Modeling, Migration and Velocity Analysis in Simple and Complex Structure

J. Bee Bednar

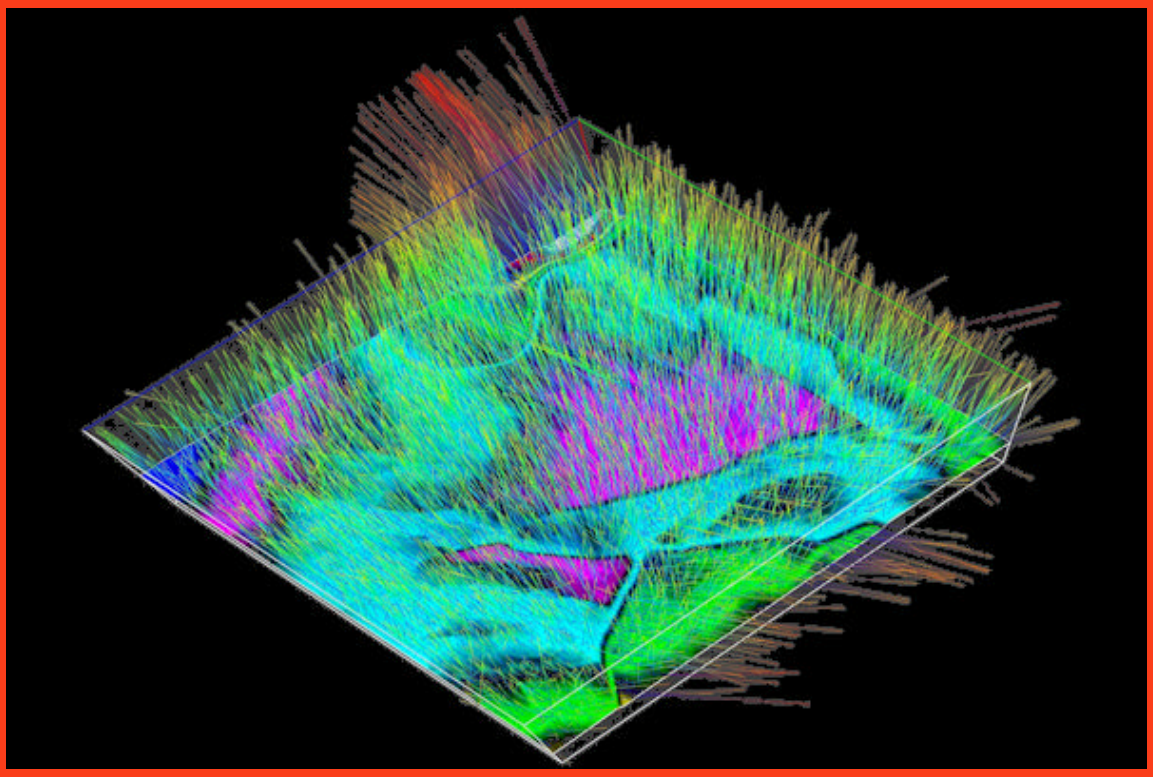

Panorama Technologies

www.panoramatech.com

Panorama Technologies, Inc.

Modeling, Migration and Velocity Analysis in Simple and Complex Structure

Preface

This book presents a hierarchy of modeling, migration, and inversion algorithms in a geometrical rather than a mathematical sense. The focus is on using simple geometrical concepts and graphical displays to explain how modeling works, how migration is in reality just a different way of doing modeling, and why true full waveform inversion must ultimately be a sequence of migrations of differences between synthetic and real data. While we do not shy away from purely mathematical explanations of the technology, the idea is to attempt to present the material in a manner accessible to the widest possible audience.

After presenting the fundamental concepts, we turn our attention to a thorough understanding and comparison of the myriad of modeling and migration algorithms. Again, the major interest is not on the mathematical details but on a visual comparison of a large number of examples and case studies.

In addition to practical comparisons, we also attempt to ensure that you get a reasonable understanding of how modern advanced technologies can be applied to reduce exploration risk. This necessarily includes an overview of the best approaches to producing the best possible result from any given migration or modeling algorithm. This necessarily implies a focus on techniques for estimating the underlying Earth model so necessary for producing accurate images.

The course underlying this book was initially developed as a tutorial for seismic interpreters working to identify, map, and develop potential hydrocarbon filled traps. Working on the extremely practical side of the exploration process, seismic interpreters have very little incentive to focus on the more mathematical aspects of how seismic data is imaged. Thus, this book is aimed at an audience with some familiarity with seismic images and their explanation relative to the underlying geology. Hopefully, you will learn where and when to use the right applied technology to produce the best possible exploration result.

Contents

Introduction 1
- Target audience . . . 2
- Overview . . . 2
  - Inversion . . . 4
  - Velocity Analysis . . . 4
  - Modeling . . . 5

Seismic Modeling 7
- Primary Concerns . . . 7
- Three Earth Models . . . 9
  - Acoustic or Fluid . . . 9
  - Isotropic Elastic . . . 9
  - Anisotropic . . . 10
  - Summary . . . 10
- Seismic Acquisition: The Basic Idea . . . 11
- Why Model? . . . 12
  - Determining Reflector Location . . . 12
  - Geologic Complexity . . . 13
  - Hypothesis Testing . . . 16
  - Acquisition . . . 17
- Waves and Wavefields . . . 17
- The Scalar Wave Equations . . . 19
  - The 1-D Scalar Wave Equation . . . 19
  - Scalar Wave Equation in Higher Dimensions . . . 22
  - Pressure Formulation of Acoustic Wave Equation . . . 24
- Stress-Strain Equations . . . 24
  - Symmetry . . . 26
  - Acoustic Symmetry . . . 27
  - Isotropic Elastic Symmetry . . . 28
  - Vertical Transverse Isotropy (VTI) Symmetry . . . 32
  - Polar Isotropy Symmetry . . . 33
  - Orthorhombic Isotropy Symmetry . . . 33

Thomsen Parameters . . . 34
Algorithms . . . 35
Variational Formulation and Finite Elements . . . 35
An Old Movie . . . 41
Finite Differences . . . 42
Polynomial Differences . . . 42
Taylor Series Differences . . . 43
Second Order Differences . . . 43
High Order Differences . . . 44
Finite Differences for the Pressure Formulation . . . 45
Graphical Descriptions . . . 45
Lax-Wendroff Method . . . 46
Elastic Finite Differences . . . 47
Staggered Grids . . . 49
Predictor-Corrector Schemes . . . 54
Splitting . . . 54
Propagation Stability . . . 56
Model Boundaries . . . 57
Free Surfaces . . . 57
Non Free Surfaces . . . 58
Sponge Boundaries—Absorbing . . . 58
Sponge Boundaries—Paraxial Boundary Conditions . . . 58
Sponge Boundaries—Perfectly Matched Layers . . . 59
FEM versus FDM Differences . . . 59
Two-Way Implicit Modeling . . . 60
One-Way Modeling . . . 60
One Way Implicit Finite Difference Methods . . . 61
Fourier-Based Methods . . . 62
FX Finite Difference Methods . . . 62
Pseudo-Spectral Methods . . . 63
Constant Velocity FK Modeling . . . 64
Phase-Shift Modeling . . . 64
Phase Shift Plus Interpolation (PSPI) Modeling . . . 66
Dual Domain or FKX One-Way Methods . . . 66
Split-Step Methods . . . 67
Extended Split Step Methods . . . 67
Higher Order FKX Methods . . . 68
A Word About Sources . . . 70
Compressional and Shear Point Sources . . . 70
Plane Wave Sources . . . 70
Huygen's Principle and Integral Methods . . . 73
The Mathematics of Huygens' Principle . . . 74
Seismic Scattering . . . 75
Raytracing . . . 76
Raytrace Modeling . . . 79
Zero Offset Modeling . . . 83

Historical 87
Data Acquisition . . . 88
Zero Offset Hand Migration . . . 90
Shot Profile Hand Migration in Two Dimensions . . . 95
Curved Rays . . . 100
Shot Profile Hand Migration in Three Dimensions . . . 105
Remarks about Migration . . . 108
Redundant Data . . . 109
Swing Arms . . . 112
Isopachs and Isochrons . . . 112
Operators . . . 113
Non-Zero Offsets . . . 115
Stacking and DMO . . . 119
What is Stacking and DMO? . . . 119
Examples . . . 125
Remarks about DMO . . . 131
Historical Summary . . . 132

Zero Offset Migration Algorithms 133
The Migration Algorithm Hierarchy . . . 133
Migration in Depth . . . 135
Explicit Two-Way XT-Reverse-Time Migration . . . 135
Implicit Two-Way XT Reverse-Time Migration . . . 137
Explicit One-Way XT Reverse-Time Migration . . . 137
Implicit One-Way XT Reverse-Time Migration . . . 137
One-Way FK Reverse-Time Migration . . . 138
FK or Stolt Migration . . . 138
Phase Shift Migration . . . 139
Phase Shift Plus Interpolation Migration . . . 139
One-Way FKX-Reverse-Time Migration . . . 140
Split Step Imaging . . . 140
Phase Screen Migration . . . 140
Kirchhoff Style Methods . . . 140
Single-Arrival Kirchhoff Migration . . . 140
Multiple-Arrival Kirchhoff Migration . . . 142
Plane-Wave Migration . . . 142
Pure Plane Wave Migration . . . 142
Beam Stack Migration . . . 143
Gaussian Beam Migration . . . 145
Migration in Time . . . 146
Converting to Vertical Time . . . 146
The Major Difference between Time and Depth Migration . . . 147
Dip Limits . . . 148
One-Way XT Time Migration . . . 149
One-Way FK Time Migration . . . 152
Phase Shift Migration . . . 152

Phase Shift Plus Interpolation . . . 152
Kirchhoff Style Time Migration . . . 152
Straight-Ray Kirchhoff Time Migration . . . 152
Curved-Ray Kirchhoff Time Migration . . . 153
Cascaded Migration . . . 155
Migration Summary . . . 156

Exploding Reflector Examples 157
Canadian Glauconitic Channel Play . . . 158
Gulf of Mexico Salt Model . . . 161
Granitic Overthrust . . . 164

Prestack Time and Depth Migration 169
Wavefield and Wave-Motion Hierarchies . . . 170
Shot Profile Prestack Migration . . . 172
Performing Shot Profile Migration . . . 172
Shot Profile Migration Example . . . 178
Partial Prestack Migration: Azimuth Moveout (AMO) . . . 179
Velocity Independent Prestack Time Imaging . . . 185
Double Downward Continuation—Common Azimuth Migration . . . 188
Common Offset Kirchhoff Ray-Based Methods . . . 190
Straight Ray Kirchhoff Prestack Time Migration . . . 190
Curved Ray Kirchhoff Prestack Time Migration . . . 191
Single Arrival Kirchhoff Depth Migration . . . 192
Multiple Arrival Kirchhoff Migration . . . 193
Kirchhoff Elastic Depth Migration . . . 194
Single Arrival Kirchhoff Depth Migration Summary . . . 194
Beam and Plane Wave Migrations . . . 195
Pure Plane Wave Migration . . . 195
Beam Stack Migration . . . 197
Delayed Shot Migration . . . 199
Gaussian Beam Migration . . . 201
Algorithmic Differences . . . 202

Prestack Migration Examples 205
Common Azimuth on the SEG/EAGE C3-NA Synthetic . . . 206
Kirchhoff versus One-Way on a Gulf of Mexico 2D Salt Synthetic . . . 207
A North Sea Sill Synthetic . . . 208
Marmousi Case Study . . . 209
An Imaging Note and the BP 2.5 Dimensional Data . . . 211
BP 2.5 D Data . . . 213
BP 2004 Salt Structure Data . . . 214
SEG AA′ Data Set . . . 215
Migration from Topography . . . 216
The SMAART JV Sigsbee Model . . . 218
SMAART JV Pluto Data Set . . . 221
SEG/EAGE C3-NA Data Imaging . . . 223

Anisotropic Earth Models . . . 225

Data Acquisition 229
Array Effects . . . 230
Aperture . . . 232
Aliasing . . . 234
Modern Acquisition Geometries . . . 239
Cross and Inline Spreads . . . 239
CATS, NATS, and WATS . . . 240
Vertical Cables (VC) . . . 242
Ocean Bottom (OBC) . . . 243
Data Acquisition Summary . . . 247

Migration Summary 249
Computational Complexity . . . 249
Velocity Sensitivity . . . 250
Amplitudes . . . 251
Conclusions . . . 251

Isotropic Migration Velocity Analysis 253
Migration Velocity Analysis Geometry . . . 255
Constant Velocity Migration Velocity Analysis . . . 257
Velocity Independent Migration Velocity Analysis . . . 258
Migrated Common Image Gathers . . . 259
Common Offset Migrated Velocity Analysis . . . 259
Common Angle Migration Velocity Analysis . . . 260
Shot Profile Migrated Image Gather Migration Velocity Analysis . . . 261
Depth Focusing Migration Velocity Analysis . . . 262
Semblance-Based Isotropic MVA on CIGs, CAGs, and SMIGs . . . 264
Painless (No Horizons) Velocity Model Construction . . . 270
Horizon-Based Velocity Analysis . . . 274
Residual Tomography . . . 278
SEG AA′ Case Study . . . 289
After Tomography . . . 295
Marmousi Case Study . . . 298
Inversion . . . 302

Anisotropic Velocity Analysis 307
Anisotropic Earth Models . . . 308
The Anisotropic Earth . . . 310
Anisotropic Normal Moveout . . . 312
Depthing . . . 315
A VTI example . . . 320

Case Studies 323
Salt Flood and Body Insert . . . 324
Amplitude Preservation . . . 329

Which One Should I Use? 330
Land Data PSTM Versus PSDM Comparison 332
Autopicking PSTM 336
Tomography 337
South Texas Fault Shadow 338
Blessing Texas Case Study 339
Data Mapping through AMO on the Blessing data 347

Course Summary 349

Bibliography 351

Chapter

Introduction

The word *migration* as it applies to seismic imaging is definitely a misnomer. It is believed to have arisen because oil migrates up dip since it is less dense than water. This knowledge proved to be exploration dynamite. Once understood, explorationists exploited it by looking for anticlines rather than synclines—and the California fields around the Brea tar pits became history. Analogously, dipping events on unmigrated seismic sections move up-dip on the final imaged or migrated section, so using the term migration in place of the more accurate imaging terms was quite natural.

It is also quite natural to think of seismic migration as being somewhat akin to photographic imagery. An image is captured, either digitally or on film, by recording the result of passing a *reflected* source of light (the sun or artificial light) through a properly focused lens on a photographic plate, film, or charge coupled device (CCD). This works because light travels in a straight line at a known constant speed and the lens, when focused, refracts the light to collect it in the proper place on the plate or CCD. We can think of this process in three steps. First, the light wavefield travels out from the source in all directions until it strikes a non-transparent reflector. Second, the reflected wavefield passes through the lens to form the image. Third, the camera's shutter captures an instant in time to record the final image. It is safe to say that radar imagery operates in much the same way and the only real difference lies in the construction of the "lens."

However, seismic migration differs from the photographic process in many ways. Sound replaces light (or radar or electro-magnetic sources) as the imaging source, and the speed of sound in subsurface rocks is definitely not constant, and it cannot be assumed to travel in a straight line. Moreover, as we will see later, each and every sound source, regardless of type, may generate three different, but coupled, wavefields as the energy spreads. As far as the author knows, there is no simple seismic analogy to the photographic lens.

Perhaps a better way to say this is that the lens for each seismic imaging effort is essentially unique to that effort. In a sense, this observation is the most crucial difference between imaging with sound and imaging with light. In the former case, we must somehow estimate the lens during the seismic imaging process. This lens is called the Earth model. In its simplest form, an Earth model is a three-dimensional velocity field that describes the subsurface speed of a compressional sound wavefield. In simple terms, a compressional wave is one wherein the particle motion occurs along the direction of propagation and represents a compression followed by a rarefraction of the particles. In its most complex form, an Earth model also includes the sound speeds of two additional waves called *shear* waves because the particle motion is perpendicular to the direction of propagation. An Earth model may also include other rock properties that influence the way in which sound propagates through the earth, but those will be of little interest here.

Seismic imaging can be considered to be a data-processing technique that creates an image of the earth's structure from the data recorded by a seismic reflection survey.

Target audience

This book and the complementary course are intended for an audience that requires a less mathematical understanding of migration and modeling than what might be required of advanced graduate students and researchers in the field. In the author's mind, this includes geophysicists and geologists who desire a fundamental principles understanding of these topics as well as a practical perspective as to where and how they may be applied for exploration advantage. We hope that, in spite of this objective, you come away with a much broader understanding of both modeling and migration as well as their application in the development and estimation of the Earth model.

Overview

Because modeling, as highlighted in this book, is so central to our ability to image, we emphasize our reasons why we believe it should become a key component to any and all exploration projects. For this, we rely on early (1936) modeling work by F. Rieber, as well as recent work by Carl Regone, J.T. Etgen, and others from British Petroleum, and the 2005 SEG Summer Research Workshop in Salt Lake City, Utah.

Three types of Earth models characterize the propagation of sound waves in the Earth. Such models range from an overly simple *acoustic* model, which only supports compressional waves, to anisotropic models that also support two coupled shear waves. Acoustic models are sometimes also referred to as isotropic models, but we will reserve that designation for isotropic elastic models. An isotropic elastic model

supports both compressional and shear waves, but the velocity of these waves is independent of the propagation angle. When the propagation velocity varies as a function of angle, the Earth model is said to be *anisotropic*. Anisotropic Earth models support one compressional and two shear waves. Thus, anisotropic Earth models contain three velocity models: one for the compressional wave, and one for each of the shear waves. Although we can think of anisotropic models in terms of three velocity fields, you should be aware that connections between the three propagation fields can be extremely complex.

The book will briefly consider sources other than sound, but since they focus on seismic migration, we ultimately are only interested in acoustic sources.

Defining the sound source and explaining its utilization to measure a synthetic seismic experiment may be the most important component of this book. We use Newton's second law in conjunction with Hooke's law to produce simple propagation equations that allow us to explain a significant percentage of the rather large number of migration algorithms that exist today.

At its best, the current ad-hoc approach for developing an acceptable seismic Earth model for imaging purposes rarely provides the necessary reflectivity required by modeling. What appears to be lacking is an understanding of how the seismic image relates to this reflectivity, so we emphasize how the needed reflectivity might be obtained.

The mathematics underlying modeling also underlies migration and, consequently, has a major impact on the acquisition geometry. The kind of data we should acquire versus the kind of data we have historically acquired is discussed in terms of optimizing migration quality.

In the belief that understanding migration is facilitated by first focusing on the simplest forms of migration, we briefly review rather quaint stacking and dip correction approaches for the production of so-called zero offset sections. We then use poststack imaging methods as they apply to stacked data sets to compare several algorithms from what we define as the migration hierarchy, and finally we move on to more modern prestack methods. These methods are applied to a wide variety of real and synthetic data in a visual, subjective attempt to evaluate the migration hierarchy's ability to produce high quality images.

Because of its clear importance, modern velocity analysis is explored in some detail. We review three different approaches producing the kinds of migration output that facilitate velocity analysis and estimation of Earth models. We provide a short review of tomographic updating. Finally, we demonstrate the conditions under which full waveform inversion might be expected to produce high quality results.

The book ends with a series of case studies designed to demonstrate the relative accuracy of the various algorithms comprising what we call the migration hierarchy.

Inversion

Estimating the appropriate lens for seismic migration is an exercise in *inversion*. This is a mathematical process by which data are used to generate a model that is consistent with the data. The most desirable outcome of a seismic inversion process would be an Earth model with sufficient detail to describe all information necessary to optimize the exploration workflow. The most comprehensive mathematical formulation of inversion provides a complete platform for estimating this information. The inversion technique iteratively combines modeling with migration to directly estimate the Earth model. At each step of what may be many iterations, the difference (the residual) between the modeled data and the recorded data is migrated to estimate a new model. When the migrated residual is zero, synthetic data generated using the estimated Earth model perfectly matches the recorded data and consequently the model is considered optimal.

One of the earliest practical tests of this so-called full-waveform inversion was an abysmal failure. Nevertheless, today, the good news is that, in a perfect setting, this process really does work. The bad news is that currently available seismic data do not entirely satisfy the mathematical requirements necessary for success.

Until recently, the modeling piece of this inversion process was by itself considered far too computationally intensive to be practical. It may also be true that the actual concept of synthesizing data over some perceived geologic model was considered to be of little practical use. However, computer power is rapidly approaching the point where modeling may not only be practical, but may even be of use in providing empirical answers to questions that are difficult to answer in any other way. While it may not be computationally possible to perform the iterative inversion described in the previous paragraph, computer power is quickly reaching the point where we may be able to consider doing the inversion for carefully selected projects.

Velocity Analysis

When concise mathematical recipes for optimal estimation of the Earth model are not practical, other more practical methods must be devised and exploited. In the last twenty-five years, a wide variety of somewhat ad-hoc velocity estimation methods have emerged and are currently used to provide reasonable estimates of the seismic lens. The importance of migration as a tool in this approach cannot be overestimated. But traditional, normal-moveout based methods applied after migration, together with tomographic techniques, have proven to be quite useful when the more optimum and concise methods fail.

How well these human-intensive techniques work are somewhat dependent on how the input data is processed. Thus, the person actually attempting to estimate the Earth model must recognize that some so-called “best practices” approaches are not amenable to the production of high quality results.

Modeling

A superficial glance at the inversion process seems to imply that we need two pieces of machinery to make it work; that is, we need to understand how to synthesize the kind of data we record (modeling), and we need to understand how to migrate it. What is really true, however, is that the only thing we really need to understand completely is how to perform the modeling, since migration is actually just two independent modeling exercises. To fully appreciate how modeling appears in the imaging process requires considerable mathematical theory and physical principles. However, there are just two fundamental principles on which modeling is based. The first, Newton's second law, is easily understood from a purely physical point of view. You experience it every time you accelerate in a car. The second, Hooke's law, is somewhat more difficult to understand, but is still quite easy to explain in simple one-dimensional terms. The combination of these two principles effectively provides us with a simple propagation methodology that is easily explained graphically and that provides the basis for making modeling and migration accessible with minimal mathematical symbolism.

Given that modeling is fundamental to seismic imaging, we obviously must put considerable emphasis on understanding how it works and the many variations of how it is implemented. In addition, it is of considerable interest to understand the types and style of Earth models that we may wish to investigate.

Chapter 2

Seismic Modeling

This chapter presents information about seismic modeling. Topics range from why we perform modeling in the first place through a brief overview of the mathematics involved in several different types of modeling.

Primary Concerns

One primary concern in seismic imaging necessarily focuses on determination of the true subsurface medium. Clearly, the accuracy of this information significantly impacts all aspects of the exploration process. Even when we do not have a completely detailed visualization of what is below us, a reasonable concept can provide guidelines for surface acquisition that improves subsurface imaging. The underlying Earth model strongly influences what we must do to migrate the data successfully and produce an optimum image.

Another primary concern focuses on which of the myriad available imaging algorithms has the best chance of producing the highest quality image. Making this choice requires an understanding of the most important such technology. Because algorithm development and implementation is a highly mathematical endeavor, acquiring this understanding can be quite difficult.

A third concern arises from the fact that, in general, the Earth does not respond well to high frequency sources since high frequency sound waves are absorbed rather quickly. Depending on rock type they penetrate only to a few thousand meters. On the other hand, low frequency sound waves are known to provide narrow bandwidth images at depths in excess of 30 or 40 kilometers.

Electromagnetic waves are frequently characterized by their penetration depth or their so called skin temperature. Although claims to the contrary abound, the skin

temperature of most electromagnetic waves is only on the order of a few hundred meters. This means that to the extent possible, changes in magnetic parameters can be observed only from approximately half of this depth. This is far too shallow to be of much use in exploration. This lack of ability to penetrate deeply into the Earth's interior eliminates most high frequency sources, and strongly implies that we cannot use light, electromagnetic, or radar sources to measure and image the Earth at the depths of interest.

Because of these issues, our best option is to use relatively low frequency sound sources on the order of a few hundred Hertz. When higher frequency sources are routinely available, their responses will be easily incorporated into the general imaging workflow, but until that happens, we must focus on low frequency data sets to achieve our exploration goals. We now know that, from an inversion point of view, accurately determining the subsurface velocity is easier when the low frequency portion of the frequency band is full. High frequencies are certainly important but have much less impact on the velocity estimation problem then lower frequencies. While somewhat contrary to intuition, the importance of very low frequency data cannot be denied.

Perhaps the final concern in seismic imaging is having a clear understanding of how sound propagates. Given a decent understand of the types of rocks we may encounter, this concern can be resolved directly through seismic synthesis or modeling. The ability to generate realistic responses to practical and physical seismic sources should move us a long way down the path toward near optimal application of the entire imaging process

Given these simple concerns, this section attempts to use mathematically based formulations for digitally synthesizing seismic data in the hopes that the issues raised above can be clarified in a relatively simple and intuitive manner.

Three Earth Models

Earth models, as we understand them, have the following three basic formulations:

- purely isotropic or acoustic
- isotropic elastic
- anisotropic

Acoustic or Fluid

Earth models, as we understand them, have three basic formulations. The first is what we usually call purely isotropic or acoustic. Acoustic models are based on the assumption that the only physical parameters defining wave propagation are density, $\rho(x,y,z)$, and interval or instantaneous velocity $v(x,y,z)$. Only fluids can be described by these two properties, but because propagation in such environments can be simulated efficiently, they are the most prevalent at this writing. Empirical evidence also seems to suggest that in many geologic settings the real Earth does not vary much from this assumption.

Isotropic Elastic

Isotropic elastic models are described by density, compressional velocity, and shear velocity. The notation for these parameters is $\rho(x,y,z)$, $v_p(x,y,z)$, and $v_s(x,y,z)$. Isotropic elastic models support two wavefields, one of which is a compressional wave and the other is a shear wave. Compressional waves in such models are identical to those in acoustic models. They are characterized by particle motions consistent with what might be called compression and rarefaction where the particle vibrations are normal to the direction of propagation. In contrast, we tend to think of waves where the the particle motion is tangential to the direction of propagation as shear waves. As a point of fact, the truth is probably somewhat different. Simulations tend to support the conclusion that the compressional wave is what we would record if we were to measure purely vertical particle motion and the shear wave is the one characterized by purely horizontal particle motions. The speed of shear waves is frequently much slower then the velocity of the compressional wave. Nevertheless, shear and compressional waves continually interact and convert from one to the other as the propagation progresses. Thus, if we are to successfully handle isotropic elastic data, we must acquire something at least directly related to the vertical and horizontal particle motions. In other words, we have to acquire *vector* data.

Anisotropic

Anisotropic models represent the Earth at its most complex. For our purposes, a model is said to be anisotropic whenever the sound speed is a function of the angle of propagation. In models of this type, not only does the velocity of sound vary with propagation angle, but there are three possible propagating modes at any given instant. One is our familiar compressional wave and the other two are shear waves, each of which propagates with its own local angle-dependent velocity profile.

Over the last 20 or so years we have come to specify what we might call the first realistic anisotropic models by density $\rho(x,y,z)$, vertical velocity $v_p(x,y,z)$, shear horizontal velocity $v_s(x,y,z)$ and three additional parameters, $\delta(z,y,z)$, $\varepsilon(x,y,z)$, and $\gamma(x,y,z)$. Models described by these "Thomsen" parameters are the so called vertically transverse isotropic or VTI models. Anisotropic VTI models have a very convenient form of symmetry that makes using them somewhat easier and less computationally complex then more complex versions of anisotropy. It is reasonable to expect anisotropic models to become the norm in future exploration exercises. In this case true anisotropic processing will also require the acquisition of vector data. The difference between this and isotropic elastic acquisition is that each vector has three components.

Summary

Regardless of the source we use, the Earth's response always contains compressional and at least one, but most probably, two shear wavefields. Thus, the expected Earth model is quite complex. While we may not have the ability to estimate the necessary parameters to image the recorded multicomponent data, there are many algorithms for doing so. It makes sense to at least understand the kinds of data we might expect to record and what it might look like. The basic idea of using modeling to help us understand the recordings has a significant history in the exploration for hydrocarbons. As this book progresses, we will attempt to define the various models currently in vogue and make some additional comments about how the required parameters might be estimated from our acoustical recordings.

Seismic Acquisition: The Basic Idea

The basic idea underlying seismic acquisition is shown in Figure 2-1. The application of a sound source at a fixed point on the surface of the Earth produces a down-going wavefield. As the wavefield propagates, it is, hopefully, reflected as an up-going wavefield that is recorded on a series of receivers located near the surface. The job of modeling is to simulate this thought experiment as accurately as possible. From a physical point of view the model is viewed as a collection of *particles* that move (compress and expand or shear) under the influence of the sound source. As we can easily infer from Figure 2-1 such compression and rarefaction can be quite complex and occur in any direction at any given time instant.

As we progress through this book, we will see that there are many approaches to synthesizing seismic data in both simple and complex Earth models. Each approach is based on a unique approximation to a governing wave equation. Each approximation has its own unique set of limitations that compromises the accuracy of the final synthetic. In the past, these approximations were a necessary evil fostered by the computational limits of the era. The list of questions posed in Figure 2-1 hint at some of the limitations of the various approximations. Ranging from algorithms based on rays (infinitely narrow paths), to wavefields that travel in only one direction, and then to wavefields traveling in all directions, these limitations can have a serious impact on the quality of both the modeling and the migration algorithm under consideration. As computers become more and more efficient, these compromises will fall by the wayside and be fully replaced by the most accurate method available for the given data.

Figure 2-1. The basic seismic acquisition concept.

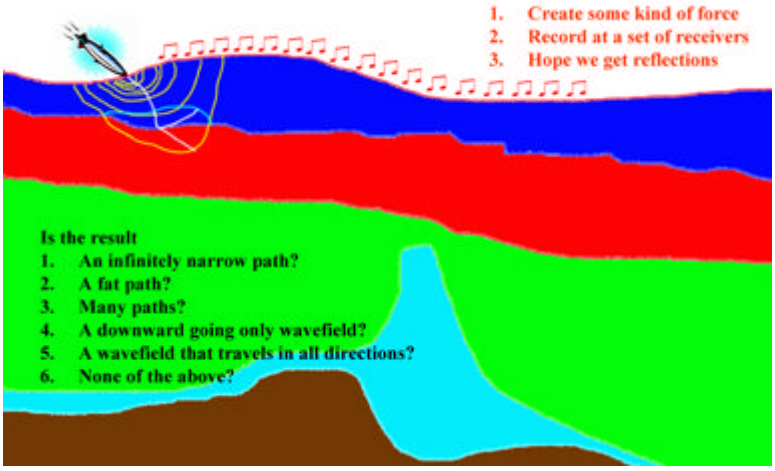

Why Model?

Modeling is fundamental to imaging, and I hope to convince you that modeling and migration are identical; that is, if you know how to do one, you know how to do the other. Consequently, it is extremely important that you understand how to synthesize seismic responses that are as close as possible to what we physically measure in the real world.

Determining Reflector Location

Before computers, simple straight-ray methods were used to determine the important parameters involved in figuring out the true sub-surface location of recorded reflected events. Figure 2-2 demonstrates the process.

Figure 2-2. Raytracing in a $v(z)$ medium.

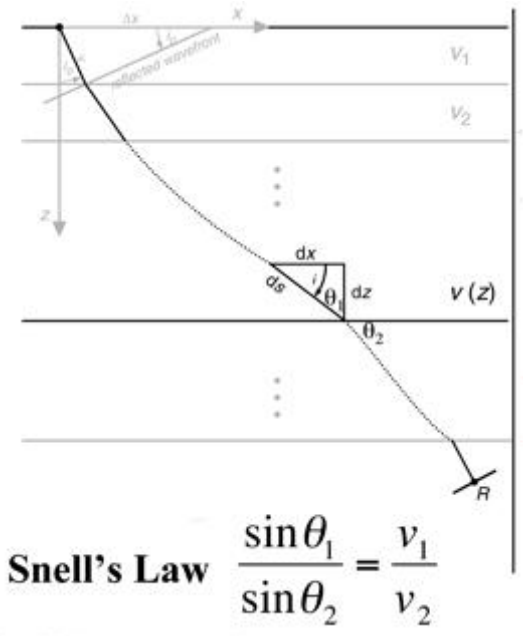

Computing the ray direction from one layer to the next requires adherence to Snell's law, Equation 2-1 or Equation 2-2. See the section on Curved Rays in Chapter 3 for information about Snell's law.

(2-1)
$$\frac{\sin\theta_1}{\sin\theta_2} = \frac{v_1}{v_2}$$

(2-2)
$$\frac{\sin\theta_1}{v_1} = \frac{\sin\theta_2}{v_2}$$

Thus, the only required elements for this form of modeling are the ability to compute the sine of angles, a ruler, and perhaps a protractor. What is important is that for a given source on the surface the normal incident ray that travels from the source to a reflector and back to the source-receiver location is uniquely determined by either the dip of the reflector or by the takeoff angle at the surface.

As we will see, this particularly simple concept is fundamental to both migration and modeling. We can estimate what we call apparent dips from seismic sections, and then compute the true dip of the reflector, along with a given velocity. Simultaneously, we can compute the surface distance from the given shot point to the surface projection of the subsurface reflector location, thereby constructing a "migrated" image.

Geologic Complexity

Perhaps the earliest and one of the most compelling reasons for modeling was presented by Frank Rieber's in his 1936 Geophysics paper. Quoting Rieber:

> The usual form of reflection seismograph operates satisfactorily over simple structural conditions, but frequently fails to obtain part or all of the desired information when structures are steeply folded, faulted or otherwise complicated. The reasons for this are plainly evident if the paths of the waves in the earth can be visualized.

In other words, he is saying that when the geology is simple, the reflection seismogram is easy to unravel, but when the geology is complex, it is difficult. He is also saying that if we can model complex structures, we may be able to better understand the problem and then develop technologies to resolve it. From my perspective, the most amazing thing is that he proceeds to do exactly that:

> This has been done by the use of a technique originally developed for acoustical measurements.
>
> A new type of equipment and technique are briefly described, with which exploration may be carried into the more complex structural regions successfully.
>
> A miniature explosion radiates waves into various models of structure, where reflection and diffraction take place in the same manner as in the earth. The various moving waves are actually photographed in flight. A series of plates is presented, showing wave patterns in various types of structures, ranging from simple to complex.
>
> Briefly, the technique is one of shadow photography, no lens of any sort being employed. A bright electric spark, lasting only about one millionth of a second, is spaced about four feet from a photographic plate. The model of

> the structure to be investigated is placed part way between the spark and the plate, in such a position that its shadow will be photographed.
>
> If no sound waves are present in the field between the light source and the plate, the shadow of this model will be the only thing shown in the photograph. The rest of the field will be uniformly exposed to the light from the spark and will correspondingly show uniform photographic density.
>
> If an abrupt sound wave happens to be passing through the field, however, the light from the spark will be bent slightly at the places where it passes through the denser air of the wave front. This bent light will be superposed upon other illumination arriving directly on the plate from the spark, thereby causing a dark line. The part of the plate from which the bent light was diverged will show, correspondingly, as a lighter line.

Thus, Rieber explains why he thinks modeling is important, and then proposes a solution to both the modeling and the visualization problem. The *why* in Rieber's case was to figure out how to interpret seismic shot records that were considered uninterpretable at the time. In the 1930's, tedious hand calculations were the only available methods for placing an event on a shot record at its correct (or nearly correct) subsurface position. These early migration methods were not well suited to positioning anything but simple reflected events. While the response of a syncline was not difficult to unravel, what Rieber's paper showed was that the so-called "no record zones" were in reality areas with even moderately complex geology. Salt structures of the size and shape we see today were generally figments of the imagination.

Figure 2-3 demonstrates the validity of Rieber's shadow method. Figure 2-3(a) shows that the response of a truncation in an otherwise constant velocity medium is a diffraction. This is a circular event that could have easily confused the typical inexperienced interpreter of the day. Part (b) shows the downward traveling wave on the edges along with the reflected wave in the center for a faulted structure. Note the clear diffractions on the left-hand side of this graphic. It is one of several similar Rieber graphics that clearly demonstrate the success of his technique. The left half of this figure shows a snapshot of the response from a syncline at some time after the explosion at the center of the image. The right half is a snapshot at a later time. What we see, particularly on the top half of the figure, is the characteristic bow-tie reflection from the syncline.

Figure 2-3. Rieber's shadow graphs of the response of simple geologic structures.

(a). Reiber's snapshots of the response of truncated structures.

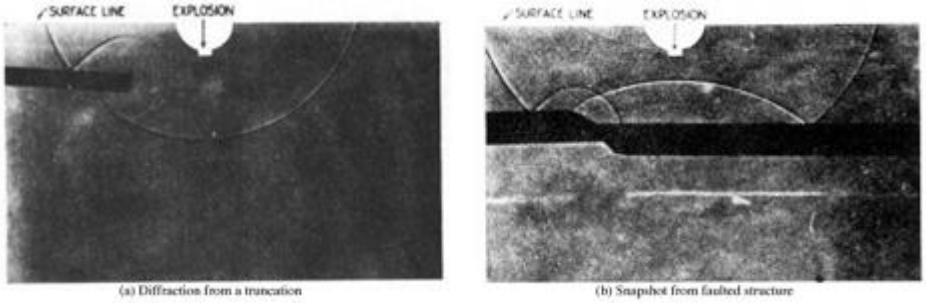

(a) Diffraction from a truncation (b) Snapshot from faulted structure

(b). Reiber's snapshots of the response of a syncline

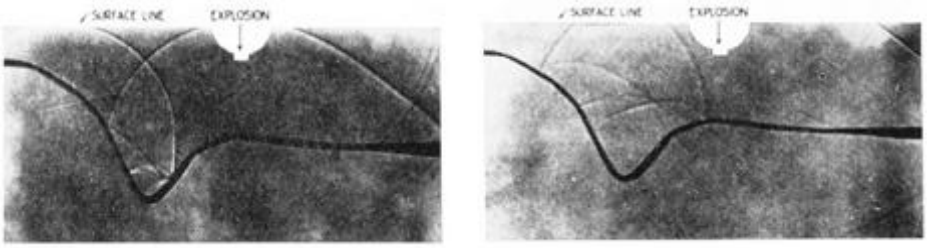

At the time of Rieber's research, the complexity of the seismic response was not well understood, and, consequently, detecting or even recognizing dip on these records was problematic. Figure 2-4 shows that Rieber understood this as well, and formulated a method for more or less automatic detection of the associated dips. It represents what is believed to be one of the first ever utilization's of what is now called slant stacking. Note that it is applied to a shot record and really detects the angle at which the given reflection emerges. The dip detector first estimates the emergence angle of a reflected wavefield at the receiver locations, which can be computed from $\frac{\Delta t}{\Delta x} = \frac{\sin\theta}{v}$. Given the emergence angle and the velocity of the wavefield (which was assumed constant in Rieber's day), we can directly calculate the location and dip of the reflector from which the wavefield came. As we will see in later chapters, this emergence angle data and the directly related subsurface dip are crucial in all modern migration methodologies.

Figure 2-4. Rieber's approach to detecting dip.

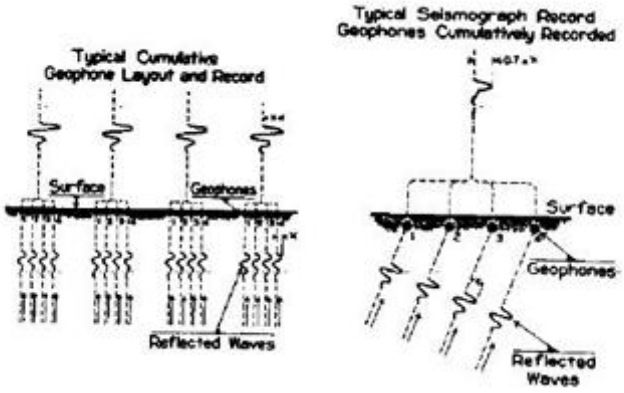

Hypothesis Testing

A more modern reason behind data synthesis is what can be called hypothesis testing. An example of this is displayed in Figure 2-5. The left hand side of this figure is an arbitrary line slice taken through a 3D prestack depth migration of a seismic data set from the Gulf of Mexico survey. It was chosen to be as close as possible to a true dip line. The right graphic is an image constructed from 2D isotropic elastic data synthesized over a 2D structure constructed from the 3D migration velocity field along with top and base salt interpretations.

Figure 2-5. Modeling multiples.

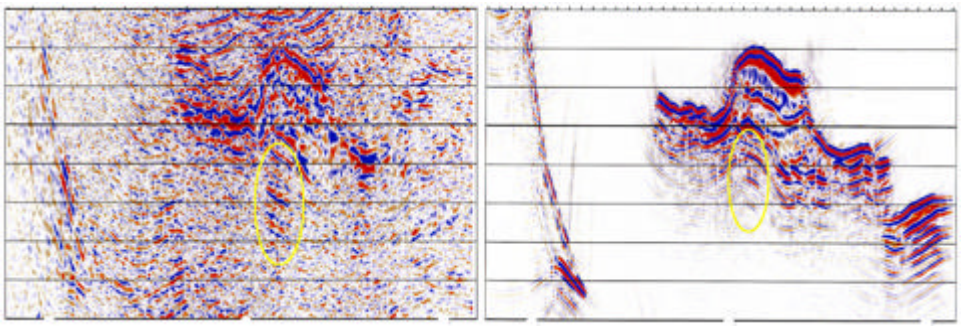

When mapped in 3D, the circled amplitude package appears to define a stacked set of hydrocarbon bearing reservoirs with significant potential. Thus, the hypothesis in this case is that the package is a valid prospect. To test this hypothesis, a 2D acoustic Earth model was constructed. The model velocity was taken to be the migration velocity with a top and base of salt used to define the salt body. Although not shown, the model includes shear velocities below the water layer, and, consequently, some converted waves have been imaged on the section.

The right side of Figure 2-5 shows the result of the modeling under the assumption that the surface of the water is not reflective. Thus, any repetitive events cannot be from water column multiples. The clear evidence of multiple amplitudes in a setting where such amplitudes cannot be due to the water layer, confirms the hypothesis that the amplitudes are from peg-leg multiples or converted ray events.

There are, of course, many other ways to utilize modeling to answer various hypotheses that are not directly related to verifying that some event or anomaly is noise. We can also build models to compare various alternative model parameters in an attempt to quantify observed amplitude versus offset or amplitude responses. In a subsequent section on full waveform inversion, we will demonstrate the importance of low frequency acquisition in the specification of the earth velocity field.

Acquisition

An important recent utilization of modeling by Carl Regone at BP dealt directly with trying to verify that wide azimuth acquisition is superior to narrow acquisition. What these studies showed was that, as actually assumed by the mathematics, wide azimuth acquisition produces superior results in all settings. We will investigate this issue in the chapter on Data Acquisition.

Waves and Wavefields

As described in Figure 2-6, wavefields are characterized and described by several well known terms:

- f = Frequency = cycles/second
- ω = Angular Frequency = radians/second = $2\pi f$
- $\frac{v}{f}$ = Wavelength = meters/cycle
- $k = \frac{\omega}{v}$ = Temporal Wave Number
- k_x = Spatial x (XLINE) Wave Number
- k_y = Spatial y (LINE) Wave Number

Figure 2-6. A single frequency sinusoid (wavefield) with amplitude $A(x, y, z, \omega)$

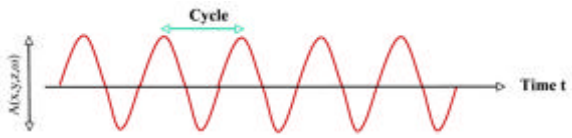

These terms completely characterize wavefields in space-time, frequency-space, and frequency-wavenumber. We can think of wavefields as actually being the sums of sinusoidal style waves having the general form of Equation 2-3, where $A = A(x, y, z, \omega = 2\pi f)$ is a positive amplitude as a function of spatial position (x, y, z) and frequency, and $\varphi = \varphi(x, y, z, t)$ is the so-called wavelet phase.

$$U(x, y, z, t) = \sum_{\omega} A\left[\cos(\omega t + \varphi) + \imath \sin(\omega t + \varphi)\right] \tag{2-3}$$

The main point is that the wavefields actually exist in three-dimensional space-time and can be characterized in many different ways. While we cannot record the full three dimensional response of any given source, the wavefield due to such a source is in fact four dimensional and effectively exists at each point where energy from the source exists. In this book, we will mostly be concerned with wavefields measured on one surface, typically where $z = 0$. But, as is the case for VSPs, we also record seismic wavefields at locations with $z > 0$.

Figure 2-7 further clarifies what we mean by Equation 2-3. As any given sinusoid propagates through the Earth, its wavelength and amplitude change as functions of both reflection strength and sound speed. Although not shown in the figure, these quantities can also change purely as a function of the material through which they are propagating.

Figure 2-7. Wavefield in space at two different velocities. Note that the wavelength and the amplitude can change purely as a function of velocity.

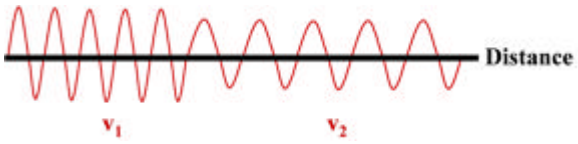

The Scalar Wave Equations

From the author's perspective, current state-of-the art practice in digital synthesis of seismic wavefields is usually based on one of four wave equation styles.

- The simplest style is called the *scalar* wave equation governing particle motion. Traditionally, this equation involves only compressional style waves and provides a wavefield describing particle motion; density is assumed constant.
- The first and second order formulations of what is usually referred to as the *stress-strain* equations can synthesize both compressional and shear wave data, although at considerable expense in 3-D. Thus, in this case, the equations govern what can be considered vector propagation. In the simplest case, there are two wavefields, one compressional and one shear. In the more complex case, there are three wavefields, one compressional and two shear. The stress-strain versions are clearly the most interesting because they allow for the most complex anisotropic wavefield propagation methods.
- The *pressure* formulation of the wave equation includes density in a form that can be used directly for synthesizing marine style acquisition.

The 1-D Scalar Wave Equation

In this section, we derive a simple one-dimensional version of the so-called scalar wave equation. Wavefields satisfying the various forms of the wave equation are currently our best guess as to how low-frequency-sound energy propagates through the Earth. As we will see, different media require specialized equations, but the basic synthesis or modeling principles remain remarkably similar.

We can gain insight into how particle movement (wave propagation) is governed by considering a simple one-dimensional model. We will start by thinking of the media as a series of discrete particles loosely connected by some form of restraint. Figure 2-8 shows a series of masses, m, connected together through a series of springs under tension, k. A source at one end of the chain creates a wavefield that travels up and down the chain.

Figure 2-8. A simple one-dimensional model.

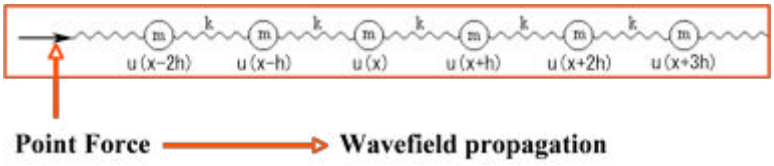

If a force is applied at one end of this one-dimensional model, the mass $u(x)$ at x reacts with and is acted on by masses $u(x - h)$ and $u(x + h)$. Each such mass accelerates and

decelerates as the wavefield generated by the source propagates up and down the model. Note that, although we have suppressed it in the notation, the fact is that $u(x) = u(x,t)$. In general, we think of each of the masses, $u(x)$, as particles that move back and forth as time progresses. What we see is a wave passing up and down the model.

Describing particle movement is accomplished through the use of two fundamental laws of physics, Newton's second law of motion, that is, *force is equal to mass times acceleration*, and Hooke's Law.

> In physics, Hooke's law of elasticity is an approximation that states that the amount by which a material body is deformed (the strain) is linearly related to the force causing the deformation (the stress). Materials for which Hooke's law is a useful approximation are known as linear-elastic or *Hookean* materials.

In mathematical form, Newton's law is given in Equation 2-4, where a is acceleration and m is the particle mass.

(2-4) $$F = ma$$

The force caused by acceleration is what you feel when you step on an automobile's accelerator. In the context of Figure 2-8, acceleration is the rate of change in velocity with respect to time. Thus, for the particle at $u(x)$, Newton's second law becomes Equation 2-5, where $\tau(x,t)$ is the force per unit area, or stress, at x.

(2-5) $$\tau(x,t) = m\left[\frac{v(x,t+\Delta t) - v(x,t)}{\Delta t}\right]$$

The fact that the velocity is the change in particle position as a function of time yields Equation 2-6, and, thus, Newton's law can be written as Equation 2-7.

(2-6) $$v(x,t) = \frac{u(x,t) - u(x,t-\Delta t)}{\Delta t}$$

(2-7) $$\tau(x,t) = m\left[\frac{u(x,t+\Delta t) - 2u(x,t) + u(x,t-\Delta t)}{\Delta t^2}\right]$$

For our purposes, Hooke's law can be rephrased as:

> A *change in force* per unit length (area or volume in higher dimensions) is equal to the bulk modulus times the increase in length divided by the original length.

Because of the way in which our small particles of mass are arranged, the force $\tau(x,t) = \frac{F(x,t)}{h}$ per unit length is really determined by the action of the particles adjacent to position x. Hooke's law can be stated mathematically as Equation 2-8 or Equation 2-9.

$$\begin{aligned}\tau(x,t) &= \tau(x+h,t) + \tau(x-h,t) \\ &= k\left[\frac{u(x+h,t)-u(x,t)}{h}\right] + k\left[\frac{u(x,t)-u(x-h,t)}{h}\right]\end{aligned} \tag{2-8}$$

$$\frac{kh^2}{m}\left[\frac{u(x+h,t)-2u(x,t)+u(x-h,t)}{h^2}\right] = \left[\frac{u(x,t+\Delta t)-2u(x,t)+u(x,t-\Delta t}{\Delta t^2}\right] \tag{2-9}$$

If we suppose that there are N masses (particles), each of density ρ, then the total length is $L = Nh$, the total mass is $M = Nm = \rho$, and the total stiffness of the array is $K = k/N$, so we get Equation 2-10.

$$\frac{kh^2}{m} = \frac{KL^2}{M} = \frac{KL}{\rho} \tag{2-10}$$

Thus, in the limit as h and Δt approach zero, we get Equation 2-11. The quantity KL is actually Young's modulus of the medium containing m.

$$\frac{KL}{\rho}\frac{\partial^2 u}{\partial x^2} = \frac{\partial^2 u}{\partial t^2} \tag{2-11}$$

It turns out that the quantity $v = \sqrt{\frac{KL}{\rho}}$ is the velocity of propagation within the medium, and so we have succeeded in deriving what is normally called the one-dimensional wave equation, Equation 2-12.

$$\frac{\partial^2 u}{\partial x^2} = \frac{1}{v^2}\frac{\partial^2 u}{\partial t^2} \tag{2-12}$$

It is interesting to note that if we combine Equation 2-7 and Equation 2-9, and then rearrange the result in the form shown in Equation 2-13, we obtain an equation that allows us to propagate a wavefield in the one-dimensional medium due to the source $s(x_0,t)$ at position x_0.

$$\begin{aligned}u(x,t+\Delta t) &= 2u(x+h,t) - u(x,t-\Delta t) \\ &\quad + v^2[(u(x+h,t) - 2u(x,t) + u(x-h,t)] + s(x_0,t)\end{aligned} \tag{2-13}$$

If we begin the discussion with both mass, m, and strain, k, as functions of position, x, the velocity, $v = v(x)$, of our one-dimensional wave equation will vary as a function of position.

It is clear from Equation 2-13 that propagation at each time step is achieved through the application of appropriate weights to the wavefields at the two previous time steps. In the case where velocity varies, the weights form a *stencil* and change for each spatial position. The wavefield at time stamp $t + \Delta t$ is computed starting at the left most spatial position and continuing to the right.

Figure 2-9 demonstrates the process. Beginning at the left each spatial output point amplitude is computed as a weighted sum of spatial points from the two previous time steps, that is, $t + \Delta t$. The stencil at t is centered around the spatial output point at $t + \Delta t$ so that waves can propagate in all directions.

Figure 2-9. Graphical interpretation of a one-dimensional propagator

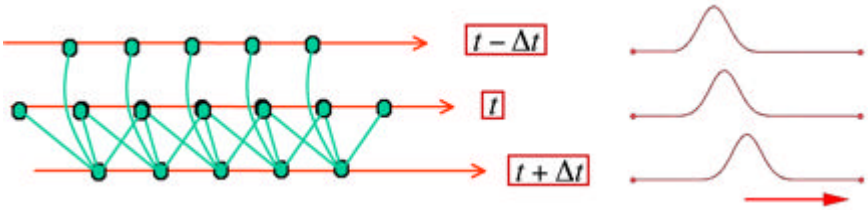

Scalar Wave Equation in Higher Dimensions

Figure 2-10 shows a simple model in two dimensions. In this case, masses, m, are connected by the equivalent of springs with tension k. A source placed as a point on the grid creates a wavefield that travels up throughout the grid in all directions.

Figure 2-10. A simple two-dimensional model.

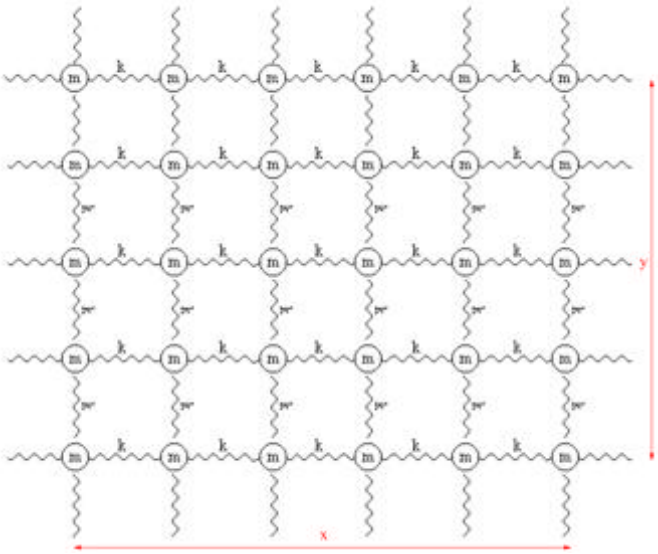

Extending the one dimensional nature of Equation 2-12 into higher dimensions is not difficult. We need only consider a two-dimensional grid of masses similar to the one-dimensional grid in Figure 2-8. Our model now has an area $A = L_x * L_y$, instead of length L, a total stiffness of $K = \frac{k}{L_x L_y}$, and total mass $M = mL_xL_y$. Our discrete equation governing wave propagation must accommodate particle motion in both the x and y directions, but, in actuality, this really only involves Equation 2-9. Thus, if we follow our approach for the one-dimensional discrete equation, Equation 2-13, we arrive at Equation 2-14.

$$\left(\frac{u(x,z,t+\Delta t) - 2u(x,z,t) + u(x,z,t-\Delta t}{\Delta t^2}\right) = \frac{kh^2}{m}\left(\frac{u(x+h,z,t) - 2u(x,z,t) + u(x-h,z,t)}{h^2} + \frac{u(x,z+h,t) - 2u(x,z,t) + u(x,z-h,t)}{h^2}\right) \tag{2-14}$$

In more compact mathematical notation, the two-dimensional Equation 2-14 becomes Equation 2-15.

$$\frac{\partial^2 u}{\partial t^2} = v^2\left(\frac{\partial^2 u}{\partial x^2} + \frac{\partial^2 u}{\partial z^2}\right) \tag{2-15}$$

After following the same procedure for a three-dimensional grid, the three-dimensional wave equation becomes Equation 2-16.

$$\frac{\partial^2 u}{\partial t^2} = v^2\left(\frac{\partial^2 u}{\partial x^2} + \frac{\partial^2 u}{\partial y^2} + \frac{\partial^2 u}{\partial z^2}\right) \tag{2-16}$$

Here, we have derived the mathematical wavefield equations for what is normally called acoustic or pure isotropic modeling. In this case, the velocity was assumed constant, but the difference between a constant velocity and variable velocity derivation is minor. Equation 2-15 and Equation 2-16 are referred to as scalar wave equations because there is only one wavefield, not a vector of two or more. Generally, the geophysical convention is to assume that z is the vertical or depth direction, but that is really just a matter of convenience. We could just as easily have used x_1 for x, x_2 for y, and x_3 for z.

Pressure Formulation of Acoustic Wave Equation

Without going into great detail, we can also derive a pressure formulation of the acoustic wave equation (see Keiiti Aki and Paul G. Richards). This equation takes the form shown in Equation 2-17.

$$\frac{\partial^2 p}{\partial t^2} = \rho(x,y,z)\, v^2(x,y,z)\left[\frac{\partial}{\partial x}\frac{1}{\rho(x,y,z)}\frac{\partial p}{\partial x} + \frac{\partial}{\partial y}\frac{1}{\rho(x,y,z)}\frac{\partial p}{\partial y} + \frac{\partial}{\partial z}\frac{1}{\rho(x,y,z)}\frac{\partial p}{\partial z}\right] \tag{2-17}$$

In contrast to the particle motion described by Equation 2-16, Equation 2-17 measures pressure changes at any given position. I like to call this the reflection formulation because of the presence of the acoustic impedance term, ρv. This equation can be put in the very compact form of Equation 2-18, where ∇ (the vector differential operator, pronounced *del*) is given by Equation 2-19.

$$\frac{\partial^2 p}{\partial t^2} = \rho v^2 \nabla \cdot \frac{1}{\rho}\nabla p \tag{2-18}$$

$$\nabla = \left(\frac{\partial}{\partial x}, \frac{\partial}{\partial y}, \frac{\partial}{\partial z}\right) \tag{2-19}$$

Ultimately, we are interested in deriving equations for more complex fully elastic wavefields, including anisotropic wavefields. These wavefields require more parameters to describe the multiplicity of wavefields that exist in such media. Before increasing the complexity of the discussion, we will focus on a graphical description of how discrete modeling works, and then turn our attention to algorithms for implementing the actual modeling exercise.

Stress-Strain Equations

As we know, isotropic elastic models are described by three familiar parameters: density, compression velocity, and shear velocity. To model elastic wavefields in such three-parameter media, we need to derive a suitable equation or set of equations that describe the wavefield propagation at any given instant. Unfortunately, these three parameters are not the most useful for this purpose. On the other hand, the required parameters are much more directly related to actual rock properties. Moreover, relating the required parameters to more useful quantities is fairly straightforward.

We begin (Equation 2-8 and Equation 2-7) by observing that Equation 2-20 is true, so that Equation 2-21 is also true.

(2-20)
$$\begin{aligned}\frac{F(x,t)}{h} &= \frac{F(x+h,t)+F(x-h,t)}{h} \\ &= k\left(\frac{u(x+h,t)-u(x,t)}{h}\right)+k\left(\frac{u(x,t)-u(x-h,t)}{h}\right) \\ &= \rho\left(\frac{u(x,t+\Delta t)-2u(x,t)+u(x,t-\Delta t)}{\Delta t^2}\right)\end{aligned}$$

(2-21)
$$\frac{\tau(x+h,t)-\tau(x,t)}{h} = \rho\left(\frac{u(x,t+\Delta t)-2u(x,t)+u(x,t-\Delta t)}{\Delta t^2}\right)$$

In continuous terms, Equation 2-21 can be restated as Equation 2-22.

(2-22)
$$\frac{\partial \tau}{\partial x} = \rho\frac{\partial^2 u}{\partial t^2}$$

Equation 2-22 is a first order partial-differential equation relating a second order change in time to a first order change in force *per unit area*. Force per unit area is generally referred to as stress, so our equation relates particle acceleration to stress. In this setting, the stress is one-dimensional and acts along or parallel to the layout of the string. There is also only one compressional wavefield described by this equation.

Stepping up to the simple isotropic elastic models described by the three familiar parameters above, means that it is necessary to include one additional wavefield in the mix, namely shear. While including just two wavefields is certainly an option, there isn't any reason not to move up to full anisotropic elasticity by incorporating two shear waves for a total of three wavefields. In three dimensions, Equation 2-22 takes the form of Equation 2-23, where $i = 1,2,3$ and we have arbitrarily chosen to set $x = x_1$, $y = x_2$, and $z = x_3$.

(2-23)
$$\frac{\partial^2 u_i}{\partial t^2} = \frac{1}{\rho}\sum_{j=1}^{3}\frac{\partial \tau_{ij}}{\partial x_j}$$

Clearly, this is a three-dimensional equation with nine stress factors, τ_{ij}, one for each of the three dimensions and wavefields. To make this into a system of equations governing the three wavefields, we must find a way to relate the stresses, τ_{ij} to the u_i. As before, Hooke's law comes to the rescue. What it says in this anisotropic case is:

> Each component of stress is linearly proportional to *every* component of strain.

Strain, which measures the deformation (compression, extension, ...) of a solid, is defined in the notation of the previous equation as Equation 2-24.

(2-24) $$E_{mn} = \frac{1}{2}\left(\frac{\partial u_m}{\partial x_n} + \frac{\partial u_n}{\partial x_m}\right)$$

The mathematical expression of Hooke's law then takes the form of Equation 2-25.

(2-25) $$\tau_{ij} = \sum_{m,n} c_{ijmn} E_{mn}$$

Inserting Equation 2-25 into Equation 2-23, we finally get the complex system ($i = 1, 2, 3$) of fully anisotropic equations of motion, Equation 2-26.

(2-26) $$\frac{\partial^2 u_i}{\partial t^2} = \sum_{m,n,j} \frac{c_{ijmn}}{\rho} \frac{\partial^2 u_m}{\partial x_n \partial x_j}$$

Symmetry

Because Equation 2-26 is three-dimensional, each of the c_{ijmn} coefficients is actually a three-dimensional volume. Even today's massive supercomputers may not have sufficient memory to handle a problem of this size.

We could easily throw up our hands at this point and give up, but, before we panic too much, we might want to analyze the situation a bit. As it turns out there are at least two things we can do to simplify the situation considerably. First, we can simplify the mathematical notation to put us into a setting where we can make some sense of the parameters, and second, we can reformulate the c_{ijmn} coefficients in a way that will make a great deal more physical sense.

We are not really interested as much in the math as we are in understanding the kinds of Earth models these c_{ijmn} coefficients define for us. We need to know how the various velocities of the wavefields that propagate in the medium are defined. We also want to see if we can understand how direction changes the speed of propagation, and then see if we can find ways to estimate parameters that can be converted into c_{ijmn} volumes so we can both synthesize data and image data we have recorded over fully elastic models.

The first simplification to the complexity of Equation 2-26 is based on the symmetry of stress and strain. Here, the ij indices representing stress can be switched so that $c_{ijmn} = c_{jimn}$. Similarly, the strain based indices can also be switched so that $c_{ijmn} = c_{ijnm}$. Finally, it is also true that $c_{ijmn} = c_{mnij}$. This triple symmetry means that the total number of c_{ijmn} volumes has been reduced to **only 21**! Thus, defining the most general model

we can imagine requires only 21 independent parameters (volumes), instead of the 81 parameters we would need without symmetry.

By applying the indexing scheme (known as the Voigt scheme) in Equation 2-27, we arrive at the 6x6 matrix shown in Equation 2-28.

(2-27)
$$\begin{array}{cccccccccc} index & ij & = & 11 & 22 & 33 & 23 & 13 & 12 \\ map & \downarrow & & \downarrow & \downarrow & \downarrow & \downarrow & \downarrow & \downarrow \\ index & k,l & = & 1 & 2 & 3 & 4 & 5 & 6 \end{array}$$

(2-28)
$$C = [c_{kl}] = \begin{bmatrix} c_{11} & c_{12} & c_{13} & c_{14} & c_{15} & c_{16} \\ c_{12} & c_{22} & c_{23} & c_{24} & c_{25} & c_{26} \\ c_{13} & c_{23} & c_{33} & c_{34} & c_{35} & c_{36} \\ c_{14} & c_{24} & c_{34} & c_{44} & c_{45} & c_{46} \\ c_{15} & c_{25} & c_{35} & c_{45} & c_{55} & c_{56} \\ c_{16} & c_{26} & c_{36} & c_{46} & c_{56} & c_{66} \end{bmatrix}$$

This matrix completely describes the unique set of 21 coefficients fully defining anisotropic elasticity. In this case, the C matrix is the most complicated form of anisotropy we can encounter. For the interested reader, this case is called “triclinic” symmetry and is probably something we will not be able to investigate computationally until computers have advance significantly beyond where they are today. Moreover, we may never be able to measure sufficient data to be able to estimate all of these parameters. Consequently, we will focus on what we consider reasonable today.

Acoustic Symmetry

In what perhaps is overkill, the C matrix takes the form shown in Equation 2-29 for a purely acoustic medium.

(2-29)
$$C = [c_{kl}] = \begin{bmatrix} \lambda & \lambda & \lambda & 0 & 0 & 0 \\ \lambda & \lambda & \lambda & 0 & 0 & 0 \\ \lambda & \lambda & \lambda & 0 & 0 & 0 \\ 0 & 0 & 0 & 0 & 0 & 0 \\ 0 & 0 & 0 & 0 & 0 & 0 \\ 0 & 0 & 0 & 0 & 0 & 0 \end{bmatrix}$$

Here, λ is the first of the two so-called “Lamè” parameters. Named after Gabriel Lamè, they are material properties (proportionality constants) that relate stress to strain. In this case, λ is directly related to the bulk modulus, K, so that the compressional velocity is $v_p = \sqrt{\frac{K}{\rho}} = \sqrt{\frac{\lambda}{\rho}}$.

If we define the actual c_{ijmn} from the elements of C, plug them back into the fully anisotropic Equation 2-26, we see that $u_1 = u_2 = u_3 = u$, and consequently that Equation 2-26 reduces to Equation 2-30, which is, of course, the normal three-dimensional scalar wave equation.

(2-30)
$$\frac{\partial^2 u}{\partial t^2} = \frac{\lambda}{\rho}\left(\frac{\partial^2 u}{\partial x_1^2} + \frac{\partial^2 u}{\partial x_2^2} + \frac{\partial^2 u}{\partial x_3^2}\right)$$

Equation 2-23 shows that $\tau_{i,j} = 0, i \neq j$, $\tau_{1,1} = \tau_{2,2} = \tau_{3,3} = \tau$, and $u_1 = u_2 = u_3 = u$, so that Equation 2-30 becomes Equation 2-31.

(2-31)
$$\begin{aligned} \frac{\partial^2 u}{\partial t^2} &= \frac{\lambda}{\rho}\left[\frac{\partial \tau}{\partial x_1} + \frac{\partial \tau}{\partial x_2} + \frac{\partial \tau}{\partial x_3}\right] \\ \tau &= \frac{\lambda}{\rho}\left[\frac{\partial u}{\partial x_1} + \frac{\partial u}{\partial x_2} + \frac{\partial u}{\partial x_3}\right] \end{aligned}$$

These two equations can also be written in first order form as Equation 2-32.

(2-32)
$$\begin{aligned} \frac{\partial v}{\partial t} &= \frac{\lambda}{\rho}\left[\frac{\partial \tau}{\partial x_1} + \frac{\partial \tau}{\partial x_2} + \frac{\partial \tau}{\partial x_3}\right] \\ \frac{\partial \tau}{\partial t} &= \frac{\lambda}{\rho}\left[\frac{\partial u}{\partial x_1} + \frac{\partial u}{\partial x_2} + \frac{\partial u}{\partial x_3}\right] \end{aligned}$$

Isotropic Elastic Symmetry

For isotropic elastic models, the C matrix takes the form in Equation 2-33, where μ is the second of the two Lamè parameters, and represents the shear modulus.

(2-33)
$$C = [c_{kl}] = \begin{bmatrix} \lambda+2\mu & \lambda & \lambda & 0 & 0 & 0 \\ \lambda & \lambda+2\mu & \lambda & 0 & 0 & 0 \\ \lambda & \lambda & \lambda+2\mu & 0 & 0 & 0 \\ 0 & 0 & 0 & \mu & 0 & 0 \\ 0 & 0 & 0 & 0 & \mu & 0 \\ 0 & 0 & 0 & 0 & 0 & \mu \end{bmatrix}$$

In this case, $v_p = \sqrt{\frac{\lambda+2\mu}{\rho}} = \sqrt{\frac{K+4\mu/3}{\rho}}$, and the shear velocity is then $v_s = \sqrt{\frac{\mu}{\rho}}$.

It is clear from these relationships, that given density, ρ, compressional velocity, v_p, and shear velocity, v_s, it is quite easy to solve for the coefficients in the C matrix, and then produce the propagation equation for synthesizing isotropic elastic seismic data. It is also

clear that modeling with this level of complexity is considerably more computationally intensive than is the case for acoustic models.

Given the matrix in Equation 2-33 and then using Equation 2-23 and Equation 2-25, we can write Equation 2-34.

(2-34)
$$
\begin{aligned}
\frac{\partial^2 u_1}{\partial t^2} &= \frac{1}{\rho}\left(\frac{\partial \tau_{1,1}}{\partial x_1} + \frac{\partial \tau_{1,2}}{\partial x_2} + \frac{\partial \tau_{1,3}}{\partial x_3}\right) \\
\frac{\partial^2 u_2}{\partial t^2} &= \frac{1}{\rho}\left(\frac{\partial \tau_{2,1}}{\partial x_1} + \frac{\partial \tau_{2,2}}{\partial x_2} + \frac{\partial \tau_{2,3}}{\partial x_3}\right) \\
\frac{\partial^2 u_3}{\partial t^2} &= \frac{1}{\rho}\left(\frac{\partial \tau_{3,1}}{\partial x_1} + \frac{\partial \tau_{3,2}}{\partial x_2} + \frac{\partial \tau_{3,3}}{\partial x_3}\right) \\
\tau_{1,1} &= \frac{\lambda + 2\mu}{\rho}\frac{\partial u_1}{\partial x_1} + \frac{\lambda}{\rho}\frac{\partial u_2}{\partial x_2} + \frac{\lambda}{\rho}\frac{\partial u_3}{\partial x_3} \\
\tau_{1,2} &= \frac{\mu}{\rho}\left(\frac{\partial u_1}{\partial x_2} + \frac{\partial u_2}{\partial x_1}\right) \\
\tau_{1,3} &= \frac{\mu}{\rho}\left(\frac{\partial u_1}{\partial x_3} + \frac{\partial u_3}{\partial x_1}\right) \\
\tau_{2,2} &= \frac{\lambda}{\rho}\frac{\partial u_1}{\partial x_1} + \frac{\lambda + 2\mu}{\rho}\frac{\partial u_2}{\partial x_2} + \frac{\lambda}{\rho}\frac{\partial u_3}{\partial x_3} \\
\tau_{2,3} &= \frac{\mu}{\rho}\left(\frac{\partial u_3}{\partial x_2} + \frac{\partial u_2}{\partial x_3}\right) \\
\tau_{3,3} &= \frac{\lambda}{\rho}\frac{\partial u_1}{\partial x_1} + \frac{\lambda}{\rho}\frac{\partial u_2}{\partial x_2} + \frac{\lambda + 2\mu}{\rho}\frac{\partial u_3}{\partial x_3}
\end{aligned}
$$

Note that each $\tau_{i,j}$ is expressed in terms of various partial derivatives of the u_i. Back substitution of these expressions into the formulas in Equation 2-34 for the second order time derivatives allows us to write the elastic particle displacement equation in the form of Equation 2-35.

(2-35)
$$
\frac{\partial^2 \mathbf{u}}{\partial t^2} = \left(\frac{\lambda + 2\mu}{\rho}\right)\nabla(\nabla \cdot \mathbf{u}) - \frac{\mu}{\rho}\nabla \times \nabla \times \mathbf{u}
$$

From a practical point of view, Equation 2-35 says that, even in the elastic case, we can solve for the vector components of particle displacement **u** in much the same way that we solve for the non-vector wavefield, u, in a scalar wave equation.

We can also write Equation 2-34 as a first order vector system. If we take the partial derivatives of the stress-strain terms, τ, in Equation 2-34 and let $v_i = \frac{\partial u_i}{\partial t}$, we obtain the

first order equation for particle velocity, Equation 2-36.

$$
\begin{aligned}
\frac{\partial v_1}{\partial t} &= \frac{1}{\rho}\left(\frac{\partial \tau_{1,1}}{\partial x_1} + \frac{\partial \tau_{1,2}}{\partial x_2} + \frac{\partial \tau_{1,3}}{\partial x_3}\right) \\
\frac{\partial v_2}{\partial t} &= \frac{1}{\rho}\left(\frac{\partial \tau_{2,1}}{\partial x_1} + \frac{\partial \tau_{2,2}}{\partial x_2} + \frac{\partial \tau_{2,3}}{\partial x_3}\right) \\
\frac{\partial v_3}{\partial t} &= \frac{1}{\rho}\left(\frac{\partial \tau_{3,1}}{\partial x_1} + \frac{\partial \tau_{3,2}}{\partial x_2} + \frac{\partial \tau_{3,3}}{\partial x_3}\right) \\
\frac{\partial \tau_{1,1}}{\partial t} &= \frac{\lambda + 2\mu}{\rho}\frac{\partial v_1}{\partial x_1} + \frac{\lambda}{\rho}\frac{\partial v_2}{\partial x_2} + \frac{\lambda}{\rho}\frac{\partial v_3}{\partial x_3} \\
\frac{\partial \tau_{1,2}}{\partial t} &= \frac{\mu}{\rho}\left(\frac{\partial v_1}{\partial x_2} + \frac{\partial v_2}{\partial x_1}\right) \\
\frac{\partial \tau_{1,3}}{\partial t} &= \frac{\mu}{\rho}\left(\frac{\partial v_1}{\partial x_3} + \frac{\partial v_3}{\partial x_1}\right) \\
\frac{\partial \tau_{2,2}}{\partial t} &= \frac{\lambda}{\rho}\frac{\partial v_1}{\partial x_1} + \frac{\lambda + 2\mu}{\rho}\frac{\partial v_2}{\partial x_2} + \frac{\lambda}{\rho}\frac{\partial v_3}{\partial x_3} \\
\frac{\partial \tau_{2,3}}{\partial t} &= \frac{\mu}{\rho}\left(\frac{\partial v_2}{\partial x_3} + \frac{\partial v_3}{\partial x_2}\right) \\
\frac{\partial \tau_{3,3}}{\partial t} &= \frac{\lambda}{\rho}\frac{\partial v_1}{\partial x_1} + \frac{\lambda}{\rho}\frac{\partial v_2}{\partial x_2} + \frac{\lambda + 2\mu}{\rho}\frac{\partial v_3}{\partial x_3}
\end{aligned}
\tag{2-36}
$$

Equation 2-36 provides a first order system of equations (in time) as opposed a second order system like that in Equation 2-26. Note that, because of symmetry, we need not write down the terms $\frac{\partial \tau_{2,1}}{\partial t} = \frac{\partial \tau_{1,2}}{\partial t}$, $\frac{\partial \tau_{3,1}}{\partial t} = \frac{\partial \tau_{1,3}}{\partial t}$, or $\frac{\partial \tau_{3,2}}{\partial t} = \frac{\partial \tau_{2,3}}{\partial t}$.

We can write Equation 2-36 in the form of Equation 2-37, where $\mathbf{S}(t)$ is a suitable vector source term, $\mathbf{v} = \left[v_1, v_2, v_3, \tau_{1,1}, \tau_{1,2}, \tau_{1,3}, \tau_{2,2}, \tau_{2,3}, \tau_{3,3}\right]^T$, and Equation 2-38 defines $\mathbf{H}$. The $\mathbf{A}$, $\mathbf{B}$, and $\mathbf{C}$ matrices in Equation 2-38 are themselves defined in Equation 2-39, Equation 2-40 and Equation 2-41, respectively.

$$
\frac{\partial \mathbf{v}}{\partial t} = \mathbf{H}\mathbf{v} + \mathbf{S} \tag{2-37}
$$

$$
\mathbf{H} = \mathbf{A}\frac{\partial \mathbf{v}}{\partial x_1} + \mathbf{B}\frac{\partial \mathbf{v}}{\partial x_2} + \mathbf{C}\frac{\partial \mathbf{v}}{\partial x_3} \tag{2-38}
$$

(2-39)
$$\mathbf{A} = \begin{bmatrix} 0 & 0 & 0 & \rho^{-1} & 0 & 0 & 0 & 0 & 0 \\ 0 & 0 & 0 & 0 & \rho^{-1} & 0 & 0 & 0 & 0 \\ 0 & 0 & 0 & 0 & 0 & \rho^{-1} & 0 & 0 & 0 \\ \frac{\lambda+2\mu}{\rho} & 0 & 0 & 0 & 0 & 0 & 0 & 0 & 0 \\ 0 & \frac{\mu}{\rho} & 0 & 0 & 0 & 0 & 0 & 0 & 0 \\ 0 & 0 & \frac{\mu}{\rho} & 0 & 0 & 0 & 0 & 0 & 0 \\ \frac{\lambda}{\rho} & 0 & 0 & 0 & 0 & 0 & 0 & 0 & 0 \\ 0 & 0 & 0 & 0 & 0 & 0 & 0 & 0 & 0 \\ \frac{\lambda}{\rho} & 0 & 0 & 0 & 0 & 0 & 0 & 0 & 0 \end{bmatrix}$$

(2-40)
$$\mathbf{B} = \begin{bmatrix} 0 & 0 & 0 & 0 & \rho^{-1} & 0 & 0 & 0 & 0 \\ 0 & 0 & 0 & 0 & 0 & 0 & \rho^{-1} & 0 & 0 \\ 0 & 0 & 0 & 0 & 0 & 0 & 0 & \rho^{-1} & 0 \\ 0 & \frac{\lambda}{\rho} & 0 & 0 & 0 & 0 & 0 & 0 & 0 \\ \frac{\mu}{\rho} & 0 & 0 & 0 & 0 & 0 & 0 & 0 & 0 \\ 0 & 0 & 0 & 0 & 0 & 0 & 0 & 0 & 0 \\ 0 & \frac{\lambda+2\mu}{\rho} & 0 & 0 & 0 & 0 & 0 & 0 & 0 \\ 0 & 0 & \frac{\mu}{\rho} & 0 & 0 & 0 & 0 & 0 & 0 \\ 0 & \frac{\lambda}{\rho} & 0 & 0 & 0 & 0 & 0 & 0 & 0 \end{bmatrix}$$

(2-41)
$$\mathbf{C} = \begin{bmatrix} 0 & 0 & 0 & 0 & 0 & \rho^{-1} & 0 & 0 & 0 \\ 0 & 0 & 0 & 0 & 0 & 0 & 0 & \rho^{-1} & 0 \\ 0 & 0 & 0 & 0 & 0 & 0 & 0 & 0 & \rho^{-1} \\ 0 & 0 & \frac{\lambda}{\rho} & 0 & 0 & 0 & 0 & 0 & 0 \\ 0 & 0 & 0 & 0 & 0 & 0 & 0 & 0 & 0 \\ \frac{\mu}{\rho} & 0 & 0 & 0 & 0 & 0 & 0 & 0 & 0 \\ 0 & 0 & \frac{\lambda}{\rho} & 0 & 0 & 0 & 0 & 0 & 0 \\ 0 & \frac{\mu}{\rho} & 0 & 0 & 0 & 0 & 0 & 0 & 0 \\ 0 & 0 & \frac{\lambda+2\mu}{\rho} & 0 & 0 & 0 & 0 & 0 & 0 \end{bmatrix}$$

Equation 2-38 is appealing because it is a one-dimensional, time-domain differential system whose solution is easily expressed as Equation 2-42, where $\mathbf{v}(0)$ represents the initial conditions. When we discuss numerical approximations to this equation, we will find this fact quite useful. It allows us to propagate wavefields one time stamp at a time without having to solve a second order system. It is also easily manipulated to produce a very efficient and accurate forward marching algorithm, the *evolution equation*.

(2-42)
$$\mathbf{v}(t) = e^{t\mathbf{H}}\mathbf{v}(0) + \int_0^t e^{\xi\mathbf{H}}\mathbf{S}(t-\xi)d\xi$$

Before developing the forward marching algorithm, we continue our discussion of the various types of data we might wish to synthesize.

Vertical Transverse Isotropy (VTI) Symmetry

The C matrix in Equation 2-43 defines what has become known as vertical transverse isotropy (VTI).

(2-43)
$$C = [c_{kl}] = \begin{bmatrix} c_{11} & c_{11}-2c_{66} & c_{13} & 0 & 0 & 0 \\ c_{11}-2c_{66} & c_{11} & c_{13} & 0 & 0 & 0 \\ c_{13} & c_{13} & c_{33} & 0 & 0 & 0 \\ 0 & 0 & 0 & c_{44} & 0 & 0 \\ 0 & 0 & 0 & 0 & c_{44} & 0 \\ 0 & 0 & 0 & 0 & 0 & c_{66} \end{bmatrix}$$

Waves propagating in media of this type exhibit a symmetry around the vertical or depth axis, z. Note that the pattern of this matrix is identical to that of the isotropic elastic C matrix. In fact, by setting $c_{11} = c_{33}$, $c_{44} = c_{55} = \mu$, and $c_{13} = \lambda$, the VTI C matrix becomes the isotropic elastic matrix. As we will see, the square roots of the ratios $\frac{c_{33}}{\rho}$ and $\frac{c_{44}}{\rho}$ specify the vertical compressional and shear velocities in the anisotropic medium. It should not be a surprise that the c_{ij} values in the matrix can be related to intuitive parameters more representative of how we think of the Earth.

We could again follow the development of Equation 2-36 to produce an equivalent for VTI media, but that is left to the reader. The important thing to notice is that implementation of a discrete version of the resulting first order system will almost certainly follow along the same lines as that for the isotropic elastic case above.

Rock types exhibiting VTI behavior include shales and thin-bed sequences.

Polar Isotropy Symmetry

The difference between VTI and polar isotropy is that the symmetry axis is tilted relative to the vertical axis. Early on, this type of anisotropic symmetry was called tilted transversely isotropic (TTI) anisotropy, but in this book I prefer to use Leon Thomsen's more general term, *polar symmetry*. Symmetry of this type is easily obtained by simply rotating the tensor c_{ijmn} of a VTI medium through a fixed angle. The new resulting C matrix produces wavefields that are symmetric around the new symmetry axis. In this case the axis can be relative to any plane through the medium and the propagation is symmetric relative to that plane. Unfortunately, when the symmetry axis is not aligned along the primary axis, neither the C matrix nor the tensor, c_{ijmn}, is particularly simple and generally does not have an easily recognized pattern. This may not be much of an issue since, when the rotation angle is known, it is possible to rotate back forth between VTI and TTI at any time.

Rock types with polar isotropy are identical to those exhibiting VTI, but in this case the symmetry is orthogonal to the dip of the rock.

Orthorhombic Isotropy Symmetry

Polar anisotropy, including VTI, is always defined by five parametric volumes and the two angles defining the symmetry axis. The C matrix with nine elements in Equation 2-44 defines orthorhombic anisotropy.

(2-44)
$$C = [c_{kl}] = \begin{bmatrix} c_{11} & c_{12} & c_{13} & 0 & 0 & 0 \\ c_{12} & c_{22} & c_{23} & 0 & 0 & 0 \\ c_{13} & c_{23} & c_{33} & 0 & 0 & 0 \\ 0 & 0 & 0 & c_{44} & 0 & 0 \\ 0 & 0 & 0 & 0 & c_{55} & 0 \\ 0 & 0 & 0 & 0 & 0 & c_{66} \end{bmatrix}$$

Orthorhombic anisotropy is probably the most realistic anisotropy that we will be able to handle or even use in the forceable future. Again, derivation of a first order system like that in Equation 2-26 is left to your discretion.

Examples of rock types that exhibit orthorhombic symmetry include

- thin-bed sequences or shale with a single set of vertical fractures
- isotropic formation with a single set of vertical, noncircular fractures
- thin-bed sequence, or shale, or a massive isotropic sandstone with orthogonal sets of vertical fractures

Thomsen Parameters

In the mid 1980's, Leon Thomsen's research into anisotropy at AMOCO's Tulsa, Oklahoma research lab lead him to define a collection of parameters that provided a much more intuitive picture of the entries in the C matrix. Thomsen began by defining Equation 2-45.

$$
\begin{aligned}
v_{P0} &= \sqrt{\frac{c_{33}}{\rho}} \\
v_{S0} &= \sqrt{\frac{c_{44}}{\rho}} \\
\varepsilon &= \frac{c_{11}-c_{33}}{2c_{33}} \\
\delta &= \frac{(c_{13}+c_{44})^2-(c_{33}-c_{44})^2}{2c_{33}(c_{33}-c_{44})} \\
\gamma &= \frac{c_{66}-c_{44}}{2c_{44}}
\end{aligned}
\tag{2-45}
$$

He then showed that the exact plane wave velocities could be expressed as a function of the propagation angle, θ, using Equation 2-46, where D' is defined by Equation 2-47.

$$
\begin{aligned}
v_p^2(\theta) &= v_{P0}^2\left[1+\varepsilon\sin^2\theta + D'\right] \\
v_{s_\perp}^2(\theta) &= v_{S0}^2\left[1+\varepsilon\frac{v_{P0}^2}{v_{S0}^2}\sin^2\theta + \frac{v_{P0}^2}{v_{S0}^2}D'\right] \\
v_{s_\parallel}^2(\theta) &= v_{S0}^2\left[1+2\gamma\sin^2\theta\right]
\end{aligned}
\tag{2-46}
$$

$$
D' = \frac{(1-\frac{v_{S0}^2}{v_{S0}^2})}{2}\left[\left\{1+\frac{4(2\delta-\varepsilon)}{1-\frac{v_{S0}^2}{v_{S0}^2}}\sin^2\theta\cos^2\theta+\frac{4(1-\frac{v_{S0}^2}{v_{S0}^2}+\varepsilon)\varepsilon}{1-\frac{v_{S0}^2}{v_{S0}^2}}\sin^4\theta\right\}^{1/2}-1\right] \tag{2-47}
$$

While these formulas have found considerable use for describing anisotropic models and for providing propagating equations for synthesis of anisotropic seismic data, the parameters of most importance for this book are the vertical and horizontal velocities. Typically, these velocities are defined from the *weak polar anisotropy* expressions in Equation 2-48 with values defined by Equation 2-49.

$$
\begin{aligned}
v_p^2(\theta) &\approx v_{P0}^2\left[1+\delta\sin^2\theta\cos^2\theta+\varepsilon\sin^4\theta\right] \\
v_{s_\perp}^2(\theta) &\approx v_{S0}^2\left[1+\frac{v_{P0}^2}{v_{S0}^2}(\varepsilon-\delta)\sin^2\theta\cos^2\theta\right] \\
v_{s_\parallel}^2(\theta) &\approx v_{S0}^2\left[1+2\gamma\sin^2\theta\right]
\end{aligned}
\tag{2-48}
$$

(2-49)
$$\begin{array}{rcl} v_p(0^\circ) & \approx & v_{P0} \\ v_p(90^\circ) & \approx & v_{P0}(1+\varepsilon) \\ v_{s_\perp}(0^\circ) & \approx & v_{S0} \\ v_{s_\perp}(90^\circ) & \approx & v_{S0} \\ v_{s_\parallel}(0^\circ) & \approx & v_{S0} \\ v_{s_\parallel}(90^\circ) & \approx & v_{S0}(1+\gamma) \end{array}$$

Clearly, ε controls the percentage of anisotropy. It determines the speed of the horizontal velocity relative to the vertical velocity v_{S0}. What will become apparent as we progress through this book is that δ controls what I will refer to as *conversion to depth*.

Expressing anisotropic parameters in this manner provides a more natural idea of the parameters defining a polar anisotropic model. While there are many possible variations, such models are defined by four volumes, the vertical velocities v_{P0} and v_{S0}, ε, and δ. Equation 2-26 is then discretized to provide the necessary propagating equation.

Algorithms

Algorithms for synthesizing seismic data abound. Here we will focus on four such methods: Ray-based, finite-difference, finite-element, and Fourier-domain-based methods. Of course, you can construct algorithms in various combinations of these domains, so it is technically possible to develop approaches that work with finite-differences in frequency-space or even perhaps time and spatial frequency. Once the basic concepts for the four are fully developed, pursuing alternative domain combinations is relative straightforward.

To keep the discussion as simple as possible we will focus all of our attention on the two-dimensional versions of Equation 2-17, and the coupled system Equation 2-36.

Variational Formulation and Finite Elements

We begin with Equation 2-18 in the frequency domain, where $g(\vec{x}_s)$ is a pressure source located at $\vec{x}_s = (x_s, y_s, z_s)$, and with $\vec{x} = (x, y, z)$, $k(\vec{x}) = \frac{\omega}{v(\vec{x})}$.

Equation 2-50 has the variational form in Equation 2-51, where V is an element of a suitable space, $\mathscr{V}$, of functions that can be used to approximate $U(\vec{x})$.

(2-50)
$$\frac{k^2}{\rho}U(x,y,z,\omega) + \nabla \cdot \frac{1}{\rho}\nabla U = -g(x_s, y_s, z_s, \omega)$$

(2-51) $$\varphi(U,V) = \int_\Omega \frac{k^2}{\rho} UV d\Omega + \int_\Omega \frac{1}{\rho} \nabla U \cdot \nabla V d\Omega = -\int_\Omega g(\vec{x}_s, t) d\Omega$$

Given a family, V_k, of basis functions spanning $\mathscr{V}$, we can approximate U and g by Equation 2-52 and Equation 2-53, respectively.

(2-52) $$U(\vec{x}) = \sum_{k=1}^{n} A_k V_k(\vec{x})$$

(2-53) $$g(\vec{x}_s, \omega) = \sum_{k=1}^{n} b_k V_k(\vec{x})$$

Thus, the variational form in Equation 2-51 can be expressed in matrix form as Equation 2-54 or Equation 2-55, where $\vec{A}^T = [A_1, A_2, \ldots, A_n]$ and $\vec{b}^T = [b_1, b_2, \ldots, b_n]$.

(2-54) $$\sum_{k=1}^{n} A_k \varphi(V_k, V_j) = \sum_{k=1}^{n} b_k \int_\Omega V_k V_j d\Omega$$

(2-55) $$\mathbf{S}\vec{A} = \mathbf{M}\vec{b}$$

In this setting, **S** is called the *complex impedance matrix* and **M** is called the *stiffness matrix*. Note that we have dropped reference to frequency, ω, so that $\mathbf{S}\vec{A} = \mathbf{M}\vec{g}$ is a single frequency equation.

If we choose our discretization scheme properly, we may assume that **S** is square, symmetric, and invertible, so that the modeling operator $\mathbf{S}^{-1}$ generates data according to the formula in Equation 2-56.

(2-56) $$\vec{U} = \mathbf{S}^{-1}\vec{f}$$

The key point to this discussion is that we have wide latitude in the choice of V_k. We can divide the model into a collection of local regions and then define V_k through polynomials, pyramids, or perhaps even boxes over each of the sub domains. This approach works well when the problem is defined by things like bridges, aeronautical structures, and other rigid bodies, but has never gained ground in seismic settings.

Dividing the medium up in this way is quite difficult mathematically, so modern methods tend to choose uniformly square or rectangular domains. It is also convenient to have basis functions that are easily differentiable and orthogonal. Thus, in some sense,

the modern version of finite element methods (FEM) tends to look more and more like a very sophisticated finite difference approach. However you accomplish the model division, the need to invert a matrix of significant size remains a serious issue.

For example, consider the one dimensional case and define $V_k(x)$ using Equation 2-57.

(2-57)
$$V_k(x) = \begin{cases} \frac{x - x_{k-1}}{x_k - x_{k-1}} & x \in [x_{k-1}, x_k] \\ \frac{x_{k+1} - x_k}{x_{k+1} - x_k} & x \in [x_k, x_{k+1}] \\ 0 & elsewhere \end{cases}$$

As illustrated in Figure 2-11, the $V_k \ = \ 1, \ldots, n$ basis is composed of shifted and scaled tent functions. For the two-dimensional case, we again choose one basis function, V_k, per vertex, x_k, of the triangulation of the planar region Ω. The function V_k is the unique function of x whose value is 1 at x_k and zero at every $x_j, \ j \ \neq \ k$. This process extends easily to three dimensions.

Figure 2-11. Basis functions V_k (blue) and a linear combination of them, which is piecewise linear (red)

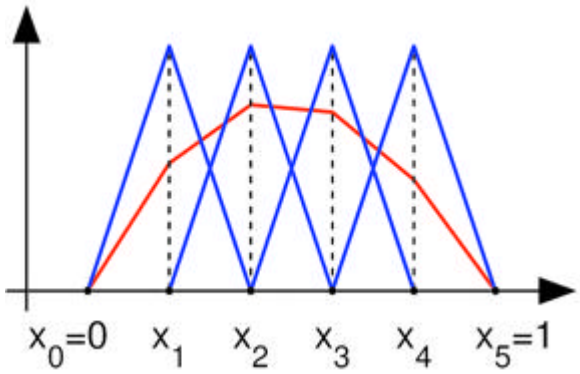

The primary advantage of this choice of basis is that the inner product in Equation 2-58 will be zero for almost all j, k.

(2-58)
$$\langle V_j, V_k \rangle = \int_0^1 V_j V_k \, dx$$

In the one dimensional case, the support of V_k is the interval $[x_{k-1}, x_{k+1}]$. Hence, the integrands of $\langle V_j, V_k \rangle$ and $\Phi(V_j, V_k)$ are identically zero whenever $|j - k| > 1$.

Similarly, in the planar case, if x_j and x_k do not share an edge of the triangulation, then the integrals 2-59 and 2-60 are both zero.

(2-59)
$$\int_\Omega V_j V_k \, ds$$

(2-60)
$$\int_{\Omega} \nabla V_j \cdot \nabla V_k \, ds$$

In two-dimensions, triangular elements can be used to approximate the domain of approximation in both regular and irregular ways. In Figure 2-12, a regular mesh is used to approximate the domain, and then through pyramids approximate the dome-like structure in the figure. Figure 2-12 illustrates a reasonably regular triangular decomposition of a domain at the bottom and the approximation to a dome accomplished through the use of the pyramidal versions of the basis functions in Figure 2-11. (From Wikipedia contributors,"Finite element method," Wikipedia, The Free Encyclopedia, http://en.wikipedia.org/w/index.php?title=Finite_element_method&oldid=298136444).

Figure 2-12. Domain triangles with pyramids as elements approximate a dome like surface. In this case the triangular basis mesh is regular. (From Wikipedia)

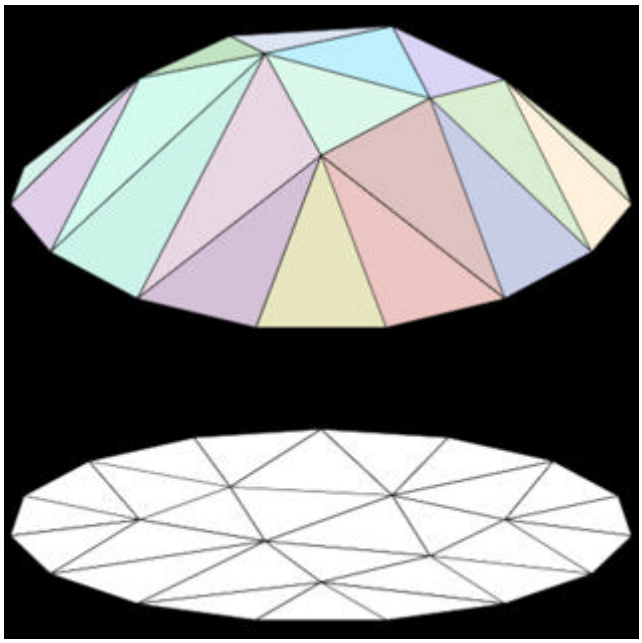

In contrast, Figure 2-13 shows an much more irregular approximation of the domain of approximation. It is an example of the utilization of irregularly sized triangles to decompose the domain of approximation. The mesh is denser in areas of interest.

Figure 2-13. Domain triangles with pyramids as elements approximate a dome like surface. Here the triangular basis mesh is irregular. (From Wikipedia)

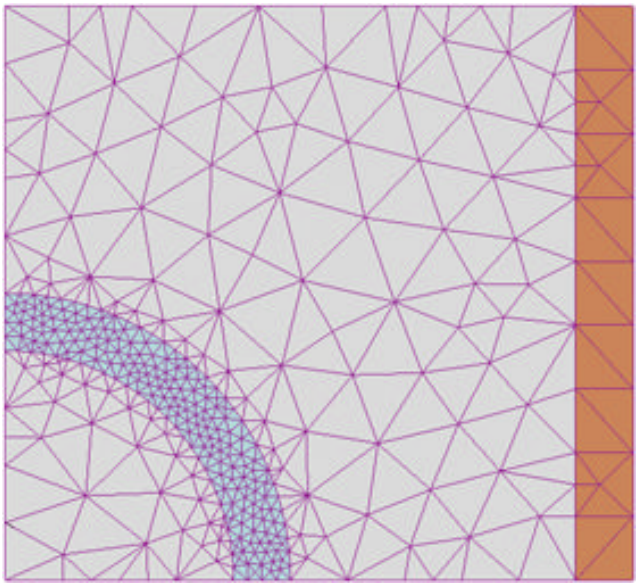

Figure 2-14 shows the general form of a 2D *S* matrix. Generally, this matrix has dimensions equal to the number of nodes or finite elements. An intriguing feature of the finite element method is that once the S-matrix is inverted, any and all shot responses can be synthesized from this single inverse.

Figure 2-14. The general form of the S-matrix in two-dimensions. (From Wikipedia)

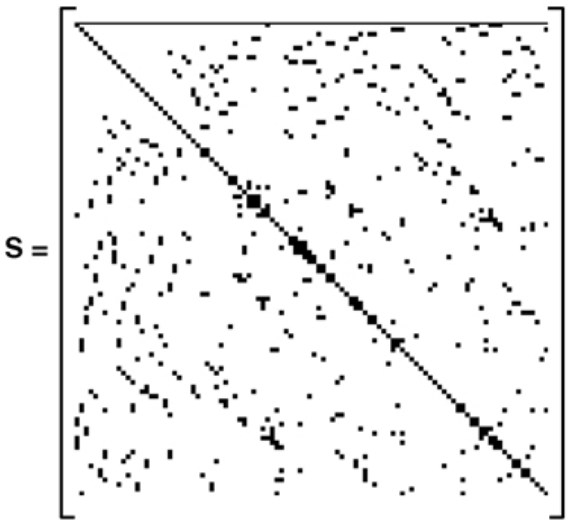

Depending on the author, the word “element” in “finite element method” refers either to the triangles in the domain, the piecewise linear basis function, or both. For our purposes, it is the latter. So, for instance, an author interested in curved domains might replace the triangles with curved primitives, in which case he might describe his elements as being curvilinear. On the other hand, some authors replace “piecewise linear” by “piecewise quadratic” or even “piecewise polynomial”. The author might then say “higher order element” instead of “higher degree polynomial”. The finite element method is not restricted to triangles (or tetrahedra in 3D, or higher order simplexes in multidimensional spaces), but can be defined on quadrilateral subdomains (hexahedra, prisms, or pyramids in 3D, and so on). Higher order shapes (curvilinear elements) can be defined with polynomial and even non-polynomial shapes (for example, ellipses or circles).

More advanced implementations (adaptive finite element methods) utilize a method to assess the quality of the results (based on error estimation theory) and modify the mesh during the solution, aiming to achieve an approximate solution within some bounds from the “exact” solution of the continuum problem. Mesh adaptivity may utilize various techniques, the most popular are:

- Moving nodes (r-adaptivity)
- Refining (and unrefining) elements (h-adaptivity)
- Changing order of base functions (p-adaptivity)
- Combinations of the above (hp-adaptivity)

In general, the finite element method is characterized by the following process.

- Choose a grid for Ω. In the preceding example the grid consisted of grid points or nodes, but one can also use triangles or curvilinear polygons.

- Choose basis functions. In our discussion, we used piecewise linear basis functions, but it is also common to use piecewise polynomial basis functions

A separate consideration is the smoothness of the basis functions. For second order elliptic boundary value problems, piecewise polynomial basis functions that are merely continuous will suffice (that is, the derivatives are discontinuous.) For higher order partial differential equations, you must use smoother basis functions. For instance, for a fourth order problem such as $u_{xxxx} + u_{yyyy} = f$, you can use piecewise quadratic basis functions that are both continuous and have first order derivatives.

An Old Movie

We can now use our modeling schema to generate synthetic shot data. Because we have a complete wavefield at each time step, we present the synthetic data in movie form. Our first movie (snapshots in Figure 2-15) was generated by R. G. Keys (now at ConocoPhillips in Houston, Texas) in February of 1982. At that time, the multiplicity of snapshots comprising these data required about 30 minutes to generate on a Cray 1S supercomputer. Today, almost any modern desktop, and even some laptops, can produce the same movie virtually in real time. As the movie progresses, please note that waves travel in all directions and the wavefield recorded at the top surface of this model would include refractions, reflections, and all forms of multiples.

Figure 2-15. Snapshot from 1982 Finite Element Pinchout Model synthesis.

Finite Differences

At first glance, finite difference modeling is by far the simplest method to grasp, since all that is necessary is to replace the continuous partial derivatives by discrete approximations. However, difficulty arises in producing an accurate approximation to the various derivatives. There are two generally accepted approaches to finding these approximations. The first is based purely on some form of fitting algorithm, frequently using polynomials, wherein a set of basis functions with known derivatives approximate the function whose derivative is required. Once the fit is obtained the derivative is defined in terms of the approximating functions.

The second way to approximate the derivatives is the finite element method (FEM). In FEM, the region of interest is divided into numerous connected subregions or elements within which approximate functions (usually polynomials) are used to represent the unknown quantity.

Polynomial Differences

The easiest approach to finite difference approximation is to simply use a difference quotient in Equation 2-61, like we did when we derived the full two-way equation. This is called a first order forward difference approximation.

(2-61)
$$\frac{du}{dx} = \frac{u(x + \Delta x) - u(x)}{\Delta x}$$

Similarly, we have the backward difference approximation in the form of Equation 2-62.

(2-62)
$$\frac{du}{dx} = \frac{u(x) - u(x - \Delta x)}{\Delta x}$$

What may not be clear is that these formulas are the result of approximating u by a straight line between $x + \Delta x$ and x and between $x - \Delta x$ and x.

One of the more popular methods for polynomial approximation is based on the Lagrange polynomial in Equation 2-63 defined for a sequence of points $[x_0, x_1, x_2, \ldots x_n]$.

(2-63)
$$L_{n,k}(x) = \prod_{\substack{i=0 \\ i \neq k}}^{i=n} \frac{(x - x_i)}{(x_k - x_i)}$$

Any function $f(x)$ can be defined such that the point sequence can then be approximated by the formula of Equation 2-64.

(2-64)
$$P(x) = \sum_{k=0}^{k=n} f(x_k) L_{n,k}(x)$$

Approximations to the derivatives of $f(x)$ can then be approximated through derivatives of the polynomial P. Since P will always be of the form in Equation 2-65, the approximate derivative will always be a weighted sum of the values of $f(x)$ at the sequence $[x_0, x_1, x_2, \ldots x_n]$.

(2-65) $$P(x) = a_0 + a_1 x + a_2 x^2 + \ldots a_n x^n$$

More accurate approximations can be obtained through the use of other polynomial bases, including the Hermite and Chebychev polynomials.

Taylor Series Differences

The Taylor series for $u(x \pm \Delta x)$ in terms of $u(x)$ is given in Equation 2-66.

(2-66) $$u(x \pm \Delta x) = u(x) \pm \frac{\partial u}{\partial x}\Delta x + \frac{\partial^2 u}{\partial x^2}\frac{\Delta x^2}{2!} \pm \frac{\partial^3 u}{\partial x^3}\frac{\Delta x^3}{3!} + \ldots$$

If we rearrange this series in the form Equation 2-67, we immediately recognize that the forward and backward differences are accurate to Δx. Mathematically, we say that the forward and backward differences are $O(\Delta x)$.

(2-67) $$\frac{u(x \pm \Delta x) - u(x)}{\Delta x} = \pm\frac{\partial u}{\partial x} + \frac{\partial^2 u}{\partial x^2}\frac{\Delta x}{2!} \pm \frac{\partial^3 u}{\partial x^3}\frac{\Delta x^2}{3!} + \ldots$$

The Taylor series in Equation 2-66 can easily form the basis for other more accurate formulas. The most obvious formula arises from the sum of the Taylor series expansions for $u(x + \Delta x) - u(x)$ and $u(x) - u(x - \Delta x)$. This immediately yields the central difference formula in Equation 2-68 which is $O(\Delta x^2)$.

(2-68) $$\frac{u(x + \Delta x) - u(x - \Delta x)}{2\Delta x} = \frac{\partial u}{\partial x} + \frac{\partial^3 u}{\partial x^3}\frac{\Delta x^2}{3!} + \frac{\partial^5 u}{\partial x^5}\frac{\Delta x^4}{5!} + \ldots$$

Since we generally think of Δx as being much less than 1 in magnitude, this central difference formula is clearly an improvement over a first-order forward or backward difference.

Second Order Differences

When we summed the formulas for $u(x + \Delta x) - u(x)$ and $u(x) - u(x - \Delta x)$, we obtained a series that contained odd order derivatives. Accordingly, if we subtract the two formulas, we obtain a series that contains only even order derivatives. This immediately produces the $O(\Delta x^2)$ formula for the second derivative with respect to x.

(2-69) $$\frac{u(x + \Delta x) - 2u(x) + u(x - \Delta x)}{\Delta x^2} = \frac{\partial u^2}{\partial x^2} + \frac{\partial^4 u}{\partial x^4}\frac{\Delta x^2}{4!} + \frac{\partial^6 u}{\partial x^6}\frac{\Delta x^4}{6!} + \ldots$$

High Order Differences

Extension of the second order central difference formula to higher orders is tedious but straight forward. For any given k (real or integer), there is Equation 2-70.

$$\frac{u(x+k\Delta x)+u(x-k\Delta x)}{2} = u(x)+k^2\frac{\partial u^2}{\partial x^2}\frac{\Delta x^2}{2!}+k^4\frac{\partial^4 u}{\partial x^4}\frac{\Delta x^4}{4!} + k^6\frac{\partial^6 u}{\partial x^6}\frac{\Delta x^6}{6!}+k^8\frac{\partial^8 u}{\partial x^8}\frac{\Delta x^8}{8!}+\ldots \tag{2-70}$$

Thus, if we want a fourth order scheme, we take the two terms in Equation 2-71 and Equation 2-72, solve the second term for the fourth order partial derivative and substitute the result into the first term to obtain Equation 2-73.

$$\frac{u(x+\Delta x)+u(x-\Delta x)}{2} = u(x)+\frac{\partial u^2}{\partial x^2}\frac{\Delta x^2}{2!}+\frac{\partial^4 u}{\partial x^4}\frac{\Delta x^4}{4!} \tag{2-71}$$

$$\frac{u(x+2\Delta x)+u(x-2\Delta x)}{2} = u(x)+4\frac{\partial u^2}{\partial x^2}\frac{\Delta x^2}{2!}+16\frac{\partial^4 u}{\partial x^4}\frac{\Delta x^4}{4!} \tag{2-72}$$

$$\frac{u(x+2\Delta x+16u(x+\Delta x)-34u(x)+16u(x-\Delta x)+u(x-2\Delta x)}{12\Delta x^2} \approx \frac{\partial u^2}{\partial x^2} \tag{2-73}$$

Higher order central difference approximations are obtained by simply adding additional terms to the mix. For example, a 10th order accurate term is obtained by back-substitution in the five equations when $k = 1, 2, 3, 4, 5$. The result is a scheme of the form in Equation 2-74, where the terms are given in Table 2.1.

$$\frac{\partial u^2}{\partial x^2} \approx \sum_{-5}^{5} w_k u(x-k\Delta x) \tag{2-74}$$

Table 2.1. Spatial Difference Terms

|k|	w
0	-5.8544444444
1	3.3333333333
2	-0.4761904762
3	0.0793650794
4	-0.0099206349
5	0.0006349206

Finite Differences for the Pressure Formulation

We can now formulate a finite difference propagation equation of just about any order we would like. However, it is of interest to reconsider the graphic in Figure 2-16(b). This figure, based on a simple second-order space-time difference equation shows that to compute any given fixed time stamp, the maximum extent of the stencil is exactly equal to three in each spatial direction and two in time. Thus, to make this process computationally efficient, it is prudent to keep the three $t - \Delta t$, t and $t + \Delta t$ volumes in memory at all times.

It is clear from Equation 2-74 that higher order differences will produce stencils with maximum extent determined by the maximum value of k. Thus, if we chose to use a 10th order scheme for each both space and time, our propagator will be 11 grid nodes wide in each spatial direction and 10 volumes in memory for each of the time stamps $t - k\Delta t$ for $k = -5, 5$. Even with current computational capabilities, holding this many volumes in memory is somewhat impractical. It is natural to try and find a procedure that avoids this memory explosion problem.

Graphical Descriptions

Figure 2-16(a) demonstrates two-dimensional propagation and Figure 2-16(b) demonstrates three-dimensional propagation in what is generally called acoustic Earth models. Note that the central difference stencil extends from time $t - \Delta t$ to time t to compute an output point at $t + \Delta t$.

Figure 2-16. Graphical interpretation of (a) 2-D and (b) 3-D propagators.

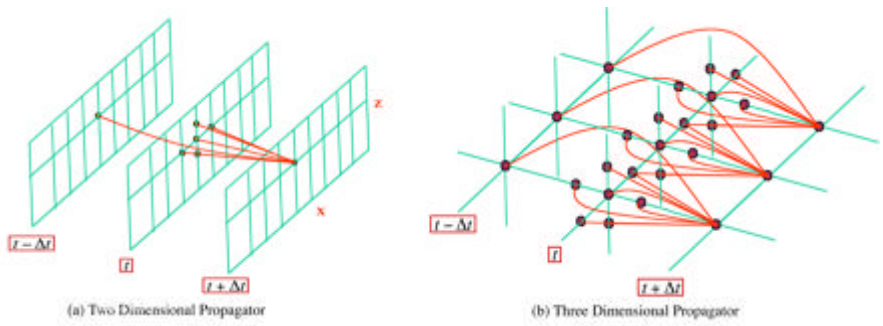

Note that in both cases, the stencil surrounds the ultimate output point to compute the new value. In the 2-D case, the stencil nodes are planar, while the 3-D nodes are volumetric. Thus, the wavefields are allowed to propagate upward, downward, and laterally in all directions as the propagation continues. It also means that we must compute all nodes at step t before we can compute any of the nodes at $t + \Delta t$. The examples in the last three figures produce what is called two-way propagation. All waveform styles (for example, refractions, free-surface, and peg-leg multiples) are possible in this setting since these propagators synthesize full waveform data.

Lax-Wendroff Method

Probably the best known "trick", initially published by Peter Lax and Burton Wendroff (see also M.A. Dablain), used the wave equation to find an accurate fourth order difference for $\frac{\partial^2}{\partial t^2}$ that does not increase the overall memory requirement. To understand this trick, consider the case in two dimensions when the velocity is constant and $\rho = 1$. From earlier efforts, we have Equation 2-75.

$$\begin{aligned} \frac{\partial^2 p}{\partial t^2} &= \frac{1}{\Delta t^2}\left(p(t+\Delta t) - 2p(t) + p(t-\Delta t) - \sum_{i=2}^{i=\infty} \frac{\partial^{2i} p}{\partial t^{2i}} \frac{\Delta t^{2i}}{2i!} \right) \\ &\approx \frac{1}{\Delta t^2}\left(p(t+\Delta t) - 2p(t) + p(t-\Delta t) - \frac{\partial^4 p}{\partial t^4} \frac{\Delta t^4}{12!} \right) \end{aligned} \tag{2-75}$$

We also know the second order derivative, $\frac{\partial^2 p}{\partial t^2}$, in Equation 2-76.

$$\frac{\partial^2 p}{\partial t^2} = v^2 \left(\frac{\partial^2 p}{\partial x^2} + \frac{\partial^2 p}{\partial z^2} \right) \tag{2-76}$$

Thus, the fourth order derivative in time is given by Equation 2-77.

$$\begin{aligned} \frac{\partial^4 p}{\partial t^4} &= v^2 \left[\frac{\partial^2 p}{\partial x^2}\left(\frac{\partial^2 p}{\partial t^2} \right) + \frac{\partial^2 p}{\partial z^2}\left(\frac{\partial^2 p}{\partial t^2} \right) \right] \\ &= v^2 \left[\frac{\partial^2 p}{\partial x^2}\left(\frac{\partial^2 p}{\partial x^2} + \frac{\partial^2 p}{\partial z^2} \right) + \frac{\partial^2 p}{\partial z^2}\left(\frac{\partial^2 p}{\partial x^2} + \frac{\partial^2 p}{\partial z^2} \right) \right] \\ &= v^4 \left(\frac{\partial^4 p}{\partial x^4} + 2\frac{\partial^4 p}{\partial x^2 \partial z^2} + \frac{\partial^4 p}{\partial x^4} \right) \end{aligned} \tag{2-77}$$

It should be noted that the assumptions of constant density and velocity are not necessary because the Lax-Wendroff scheme generalizes our scheme for finding higher order central difference terms through the recursive formula in Equation 2-78.

$$\frac{\partial^{2i} p}{\partial t^{2i}} = -\left(\rho v^2 \nabla \cdot \frac{1}{\rho} \nabla p \right) \frac{\partial^{2i-2} p}{\partial t^{2i-2}} \tag{2-78}$$

In this case, the higher order time derivatives can be computed from higher order spatial derivatives by applying the spatial side of the original wave equation.

If we now replace the spatial derivatives using formulas like that in Equation 2-74, we arrive at a fourth order formula for the second partial derivative in time. After

calculating all the various weights, replacing partial derivatives with central differences, and solving for $p_{i,j,n+1} = p(i\Delta x, j\Delta z, n\Delta t + \Delta t)$, we arrive at a discrete central difference formula of general form shown in Equation 2-79.

$$p_{i,j,n+1} = -2p_{i,j,n} + p_{i,j,n-1} + \Delta t^2 \left[v^4 \sum_k \sum_m a_{k,m} p_{i-k,j-m,n} + v^2 \left(\sum_k b_k p_{i-k,j,n} + \sum_m c_m p_{i,j-m,n} \right) \right] + s_{i_0,j_0,n} \quad (2\text{-}79)$$

For clarity, Δx^2 and Δy^2 have been suppressed, and $s_{i_0,j_0,n}$ represents a source at the location specified by i_0 and j_0.

Formulas of this kind are generally called *difference equations* and provide what is usually called an *explicit* forward marching algorithm for data synthesis. Schemes of this kind are also called *quadrature methods* because they are integrating the wave equation to synthesize a response to a given stimulus.

Figure 2-17 shows a simple pyramid model and data. The finite difference data over this model was synthesized on VAX 11-780 computers in late 1981 and early 1982. At that time, the calculations necessary to compute each shot required on the order of 48 hours. Today, most laptops can compute the entire set of 24 shots in minutes.

Figure 2-17. A simple pyramid model and data.

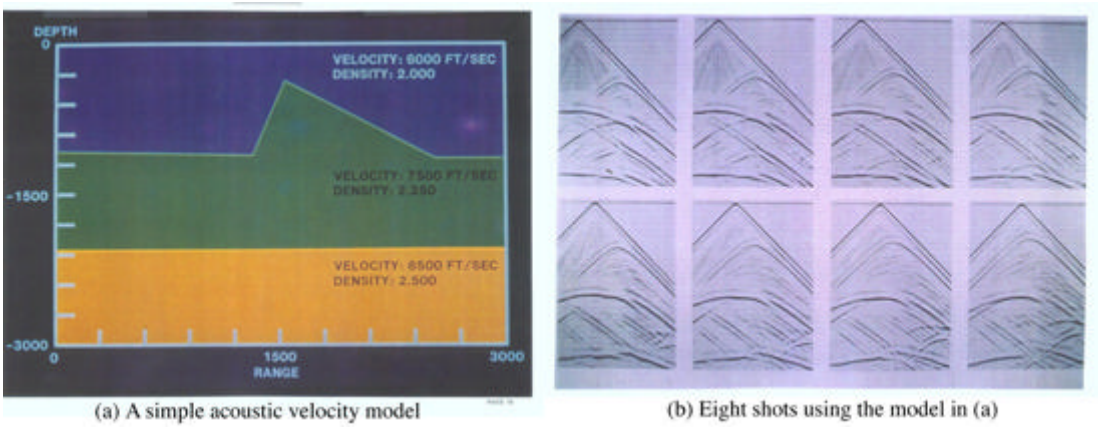

(a) A simple acoustic velocity model

(b) Eight shots using the model in (a)

Elastic Finite Differences

We now turn our attention to discrete simulation of vector elastic data. We can do this using either Equation 2-35 or Equation 2-36. Choosing the first equation leads to a method that is essentially the same as the pure explicit finite difference algorithm discussed in the previous section. To gain a slightly different perspective, we base our

formulation on Equation 2-36 and again we limit ourselves to the 2D case. In somewhat more familiar notation, Equation 2-36 becomes Equation 2-80.

$$
\begin{aligned}
\frac{\partial v_1}{\partial t} &= \rho^{-1}\left(\frac{\partial \tau_{1,1}}{\partial x_1} + \frac{\partial \tau_{1,2}}{\partial x_2}\right) \\
\frac{\partial v_2}{\partial t} &= \rho^{-1}\left(\frac{\partial \tau_{1,2}}{\partial x_1} + \frac{\partial \tau_{2,2}}{\partial x_2}\right) \\
\frac{\partial \tau_{1,1}}{\partial t} &= (\lambda + 2\mu)\frac{\partial v_1}{\partial x_1} + \lambda\frac{\partial v_2}{\partial x_2} \\
\frac{\partial \tau_{1,2}}{\partial t} &= \mu\left(\frac{\partial v_1}{\partial x_2} + \frac{\partial v_2}{\partial x_1}\right) \\
\frac{\partial \tau_{2,2}}{\partial t} &= \lambda\frac{\partial v_1}{\partial x_1} + (\lambda + 2\mu)\frac{\partial v_2}{\partial x_2}
\end{aligned}
\tag{2-80}
$$

We note that v_1 is the horizontal velocity and v_2 is the vertical velocity of a particle at any given position in space.

In this case, Equation 2-42 (the evolution equation) becomes Equation 2-81, where **v**, **H**, **A** and **B** are given by Equation 2-82 through Equation 2-85, respectively.

$$\frac{\partial \mathbf{v}}{\partial t} = \mathbf{H}\mathbf{v} + \mathbf{S} \tag{2-81}$$

$$\mathbf{v} = \left[v_1, v_2, \tau_{1.1}, \tau_{1,2}, \tau_{2,2}\right]^T \tag{2-82}$$

$$\mathbf{H} = \mathbf{A}\frac{\partial \mathbf{v}}{\partial x_1} + \mathbf{B}\frac{\partial \mathbf{v}}{\partial x_2} \tag{2-83}$$

$$\mathbf{A} = \begin{bmatrix} 0 & 0 & \rho^{-1} & 0 & 0 \\ 0 & 0 & 0 & \rho^{-1} & 0 \\ \lambda + 2\mu & 0 & 0 & 0 & 0 \\ 0 & \mu & 0 & 0 & 0 \\ \lambda & 0 & 0 & 0 & 0 \end{bmatrix} \tag{2-84}$$

$$\mathbf{B} = \begin{bmatrix} 0 & 0 & 0 & \rho^{-1} & 0 \\ 0 & 0 & 0 & 0 & \rho^{-1} \\ 0 & \lambda & 0 & 0 & 0 \\ \mu & 0 & 0 & 0 & 0 \\ 0 & \lambda + 2\mu & 0 & 0 & 0 \end{bmatrix} \tag{2-85}$$

Recall that the solution of Equation 2-81 has the form of Equation 2-86.

$$\mathbf{v}(t) = e^{t\mathbf{H}}\mathbf{v}(0) + \int_0^t e^{\tau\mathbf{H}}\mathbf{S}(t-\tau)d\tau \tag{2-86}$$

Equation 2-86 is immediately recognizable as a convolution in time. Thus, the progression from initial state to final state is really just a recursive convolution at each time stamp t. The well known series expansion for e^x provides an immediate approach to providing a discrete evolution equation for the solution vector $\mathbf{v}(t)$. The resulting scheme is equivalent to the Lax-Wendroff methodology and so will not be discussed further. If you are interested, you are encouraged to work out the mathematical details.

Staggered Grids

What we would like to develop is a finite difference solution to the system in Equation 2-81. We could, of course, use the higher order difference formulas developed through the use of the system in Equation 2-72. Several authors (Jean Virieux and A. Lavender) have suggested that somewhat higher accuracy might be achieved through the use of smaller time and space increments. Thus, their idea was to simply rewrite Equation 2-72 in the form of Equation 2-87 and Equation 2-88.

$$\frac{u(x+\frac{\Delta x}{2}) + u(x-\frac{\Delta x}{2})}{2} = u(x) + \frac{\partial u^2}{\partial x^2}\frac{\Delta x^2}{4\times 2!} + \frac{\partial^4 u}{\partial x^4}\frac{\Delta x^4}{16\times 4!} \tag{2-87}$$

$$\frac{u(x+\Delta x) + u(x-\Delta x)}{2} = u(x) + \frac{\partial u^2}{\partial x^2}\frac{\Delta x^2}{2!} + \frac{\partial^4 u}{\partial x^4}\frac{\Delta x^4}{4!} \tag{2-88}$$

This equation, of course, results in a difference formula of the form in Equation 2-89.

$$\frac{\partial^2 u}{\partial x^2} \approx \sum_{i=0}^{i=N} w_i u(x - \frac{i}{2}\Delta x) \tag{2-89}$$

Note that in Equation 2-89, the actual derivative is still estimated at a fixed grid point, but the accuracy is based on half the sampling increment.

At first glance, it might seem that a discrete solution of the system in Equation 2-80 using formulas based on half derivatives would require significantly more storage than using formulas defined at the normal sampling increments. However, it turns out that this is not the case if we first simplify the notation by defining $[v, w, \sigma, \xi, \zeta] = \left[v_1, v_2, \tau_{1,2}, \tau_{1,2}, \tau_{2,2}\right]$ so that we can then write $v_{i,j}^k = v_1(i\Delta x, j\Delta y, k\Delta t)$ for any sampling rate, and similarly for w, σ, ξ, and ζ.

A fourth order scheme in space and a second order scheme in time to solve Equation 2-80 can then be expressed as Equation 2-90.

$$
\begin{aligned}
v_{i,j}^{k+1/2} &= v^{k-1/2} + \rho_{i,j}^{-1}\frac{\Delta t}{\Delta x}\left(\sigma_{i+1/2,j}^{k} - \sigma_{i-1/2,j}^{k}\right) \\
&\quad + \rho_{i,j}^{-1}\frac{\Delta t}{\Delta z}\left(\sigma_{i,j+1/2}^{k} - \sigma_{i,j-1/2}^{k}\right)
\end{aligned}
$$

$$
\begin{aligned}
w_{i+1/2,j+1/2}^{k+1/2} &= w_{i+1/2,j+1/2}^{k-1/2} + \rho_{i+1/2,j+1/2}^{-1}\frac{\Delta t}{\Delta x}\left(\sigma_{i+1,j+1/2}^{k} - \sigma_{i,j+1/2}^{k}\right) \\
&\quad + \rho_{i+1/2,j+1/2}^{-1}\frac{\Delta t}{\Delta z}\left(\zeta_{i+1/2,j+1}^{k} - \zeta_{i+1/2,j}^{k}\right)
\end{aligned}
$$

(2-90)

$$
\begin{aligned}
\sigma_{i+1/2,j}^{k+1} &= \sigma_{i+1/2,j}^{k} + \left(\lambda + 2\mu\right)_{i+1/2,j}\frac{\Delta t}{\Delta x}\left(v_{i+1,j}^{k+1/2} - v_{i,j}^{k+1/2}\right) \\
&\quad + \lambda_{i+1/2,j}\frac{\Delta t}{\Delta z}\left(w_{i,j+1}^{k+1/2} - w_{i,j}^{k+1/2}\right)
\end{aligned}
$$

$$
\begin{aligned}
\zeta_{i+1/2,j}^{k+1} &= \zeta_{i+1/2,j}^{k} + \left(\lambda + 2\mu\right)_{i+1/2,j}\frac{\Delta t}{\Delta x}\left(w_{i+1,j}^{k+1/2} - w_{i,j}^{k+1/2}\right) \\
&\quad + \lambda_{i+1/2,j}\frac{\Delta t}{\Delta z}\left(u_{i,j+1}^{k+1/2} - u_{i,j}^{k+1/2}\right)
\end{aligned}
$$

$$
\begin{aligned}
\xi_{i,j+1/2}^{k+1} &= \xi_{i,j+1/2}^{k} + \mu_{i,j+1/2}\frac{\Delta t}{\Delta z}\left(u_{i,j+1}^{k+1/2} - u_{i,j}^{k+1/2}\right) \\
&\quad + \mu_{i,j+1/2}\frac{\Delta t}{\Delta x}\left(w_{i+1,j}^{k+1/2} - u_{i,j}^{k+1/2}\right)
\end{aligned}
$$

The major difference between this and the usual sampling increment scheme is that the different components of the velocity field are not known at the same node. The actual size of each grid is identical to that of a more traditional equally spaced approach so staggering the grid does not change the overall size of the problem

Figure 2-18 and Figure 2-19 demonstrate staggered grid propagation graphically. The first of these figures show how the model parameters intermingle with data values at each grid node. The second figure shows how each stencil for each of the propagating wavefields is applied. Note that going from one time stamp to the next requires you to cycle through an application of four different stencils.

Figure 2-18. Distribution of variables and parameters (ρ, c_{ij}) in a 2D staggered grid mesh.

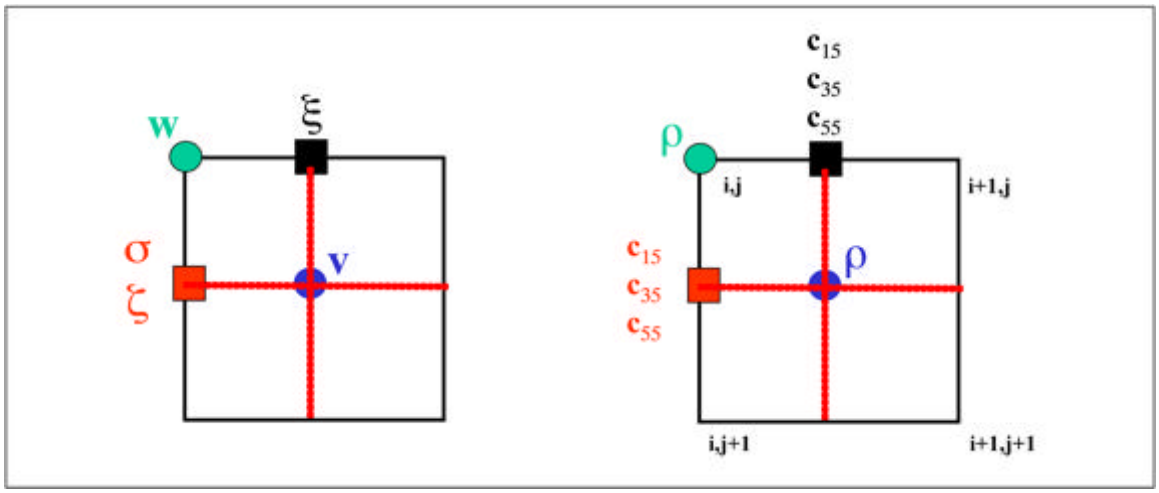

Figure 2-19. Staggered grid fnite difference stencils.

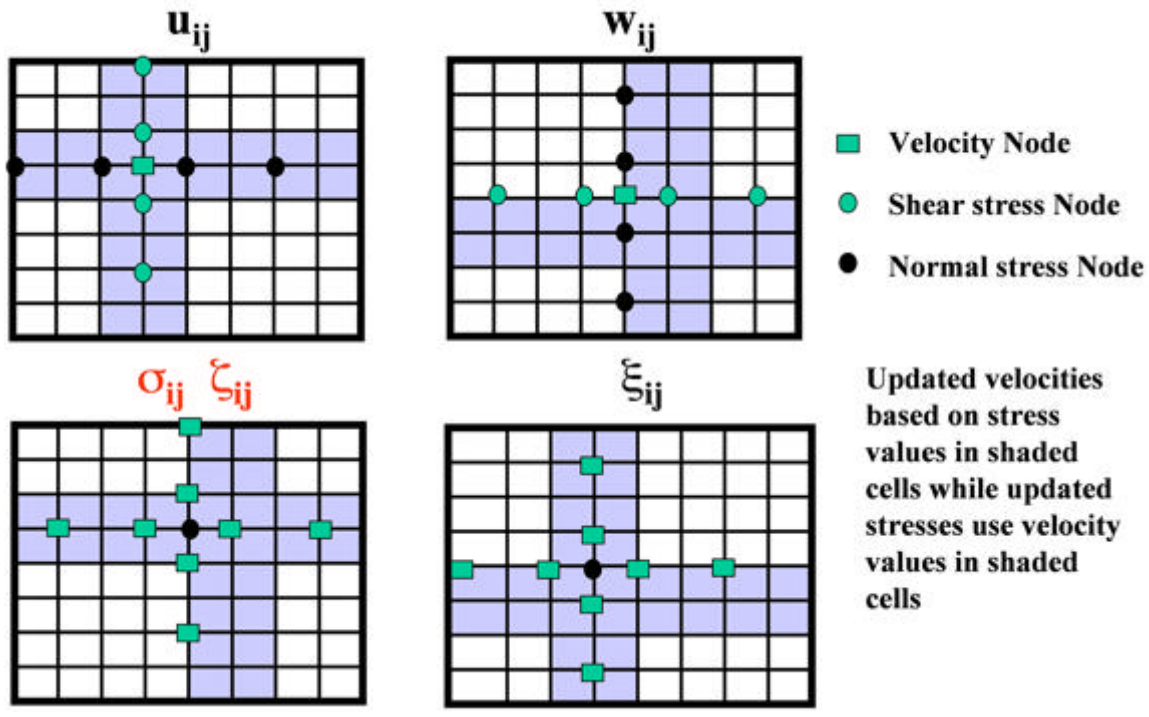

It is clear that synthesizing data over elastic models requires significantly more computational resources than when the model is acoustic. Simple isotropic elastic models are described by six volumes, while VTI and full elastic models require seven and eight volumes, respectively. In addition to this increase in storage, the computational load increases by at least one order of magnitude.

Figures 2-20 through 2-24 provide clear examples of simulations over both isotropic elastic and VTI models. Figure 2-20 illustrates an isotropic elastic version of the SEG/EAGE salt model along with representative inline compressional and shear responses. Figure 2-21 and Figure 2-22 show similar images over the Marmousi2 isotropic elastic model. Figure 2-23 and Figure 2-24 provide graphics of the full VTI model and VTI shot responses.

Figure 2-20. Isotropic elastic SEG/EAGE salt model with compressional and shear shot response.

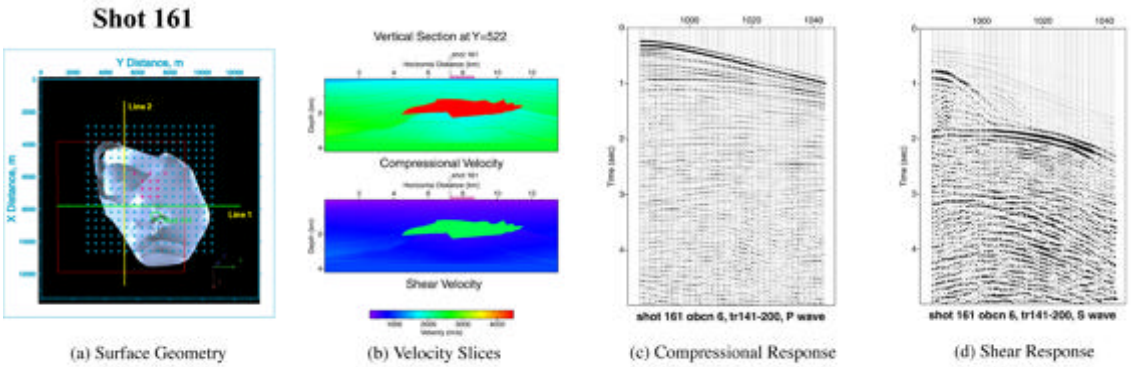

(a) Surface Geometry (b) Velocity Slices (c) Compressional Response (d) Shear Response

Figure 2-21. Marmousi2. Isotropic elastic version of the original Marmousi data.

(a). Compressional Velocity **(b).** Shear Velocity **(c).** Density

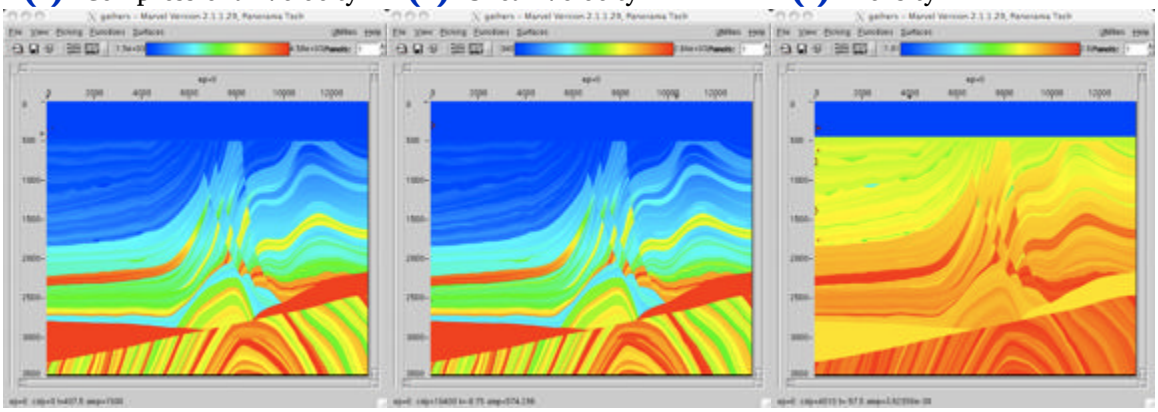

Figure 2-22. Marmousi2. Synthetic horizontal particle velocity and vertical particle velocity.

(a). Horizontal Shot-VSP **(b).** Vertical Shot-VSP

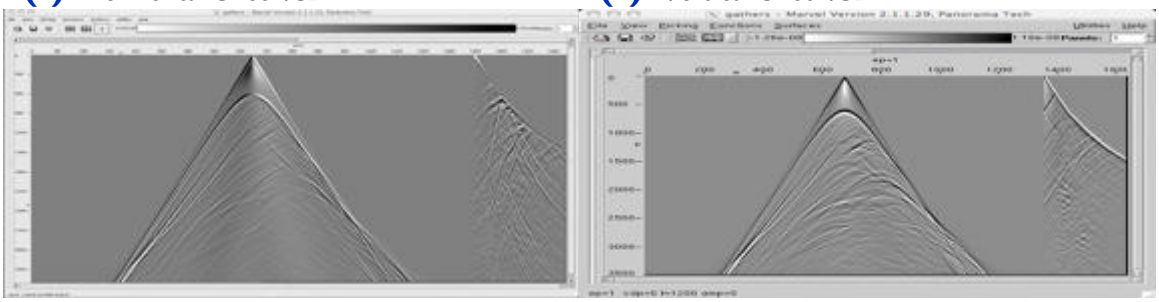

Figure 2-23. Hess Corporation VTI model. Available from the SEG.

(a). c11 **(b).** c13 **(c).** c33

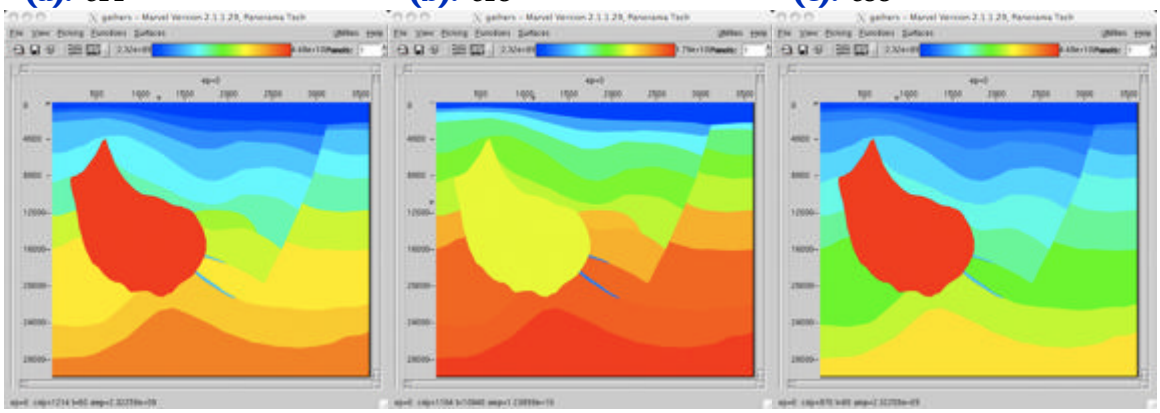

(d). c55 **(e).** Density

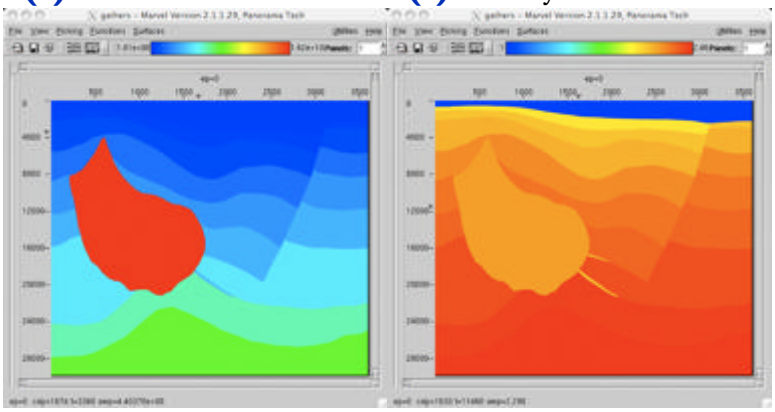

Figure 2-24. Hess-VTI. Synthetic Particle Velocities

(a). Horizontal Particle Velocity **(b).** Vertical Particle Velocity

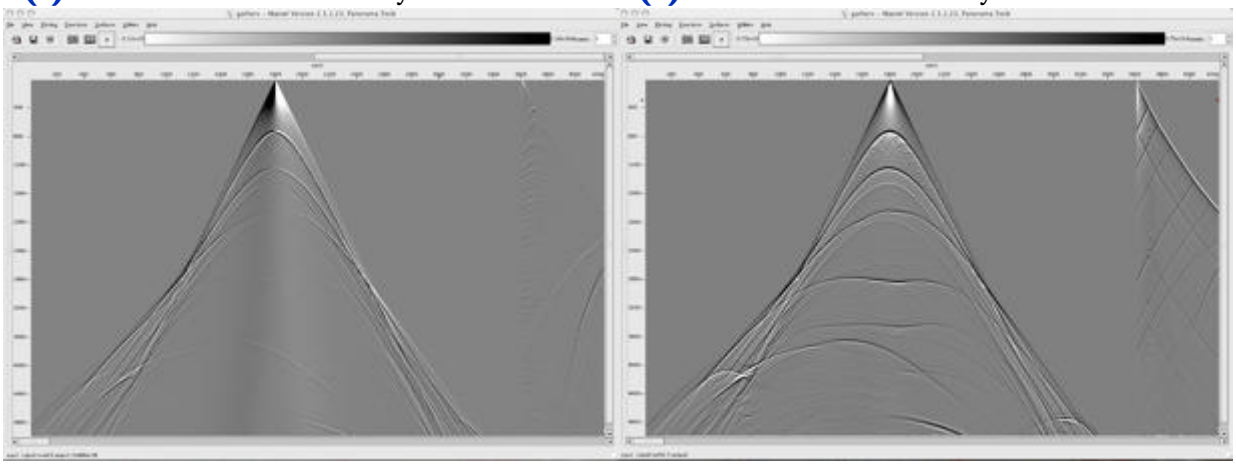

Predictor-Corrector Schemes

Equation 2-86 can be approximated by a first-order difference to produce the Euler or forward predictor scheme in Equation 2-91.

(2-91) $$\overline{\mathbf{v}}[(n+1)\Delta t] = \mathbf{v}(n\Delta t) + \Delta t\mathbf{H}\mathbf{v}(n\Delta t)$$

You can get a second order scheme by averaging the predicted value with the current value as shown in Equation 2-92.

(2-92) $$\mathbf{v}[(n+1)\Delta t] = \mathbf{v}(n\Delta t) + \frac{\Delta t}{2}[\mathbf{H}\mathbf{v}(n\Delta t) + \mathbf{H}\overline{\mathbf{v}}(n\Delta t)]$$

In this case, the x_1, x_2, and x_3 differentials are replaced with suitable central differences, and Equation 2-92 is used as a predictor-corrector scheme of second order.

Splitting

It is possible to rewrite Equation 2-81 as Equation 2-93, where $\mathbf{A}_0$, $\mathbf{B}_0$, and $\mathbf{E}_0$ are given by Equation 2-94 and Equation 2-95, respectively.

(2-93) $$\mathbf{E}\frac{\partial \mathbf{v}}{\partial t} = \mathbf{A}_0\frac{\partial \mathbf{v}}{\partial x} + \mathbf{B}_0\frac{\partial \mathbf{v}}{\partial y}$$

(2-94)
$$\mathbf{A_0} = \begin{bmatrix} 0 & 0 & 1 & 0 & 0 \\ 0 & 0 & 0 & 1 & 0 \\ 1 & 0 & 0 & 0 & 0 \\ 0 & 0 & 0 & 0 & 0 \\ 0 & 1 & 0 & 0 & 0 \end{bmatrix} \quad \mathbf{B_0} = \begin{bmatrix} 0 & 0 & 0 & 0 & 1 \\ 0 & 0 & 0 & 1 & 0 \\ 0 & 0 & 0 & 0 & 0 \\ 0 & 1 & 0 & 0 & 0 \\ 1 & 0 & 0 & 0 & 0 \end{bmatrix}$$

(2-95)
$$\mathbf{E_0} = \begin{bmatrix} \rho & 0 & 0 & 0 & 1 \\ 0 & \rho & 0 & 1 & 0 \\ 0 & 0 & \frac{\lambda+2\mu}{(\lambda+2\mu)^2-\mu^2} & \frac{-\mu}{(\lambda+2\mu)^2-\mu^2} & 0 \\ 0 & 0 & \frac{-\mu}{(\lambda+2\mu)^2-\mu^2} & \frac{\lambda+2\mu}{(\lambda+2\mu)^2-\mu^2} & 0 \\ 0 & 0 & 0 & 0 & \frac{1}{\mu} \end{bmatrix}$$

If we let $\mathbf{V} = \mathbf{E_0 v}$, $\mathbf{F} = \mathbf{A_0 v}$, and $\mathbf{K} = \mathbf{B_0 v}$, then Equation 2-93 takes the form of Equation 2-96.

(2-96)
$$\frac{\partial \mathbf{V}}{\partial t} = \frac{\partial \mathbf{F}}{\partial x} + \frac{\partial \mathbf{K}}{\partial y}$$

Equations of the form in Equation 2-96 are called *divergence free*. These equations are easily *split* into two much simpler equations which are then solved by splitting methods. The simple conceptual idea is to solve the equation in one direction and then the other, followed by reversing the solution order for the next time stamp. Suppose we let L_x represent one finite difference update using only the x variables and L_y represent one finite difference update using only the y variables. The general process for updating then uses the formula in Equation 2-97.

(2-97)
$$\mathbf{V^{n+2}} = L_x L_y L_y L_x \mathbf{V}^n$$

Thus, all we have to do is specify one or the other of the solution schemes L_x, or L_y, and we will have the other, completely by symmetry. A fourth order in space, second order in time predictor-corrector scheme for L_x takes the form of Equation 2-98.

(2-98)
$$\begin{aligned} \overline{\mathbf{V}}_{i,j} &= \mathbf{V}^k_{i,j} + \frac{\Delta t}{\Delta x}\left[(7\mathbf{F}^k_{i+1,j} - \mathbf{F}^k_{i,j}) - (\mathbf{F}^k_{i+2,j} - \mathbf{F}^k_{i+1,j})\right] \\ \mathbf{V}^{k+1}_{i+1,j} &= \frac{1}{2}\left[V^k_{i,j} + \overline{\mathbf{V}}_{i,j} + \frac{\Delta t}{\Delta x}\left\{(7\overline{\mathbf{F}}_{i,j} - \overline{\mathbf{F}}_{i-1,j}) - (\overline{\mathbf{F}}_{i-2,j} - \overline{\mathbf{F}}_{i-1j})\right\}\right] \end{aligned}$$

Propagation Stability

Each of the various finite difference methods you might construct contains a ratio of the form $\frac{v\Delta t}{\Delta v}$, where v is one of the spatial increments Δx, Δy or Δz. It might come as somewhat of a surprise that if this ratio is too large, the propagation scheme it helps define will not be stable. An unstable scheme will eventually produce excessively large numbers and exceed the numerical accuracy of the machine it is running on.

Derivation of a formula that can provide an accurate bound for these ratios requires that we first relate frequency to wavenumber. To do this in a simple manner, we begin with the 1-D version of the Lax-Wendroff discrete pressure equation (Equation 2-17), as shown in Equation 2-99, where v is velocity.

$$\frac{1}{\Delta t^2}\left(p(t+\Delta t) - 2p(t) + p(t-\Delta t) - \sum_{i=2}^{i=\infty} \frac{\partial^{2i} p}{\partial t^{2i}} \frac{\Delta t^{2i}}{2i!}\right) = v^2 \frac{\partial^2 p}{\partial t^2} \tag{2-99}$$

To make our life a bit easier, we assume a solution of the form $\exp[ik_x x - \omega\Delta t]$ and ignore the higher order terms to obtain the dispersion relation in Equation 2-100 and Equation 2-101.

$$\frac{1}{\Delta t^2}[2\cos(\omega\Delta t) - 2] = \frac{4}{\Delta t^2}\sin^2\left(\frac{\omega\Delta t}{2}\right) = v^2 k_x^2 \tag{2-100}$$

$$\frac{2}{\Delta t}\sin\left(\frac{\omega\Delta t}{2}\right) = v k_x \tag{2-101}$$

Although the true dispersion relation for the 1-D equation has $c = \frac{\omega}{k_x}$, Equation 2-102 says that the discrete velocity is greater than the true velocity.

$$\bar{v} = \frac{v}{\frac{\sin(\pi f \Delta t)}{\pi f \Delta t}} \tag{2-102}$$

Thus, to avoid explosive growth, we must have the relation in Equation 2-103.

$$\Delta t \le \frac{2}{\pi}\left(\frac{\Delta x_{min}}{v_{max}}\right) \tag{2-103}$$

A similar analysis shows that to achieve stable isotropic elastic ($P - SV$) waves, we must have the relation in Equation 2-104.

$$\Delta t \le \frac{\Delta x_{min}}{\sqrt{v_P^2 + v_{SV}^2}} \tag{2-104}$$

The important aspect of this analysis is that we cannot choose our time step size arbitrarily. We must use the appropriate version of Equation 2-103 or Equation 2-104 to assure ourselves that the calculations we perform and, consequently, the waveform we produce will not grow exponentially.

Model Boundaries

This section describes the things we must do to handle model boundaries, which can consist of either free or non-free surfaces.

Free Surfaces

Handling a free surface is probably the most complex of the various problems that arise in seismic modeling exercises. The literature on this aspect of the synthesis is quite vast and outside the scope of what we wish to discuss here. We leave detailed investigation of this to you, if you are interested.

However, one of the more appealing methods is discussed by Lavendar in his 1988 paper on P-SV modeling, and illustrated in Figure 2-25. The essential difference lies in how each layer is handled. Turning free surface reverberations on (or off) controls whether or not synthetic data contains multiples and ghosts.

Figure 2-25. Free Surface versus Non-Free Surface Layers

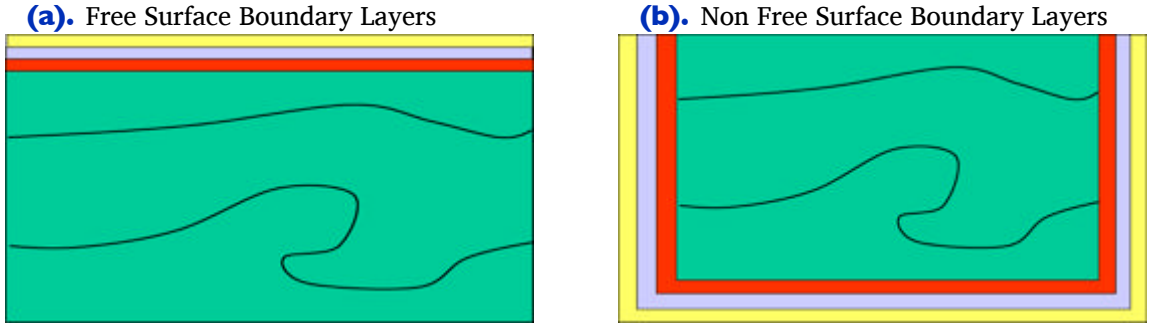

The free surface at the top of the model is padded above with a fictitious set of nodes. Since a free surface implies that no normal or shear stresses are active there, we can set $\tau_{2,2} = 0$ and $\tau_{1,2} = 0$ at the top. The shear stress boundary condition is handled by setting it to zero at $z = 0$ as well. The normal stress is not defined at the top boundary but is forced to zero by making the normal stress antisymmetric for the first two rows above

the free surface, as shown in Equation 2-105.

$$(\tau_{22})_{-1,i} = -(\tau_{22})_{0,i}$$
$$(\tau_{22})_{-2,i} = -(\tau_{22})_{1,i} \quad (2\text{-}105)$$

Non Free Surfaces

There are a variety of approaches for handling the other boundaries in a typical seismic Earth model. The three most popular methods are what are called sponge boundary conditions: Absorbing, boundary conditions, and the so-called perfectly matched layers.

Sponge Boundaries—Absorbing

The idea behind sponge boundary conditions is to modify the propagating equation by adding viscosity to the equation along the boundary. This is normally accomplished by writing Equation 2-106, where γ is an absorbing parameter chosen to produce a wave that decreases in amplitude with distance.

$$\frac{\partial}{\partial t}\begin{bmatrix} p \\ q \end{bmatrix} = \begin{bmatrix} -\gamma & 1 \\ -\rho v^2 \nabla \cdot \frac{1}{\rho}\nabla & -\gamma \end{bmatrix}\begin{bmatrix} p \\ q \end{bmatrix} + \begin{bmatrix} 0 \end{bmatrix} \quad (2\text{-}106)$$

The value of γ is usually chosen to have exponential decay within the defined boundary zone and is zero within the model dimensions. Note that when $\gamma = 0$, the solution to the equation is, in fact, p.

For the finite element method, sponge boundaries can be implemented by changing the definition of $\varphi(U, V)$ to Equation 2-107, where α and β are the damping factors in each of the boundary layers.

$$\varphi(U, V) = (1 + \alpha)\int_{\Omega} \frac{k^2}{\rho} UV d\Omega + \left(\beta + 1\right)\int_{\Omega} \frac{1}{\rho}\nabla U \cdot \nabla V d\Omega \quad (2\text{-}107)$$

Sponge Boundaries—Paraxial Boundary Conditions

Paraxial boundaries are based on the one-way wave equation and within the boundary layers take the form in Equation 2-108, where $|\alpha_j| < \frac{\pi}{2}$ for all j (Higdon 1991).

$$\left\{\prod_{j=1}^{j=J}\left[\left(cos\alpha_j\right)\frac{\partial}{\partial t} - v\frac{\partial}{\partial x}\right]\right\} p = 0 \quad (2\text{-}108)$$

This equation works because each factor, $\cos(\alpha_j)\frac{\partial p}{\partial t} - v\frac{\partial p}{\partial x}$, is an annihilator of any wave arriving at an angle α_j.

Sponge Boundaries—Perfectly Matched Layers

Perfectly matched layers are a modern treatment of the sponge boundary conditions. In this setting, the spatial derivatives are modified so that we have Equation 2-109.

(2-109)
$$\frac{\partial}{\partial x} \longrightarrow \frac{1}{1 + \frac{i\sigma(x)}{\omega}} \frac{\partial}{\partial x}$$

FEM versus FDM Differences

The finite element method (FEM) and finite difference method (FDM) are alternative ways of approximating solutions of partial differential equations. The differences between FEM and FDM are:

- FDM is an approximation to the differential equation while FEM is an approximation to its solution.
- The most attractive feature of FEM is its ability to handle complicated geometries (and boundaries) with relative ease. While FDM is restricted, in its basic form, to handling rectangular shapes and simple alterations of those shapes, the handling of geometries in FEM is theoretically straightforward.
- The most attractive feature of FDM is that it can be very easy to implement and does not require the inversion of an extremely large matrix.
- In some cases, FEM can be considered to be equivalent to FDM. Choosing basis functions as either piecewise constant functions or Dirac delta functions produce a FDM type method. In both approaches, the approximations are defined on the entire domain, but need not be continuous.
- FEM is generally considered to be more mathematically sound then FDM, and more accurate. Typically, the quality of the approximation between grid points is excellent in FEM but poor in FDM.
- The quality of an FEM approximation is often higher than in the corresponding FDM approach, but this is extremely problem dependent. There are numerous examples to the contrary.

Generally, FEM is the method of choice in all types of structural analysis problems, but it has not proven to be of tremendous value in seismic simulation or migration. The biggest reason for this is the tremendous size of the impedance matrix, **S**, which means it is quite difficult to handle.

Two-Way Implicit Modeling

With the exception of the finite element method, the two-way approaches described earlier are what are usually referred to as *explicit* schemes. They forward march source samples one step at a time. The finite element method is close to an *implicit* approach since finding the solution requires the inversion of a matrix. There are certainly approaches to seismic modeling that can be framed in an implicit sense, but those are equation dependent and will not be discussed further in this book.

One-Way Modeling

Although its not quite mathematically correct, Equation 2-17 is sometimes factored into two first order equations. The factorization leads to two separate first-order equations in z. Equation 2-110 illustrates the nature of the factorization.

$$\left(\frac{\partial}{\partial z} - \sqrt{\frac{1}{v^2}\frac{\partial^2}{\partial t^2} - \frac{\partial}{\partial x}\frac{1}{\rho}\frac{\partial}{\partial x}}\right)\left(\frac{\partial}{\partial z} + \sqrt{\frac{1}{v^2}\frac{\partial^2}{\partial t^2} - \frac{\partial}{\partial x}\frac{1}{\rho}\frac{\partial}{\partial x}}\right)p = 0 \tag{2-110}$$

In the case where the density, ρ, is constant, or, even better, equal to 1, the equations simplify further and are what are usually used when applied as part of a migration.

Clearly, the thought process to arrive at this product assumes that the two cross-product terms commute, and thus their difference is zero, but this assumption of commutation is simply not mathematically correct. Nevertheless, is can be shown that suitable approximations to either of the first-order equations that result from the factorization honor the wavefront travel times of the original two-way equation. Because wavefields are no longer allowed to travel in any direction other than upward or downward, the amplitude of the propagation cannot be correct.

In the case of normal full-wave propagation, the impinging wavefield energy creates a new source at the point of impact. Regardless of source wavefield type (that is, compressional or shear), the new source radiates energy in all directions weighted by the reflection strength for upward traveling wave, transmission strength for the downward traveling waves, and angle of the reflecting bed. This is an extremely important concept for all of the discussion that follows. It actually allows us to think in terms of separating wavefields into upward only and downward only propagation directions. Each factor in Equation 2-110 does precisely that. The first factor governs downward only traveling waves while the second permits only upward traveling waves.

Once a suitable approximation for the square root term has been found, almost any of these methods can be applied to synthesize data of the type required by the equation. That is, when the downward factor is used, you can propagate wavefields downward but not upward; when the upward factor is used, you can propagate wavefields upward but not downward. Thus, these equations greatly limit the extent to which full wavefield seismic can be generated.

One Way Implicit Finite Difference Methods

There are many known approximations for the square root in Equation 2-110. Each such approximation has its own pros and cons, and each has its own unique limit to the downward propagation angle it will tolerate. One of the better known square-root approximations is Equation 2-111.

$$\sqrt{1 - X^2} = 1 - \frac{4 - 3X^2}{4 - X^2} \tag{2-111}$$

If we apply this approximation to the square root in Equation 2-110, we obtain Equation 2-112.

$$\sqrt{\frac{1}{v^2}\frac{\partial^2}{\partial t^2} - \frac{\partial}{\partial x}\frac{1}{\rho}\frac{\partial}{\partial x}} \approx \frac{1}{v}\frac{\partial}{\partial t} - \frac{\frac{4}{v^2}\frac{\partial^2}{\partial t^2} - 3\frac{\partial}{\partial x}\frac{1}{\rho}\frac{\partial}{\partial x}}{\frac{4}{v^2}\frac{\partial^2}{\partial t^2} - \frac{\partial}{\partial x}\frac{1}{\rho}\frac{\partial}{\partial x}} \tag{2-112}$$

Equation 2-112 leads directly to a downward propagation equation of the rather complex form in Equation 2-113.

$$\frac{\partial p}{\partial z} = \frac{1}{v}\frac{\partial p}{\partial t} - \frac{\frac{4}{v^2}\frac{\partial^2 p}{\partial t^2} - 3\frac{\partial p}{\partial x}\frac{1}{\rho}\frac{\partial p}{\partial x}}{\frac{4}{v^2}\frac{\partial^2}{\partial t^2} - \frac{\partial}{\partial x}\frac{1}{\rho}\frac{\partial}{\partial x}} \tag{2-113}$$

At first glance, this equation may seem to be somewhat intractable for any finite difference approach. The trick to putting this into a more useable form is to clear fractions to obtain Equation 2-114.

$$\left(\frac{4}{v^2}\frac{\partial^2 p}{\partial t^2} - \frac{\partial p}{\partial x}\frac{1}{\rho}\frac{\partial p}{\partial x}\right)\frac{\partial p}{\partial z} = \left(\frac{4}{v^2}\frac{\partial^2 p}{\partial t^2} - \frac{\partial p}{\partial x}\frac{1}{\rho}\frac{\partial p}{\partial x}\right)\frac{1}{v}\frac{\partial p}{\partial t} + 3\frac{\partial p}{\partial x}\frac{1}{\rho}\frac{\partial p}{\partial x} - \frac{4}{v^2}\frac{\partial^2 p}{\partial t^2} \tag{2-114}$$

Equation 2-114 in 3D becomes Equation 2-115.

$$\begin{aligned}\left(\frac{4}{v^2}\frac{\partial^2 p}{\partial t^2} - \frac{\partial p}{\partial x}\frac{1}{\rho}\frac{\partial p}{\partial x} - \frac{\partial p}{\partial y}\frac{1}{\rho}\frac{\partial p}{\partial y}\right)\frac{\partial p}{\partial z} \;=\; &\left(\frac{4}{v^2}\frac{\partial^2 p}{\partial t^2} - \frac{\partial p}{\partial x}\frac{1}{\rho}\frac{\partial p}{\partial x} - \frac{\partial p}{\partial y}\frac{1}{\rho}\frac{\partial p}{\partial y}\right)\frac{1}{v}\frac{\partial p}{\partial t} \\ &+ 3\left(\frac{\partial p}{\partial x}\frac{1}{\rho}\frac{\partial p}{\partial x} + \frac{\partial p}{\partial y}\frac{1}{\rho}\frac{\partial p}{\partial y}\right) - \frac{4}{v^2}\frac{\partial^2 p}{\partial t^2}\end{aligned} \tag{2-115}$$

If we then approximate the derivatives via some form of the finite difference stencils discussed in previous sections, we can rearrange the problem, converting Equation 2-113 into a matrix style system of the form in Equation 2-116.

$$\mathbf{A}p(z + \Delta z) = \mathbf{B}p(z) \tag{2-116}$$

Solving this system amounts to inverting **A**. The need to employ finite-differences in time can make this a very complicated task in 3D. Consequently, this XT method has not enjoyed a lot of popularity in either forward modeling or imaging for 3D projects.

Fourier-Based Methods

This section discusses the several Fourier-based methods for solving modeling and imaging projects.

FX Finite Difference Methods

The factorization in Equation 2-110 can also be done in the Fourier or frequency domain by simply rewriting it in the form of Equation 2-117.

(2-117) $$\left(\frac{\partial}{\partial z} - i\sqrt{\frac{\omega^2}{v^2} + \frac{\partial}{\partial x}\frac{1}{\rho}\frac{\partial}{\partial x}}\right)\left(\frac{\partial}{\partial z} + i\sqrt{\frac{\omega^2}{v^2} + \frac{\partial}{\partial x}\frac{1}{\rho}\frac{\partial}{\partial x}}\right)p = 0.$$

In this case, Equation 2-114 becomes Equation 2-118.

(2-118) $$\left(\frac{4\omega^2}{v^2}p + \frac{\partial p}{\partial x}\frac{1}{\rho}\frac{\partial p}{\partial x}\right)\frac{\partial p}{\partial z} = \left(\frac{4\omega^2}{v^2}p + \frac{\partial p}{\partial x}\frac{1}{\rho}\frac{\partial p}{\partial x}\right)\frac{i\omega}{v}p - 3\frac{\partial p}{\partial x}\frac{1}{\rho}\frac{\partial p}{\partial x} - \frac{4\omega^2 p}{v^2}$$

In 3D, Equation 2-118 becomes Equation 2-119.

(2-119) $$\left(\frac{4\omega^2}{v^2}p + \frac{\partial p}{\partial x}\frac{1}{\rho}\frac{\partial p}{\partial x} + \frac{\partial p}{\partial y}\frac{1}{\rho}\frac{\partial p}{\partial y}\right)\frac{\partial p}{\partial z} = \left(\frac{4\omega^2}{v^2}p + \frac{\partial p}{\partial x}\frac{1}{\rho}\frac{\partial p}{\partial x} + \frac{\partial p}{\partial y}\frac{1}{\rho}\frac{\partial p}{\partial y}\right)\frac{i\omega}{v}p - \left(3\frac{\partial p}{\partial x}\frac{1}{\rho}\frac{\partial p}{\partial x} + \frac{\partial p}{\partial y}\frac{1}{\rho}\frac{\partial p}{\partial y}\right) - \frac{4\omega^2 p}{v^2}$$

Equation 2-119 has the generalized form in Equation 2-120.

(2-120) $$\mathbf{A}(\omega)p(z + \Delta z) = \mathbf{B}(\omega)p(z)$$

Once again, inversion of $\mathbf{A}(\omega)$ is a necessity. In the frequency domain, this matrix is normally diagonally dominant and usually relatively easy to compute. Note that we are

solving this as an equation in z for each ω. We are in effect computing $p(z + \Delta z)$ from $p(z)$ so that the $\mathbf{A}(\omega)$ matrix has two dimensions and not three. This further simplifies the issue and makes this method one of the more tractable one way implicit methodologies. Nevertheless, the process is not straightforward and usually requires a splitting approach to make it efficient.

One clear advantage of this approach to one-way forward modeling is the elimination of finite difference approximations in time. In the frequency domain, the partial differentials are simple complex multiplications. Since they are applied across the entire frequency band, the temporal derivatives are as precise as they can be.

Pseudo-Spectral Methods

Pseudo-spectral methods are based on the utilization of Fourier transforms in the calculation of spatial derivatives (see D. Kosloff and E. Baysal). Again, using the 2D version of Equation 2-17 as the base, we first apply a central difference scheme in the time direction and then use Fourier transforms to calculate all spatial derivatives. As an example, consider the discrete formulation in Equation 2-121, where L represents the discrete operator containing the spatial derivatives in both x and z.

(2-121) $$p_{i,j}^{k+1} = 2p_{i,j}^{k} - p_{i,j}^{k-1} - v^2 \Delta t^2 L p_{i,j}^{k} + s_{i,j}^{k}$$

To calculate the discrete version of the term $\frac{\partial p}{\partial x}\frac{1}{\rho}\frac{\partial p}{\partial x}$, we first Fourier transform in the x-direction on p, multiply by the discrete-spatial wave-number ik_x, and then inverse Fourier transform to get $\frac{\partial p}{\partial x}$.

This is followed by a repeat of a Fourier-multiply-Fourier inverse step to get $\frac{\partial p}{\partial x}\frac{1}{\rho}\frac{\partial p}{\partial x}$.

When the process has been completed along all x-lines, a similar calculation is performed to get $\frac{\partial p}{\partial z}\frac{1}{\rho}\frac{\partial p}{\partial z}$.

Working in 3D is just as simple and requires only that we perform one more transform sequence in the y direction.

The great advantage of this process is accuracy. Using the Fourier transform for the spatial derivatives is identical to applying a central difference with the number of coefficients equal to the half length of the discrete transform.

Once we understand that the Fourier transformation converts differentials, $\frac{\partial u}{\partial x}$, into frequency domain multiplications of the form $ik_x u(x)$, it is quite natural to want to Fourier transform Equation 2-17 over all variables and convert the resulting PDE into a simple algebraic equation. Unfortunately, because the velocity, $v(x,y,z)$, and the

density, $\rho(x,y,z)$, are both potentially functions of three independent variables, Fourier transformation would result in a frequency domain convolution, which is not a much simpler algebraic equation.

Constant Velocity FK Modeling

When the velocity, v, is constant, Fourier transformation over all the variables produces Equation 2-122 everywhere except at the source.

(2-122) $$(k_z^2 + k_z^2 - \frac{\omega^2}{v^2})\, u(k_z, k_x, \omega) = 0$$

Thus, for k_z and $u(k_z, k_x, \omega)$, we get Equation 2-123 and Equation 2-124, respectively.

(2-123) $$k_z = \pm\sqrt{\frac{\omega^2}{v^2} - k_x^2}$$

(2-124) $$u(k_z, k_x, \omega) = u\left(\sqrt{\frac{\omega^2}{v^2} - k_x^2}, k_x, \omega\right)$$

The key point is that we only need to know $p(z = 0, x, t)$ to determine k_z through a Fourier transform over x and t.

Thus, to do modeling, we simply define $p(0, x_0, t) = s(x_0, t)$, set $p(0, x, t) = 0$ elsewhere, Fourier transform over x and t, define $p(k_z, k_x, \omega)$ through Equation 2-123, and then inverse transform to get our one-way modeled data $p(z, x, t)$. Whether this represents upward or downward traveling waves is purely dependent on the choice of sign in Equation 2-123.

Since this method is almost totally dependent on extremely efficient Fourier transforms, you would think that modeling using this method would be very popular. Unfortunately, the equations in this section are valid only when the velocity is constant. As we will see, overcoming this limitation has produced many of the modern one-way algorithms for imaging, but has not resulted in a satisfactory formalism for detailed high resolution modeling. Methods in this section can progress wavefields in one direction or the other, but unlike the two-way methods, they do not automatically generate waves traveling in every possible direction.

Phase-Shift Modeling

When the velocity, $v = v(z)$, is just a function of z alone, and the density, ρ, is constant, we can Fourier transform over t, x to get Equation 2-125.

(2-125) $$\frac{\partial^2 p}{\partial z^2} = \left[-\frac{\omega^2}{v^2(z)} + k_x^2\right] p$$

If we now factor Equation 2-125 and choose the downward propagating equation as the one of interest, we can write Equation 2-126.

(2-126) $$\frac{\partial p}{\partial z} = -\left[\sqrt{\frac{\omega^2}{v^2(z)} - k_x^2}\right] p$$

If we think of this equation as a first order ordinary differential equation in z, we can immediately write its solution in the form of Equation 2-127, where k_z has the value in Equation 2-128.

(2-127) $$p(k_x, z + \Delta z, \omega) = \exp[ik_z \Delta z]\ p(k_x, z, \omega)$$

(2-128) $$k_z = \sqrt{\frac{\omega^2}{v^2(z)} - k_x^2}$$

Note that the exponential term in Equation 2-127 represents a pure phase shift for each frequency ω. The process is visualized quite naturally in Figure 2-26. Starting at the top for downward propagation and at the bottom for upward propagation, the one-way phase shift method simply shifts the wavefield from one layer to the next in a simple and straightforward manner. To start the modeling process, you initialize the wavefield $p(z = 0, x_0, t) = s(x_0, t)$ at $z = 0$ with a suitable source, Fourier transform over time and begin downward propagation using Equation 2-127

Figure 2-26. FK domain depth-slice by depth-slice continuation for $v(z)$ velocity models. This is called phase shift modeling.

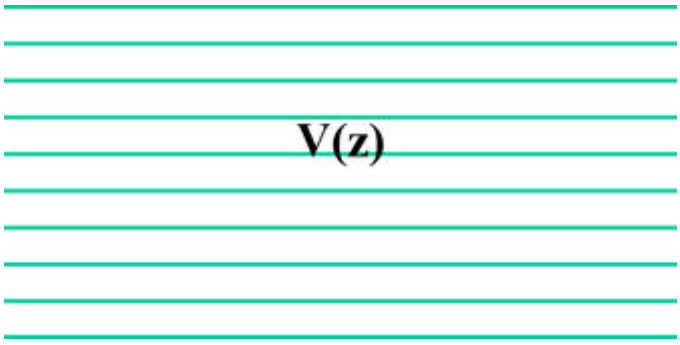

While we recognize that the accuracy of the phase-shift method is highly dependent on the number of terms we use to approximate the series for the exponential, the ultimate accuracy is dependent only on the current computer language approximations for the exponential and the square root. The ultimate limitation of this method, like the pure FK method discussed previously, is the restriction that the velocity vary only in the vertical direction. The frequency slice process specified by Equation 2-127 has an immediate and more or less obvious extension to 3D.

Phase Shift Plus Interpolation (PSPI) Modeling

When the sound speed, $v(x,z)$, varies laterally as well as vertically, the wavefield shifts are no longer uniform. One approach to handling this problem is to first perform a number, n, of pure phase shifts using a uniform set of of velocities lying between the minimum and maximum values of $v(x,z)$. Interpolation of the appropriate wavefields at any given x along the common depth slice at z approximates the wavefield corresponding to the true velocity $v(x,z)$ at x. Figure 2-27 illustrates the concept.

Figure 2-27. PSPI FK domain depth-slice by depth-slice continuation for $v(x,z)$ velocity models.

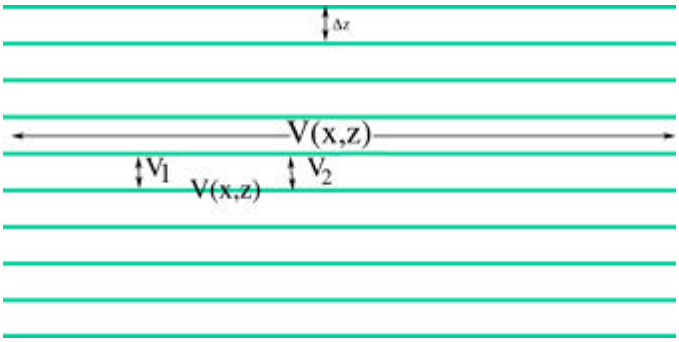

The problem with this approach revolves around the complexities of performing the interpolation. Key questions arise as to whether interpolation in space-time or frequency-space is the more optimum method. Because of the difficulties associated with the need for interpolation, PSPI continuations frequently have difficulty imaging steeply dipping events. As a result, considerable research focused on finding a better approach.

Dual Domain or FKX One-Way Methods

Because of the incredible efficiency of the Fast Fourier transform, it did not take long for several authors to investigate the possibility of avoiding the need for wavefield interpolation by using approximations that split the computations between the FK and FX domains. This required multiple transforms for each up or down shift, but because of the efficiency of the Fourier transform, this was considered worth the extra effort. The idea underlying this form of the process is again a Taylor series approximation. If the velocity, $v(x,z)$ varies laterally, the first-term Taylor series expansion of the k_z term in Equation 2-128 around some fixed reference velocity, $v_{ref} = v_{ref}(z)$, has the form of Equation 2-129, where $s_{ref} = \frac{1}{v_{ref}}$ is the reference slowness and $k_z^{ref} = \sqrt{s_{ref}^2\omega^2 - k_x^2}$.

(2-129)
$$k_z = k_z^{ref} + \frac{dk_z}{ds_{ref}}\Delta s$$

In this case,

(2-130) $$\frac{dk_z}{ds_{ref}} = \frac{\omega}{\sqrt{s_{ref}^2\omega^2 - k_x^2}}$$

Using the approximation in Equation 2-111, a little algebraic manipulation yields Equation 2-131, so that Equation 2-132, where $k_{ref}^2 = \frac{\omega^2}{v_{ref}^2}$.

(2-131) $$\frac{dk_z}{ds_{ref}} = \omega\left[1 + \frac{2k_x^2}{4k_{ref}^2 - 3k_x^2}\right]$$

(2-132) $$k_z \approx \sqrt{k_{ref}^2 - k_x^2} + \omega\Delta s + \omega\Delta s\frac{2k_x^2}{4k_{ref}^2 - 3k_x^2}$$

You could, of course, use additional terms of the Taylor series to try to increase the accuracy of the approximation, but, as we will see, the third term in Equation 2-132 can be quite difficult to implement.

Split-Step Methods

Paul Stoffa at the University of Texas in Austin was one of the first to utilize Equation 2-132. He and his colleagues in Austin and at Delft University in Holland simply truncated the series for k_z to Equation 2-133, and then noted that the first term was just a phase shift in the FK domain while the second is a similar phase-shift in the FX domain.

(2-133) $$k_z \approx \sqrt{k_{ref}^2 - k_x^2} + \omega\left[\frac{1}{v} - \frac{1}{v_{ref}}\right]$$

Summing over all frequencies produces the image at the current Δz. Fourier transforming back to the FK domain begins the process for the next $z + \Delta z$. Although this method proves to be somewhat inaccurate when compared to good implementations of PSPI, it is significant in that it requires no interpolation at all. It provides a direct correction in the FX domain after an initial phase shift.

Extended Split Step Methods

The extended phase screen method is probably more accurately referred to as split-step plus interpolation or $SSPI$. It attempts to increase the overall accuracy of the preceding process by using multiple reference velocities in exactly the same manner as $PSPI$.

Higher Order FKX Methods

Higher order methods based on Equation 2-132 must find ways to handle the third term, Equation 2-134.

(2-134) $$k_z^{fd} = \omega \Delta s \frac{2k_x^2}{4k_{ref}^2 - 3k_x^2}$$

While it might appear that this term can be handled directly by some form of transform between the FK and KX or maybe FX domains, the denominator implies the existence of a singularity and therefore a potentially difficult instability. Two approaches have evolved in an attempt to handle the instability. One is the phase-screen or pseudo-phase screen method of Ru Shan Wu at the University of California at Santa Cruz and the other is the Fourier Finite Difference (FFD) method of D. Ristow and T. Rühl. In fact, both of these methods use what is called an implicit finite difference technique to implement the term stably.

Note that from an implementation point of view, what we do in practice is first form Equation 2-135, inverse Fourier transform over k_x and form Equation 2-136, and finally try to compute Equation 2-137 in some domain or the other.

(2-135) $$p_1(k_x, z + \Delta z, \omega) = \exp\left(ik_z^{ref} \Delta z\right) p(k_x, z, \omega)$$

(2-136) $$p_2(x, z + \Delta z, \omega) = \exp\left(i\omega \Delta s \Delta z\right)$$

(2-137) $$p(x, z + \Delta z, t) = \exp\left(ik_z^{fd} \Delta z\right) p_2(k_x, z, \omega)$$

It should be clear that because the third term contains both spatial and wavenumber terms, this calculation might not be straightforward. The actual trick is to approximate the exponential one more time in the form of Equation 2-138, substitute into Equation 2-137, and clear fractions to get Equation 2-139.

(2-138) $$\exp\left(ik_z^{fd} \Delta z\right) = \frac{1 + i\omega \Delta s \frac{2k_x^2}{4k_{ref}^2 - 3k_x^2} \frac{\Delta z}{2}}{1 - i\omega \Delta s \frac{2k_x^2}{4k_{ref}^2 - 3k_x^2} \frac{\Delta z}{2}}$$

(2-139) $$\left(4k_{ref}^2 - 3k_x^2 - i\omega \Delta s 2k_x^2 \Delta z\right) p(k_x, z + \Delta z, \omega) = \left(4k_{ref}^2 - 3k_x^2 + i\omega \Delta s 2k_x^2 \Delta z\right) p_2(k_x, z, \omega)$$

If we now inverse transform back to the FX domain, we see that each k_x^2 term becomes a second order partial derivative with respect to x. When these are replaced by central difference approximations, we arrive at a matrix equation of the form in Equation 2-140, so that Equation 2-141.

(2-140) $$\mathbf{Ap} = \mathbf{Bp}_2$$

(2-141) $$\mathbf{p} = \mathbf{A}^{-1}\mathbf{Bp}_2$$

What is nice about this method is that the matrix **A** is usually sparse with a limited number of terms along the diagonal, so in 2D, as described here, inverting the matrix is relatively fast. Moreover, the result is easily stabilized.

However, in 3D, the equivalent **A** matrix is huge and is quite difficult to invert. The problem is usually solved by a splitting technique similar to that in previous sections. Essentially, Equation 2-139 is solved in the x-direction, and then the similar y-direction formula is used to provide a solution in that direction. These methods are alternated as the process proceeds depth-slice by depth-slice until all data is propagated to the appropriate depth.

Figure 2-28 is a simple graphic of how one-way propagators work. Figure 2-28(a) provides the schema for synthesizing purely downward traveling waves, and part (b) is the corresponding propagator for purely upward traveling waves. While these kinds of propagators limit the type of wave that can be propagated, their significance lies mostly in the fact that they are much more computationally efficient then the full two-way versions shown in previous figures. One-way computations can be performed on a depth-slice by depth-slice basis so there is no need to fill in the value at every previous node before continuing. Moreover, extremely efficient Fourier domain methods can be used to reduce computational complexity even further. As a result, one-way methods have enjoyed great popularity and have been the subject of considerable research.

Figure 2-28. A one-way propagator. The black dots have been removed from the propagating stencil. Graphic (a) calculates only downward traveling waves while (b) only permits upward traveling waves.

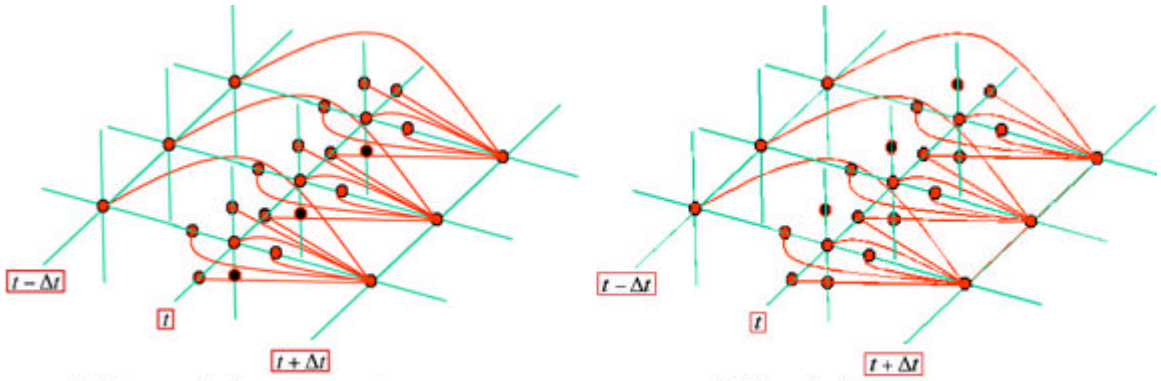

(a) Downward only wave propagator (b) Upward only wave propagator

A Word About Sources

This section describes the sources used to generate the sound waves that are at the center of the seismic migration and modeling process.

Compressional and Shear Point Sources

So far the discussion has been focused on compressional, wave-point sources. Theoretically, such sources radiate energy uniformly in all directions. Mainly because they are easy to generate, point-sources represent the norm in modern seismic data synthesis and acquisition. In media that support shear wave propagation, pure compressional sources also generate shear waves uniformly in all directions. In contrast, real shear wave sources are not so easy to generate, and are impossible to generate in any liquid. Over any media that supports their propagation, shear waves are frequently generated using some kind of scratcher or angled compressional source. In the first case, the scratcher is actually generating a physical source that is fundamentally angled downward, while in the second case the angled compressional source generates most of its energy close to the angle of the compression gun. In either case, the resulting converted-shear wave is frequently too weak to generate sufficient energy for practical use.

Plane Wave Sources

Plane wave sources are all but impossible to generate in the field. However, any reasonable set of shot profiles, $u(x_s, x_r, t)$, from either real data or synthetic data, can be transformed to simulate a plane wave source at some fixed position, x_{s_0}, by simply performing a slant stack over the sources surrounding this central point. The mathematical formula for this in 2D is given by Equation 2-142.

(2-142) $$U(p_s, x_{s_0}, x_r, \tau) = \int u(x_s, x_r, \tau - p \cdot (x_s - x_{s_0}))\, dx_s$$

This formula has a natural extension to 3D, so plane wave shots can be generated for linear moveout in each coordinate direction.

Figure 2-29 describes graphically how a plane wave source is generated from a set of shot profiles. Each source in the set is delayed (or advanced) in time by an amount determined by the desired plane wave moveout and its distance from the central source. The delayed shots are then summed to produced the desired plane wave response. This process is repeated for each required plane wave.

Figure 2-29. Generating a plane wave source by delaying shots.

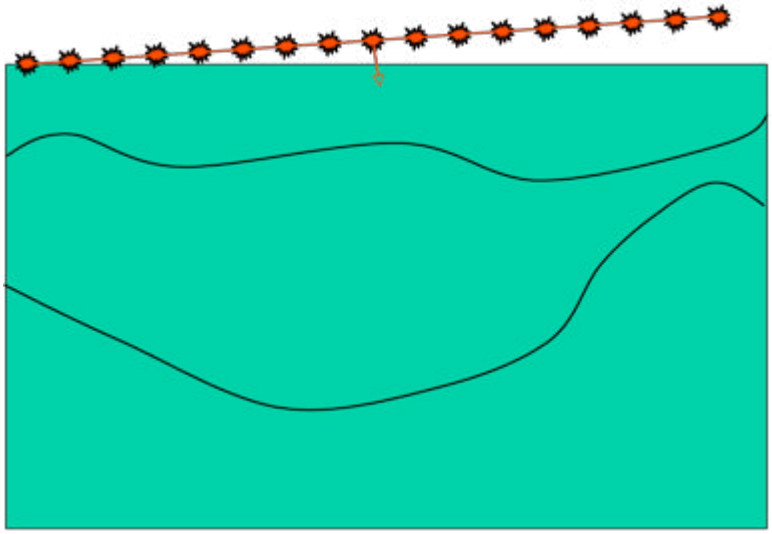

Plane wave sources produce a wavefield with a particular *takeoff* angle. Normally, takeoff angles are measured in degrees from level with zero representing a plane wave in the vertical direction. In the sense that only one plane wave can be generated with this take off angle, the resulting track is unique and the full plane wave is completely determined by this takeoff angle. Figure 2-30 conceptualizes the basic idea in ray theoretic terms. Here we see a plane wave with an apparent takeoff angle of approximately 30 degrees traveling through the subsurface media, as indicated by the ray, and striking a steeply dipping reflection event. The angle of the plane wave at this point also uniquely determines the raypath back to the source so either angle contains sufficient information to completely determine the raypath.

Figure 2-30. A plane wave source and ray.

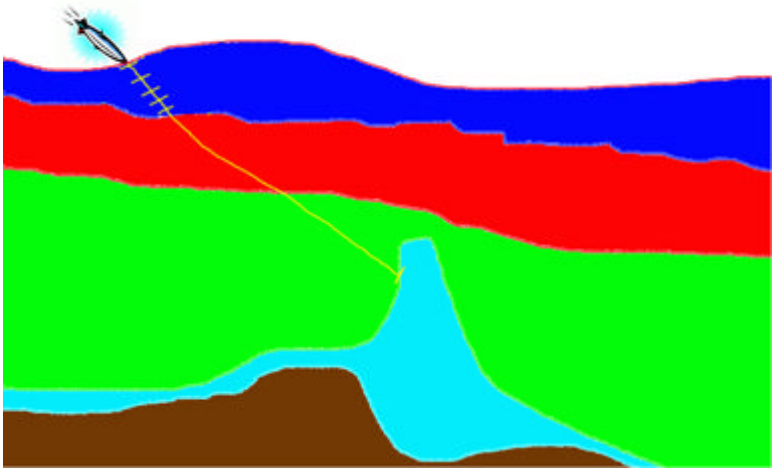

Figure 2-31 illustrates a plane wave propagating through the Marmousi2 model. Figure 2-32 is the actual response of the plane wave in Figure 2-31. While not something the typical geophysicist is familiar with this plane wave shot response can be migrated and imaged just like any traditional point source response.

Figure 2-31. Plane wave sources in the Marmousi2 isotropic elastic model.

(a). Plane Waves at 688 ms **(b).** Plane Waves at 1360 ms

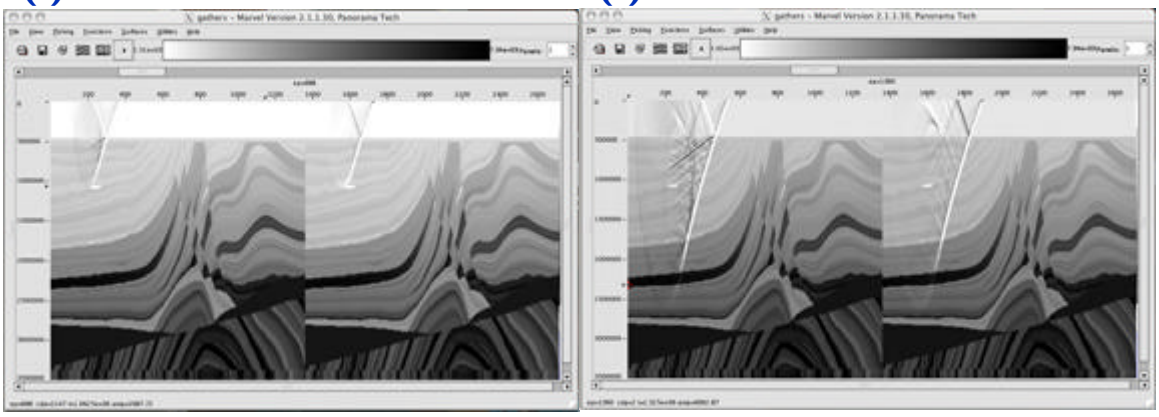

Figure 2-32. Plane wave response over the Marmousi2 model.

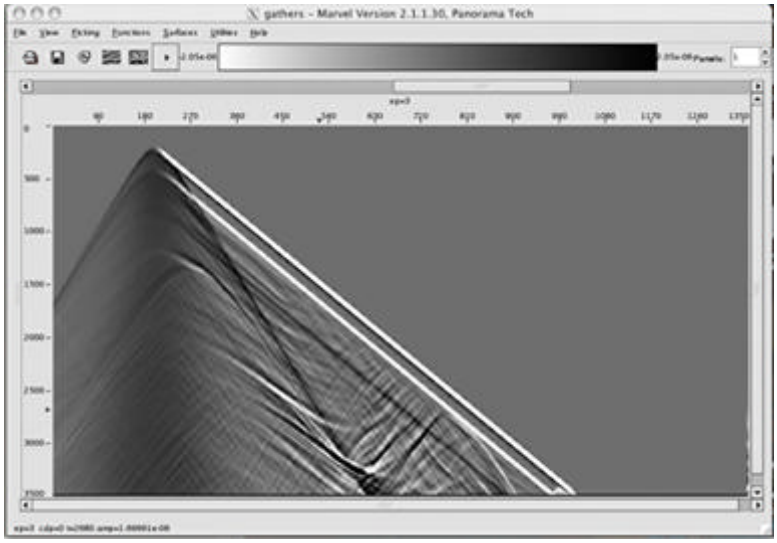

Huygen's Principle and Integral Methods

One of the most powerful seismic modeling concepts, known today as simply the *Huygens Principle*, was expressed some 350 years ago by both Christiaan Huygens and Augustin-Jean Fresnel (Wikipedia contributors, "Huygens–Fresnel principle", Wikipedia, The Free Encyclopedia, Wikipedia link):

> The Huygens–Fresnel principle (named for Dutch physicist Christiaan Huygens, and French physicist Augustin-Jean Fresnel) is a method of analysis applied to problems of wave propagation (both in the far field limit and in near field diffraction). It recognizes that each point of an advancing wave front is in fact the center of a fresh disturbance and the source of a new train of waves; and that the advancing wave as a whole may be regarded as the sum of all the secondary waves arising from points in the medium already traversed. This view of wave propagation helps better understand a variety of wave phenomena, such as diffraction.
>
> For example, if two rooms are connected by an open doorway and a sound is produced in a remote corner of one of them, a person in the other room will hear the sound as if it originated at the doorway. As far as the second room is concerned, the vibrating air in the doorway is the source of the sound. The same is true of light passing the edge of an obstacle, but this is not as easily observed because of the short wavelength of visible light.
>
> Huygens principle follows formally from the fundamental postulate of quantum electrodynamics that wavefunctions of every object propagate over any and all allowed (unobstructed) paths from the source to the given point. It is then the result of interference (addition) of all path integrals that defines the amplitude and phase of the WAVEFUNCTION of the object at this given point, and thus defines the probability of finding the object (say, a photon) at this point. Not only light quanta (photons), but electrons, neutrons, protons, atoms, molecules, and all other objects obey this simple principle.

While we frequently drop his name and simply call this Huygens principle, Fresnel's contribution cannot be minimized, but the part we really need to understand is visualized in Figure 2-33. This principle is usually explained conceptually by saying that the way Huygens arrived at it was based on observations of what happened when he dropped a finite number of balls, N, into the Zuider Zee. When the balls were arranged in a line, what he saw was not N independent events, but something like to a moving line. He saw an envelope of the wavefields rather than the independent wavefield of each separate ball. That being said, it is much more important to think in terms of the formal discussion above. Perhaps a better example of the Huygens–Fresnel principle would be to recognize that a discussion in an adjacent room would actually appear to come from the connecting door. Clearly, the door is acting as a new source and the listener only hears the sound coming from that source.

Figure 2-33(a) shows this for two-way waves and emphasizes that fact we need not think of a single reflector. Parts (b) and (c) of this figure show what happens when waves are allowed to travel in only one direction.

Figure 2-33. A simple graphical interpretation of the Huygens–Fresnel Principle.

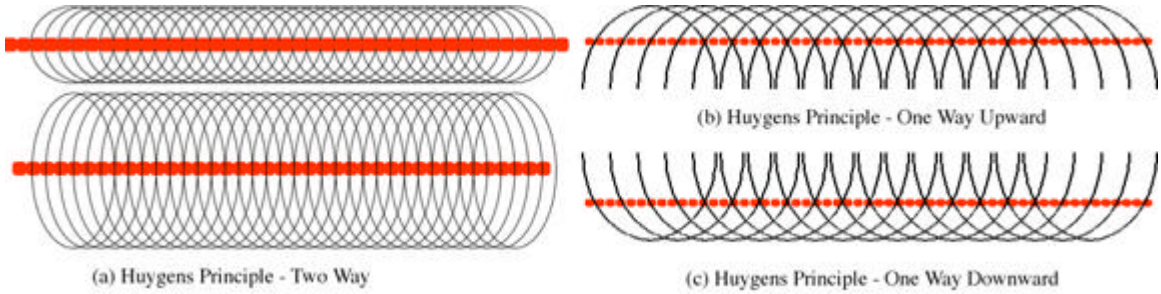

We see that the wavefield due to a reflector, the red flat line in parts (a), (b), and (c), can be thought of as the envelope of an infinite series of point sources. Each point source can be thought of as having been ignited by an impinging wavefront which in part (a) results in both a reflection and a transmission. Parts (b) and (c) visualize what happens when propagation is only allowed upward (b) or downward (c).

The Mathematics of Huygens' Principle

One of the more mathematically complex ways to use this principle is to recognize that regardless of the type of media (that is, acoustic, elastic, or anisotropic), we can think of the total response of any give source in terms of what happens at any given point in the actual model. For example, a source on the surface eventually arrives at some point (x, y, z) with reflectivity $R(x, y, z)$. According to Huygens' principle, the energy of the source then generates a virtual source at (x, y, z), the energy from which then propagates through the entire model, and then perhaps to receivers on the recording surface. In a nutshell, what this really means is that we need only know the response of each point in our model to completely reconstruct the entire wavefield $u(x, y, z, t)$. For the pressure formulation, this concept is mathematically expressed in terms of the so-called Greens' function $G(\vec{x}, \vec{x}_s, t)$ as shown in Equation 2-143, where $\vec{x} = (x, y, z)$ is a generic point in the medium and $\vec{x}_s$ is the vector location of the source.

(2-143)
$$\frac{\partial^2 G}{\partial t^2} - \rho v^2 \nabla \cdot \frac{1}{\rho} \nabla G = \delta(\vec{x} - \vec{x}_s)$$

For a given source, $s(\vec{x}_0, t)$, integration by parts allows us to express the solution p of Equation 2-17 in the integral form of Equation 2-144.

(2-144)
$$p(\vec{x}, t) = \int_{\Omega} G(\vec{x}, \vec{x}_s, t)\, s(\vec{x}_0, t)\, dx_s\, dt$$

This means that the solution to the equation is just the sum of all the point responses of the medium under consideration.

For example, when the velocity and density are constant, the Green's function takes the form in Equation 2-145 and Equation 2-146.

(2-145) $$G(\vec{x},\vec{x}_s,t)=\frac{\delta(t-\frac{|\vec{x}-\vec{x}_s|}{v})}{4\pi|\vec{x}-\vec{x}_s|}$$

(2-146) $$p(\vec{x},t)=\int_\Omega \frac{s(\vec{x}_0,t-\frac{|\vec{x}-\vec{x}_s|}{v})}{4\pi|\vec{x}-\vec{x}_s|}$$

Thus, $p(\vec{x},t)$ is the superposition of all the point responses in the medium due to a source at the point $\vec{x}_0=(x_0,y_0,z_0)$. Another way to say this is that the Green's function, G, is the inverse of the operator in Equation 2-147.

(2-147) $$G=\left(\frac{\partial^2}{\partial t^2}-\rho v^2\nabla\cdot\frac{1}{\rho}\nabla\right)^{-1}$$

Seismic Scattering

In integral form, these formulas lead to what has become known as *domain-integral methods* for solving seismic scattering problems. Although they are important because they divide the seismic propagation scheme into incident and scattered parts, these methods have not been popular for seismic modeling so they are of only a little interest to us.

In theory, the ideas can be based on any of the equations above, but for illustrative purposes, we only consider the pressure case when the density is constant. The basic idea is to assume that the velocity, v, can be expressed as the slowness difference $\frac{1}{v}=\frac{1}{c}-\frac{1}{c_0}$, where c_0 is constant. We can then write Equation 2-148, so that our solution takes the form of Equation 2-149, where p^{inc} is defined by Equation 2-150.

(2-148) $$\left(\nabla\cdot\nabla-\frac{1}{c_0}\frac{\partial^2}{\partial t^2}\right)p=s(\vec{x}_s,t)-\left(\frac{1}{c_0}-\frac{1}{c}\right)\frac{\partial^2 p}{\partial t^2}$$

(2-149) $$p(\vec{x},t)=p^{inc}+\int_\Omega\left(\frac{1}{c_0}-\frac{1}{c}\right)\frac{\partial^2 p}{\partial t^2}$$

(2-150) $$p^{inc} = \int_{\Omega} \frac{s(\vec{x_0}, t - |\vec{x} - \vec{x}_s|/v)}{4\pi|\vec{x} - \vec{x}_s|}$$

Although a bit of a stretch, Figure 2-34 illustrates Huygens' principle in considerable detail. Here we see the wave reflections and transmissions at each point in a given medium.

Figure 2-34. Wave directions and exploding reflectors.

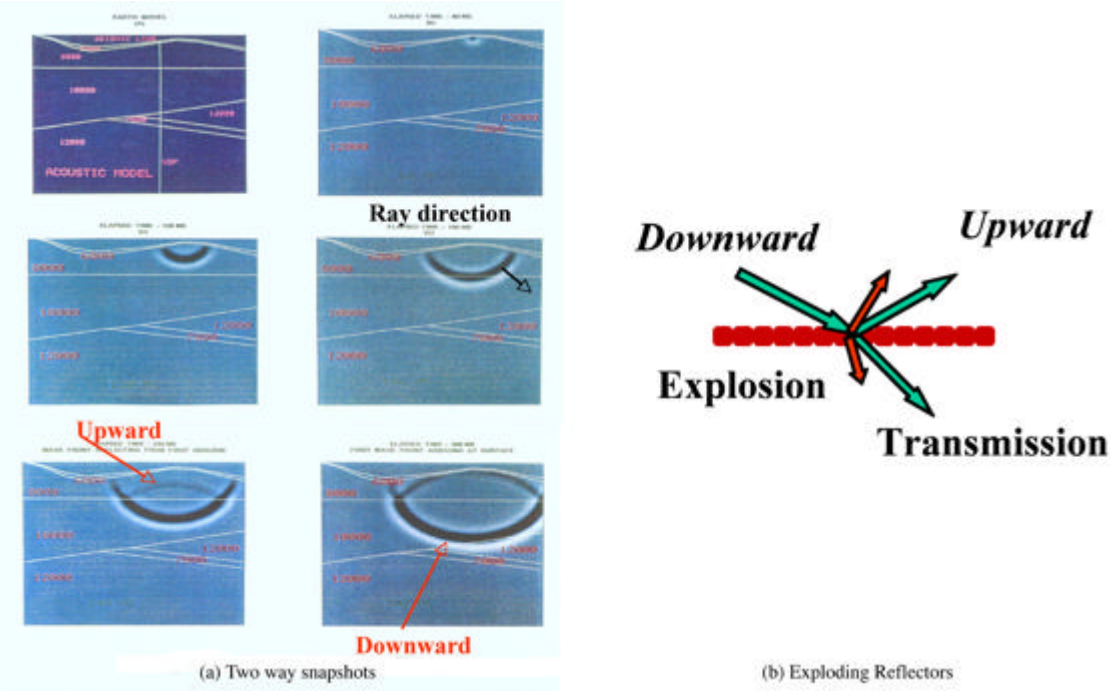

Raytracing

For a source at x_s and receiver at x_r, if we denote the traveltime or *phase* from x_s to x_r by $\varphi(x_r, x_s)$ and the amplitude decay by $A(x_r, x_s)$, we can then write Equation 2-151 in space-time and Equation 2-152 in frequency.

(2-151) $$G(x_r, x_s, t) \approx A(x_r, x_s)\delta(t - \varphi(x_r, x_s)$$

(2-152) $$G(x_r, x_s, \omega) \approx A(x_r, x_s)e^{i\omega\varphi(x_r, x_s)}$$

Substituting into the wave equation in Equation 2-153, we get Equation 2-154.

(2-153) $$\left(\nabla \cdot \nabla - \frac{i\omega^2}{v^2}\right) G(x_r, x_s, \omega) = 0$$

(2-154) $$\left\{ i\omega^2 \left[\left(\nabla\varphi \right)^2 - \frac{1}{v^2(\mathbf{x})} \right] + i\omega \left(2\nabla A \cdot \nabla\varphi + A\Delta\varphi \right) \Delta A \right\} e^{i\omega\varphi} = 0$$

Equating coefficients of powers of $i\omega$ to zero yields the Eikonal equation, Equation 2-155, and the transport equation, Equation 2-156.

(2-155) $$\left(\nabla\varphi \right)^2 - \frac{1}{v^2(\mathbf{x})} = 0$$

(2-156) $$2\nabla A \cdot \nabla\varphi + A\Delta\varphi = 0$$

Simultaneous solution of Equation 2-155 and Equation 2-156 provides the traveltimes and amplitudes necessary to approximate the Green's function in an efficient manner.

While not straightforward, the Eikonal equation, as given here, can be solved by finite differences and/or the method of characteristics. It is called the method of characteristics because it solves the Eikonal equation along rays by simultaneously solving Equation 2-157 and Equation 2-158. The method of characteristics is usually referred to more traditionally as raytracing.

(2-157) $$\frac{d\mathbf{x}}{d\sigma} = \mathbf{p}$$

(2-158) $$\frac{d\mathbf{p}}{d\sigma} = \nabla \left[\frac{1}{2v(\mathbf{x}(\sigma))} \right]$$

In this case, σ typically represents arc length along the characteristic or ray, and $\mathbf{x}(\sigma)$ is the position of the ray vector at the distance σ from the initial position of the ray. The process is usually initialized by setting $\mathbf{x}(0) = \mathbf{x}_s$ to the initial source position and setting, as shown in Equation 2-159.

(2-159) $$\mathbf{p}(0) = \frac{1}{v(\mathbf{x}_s)} \begin{pmatrix} \sin\alpha\cos\beta \\ \sin\alpha\sin\beta \\ \cos\alpha \end{pmatrix}$$

Once $\mathbf{x}(\sigma)$ is known, the desired traveltime is computed by integrating along the characteristic curve in Equation 2-160.

(2-160) $$\varphi(\mathbf{x}(\alpha,\beta,\sigma)) = \int_0^\sigma \frac{d\sigma'}{v^2(x(\alpha,\beta,\sigma'))}$$

Figure 2-35. Ray Fan versus Eikonal traveltime phase

(a). Ray Phase Function

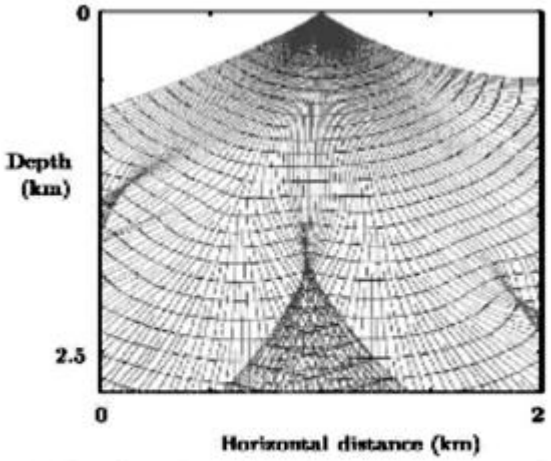

FIG. 8. A fan of rays in two dimensions starting from a surface location and the associated wavefronts. The ray coverage is kept sufficiently high by filling in shadows with new rays (see the section on wavefront construction).

(b). Eikonal Phase Function

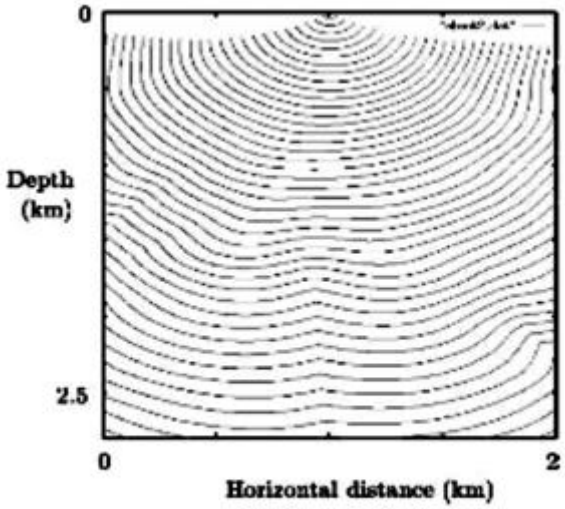

FIG. 10. Propagation of first-arrival wavefronts for the same shot and model as used in Figure 8.

Figure 2-36. Anisotropic model and traveltimes.

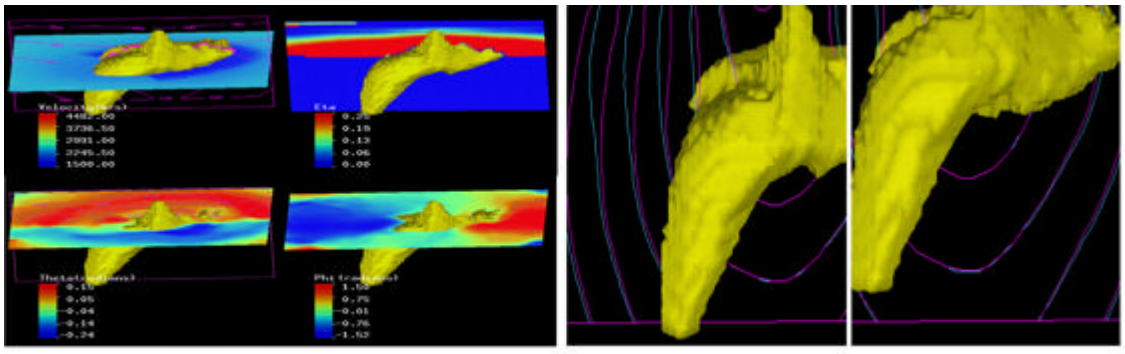

(a) Anisotropic Model

(b) Anisotropic Traveltimes

Raytrace Modeling

Figure 2-37(a) provides an example of how Huygens principle factors into construction of a raytrace-based response to exploding reflectors. Given a point on a reflecting surface (the red circle in the figure), a ray from a source point simulates an exploding the point. Rays emanate from the point in all directions and are recorded at surface receivers. Since any reflecting surface can be considered as a set of such points, the sum of all their point responses will produce, in the worst case, a reasonable approximation of what we would see if we ran our full two-way propagator for this model.

Figure 2-37. Huygens Principle as it applies to raytrace modeling

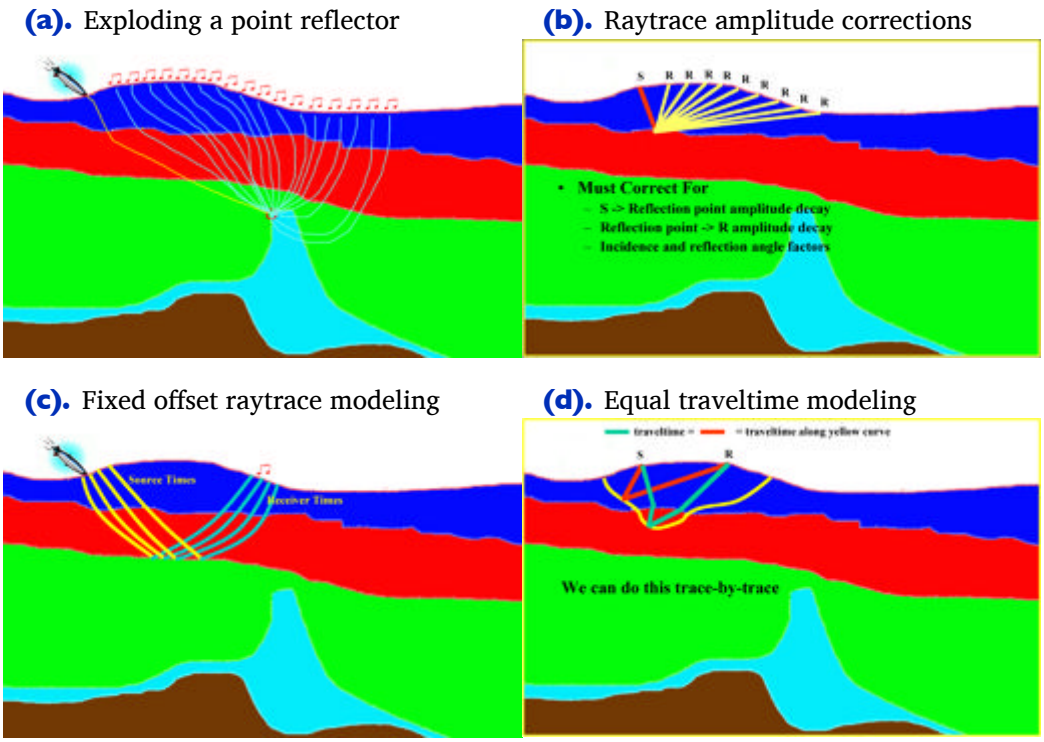

Figure 2-37(b) hints at one of the more complicated parts of accurate raytrace modeling. Reasonably accurate raytrace amplitude responses require that we correct for several important factors. These include source-to-reflection point decay and reflection-point-to-receiver amplitude decay, as well as obliquity factors based on the incidence and reflection angles. The phase of secondary arrivals also require correction.

Depending on how it is structured, raytrace modeling can be one of the most computationally efficient modeling methods available, and can easily model virtually any type of recording geometry. As indicated in Figure 2-37(c), raytrace modeling is easily modified to achieve fixed or common offset modeling. Its chief drawback is that multiples and other multiple arrival events are very difficult to include in the model.

While we tend to think of raytrace modeling in the sense of the isochron in Figure 2-37(a), this may not be optimum. Figure 2-37(d) shows raytrace modeling formulated in terms of equal traveltime curves or surfaces. The yellow curve in this figure represents all the reflection points for which the sum of the traveltime from a source to any point on the yellow line and back to a receiver is identical to that from any other reflection point. To produce the amplitude response at this time requires only that we sum all reflection amplitudes at these locations into the trace at this fixed time. If you already understand Kirchhoff migration to some degree, this concept should be very familiar.

Figure 2-38 provides proof of concept that the ray-based synthesis methods outlined here actually work. In this figure, the model is on the left and the ray based synthetic shot is on the right. The phase function, φ, and amplitude decays, A, were calculated using the method of characteristics along with a simultaneous solution to the transport equation.

Figure 2-38. A raytrace shot over the SEG AA′ 2D model.

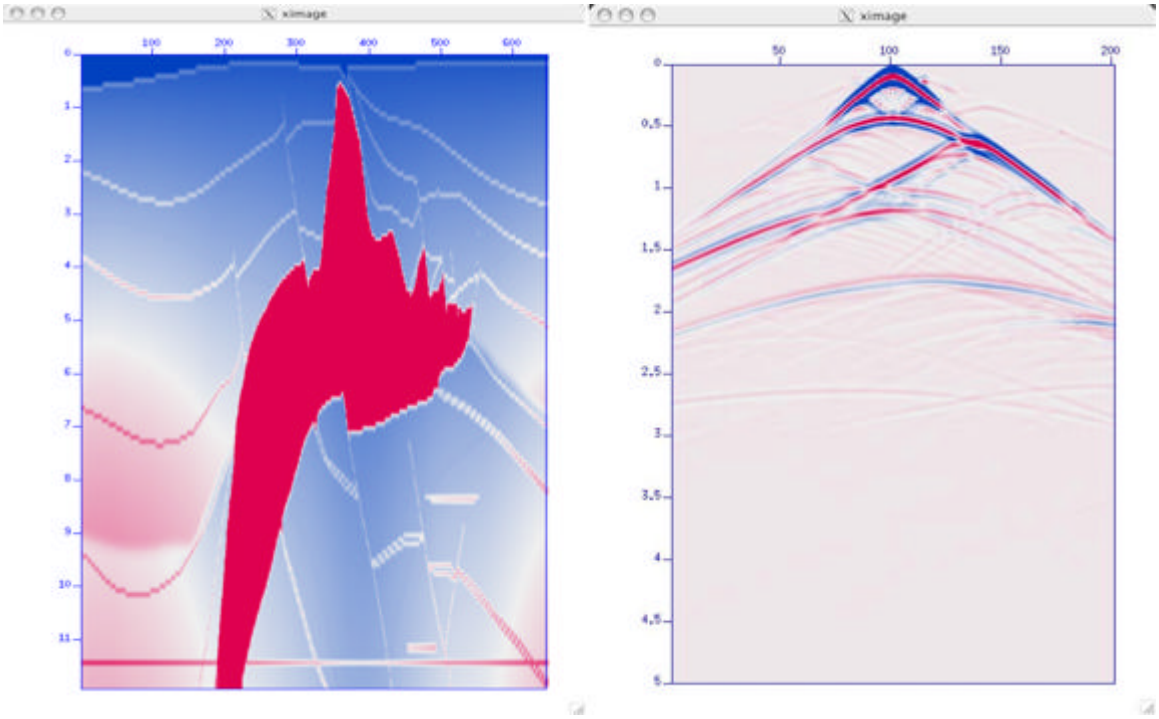

While the raypath concept is sufficient to understand plane wave issues, in most cases, we emphasize that the full plane wave generated by the source is much more complicated. Because of this fact, it is possible to generate a full wave response from an appropriately sampled bundle of ray theoretic plane waves. Figure 2-39 demonstrates this in terms of what are more precisely called *Gaussian beams*. What we see in this figure is part of the full response due to two plane wave raypaths. The blue lines indicate what are called central rays, while the red lines indicate wavefronts calculated directly from the central rays. The wavefronts are actually calculated using a finite difference technique specified by theoretical formulas analogous to those on which our one and two-way propagators are based. In addition to dynamically determining the amplitude

at each point on the red lines, a Gaussian weight is applied to ensure that the sum of all such waves faithfully represents the forward traveling wavefront. The name Gaussian beam is derived from this weighting methodology.

Figure 2-39. A partial wave response due to two rays.

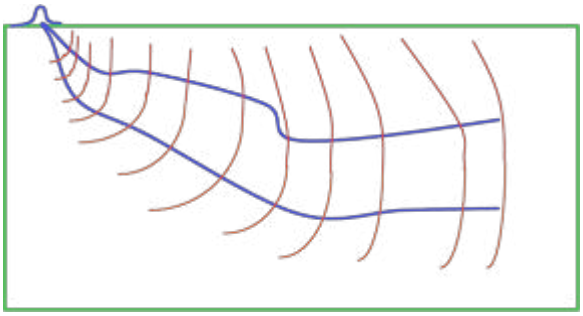

Figure 2-40 shows the kinds of events that each of our schemes can model successfully.

Figure 2-40. A brief comparison of modeling methods.

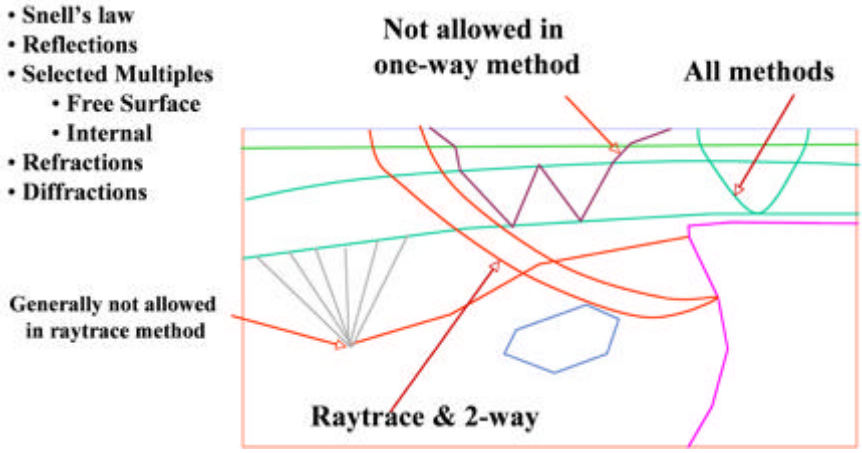

Figure 2-41 summarizes the differences between three modeling algorithms. The left hand side represents full two-way propagation, the middle image shows one-way propagation, and the right side shows single arrival raytrace-based modeling. Note that neither the full one-way nor the single arrival raytrace-based response have any reflected waves.

Figure 2-41. Basic model differences. Left is full two-way, middle is one-way, and right is single arrival Kirchhoff shot response for shot in center of model.

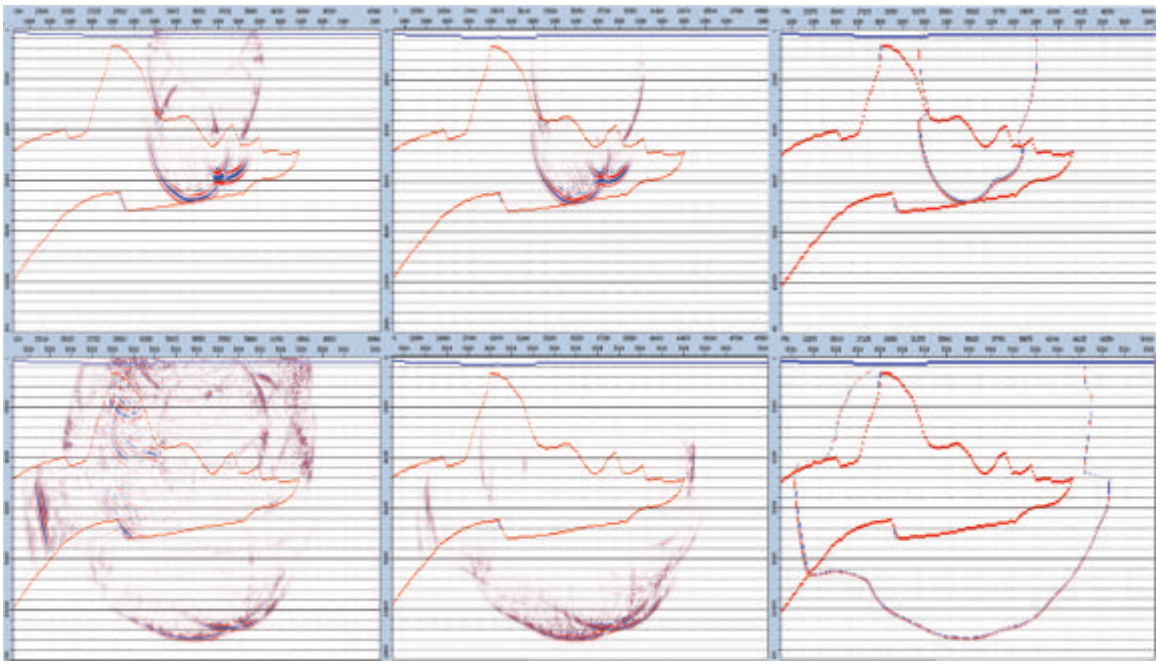

Zero Offset Modeling

At this point, our understanding of modeling is based on a two-step process. A source of some kind is initiated at time, $t = 0$, and it is then allowed to propagate into the Earth according to some form of propagating equation. We also understand that each subsurface point in the Earth, whether part of a reflector or not, can be considered as a point reflector. After some length of time, energy from the source reaches the point, and, according to Huygens Principle, initiates a new source at the location of the point reflector. The point reflector then acts as a internal source which radiates energy in all directions. Some of this energy reaches the surface as a reflection and some of it continues into the Earth to ignite other point reflectors creating additional sources until the energy is exhausted. What we record at the surface is the reflected energy at a widespread array of receivers with some offset from the source position. What we lose is the energy that never manages to get reflected. In such synthetic experiments, we can record all the information we want. If desired, we can even record zero-offset data, but to do that we have to set off sources at each location where we want a receiver. This means that, at considerable computational expense, we must forward propagate a source for every coincident receiver location.

In the early days of reflection seismic processing and interpretation, there was seldom enough computer power to produce an appropriate number of shots to enable synthesis of stacked sections. It was natural to attempt to find a way to produce all the traces in zero or short offset ensembles. It does not take much effort to come up with a reasonable approach. The Huygens principle tells us that if we can determine the response from any single subsurface point, all we have to do to produce the receiver wavefield is to sum all such responses into the receiver and we are done.

Let's consider the zero-offset response of a single point-reflector. If the traveltime from the source at s_i to the point-reflector at r is $t_{s_i r}$, the traveltime from the reflector back to the source is also $t_{s_i r}$ because the energy reaching the receiver at the source position must travel the path (or paths) from the source to the point-reflector in reverse. This means that the total traveltime from the source to the reflecting point and back to the receiver at the coincident source location is just $2t_{s_i}$. This statement must be true for every coincident source and receiver on the recording surface, so the zero offset response of the point reflector is the sum of the response for each source, s_i, on the recording surface.

The trick to understanding how to efficiently synthesize zero-offset responses is simply to realize that if the velocity, v, of the medium is divided by two and we set off an explosion at the point reflector at $t = 0$, then what we will record on the recording surface is exactly the time $2t_{s_i}$. Thus, exploiting Huygens Principle in Figure 2-33, the zero offset response for any given model can be obtained by simply dividing the velocity by two, setting off explosions at each subsurface point reflector, and recording the response at the surface. The only problem with this trick is that the zero-offset response obtained in this fashion will have odd period multiples whenever a free-surface is present.

Figure 2-42 shows what happens in the subsurface, and Figure 2-43 shows what we get at the surface when we synthesize exploding-reflector-zero-offset data. The far upper left image shows the subsurface exploding reflectors just before they explode. The remaining figures demonstrate how the wavefield propagates to the receivers.

Figure 2-42. Exploding reflector synthesis.

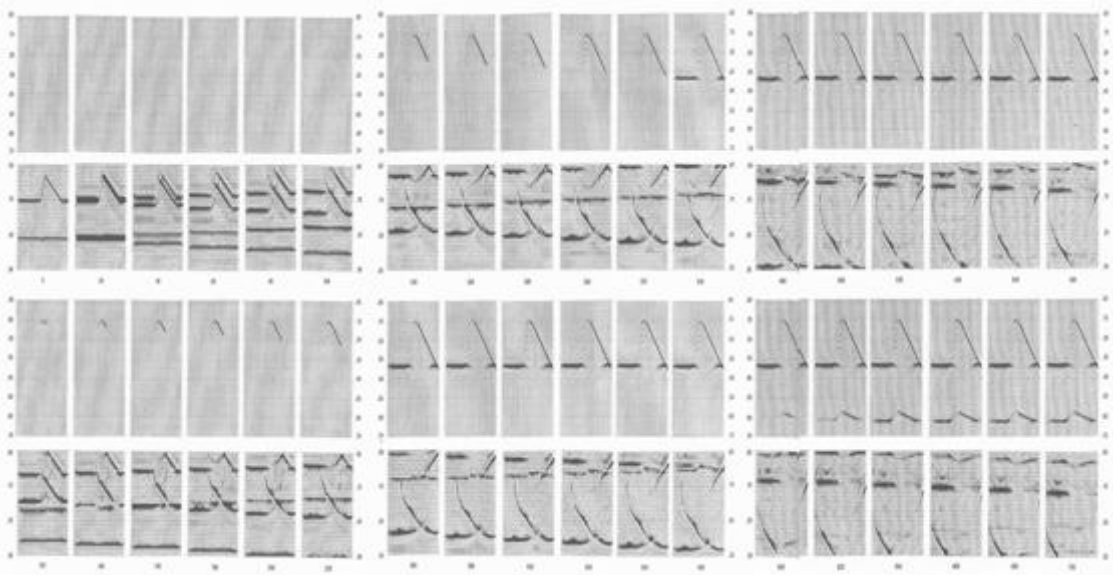

Figure 2-43. Surface response of the exploding reflectors from Figure 2-42

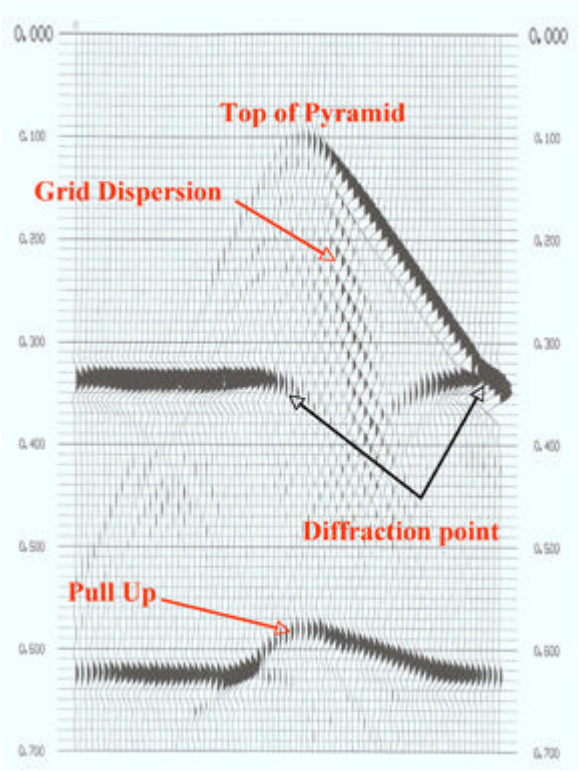

An easy way to understand the comments in the previous paragraph is through watching the movie schematized in Figure 2-44. This move was made in the late 1980's or early 1990's from a model derived from a 3D two-way migration of *DMO*-corrected Gulf of Mexico stacked data. It is based on what turned out to be an inaccurate interpretation of the salt flank, but it is still an interesting case study.

Figure 2-44. Exploding reflector movie. The best way to understand exploding reflector modeling is through a movie.

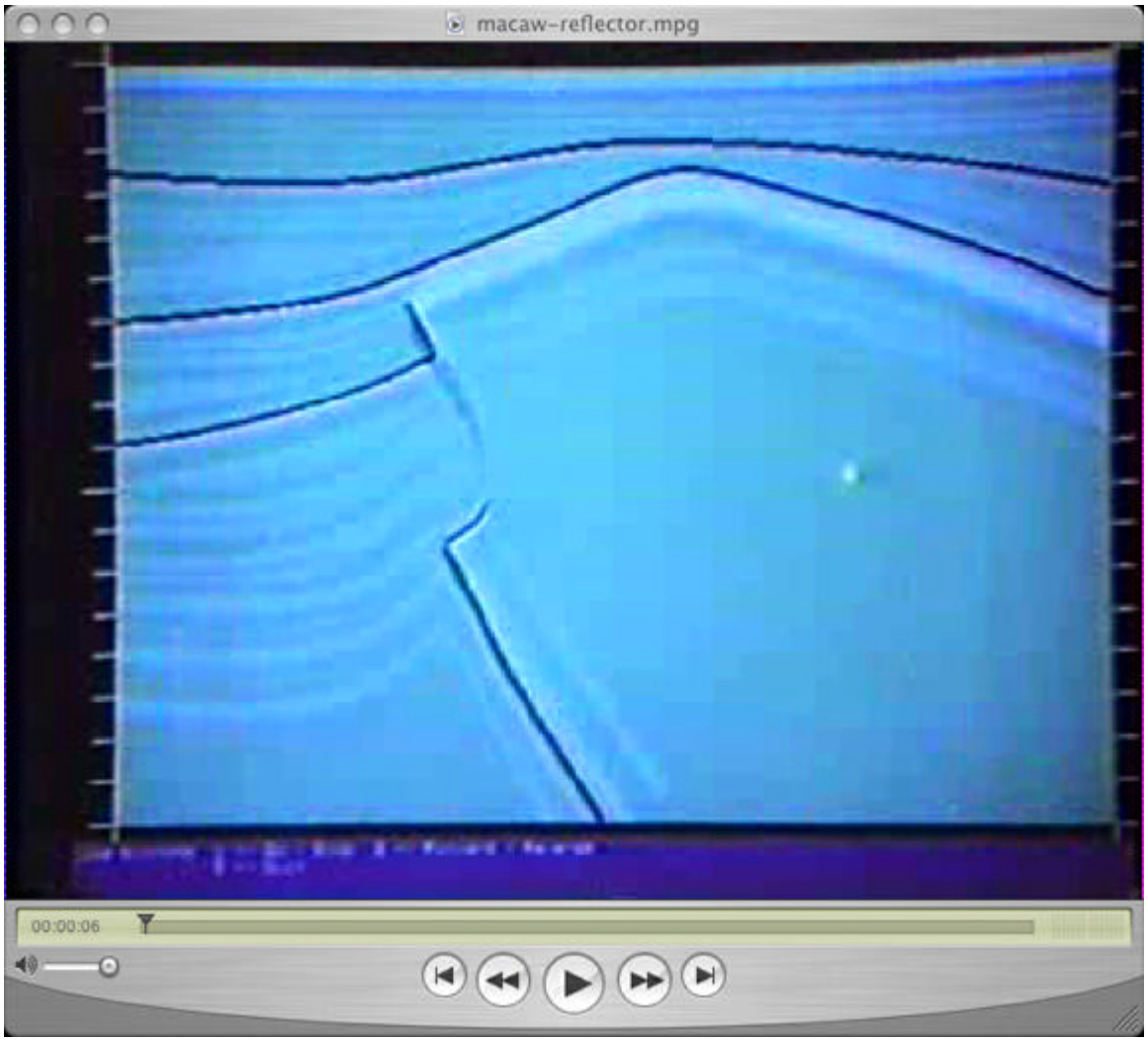

Chapter 3

Historical

This chapter examines the history and evolution of modern seismic migration methods. Modern migration methods evolved from simple geometric concepts to complex wave-equation techniques. The major driving force for such dynamic changes is the overwhelming need to transition from doing calculations using pencils and paper to analog calculators and finally to modern digital computers. This section reviews that process and provides a firm foundation for the geometric concepts that led to the modern era.

It should be noted that modern geophysical mathematical concepts governing wave propagation in complex geologic media have been studied and developed before the current epoch. Many of these theories date back to the early 20th, the 19th, and even, in some cases, the late 18th centuries. While the scientific foundations were definitely available, many early geophysical explorationists tended to ignore them and rely instead on what might be called more *ad hoc* methodologies. What we use today is the result of a lengthy trial and error stumble urged on by the need to find hydrocarbons hidden in more and more difficult to find traps.

Data Acquisition

During World War I (1914-1918), sound waves from exploding bombs and other ordinance were detected many miles from the explosion point. Noise from the operation of submarines was detected over even greater distances. These two observable events are thought to have lead to the speculation that one could detect geologic bedding planes by recording the sound energy from a surface explosion. Oil companies around the world began to research whether or not such an idea might be possible. One of the early investigators into this idea was a physicist named Reginald Fessenden. Figure 3-1 describes Fessenden's scheme for locating geological formations using a sound source. The source in this case was essentially a vibrator not unlike what we call a vibroseis today. The technique is also virtually identical to what would ultimately became sonar for locating submerged submarines.

Figure 3-1. A graphic describing the essence of R. Fessenden's 1917 patent for devices to generate and record seismic energy.

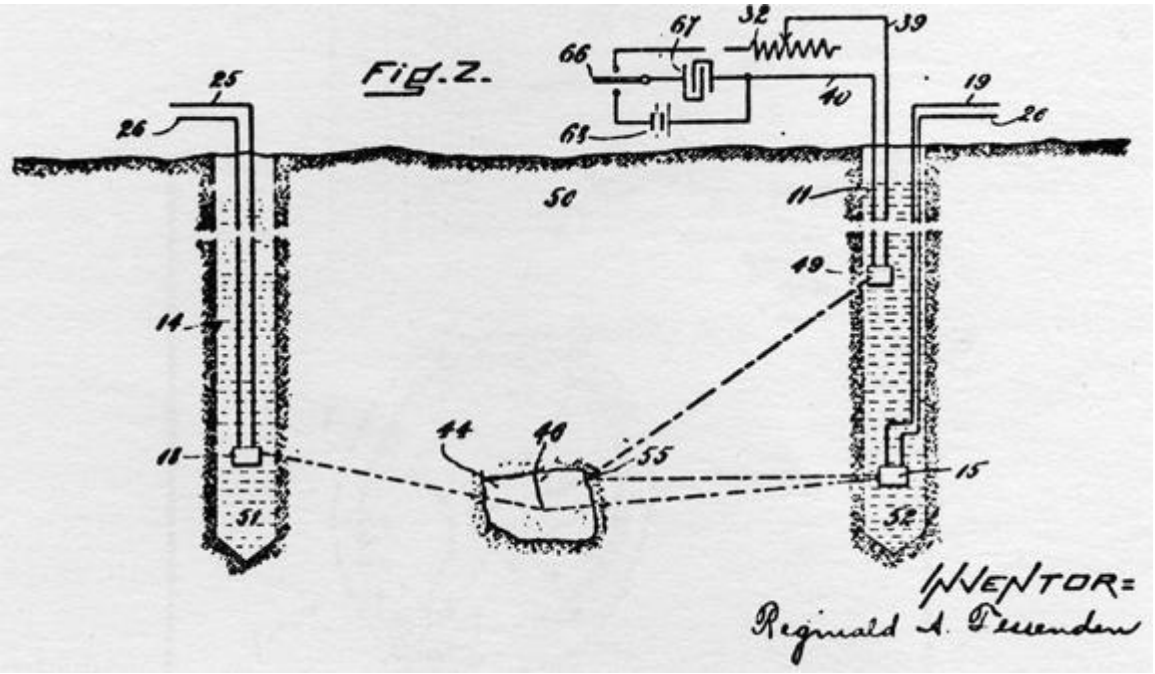

While I am quite sure that Fessenden was completely convinced that his device would work, his belief was not shared by all. Thus, it was necessary to prove empirically that a surface sound source would generate reflections from geologic formations, and that such reflections could be recorded at the surface and mapped or interpreted to find hydrocarbon bearing traps.

At this point in time, making a microphone, or what we now call a geophone, was very expensive and each such device was very heavy. Thus, in the very early days, very few receivers were used to record the response of each shot. Figure 3-2 shows a typical four

microphone recording from 1928. It is believed to be one of the first seismic recordings to empirically verify that reflections from subsurface formations occurred and could be detected. The large oscillations at the beginning of this shot profile indicate the first arrival of energy from the source. The arrival indicated by the arrow as well as those above it are all reflections from the Cimarron anhydrite in central Kansas on the Seminole Plateau. The fact that these amplitudes were actually reflections was verified by drilling a well at the end of a line of four receiver shots.

Figure 3-2. A single trace recording

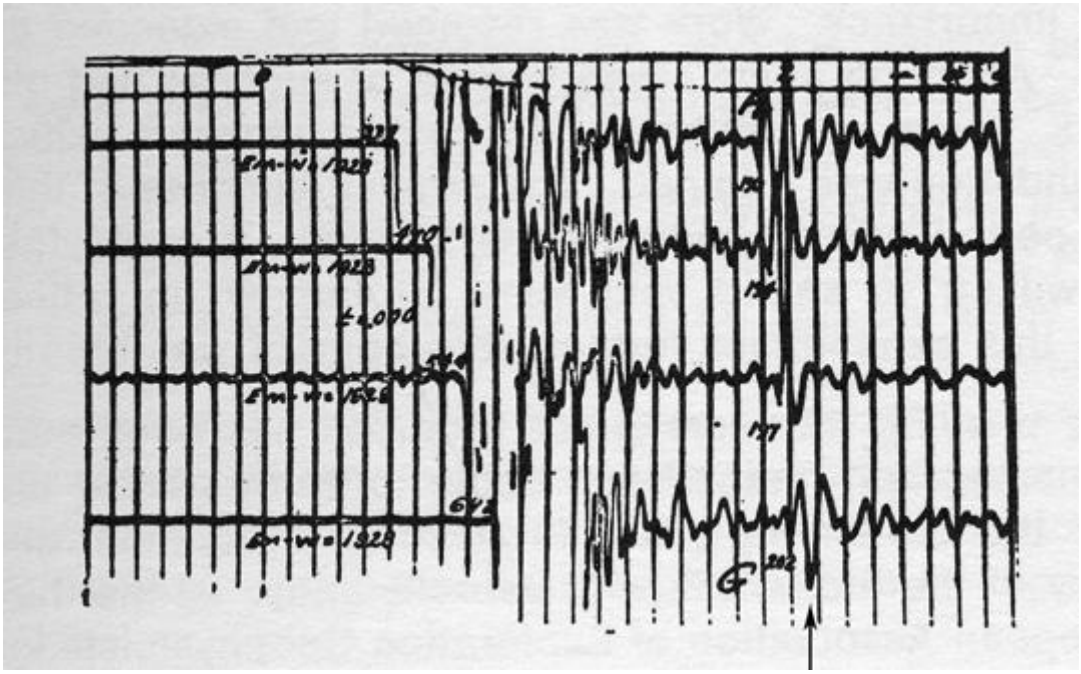

Zero Offset Hand Migration

Given records like that in Figure 3-2, early explorers made a *stickmap* that might have looked something like the one displayed in Figure 3-3. The times defining the event in this figure would most likely have been based on the identified arrival from the closest trace to the shot point. They would have liked to have a trace in which the shot and receiver were coincident. But, because they were using dynamite, this would have resulted in the destruction of the receiver, and so they settled for receivers that were close to the shot. In Figure 3-2, the closest trace would have been the time pointed to by the arrow with a shot-receiver separation (offset) of about 100 meters. This separation would have to suffice as an approximation to a trace with coincident source and receiver. Such traces were called zero-offset traces.

Figure 3-3. A simple non-flat horizon

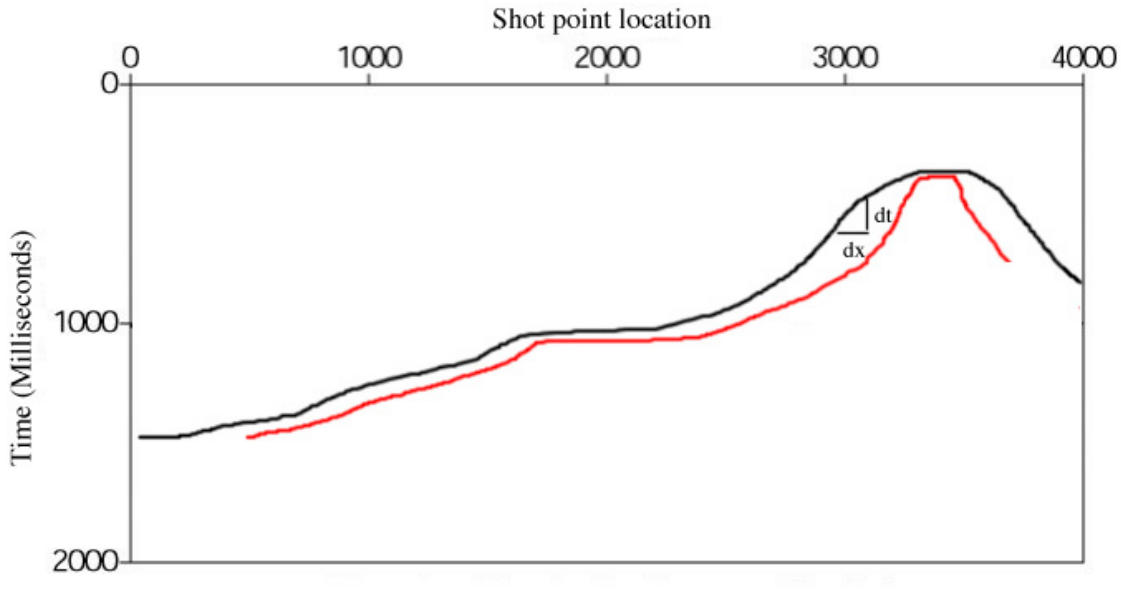

The black line graph in Figure 3-3 represents what is called a zero-offset or unmigrated time *section*. What is necessary for exploration and drilling is a depth map, or, when the velocity is constant, a migrated time map as conceptualized by the red line graph. In this case, the red line was simply drawn in free-hand, but represents the major features of what might be the true migration position of a reflected horizon. Note in particular that after migration, the peak of the anticline has not changed position, but its width has shrunk. It is also true that the positions of dipping events have moved up-dip in every case.

To produce the red-line section in Figure 3-3, we need to know how to convert unmigrated arrivals into migrated arrivals. Figure 3-4 shows the relationship between zero-offset reflections and their correct migrated position. The true reflector has a true dip angle of α, while the apparent or recorded event is at dip angle β. In this figure, the data is assumed to have been recorded over a constant velocity medium. Note that the location of the migrated event is placed relative to vertical time or depth, but remember that this vertical positioning is only valid for constant velocity media. Since the velocity is constant, vertical depth is given formally by the traditional relationship, where depth is equal to velocity times one-way time, that is, $d = vt/2$ or $t = 2d/v$.

Figure 3-4. Fundamental migration geometry between the apparent location and dip β versus the migrated location and dip α.

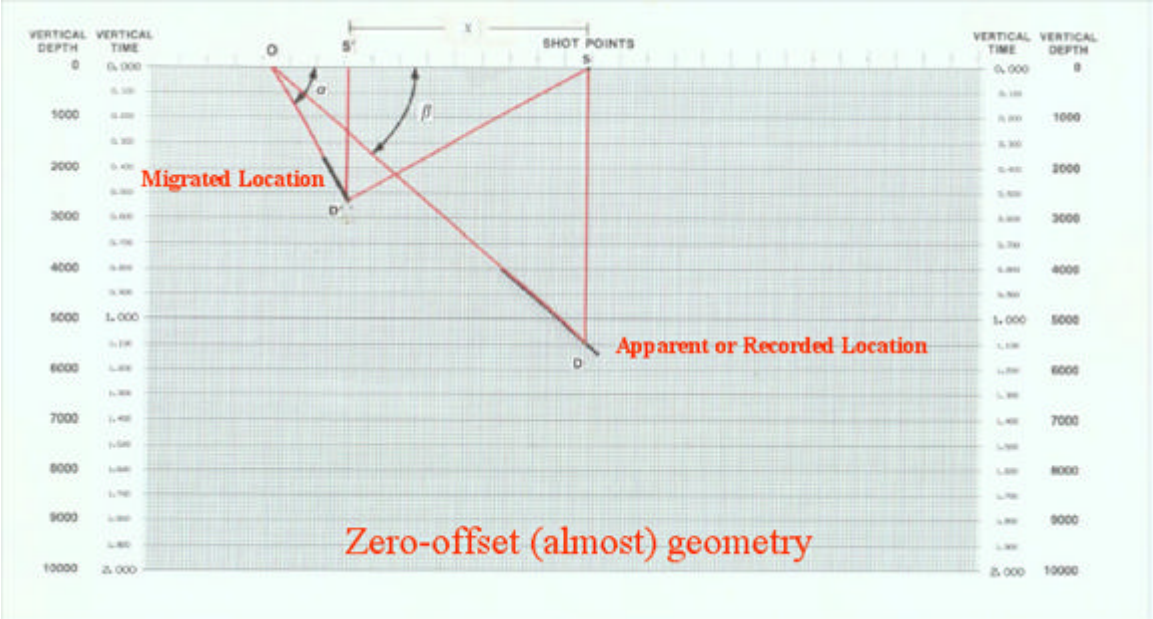

Migration in a two-dimensional, constant velocity medium requires only that we know the sound speed in the medium, and can measure the ratio of the change in arrival time to the corresponding horizontal change. As indicated in Figure 3-5, this is usually specified in seconds per trace divided by the trace spacing, but any time interval and corresponding spatial interval will do. The formulas listed in the figure provide all necessary calculations to determine the migrated position of any given event. Note again that in this simple medium, vertical depth is easily obtained by multiplying the vertical time, t, by the medium sound speed, v. Note also that events with any given apparent dip migrate up-dip. Consequently, we can ignore the sign of any given value and simply place the migrated dip element at its appropriate up-dip position. As we will see, extension of this formula to a vertically varying medium is quite easy.

Figure 3-5. Fundamental migration trigonometry relating the apparent location and dip specified by S and β versus the migrated location and dip specified by S' and α.

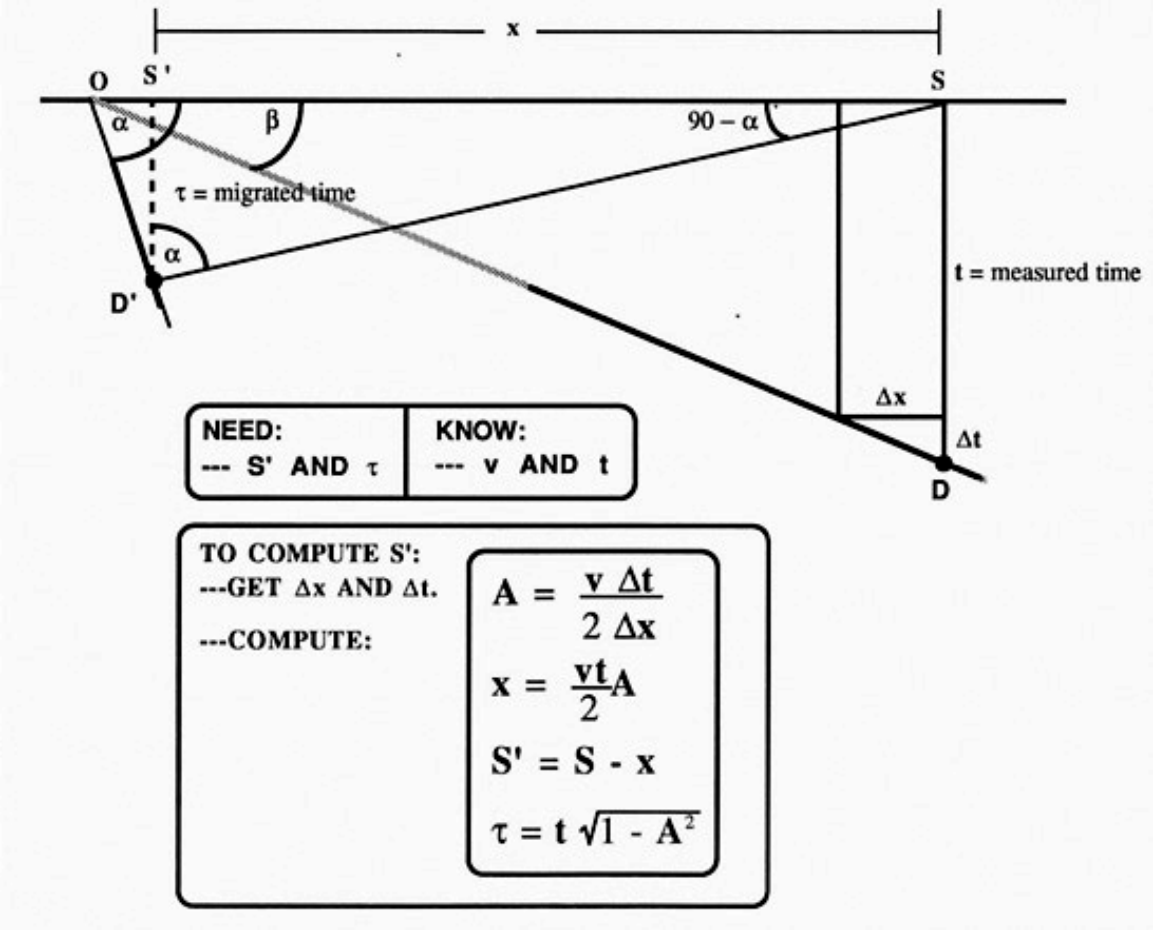

Figure 3-6 extends the migration formulas in Figure 3-5 to a three-dimensional constant-velocity medium. These equations provide the necessary computational formulas to complete the migration process. Here, however, it is a bit more difficult to actually do the migration by hand. At this point, the migrated position must be contoured to produce a migrated map of the recorded event.

Figure 3-6. Fundamental migration trigonometry relating the apparent location and dip specified by the S and β versus the migrated location and dip specified by S' and α.

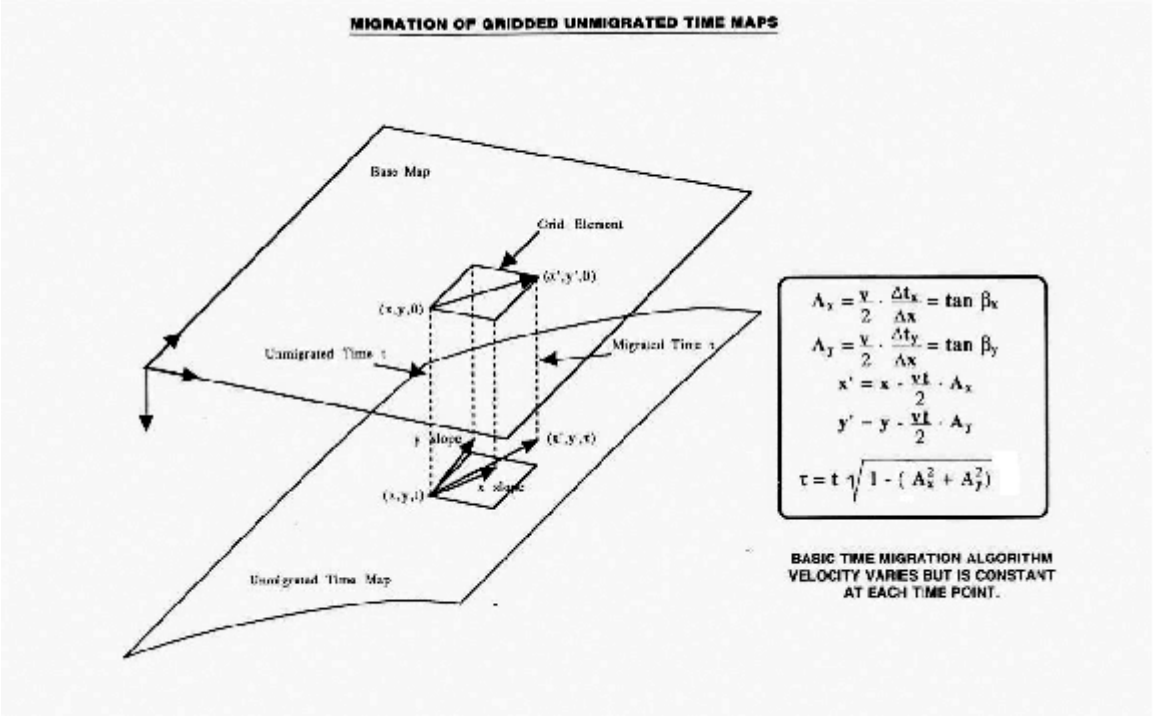

Beginning in the late 1940's and continuing until the early 1960's, all interpreters used this approach to produce migrated prospect maps. The equations were employed in a two-step manner, where calculations proceeded in the line direction, and were then followed by similar calculations in the cross-line direction.

Figure 3-7 shows an example of an unmigrated or zero-offset map. This map is from an early interpretation done over a salt dome in the Gulf of Mexico at South Pass Block 89. Faults and the large truncation surrounding the large salt dome are clearly evident.

Figure 3-7. An unmigrated (zero-offset) time map of a salt structure in the Gulf of Mexico. This particular map was contoured in 1972 or 1973 from a two-dimensional grid.

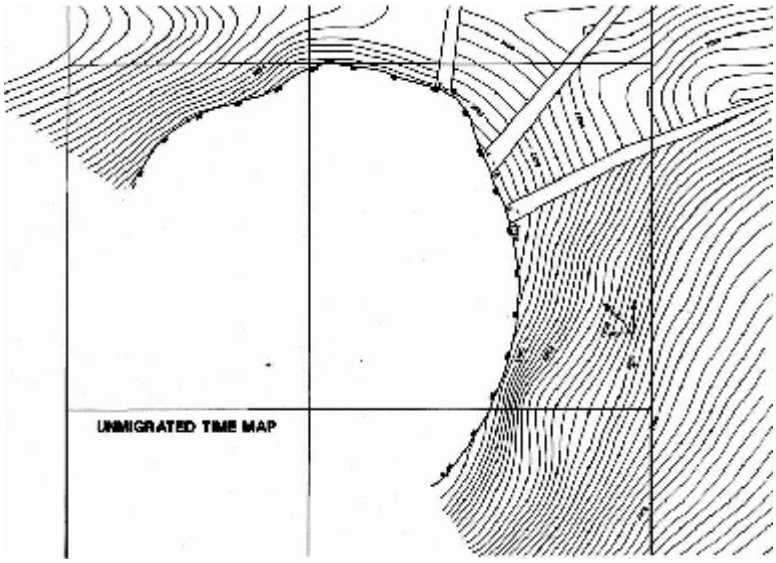

The vectors graphed in Figure 3-8 are the result of using the equations in Figure 3-6. A computer was used to generate and plot the vectors. Note the significant change in the shape of the salt structure and note also that some of these vectors are over two miles in length. It is important to observe that any 2D migration of the red line will be inaccurate. Not only does its subsurface position migrate up-dip, but its shape can change quite dramatically. This is a basic reason why 3D imaging is so superior to 2D.

Figure 3-8. Migrated vectors from the map in Figure 3-7 computed using the formulas in Figure 3-6.

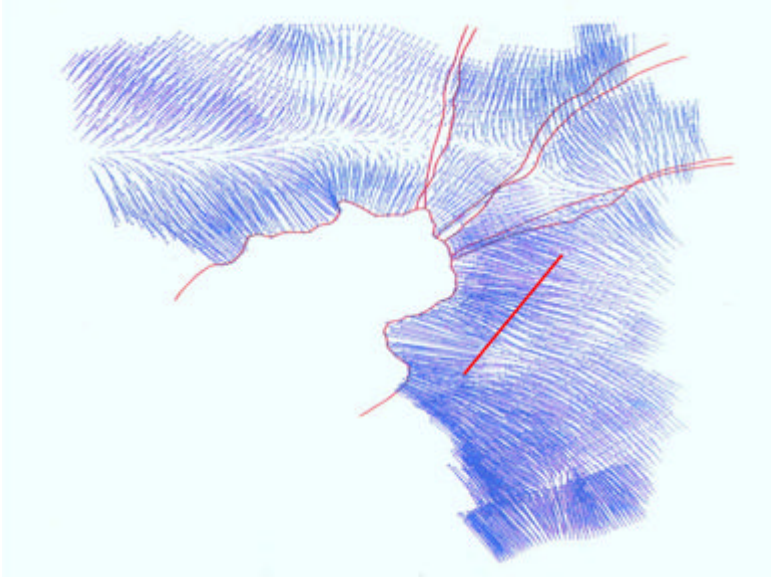

Shot Profile Hand Migration in Two Dimensions

Picking traveltimes from a short-offset trace to approximate zero-offset arrivals and thereby produce a zero-offset section works well when neither the velocity nor the geometry of the local formations vary dramatically. It breaks down when velocity variation is strong, when the structure of the subsurface horizons is complex and when assuring that the current pick is on the same formation as the last pick is difficult.

The first approach to alleviating at least some of these problems was to increase the number of geophones in each shot profile. Instead of using a handful of receivers on one side of a shot, “split-spread” shooting, as shown in Figure 3-9, became prominent. After each shot was recorded into multiple receivers, one half of the receivers were picked up and moved to produce a new split-spread array for the next shot. For example, in the diagram in this figure, the receivers on the left would be moved so that the left-most receiver is just to the right of the right-most receiver. A new source would be discharged and recorded into the newly positioned array. As this process continued, complete coverage of the subsurface reflector is accomplished. As shown in the left hand trace graphic in Figure 3-10, trace-to-trace correlation is now much easier, and subsurface mapping is supposedly simplified.

Figure 3-9. A typical 2D shot diagram from the mid 1960's to around 1975. These were used in split-spread shooting arrangements.

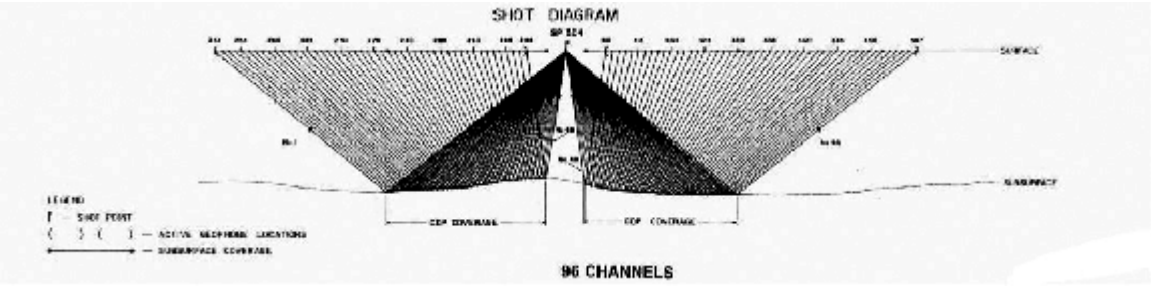

Figure 3-10. Detecting dip. The amplitude and direction were defined by a slant stack.

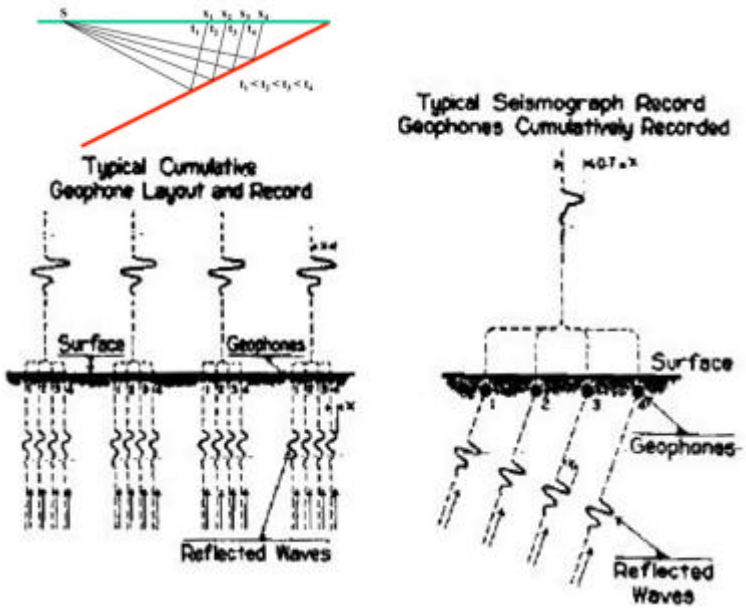

A key question that needed an answer was what does dip really look like on a shot record with a large number of receivers. Could shot-record dip be used to estimate the location of the reflecting horizon?

These questions were not focused so much on dip, but on whether or not you could estimate the dip from the shot profile and then figure out where the reflection came from. Figure 3-10 shows Rieber's 1936 solution to the question of estimating dip. He delayed each shot linearly (right hand side of the figure) and summed up the amplitudes. When a large amplitude was found, the delay required to find it defined the emergence angle, and so gave insight into both the arrival direction and the amount of subsurface dip that produced it. He was probably the first to recognize the importance of summing over lines (slant stacks) to reduce the problem to one of simply detecting an amplitude.

Unfortunately, I am not aware of anyone who took advantage of Rieber's methods in any detail during his day. It was not until the advent of modern computers that his method came to the forefront in the form of plane-wave or beam stack approaches to imaging. However, using information from a shot profile still became a viable approach to more accurate subsurface mapping.

Figure 3-11 shows what an aspiring geophysicist named Klaus Helbig was given as a test in 1952. It was his introduction to geophysics. He is a well known German geophysicist who is still alive at this writing and is a wonderful source of historical information about how geophysics was done prior to the advent of powerful computers. I am indebted to him for many of the figures and exercises in this section. Figure 3-11 shows a synthetic shot profile on the right. The problem, given an assumed velocity of 3000 meters per second, is to find the reflection point that generated the shot record on the right. As described in Figure 3-12, the problem is easily solved by applying Pythagorus' theorem, and Figure 3-13 provides the numerical answer to the problem. This calculation requires close attention to the different signs, but essentially everything still moves up dip. Even at the modest production rates of the fifties, it was unavoidable that errors crept into the several hundred calculations that had to be performed by hand. As Helbig says:

> Other companies must have had their way of dealing with this problem. In our company, a two-dimensional slide rule was used. While it was not absolutely fool proof, it simplified the calculations drastically and forced the operator to be consistent. Consistent sign errors are more easily detected than random errors.

Figure 3-11. A test for an aspiring geophysicist.

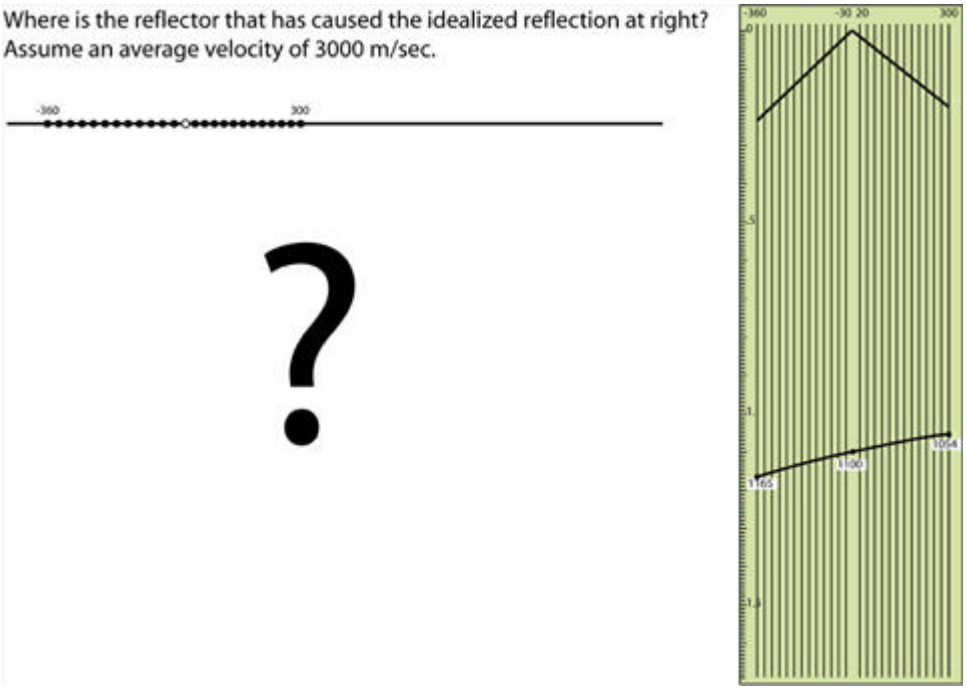

Figure 3-12. Klaus Helbig's solution to the problem of Figure 3-11.

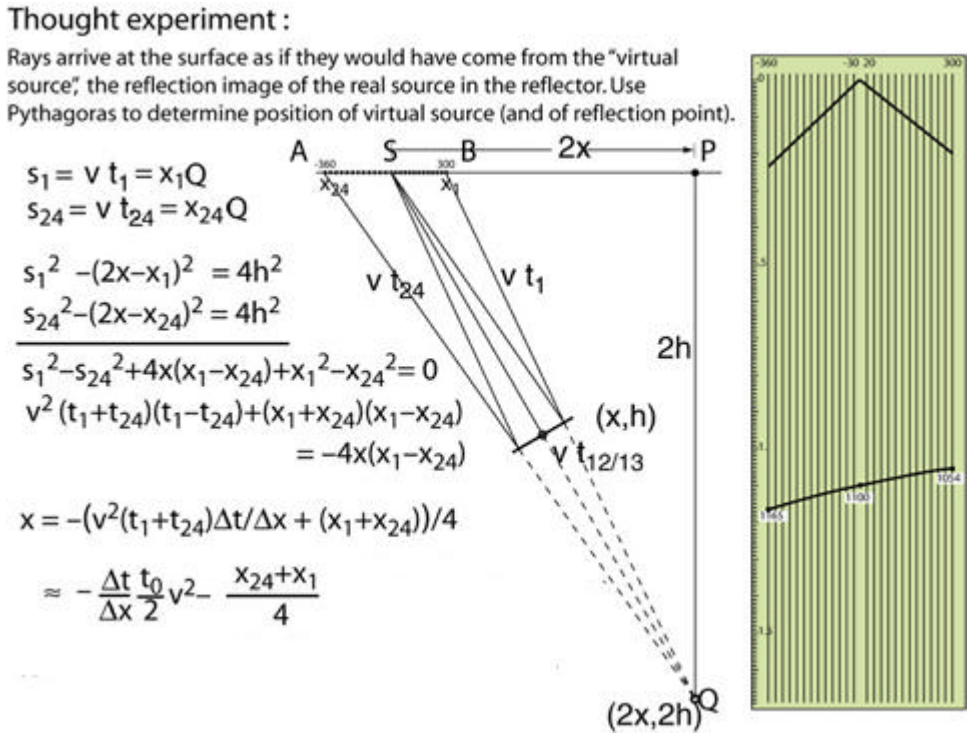

Figure 3-13. The numerical solution to the problem in Figure 3-11.

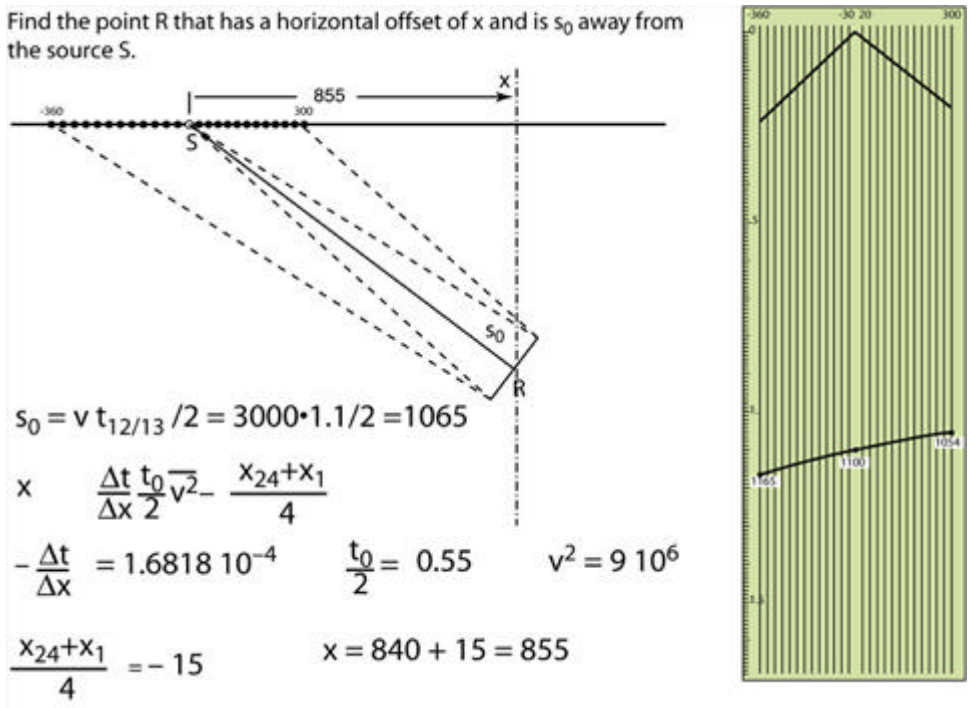

It is worth noting that we can use virtually any two picks from the shot record displayed in Figures 3-11, 3-12, and 3-13 to perform a migration. Such picks can be from any pair of traces within the shot profile, so, technically speaking, we can migrate the shot record in a very detailed manner. It is also worth mentioning that what is happening is shot-by-shot migration. It was done by humans as opposed to a digital computer, but it is still a shot-by-shot or shot profile migration.

Performing the computations involved in migration by hand is clearly difficult. Even in two-dimensions, this process was fraught with error. As a result, there was a strong push to automate the process to be able to choose well locations quickly and more accurately. One of the first such devices, as shown schematically in Figure 3-14, might best be described as a plotting device.

Figure 3-14. A simple machine for drawing reflectors at positions determined by the solution to Klaus Helbig's "thought problem."

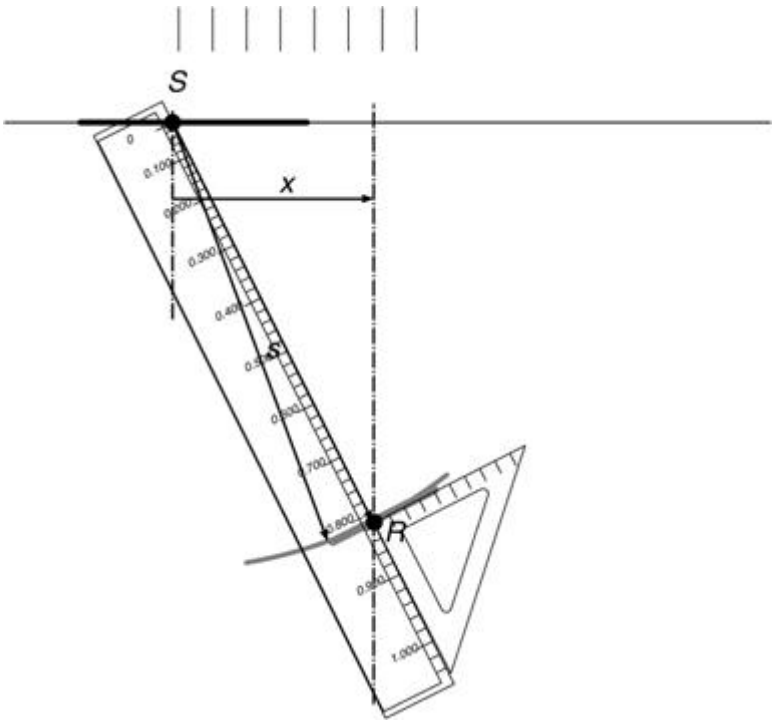

As drawn, it cannot directly calculate the value of x (Equation 3-1) in Figure 3-12, but given a bit of experience by the interpreter, it can produce very accurate *stickmap* interpretations of true subsurface horizon locations.

(3-1)
$$x = \frac{\Delta t}{\Delta x}\frac{t_0}{2}v^2 - \frac{x_{24} + x_1}{4}$$

Again, according to Klaus:

> A temporary vertical line is drawn at horizontal distance x down to the (expected) position of the reflector element. A ruler graduated in distance traveled for given times (times are displayed on the scale) is placed so that the zero-mark is at the source S and the actual traveltime at the intersection with the temporary vertical line. With the ruler firmly held in place, a small set square is placed against the ruler to draw the forward part of the reflector elements. The set square is graduated at half the scale of the rest of the drawing. This simplifies the drawing of the lengths of the parts of the reflector elements (about half as long as the corresponding surface spreads).

While it is not really a migration machine, it does foretell the kind of device that would follow to reduce the computational complexities associated with the constant velocity and straight ray formula of Figure 3-12.

Curved Rays

Until this point in time, rays underlying seismic imaging were implicitly assumed to be straight. Allowing the velocities in our Earth model to vary requires that we allow rays to refract or bend. The concept is illustrated in the cartoon of Figure 3-15. Because light travels at different speeds in air and water, it refracts. Thus, the bowman must shoot below the image of the fish he sees in the water to hit it. When velocities vary significantly, failure to accurately account for reflections along bent rays can cause significant misplacement of subsurface events. This is particularly true in subsalt plays, but is generally true for almost all prospective areas. When this was recognized, migrations began to enter what might be called the depth era. Doing this properly increased the need for a more automated method for producing the stick map images.

Figure 3-15. Fishing with a bow and arrow

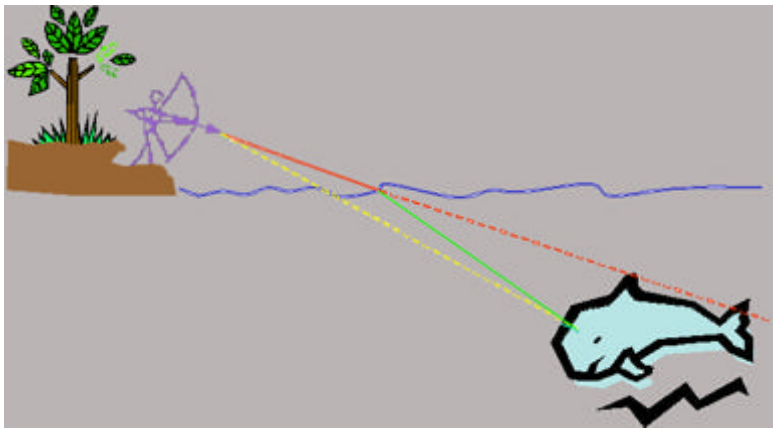

If the bowman is to hit the fish, he must properly account for the way in which light refracts as it passes from the water into the air. Similarly, the seismic program must account for the way sound is refracted when it passes from one layer to another. Both processes, in fact, obey Snell's law, which states that the ratio of the sines of the angles of incidence and refraction is equivalent to the ratio of velocities in the two media, and is also equivalent to the inverse of the ratio of the indices of refraction. For example, when a sound wave is reflected from *R* in Figure 3-16 and travels toward the surface, it is transmitted through each layer according to Snell's law. This relationship is stated mathematically in Equation 3-2.

Figure 3-16. Illustration of Snell's Law

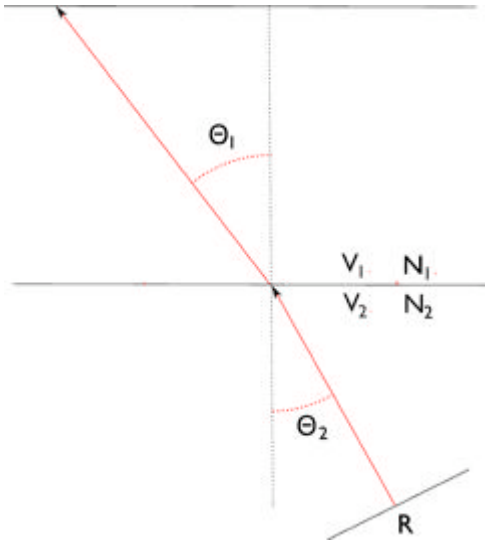

(3-2)
$$\frac{\sin i_1}{\sin i_2} = \frac{V_1}{V_2} = \frac{N_2}{N_1}$$

As long as the velocity depends on depth only, curved rays can be incorporated into the migration process by solving the problem layer-for-layer and then integrating. Since depth is unknown beforehand, it is more consistent to sum over *vertical* time, that is, over the time along a vertical ray. While specific cases can be solved exactly, the general case of arbitrary dependence of velocity on depth requires the two approximations shown Figure 3-17. As will be seen in later sections, the exact traveltime from surface to reflector is given by an infinite series.

Figure 3-17. Curved ray corrections

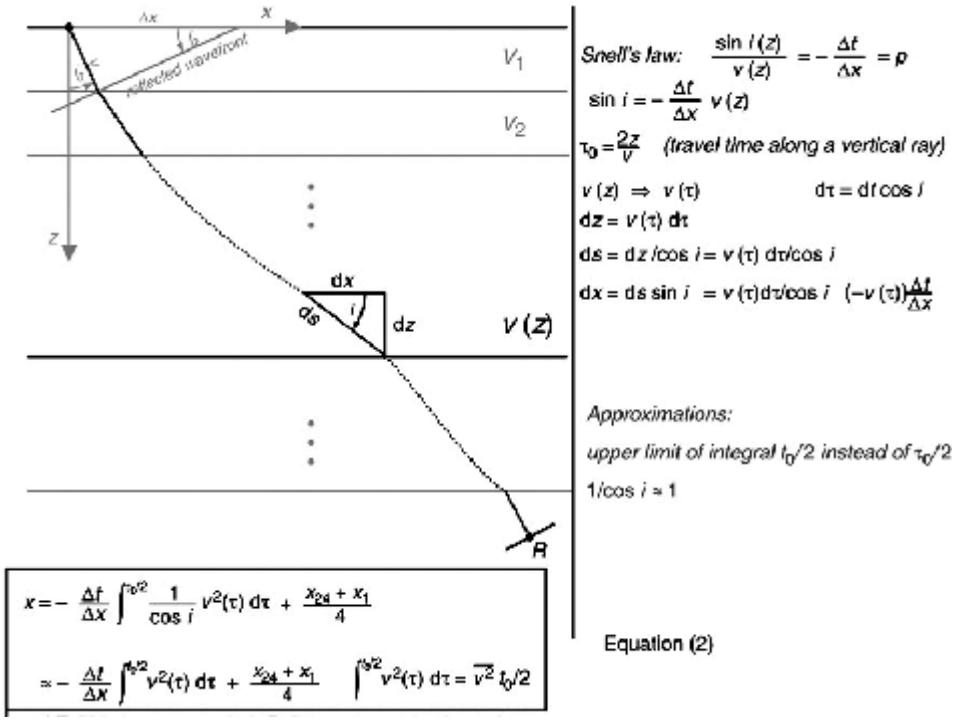

Thus, the upward traveling wave refracts based on its emergence angle, i, in the layer just above it. When it finally reaches the surface with an emergence angle of i_0, it has traversed the path indicated in Figure 3-17. The formulas integrating $v(\tau)$ over τ, provide the necessary estimate of x. The curved ray formula for x is given by Equation 3-3, where $\bar{v}$, the well known root-mean-square (RMS) velocity, is given by Equation 3-4.

(3-3) $$x = \frac{\Delta t}{\Delta x}\frac{t_0}{2}\bar{v}^2 - \frac{x_{24} + x_1}{4}$$

(3-4) $$\bar{v} = \sqrt{\frac{2}{t_0}\int^{\frac{t_0}{2}} v^2(\tau)\,d\tau}$$

Equation 3-3 is important because it tells us how to do an approximate migration when the velocity varies vertically and when rays are allowed to bend or refract. It also provides the mathematical basis for a machine doing the complex migration calculations.

Figure 3-18 shows how the migration formulas in Figure 3-17 can be used, in principle, to construct a machine for performing the migration for a given $\frac{\Delta t}{\Delta x}$ and an average squared velocity given by Equation 3-5.

(3-5) $$\bar{v}^2 = \frac{2}{t_0}\int^{\frac{t_0}{2}} v^2(\tau)\,d\tau$$

Figure 3-18. Principle for a analog device for event migration.

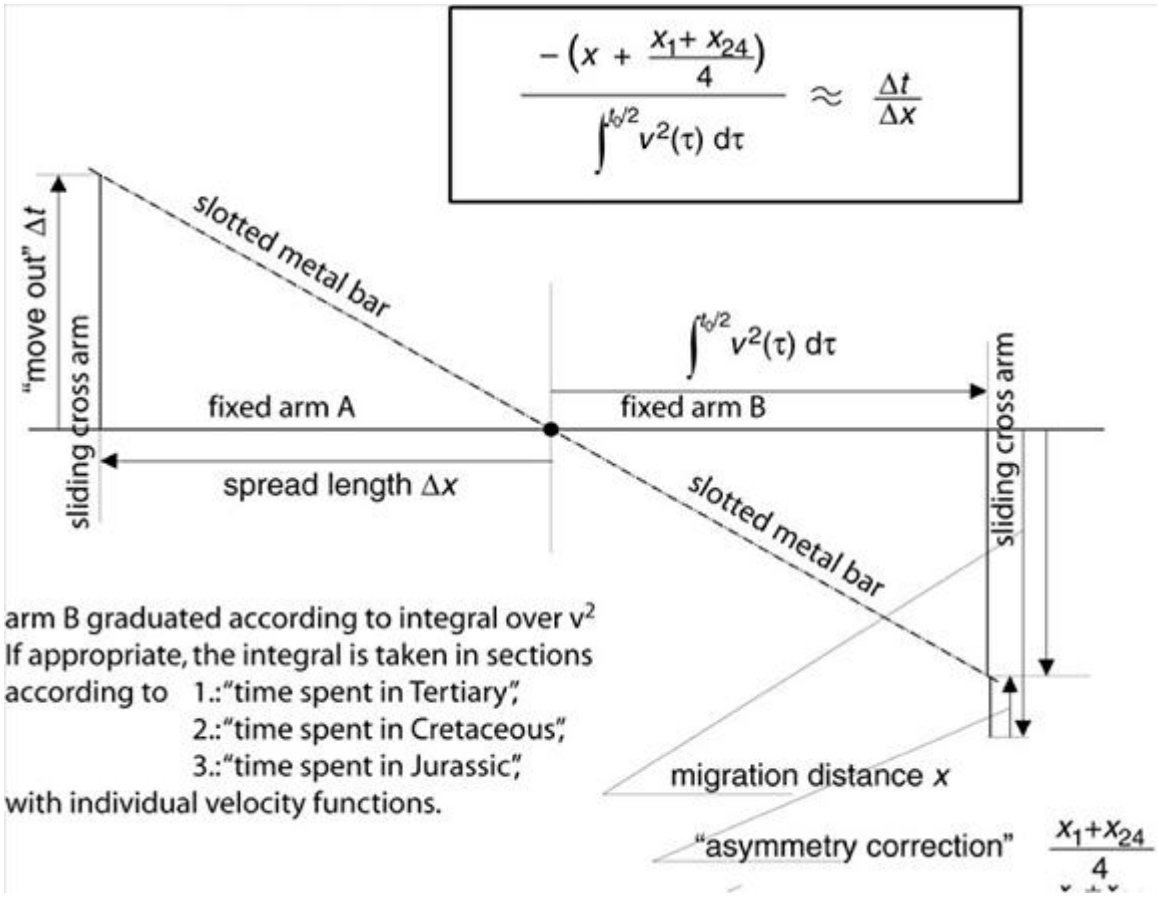

For a given $\frac{x_1+x_{24}}{4}$, the input values for Δt and Δx are input on the left and the migration distance is read off the sliding cross arm on the right. The different parts of this relation are assigned to corresponding sides of two similar triangles.

Figure 3-19 should clarify these comments. Since most reflections were visible on all 24 traces, the Δx setting and the $\bar{v}^2$ setting remains generally constant, at least during the calculation for a single shot record. Since lateral velocity variation was considered to be small, $\bar{v}^2$ also did not change appreciably. What did change was Δt. This change resulted in a *swing* of the machine's arm and consequently devices like that in Figure 3-19 became know as *Swing Arms*. Figure 3-20, from A. W. Musgrave's dissertation at the Colorado School of Mines, shows a real migration machine of the type described figuratively in Figure 3-19.

Figure 3-19. An early migration machine design.

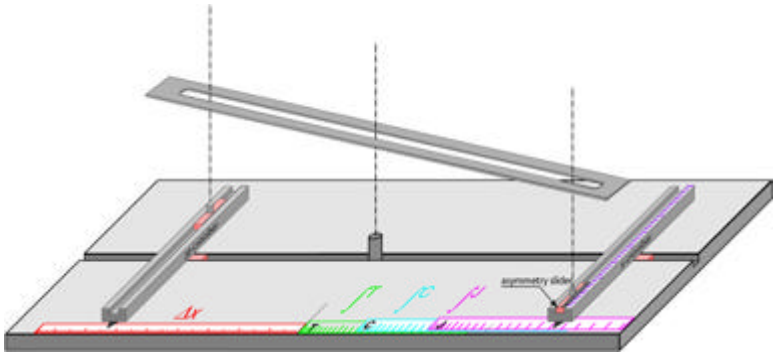

Figure 3-20. A. W. Musgrave's version of a swing arm migration machine

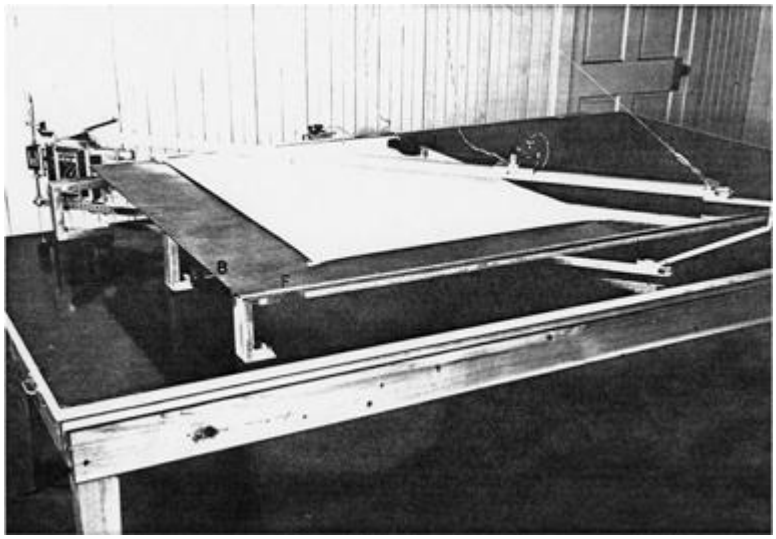

Shot Profile Hand Migration in Three Dimensions

Dipping events are usually from three dimensional reflectors. Figure 3-21 shows one possible approach to figuring out the 3D nature of reflections from dipping events by recording into orthogonal receivers. The idea is to measure and use apparent dips in crossline and inline directions as we did in Figure 3-6 to estimate the distance and direction of the migrated position from the current one.

Figure 3-21. Using a "tee" to detect dip in three dimensions.

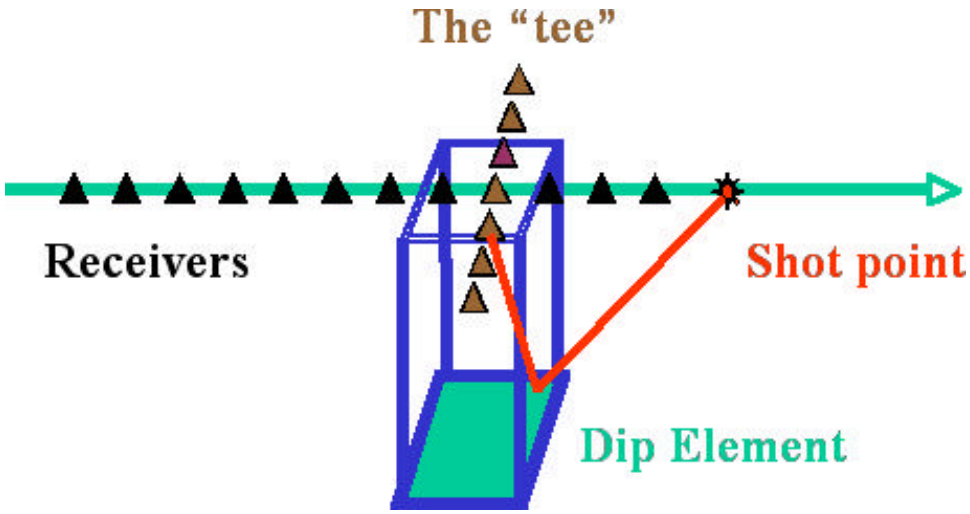

Figure 3-22 shows two late 1940's vintage Amerada Petroleum seismic records showing a "single-end shot record" and what they called a "tee" record for determining the parameters for the calculations described in previous figures. The right-hand side of each record is the single ender while the left-hand side represents the "tee". This kind of cross-spread shooting foreshadowed acquisition of seismic data using orthogonal shot and receiver lines.

Figure 3-22. A “tee” on the left and a single-ended spread on the right in both panels. The “tee” was a string of receivers orthogonal to the direction of the shot line.

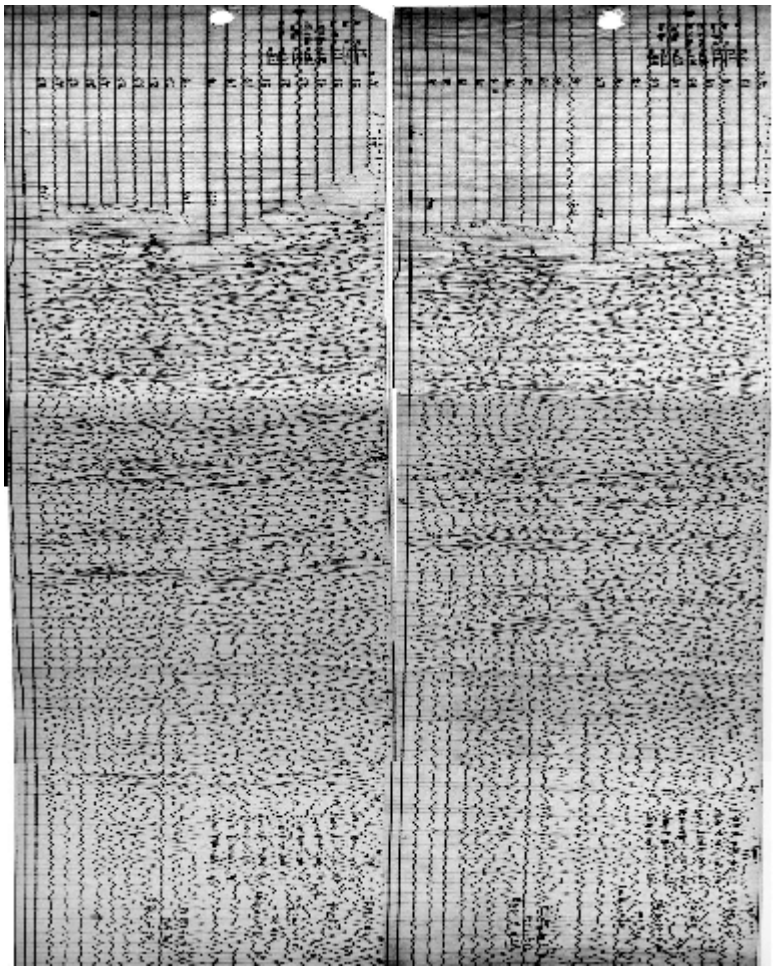

Figure 3-23 shows the simple mathematics of locating the source of the reflected event when there is dip in the x and y directions. This is a 1940's vintage description of how Amerada Petroleum's scientists approached the problem. This kind of solution was considered a top-secret technology in all oil companies of the day.

Figure 3-23. Amerada Petroleum's solution to using the "tee" to resolve 3D dip.

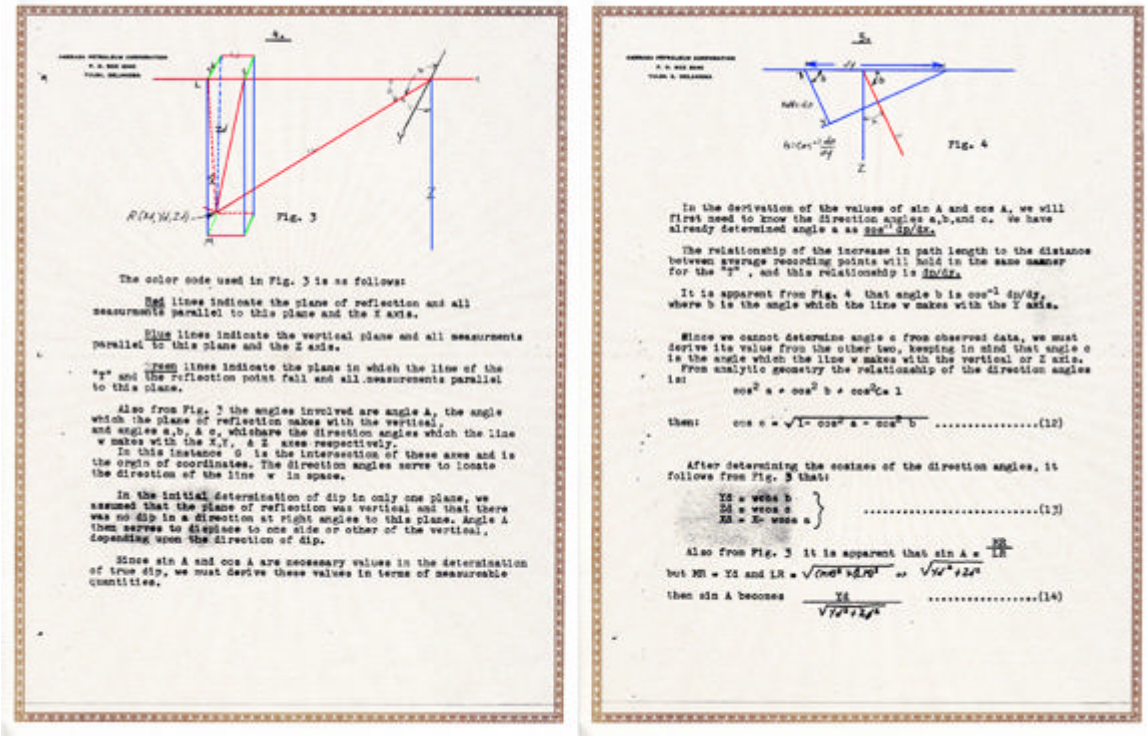

Fig. 3

The color code used in Fig. 3 is as follows:

Red lines indicate the plane of reflection and all measurments parallel to this plane and the X axis.

Blue lines indicate the vertical plane and all measurments parallel to this plane and the Z axis.

Green lines indicate the plane in which the line of the "r" and the reflection point fall and all measurements parallel to this plane.

Also from Fig. 3 the angles involved are angle A, the angle which the plane of reflection makes with the vertical, and angles a,b, & c, whichare the direction angles which the line w makes with the X,Y, & Z axes respectively.

In this instance O is the intersection of these axes and is the origin of coordinates. The direction angles serve to locate the direction of the line w in space.

In the initial determination of dip in only one plane, we assumed that the plane of reflection was vertical and that there was no dip in a direction at right angles to this plane. Angle A then serves to displace to one side or other of the vertical, depending upon the direction of dip.

Since sin A and cos A are necessary values in the determination of true dip, we must derive these values in terms of measureable quantities.

Fig. 4

In the derivation of the values of sin A and cos A, we will first need to know the direction angles a,b,and c. We have already determined angle a as $\cos^{-1} dp/dx$.

The relationship of the increase in path length to the distance between average recording points will hold in the same manner for the "r" , and this relationship is dp/dr.

It is apparent from Fig. 4 that angle b is $\cos^{-1} dp/dy$, where b is the angle which the line w makes with the Y axis.

Since we cannot determine angle c from observed data, we must derive its value from the other two, keeping in mind that angle c is the angle which the line w makes with the vertical or Z axis.

From analytic geometry the relationship of the direction angles is:

$$\cos^2 a + \cos^2 b + \cos^2 c = 1$$

then: $\cos c = \sqrt{1 - \cos^2 a - \cos^2 b}$ .....(12)

After determining the cosines of the direction angles, it follows from Fig. 3 that:

$$\left.\begin{aligned} YS &= w\cos b \\ ZS &= w\cos c \\ XS &= w\cos a \end{aligned}\right\}$$ .....(13)

Also from Fig. 3 it is apparent that $\sin A = \frac{MR}{LR}$

but $MR = YS$ and $LR = \sqrt{(ms)^2 + (LM)^2}$ or $\sqrt{ys^2 + zs^2}$

then sin A becomes $\frac{YS}{\sqrt{ys^2 + zs^2}}$ .....(14)

Remarks about Migration

Much of what has been discussed so far is what we might call early shot-by-shot migration. Early practitioners of the imaging art were forced to use what they had. They did not have access to modern computers, so sorting data into any other order was impossible because it had not been recorded, impossible because the technology of the day was not capable of doing it, or impossible because it was just too difficult and expensive to consider. There wasn't any way to estimate velocities from recorded data, so shot-by-shot event imaging was the only practical approach.

Without redundancy, velocity information was obtained only by trial and error. If, when tested, a given $v(z)$ was shown to be in error, a new $v(z)$ was selected and used to produce a new stick image. This process was repeated until the result was considered geologically reasonable. This meant that a different flat Earth, vertically varying velocity was being used for each new geologic setting, even if the new location was close to the previous one. It also meant that a large number of different velocity functions might have to be tried before a suitable one was found.

The basic steps in historical *shot-by-shot imaging* are summarized in the following list:

1. Estimate little dip elements from shot-profile records: Single-ended, split-spreads, and "tees".

2. Calculate the distance from the shot-point to the image point using relatively simple math.

3. Place the image point at the estimated depth or vertical (migrated) time to produce a "stick" image.

From a computational viewpoint, this suggests that more than one set of calculations based on Figure 3-17 might be necessary to produce an accurate stick image of any given horizon of interest.

Redundant Data

When multi-fold acquisition consisted mostly of 2D data, receivers were laid out on either side of a centrally placed source. Figure 3-24 shows that this split-spread shooting resulted in redundant data that can be sorted in a variety of ensembles or gathers. In this figure, we see common or fixed-offset, common-receiver, and common-mid-point or common-depth-point gathers. Holding the offset fixed produces sections that, when the offset distance is small, look remarkably like zero-offset profiles. Notice that the term *common-depth-point* really has very little to do with a subsurface point. It is exactly equivalent to a surface source-receiver midpoint. This is also true of common-offset data, where the offset is measured at the surface. Moreover, these data are completely described when the source and receiver locations for the given trace are known. All other information can be computed from these locations.

Figure 3-24. Split-spread acquisition geometry.

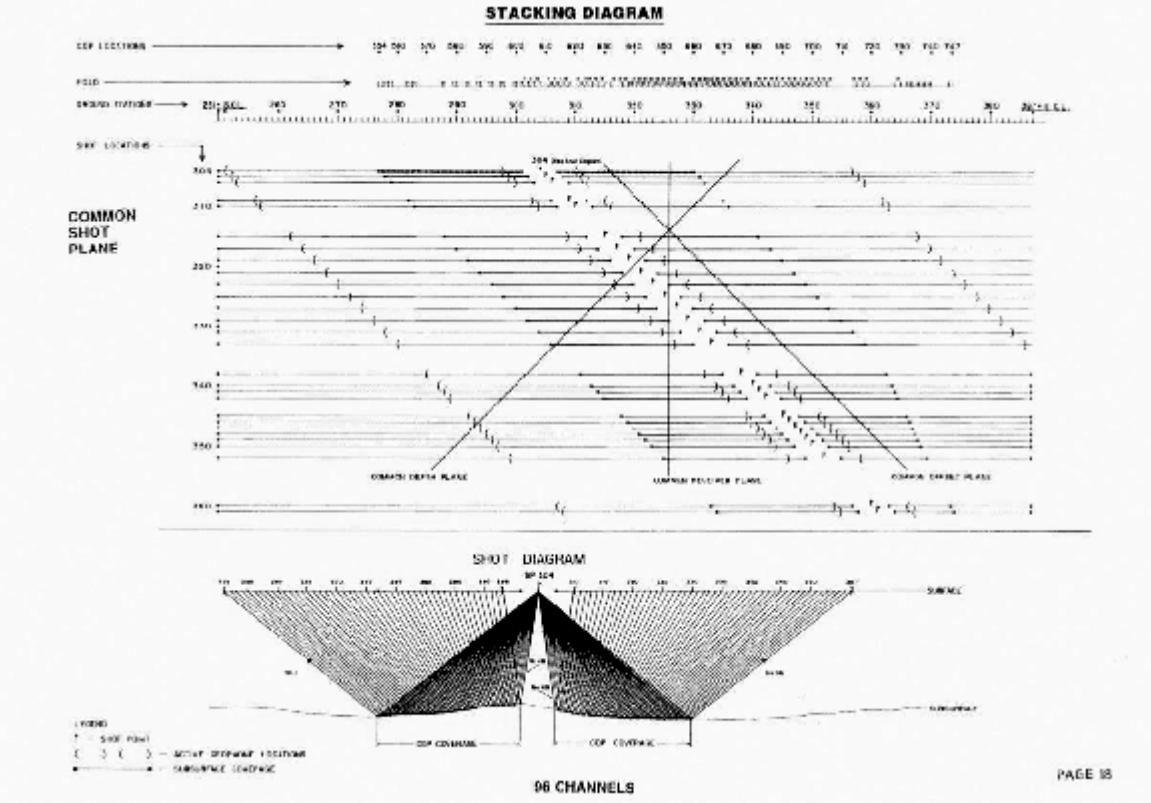

These data, while usually referred to as 2D, actually have three dimensions: source position, receiver position and time. Alternatively, they can be thought of as having common-midpoint, offset, and time as their coordinate system. However we specify the surface data, the resulting volume is three dimensional.

Figure 3-25 shows the split-spread response of a subsurface containing a single reflection point. At the top left, we see the entire response and then, clockwise, the next four figures show a common-offset slice, a common-time slice, a common-angle slice, and a common-midpoint slice. We will see that there are migration algorithms that allow us to migrate data organized in any of these domains.

Figure 3-25. Split-spread point response. The response of a single point to split-spread acquisition.

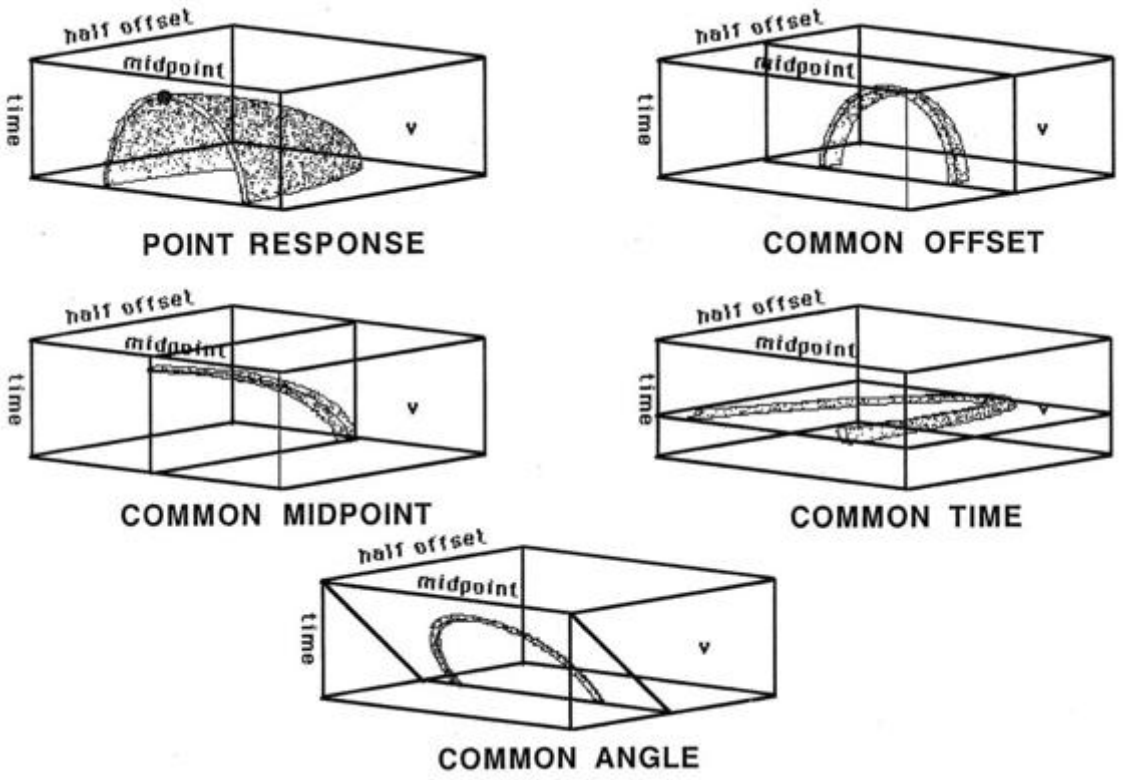

Redundant data have many advantages. In the early days, the major advantage arose because they can be sorted into common-mid-point (CMP) order to produce rough estimates of velocity. Although not completely accurate, these velocity estimates were thought to provide the velocity $\bar{v}^2$ so important in the migration approach discussed above. The accuracy of velocities estimated in this way is a function of many things, but the lateral velocity variation due to reflector dip and the velocity variation due angle of propagation can render such estimates almost useless. Only when the Earth is absolutely flat, and there is no variation of velocity with angle of propagation, can such velocity analysis produce accurate values. Nevertheless, the velocities estimated in this way represented a major step forward in improving the accuracy of migrations. Without these estimates, the production of subsurface images probably would not have arrived as early as it did.

Figure 3-26 shows how redundant data provides estimates of velocity. The left side of this figure shows a typical common-midpoint gather. The traces all have the same midpoint, and, if the subsurface reflectors are all flat, the hyperbolic curve in red defines the appropriate velocity to use to correct the data to zero offset time, t_0, and ultimately to produce zero-offset data. Special analog computers were designed and used to estimate $\bar{v}^2(t_0)$ at as many midpoints as possible. Another analog computer stacked the traces in the CMP and the resulting section was migrated using formulas just like those in the previous paragraphs.

Figure 3-26. Flat Earth Society processing to zero offset

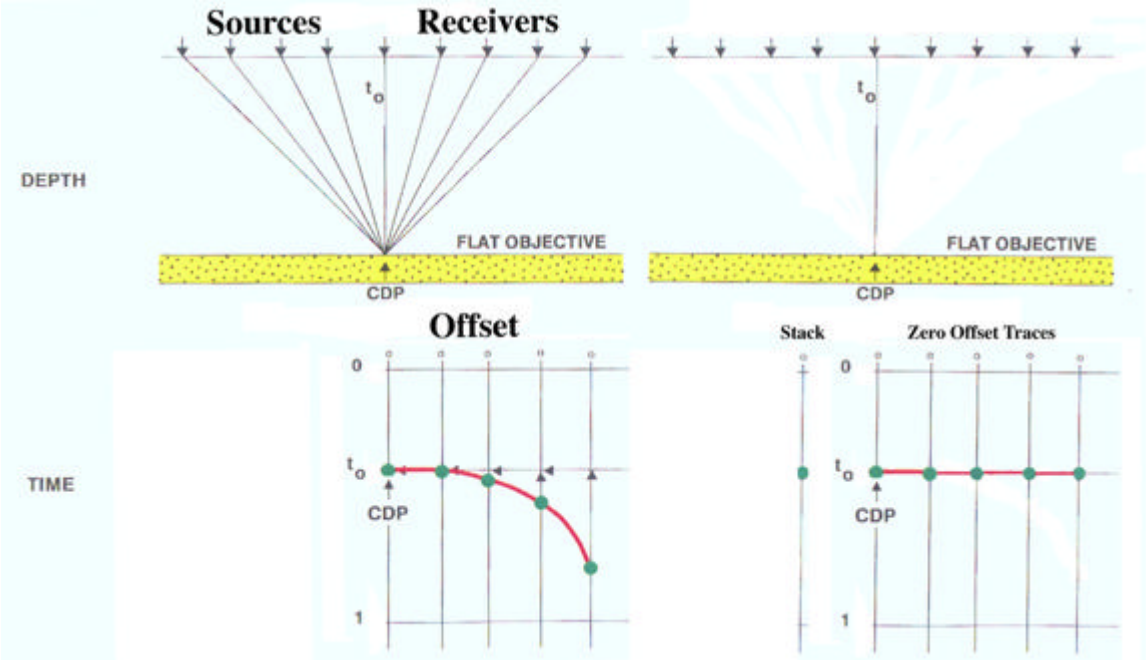

The right hand side of Figure 3-26 shows the application of a dynamic correction known as normal moveout (NMO) to correct the hyperbolic response to a flat one. Part of the definition of NMO from Wikipedia (Wikipedia contributors, "Normal Move Out" Wikipedia, The Free Encyclopedia, Wikipedia link):

> Because the wave must travel along the hypotenuse created between the depth of the event and source-receiver offset, the time delay increases hyperbolically along equally spaced geophones. The hyperbolic distortion must be corrected in order to accurately image the subsurface.

The result of summing the dynamically corrected traces for every CMP is called a *stacked section*.

Swing Arms

This section presents additional information about swing arms, which were mechanical devices enabling you to migrate dip data. See also Curved Rays on page 100 for more information about swing arms.

Isopachs and Isochrons

In view of the comments in the preceding sections, one conclusion becomes quite clear—any apparent reflection on any given trace could have come from any point on an equal traveltime subsurface *isopach*. An equal traveltime isopach is that set of points in the subsurface whose traveltimes from the surface and back (two-way times) are identical. Figure 3-27(a) shows an equal traveltime curve in a constant velocity medium for zero-offset reflections. Clearly, if all we have is a zero-offset trace, we can only infer that the reflection could have come from any point on the equal-traveltime isopach defined by the reflection time.

Figure 3-27(b) provides the simplest mathematics defining an equal traveltime curve. It also shows how the apparent horizon (dotted line) is imaged as the envelope (dark solid line) of a set of equal traveltime curves.

Figure 3-27. Equal traveltime curves in a constant velocity medium.

(a). Equal traveltime curves for zero offset data

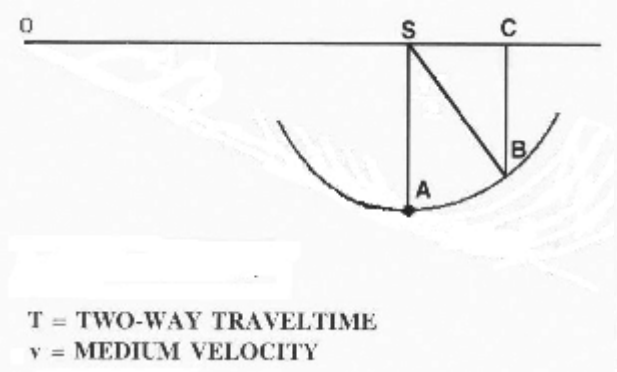

(b). Migration with equal traveltime curves

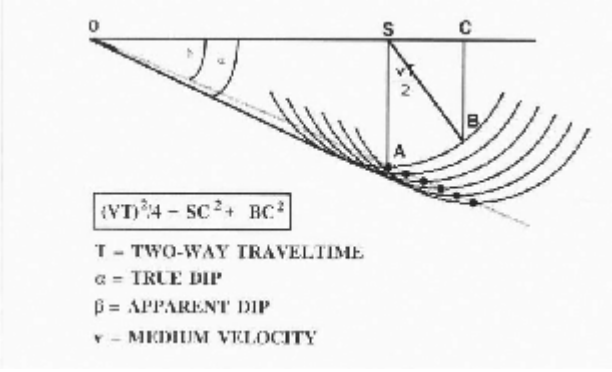

For any given arrival on a recorded seismic trace, all potential locations from which this arrival could have been reflected lie on a circle with the source point as the center and the velocity-time depth as the radius. If we trace out a circular isopach for each source, the envelope of all such isopachs will be the location of the actual reflecting surface. Since the velocity is assumed to be constant, these circular isopachs can also be thought of as isochrons, or curves and surfaces in time rather than depth. Regardless of terminology, a swing-arm built on this principle has a significant advantage over hand

plotting each vector to migrate the given dip data. An entire zero-offset stick map could be migrated with a constant velocity without every resorting to any calculations at all. Of course, the constant velocity assumption meant that the results might not be accurate, but they could be redone quickly. A different constant velocity could be used for each surface position to at least make the resulting migrated stick map as close as possible to subsurface truth.

Operators

Figure 3-28 provides the time response on the surface for a single point reflector in the subsurface.

Figure 3-28. Operators and operator migration—Point reflector zero-offset response

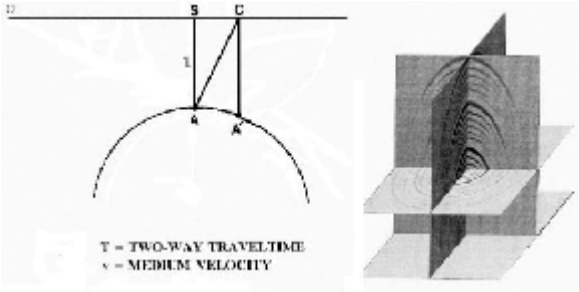

Every time on this time domain curve is the two-way time from the surface source to the point reflector and back to a receiver at exactly the same location as the source. The time recorded at A' below C is actually the time it would take for sound to travel from a source at C to the point reflector below S and back to a receiver at C. As indicated in Figure 3-28 for a constant velocity medium, the set of all such times can be calculated quite easily using Pythagorus' theorem.

(3-6)
$$T = \sqrt{T_0^2 + \frac{(C-S)^2}{v}}$$

In a more complex velocity medium, the curve would not be a circle, but would still represent the zero-offset reflection times from the point reflector. Zero offset responses are quite easy to calculate, and raytrace modeling is fully capable of calculating such responses in virtually any medium.

The operator approach to migration computes an operator curve, intersects it with each input trace, selects the amplitude at the intersection time, and then adds it to the image point or output location on or near the top of a downward facing frown. In actuality, this is completely equivalent to the previous diffraction-based approach. They both produce the same result, but this one is a bit more difficult to understand. Figure 3-29 shows an amplitude at *A* being moved to the top of the zero-offset response curve and added to the reflection point location at *B*. In general, all the amplitudes that intersect the operator would be summed into the top of this curve at point *B*. However, the only non-zero amplitude point that we can see is at *A*. As the process continues, each and every point on the apparent or unmigrated reflector is moved to the top of the associated zero-offset response curve and added to the appropriate spot on the migrated image represented by the solid line in Figure 3-29.

Figure 3-29. Operators and operator migration—Zero-offset response or operator migration

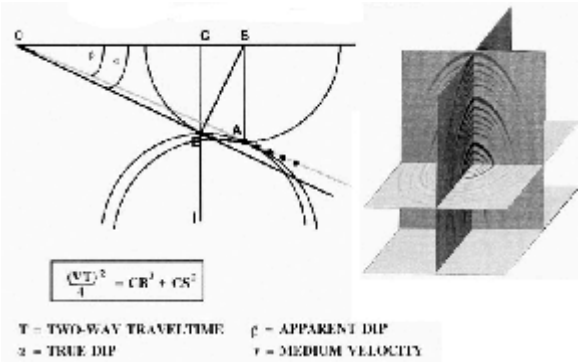

The three-dimensional figure on the right illustrates all the amplitudes from surrounding traces that contribute to the trace in the middle. These frowns are called operators, but they are really the modeled response of a point reflector at some subsurface location. The important thing is the process and not the shape of the zero-offset response.

This approach to migration is somewhat more difficult to understand than the *spray* approach of the previous section. Why it works should become much clearer in the chapter on seismic modeling. However, one thing should be clear, it is based on modeling a point reflector and not on the possible locations from where the reflector might have come.

Non-Zero Offsets

Figure 3-30 shows the ellipse representing the set of points whose traveltimes from a source at *S* to a receiver at *R* are identical. Producing this kind of curve in variable velocity mediums became practical with the advent of digital computers. Migration of fixed-offset data follows the same principles at shown in the zero offset case shown in the bottom image in Figure 3-27. There is, of course, a corresponding non-zero-offset operator-based approach to migration. Raytracing is used to compute the traveltime from any given source to a reflection point, then from the reflection point back to the receiver on the surface. Operator migration then proceeds in the same manner as it did in Figure 3-28.

Figure 3-30. Fixed offset equal-travel-time curves.

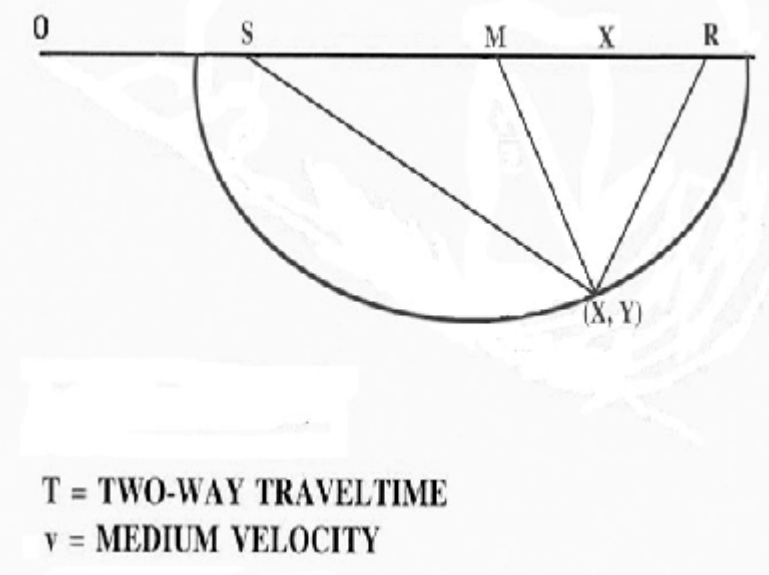

It is clear from Figures 3-27 through 3-30 that if we wish to use the concepts involved in the most general possible case, we must compute traveltimes from any given source to a potential reflection point and then back to a fixed receiver. Just prior to the advent of digital computers and to some extent beyond that time, efforts were made to do just that. Analog devices were designed to compute these traveltimes in the form of *wavefront charts*.

The mathematics in Figure 3-31 was used to compute the wavefront charts in Figure 3-32. It is not important to understand the mathematics. What is important is that the formulas provide a method for calculating the two-way traveltimes from any point on the surface to any point in the subsurface of a $v(z)$ medium and back. Today, the traveltimes originally chosen from wavefront charts are easily and very repetitively computed via raytracing. What is also important is that this approach was known and used in the mid 1950's for performing complex migrated stick figure reconstruction of picked seismic arrivals.

Figure 3-31. Wavefront chart mathematics

$$x(i) = \frac{2z_0^{(2)}}{\sin^2 i_0}\int_{i_0}^{i}\sin^2\chi d\chi = \frac{z_0^{(2)}}{2\sin^2 i_0}\left(2i - 2i_0 - \sin 2i - \sin 2i_0\right),$$

$$z(i) = z_0^{(2)}\left(\left(\frac{\sin i}{\sin i_0}\right)^2 - 1\right) = \frac{z_0^{(2)}}{2\sin^2 i_0}\left(1 - \cos 2i - \cos 2i_0\right),$$

$$t(i) = \frac{2z_0^{(2)}}{v_0 \sin i_0}\int_{i_0}^{i}\chi d\chi = \frac{i - i_0}{\sin i_0}\tau_0 .$$

These are the equation of a right cycloid generated by a circle with

$$R = \frac{1}{2}\frac{z_0}{\sin^2 i_0} = \frac{1}{2}\frac{z}{\sin^2 i}$$

The wave front charts in Figure 3-32 are based on the mathematics of Figure 3-31. The charts represent the velocity functions in Equation 3-7, where $n = 0$ is constant velocity, $n = 1$ is standard chart (constant velocity gradient, rays are circles, fronts are spheres), and $n = 2$, which is more realistic, but in the pre-computer days, difficult to generate.

(3-7)
$$\left(\frac{v}{v_0}\right)^n = \frac{z + z_0}{z_0}$$

Figure 3-32. Wavefront charts

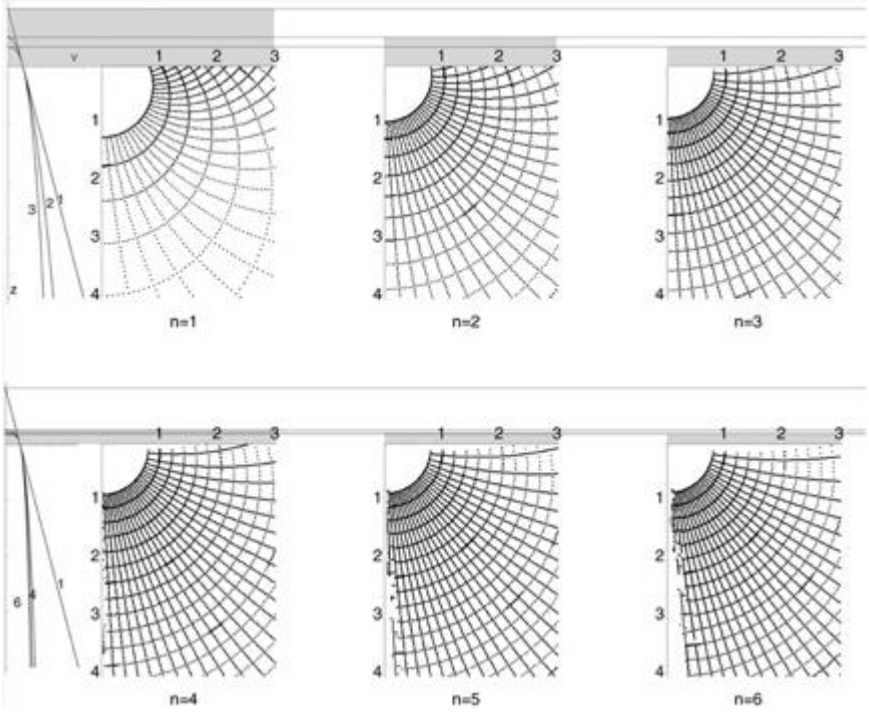

It may not be clear from these figures, but the construction of any given wavefront chart is based on the utilization of circles to generate rays. This should not be too surprising since, for any given constant velocity, the point response is defined by the equation of a circle.

Once the concept, as shown in Figure 3-33, is understood, it is quite reasonable to construct a mechanical device to both calculate the wavefronts and also produce stick figure images. By the late 1950's and into the early 1960's, machines were constructed to perform migration based on the wavefront charts in Figure 3-32. Thus, Figure 3-33 is a geometrical picture of the mechanical basis for a machine such as A. W. Musgrave's wavefront charting machine shown in Figure 3-34. Note the charts on the surface. This machine is actually an analog device for raytracing. I don't know about you, but this looks like a printing press to me. Unfortunately, no such machine appears to have survived.

Figure 3-33. The geometric basis for A. W. Musgrave's migration machine

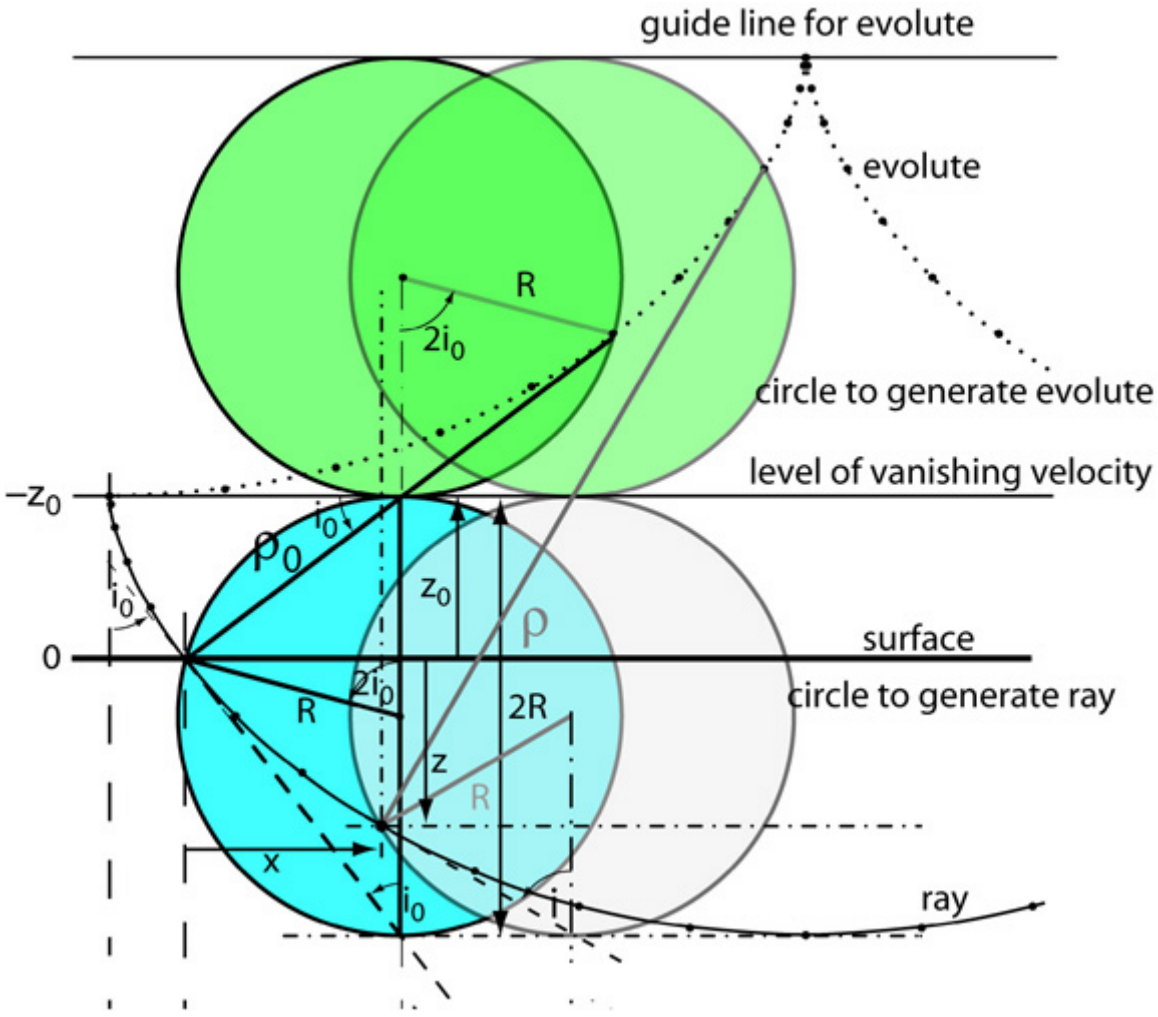

Figure 3-34. A. W. Musgrave's migration machine

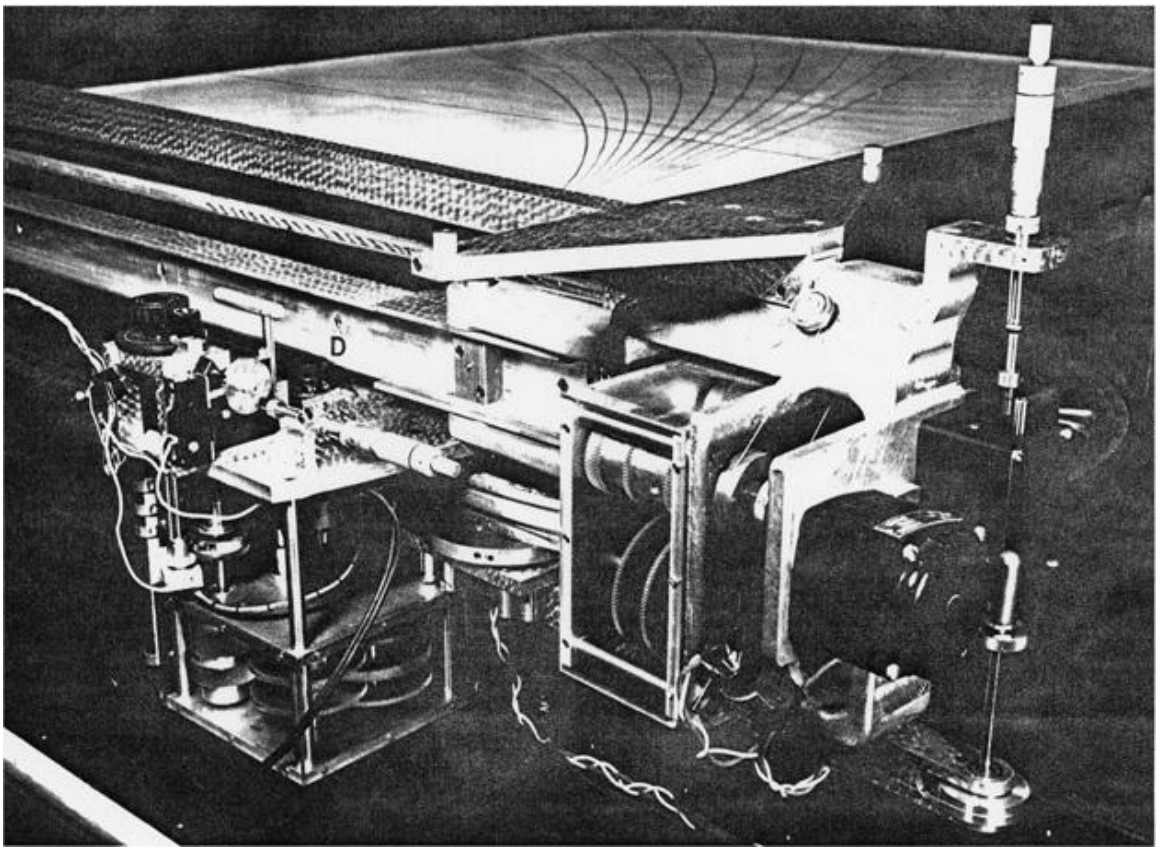

It is important to note that in the real world, because the sources and receivers are at discrete locations, we must consider our measured seismic data to be digital in character. Since modern data is also digital in time, reflection seismic processing today is purely digital. Since the wavenumbers of propagating plane waves carry information about the angle of propagation, this suggests that there will be some issues with regard to the aliasing of dipping subsurface reflectors. The impact of aliasing on our ability to image subsurface events will be discussed in subsequent sections.

Stacking and DMO

The primary purpose of this section is to provide a simple understanding of why certain parts of early digital processing techniques did not image all of the Earth's structures. This, in effect, is an interpretation issue. We will see that what might be considered easily imaged events are sometimes totally invisible in the seismic record. In many such cases, parts of the subsurface structure may be invisible simply because we have not applied the most accurate available technique to image it. In other cases, its absence may be due to improper noise suppression techniques applied during the preprocessing steps. Whatever the cause, the idea is always to be able to understand what approach produces the best image.

What is Stacking and DMO?

As we will see, migration can be split into four conceptual pieces. As a rule of thumb, these four pieces will help us understand what migration is and how it naturally completes the imaging process.

1. The first piece is called *normal moveout* (NMO). When the world is flat, NMO corrects for the fact that the source and receiver are not coincident, but it cannot do so when the reflections come from dipping horizons.

2. The second piece of migration corrects for dip. Historically, this second piece was called *dip-moveout* (DMO), but, in the cases of interest here, it happens within the migration methodology itself.

3. The third migration piece shifts events on each moveout-corrected offset to its true subsurface position.

4. The fourth and final piece sums (stacks) all the redundant traces into the final image.

When the Earth's velocity has very little lateral variation, these four operations can be split apart and applied in any desired order. The most familiar order is NMO, DMO, stack, and finally migration. However, when the velocity is almost constant, it is quite possible to use the order DMO, migration, NMO, and stack. Full prestack migration can be thought to have the order DMO, NMO, imaging, and stack, but in reality the sequence DMO, NMO, and imaging is usually done in one giant process.

Initial attempts at subsurface imaging forced the geophysicist to join the Flat Earth Society. For a constant velocity medium, Figure 3-35 shows that Greek mathematics can be used to provide the total travel time, t, from a surface source to a flat subsurface reflector and back to a surface receiver. This is done in terms of the two-way vertical travel time, t_0, from the midpoint, M, to the reflector and back to the surface. Since neither the velocity, v, nor the vertical or "zero-offset" traveltime is usually available directly, redundant source and receiver configurations must be used to estimate the traveltimes. For most acquisition geometries, redundancy is usually sufficient to simultaneously estimate both t_0 and v.

Figure 3-35. Constant velocity NMO.

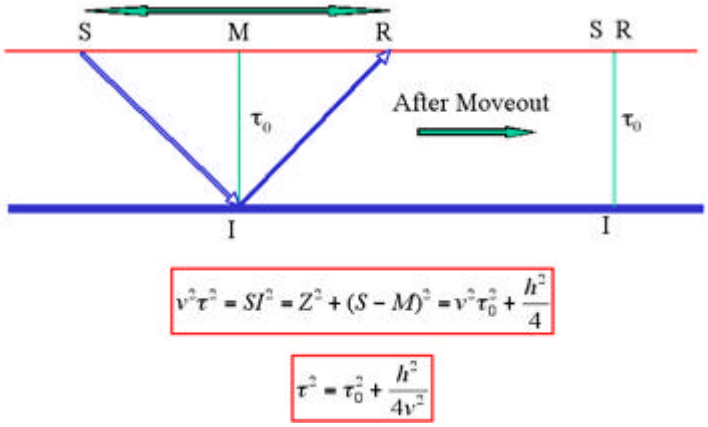

The subsurface image point, I, is usually referred to as the *common-depth-point* (CDP). The common depth point is the halfway point in the travel of a wave from a source to a flat-lying reflector to a receiver. When we know the velocity, the arrival at time t and offset h can be moved to time t_0. This process is usually called *normal moveout correction* (NMO). After NMO, all traces with a common-midpoint are summed to remove the redundancy and produce a zero-offset trace.

However, for our purposes, the important thing is that this vertical time shift is the first step in formulating a prestack approach to imaging. The shift corrects to the arrival time consistent with coincident sources and receivers. After NMO, the result is as though the source, S, and receiver, R, were located at the midpoint, M.

The traces in the CDP gather of Figure 3-36 all have the same midpoint. When the subsurface reflectors are all flat, the hyperbolic curve in red defines the appropriate velocity to use to correct the data to zero offset time t_0. A modern computer easily fits the data and provides the graphics to estimate both the vertical traveltime and the velocity. The vertical traveltime, t_0, in this figure is extremely important. Keep this in mind as the book continues.

Figure 3-36. Typical midpoint gather.

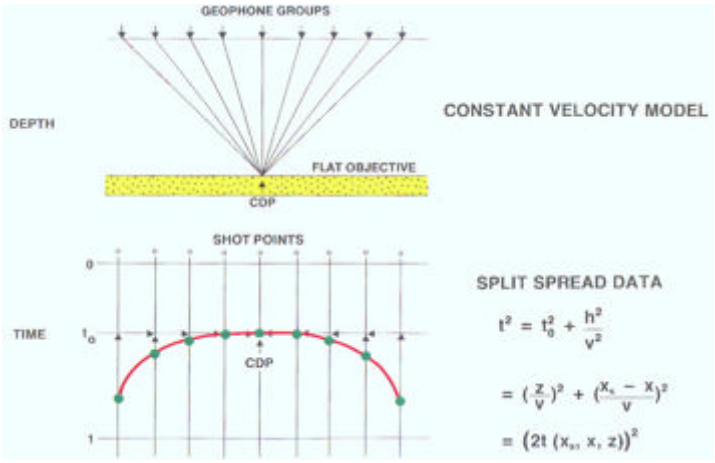

The shots in Figure 3-37 are from the pyramid model in Figure 3-38.

Figure 3-37. Shots 1-24 from the Pyramid model

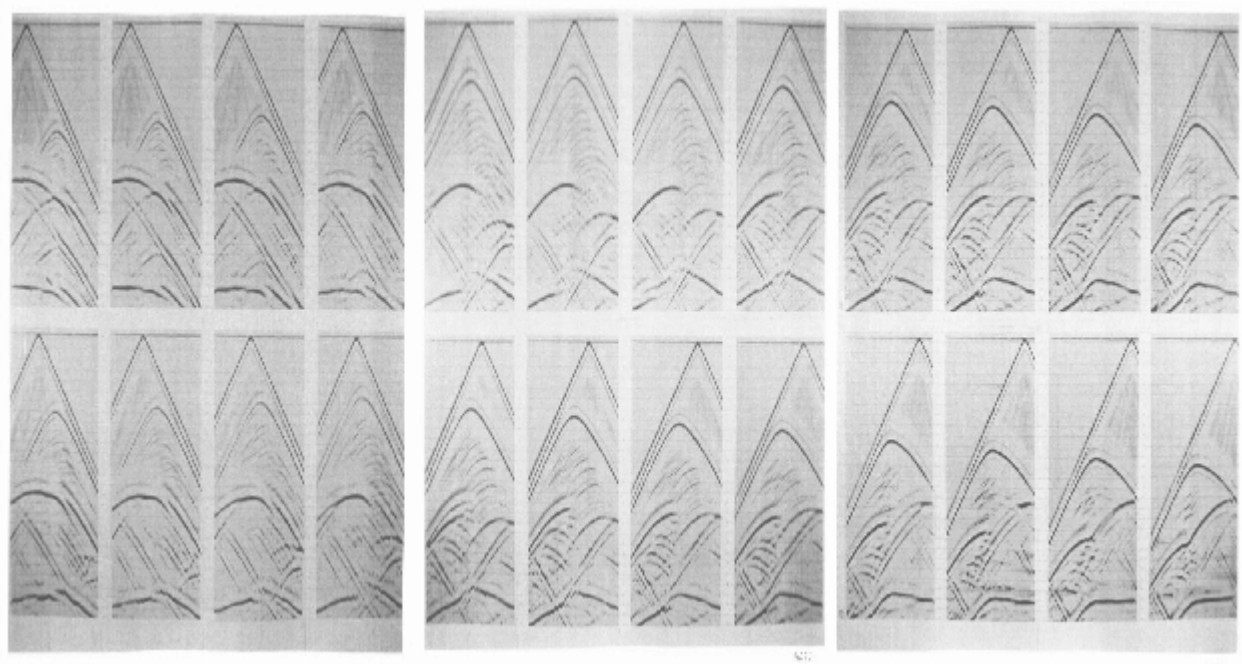

Figure 3-38. The Pyramid Model

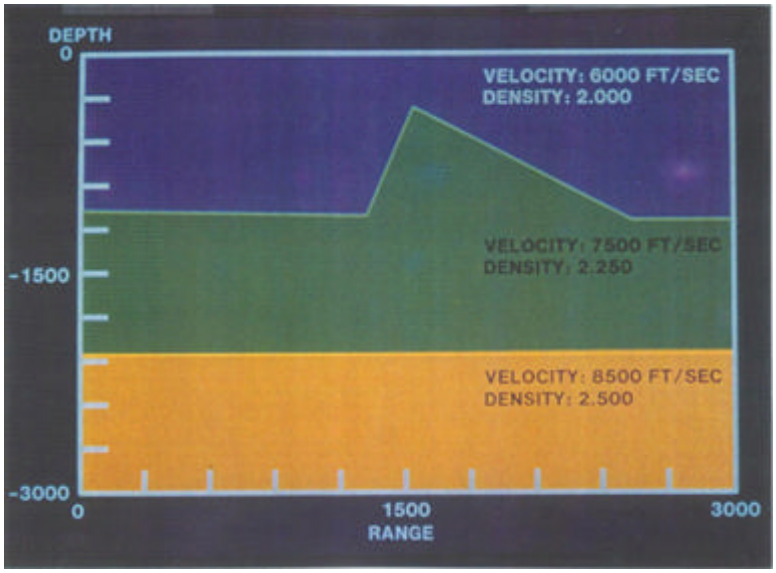

Figure 3-39 is a stack of the common-midpoint ordered data in Figure 3-37. NMO was performed using the root-mean-square velocity from the model used to generate the data. The “noise” in this data set is representative of a poor implementation of the approximations to the differential equation used to model the data. This kind of noise is related either to the fact that the differences have not been approximated well, or because damping at the boundaries is poor.

Figure 3-39. The stack of Shots 1-24 from Figure 3-37.

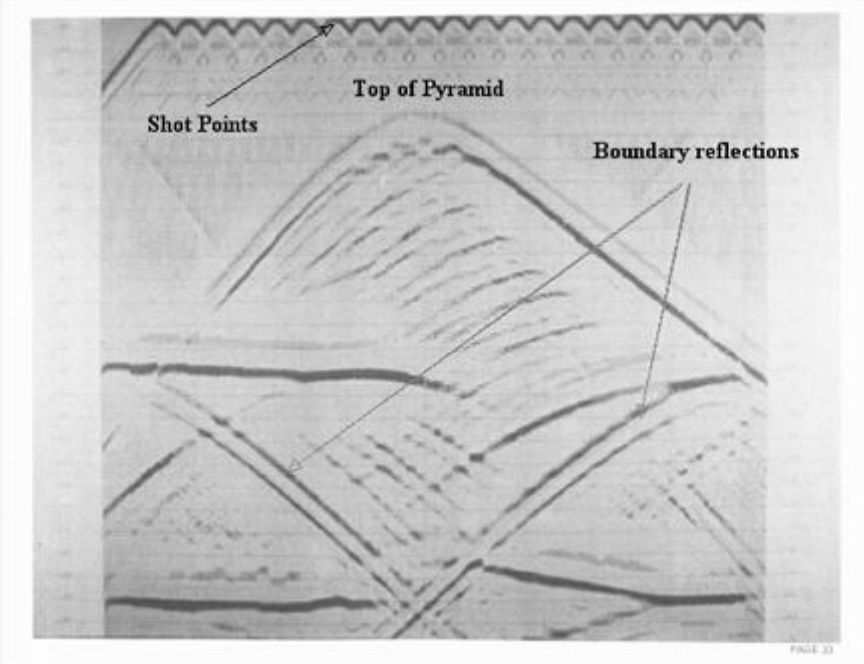

Figure 3-40 shows how dip affects arrival times as a function of half-offset.

Figure 3-40. Moveout for a dipping reflector.

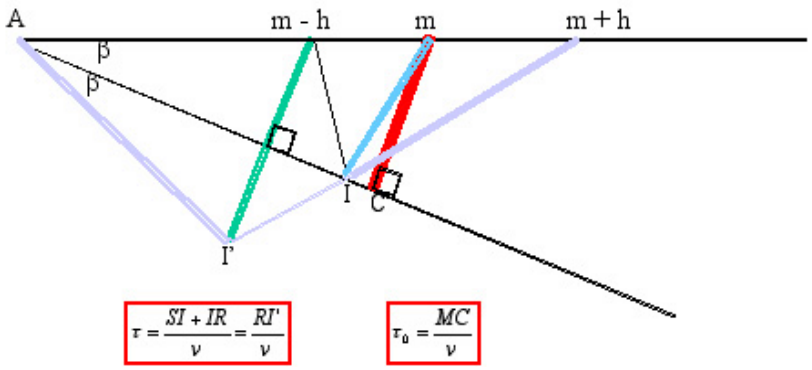

$$\tau^2 = \tau_0^2 + \frac{h^2 \cos^2 \beta}{v^2} = \tau_0^2 + \frac{h^2}{\frac{v^2}{\cos^2 \beta}}$$

To relate the traveltime from source at $m - h$ (S) to the image point, I, and back to the receiver at $m + h$ (R), note that in Figure 3-40, the length of the path from S to I and then to R is the same as the length from R to I'. Using the law of cosines, we have Equation 3-8.

(3-8)
$$\begin{aligned}(RI')^2 &= (AI')^2 + (AR)^2 - 2(AI')(AR)\cos 2\beta \\ &= (m-h-A)^2 + (m+h-A)^2 - 2(m-h-A)(m+h-A)\cos 2\beta \\ &= 2(m-A)^2 + 2h^2 - 2(m-A)^2 \cos 2\beta + 2h^2 \cos 2\beta \\ &= 2(m-A)^2(1 - cos2\beta) + 2h^2(1 + \cos 2\beta) \\ &= 4(m-A)^2 \sin^2 \beta + 4h^2 \cos^2 \beta\end{aligned}$$

To get the time over the path from R to I', divide each side of Equation 3-8 by v^2, as shown in Equation 3-9.

(3-9)
$$\frac{(RI')^2}{v^2} = \frac{4(m-A)^2 \sin^2 \beta}{v^2} + \frac{4h^2 \cos^2 \beta}{v^2}$$

Since the vertical traveltime is given by Equation 3-10, we get the final equation, Equation 3-11.

(3-10)
$$\tau_0 = \frac{MC}{v} = \frac{(m-A)\sin\beta}{v}$$

(3-11)
$$\tau^2 = \tau_0^2 + \frac{h^2 \cos^2 \beta}{v^2} = \tau_0^2 + \frac{h^2}{\frac{v^2}{\cos^2 \beta}}$$

The cosine term in the denominator of Equation 3-11 essentially increases the apparent velocity of the dipping reflector. For example, the apparent velocity of a bed dipping at 60 degrees will be exactly twice that of a flat reflector in the same velocity medium.

Figure 3-41 shows that reflections from a dipping reflector in a constant velocity medium appear to be from a flat reflector with a velocity of $\frac{v}{\cos\beta}$. The blue hyperbola is what actually defines the dipping event. The red curve is the hyperbola from a flat reflector with the same velocity, v.

Figure 3-41. The impact of dip as seen on a common-midpoint gather.

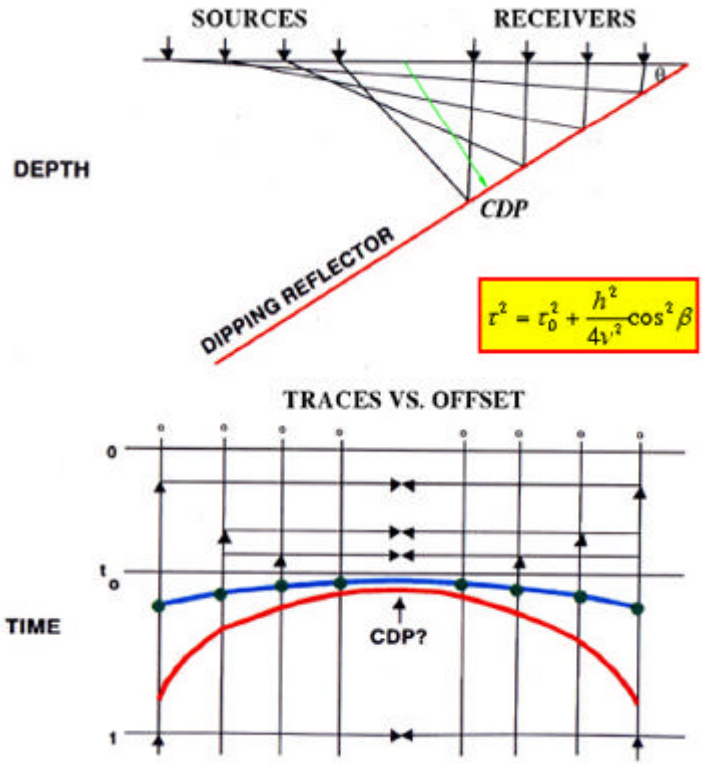

Note that for traces with a fixed midpoint, reflections from the dipping horizon do not correspond to a fixed common-depth-point (CDP) location (the intersection of the green line and the dipping reflector). In fact, the larger the offset between source and receiver, the greater the CDP-reflection point separation. This separation is referred to as *CDP smear*. To correct precisely for CDP smear requires that we prestack migrate the traces, since normal moveout will not work.

Nevertheless, the hyperbolic curve (blue in the figure) can still be corrected and stacked, it just cannot be stacked with the true velocity v, but must be stacked with the normally much faster velocity, $\frac{v}{\cos\beta}$. Thus, if we assume that the CDP smear is small, we could, in principle, stack the data with the faster velocity and produce some kind of representation of the dipping event. One way to do this, and then combine the dipping information

with the standard stack, is to NMO with the faster velocity, filter out anything that is not flat, stack and then add the result back to the NMO stack.

Examples

To see how this might work, we will stack the data with velocities of the form $\frac{v}{\cos\beta_i}$ over a uniform range of angles β_i, filter out anything that is not flat on the CDP gathers, and then stack.

Figure 3-42 is an example stack of a two-dimensional Gulf of Mexico data set over an obvious salt structure. The process used to generate this unmigrated image was simply NMO followed by stack. There was no intermediate dip correction or migration.

Figure 3-42. A typical stack of a 2D data set from the Gulf of Mexico. This data was shot sometime in the 1980's.

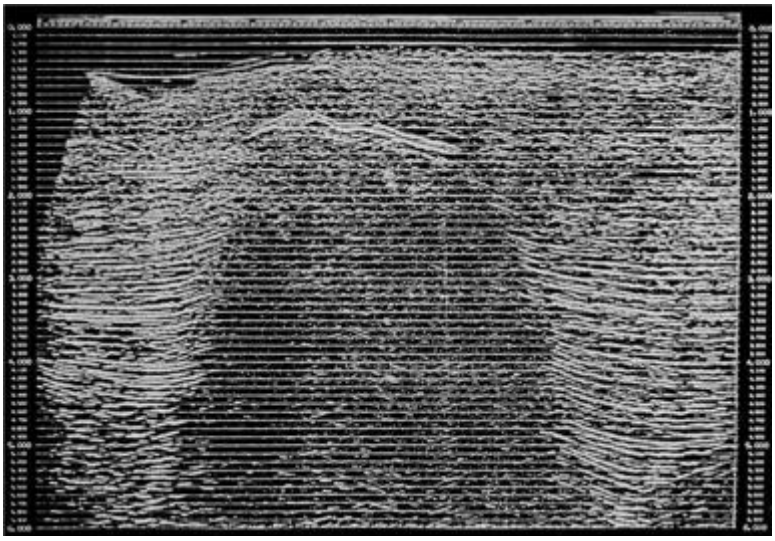

Figure 3-43 is a stack of a Gulf of Mexico salt structure using parameters and filters that attempt to image dip up from 0 to 15 degrees. What we actually did was find a set of velocities that we thought represented the sediment velocities, and then filter out all of the events that were over-corrected by normal moveout. Our best estimate is that the actual dips of the reflections comprising this image are no larger than 35 degrees.

Figure 3-43. Stack of the data in Figure 3-42 using an assumed dip of 7.5 degrees. At the bandwidth of these data the effect is to stack everything up to approximate 15 degrees.

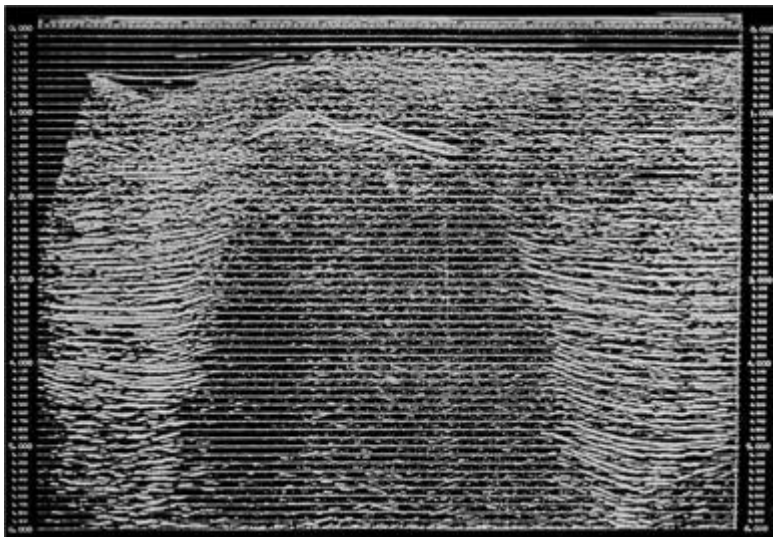

Figure 3-44 is a stack of a the Gulf of Mexico salt structure with parameters chosen to image events from beds with 15 to 30 degree dips. Note that what we are seeing are mostly reflections from beds whose dip is increasing as they approach the salt dome.

Figure 3-44. Stack of the data using an assumed dip of 22.5 degrees. At the bandwidth of these data the effect is to stack everything between 15 and 30 degrees of dip.

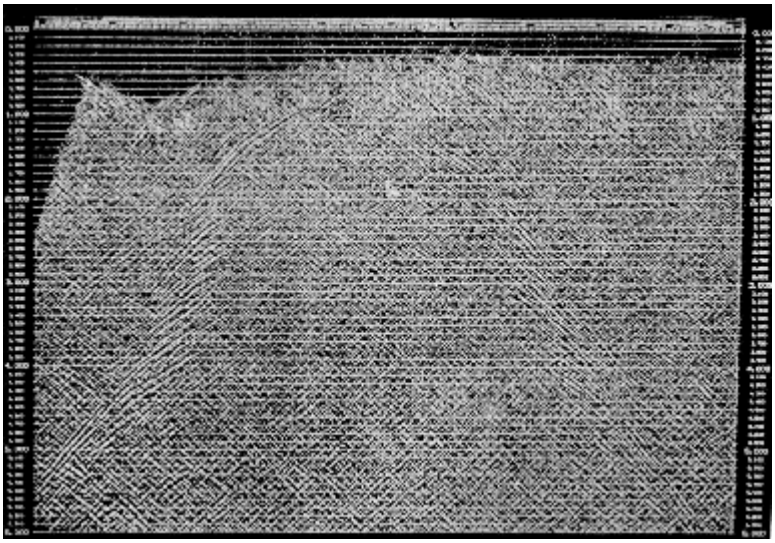

Figure 3-45 shows the stack of data over a Gulf of Mexico salt dome with parameters chosen to image reflections from events with 30 to 45 degree dips. As we increase the angle of the dips we are trying to image, we see that events reflected from more steeply dipping beds begin to appear. Again, this unmigrated image was produced by modifying the normal stacking velocity field to produce an apparent velocity field closely associated with dipping events in the 30 to 35 degree range.

Figure 3-45. Stack of the data using an assumed dip of 37.5 degrees. At the bandwidth of these data the effect is to stack everything between 30 and 45 degrees of dip.

By increasing the dip range to 45 to 60 degrees, Figure 3-46 shows that, in fact, there are reflections in this data set from beds that dip in excess of 45 degrees. What is more important is that these reflections cannot be seen in a typical stack which has not been dip-moveout corrected. Thus, if they are not imaged in a traditional stack, we cannot be expected to image them on post-stack migrated sections.

Figure 3-46. Stack of the data using an assumed dip of 52.5 degrees. At the bandwidth of these data the effect is to stack everything between 45 and 60 degrees of dip.

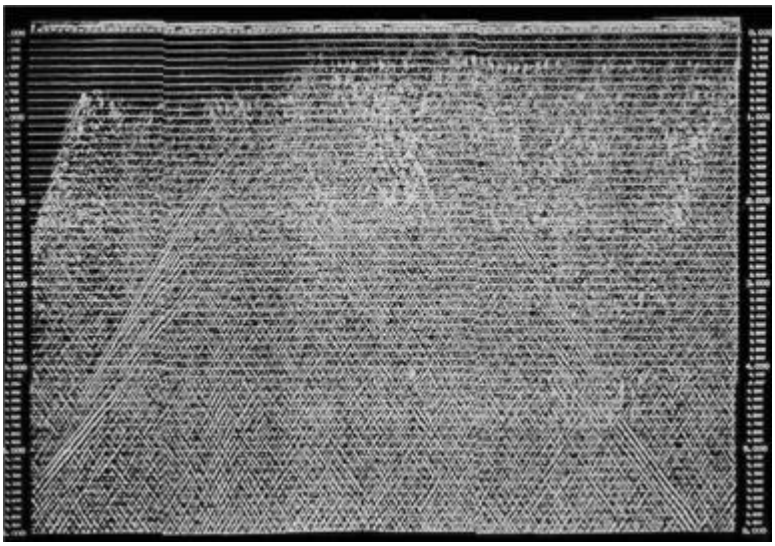

Figure 3-47 is a linear stack of the 15 to 60 degree dipping events. By stacking the sections from the last three figures, we get an idea of the events that should be in the original NMO-only based stack, but are not visible there. When these are migrated, a much clearer picture of the salt structure appears.

Figure 3-47. The sum of the sections in Figures 3-43 through 3-46.

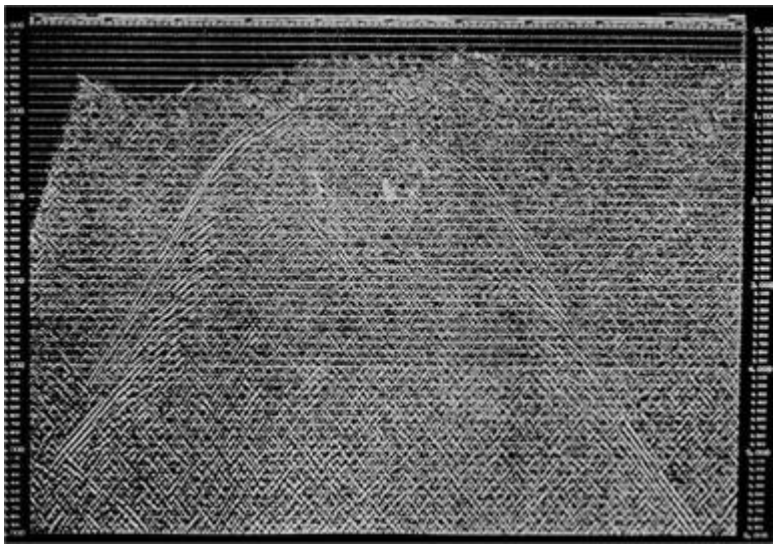

Adding all of the sections together provides the final NMO-DMO corrected stack in Figure 3-48. This DMO corrected data set is much closer to a true zero-offset profile, and now includes reflections from steeply dipping events. Migration of this section will produce a much clearer picture of the salt structure.

Figure 3-48. The sum of the sections in Figures 3-42, and 3-47.

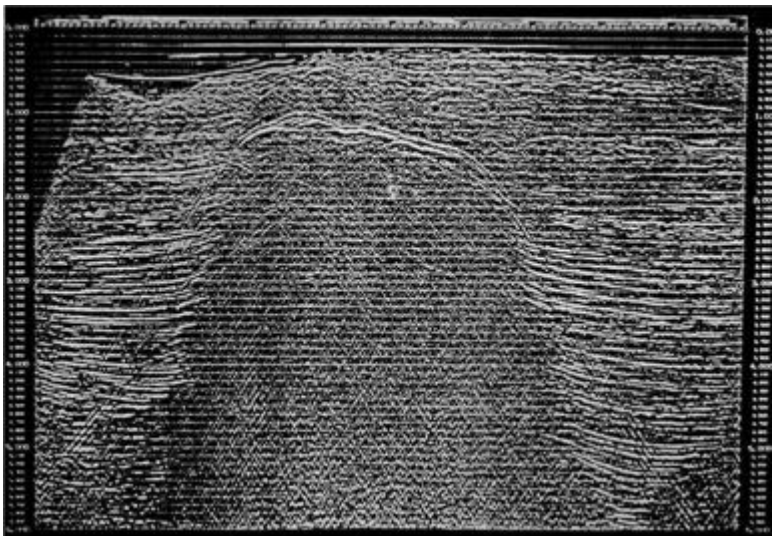

Remarks about DMO

In summary, correcting for dip using DMO partially migrates the data to address the fact that CDP arrival time curves have apparent velocities much faster than flat events. It converts upward sweeping hyperbolas in each and every NMO-corrected CDP into flat events at zero-offset traveltimes. Although it is possible to perform DMO using non-constant velocity fields, in practice, most DMO algorithms are constant velocity methods. They achieve their goals in much the same manner as an ordinary migration, but with much smaller operators. As seen in the earlier figures, it is possible to image dipping events using existing stacking and dip filter methods. What is even more surprising is that constant velocity DMO and even prestack time migration can be accomplished without knowing anything about the velocity.

The NMO-DMO-STACK combination is usually called *partial prestack migration* because it performs three of the four tasks involved in performing a prestack migration. After its application, the only remaining task is to position subsurface events properly. Because NMO-DMO-STACK is relatively cheap, this process played an important early role in improved imaging, and for a time became a standard part of every processing sequence.

However, since most DMO processes are based on constant velocity assumptions, or, at best, $v(z)$ assumptions, they have considerable difficulty producing images below strong velocity variations. Thus, DMO-NMO is a useful tool for imaging steep dips, but is impractical when the objective is subsalt.

With the advent of inexpensive computers and the resulting ability to perform full prestack migration, DMO-NMO no longer reigns as the optimum approach to seismic imaging.

Historical Summary

Absolutely all migration algorithms can be considered to do one or the other of the processes described in this section. Which method we choose to use to explain observed events on imaged sections is pretty much a matter of choice. Diffracting amplitudes over specific curves or smiles is by far the most popular. Nevertheless, it is sometimes helpful to understand the alternative frown-based method. Before this frown-based approach can be fully appreciated, it is necessary to consider the geometrical aspects of data synthesis or seismic modeling. Chapter 3 reviews seismic modeling. Since seismic modeling must of course acquire data in some sense equivalent to normal acquisition procedures, Chapter 4 reviews how seismic data is acquired today.

Chapter 4

Zero Offset Migration Algorithms

The sections on imaging are clearly the heart of the book—this chapter contains a discussion of zero-offset poststack migration, including time migrations, and Chapter 6 discusses prestack migration. The wide selection of algorithms are from what we call the migration hierarchy, but not all of those algorithms are covered completely. Considerable importance is placed on the impact of aliasing and on how full wave-equation-based methods function in exactly the same manner as much simpler approaches, although they are more difficult to understand.

The Migration Algorithm Hierarchy

We again appeal to history to organize the material as we discuss various algorithms in terms of the Migration Hierarchy shown in Figure 4-1. This figure is a very simplified diagram of the variety of migration approaches available to image reflection seismic data. In a manner analogous to what was discussed in the modeling section (Chapter 3), this hierarchy refers to the theoretical assumptions made in algebraic manipulations of the initial propagator equations. It is important to note that, although we will address this hierarchy in a top down manner, this is definitely not the order in which the algorithms were developed. It is also interesting to observe that computational efficiency generally improves as we go down the figure; that is, full two-way extrapolation at the top is much more computationally intensive than almost any of the one-way methods at the bottom.

Figure 4-1. A modern hierarchy of migration algorithms.

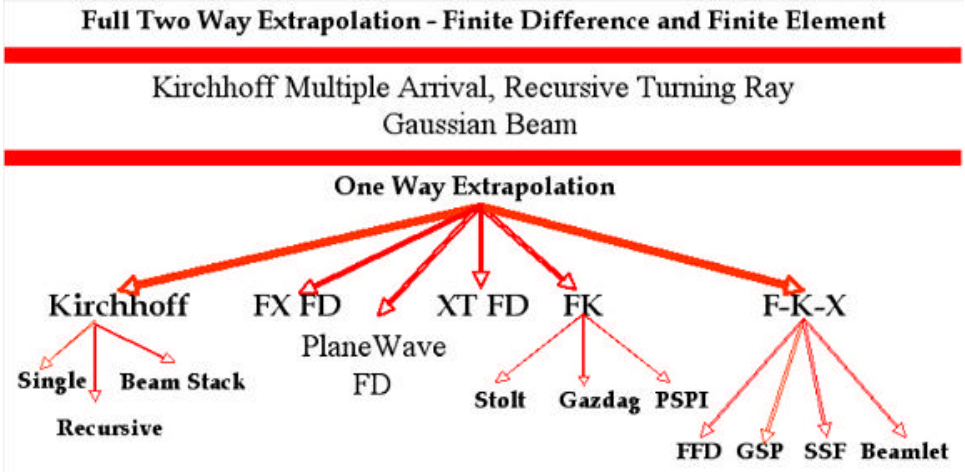

Each symbol or phrase in the figure references a particular approach to migration. In general, capital *F* indicates a frequency domain method, K is a wavenumber method, X is a method in space, and T is a method in time. Thus, FX migration means an algorithm that works essentially in the frequency-space domain, while XT is a space-time method. FKX methods are the dual-domain methods that achieve their goals by bouncing back and forth between frequency, wavenumber, and space. We could conceivably have a FKXT or multi-domain method, but, to date, such methods have not gained much popularity.

All of the methods in the hierarchy, including all of the Kirchhoff approaches, were derived from a three-dimensional version of the one-dimensional forward modeling propagator. Fundamentally, the geometry dictated by the wave equation from which they arose is the same for each and every approach. Wave equation propagators are all derived from continuous versions of discrete equations like Equation 4-1, where v is the speed of sound in the medium.

$$\frac{u(x+h,t)-2u(x,t)+u(x-h,t)}{\Delta x^2}=\frac{1}{v^2}\left(\frac{u(x,t+\Delta t)-2u(x,t)+u(x,t-\Delta t)}{\Delta t^2}\right) \tag{4-1}$$

Equation 4-1 is written in continuous form as Equation 4-2.

$$\frac{\partial^2 u}{\partial x^2}=\frac{1}{v^2}\frac{\partial^2 u}{\partial t^2} \tag{4-2}$$

By extension, the basic three-dimensional partial differential equation then takes the form of Equation 4-3.

$$\frac{\partial^2 u}{\partial x^2}+\frac{\partial^2 u}{\partial y^2}+\frac{\partial^2 u}{\partial z^2}=\frac{1}{v^2}\frac{\partial^2 u}{\partial t^2} \tag{4-3}$$

This wave equation is the simplest form from which all migration algorithms arise, but that does not mean it is the correct one. It just means that it was easier to start with this one rather than the general heterogeneous version shown in Equation 4-4, where ρ is density, v is sound speed, and ∇ is the vector differential operator given by Equation 2-19. Regardless of the complexity of the original equation, the fundamental migration concepts do not change.

$$\frac{\partial^2 U}{\partial t^2} - \rho(x,y,z)\, v^2(x,y,z)\, \nabla \cdot \frac{1}{\rho(x,y,z)} \nabla U = s(x_s, t) \tag{4-4}$$

Migration in Depth

This section describes a number of the methods used to perform migrations in depth. In depth migration, reflections in seismic data are moved to their correct locations in space. These methods include both explicit and implicit one- and two-way methods, two-way reverse time methods, Kirchhoff style methods, and plane wave techniques.

Explicit Two-Way XT-Reverse-Time Migration

Perhaps the easiest way to understand migration is to consider what we learned in the section on Zero Offset Modeling. To produce true zero-offset data, we started with a given model, halved the velocity, computed reflection amplitudes for each point on a reflector, and then simulated explosions at each such point reflector. These simulated explosions were ignited at $t = 0$. The surface wavefield at $z = 0$ for all possible recording times, t, became a zero-offset subsection. The trick of halving the velocity was all that was necessary to ensure proper arrival times in our zero-offset experiment. It does not take a lot of thought to see that if we simply reverse this process, we will arrive at an algorithm that will produce an image of the subsurface at the original $t = 0$.

"Reverse time migration" uses the reversed time data as a source term for a seismic modeling exercise. Thus, the "source" in this case is a multiplicity of traces. In 3D, it is a common-offset volume where the distance between the source and receiver is zero. Figure 4-2 is a schematic example of the process. The first and second lines of Figure 4-2 show what remains as each time slice is propagated into the output image, while the second and fourth lines show the current image at each propagation step. Thus, the upper first and second images in the upper left show the initial condition of the zero-offset wavefield and the subsurface. In practice, the initial subsurface subsection would be filed with zeros. Here, we just reversed the modeling images from the subsection on modeling. Note that as the process continues, the final subsurface at the bottom right contains the fully migrated image—all amplitudes in the original recorded zero-offset subsection have been exhausted and are now zero; that is, the entire recorded wavefield

has been back propagated into the Earth. In these images, all subsurface reflectors are clearly being imaged from above and from below.

Figure 4-2. Reverse time migration snapshots.

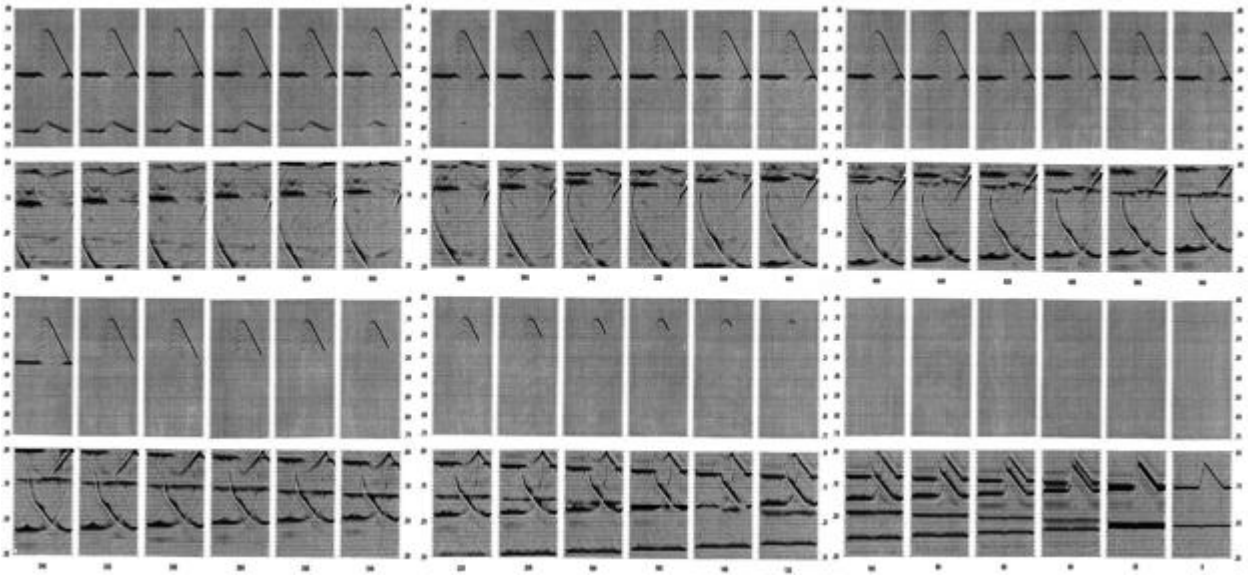

Figure 4-3 visualizes what happens locally during the process described by Figure 4-2 and its associated comments. Input traces are reversed in time and fed directly into the modeling algorithm to produce the final image. This kind of method is called an *explicit method* because it back propagates time-reversed data one step at a time.

Figure 4-3. Using time-reversed traces with a modeling propagator to produce subsurface images

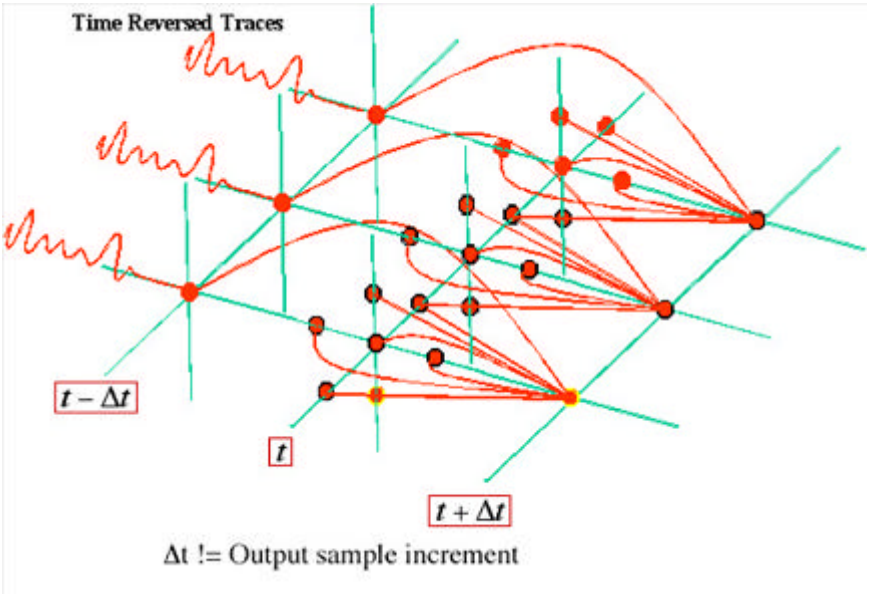

Implicit Two-Way XT Reverse-Time Migration

The only difference between explicit and implicit zero offset migration is that the former explicitly employs the mesh shown in Figure 4-3, while the latter inverts a rather large matrix to obtain the migrated image. The “sources” in both are the time-reversed stacked or zero-offset traces, so the only differences between the explicit and implicit versions involve the implementation.

Explicit One-Way XT Reverse-Time Migration

Again, going back to our modeling discussion, it is quite easy to make a one-way migration method. Figure 4-4 illustrates this point quite accurately. Note that three-dimensional, one-way-reverse-time migration differs from its two-way counterpart only in that the propagating stencil is free of coefficients below the current time or depth slice. Thus, unlike the two-way algorithm, one-way imaging proceeds one time or depth slice at a time. It is precisely this feature that makes one-way wave equation imaging vastly more efficient than its full two-way cousin.

Figure 4-4. Three-dimensional non-Kirchhoff time or depth migration.

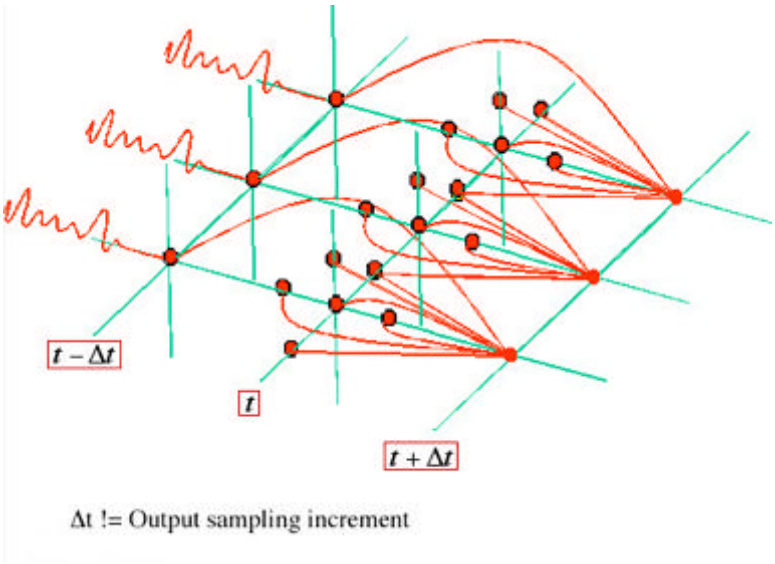

Implicit One-Way XT Reverse-Time Migration

Here we only need to invert the appropriate upper-diagonal matrix to find the imaged solution. Because the process is based on a back-substitution method, it is extremely efficient and therefore much faster than the full two-way-implicit scheme.

One-Way FK Reverse-Time Migration

One-Way-FK-Reverse-Time Migration methods can be divided into FK, phase shift methods, and phase shift plus interpolation methods.

FK or Stolt Migration

In the mid 1970's, R. H. Stolt at Conoco's Ponca City, Oklahoma research facility invented what has become known as Stolt or FK migration, as shown in Figure 4-5.

Figure 4-5. R. H. Stolt's frequency-wavenumber Migration.

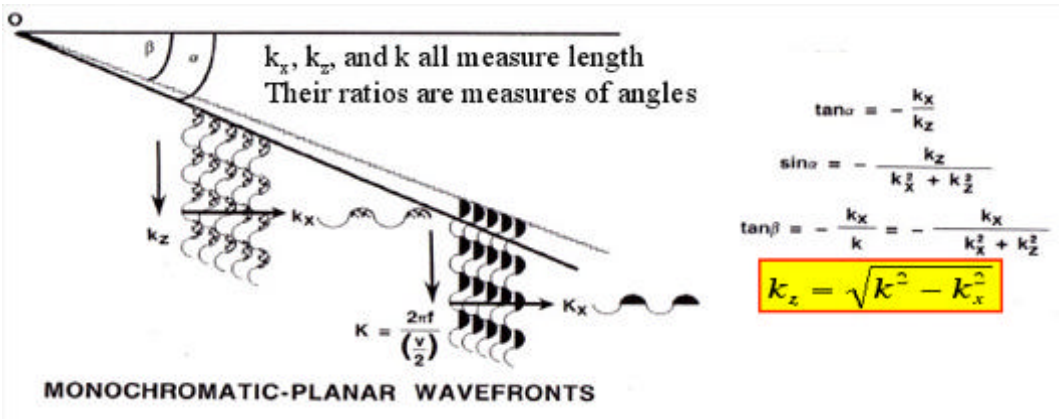

What Stolt recognized was that in a normal zero-offset seismic experiment, we are given time data, $u(x, y, 0, t)$, measured at $z = 0$, and what we want is the exploding reflector depth data, $u(x, y, z, 0)$. He also understood that if he could compute the depth wavenumber, k_z, from frequency, $\omega = 2\pi f$, and the x and y wavenumbers, he could produce a very fast FK domain method.

Figure 4-5 shows how he did migration. The vertical wavenumber k_z in depth is directly computable from the 2D dispersion relation $k^2 = k_x^2 + k_z^2$ where $k = \frac{\omega}{v}$. Because the dispersion relation in Equation 4-5 holds in 3D, extension to three dimensions is straightforward.

(4-5) $$k^2 = k_x^2 + k_y^2 + k_z^2$$

The assumption of constant velocity is the Achilles' heel of Stolt's method. It cannot be derived mathematically unless the velocity is constant, and no method has ever been found to overcome this weakness. However, since it was Fourier-based, it was much faster than any of the other methods of the day. Researchers quickly tried to get around the constant velocity issue.

Phase Shift Migration

The FK domain phase shift method shown in Figure 4-6 was based purely on reverse-time modeling. It was one of the first approaches to successfully remove the constant velocity criteria imposed by the Stolt approach. It was also the first and, perhaps until very recently, the only method that was capable of imaging up to 90 degrees. The phase shift approach was invented by Jeno Gazdag shortly after the Stolt method appeared. It, in effect, applies the Stolt method to each slice in a Earth model where the propagation velocity varies only vertically. Thus, it is a recursive technique that repetitively applies the formula for k_z in Figure 4-5 to each constant velocity depth slice in the $v(z)$ model. It begins at zero depth ($z = 0$) and proceeds until the desired depth is reached. As long as the Earth's velocity varies only vertically, it does a remarkably good job of imaging steeply dipping events. This approach can be modified to include at least some two-way propagation, so it is also very versatile.

Figure 4-6. FK domain depth-slice by depth-slice migration

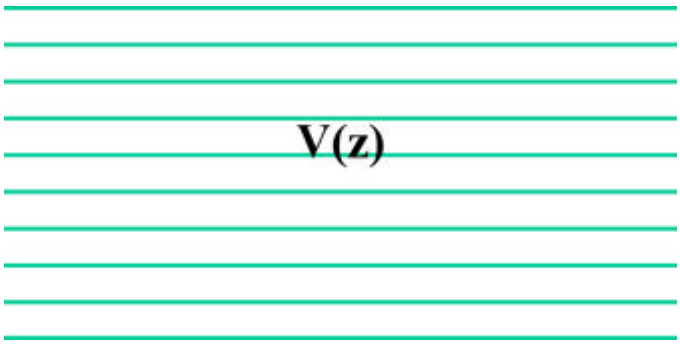

Phase Shift Plus Interpolation Migration

As discussed in the chapter on seismic modeling, phase shift plus interpolation (PSPI) modeling is easily adapted to produce a phase-shift-plus-interpolation style reverse-time migration, as shown in Figure 4-7. The sources in this case are again the time reversed traces and the result is a depth image of the zero-offset input data.

Figure 4-7. PSPI FK domain depth-slice by depth-slice migration

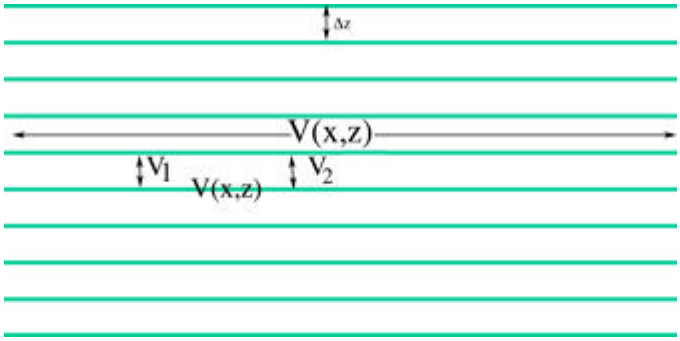

One-Way FKX-Reverse-Time Migration

One-way FKX-reverse-time migration methods can be divided into split-step and phase screen methods.

Split Step Imaging

The split-step imaging method is a direct application of the split-step modeling method in Split-Step Methods on page 67. Explaining this method in considerable detail is beyond the scope of this book. For the purposes here, it is enough to say that the method splits all downward propagation between the FK and FX domains.

Phase Screen Migration

The so-called phase-screen method, as envisioned by Ru Shan Wu at the University of California at Santa Cruz, is briefly discussed in Higher Order FKX Methods on page 68. This method, when compared to the split-step approach, is based on an improved set of approximations for utilization in the FX domain.

Kirchhoff Style Methods

Kirchhoff migrations are a method of seismic migration that uses the integral form (Kirchhoff equation) of the wave equation. Kirchhoff style methods can be separated into single-arrival methods and multiple-arrival methods.

Single-Arrival Kirchhoff Migration

In single arrival Kirchhoff depth migration, as shown in Figure 4-8, either a direct finite difference solution to the Eikonal equation or full 3D raytracing is used to calculate exact traveltimes from the source/receiver point to the output image point.

Figure 4-8. Single arrival Kirchhoff depth migration.

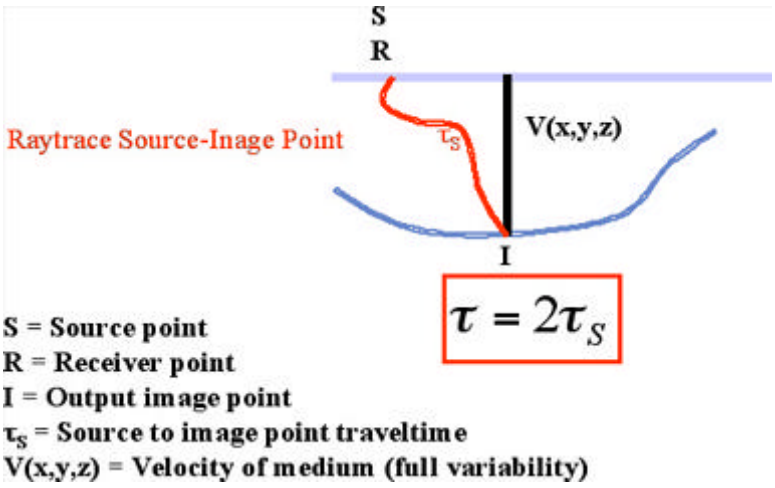

Because Eikonal-based methods are generally able to calculate only first arrivals, they are no longer popular as part of the general depth migration methodology.

However, raytrace methods facilitate the calculation of multiple arrivals, and the selection of those arrivals better serves the migration process. Typical arrivals of this type are maximum energy, minimum distance, or minimum velocity. In areas with strong lateral velocity variations, such as salt regimes, the minimum velocity methodology is considered to be optimum since they avoid headwaves caused by proximity to salt or other high velocity structures.

The utilization of a single arrival in Kirchhoff depth migration technology is one of the chief reasons these methods cannot image below complex structure.

Multiple-Arrival Kirchhoff Migration

When we use all of the possible arrivals, as shown in Figure 4-9, we can achieve a superior result to what is achieved with the single arrival approach. While multiple arrivals complicate the migration algorithm and generally make it more computationally costly, the benefit of including more arrivals usually outweighs the increased cost.

Figure 4-9. Multiple arrival Kirchhoff depth migration.

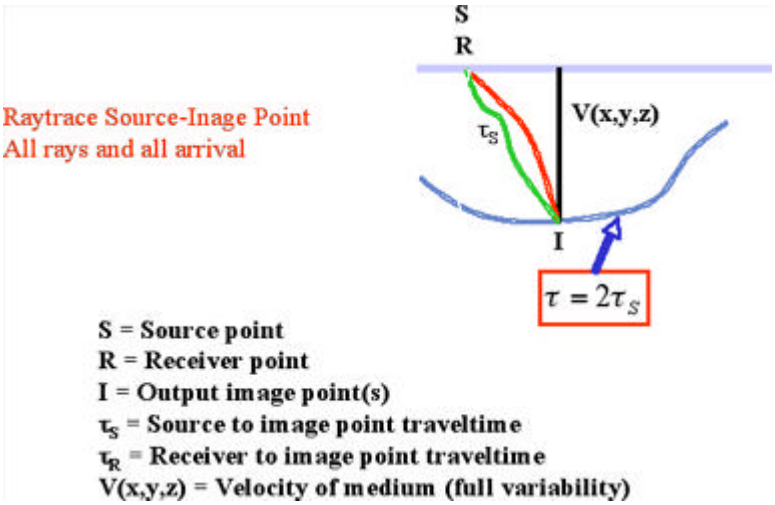

Plane-Wave Migration

Plane-wave migration methods can be divided into pure plane wave methods, beam stack methods, and Gaussian beam methods.

Pure Plane Wave Migration

The hand migration discussed in the chapter on historical methods and displayed in Figure 3-5 is in actuality one of the first plane wave migration techniques. The constant velocity trigonometric solution in that figure provides the formulas for calculating the migration time, τ, and the lateral shift, x, to determine the migrated position, S'.

Figure 4-10 shows how you can avoid the constant velocity assumption completely. In this figure, the $\frac{dt}{dx}$ measured from the unmigrated data, together with the near surface velocity, determines the cosine of the plane wave takeoff angle, θ, at the zero-offset location of the reflected arrival from the steeply dipping structure. If we shoot a ray with this takeoff angle into the subsurface model and continue it until the recorded time at A is exhausted, the orthogonal to the ray will be the dip of the reflected event and the position of the end of the ray will be its location. Repeating this process for every

estimated dip ultimately produces a full migration of the recorded zero-offset or stacked subsection.

Figure 4-10. Hand migration as a beam or plane wave migration.

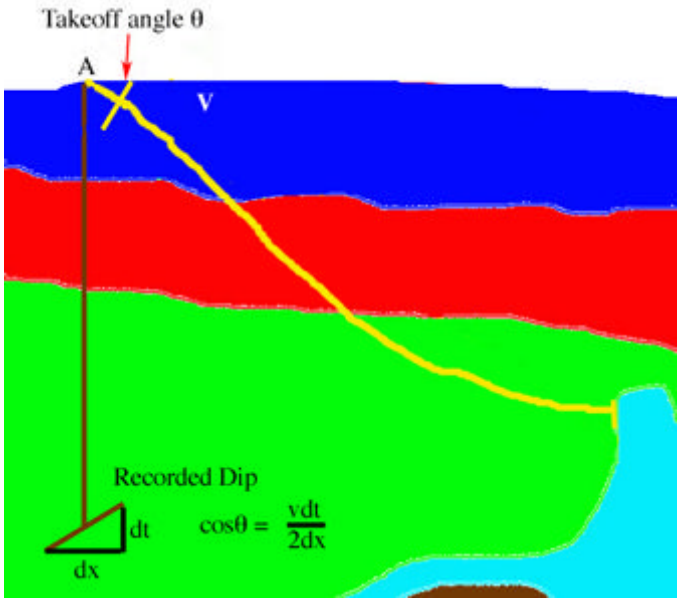

Beam Stack Migration

Kirchhoff methods are converted to a beam or slant stack approach by simplifying the manner in which traveltimes are calculated. The idea is to try to use the distance from a central source or receiver to calculate another traveltime at a nearby location. In two dimensions, the formula is something like that shown in Equation 4-6, where $\tau_{x_{s_0}}$ is the raytraced traveltime from the central location, x_{s_0}, and $p_{x_{s_0}}$ are suitably chosen scalars.

(4-6) $$\tau_{x_s} = \tau_{x_{s_0}} + p_{x_{s_0}}(x - x_s)$$

Noting that $p_{x_{s_0}}$ must have units of time over distance, we can easily infer that this value must tell us how $\tau_{x_{s_0}}$ changes incrementally versus an incremental change in the central source position. That is, $p_{x_{s_0}}$ must have the form in Equation 4-7, which is just the derivative (gradient in 3D) of the traveltime with respect to source position.

(4-7) $$p_{x_{s_0}} = \frac{\Delta\tau_{x_{s_0}}}{\Delta x}$$

Traveltimes at a position close to the central point can then be calculated from Equation 4-8.

(4-8) $$\tau_{x_s} = \tau_{x_{s_0}} + \frac{\Delta\tau_{x_{s_0}}}{\Delta x}(x - x_s) = \tau_{x_{s_0}} + \frac{d\tau_{x_{s_0}}}{dx}$$

Equation 4-9 performs a standard zero-offset Kirchhoff migration in 2D, where A is a traveltime correction factor, $\tau_{x_s}(x,z)$ is the traveltime from the surface location x_s to (x,z), and $D(x_s,t)$ is the zero-offset data to be imaged as $I(x,z)$.

(4-9) $$I(x,z) = \Sigma_{x_s} A(x_s) D(x_s, \tau_{x_s}(x,z))$$

The basic ideas for this kind of traveltime computation is shown in Figure 4-11.

Figure 4-11. Traveltime computation in terms of local distance from a given centrally located shot.

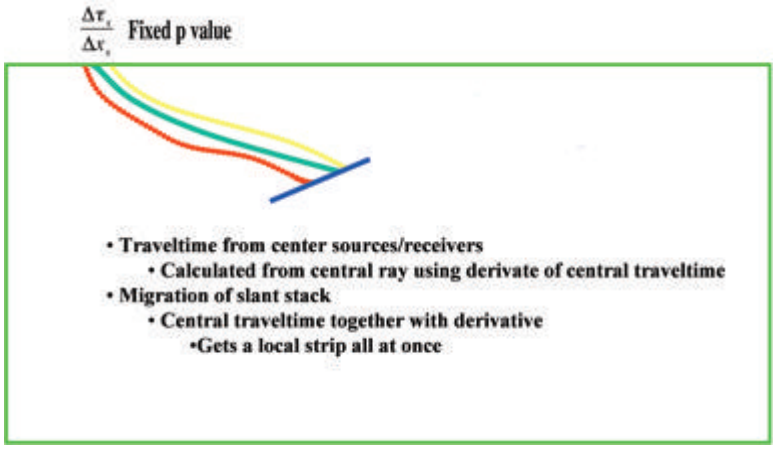

Inserting the formula for calculating τ_{x_s} results in Equation 4-10.

(4-10) $$I(x,z) = \Sigma_{x_s} A(x_s) D(x_s, \tau_{x_{s_0}} + p_{x_{s_0}}(x - x_s))$$

Equation 4-10 suggests that we can perform this operation in two independent steps. First, we calculate the slant stack of our input zero-offset data, $D(x,t)$, using Equation 4-11. Then we simply Kirchhoff migrate this slant stack bundle using Equation 4-12, where the sum is taken over all x_s that are sufficiently close to x_{s_0}. The image $I(x,z)$ is then just the sum of all the bundles.

(4-11) $$D_S(x_{s_0}, p, \tau) = \Sigma_{x_{s_0}} D(x_{s_0}, \tau + p(x - x_{s_0}))$$

(4-12) $$I(x_s, z) = \Sigma A(x_{s_0}) D_S(x_{s_0}, p_{x_{s_0}}, \tau_{x_{s_0}})$$

Since the slant stack can be calculated independently of the migration, and since the derivative of the traveltime can be calculated during the raytracing, the computational cost of performing the necessary steps prior to the migration stage is only slightly greater than that required for a standard Kirchhoff migration.

On the other hand, since the entire slant stack bundle replaces many traces in the migration process, Kirchhoff-beam-stack methods can be significantly more efficient than their traditional straight-forward implementations. Typically, these Kirchhoff-beam-stack migrations are about 10 times as fast as a traditional Kirchhoff approach.

Gaussian Beam Migration

Figure 4-12 demonstrates graphically how we can construct a significant portion of the required impulse response for a zero-offset trace using what are called *Gaussian beams*. The mathematics associated with Gaussian beams is beyond the scope of this book, but the concepts are worth some explanation. Although somewhat of an over-simplification, we can think of a Gaussian beam as being equivalent to a phase shift calculation using a $v(\rho)$ velocity function extracted using the arc-length along the ray, ρ, as the depth parameter.

Figure 4-12. A partial wave response due to two rays.

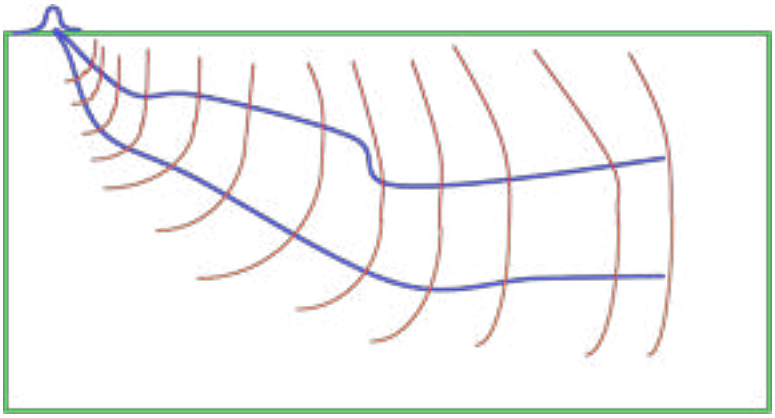

Several corrections to this phase shift are made to ensure that the process works correctly. First, as the ray calculations proceed, two special functions are calculated at each increment, $\Delta\rho$, of the arc length. These functions provide the necessary amplitude decays parallel and orthogonal to the ray at any given location. Second, the beam is weighted with the normal Gaussian function to ensure that the sum of all such beams accurately represents the true impulse response of the migration operator. The result of applying the corrections is called a Gaussian beam, and its amplitudes are then summed into corresponding subsurface locations on either side of the central ray. The sum of all such beams produces the completed impulse response.

Migration in Time

Time migration moves dipping events from their apparent locations to their true locations in time. The resulting image is shown in terms of traveltime rather than depth, and must then be converted to depth with an accurate velocity model. Because of the clear and direct connection to data synthesis over media described in terms of depth, it is easy to explain depth migration in the time-reversed sense.

However, even though it can be one of the most accurate imaging methods, depth migration has not yet reached the acceptance level it deserves. There are many reasons for this. One reason is the belief by many people that finding the most accurate velocity is still beyond the reach of most depth-migration methods. This was certainly true when actually performing a prestack migration of any form was beyond the reach of the computational capacities of the period. Historically, imaging in time by hand (see Chapter 1) was easy to explain with virtually no need to even consider partial differential equations. Interpreters were required to have only limited mathematical ability to do the migration and could perform all depth conversions as a simple vertical stretch.

Moreover, as shown in Figure 3-17 and discussed in Chapter 1, interpreters could compute the migration position and time quite easily using only an appropriate RMS velocity and locally estimated dip. Consequently, the coupling of readily available computer power with multi-fold data for estimating stacking velocities led directly to a plethora of time-migration versions of the depth migration algorithms listed in the previous sections.

Converting to Vertical Time

Converting depth migration algorithms into time migration algorithms is not difficult, but the process is not easy to explain fully without detailed mathematical analysis.

In 2D, vertical time, τ, is defined by Equation 4-13, where z is depth, and $v(x,z)$ is a two-dimensional velocity function.

(4-13)
$$\tau(z) = \int_0^z \frac{dz}{v(x,z)}$$

There is, of course, a 3D version of this equation, but for simplicity we will only consider the 2D case.

With this as our variable of choice, the two-dimensional equation governing our wavefield takes the form of Equation 4-14, which, on the surface, appears to be little different from the depth equation on which all modeling and depth imaging is based.

(4-14)
$$\frac{\partial^2 u}{\partial \tau^2} + \frac{\partial^2 u}{\partial x^2} = \frac{1}{v^2}\frac{\partial^2 u}{\partial t^2}$$

The problem is that this equation has two time variables. One, t, is the actual time governing wavefield propagation, and it is what we record in the form of arrival times. The other, τ, is simply the conversion of vertical depth to time. The key point to all of this is that wavefields do not travel in vertical time, they propagate in space. Therefore, the problem is how can we solve Equation 4-14 for the image at time τ.

Jon Claerbout (1976) found a unique solution to this problem. He first recognized that vertically propagating solutions of this equation are constant along level lines, $t + \tau = constant$. He then made a change of variables from t to $t' = t + \tau$, and then ignored all higher order derivatives. The result is

$$\frac{\partial^2 u}{\partial x^2} = \frac{1}{v^2}\frac{\partial u}{\partial t'}\frac{\partial u}{\partial \tau} \tag{4-15}$$

This equation can be solved discretely quite easily. The transformation from Equation 4-14 to 4-15 is not unlike the factorization into one-way equations in the Modeling chapter (Chapter 2), and so virtually all of the concepts and ideas incorporated in depth migration algorithms are also part and parcel of the time migration scene. In the same manner that factoring the full two-way equation into two one-way equations theoretically limited propagation to no more than 90 degrees, approximating Equation 4-14, another easily solvable equation, also reduces the dip response of any image.

Perhaps the only significant difference between the one-way depth approach and the one-way time migration approach is that the latter is almost always cast as an implicit scheme. Because the required matrix inversion is relatively simple, this does not result in a computationally intense algorithm. Thus, time migration as practiced in the past is quite efficient.

The Major Difference between Time and Depth Migration

The major difference between time and depth migration is directly related to the transformation from depth, z, to vertical time, τ. This difference is illustrated in Figure 4-13, which provides a graphic of what happens when the velocity varies in any direction. Depth migration accurately places the imaged event at its image ray time location, while time migration continues to place the migrated event at vertical time. Large lateral placement errors are the rule when the velocity varies strongly. This is a major reason to prefer depth migration over pure time-migration approaches, but it is not the only reason. Ray bending is also extremely limited because time migrations utilize RMS velocities instead of true interval velocities.

Figure 4-13. The major difference between time and depth.

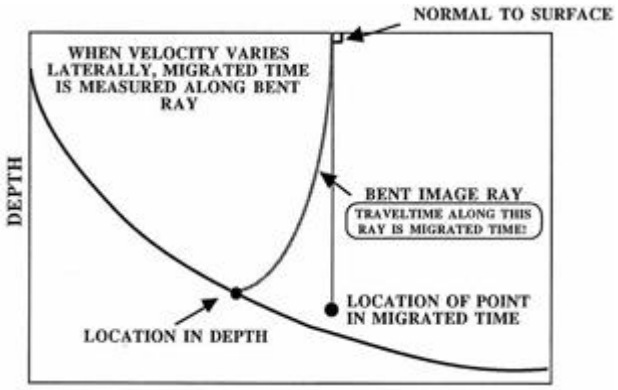

Dip Limits

As we saw in the chapter on modeling, factoring the full two-way equation limited one-way propagation to 90 degrees, since almost any implementation of a one-way method decreases the dip response. In depth migration, the basic problem arises from the need to approximate the square-root term in the one-way equation. The approximation is usually the result of truncating a Taylor series, but it can also result from other approximations.

In vertical-time migrations, an entirely different equation replaces the fundamental wave equation, but its approximation is the result of truncation and also results in a decreased dip response. This decrease is clearly evident on any comparison between the algorithmic and exact impulse responses. It is not surprising that the recognized definition of dip limits was based on where the impulse response breaks down. Figure 4-14 shows how dip limits are defined.

Figure 4-14. Algorithmic dip limit definitions.

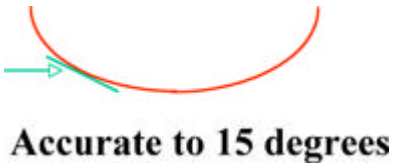

Using this definition, it is possible to show that the dip limit of early time migration algorithms did not exceed 15 degrees. Consequently, they were called 15 degree algorithms. Increasing the approximation accuracy by using additional terms in series approximations produced algorithms with 45 and even in some cases 60 degree limits. Using three or more terms ultimately resulted in diminishing returns and there was an upper limit of around 80 degrees. Although there are many different domains of application, the process almost always revolves around some type of series expansion of either the square root term or its time-domain equivalent.

One-Way XT Time Migration

The simple model shown at the top of Figure 4-15 was designed to test the basic concepts of zero-offset seismic migration or imaging. The model consists of 16 flat and 16 dipping events in a constant velocity medium, where the first dipping event is actually flat. Since the medium has constant velocity, there is absolutely no difference between running a time or a depth migration algorithm. We will test our first migration by running one-way time migration algorithms that are limited to 15 and 45 degree dip responses. The idea is to see just how good of a job we can do with a more or less naive approach.

Figure 4-15. Simple constant velocity model with dipping events from 0 to 70 degrees.

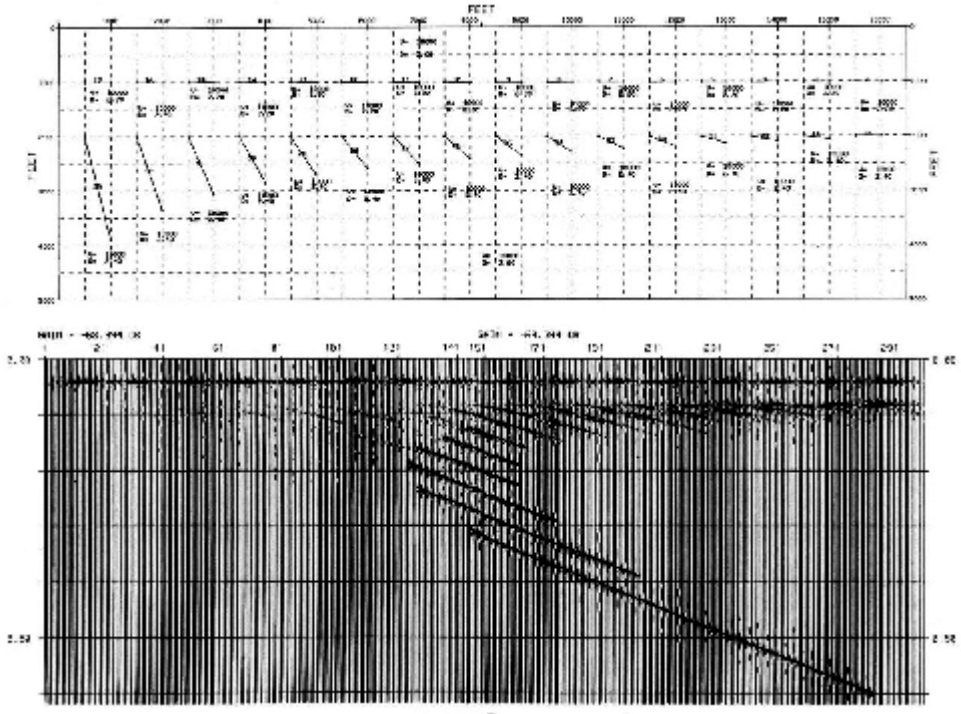

The data shown at the bottom of Figure 4-15 demonstrates several of the usual rules of thumb concerning seismic data. In this case, since the data was synthesized numerically, it is pure zero-offset data; that is, there is no separation between the source and receiver used to synthesize it.

The 15 degree approach shown in Figure 4-16 exhibits one of the most difficult aspects of migration. Imaging steeply dipping events is very much a function of the accuracy of the approximations used to make the algorithm workable.

Figure 4-16. Application of a 15 degree equation and the impact of interpolation.

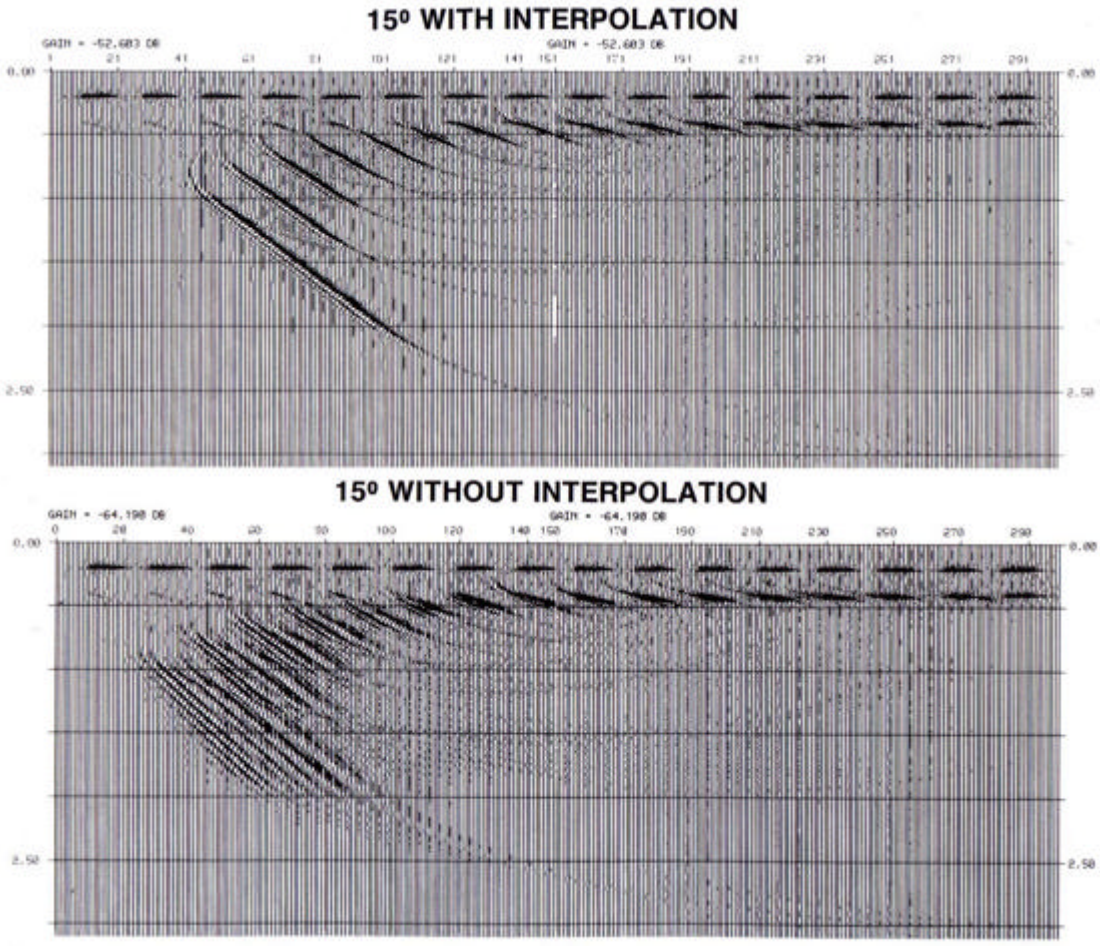

In the lower half of this figure, we see under-migrated events. Visual inspection reveals that the highest correct dip on the section is approximately 20 degrees. This is a bit higher than the 15 degrees the model study suggests is possible, but well within the expected error of the method. The bottom of this figure also demonstrates something called *grid dispersion*. This phenomenon is a complex part of the algorithm's implementations, but is easily handled by interpolating to a finer sample interval. The top half of the figure demonstrates that although the grid dispersion can be removed quite easily, the improper placement of the steep dips is still apparent.

If we move to a more accurate algorithm, in this case a 45 degree approximation, as shown in Figure 4-17, we see that we can easily achieve proper placement up to approximately 55 degrees. In this case, grid dispersion is not as much of a problem, even though it is still present. The more accurate implementation has achieved much better overall results.

Figure 4-17. Application of a 45 degree equation and the impact of interpolation.

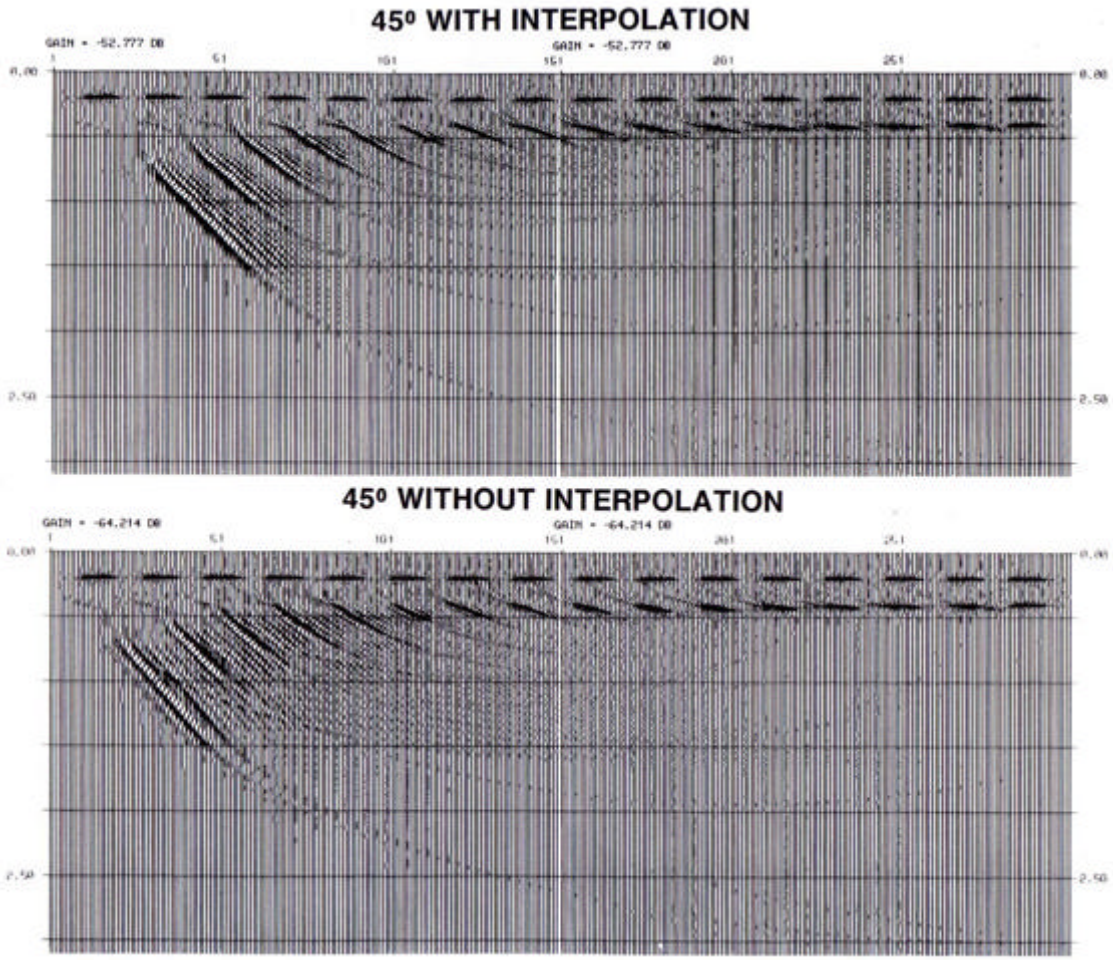

One-Way FK Time Migration

One-way FK time migration can be separated into a phase shift migration method and a phase shift plus interpolation (PSPI) method.

Phase Shift Migration

Phase shift migration in time is actually based on an approximation of the transformed wave equation, Equation 4-15. However, the process of down shifting the surface exploding reflector data is given by Equation 4-16, where φ is defined by Equation 4-17. Variable v_{rms} is the RMS velocity between τ and $\tau + \Delta\tau$, and is virtually identical to its depth counterpart given by Equation 2-127.

(4-16) $$U(k_x, \tau + \Delta\tau) = \exp(-\imath\omega\varphi\Delta\tau)\, U(k_x, \omega)$$

(4-17) $$\varphi = k_x^2\left(\frac{v_{rms}}{\omega}\right)^2$$

Phase Shift Plus Interpolation

Phase-shift-plus-interpolation (PSPI) time migration is identical to the depth migration explained in Phase Shift Plus Interpolation Migration on page 139. The only noticeable difference is that the down shift takes place in migrated time rather than migrated or imaged depth. Multiple velocities can be phase shifted to form the basis of an interpolation scheme in either space-time or frequency-space to make sure that the process is accurate, effective, and fast.

Kirchhoff Style Time Migration

Kirchhoff style time migration can be separated into straight-ray Kirchhoff time migration and curved-ray Kirchhoff time migration.

Straight-Ray Kirchhoff Time Migration

Straight ray Kirchhoff migration does not really do what the name implies. The method is patterned on Figure 3-17 and the RMS velocity as defined in Equation 3-4.

As shown in Figure 4-18, the method selects an RMS velocity function at the output image location, I, and then uses it in the traditional traveltime Equation 4-18 to compute

the required traveltime from the source to the image point and back to the coincident receiver. Once this time, $2\tau_S$, is available, the method selects the amplitude from the trace at surface location S, and adds the output to the location A at time τ.

Figure 4-18. Straight ray Kirchhoff Migration.

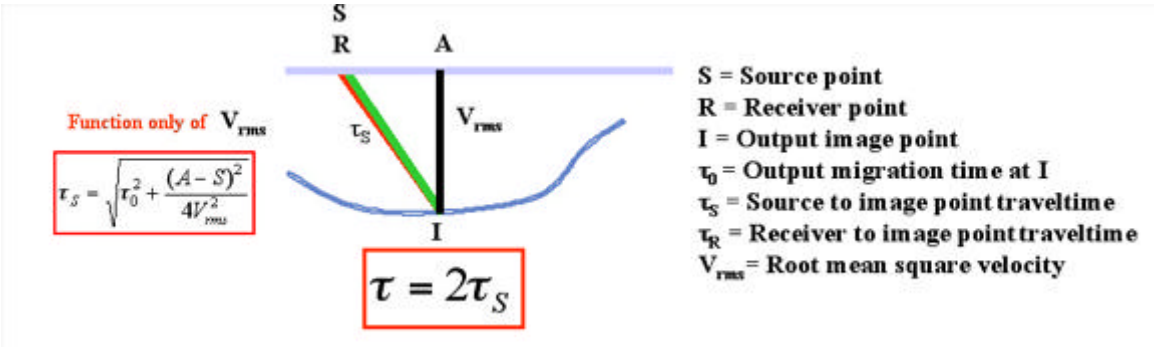

The blue line indicates all image points with the same output migration time. In a constant velocity medium, this equal-traveltime curve is actually a circle and represents the set of points which are equally likely points from which energy might be reflected. This process was the *de facto* Kirchhoff algorithm for many years and was one of the first to be computerized.

Curved-Ray Kirchhoff Time Migration

Equation 4-18 is the traditional traveltime formula for the time between a source at a distance from a surface point, m, and an image point located directly below m with a vertical traveltime of τ_0.

(4-18) $$\tau = \sqrt{\tau_0^2 + \frac{h^2}{4v^2}}$$

This is a truncation of a series of the form shown in Equation 4-19, where $c_1 = \frac{1}{v^2}$ is the reciprocal of the RMS velocity, v. As shown in Figure 4-19, the rest of the c_i values are complicated modes of the interval velocity function, $v(i\Delta z)$.

(4-19) $$\tau^2 = \tau_0^2 + c_1(m-S)^2 - c_2(m-S)^4 + c_3(m-S)^6 - \ldots$$

Figure 4-19. Curved ray traveltimes.

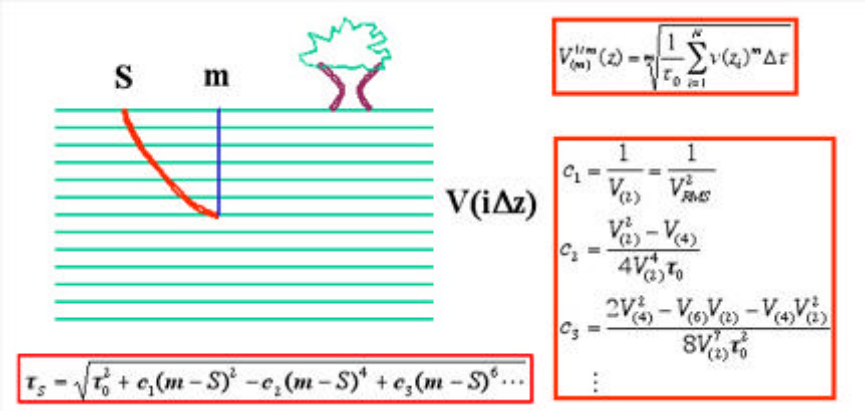

Figure 4-20 shows how curved ray Kirchhoff migration works using the full series representation shown in Figure 4-19.

Figure 4-20. Curved ray Kirchhoff time migration.

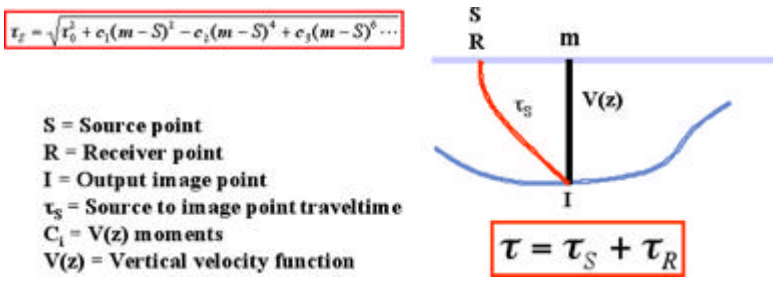

Calculating the traveltime through a velocity medium that varies only in the vertical direction ensures that the migration is identical to those that would be obtained using a raytracer. In effect, a curved ray time migration is identical to performing a depth migration using a different $v(z)$ for each output location and then outputting the result in vertical time.

Cascaded Migration

Figure 4-21 shows how migration algorithms can be cascaded to improve the overall response of the final migration.

Figure 4-21. Cascaded Migration.

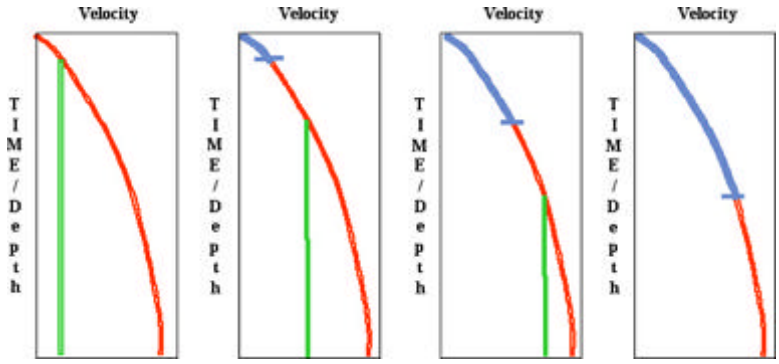

In some cases, the combination of several poor migration techniques produces a migration that is superior to each individual migration methodology. Each successive migration takes place with a migration field that is constructed from a small portion of the final velocity field and a constant velocity. Usually, the piece of the final field is chosen so as not to have any strong variations. After migrating with the constructed field, the next migration begins where the last one left off. That is, the new time zero is defined by the time at which the constant velocity functions intersect that portion of the final velocity field used during this stage of the cascade.

Almost any migration algorithm can be cascaded. The basic problem is that cascaded migrations are theoretically correct only when the cascade is performed after a constant velocity migration. This, in effect, means that the cascade concept can only be applied effectively after a completely straight-ray time migration.

Migration Summary

There is no question that two-way finite difference methods offer the potential for the most accurate images any migration algorithm can produce. If we know the exact subsurface wavefield at the last recorded time, the output from this technique provides an exact answer. It images all events from which reflections occur at precisely the correct reflectivity. Consequently, it is the ultimate goal of all migration algorithm developers. Its only algorithmic problems are its extreme computational requirements and that it can produce unusual artifacts that are difficult to explain when incorrect Earth models are used.

However, full two-way reverse time migration has no velocity sensitivities, it has no dip limitations, and, in the prestack sense, it is the only approach that accurately handles all amplitude issues.

Phase-shift-plus-interpolation (PSPI) represents a very simple extension to the pure phase-shift approach. It uses the phase shift algorithm with multiple constant velocities, and then interpolates as needed to achieve the proper image at each image point on the current depth or time slice. It was very likely the first FK-style method that was able to at least partially remove both the $v(z)$ assumption and still retain a reasonable dip response. The quality of PSPI algorithms is still a function of the accuracy of the implementation, but, nevertheless, most such algorithms are quite good. Like its phase-shift counterpart, it can be extended to include some full two-way propagation. Because the interpolation step in PSPI can be somewhat difficult, and because each application of the phase shift method adds to the overall cost, alternatives to the method have been sought.

Split-step methods attempt to avoid the interpolation step of PSPI methods through a different approximation to the underlying wave-equation. In effect, this approach was one of the first to use a dual domain approach. The “shift” is accomplished in the FK domain, while the modification of the interpolation step is accomplished in the FX domain. When this method was published, it was thought to provide an improved approach to PSPI, but this did not prove to be the case.

Generalized phase screens are really split-step algorithms with additional terms to increase the overall dip-response and improve accuracy. The key difference between a split-step algorithm and a phase screen method is that the phase screen methods have additional correction terms in (F, X) space, and, as a result, should produce a more accurate, less sensitive algorithm when properly implemented. Again, like the original phase shift method, generalized phase screens can be modified to include some forms of two-way propagation.

Chapter 5

Exploding Reflector Examples

Let's turn our attention to a few simple zero-offset examples. In this case, we only want to compare algorithms. True zero offset data should provide a complete and accurate image of the subsurface. Since the data we will image is synthetic, we will have an exact representation of the true result.

Using our exploding reflector modeling approach, we generate what might be called true zero-offset seismic sections. These sections are then migrated using some new and some very old methods. Visual comparisons provide conclusive evidence that using the most accurate algorithm usually produces the best possible image.

If we are correct in our theoretical analysis, reverse time migration should produce almost exactly the correct answer in the following examples. Since reverse-time migration does not have any information about amplitudes in the subsurface at the start of the migration, we should not expect a perfect result. Nevertheless, the final reverse-time image should be the best, so we will use it as the baseline throughout the following examples.

Canadian Glauconitic Channel Play

Figure 5-1 shows a hard rock channel play velocity model together with a zero-offset exploding reflector simulation. Two channels are visible just below 700 meters. This model is based on glauconitic channel plays in Canada. The job is to image the channels just below 1300 milliseconds.

Figure 5-1. A shallow hard-rock-channel play from Alberta Province in Canada.

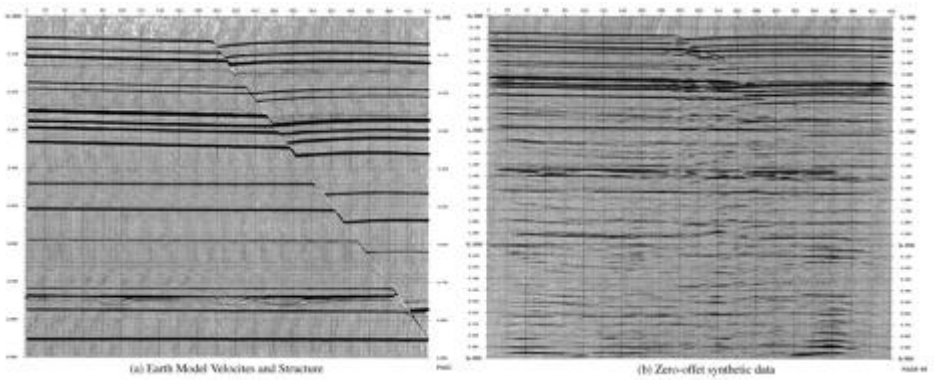

Figure 5-2 shows a pure phase-shift migration versus a two-way reverse time migration. Note that while the phase-shift was performed as a time migration, and the reverse time migration was actually a depth migration, a simple squeeze plot of the depth migration provides an excellent basis for direct comparison between the two images.

Figure 5-2. Phase shift versus full two-way-reverse-time migration.

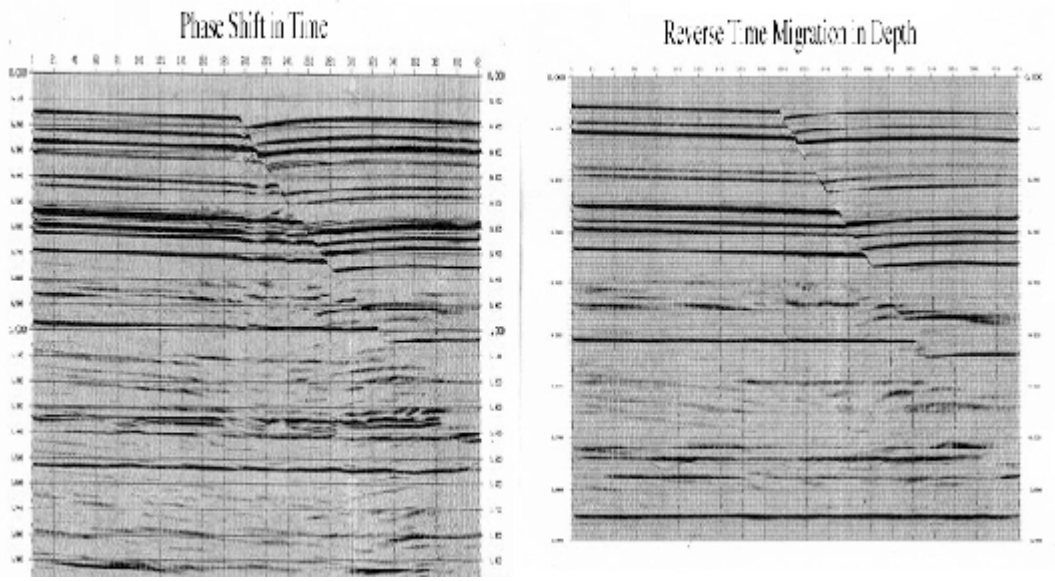

In Figure 5-3, the 45 degree migration was produced by an approximation to the one-way wave equation that was expected to image dips only up to approximately 45 degrees. Such migrations were the rule for many years and were considered to be the best possible migrations by many contractors. Clearly, the reverse-time migration on the right is superior to the 45 degree migration on the left. In this case, the improved accuracy of the reverse time method is preferable.

Figure 5-3. 45 degree time migration versus full two-way-reverse-time migration.

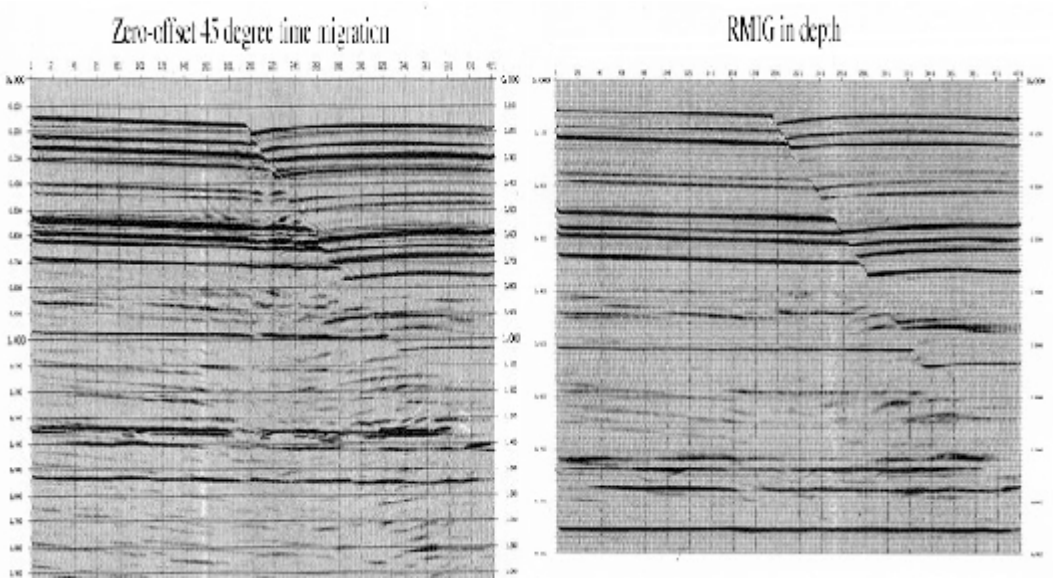

The FK or Stolt migration on the left of Figure 5-4 works well for this example. Velocity variations are not strong, so the constant velocity assumptions inherent in this approach are not a serious issue. Still, the reverse-time migration on the right is probably better.

Figure 5-4. FK versus full two-way-reverse-time migration.

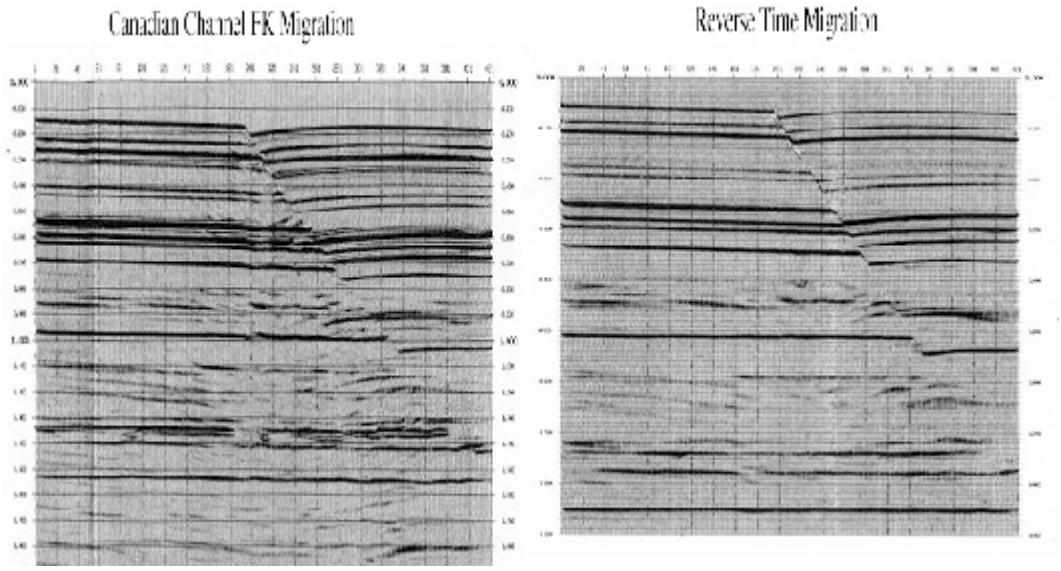

Figure 5-5 shows that cascading migrations produce the best comparison between migration techniques. However, the reverse-time migration still has fewer artifacts and appears much clearer.

Figure 5-5. Cascade versus full two-way-reverse-time migration.

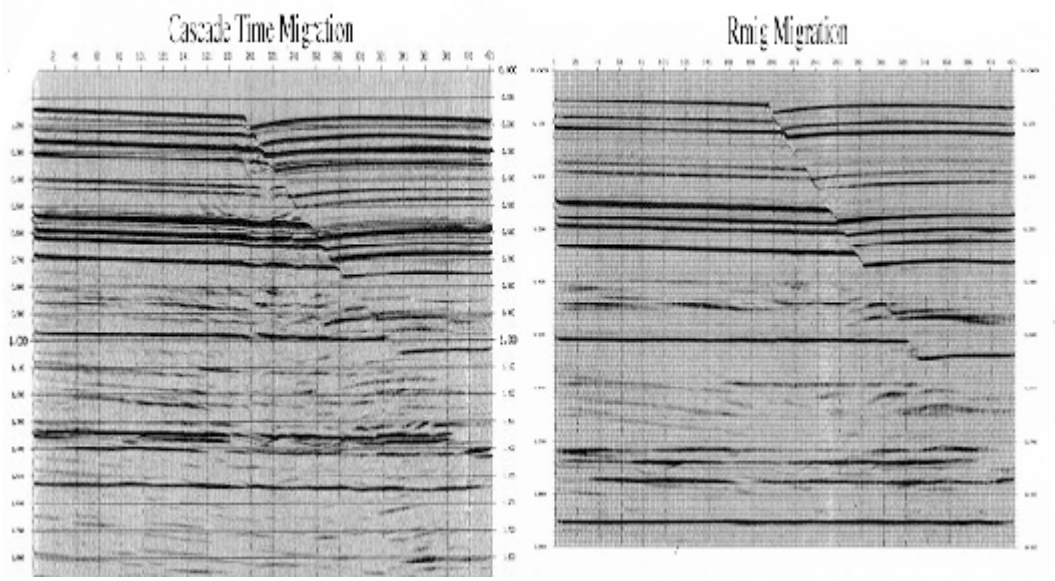

Gulf of Mexico Salt Model

Figure 5-6 shows a typical Gulf of Mexico salt structure with associated zero-offset exploding reflector synthetic data. The play here is in the beds that terminate at the salt-sediment interface. The geology is such that, except for the salt-sediment interface, velocity variation is relatively small.

However, from an imaging point of view, the extreme 2:1 or even in some cases 3:1, velocity contrast between the sediment and the salt represents a very difficult problem for most imaging algorithms to handle. The challenge is to image the salt face and the corresponding sediment terminations. The Gulf of Mexico salt structure has some of the steepest dips of all the models considered in this section. We should expect reverse time migration to win this contest easily.

Figure 5-6. A Gulf of Mexico Salt Earth Model and Exploding Reflector Data.

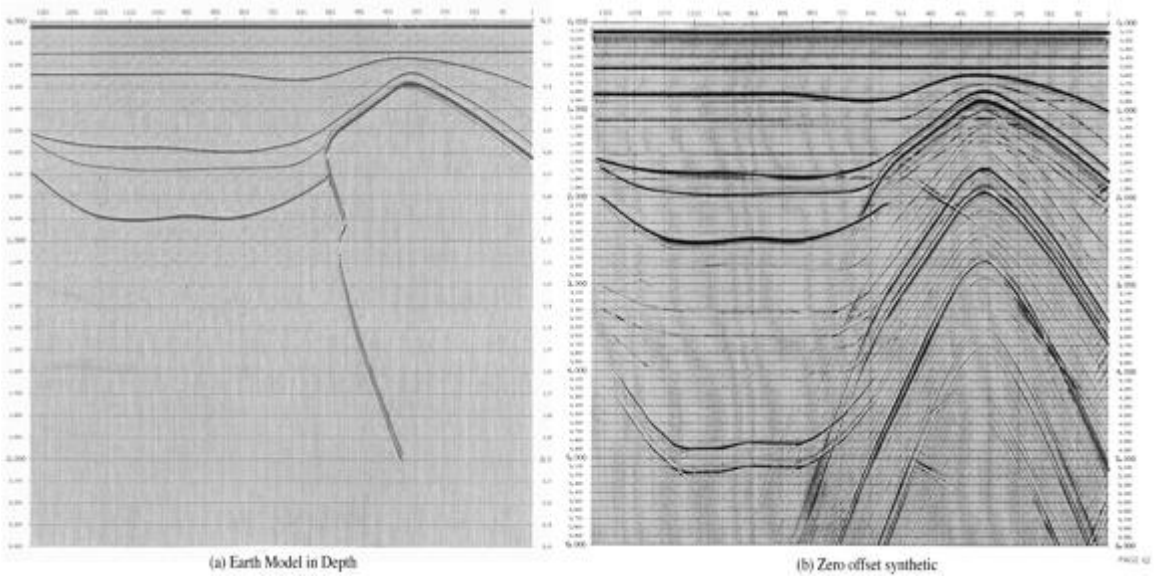

Figure 5-7 compares phase shift migration versus two-way reverse time migration. As we will see, regardless of which migration algorithm we use, the reverse time approach does the best job of placing all the events at their proper location. Unlike its time-domain based counterparts, it places all events as close as possible to where the velocity model says they should be.

Figure 5-7. Phase shift versus full two-way-reverse-time migration.

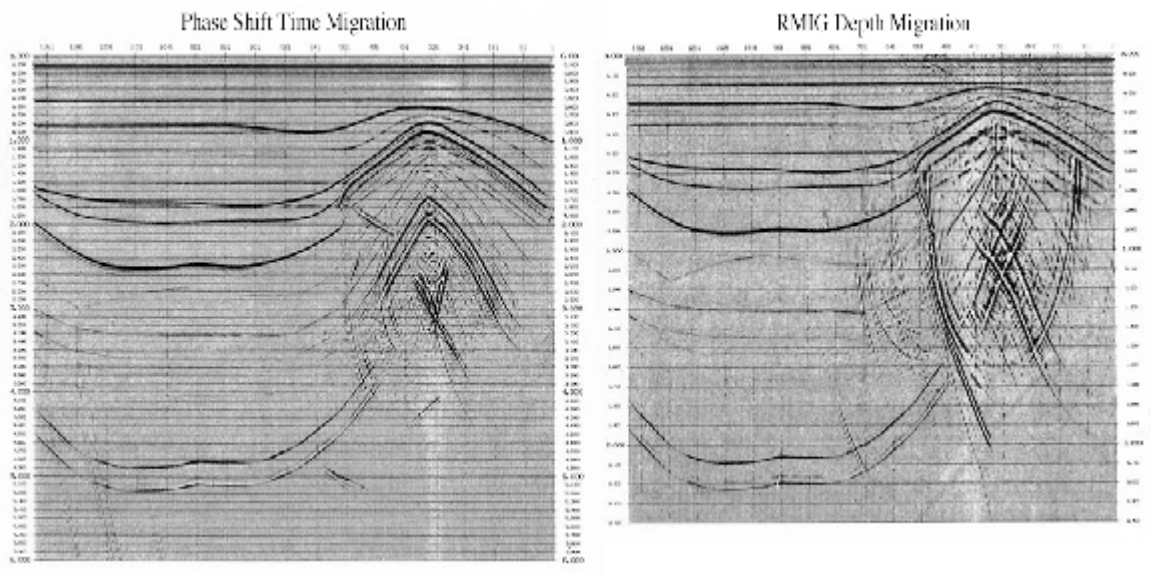

Figure 5-8 compares 45 degree migration versus two-way reverse time migration. From a purely esthetic point of view, we could argue that the 45 degree migration on the left is superior to the reverse-time migration on the left. One reason for this is the inherent dip-filtering that the 45 degree limit produces. Dips beyond 45 degrees are essentially lost, so the salt face will never be properly imaged, but because they are lost, the image looks much cleaner.

Figure 5-8. 45 degree versus full two-wayreverse-time migration.

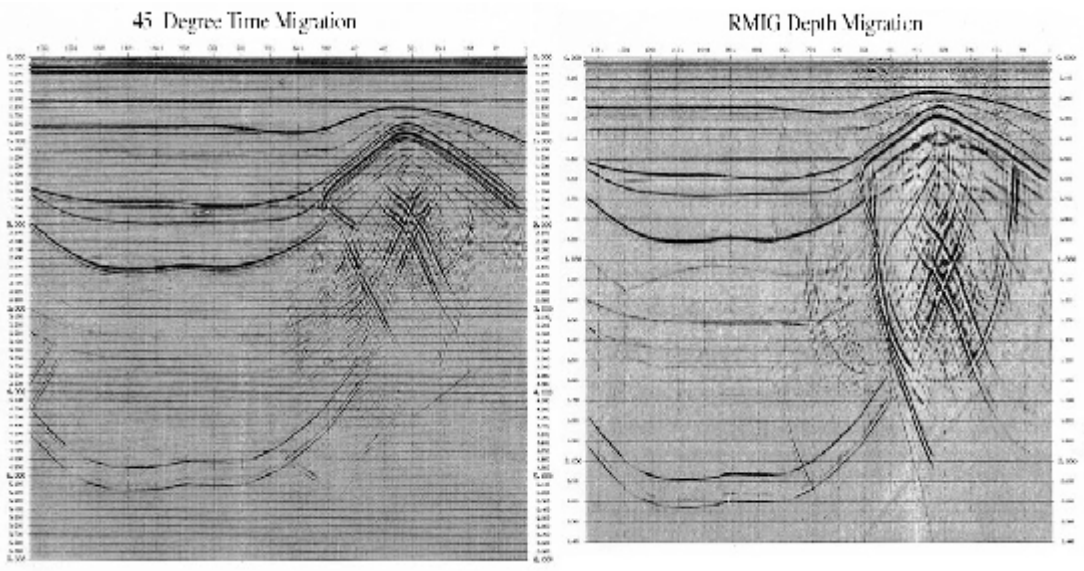

Figure 5-9 compares FK migration versus two-way reverse time migration. Because it is so sensitive to the constant velocity assumption used to derive it, an FK migration has no chance of imaging the salt face at its proper position. What is more surprising is that the salt face is almost not imaged at all.

Figure 5-9. FK versus full two-way reverse-time migration.

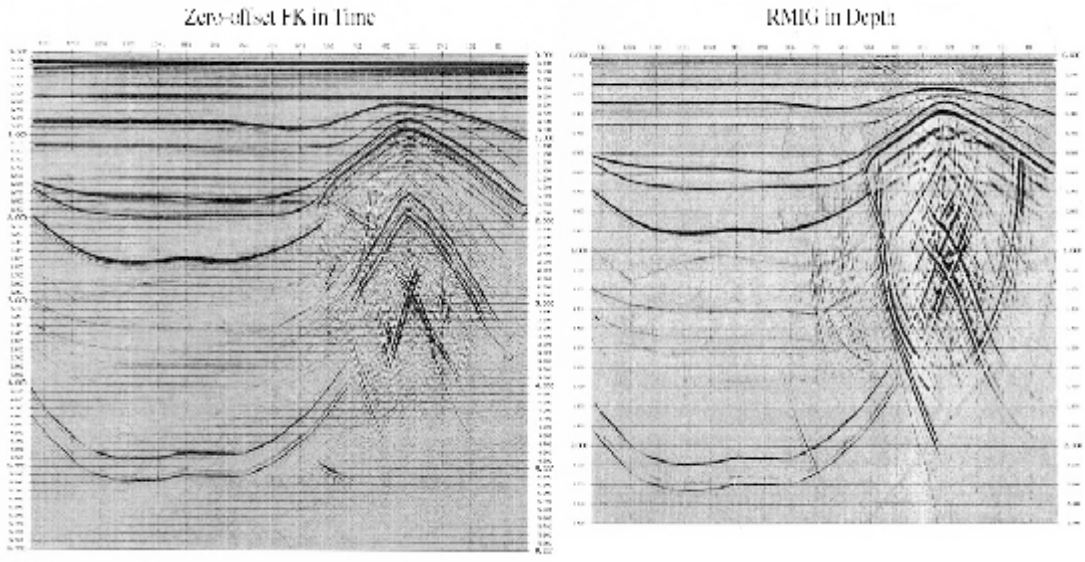

The cascade migration in Figure 5-10 does a very nice job on this zero-offset data set. We can argue that it is in fact the best of all the time-migration results. Nevertheless, the image is not nearly as good as the two-way graphic on the right.

Figure 5-10. Cascade versus full two-way-reverse-time migration.

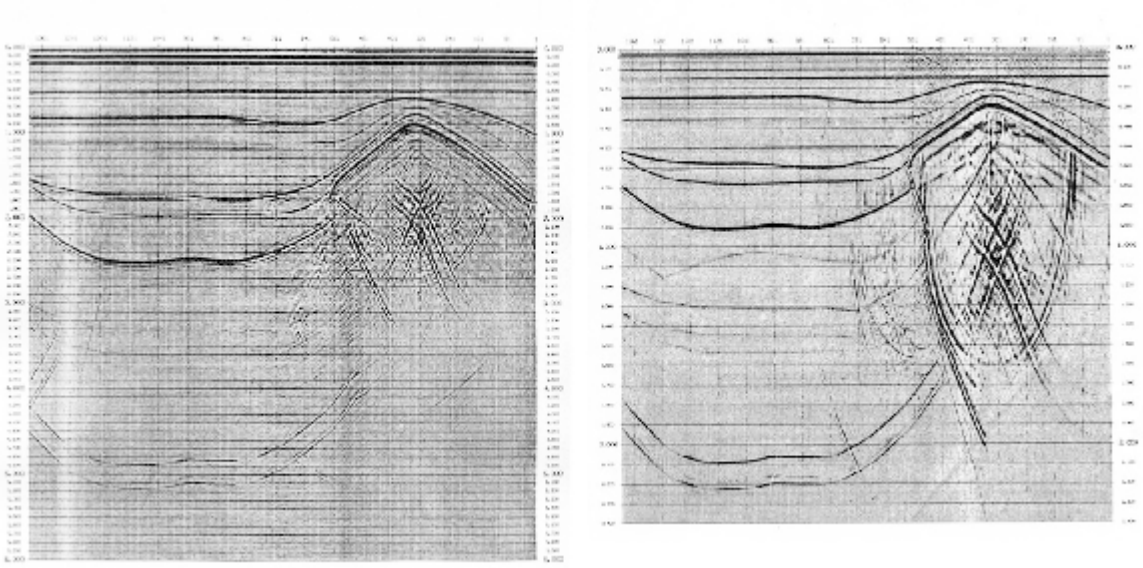

Granitic Overthrust

Figure 5-11 shows a granitic overthrust model from the Northern United States together with a simulation of a zero-offset section using that model. The problem is to unravel this data and put it back in its proper location. The objective are the sediments below the granite thrust.

Figure 5-11. A Granitic overthrust example from the state of Wyoming in the United States of America.

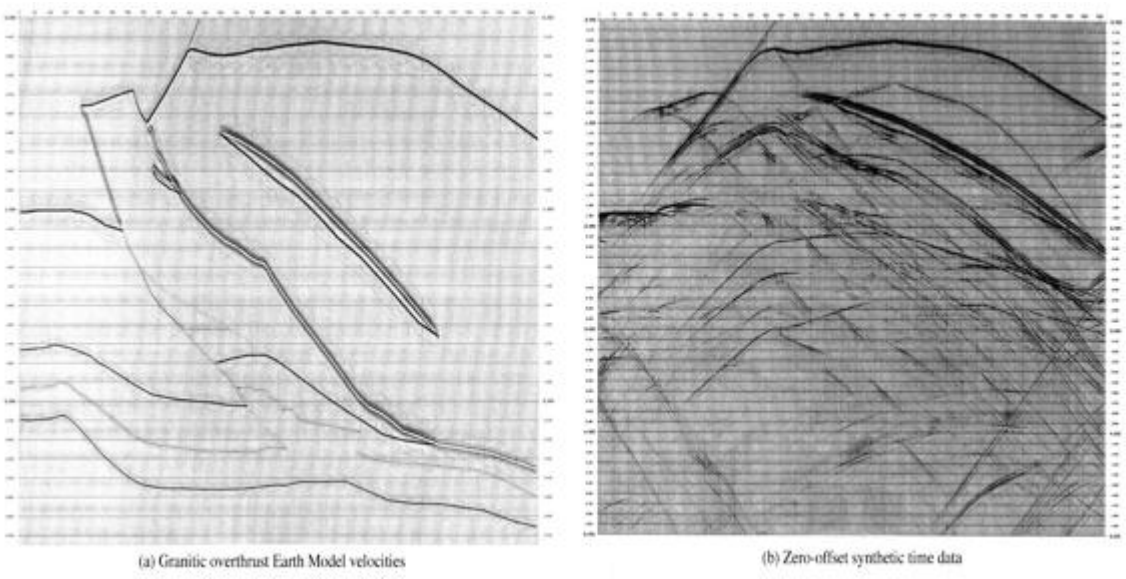

Granitic overthrusts are certainly as difficult to image as salt structures. Granitic structures are representative of structures with velocity contrasts between 3 and 3.6 to 1, where granite velocities are usually between 6800 and 7000 m/s, while near surface velocities are in the neighborhood of 1800 m/s.

Imaging the top and base of such structures with a time migration is almost impossible.

Figure 5-12 shows that a comparison of phase shift migration with reverse time migration is in reality no comparison at all. A single velocity function simply cannot cope with the extreme variation in the actual Earth model.

Figure 5-12. Phase shift versus full two-way-reverse-time migration.

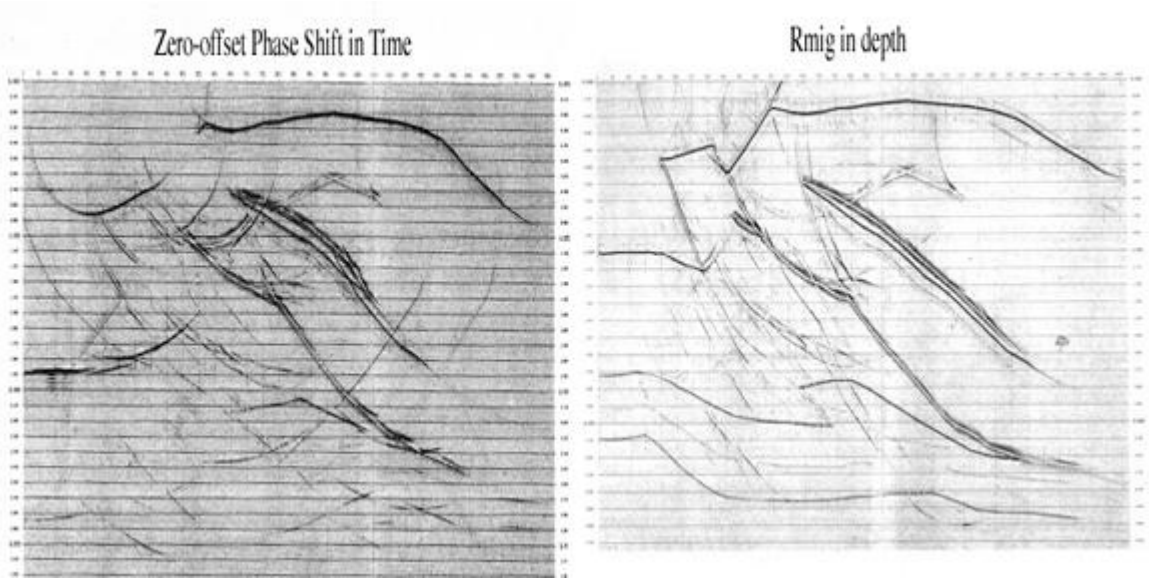

Figure 5-13 shows that an FK migration is no better than the phase shift of the previous figure.

Figure 5-13. FK versus full two-way-reverse-time migration.

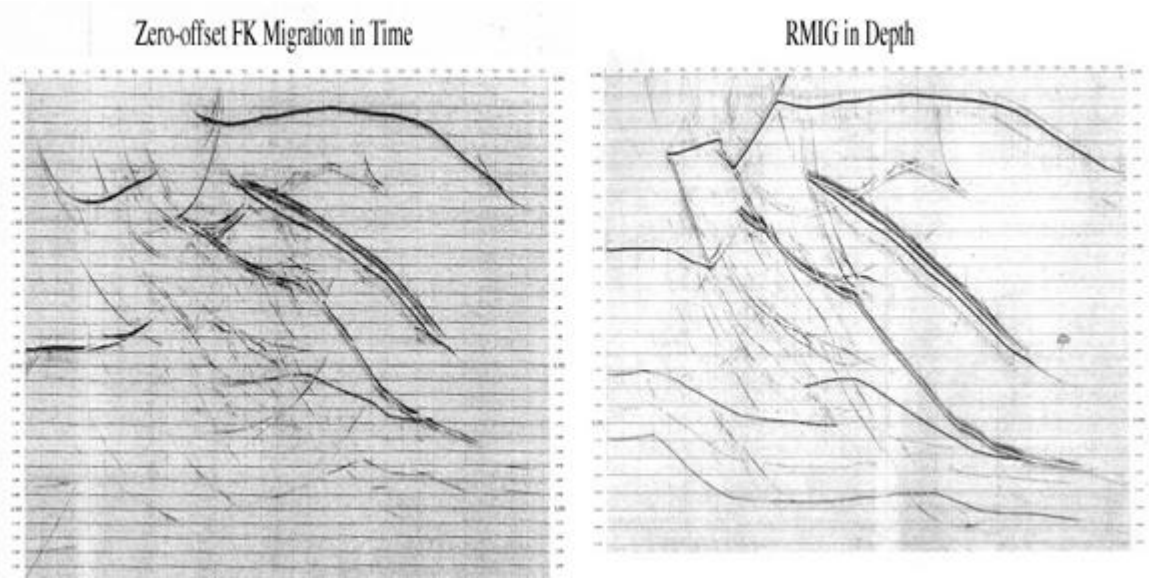

In contrast to the previous methods, the cascade migration shown in Figure 5-14 does a superior job of imaging above and to the left of the granitic intrusion, but simply cannot image anything below the granitic overthrust accurately.

Figure 5-14. Cascade versus full two-way-reverse-time migration.

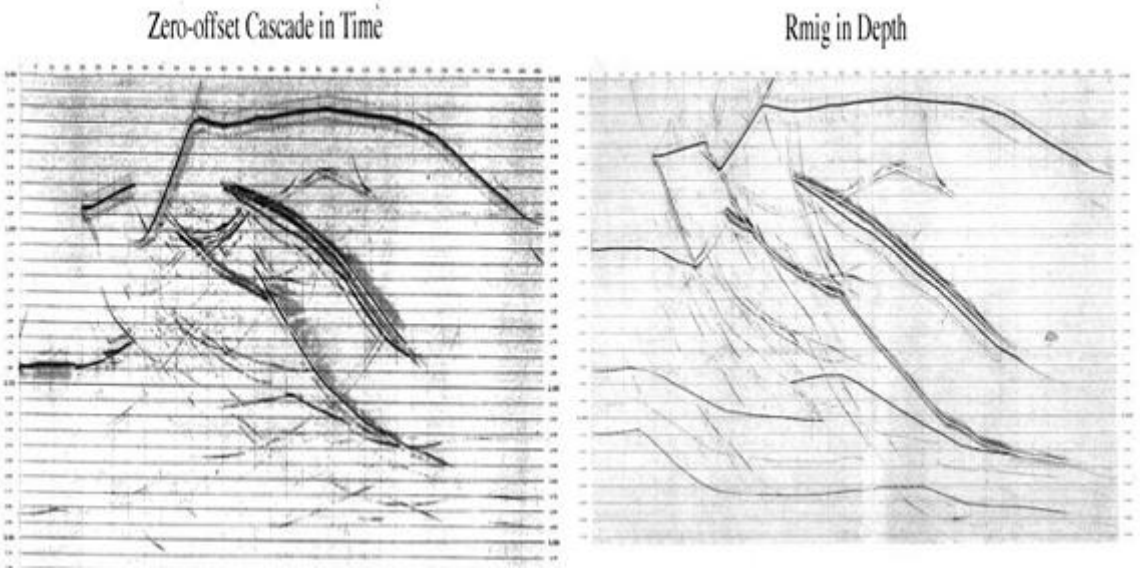

Chapter 6

Prestack Time and Depth Migration

Prestack migration algorithms are relatively simple variants of the poststack methodologies. The primary difference lies not in the mathematical theory but in the way in which any given algorithm is structured and applied to recorded multi-fold data. The basic differences arise because the prestack method must handle non-coincident sources and receivers. This means that it must handle the traveltime issues and amplitude correction factors associated with the source and similar issues for each and every receiver.

To resolve this issue, it is normal to split the imaging problem into two independent pieces. One piece handles the traveltime and amplitude from the source to the image point, while the other handles the traveltime and amplitude from the image point to the receiver. When both pieces are based on the same modeling approach, the names of the prestack algorithms are frequently identical to those given to the poststack methods from which they arose. When the two pieces are based on technically different methods, the resulting algorithm is assigned a hybrid combination of the two names. Figure 4-1 details these methodologies and becomes the framework for the discussion on zero offset technologies.

Wavefield and Wave-Motion Hierarchies

In Chapter 8, we noted the possibility of recording elastic as well as acoustic data. Figure 6-1 shows a simplified diagram of the kinds of waves you might encounter in a typical seismic acquisition experiment.

Figure 6-1. Wavefield hierarchy

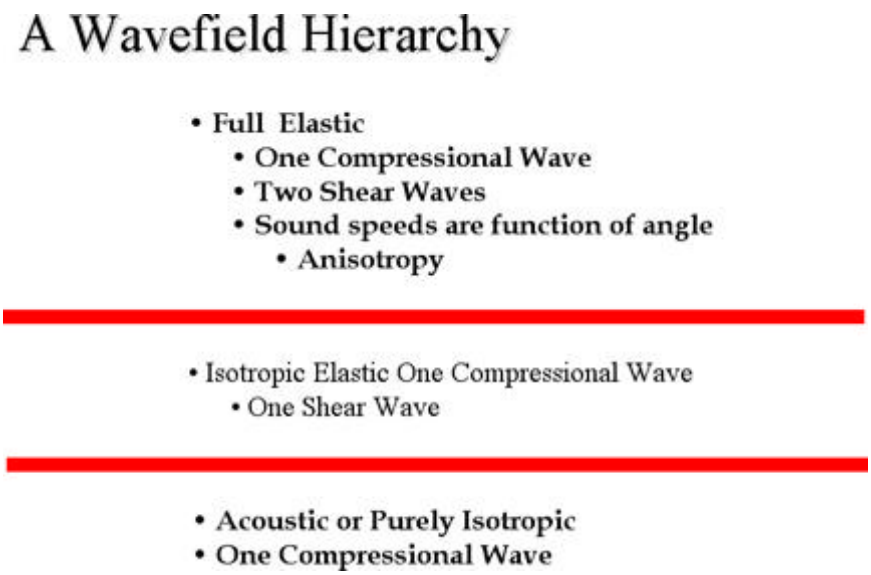

At the top of Figure 6-1, we see what is probably closest to what happens in the real earth. It is what we should record if we are serious about producing the best possible representation of the subsurface rocks. At the bottom, we see the kinds of waves that most of the migration algorithms of the recent past were designed to handle. This focus on the lowest rung of the ladder was dictated by the lack of sufficient computer power to consider imaging anything other than acoustic waves.

Between these two extremes, we see a wavefield middle ground that was once considered to define a sufficient data set for most, if not all, exploration goals. This has also proven to be false. While it is quite easy to construct middle-ground algorithms based on the technology we have discussed to this point, the possibility of stepping from the bottom rung to the top rung is rapidly making the middle rung obsolete. Moreover, what is important is that zero-offset methods have little or no chance of imaging the complex kinds of waves that occur in the earth. Effective imaging of compressional and shear waves that constantly convert from one to the other can only be contemplated through the use of prestack methods.

Wavefields in almost any medium radiate in all directions. The normal at any given subsurface location to the propagating wave front points in the direction of what we commonly think of as a ray. Since the propagation is normally not constrained with regard to direction, this normal is allowed to point in any direction consistent with the

sound speed of the medium. If the normal points upward, we say that this is an upward traveling wave. If it points downward, we call it a downward traveling wave. Clearly, such fields change directions at 45 degrees and become purely horizontal waves at 90 degrees. As we track any given normal or ray, we quickly observe that not only can it travel horizontally but it can also turn up and propagate upward.

Figure 6-2 shows the kind of wavefields we can model based purely on choice of algorithm. Choosing one of the algorithms defined in Figure 4-1 means that we inherently assume the propagation characteristics of that particular approach. Unless we happen to choose the algorithm that exactly fits the actual earth propagation, some part of the true wavefield will not be properly imaged. It should be clear that any assumption limiting wavefield directions cannot be correct: It cannot accurately handle amplitudes; it will likely produce artifacts; and it may not be able to image recorded events.

Figure 6-2. A wave-motion hierarchy.

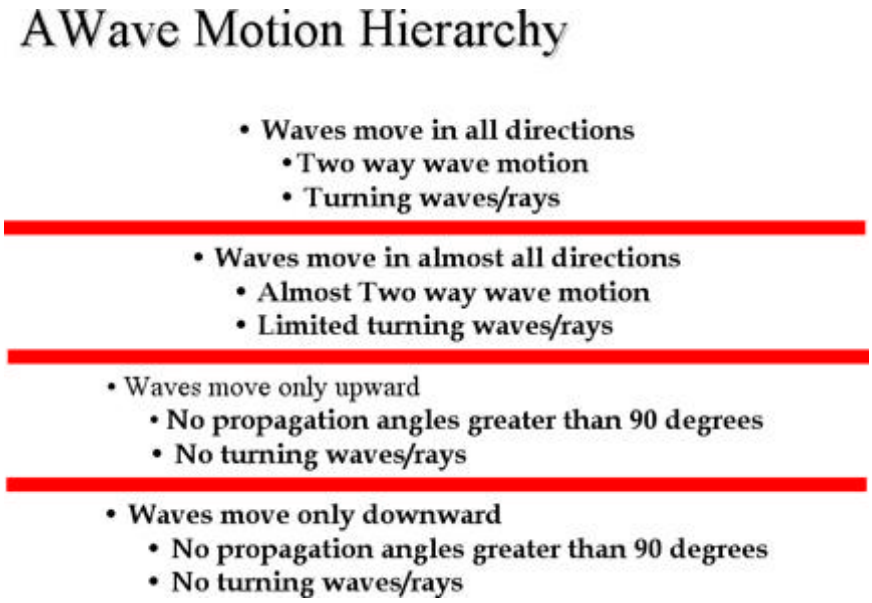

The only good news is that every algorithm in Figure 4-1 on page 134 is simply an approximation to the more accurate one at the top. Thus, given results from the bottom level, we should be able to step up to the next level, by simply running the more accurate approach.

Shot Profile Prestack Migration

Shot profile migration is a process by which each shot record is migrated separately and the result is summed into the final image volume. This process is sometimes also called *common-shot migration* or just *shot migration*.

Performing Shot Profile Migration

Shot-profile migration consists of three steps. In the first step, a synthetic shot is generated and propagated into the Earth. In the second step, receiver traces are reversed in time, used as sources in the modeling code, and then downward continued into the Earth. The third step forms an image at each depth or time slice through the application of an appropriate *imaging condition*.

This three-step approach is based on what is known as the *cross-correlation method* and was popularized by Jon Claerbout (1971, 1986). Figure 6-3 conceptualizes the basic ideas. The left hand side of this figure represents the forward propagation of the shot into the Earth, while the right hand side shows the backward propagation of the traces corresponding to this shot. In this figure, shot synthesis is generating a downward traveling wavefield, while the backward propagation of the receiver traces is generating what ultimately becomes an upward traveling wavefield.

Figure 6-3. Migration of common shot profiles

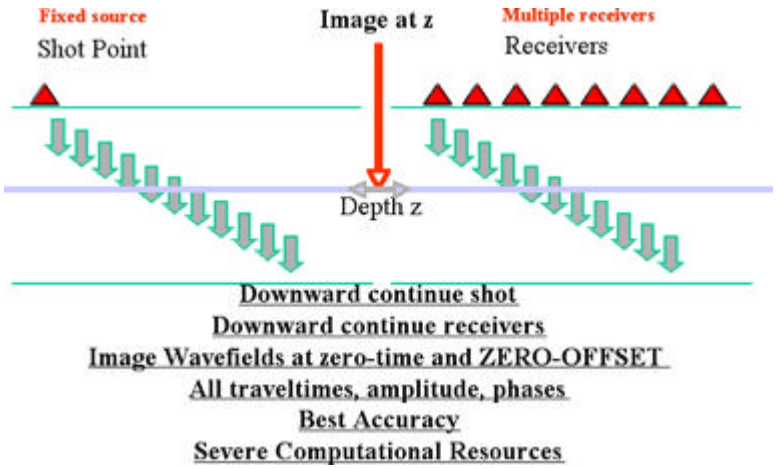

Note that we can choose virtually any pair of modeling algorithms for the basis of shot-profile migration. When a full two-way approach is used for both the shot and receiver steps, the result is a full two-way algorithm. When a one-way wave equation is used for both the shot synthesis and receiver back-propagation, the result is definitely a one-way method. Of course, it is possible to use two different modeling methods. We could use

a raytrace-based method for the shot synthesis and a full two-way back-propagation for the time-reversed receiver traces. Virtually any combination of the modeling algorithms discussed in Chapter 2 on page 7 is possible, so the number of prestack shot profile methods is quite large. We will avoid giving these hybrid methods names, but we will attach names to methods for which the shot synthesis and receiver back-propagation methods are algorithmically identical.

Understanding shot-profile migration is mainly dependent on comprehension of the third (imaging-condition) step of the shot-profile migration methodology since the modeling pieces are straight forward. To help understand the imaging condition, recognize that, as shown by the red dot in the movie corresponding to the image in Figure 6-4, each subsurface image point can be thought of as a seismic receiver that records signals from both the source and the receivers. The trace from the downward traveling source wavefield registers no arrivals until the first source amplitude arrives after τ_S seconds. This, of course, is the time it takes for energy from the source to ignite the virtual reflector at the image point.

Figure 6-4. A wavefield arriving at a subsurface image point (in red)

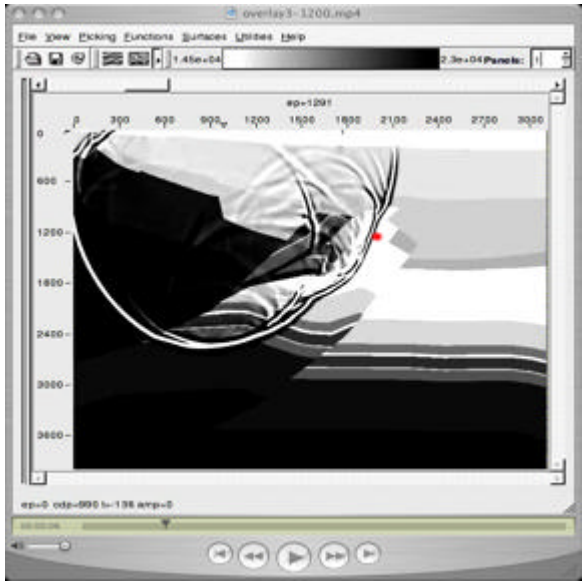

An example of such a trace showing two arrivals recorded from a source is shown in the top trace in Figure 6-5. An example of a second trace showing three arrivals from the backward propagated receivers is shown in the bottom trace. Because it was generated from time-reversed traces, amplitudes at the longest time are due to amplitudes recorded at the maximum recording time, τ_{max}. After backpropagating for $\tau_{max} - \tau_S$ seconds, the full wavefield that radiated out from the image point as it acted as a virtual source has arrived at the receiver located at the image point. At this time stamp, there are still τ_S seconds left to propagate, but none of these amplitudes will be recorded at the image point. Thus, both traces contain exactly two arrivals. Imaging is accomplished by summing all the amplitudes in a a point-by-point multiplication of the two traces and then adding the result to the image point location. This is exactly Jon Claerbout's cross-correlation imaging condition (1971, 1976) in graphic detail.

Figure 6-5. Downward (source) and Upward (receiver) arrivals at a subsurface image point

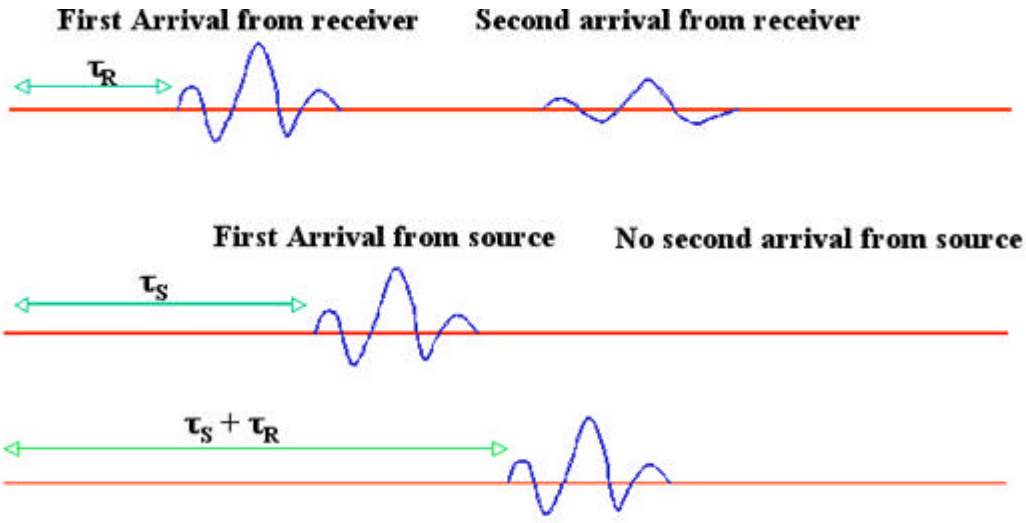

Figure 6-6 is a further attempt to clarify Claerbout's imaging condition. This figure shows a subsurface model with a single point reflector in red on the face and the time section indicated by the blue arc on the top. It contains three potential point reflectors indicated by two black dots and one red dot. The red dot is the only point reflector in the model.

Figure 6-6. Point reflector response with forward source and backward receiver wavefields at two subsurface locations.

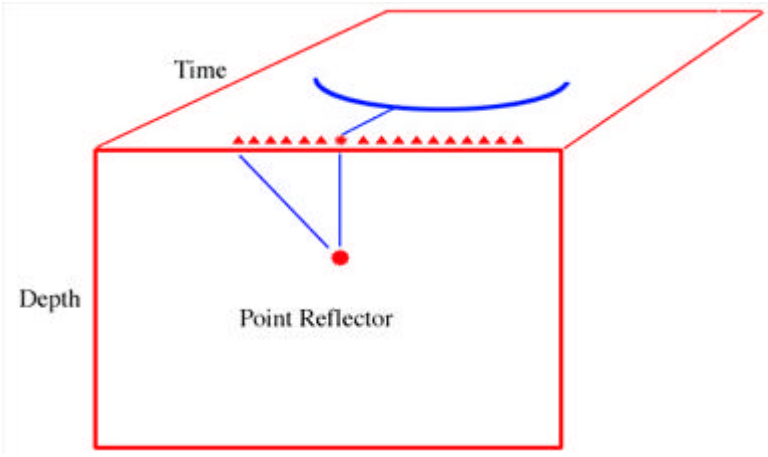

We see that events on the two recorded traces do not overlap at the upper black image point. Thus, applying the imaging condition produces zero amplitude and no reflectivity, as predicted, and no point reflector is detected. On the other hand, at the black dot that is near the red point reflector, the events on the two traces may be close enough to the red dot to produce a small amplitude, and as a result the point reflector begins to be detected. Claerbout's imaging condition is just the ticket for detecting the only point reflector in the model.

It may not be surprising that there was more than one arrival in each of the two traces at the image point. As indicated in the propagating wavefield in Figure 6-4(a), multiple paths from the source location to any subsurface image point is probably the norm in complex geology. In spite of that, it is important to recognize that there are several algorithms that make the surprising assumption that only one arrival is present at each subsurface location. We will see that single arrival methods, while useful, are very sensitive to the kinds of velocity variations seen in even relatively simple geologic settings.

As was the case on historical approaches in Chapter 3, migration was performed by hand on a shot-by-shot basis. In that case, the imaging was based on direct estimation of local dips coupled with a crude velocity guess. To emulate this process using our modeling methods, it was necessary account for the propagation from the source to the reflection point, and from the reflection-point to the receiver for each and every trace in our survey. This was accomplished by a forward shot propagation and a backward propagation using the recorded data reversed in time as sources. Clearly, both steps could employ exactly the same modeling code. The only real difference between the two is that one used synthetic source data while the other used the actual recorded data in reverse time order. Do not be discouraged if this does not seem simple or intuitive. In 1971, very few practicing geophysicists thought anything like this would ever be possible and many thought Claerbout's method would never be practical. They were wrong.

In precise mathematical terms, Claerbout's time-coincident imaging condition is mathematically represented by Equation 6-1, where $I(x,z)$ represents the seismic amplitude at the position (x,z) in space and depth, $S(t,x,z)$ is the downward traveling source wavefield, and $P(t,x,z)$ is the backward-propagating seismic-shot record.

(6-1) $$I(x,z) = S(t,x,z) \otimes P(t,x,z) \Rightarrow t = 0$$

In this case, $\otimes$ is interpreted to mean cross-correlation and $\Rightarrow t = 0$ means to evaluate at zero time for this depth. This process usually takes place in the frequency domain, so evaluation at time zero just means to sum over frequency. In this case, the formula is given by Equation 6-2.

(6-2) $$I(x,z) = \sum_{\omega} \overline{S(\omega,x,z)} P(\omega,x,z)$$

Refinements to this simple process abound. One of the simplest improvements is given by Equation 6-3.

(6-3) $$I(x,z) = \frac{\sum_{\omega} \overline{S(\omega,x,z)} P(\omega,x,z)}{\sum_{\omega} \overline{S(\omega,x,z)} S(\omega,x,z)}$$

This improvement in the frequency domain normalizes Equation 6-2 by the spectrum of the source wavefield. Because the source wavefield is what illuminated the subsurface in the first place, dividing by this value has the general affect of correcting for uneven illumination. It generally results in improved amplitude preservation, but should not be considered as the final word in amplitude preservation.

When the velocity field is exact, the imaging condition, as described by equations 6-1 and 6-3, produces sharp and accurate maps of subsurface reflectivity. When the velocity field is incorrect, many point reflectors may not be imaged or may be imaged very poorly.

It is quite natural to ask if there is some modification to the image condition that might make it possible to assess the accuracy of the velocity field or even to produce a method to estimate velocity corrections. One answer to this question is given by the non-zero offset imaging condition in Equation 6-4, and the other by the time shift zero offset condition in Equation 6-5.

(6-4) $$I(x,z,h) = S(t,x-h,z) \otimes P(t,x+h,z) \Rightarrow t = 0$$

(6-5) $$I(x,z,\tau) = S(t-\tau,x,z) \otimes P(t,x,z)$$

In Equation 6-4, h is a scalar with units of feet or meters at depth that measures where the two wavefields achieve maximum lateral correlation. It defines a range of subsurface

offsets that, in principle, offers the possibility for sensing and correcting for velocity errors. When the migration velocity is incorrect, the best image will appear at some positive or negative h. How far the wavefields are separated can be used to estimate a new velocity volume or field.

In Equation 6-5, τ is a scalar at depth with units of time that tells us how close the two wavefields are in time at depth. The scalar τ is not directly related to surface time; it is merely a value indicating the difference between forward source and backward receiver times. Instances where non-zero τ's produce the best image indicate inaccurate velocities, and the value of τ becomes useful in estimating a new velocity field.

It is worth noting that both of these approaches can be converted to methods that produce gathers parameterized by opening or reflection angle and azimuth in 3D. The mathematics are beyond the objectives of this book, but these migration angle gathers can be analyzed in much the same way that more traditional offset gathers are currently used to estimate subsurface velocities.

In the frequency domain, equations 6-4 and 6-5 have the forms in equations 6-6 and 6-7.

(6-6)
$$I(x,z,h) = \frac{\sum_{\omega} \overline{S(\omega, x-h, z)} P(\omega, x+h, z)}{\sum_{\omega} \overline{S(\omega, x-h, z)} S(\omega, x+h, z)}$$

(6-7)
$$I(x,z,h) = \frac{\sum_{\omega} \overline{e^{i\omega\tau} S(\omega, x, z)} P(\omega, x, z)}{\sum_{\omega} \overline{e^{i\omega\tau} S(\omega, x, z)} S(\omega, x, z)}.$$

Shot Profile Migration Example

The black lines in Figure 6-7(a) show the location of three shots with receivers spanning the entire model. Part (b) shows one-way shot profile migrations of these shots. Note that each migration images a substantial portion of the subsurface. These images were actually produced using the imaging condition of Equation 6-3. Thus, the process included approximate correction for illumination.

Figure 6-7. Shot profile images

(a). A Gulf of Mexico Earth model and synthetic shot profile

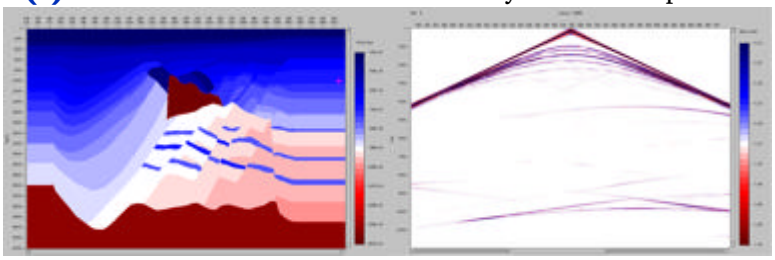

(b). Shot profile migrations of shots over the model in (a)

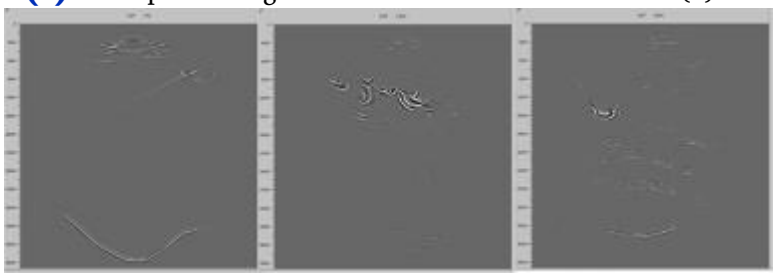

As noted earlier, every algorithm in Figure 4-1 can be used as part of a shot profile style migration method.

- Pure XT algorithms are either one-way or two-way and are usually implemented using finite difference approximations.
- Of the FK methods, only the PSPI method is popular.
- The most popular one-way method is based on the FKX phase screen method of Ru Shan Wu and colleagues, or on methods that are slight variants of this technique.
- Plane wave modeling techniques are also in demand because they can be applied very efficiently.
- In contrast, raytrace (Kirchhoff) shot-profile approaches are not popular because this method is usually implemented to image common-offset volumes rather than shots. This structure facilitates the production of common-offset image gathers, and their use directly affects estimation of interval velocities.

Combinations of these methods are rare. Some that probably should have received attention include combinations of Gaussian Beam and two-way-reverse-time, as well as Gaussian Beam and one-way-phase screen or PSPI.

Partial Prestack Migration: Azimuth Moveout (AMO)

Except for pure land acquisition, it is generally very difficult to record pure common offset or pure common azimuth data. Economics limits such recording on land, and cable feather makes marine acquisition of such data almost impossible. Consequently, methods have been developed to map recorded data into the proper framework. One such approach is *azimuth moveout* (AMO), which is the combination of DMO to a zero offset, followed by inverse DMO to a fixed non-zero offset. Figure 6-8 is a revision of Figure 3-30.

Figure 6-8. Constant velocity non-zero offset equal traveltime curve.

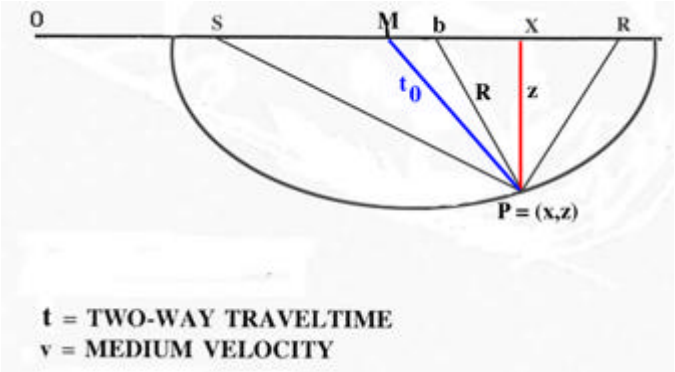

With a little bit of Greek mathematics, it shows that the time, t, of the equal traveltime curve in a constant velocity medium satisfies the elliptical equation in Equation 6-8, where, of course, t is the traveltime from S to P to R, and $h = (R - S)/2$ is the half offset.

(6-8)
$$\frac{x^2}{\frac{(vt)^2}{4}} + \frac{z^2}{\frac{(vt)^2}{4} - h^2} = 1$$

It is interesting to determine the time, t_0, in terms of v, t, and h, but doing so is not completely straightforward mathematically. What we first need to recognize is that t_0 in Equation 6-8 lies on the circle defined by Equation 6-9.

(6-9)
$$(x - b)^2 + z^2 = \frac{(vt)^2}{4}$$

For readers with a bit of calculus, if we take the derivatives of Equations 6-8 and 6-9 with respect to x, we get, respectively, Equation 6-10 and Equation 6-11.

(6-10) $$\frac{x}{\frac{(vt)^2}{4}} + \frac{z\frac{\Delta z}{\Delta x}}{\frac{(vt)^2}{4} - h^2} = 0$$

(6-11) $$(x - b) + z\frac{\Delta z}{\Delta x} = 0$$

Note that $\Delta z/\Delta x$ is the slope of the local tangent or, more practically, the slope of the reflecting migrated event if P was its location. Using Equation 6-11 to eliminate $\Delta z/\Delta x$ from Equation 6-10 yields Equation 6-12.

(6-12) $$b = \left(1 - \frac{\frac{(vt)^2}{4} - h^2}{\frac{(vt)^2}{4}}\right) x$$

After simple algebraic manipulations, the result is Equation 6-13. What this formula tells us is that the zero-offset time, t_0, is a function of the offset, h, the velocity, v, and the traveltime, t.

(6-13) $$t_0^2 = \left(t^2 - \frac{4h^2}{v^2}\right)\left(1 - \frac{b^2}{h^2}\right) = t^2\left(1 - \frac{b^2}{h^2}\right) - \frac{4h^2}{v^2}\left(1 - \frac{b^2}{h^2}\right)$$

A key point is that t is the input time on the input trace and t_0 is the zero-offset time. What we want a DMO process to do is to map data at time t to data at time t_0. A bit of trickery due to D. Forel and G.H.F. Gardner (1986) makes this possible. What they wanted after DMO processing was a data set that satisfied an equation of the form in Equation 6-14 for each *new* offset k.

(6-14) $$t_1^2 = t_0^2 + \frac{4k^2}{v^2}$$

They realized that, given t_1 and k, they could rewrite Equation 6-13 in the form of Equation 6-15.

(6-15) $$t_1^2 = t^2\left(1 - \frac{b^2}{h^2}\right) + \frac{4}{v^2}[k^2 - (h^2 - b^2)]$$

Then, if they chose $k^2 = h^2 - b^2$, the result would be Equation 6-16, which simplifies to Equation 6-17.

(6-16) $$t_1^2 = t^2\frac{k^2}{h^2}$$

(6-17) $$t_1 = t\frac{k}{h}$$

Thus, all DMO amounts to is a simple mapping from offset h at time t to offset k at time t_1. Moreover, this mapping is entirely velocity independent. This means that DMO and, consequently, DMO inversion can both be performed in a completely velocity independent manner. Forel and Gardner also realized that this process can be carried out by replacing each input trace with an ensemble of output traces having offsets determined by k through b at time t_1.

Figure 6-9(a) shows an ensemble of replacement traces for DMO on the left and DMO inverse on the right. As we might expect, what we see are smiles for the former and frowns for the latter. Figure 6-9(b) shows what happens to a purely inline common-midpoint gather after DMO is applied. Note that, after DMO, the source-receiver axis is orthogonal to the input source receiver axis. If we apply DMO inverse to the DMO'd data, the result would be to simply rotate back to the original orientation.

Figure 6-9. DMO in pieces

(a). DMO impulse response on the left and DMO inverse on the right

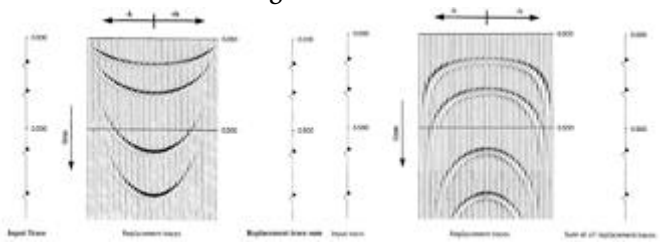

(b). DMO is essentially a 90 degree rotation

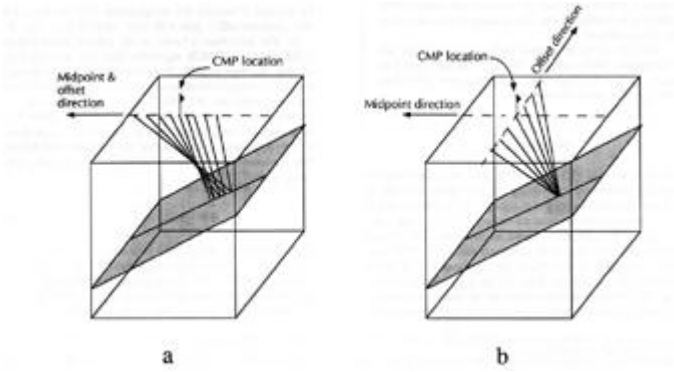

Figure 6-10 shows how to modify AMO (DMO followed by DMO inverse) to achieve an output source-receiver orientation of any desired angle. DMO is first applied along the output trace orientation indicated by the h_O vector in part (b). DMO inversion is then applied orthogonally to this direction. This process transforms an input volume with virtually random azimuths into one with a fixed azimuth and only four dimensions.

Figure 6-10. Arbitrary angle AMO

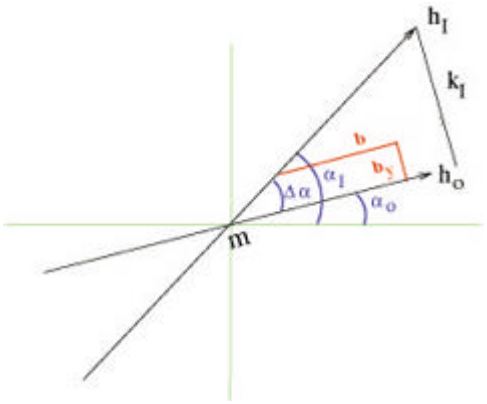

Figure 6-11 shows an AMO impulse response on the left and a full 3D volume on the right. The input trace from the SEG/EAGE C3-NA synthetic data volume used for the impulse response had an azimuth of -2 degrees and an offset of 1600 meters. All traces from the SEG/EAGE C3-NA data were used to produce the 1000 meter offset volume on the right. The azimuth of this volume was 45 degrees.

Figure 6-11. AMO impulse and 45 degree azimuth at 1000m offset.

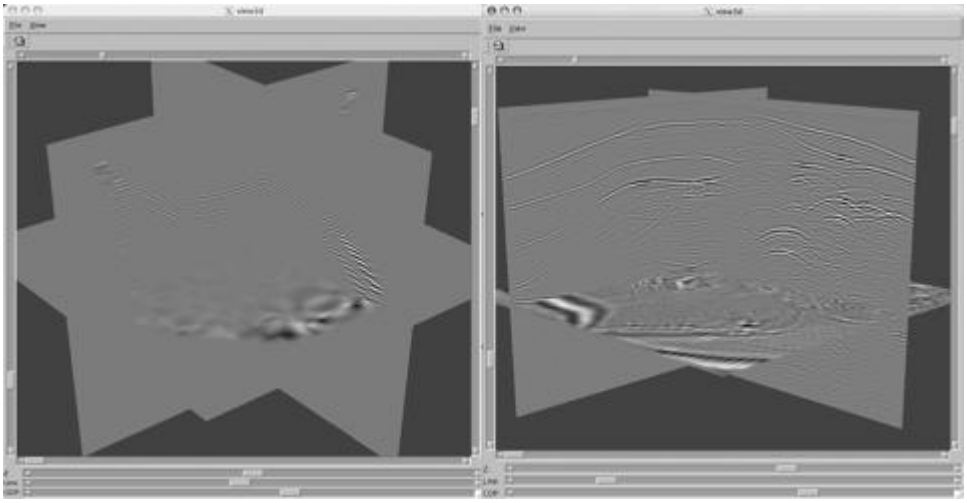

The left hand side of Figure 6-12 shows a 1000 meter offset slice through an AMO'd volume processed to achieve zero degrees azimuth. The right hand side shows the same line from a similarly processed volume at 45 degrees. Note the considerable differences in reflector position even though the model is the same.

Figure 6-12. A comparison of zero degree and 45 degree azimuths.

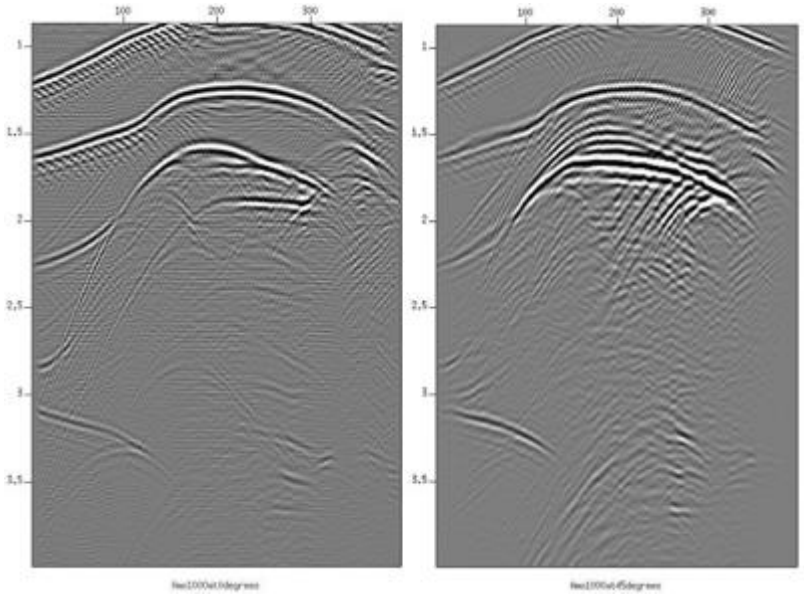

The top half of Figure 6-13 shows a fixed 15 degree azimuth line selected from a single streamer marine acquisition from offshore Indonesia. Shots with mostly shorter offsets are on the left, while those with mostly longer offsets are on the right. The bottom part of this figure shows a selected set of shots from the 3D AMO processed data set. Note the similarity of these data as well as that all offsets are now present in the common azimuth line.

Figure 6-13. Real data AMO example

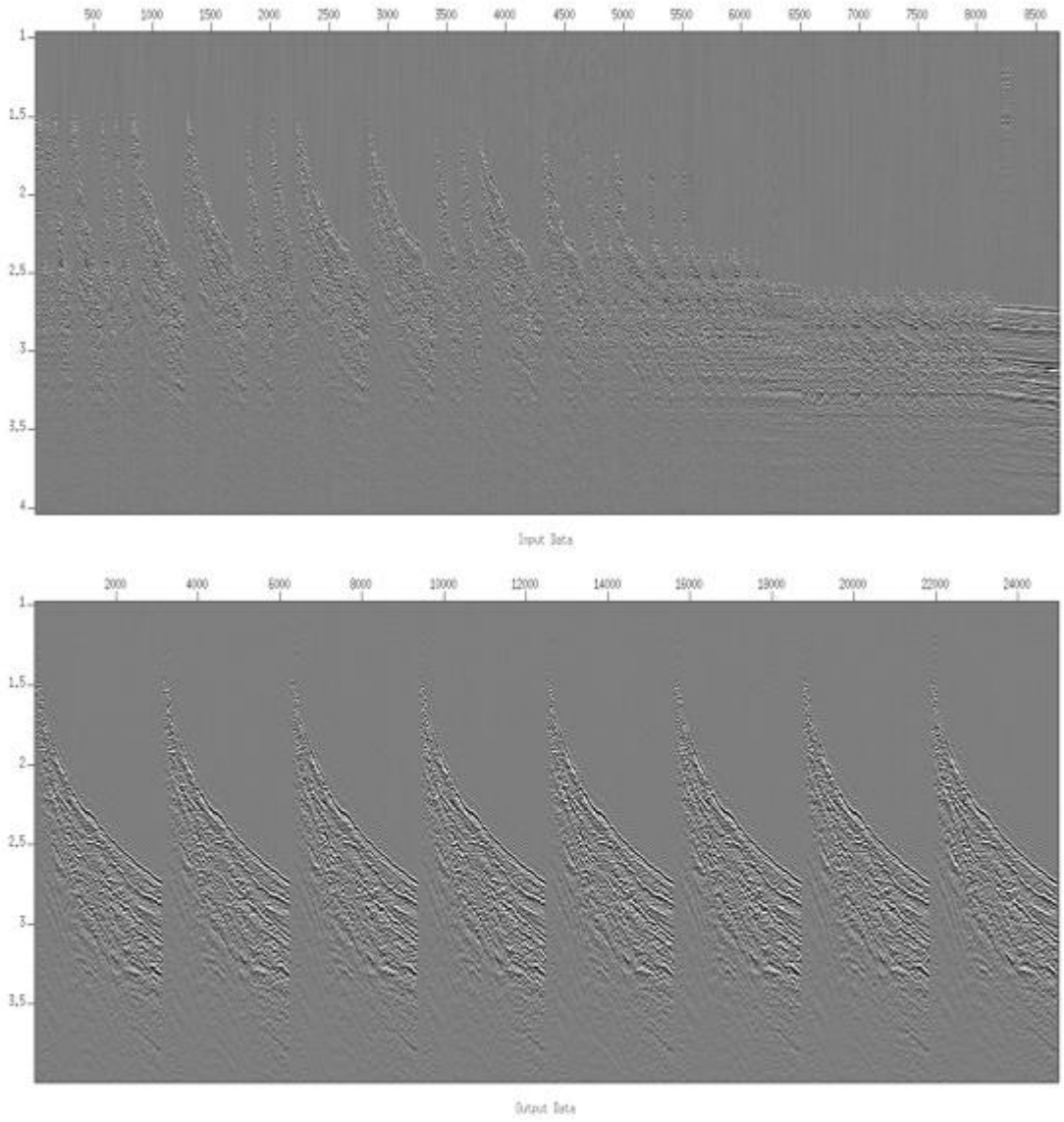

Velocity Independent Prestack Time Imaging

Figure 6-14 shows various slices through the seismic response for a point reflector in a purely constant velocity medium. The top left figure is the response due to a single point reflector. Proceeding in a counterclockwise manner, we see a common-depth point slice, a radial or common-angle slice, a common-time-slice, and finally in the upper right, a common offset slice. In this constant velocity world, it should not be difficult to envision a method for imaging each of these particular orientations of the data.

Figure 6-14. Point response in a constant velocity medium

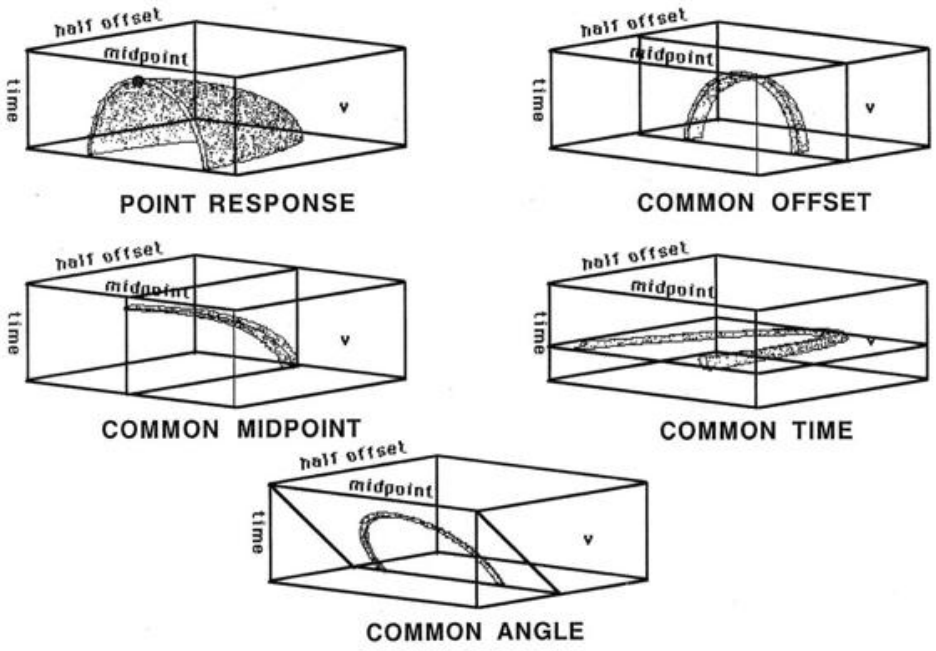

Common-offset sections actually look like normal stacked seismic sections, but there is a difference. In the near offset on the left side of Figure 6-15, the section closely resembles a normal stack, while the far offset on the right appears to be a squeezed version of the section on the right. Even though these sections are from the two dimensional anisotropic model in the lower right hand corner, anisotropy is not really visible to the naked eye. Moreover, traditional normal moveout correction, even though it supposedly stretches the data to equivalent zero-offset time, will not ultimately produce anything close to a true zero-offset stack.

Figure 6-15. Near and far offsets

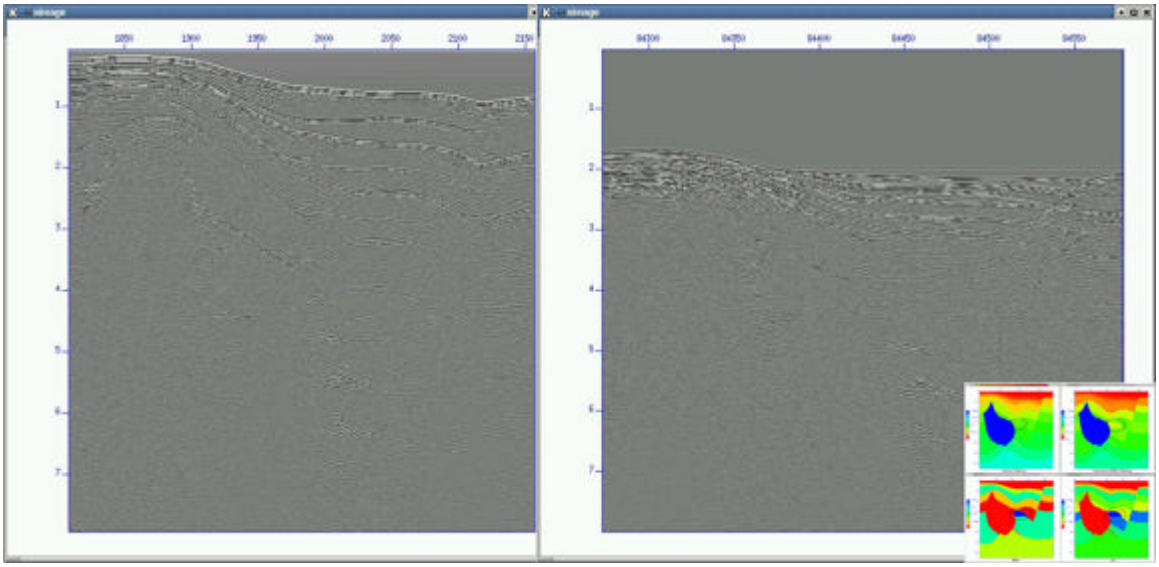

Figure 6-16 details an unusual methodology for imaging or migrating data in constant velocity media. It combines what we have learned in the previous figures to allow us to image the point source response while delaying the velocity analysis until the very end.

Figure 6-16. Dip independent prestack imaging

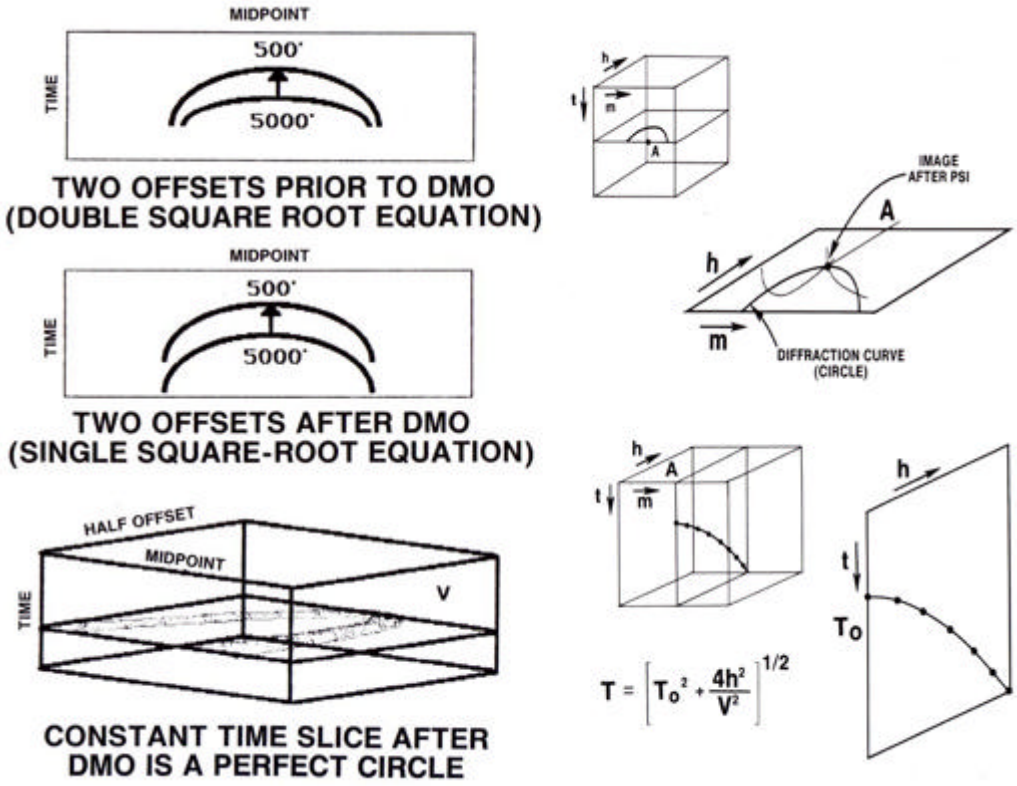

The left hand side of this image essentially shows what happens when we apply DMO. The top graphic shows the input data from a single point source. That is, it represents two different common-offset slices superimposed on one another. The middle figure on the left hand side shows the same two offset slices after DMO. Note that, in this case, the two common-offset images differ only by moveout time.

In the bottom part of the left hand side, we see that, after DMO, any time slice appears to be a circle. That being the case, we can image this circle to a point by simply migrating it as in the previous figures. Once this is done, as indicated by the top figure on the right, we will have reduced the point source response to a single CDP whose moveout velocity provides the necessary information to image the point at its correct subsurface location.

The completely velocity independent prestack imaging method that produced Figure 6-17 delayed velocity analysis until the very end of the process. This means that the velocities obtained from this approach are actually migrated velocities, and consequently are measured almost vertically. The importance of this statement is that this set of velocities are much more consistent with the assumptions made to ensure the accuracy of the traditional Dix vertical inversion scheme.

Figure 6-17. Application of dip independent prestack imaging in the Gulf of Mexico

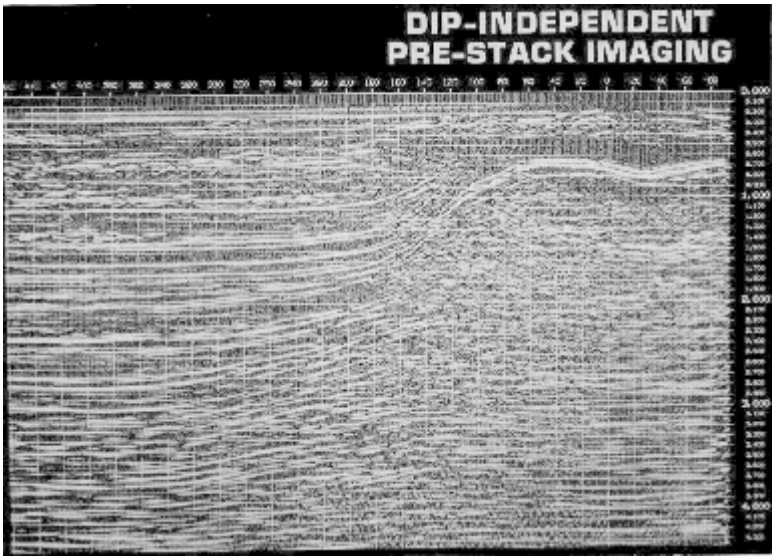

Double Downward Continuation—Common Azimuth Migration

Among the several approaches to prestack imaging, common azimuth migration is one of the fastest. While it may suffer from off-azimuth response problems, it produces usable output at a speed that makes it a viable technique for velocity analysis and velocity model construction.

Figure 6-18 shows a common azimuth migration. A common azimuth migration parameterizes input data by CDP and offset. Since the data are assumed to have been recorded with one and only one azimuth, the source and receiver locations can be computed from the midpoint (or CDP) and offset. This means that the data are defined by only four parameters: midpoint (2), offset (1), and time, and, as a consequence, are four-dimensional. Normally, data sets with more than one azimuth are really five-dimensional: source(2), receiver(2) and time (1).

Figure 6-18. Common azimuth downward continuation migration

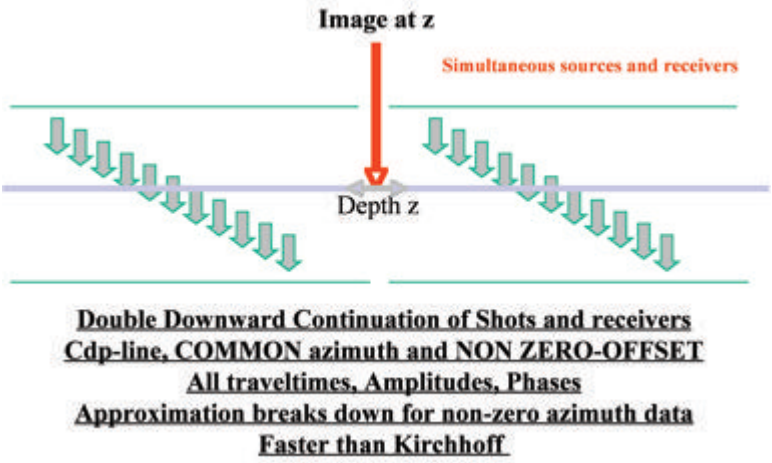

The nice thing about common azimuth data is that they can be continued downward in the same manner as poststack data. Even though the poststack data set has only three-dimensions, the methodology of the two approaches is so similar that we can certainly think of them as being the same.

The disadvantage of the common azimuth approach is that real world data is never acquired in common azimuth form. Moreover, the approximations used to produce the algorithm usually result in a methodology that cannot image steeply dipping events well.

Perhaps the saving grace of this algorithm lies in its speed. For full volume migrations, it has the potential to be the fastest algorithm ever invented for prestack imaging.

Again, as was the case for poststack data, common azimuth approaches image the data one depth slice at a time. Figure 6-19 is just an illustration to emphasize that almost all one-way methods image the data one depth or time slice at at time.

Figure 6-19. Common azimuth depth slice from a migration of the SEG/EAGE C3-NA data set

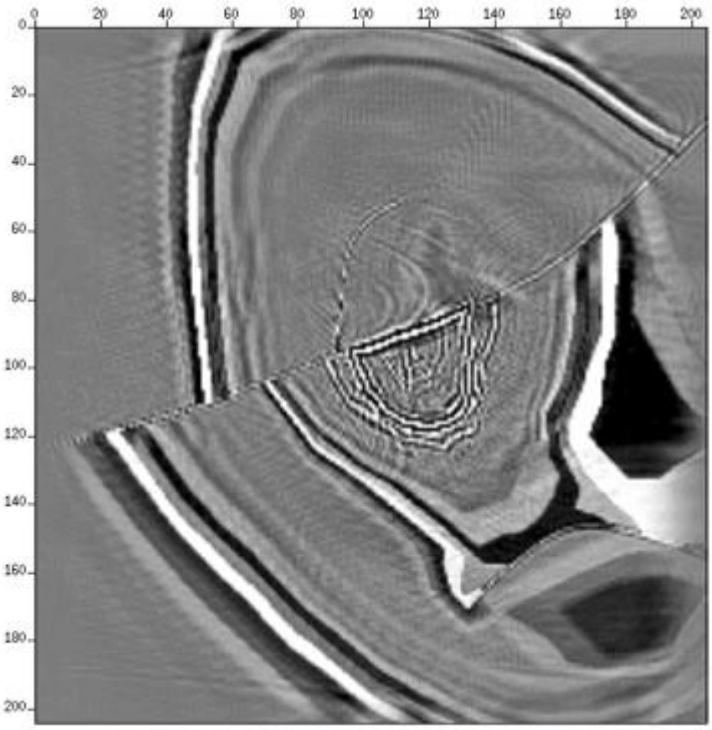

The nice thing about common azimuth migration is that it reduces the complexity of the input data set by one dimension. Normal 2D data is actually three-dimensional—it is indexed by one space variable for the shot location, one for the receiver, and one for time. In contrast, 3D data is characterized by being five dimensional, where each shot location has at least two surface coordinates, each receiver also has two surface coordinates, and, of course, there is one time dimension. Since shot, $m + h/2$, and receiver locations, $m - h/2$, are a simple function of the midpoint coordinate vector, m, common azimuth data has four dimensions, with two midpoint coordinates, one offset, and time. As a result, downward continuation of data of this type is much simpler that downward continuation of more typical five-dimensional 3D data sets.

However, common azimuth processes are not without problems. For example, the approximations necessary to make the methodology efficient are known to break down at 45 degrees. Furthermore, dip limits can be severe if the implementation does not properly account for different velocities at source and receiver coordinates. Nevertheless, for a large percentage of the subsurface, common azimuth migration is a useful, efficient tool for velocity model construction on a densely-spaced grid.

Aliasing is as much of an issue for common azimuth migration as it is for almost any other type of wave-equation based method. Whether data is recorded at good or bad spatial increments, aliasing must be considered and handled. For example, if it is based on the formulas above, the acquisition *dx*, *dy* and desired *dz* do not support a maximum frequency consistent with the recording parameters, the output spacing can be adjusted so that these frequencies will be imaged without aliasing. Normally, this consideration is not an issue with Kirchhoff-based technologies, since implementations of this type usually handle aliasing correctly without much user consideration. Because it is a recursive process, one-way downward continuation must be performed so that the output spacing precludes any aliasing at every depth step. This is particularly true at the initial downward propagation, but must be maintained until the recorded frequency has dropped below the point where the surface acquisition increments are satisfactory.

In addition to requiring proper spatial increments, common azimuth approaches require input data that is properly sampled in offset. The input offset increment must be chosen to ensure that offset dependent arrivals are not aliased.

Common Offset Kirchhoff Ray-Based Methods

Kirchhoff migrations have long been a staple of imaging technology. As a result, there are many excellent implementations of this methodology. Almost all are so-called single arrival approaches, whether in time or depth. Generally speaking, when the velocity gradients are reasonable, single arrival methods have excellent capabilities and can produce excellent images. On the other hand, when overburden velocity variations are strong, Kirchhoff methods can have significant problems imaging below these variations.

Straight Ray Kirchhoff Prestack Time Migration

The process described in Figure 6-20 provides the basic schema for all single arrival prestack Kirchhoff time and depth migrations.

Figure 6-20. Straight ray prestack Kirchhoff time migration.

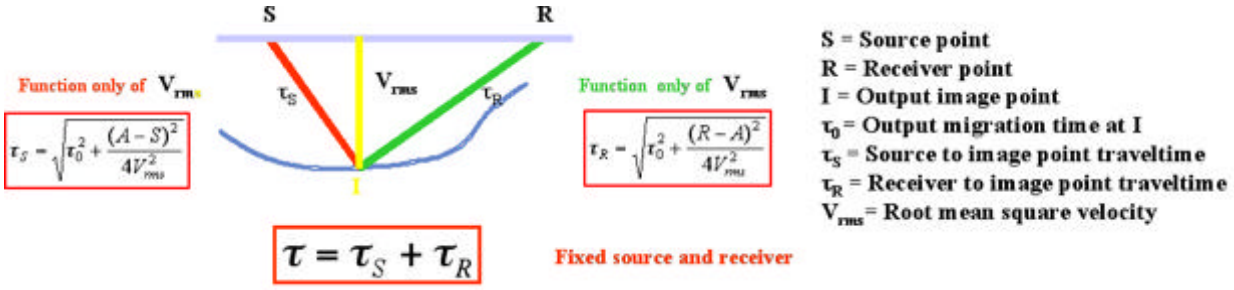

The process gives a simple velocity dependent recipe for computing a source to image-point traveltime and an image-point to receiver traveltime for use in the migration. In this prestack case, a closed form local RMS velocity formula produces the required times. The sum of these two traveltimes is then used to select an amplitude from the trace with this source and receiver. We then calculate a correction amplitude for this image point, multiply it times the amplitude selected from the trace, and add the result to the output image location. To avoid aliasing, it is normal to filter the trace using the usual aliasing equation in Equation 6-18.

(6-18)
$$f_{max} = \frac{v_{min}}{4\,dx\cos\theta}$$

Equation 6-18 is used to compute a dip dependent upper frequency to restrict the frequency content of the trace prior to adding the extracted amplitude into the corresponding output image point. The simplest version of this type of anti-aliasing pre-computes several traces with decreasing frequency bands and then selects the desired amplitude from the one most likely to avoid aliasing issues.

Curved Ray Kirchhoff Prestack Time Migration

The curved ray Kirchhoff prestack time migration algorithm shown in Figure 6-21 is based solely on the curved ray formulas in Figure 4-19. Those formulas are used to compute source to image point and image point to receiver traveltimes. Typically, the required $v(z)$ velocity is selected at the image point, but it is clearly possible to select one at the source and a different one at the receiver.

Figure 6-21. Curved-ray-prestack-time-Kirchhoff migration.

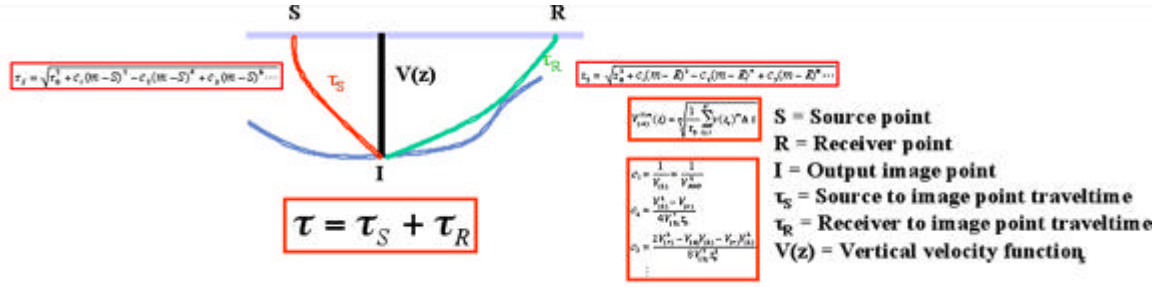

Single Arrival Kirchhoff Depth Migration

As indicated in Figure 6-22, the only difference between various Kirchhoff prestack time migrations and Kirchhoff depth migrations lies in how the required traveltimes are computed.

Figure 6-22. Single-arrival-Kirchhoff-depth migraiton

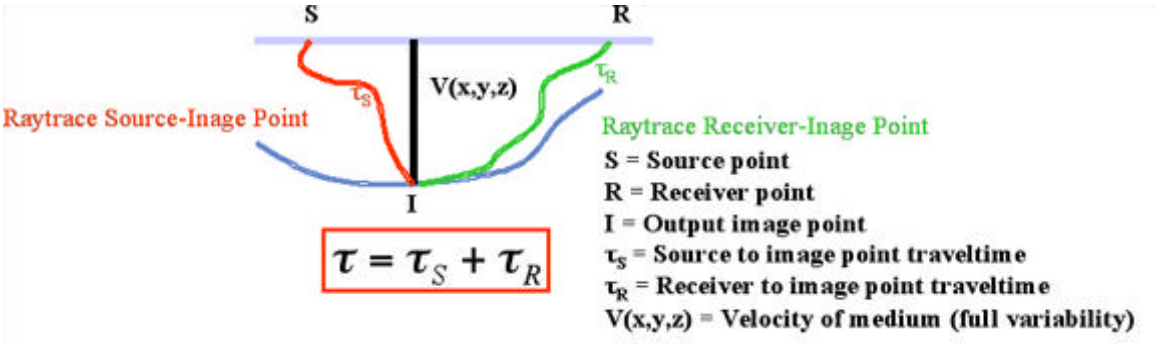

Raytracing is by far the dominant method for calculating these traveltimes. In this figure, rays are traced from the source and the receiver to the output image point. The traveltime sum, along with appropriate amplitude corrections, is then used to sum the trace amplitude into the output image point. On the surface, this process requires that rays be traced from each source and receiver to each output image point. Computing a traveltime volume for each and every source and receiver location can be very expensive, so as shown in Figure 6-23, most modern Kirchhoff implementations precompute traveltimes on a regular grid.

Figure 6-23. Raytracing issues for all 3D raytrace based imaging methods

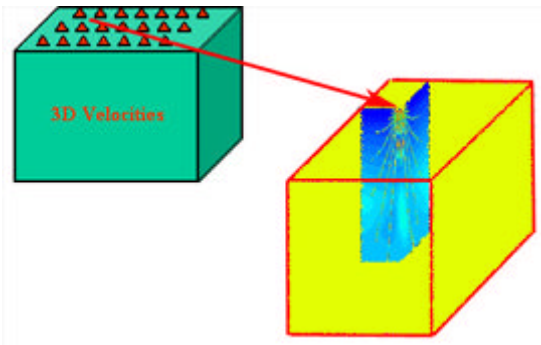

It is possible that more than one ray will arrive at any given image point during the calculation. Since keeping track of every such arrival is an extremely complex bookkeeping problem, it usually easier to choose a single arrival, but the selection of the arrival best serving the migration process is not always easy. Typical arrivals of this type are maximum energy, minimum distance, or minimum velocity.

Minimum velocity arrivals avoid headwaves caused by proximity to salt or other high velocity structures. Thus, in areas with strong lateral velocity variations, such as salt regimes, the minimum velocity methodology is considered to be optimum. In such cases, the minimum velocity ray is defined to be that ray for which the sum of all velocities along the ray has the smallest value. Interpolation is used to compute the desired traveltime at each source, receiver, and image point, thus reducing the overall computation costs and generally improving the speed of the migration step.

Clearly, the accuracy of the migration is controlled by how well the implementation handles both the traveltime computations and the interpolation of the traveltime volumes.

Multiple Arrival Kirchhoff Migration

Energy from a seismic source can reach any given subsurface point in more than one way. Figure 6-24 characterizes this concept graphically in terms of rays. Each ray is uniquely determined by either its take-off angle or by its arrival (incidence) angle, and there is no restriction on how many rays from a fixed source location can reach any given subsurface point. To properly implement an algorithm of this type we must, at least in theory, calculate an amplitude and a phase-shift for each arrival to correct the selected amplitude from the current input trace.

Figure 6-24. Multiple-arrival-prestack-Kirchhoff-depth migration

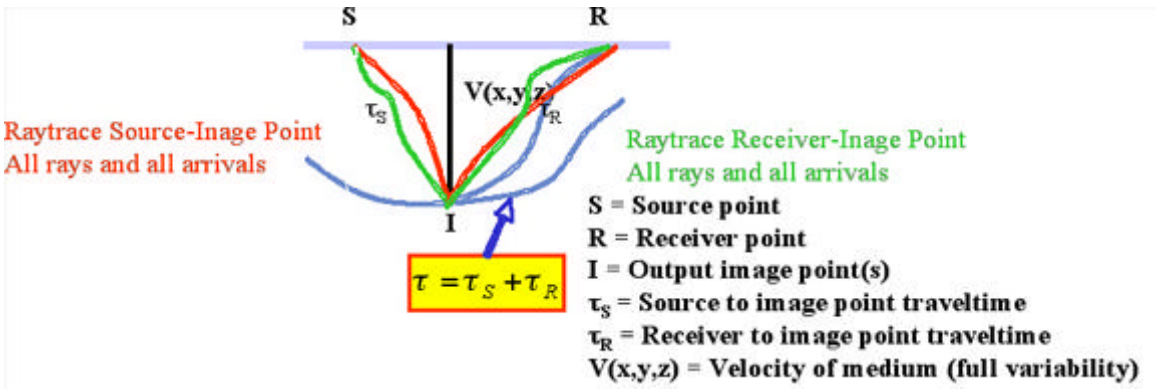

Multi-arrival Kirchhoff migration is very difficult to implement since it presents a rather complex bookkeeping problem that apparently has no efficient solution. This is unfortunate because multi-arrival Kirchhoff migration has the greatest potential for providing an algorithm with a near optimum percentage of the features of full two-way imaging. Based on empirical observations from the myriad implementations of its single-arrival brother, it would have super dip response, excellent amplitude handling, as well as the ability to include turning rays and diffractions.

Kirchhoff Elastic Depth Migration

The separation between acoustic and elastic Kirchhoff migration algorithms is solely determined by traveltime calculations. The migration step is not dependent on how the traveltime volumes are computed. If the traveltime volumes are based on acoustic equations, the result is an acoustic migration. If they are based on anisotropic calculations, the result is an anisotropic migration. If the source traveltimes are based on compressional velocities and the receiver traveltimes are based on shear velocities, the resulting algorithm is a converted wave migration.

Single Arrival Kirchhoff Depth Migration Summary

As the current work-horse of seismic depth migration and migration velocity analysis, single arrival Kirchhoff migration has proven to have excellent dip response, good amplitude response, and has shown some ability to image turning ray energy. Its great flexibility as a velocity analysis tool suggests that it will be around for some time to come. Its single biggest drawback is that it is very sensitive to strong lateral velocity variations, particularly below salt structures. This is very likely due to the use of a single arrival.

Raytrace-based migrations rely heavily on the quality and accuracy of their traveltime generators. As a high-frequency approximation to forward wave-field propagation, raytracing can be very sensitive to even relatively minor velocity variations. Reducing this sensitivity usually means that the input velocity field must be smoothed before calculating traveltime tables. In some cases, this is not an issue, but when the velocity variation is strong, significant depth errors may result. The raytrace module must compute both the traveltime to a given image point and any and all amplitude correction factors. If the raytracer is inaccurate, so is the output image, and no raytracer can recover from an incorrect velocity field. Likewise, no velocity field can be recovered from an incorrect raytracer.

When using Kirchhoff style methods, it is extremely important to understand how, when and where traveltime volumes are computed. If the migration algorithm is based only on downward, single arrival raytracing, then each volume must be sampled sufficiently well in all directions to ensure proper accuracy. In some Kirchhoff implementations, traveltime generators are based on finite difference solutions to the basic Eikonal equation that governs ray propagation. Because Eikonal-based methods are generally only able to calculate first arrivals, they are prone to producing spurious results in complex geological models.

Raytrace methods facilitate the calculation of multiple arrivals, and the selection of the most appropriate arrival better serves the migration process. Raytracing is the preferred traveltime generation method.

The utilization of a single arrival in Kirchhoff depth migration technology is one of the chief reasons these methods have difficulty imaging below complex structures. When we use all of the possible arrivals, as shown in Figure 6-24, we can achieve a superior result to what is achieved with the single arrival approach. While multiple arrivals complicate the migration algorithm and generally make it more computationally costly, the benefit of including more arrivals usually outweighs the increased cost. However, because it is so difficult to solve the general bookkeeping problem involved in making a multi-arrival Kirchhoff practical, this approach is seldom used.

Beam and Plane Wave Migrations

Beam and plane wave migrations can be divided into the following cases:

- pure plane wave
- beam stack
- delayed shot
- Gaussian beam

Pure Plane Wave Migration

The migration algorithms in the previous section are all based on downward continuation concepts. Conceptually, each such approach either uses the reversed wavefield as a source term and models the response in reverse, or it uses the reversed wavefield to downward continue the recorded data and produce an image at each depth slice.

The next two algorithms are based on concepts that use surface emergence angles to develop algorithms that produce similar images although they use widely different techniques.

We can also do the decomposition on common-offset sections shown in Figure 6-25. This is similar to slant stacking a stack. In this case, the section is a synthetic at 1000 meters offset, but for all intents and purposes, it looks just like a stacked section. Note that the short black dip element carries the sum of the information necessary to figure out its final position (the red dip element). A two-point raytracer can figure this out quite easily.

Figure 6-25. Fixed offset hand migration

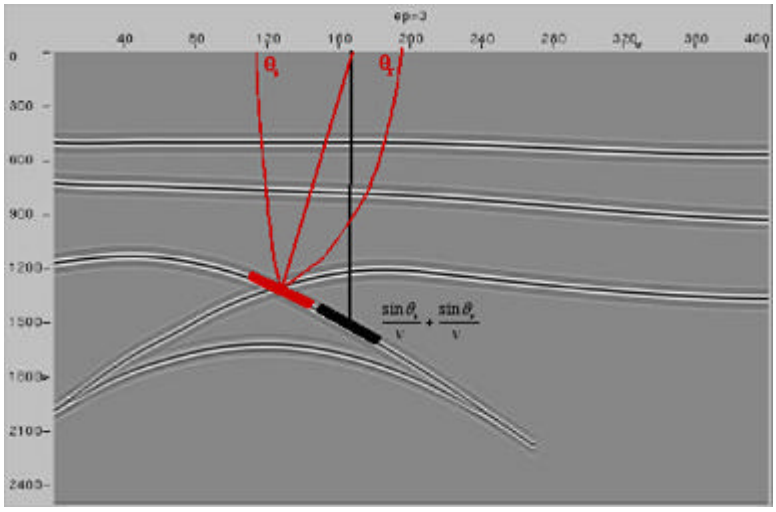

Figure 6-26 illustrates the process for one of the fastest migrations possible. Given the local dip information from the previous figure, a two-point raytracer gives us the position of the dip element. All we need is a bit of the local wavelet to place at the center of the image zone rectangle.

Figure 6-26. Ultra fast beam migration

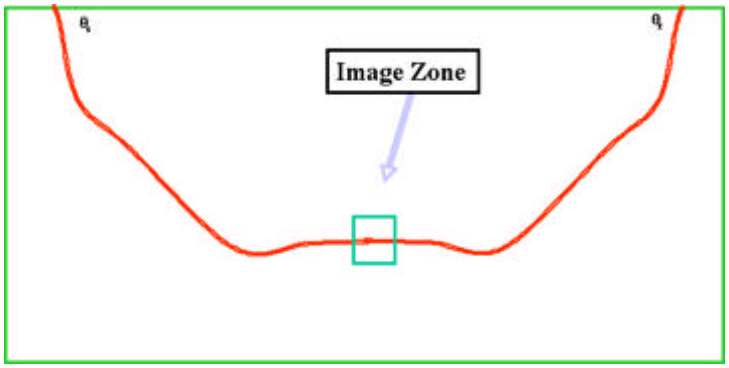

Beam Stack Migration

We get a bit more than just the emergence angles when we find the local dip element shown in Figure 6-27. In this case, the local dip is the sum of the source traveltime gradient and the receiver gradients. Since we know these two values when we calculate the traveltimes, we can construct another beam style migration element through a diffraction stack.

Figure 6-27. Using local dip estimates

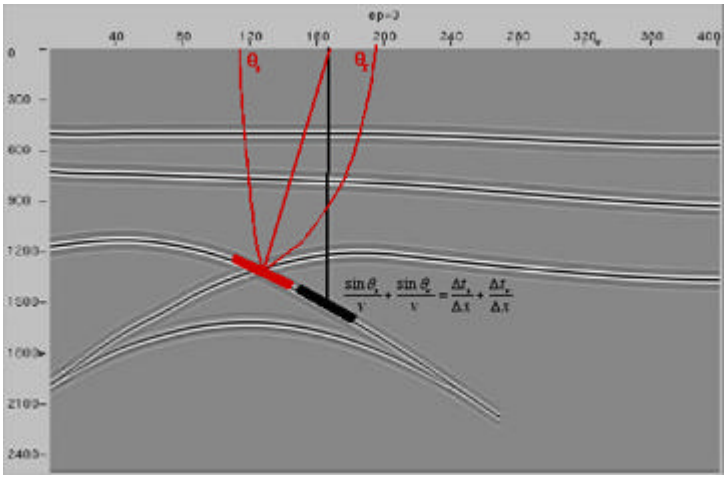

Converting a Kirchhoff method to a beam or slant stack approach requires that we expand traveltime around a central source (or receiver) location in a Taylor series. In two-dimensions, the proper formula is given by Equation 6-19.

(6-19) $$\tau_0 + p_{x_s} \bullet (x = x_s)$$

Here, p_{x_s} actually turns out to be the derivative (gradient in 3D) of the traveltime with respect to source position; that is,

(6-20) $$p_{x_s} = \frac{\Delta \tau_s}{\Delta x_s}$$

Since p_{x_s} can be calculated during the raytracing part of the Kirchhoff method, there is little added computational cost. On the other hand, since the entire slant stack bundle replaces many traces in the migration process, Kirchhoff-beam-stack methods can be significantly more efficient than their traditional straight-forward implementations.

Figure 6-28. Generalized Traveltimes and Beam-Stack Kirchhoff Migration

(a). Computing traveltimes from centered traveltimes

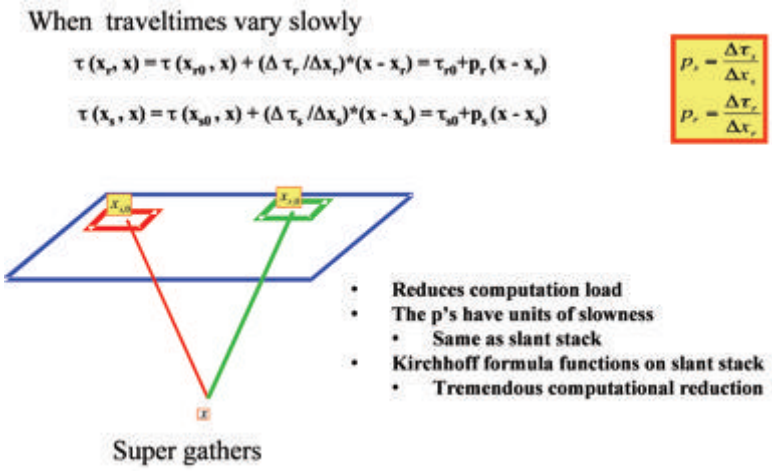

(b). Schematic of a traveltime bundle

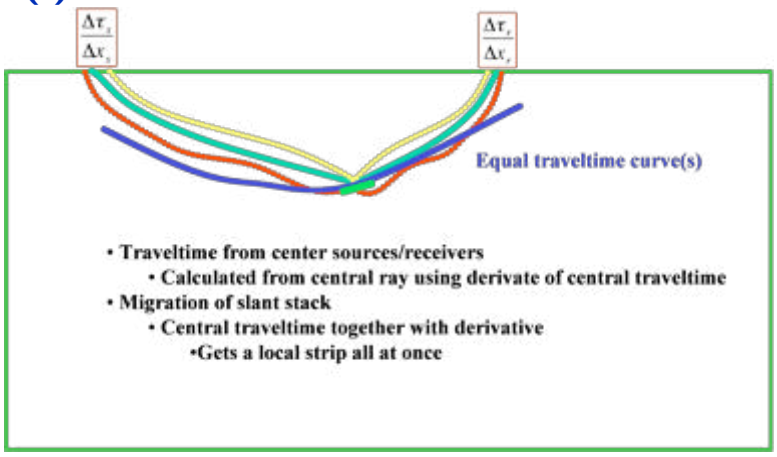

Delayed Shot Migration

Figure 6-29 illustrates the basic concepts underlying plane-wave or common-emergence angle calculations for source and receiver gather plane wave decomposition. The first step is to decompose the data into plane wave sections. In the case of a synthetic source, we simply decompose the source along the normal to the p value. For receiver gathers, holding p fixed produces a p gather or p-section. Such sections are obtained through a simple slant stack of the data around some central point. To propagate a source, we simply do the propagation along the common angle. To back propagate a receiver decomposition, we simply back-propagate each p. Depending on which algorithm we choose, each common p-section can be migrated individually. After migration, we only need to sum the results to produce a final migrated result.

Figure 6-29. Delayed shot and receiver migration

(a). Delaying shots or receivers to synthesize a plane wave source

(b). Shot and receiver delay migration principles

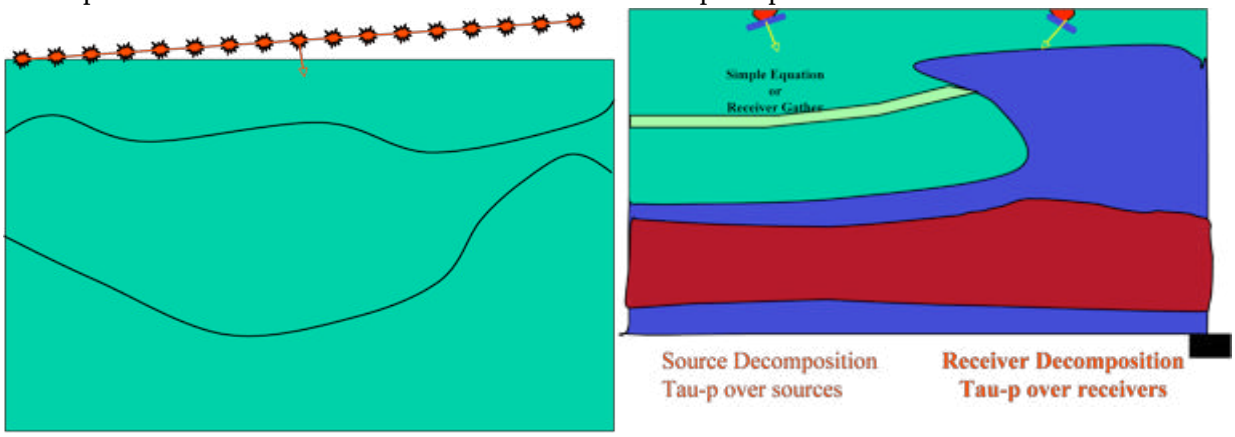

Figure 6-30 illustrates that each p-value in the slant stack produces a common emergence section that can be migrated in much the same manner as a common-offset stack, or even, conceptually, a zero-offset stack.

Figure 6-30. A common p section

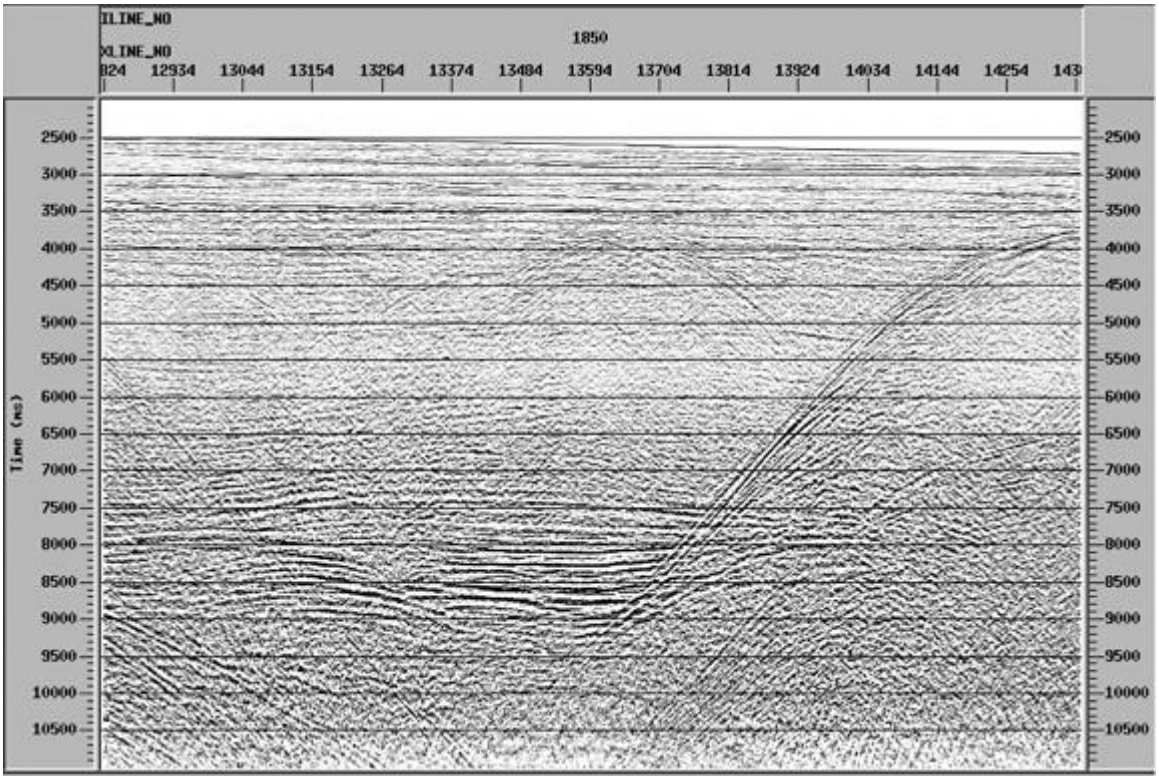

The utilization of slant-stacked data has many advantages and many draw-backs. An important drawback is the need to use a large number of p-values to adequately cover the entire impulse or operator response. Typically, theory requires us to use hundreds of such values, but most implementations are efficient only if the process uses a few values.

Gaussian Beam Migration

Figure 6-31(a) shows how a forward propagated shot can be constructed through the use of what are called Gaussian beams. Computation of each such beam requires that we first shoot a central ray. The velocity function, $v(s)$, selected along the ray path is then used to propagate source energy forward along this ray. We can use almost any kind of propagator for this process, but usually something like a phase shift is the algorithm of choice. During the back-propagation, energy is allowed to expand from the central ray, and is controlled predominantly by a Gaussian bell-style weight, with the local size depending on the propagation distance and local sound speeds. Because each central ray is defined by its take-off angle, and each such angle is in turn a plane wave direction, we can say that Gaussian beam modeling is really a plane wave modeler.

Figure 6-31. Shot modeling and prestack migration via Gaussian beams

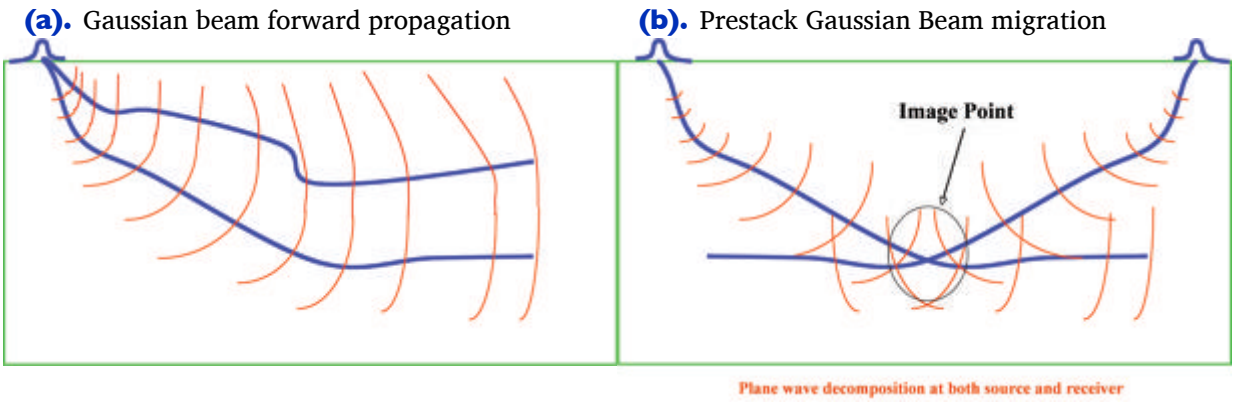

Figure 6-31(b) shows how to use the concepts discussed in part (a) to construct a Gaussian beam approach to prestack migration. Note that Gaussian weighting is applied to each p-value in the slant stack of a bundle of local traces.

Gaussian beam migration has many positives, including that it does not suffer from the single arrival problems associated with traditional Kirchhoff migrations, and it can be implemented in a manner that correctly handles amplitudes and even multiple arrivals. Consequently, Gaussian beam methodologies tend to produce images that are extremely close to full-wave equation methods. In fact, they are much closer to two-way methods than one-way approximations to the wave equation.

Algorithmic Differences

Figure 6-32 shows the basic differences between different migration algorithm classes.

Figure 6-32. Prestack migration differences

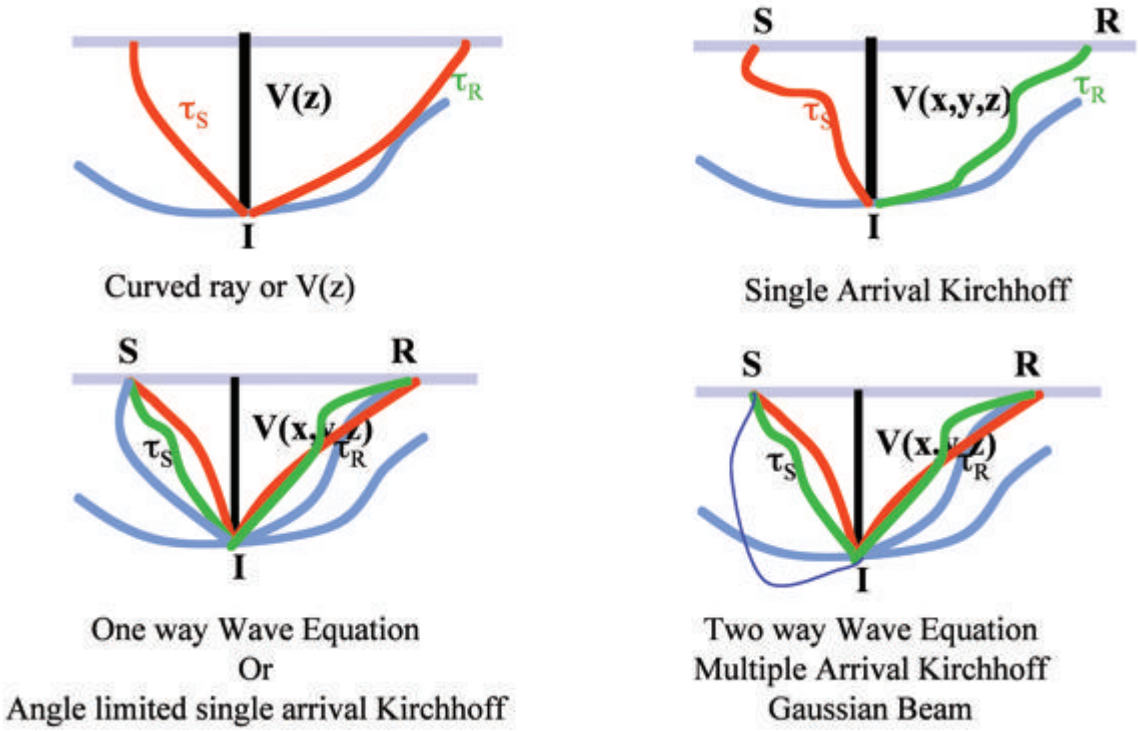

The top left part of the figure is a schematic of a typical curved-ray time migration. Note that this approach uses a single arrival and also uses a single $v(z)$ velocity for each output image point. This means is that the curved ray time migration is really a $v(z)$ depth migration that uses a completely different model for each and every output point.

The top right part of Figure 6-32 conceptualizes a single arrival Kirchhoff depth migration. Here, the single arrival is chosen by shooting rays in a fully three-dimensional Earth model. In this case, the migration is a truly three-dimensional process. In complex media, the forced choice of a single arrival increases this method's sensitivity to rapid and strong velocity variation. It is not surprising that single arrival Kirchhoff depth migration has considerable difficulty imaging below salt structures. Nevertheless, the flexibility of this approach means that it will remain the workhorse of migration velocity analysis for Earth model estimation.

The bottom left part of the figure shows a characteristic multiple arrival migration methodology. Among the techniques that achieve this goal are one-way FKX wave-equation algorithms and multi-arrival Kirchhoff methods that do not allow turning rays. Because turning rays have been eliminated, the methods envisioned in this figure cannot image beyond 90 degrees.

The bottom right part of Figure 6-32 illustrates a full, or at least nearly full, two-way methodology. In this setting, waves described by all incidence and reflections angles are imaged. The methods that have this kind of capability include full multiple-arrival Kirchhoff algorithms, Gaussian beam methods, and, of course, full finite difference reverse time migration.

To further understand migration differences, Figure 6-33 shows impulse responses from two different algorithms at three different trace locations in the velocity model. The vertical black lines mark the position of synthetic traces from the data set generated over the model. The top row of impulse responses are based on one-way FKX algorithms while the bottom row are based on a single arrival Kirchhoff method.

Figure 6-33. Comparison of impulse responses from a complex salt structure model

(a). Velocity Model **(b).** Impulse Responses

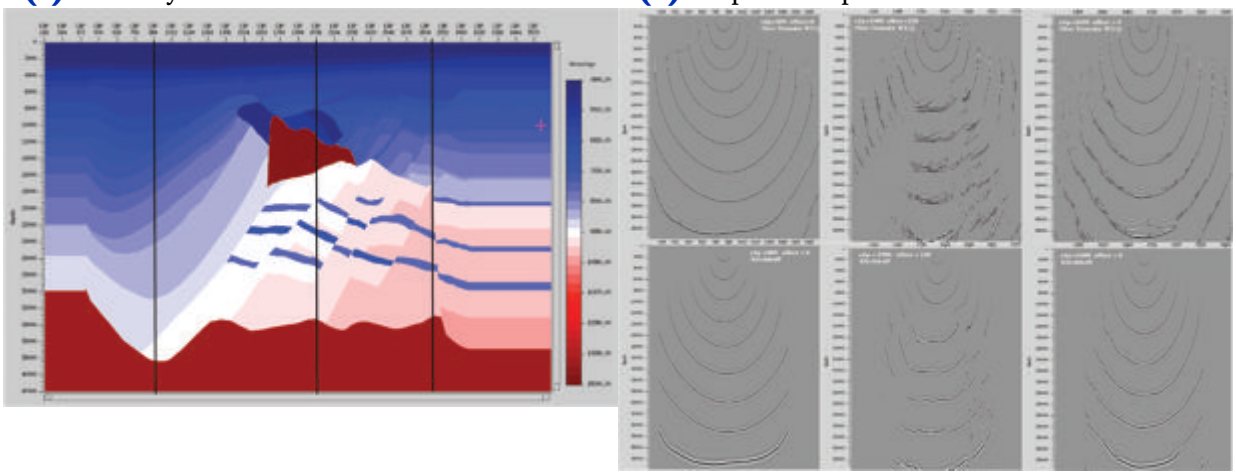

Because the left hand impulse response column represents a trace from that side of the model, the lack of strong lateral velocity variation results in almost identical wave-equation and Kirchhoff responses.

In contrast, the middle column represents a trace with a midpoint directly over the salt structure in the center of the model. Note that while the Kirchhoff amplitudes are comparable to those of the response in the top row, the tremendous number of multiple arrivals and phase changes are quite evident. It is possible to program the Kirchhoff response to almost exactly match the wave-equation response, but the effect is difficult to achieve.

Since the trace used to compute the right hand column is also out of the strong lateral velocity zone, its affect on arrivals is not as noticeable as the center column. Nevertheless, the need to compute a large number of multiple arrivals is still quite clear.

Figure 6-34 shows the extremely complicated impulse of both the two-way and one-way methods, and demonstrates the need to use highly accurate algorithms in complex

geological media. Many people would argue that the smooth structure of the Kirchhoff impulse response on the right is the correct approach. However, the best results are produced using the full two-way method on the left. In some cases, the most pleasing image to the eye is not the best approach to producing a full image.

Figure 6-34. A simple comparison of Kirchhoff, one-way and two-way impulse responses over the SEG/EAGE AA′ data set.

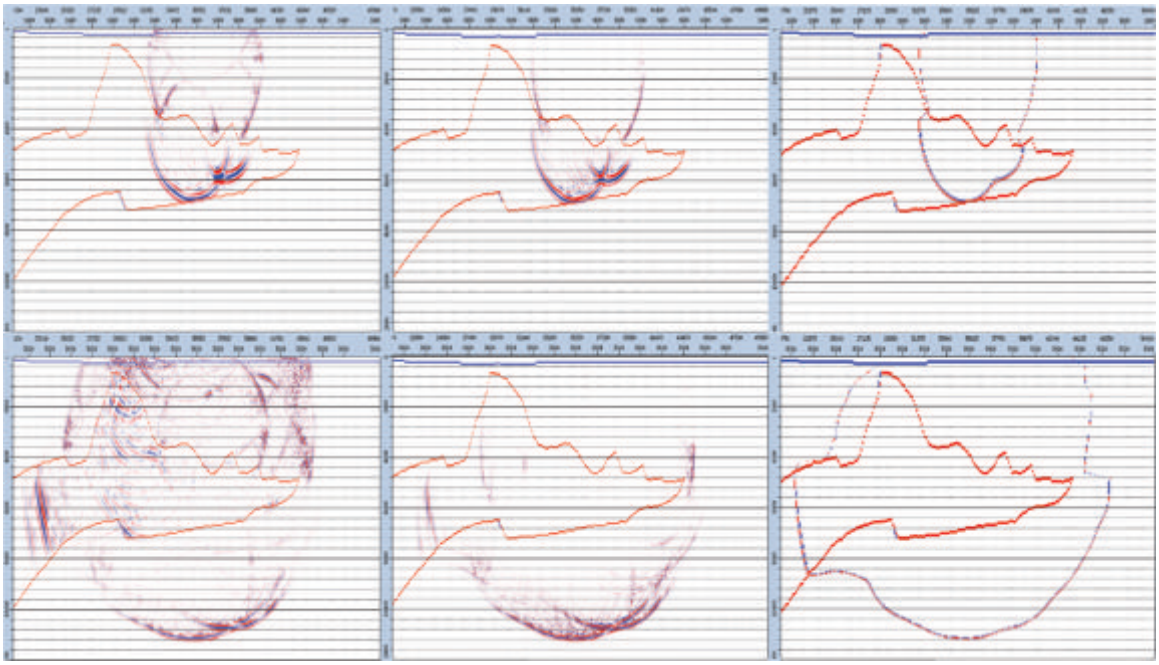

Chapter 7

Prestack Migration Examples

This chapter is devoted to assessing the quality and usability of a wide variety of prestack imaging algorithms. Visual side-by-side comparisons provide ample empirical evidence to conclude that the more accurate the algorithm, the wider the aperture, and the more careful the application, the better the result. Ultimately, we will argue that the full two-way method is by far the best at providing optimum imaging. When computational expense is not an issue, this should definitely be the method of choice.

The images in this chapter are self-explanatory and require little or no real attention to visual detail. Because they are so small, it is better to see them on the screen.

Common Azimuth on the SEG/EAGE C3-NA Synthetic

Figure 7-1, after Biondi *et al.*, represents a direct comparison between a Kirchhoff migration and a full one-way common azimuth migration.

Figure 7-1. Common azimuth versus a single arrival Kirchhoff migration of the SEG/EAGE C3-NA data volume.

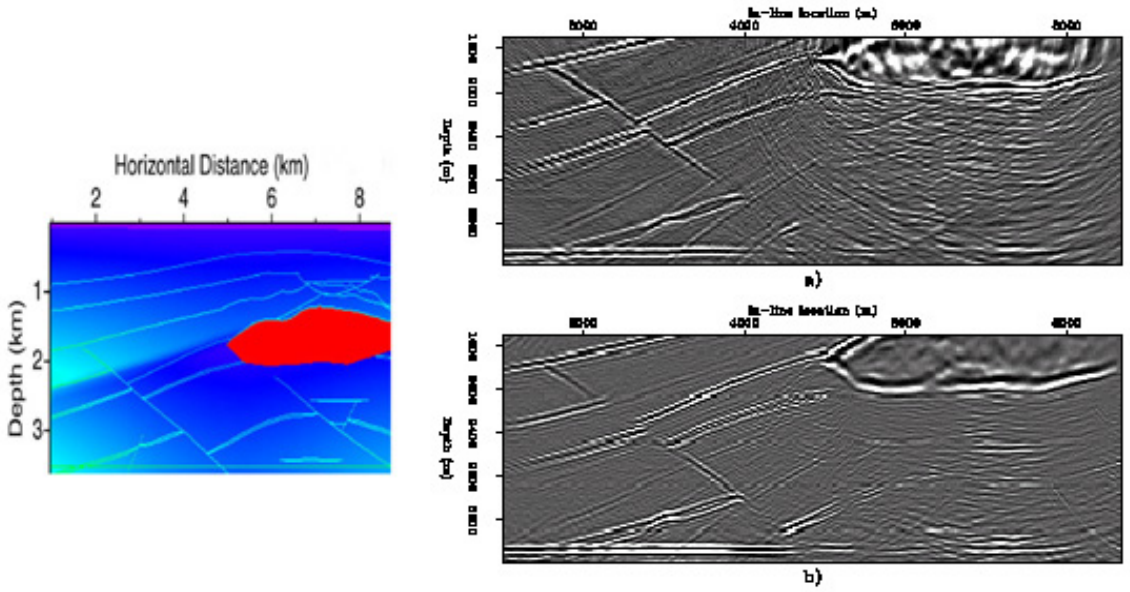

Kirchhoff versus One-Way on a Gulf of Mexico 2D Salt Synthetic

This short section looks at a major reason we should use highly accurate imaging techniques. It compares a one-way phase screen to a maximum amplitude Kirchhoff method. Improvements at both the salt-sediment interface and below the salt provide clear evidence of the superiority of the more accurate one-way technique.

A series of widely spaced shots were synthesized over the model shown in the upper right corners of both halves of Figure 7-2. Receivers for each shot were spread across the entire model surface. The one-way technique clearly does a better job overall and is much better at the salt-sediment interface and in the sub salt section of the model.

Figure 7-2. A comparison of Kirchhoff and one-way migrations Algorithms.

(a). Model and prestack Kirchhoff migration **(b).** Model and one-way phase screen

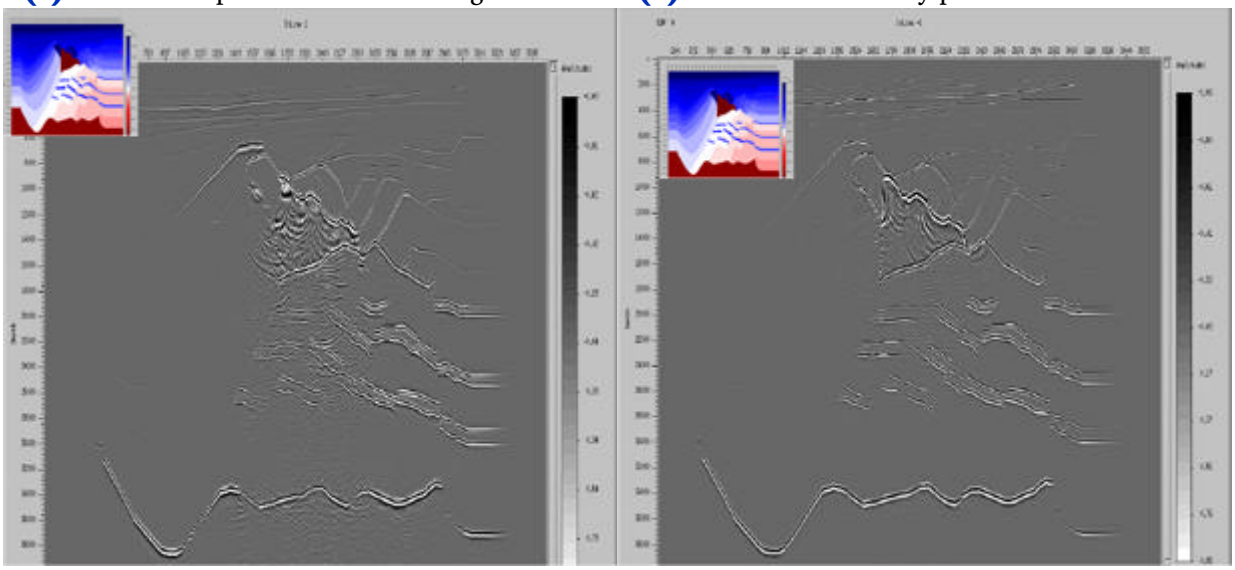

A North Sea Sill Synthetic

The model in Figure 7-3 was designed by Dr. Rob Hardy at Trinity University in Dublin, Ireland. The synthetic data were generated using Panorama Technologies advanced finite difference modeling technology. All images in this figure were based on the same input data. The Kirchhoff image was the result of an application of Seismic Unix's Kirchhoff migration from the Colorado School of Mines.

Figure 7-3. Volcanic Sills Model and Migrated images

(a). Volcanic Sills Model

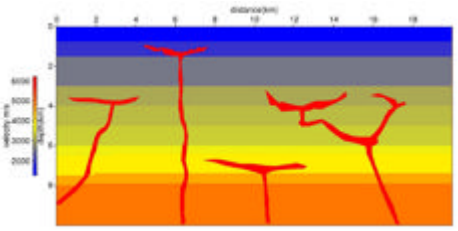

(b). SU Kirchhoff of the Sills Data

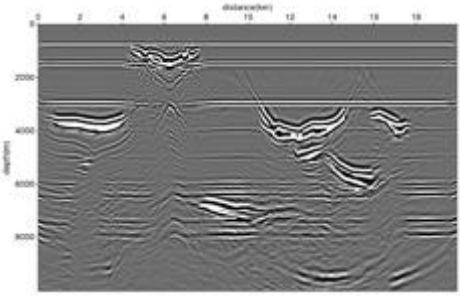

(c). One-way FKX image of the Sills Data

(d). Two-way XT image of the Sills Data

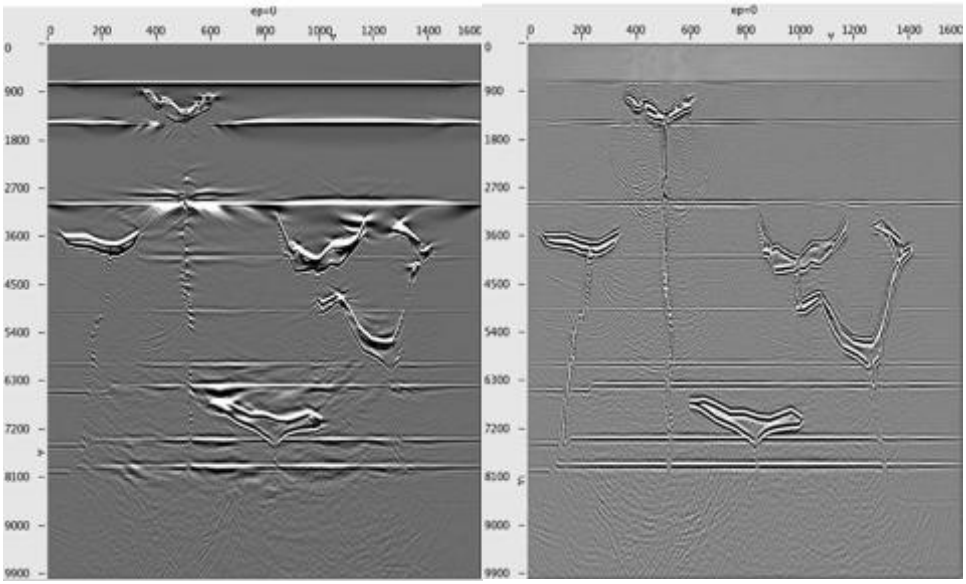

Marmousi Case Study

The Marmousi data set was generated under the direction of Roloff Versteeg (1990), while at the Institute de Francis du Petrol (IFP) in Paris, France. The velocity or Earth model is based on an actual prospect from offshore Western Africa. The Marmousi data have proven to be a gold mine for both development of imaging algorithms and for showing practitioners of the art that the world is not as simple as they originally thought. Here we see that problems with Kirchhoff techniques are not strictly limited to Gulf of Mexico style salt structures.

The various parts of Figure 7-4 are self-explanatory. The only conclusion we can reach is that multi-arrival methods are absolutely necessary to ensure optimum imaging. In the author's mind, the full two-way image in the lower right corner (Figure 7-4(f)) is superior to all the others, but at least three of the other methodologies would give satisfactory results for exploration purposes.

Figure 7-4. A comparison of prestack algorithms on the Marmousi data set.

(a). The Marmousi velocity model

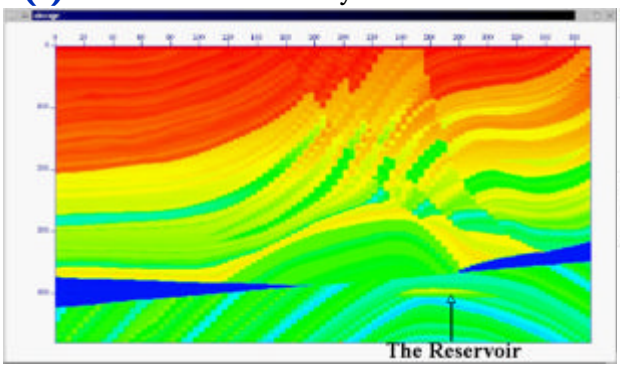

(b). Multi arrival Kirchhoff after Sam Gray Veritas

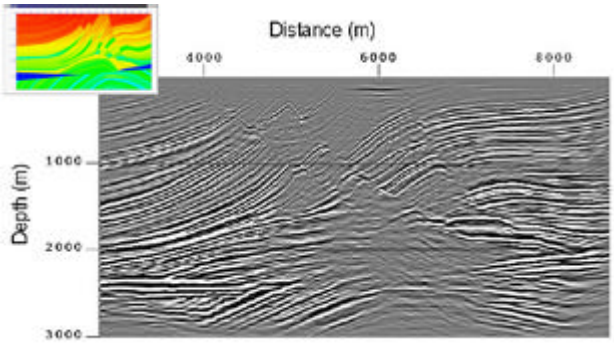

(c). Gaussian Beam after Hill 2001

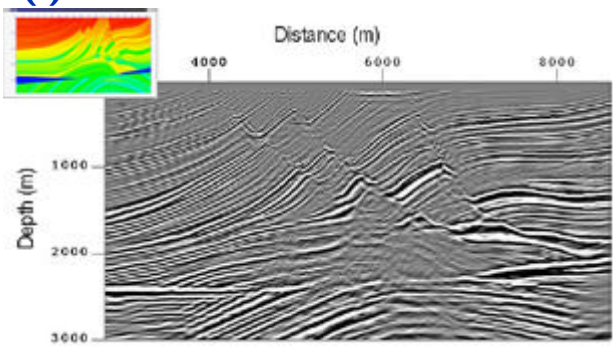

(d). Single arrival Kirchhoff migration

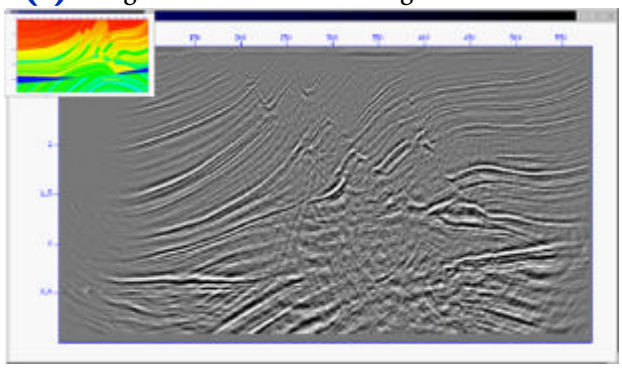

(e). One-way phase screen migration

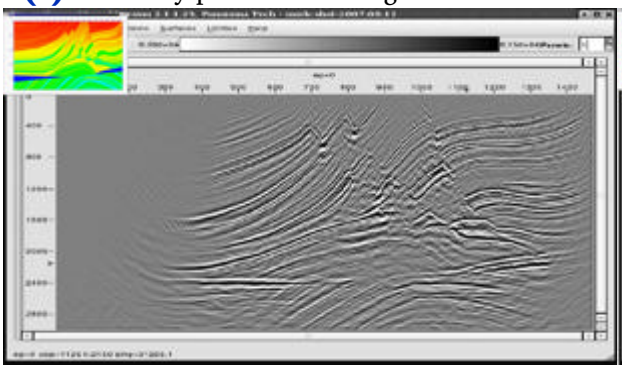

(f). Full two-way finite difference migration

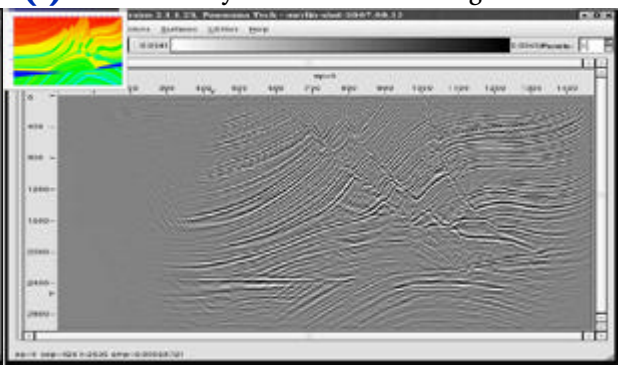

An Imaging Note and the BP 2.5 Dimensional Data

Before providing some comparisons of one- and two-way migrations on complex data sets, it is worth discussing imaging data sets that, because of severe illumination or surface issues, might have wide ranging differences in both source generated and receiver suppressed energy levels. This issue was brought to light by several researchers at AMOCO and later BP. J. T. Etgen, Carl Regone and colleagues generated the model, which, when migrated, produced such a wide range of output reflection strengths that just displaying it was difficult.

Figure 7-5 shows how this reflection strength disparage can be overcome by a careful compensation for illumination. The bottom part of this figure shows a straightforward migration of the original input data. The middle part represents the illumination in space and depth. Simply dividing by this quantity produces the image at the top of Figure 7-5. Note that this process is not equivalent to an automatic gain control. It is actually based on being able to correctly handle energy differences specified by the Earth model and correct the output image for lateral and vertical differences.

Figure 7-5. Using illumination corrections to properly gain imaged data.

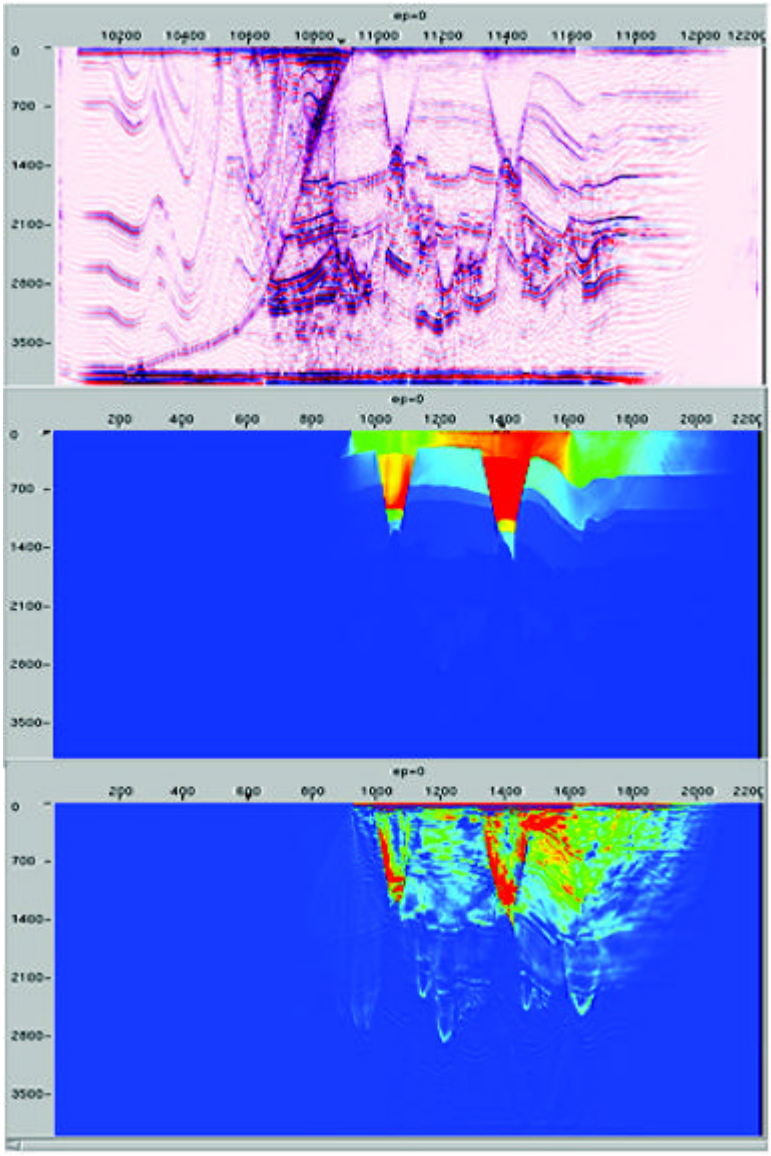

BP 2.5 D Data

Each graphic in Figure 7-6 represents application of either a one-way or a two-way method to the original BP 2.5D data set. Parts (a) and (b) show an image of the velocity model overlaid on a one-way image of the raw input data along with the one-way image without the overlay. Parts (c) and (d) show the need to properly account for differences in both illumination and energy spreading losses. Parts (e) and (f) show that use of a well implemented imaging condition can produce dramatic results.

Figure 7-6. Imaging with proper illumination correction.

(a). One-way BP 2.5D data with velocity overlay

(b). Two-way BP 2.5D data without illumination

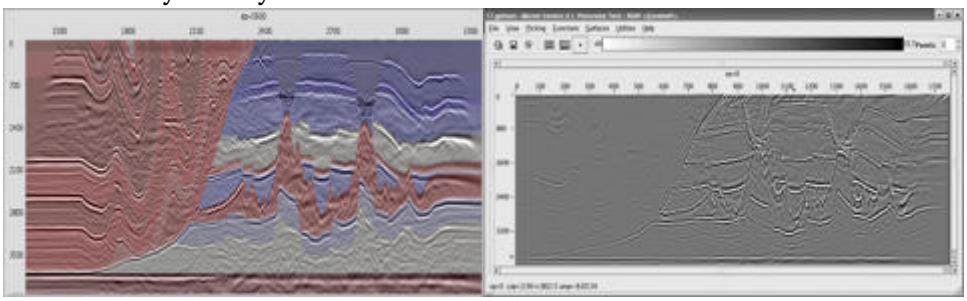

(c). Two-way BP 2.5D data with normal imaging

(d). One-way BP 2.5Dl data with overlay

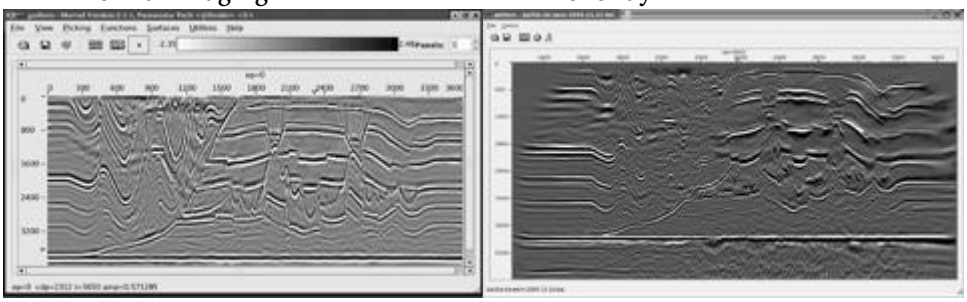

(e). Two-way BP 2.5D data with illumination

(f). Two-way BP 2.5D with optimum imaging

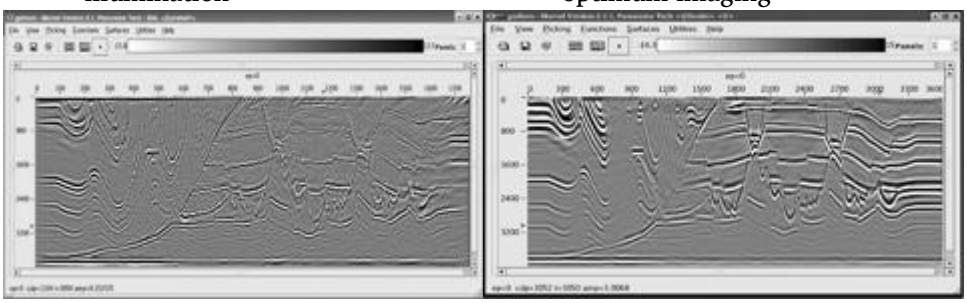

BP 2004 Salt Structure Data

Figure 7-7(a) is a graphic of the velocity model for the Earth model used to generate realistic data for evaluation of imaging techniques. This model is very complex, with lateral velocity ratios close to 2:1 at many depth levels. Part (b) of this figure compares two partial images. The image on the left in part (b) was obtained from a one-way method, while the image on the right is a two-way image using exactly the same parameters and input data. Clearly, the two-way method images much more of the subsurface than does the one-way method. This is very likely because the two-way method produces a much more accurate impulse response at all angles. Part (c) shows that the two-way method can provide an excellent response even without multiple suppression.

Figure 7-7. Migration of the complex BP2004 data.

(a). BP 2004 Model after F. Billette

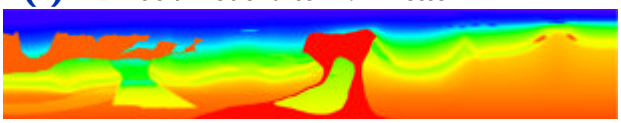

(b). One-way versus two-way on the same input data

(c). Full two-way migration on the BP 2004 data volume

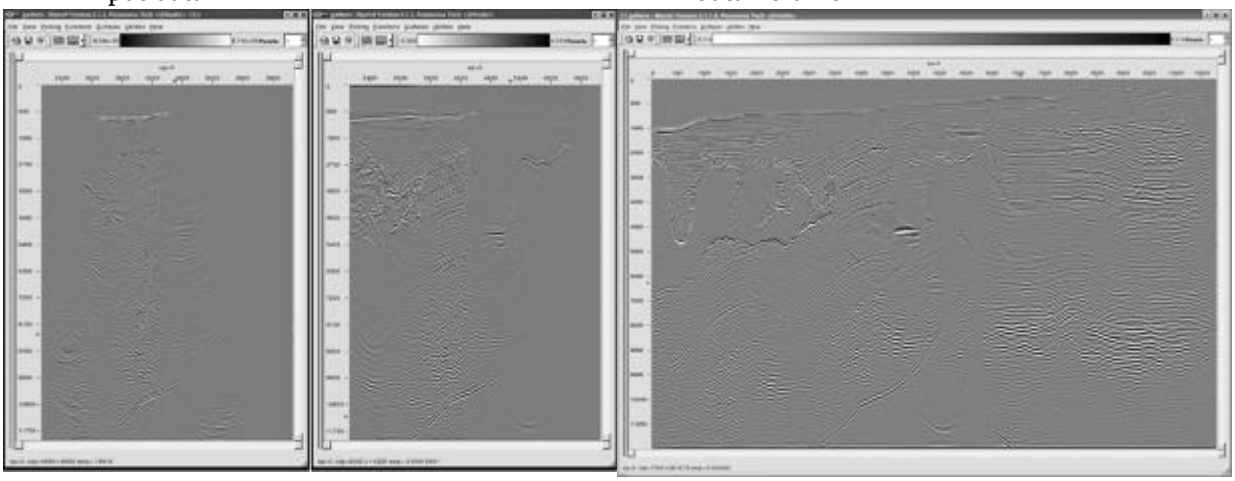

SEG AA′ Data Set

The SEG AA′ data set was originally a test 2D data set shot over a selected line from the full SEG/EAGE model. It has been said (personal communication from Sam Gray) that almost any algorithm can be made to image this data set reasonably well. Here, we simply compare a one-way split step method to a more accurate full two-way method.

Figure 7-8(a) is the original SEG AA′ velocity model. Figure 7-8(b) is an image of the prestack data originally shot over this model at AMOCO production before it became part of BP. Part (b) is a two-way image of this data, and is clearly better than the one-way result.

Figure 7-8. SEG AA′ model and associate one and two-way images.

(a). The SEG AA′ velocity model

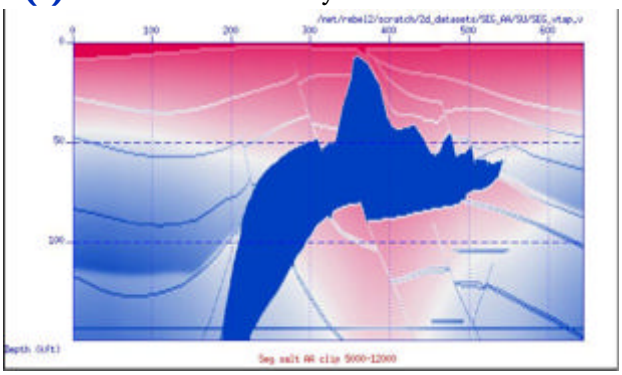

(b). One-way image of the AA′ data

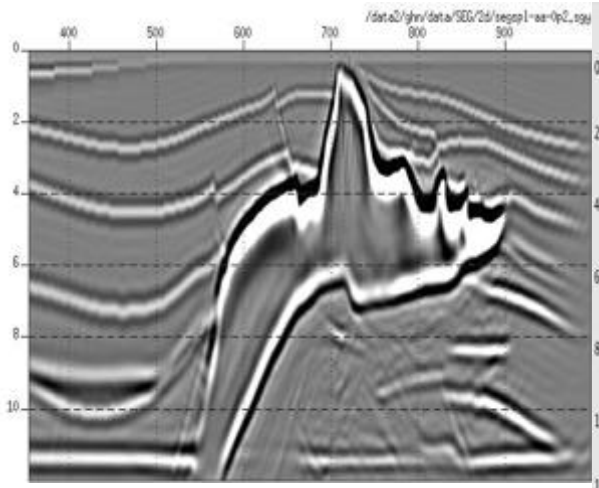

(c). Two-way image of the AA′ data

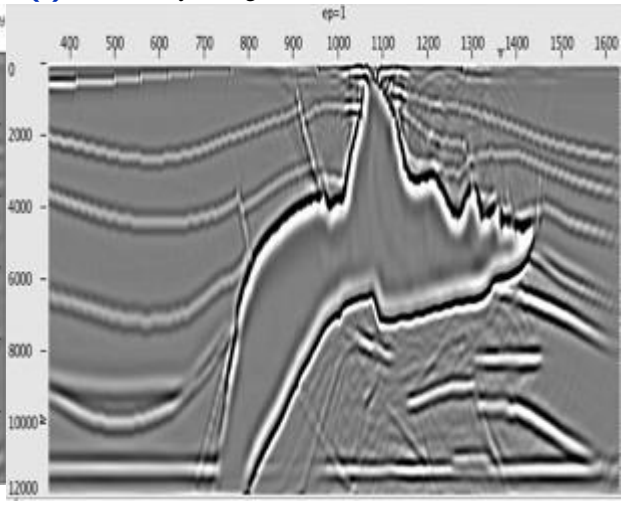

Migration from Topography

The traditional approach to handling data taken in areas of extreme (or even modest) topography is to statically correct the data to some datum, and then migrate as if the source and receivers were on the usually absolutely flat plane. It is quite easy to perform the migration directly from the topography. The major difficulty is not in making the algorithm handle the topography, but, instead, the difficulty arises in having accurate topographic data available and in being able to estimate an accurate near surface velocity field. What this section shows is that migrating from topography is not an issue.

Migration from topography requires the exact specification of the location and elevation of each and every source and receiver in the acquisition. Even though this information is routinely available, it is frequently not stored concomitant with the data, or it is lost after static corrections. Implementation of migration from topography requires only that wavefields be generated at the source or back-propagated from the receiver locations and elevations. Part (a) of Figure 7-9 shows a relatively simple model with relatively complex topography. Parts (b) and (c) show Kirchhoff and two-way images of these data. Visual comparison suggests that, again, the two-way approach is vastly superior to the Kirchhoff method.

Figure 7-9. Migration from topography.

(a). The BP (AMOCO) Canadian foothills topographic model

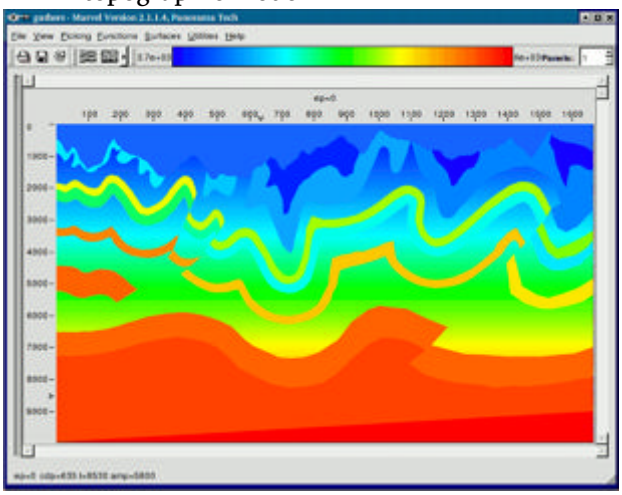

(b). Kirchhoff migration of the BP tomographic data

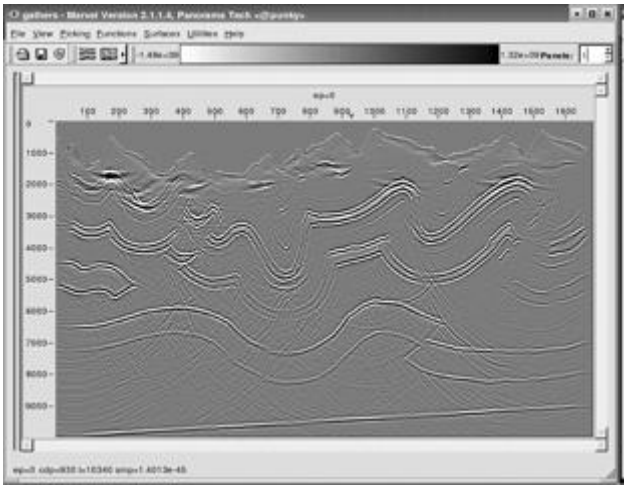

(c). Full wavefield migration of the BP tomographic data

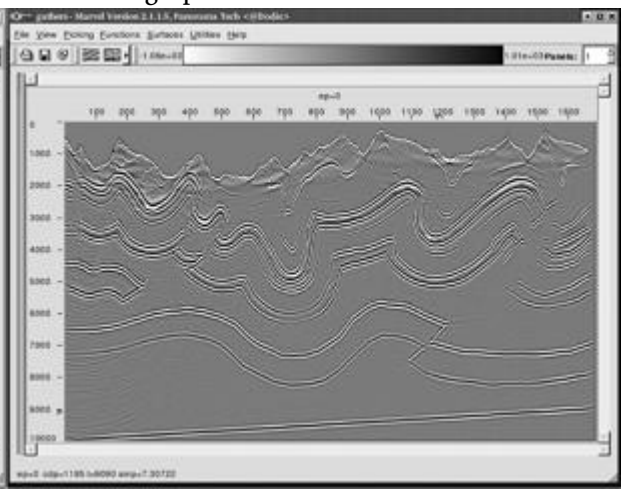

The SMAART JV Sigsbee Model

The SMAART JV (Subsalt Multiples Attenuation And Reduction Team Joint Venture) was an industry-sponsored joint venture focused on designing realistic Earth models and acquiring data over them to test the then current methodologies for imaging and multiple suppression. The first of the two images in Figure 7-10 shows the model used to synthesize the data as well as several images of the synthetic data. What is most interesting is the excellent amplitude response of the two-way algorithm.

Figure 7-10 shows the Sigsbee model in part (a), a Kirchhoff vertically varying gained image in part (b), a one-way image with no gain in part (c), and a full illumination corrected two-way image in part (d). The two-way image shows outstanding amplitude restoration and, in fact, when compared to the model in part (a), provides an excellent image proportional to reflectivity.

Figure 7-10. Sigsbee model and images from the SMAART Joint Venture project

(a). SMAART JV Sigsbee salt model

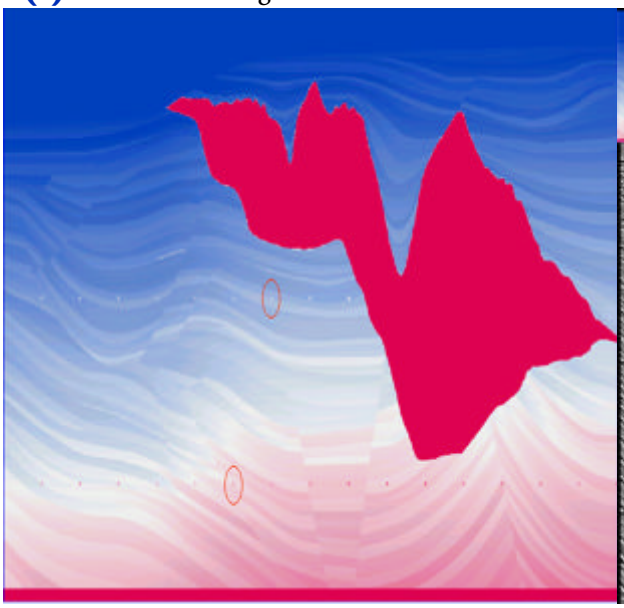

(b). Kirchhoff image (Sam Gray et. al)

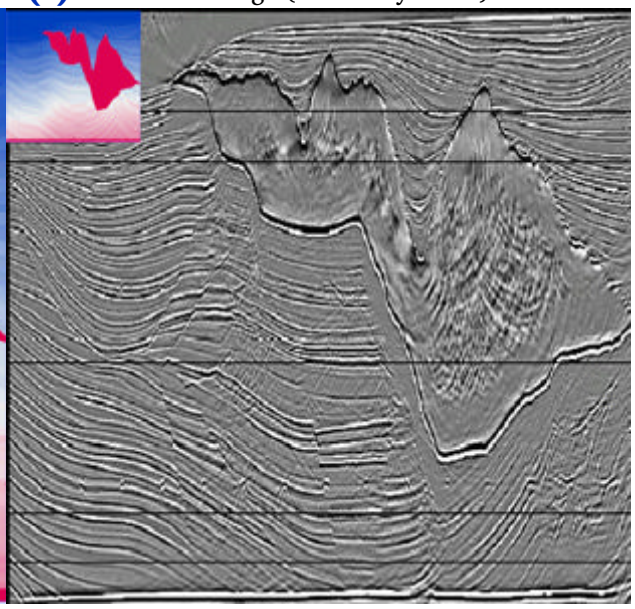

(c). One-way image

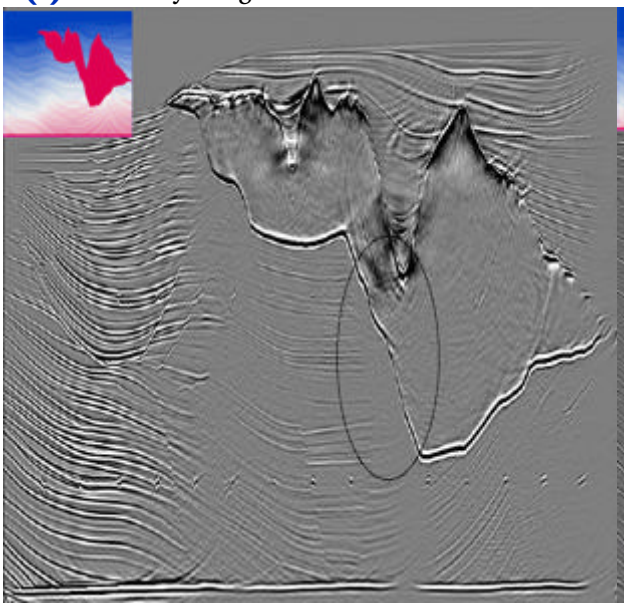

(d). Two-way image

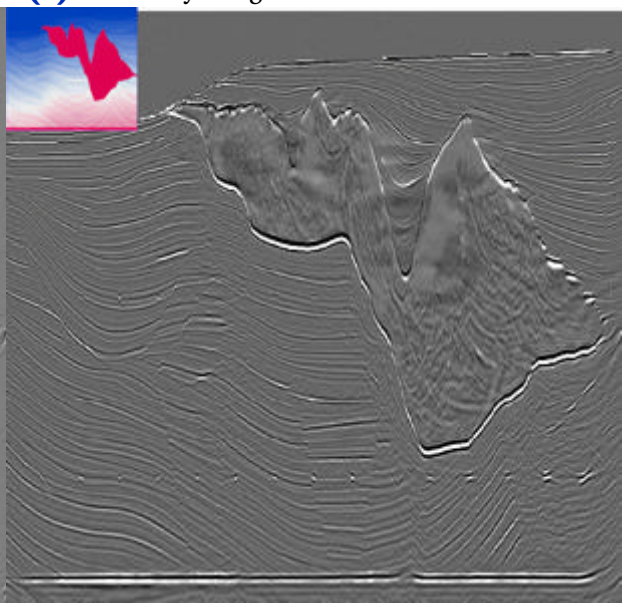

The zoomed images in Figure 7-11 that came from the original images in Figure 7-10 confirm the much higher quality imaging capabilities of two-way methodology.

Figure 7-11. Zoomed images from Figure 7-10

(a). Zoom comparison of one-way on the left and two-way on the right

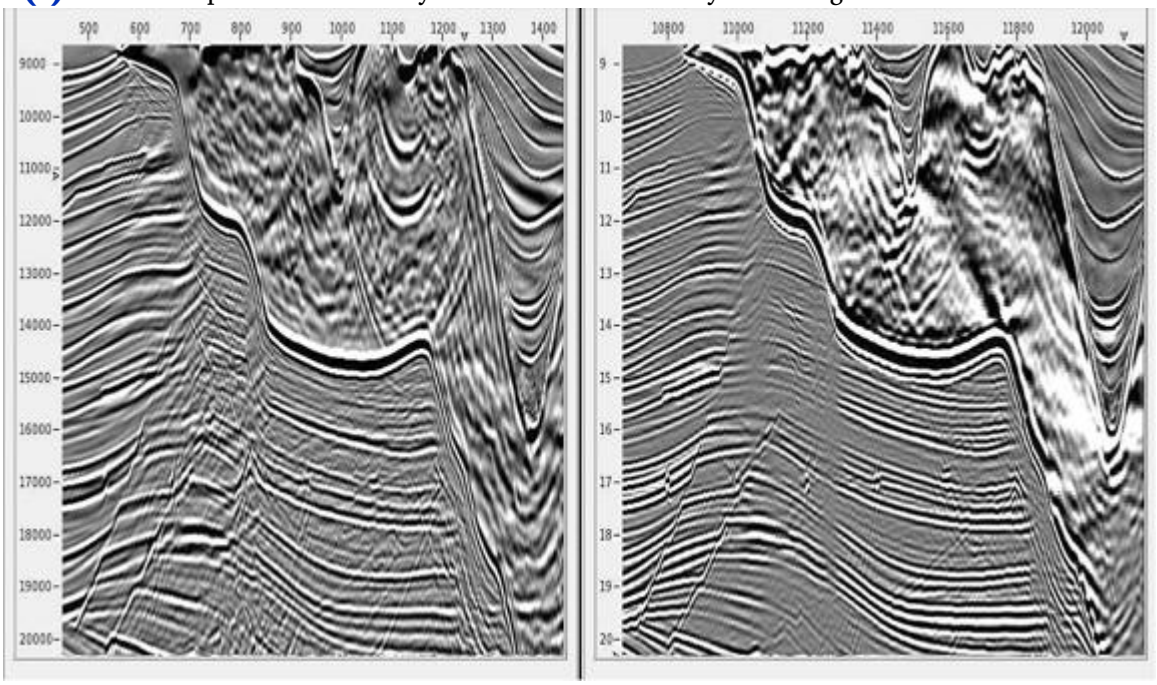

(b). Zoom comparison of one-way on the left and two-way on the right

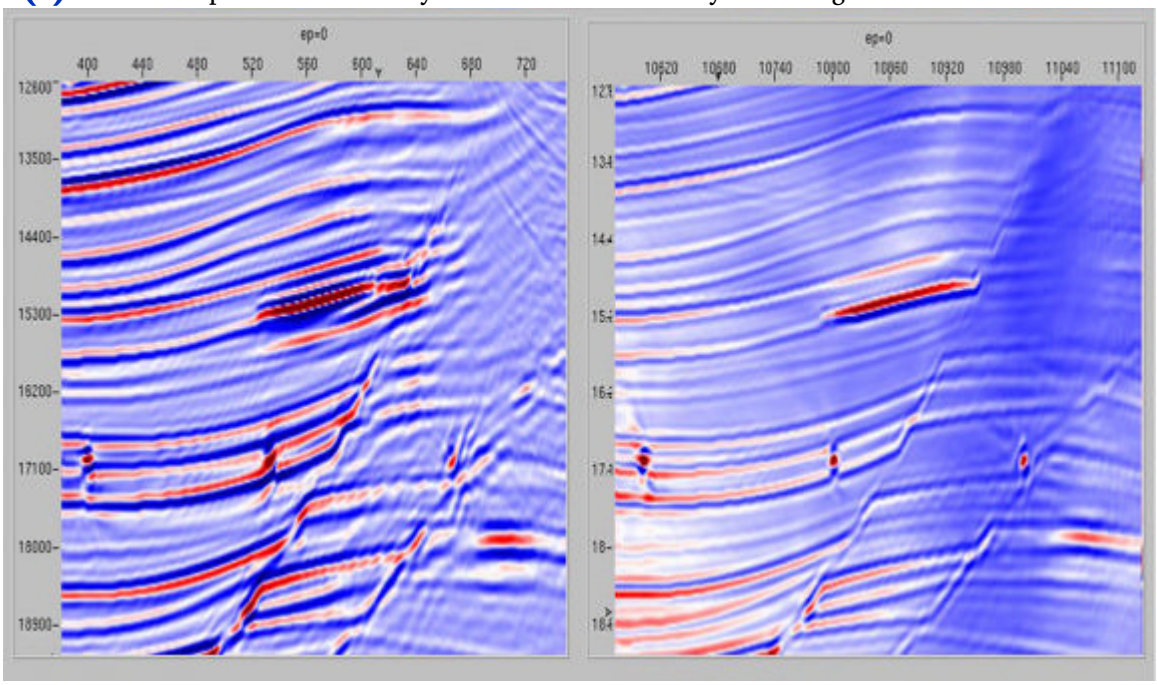

SMAART JV Pluto Data Set

In addition to designing and synthesizing data over a complex salt model, the SMAART JV data sets also produce data over a model designed specifically to test surface-related multiple elimination (SRME) algorithms. The Pluto data set is somewhat unusual because it contains a full set of zero-offset traces.

The images in Figure 7-12 visually quantify the impact of multiple energy on the higher technology migration algorithms. Part (a) provides a glimpse of the impact of multiples on a one-way phase screen migration of the Pluto data. Part (b) shows improved results when the multiples have been suppressed by SRME, but the two-way image in (c) is a better image still, even though it was produced with only 50% of the input data.

Figure 7-12. SMAART JV Pluto data set images.

(a). One-way migration with no SRME

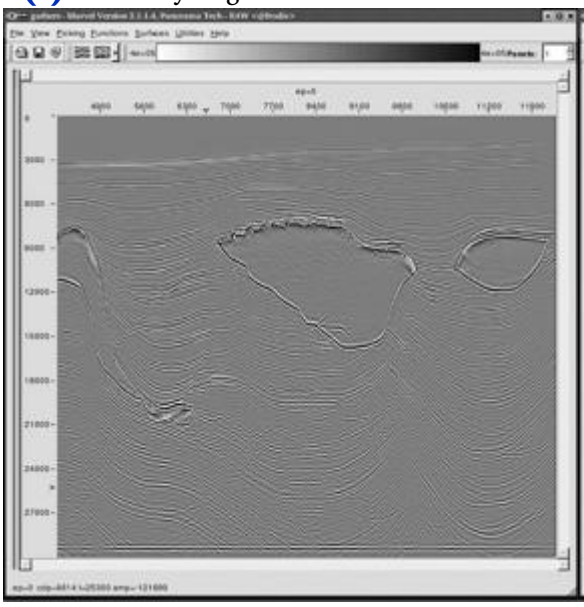

(b). One-way migration with SRME

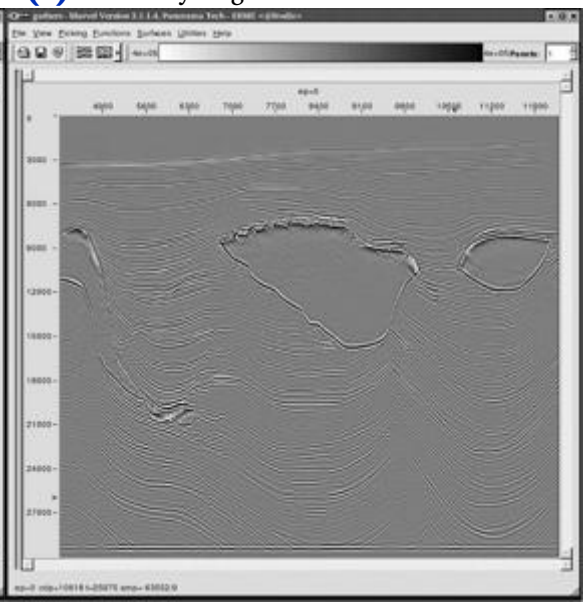

(c). Two-way image of 50% of the input data

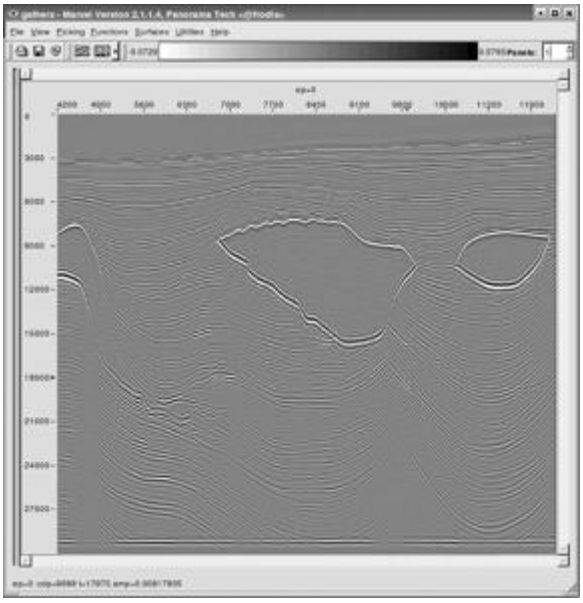

SEG/EAGE C3-NA Data Imaging

In this section, we consider the question of why imaging below salt for the C3-NA data set is so difficult

The two-way migration of the SEG/EAGE salt data represented in Figure 7-13(a) and (b) is quite good and compares favorably with the one-way migration in the left hand side of Figure 7-13(c). However, it is quite clear that, in spite of the excellent imaging, neither method provides a satisfactory image below salt.

Figure 7-13. SEG/EAGE C3-NA salt images

(a). A 3D two-way image

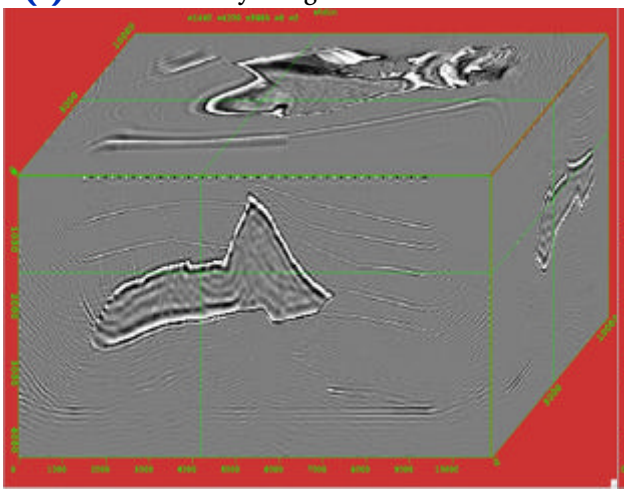

(b). A 3D two-way image

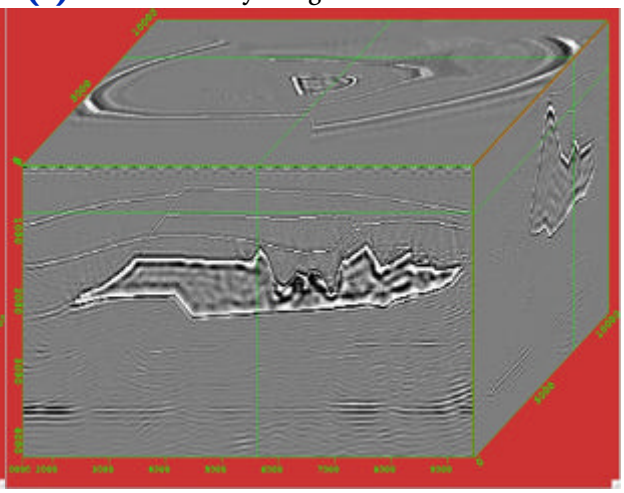

(c). A comparison one-way and two-way on Line 289

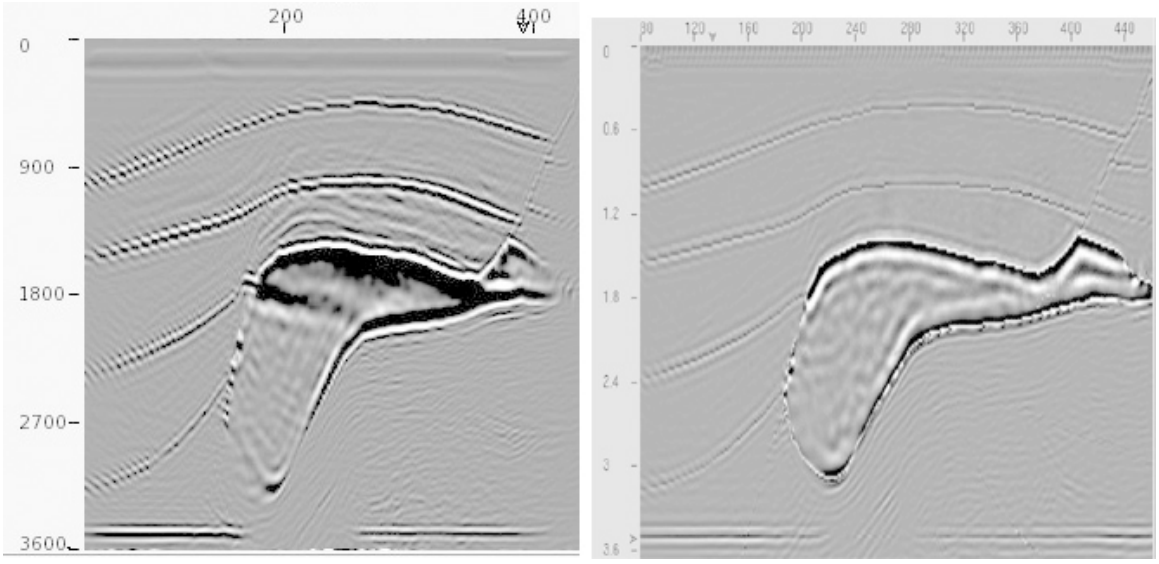

Figure 7-14 shows the result of proper data acquisition. The model in part (a) was used to synthesize densely spaced shots with apertures that covered the entire model. These data were then migrated to produce the image in parts (b) and (c). The graphic in part (b) of this figure is an excellent image of the sub salt reflectors. The same is true for the two-way image in part (c). The only possible conclusion is that proper acquisition is required for optimum imaging.

Figure 7-14. Imaging below salt

(a). A 2D line extraction from the 3D SEG/EAGE salt model

(b). One-way image of a 2D acquisition over the model in (a)

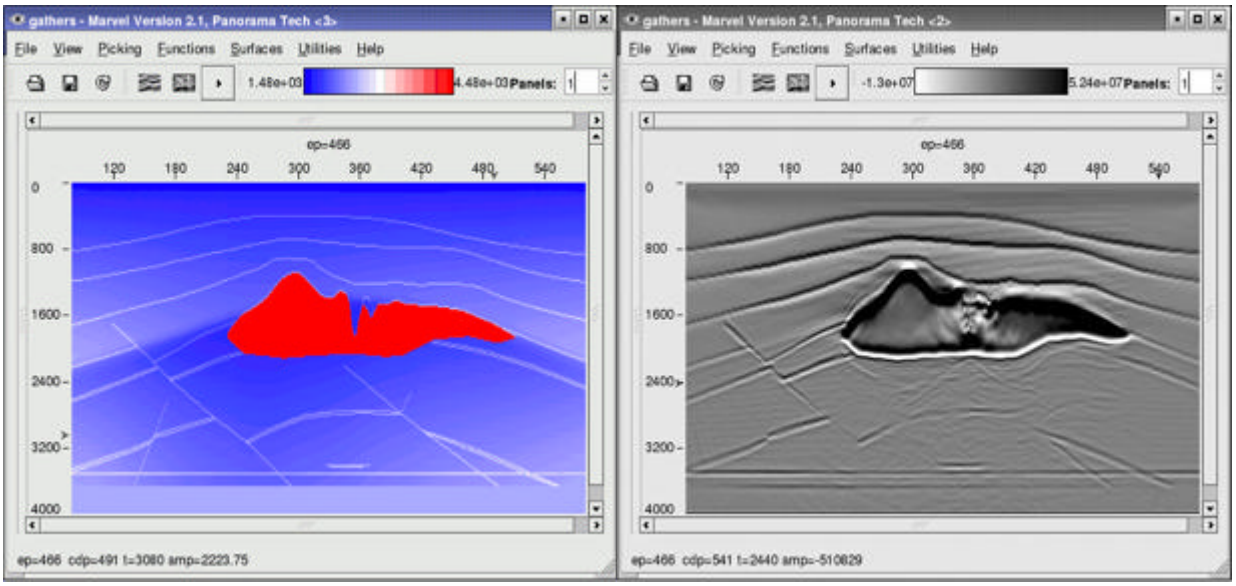

(c). Two-way image of a 2D acquisition over the model in (b)

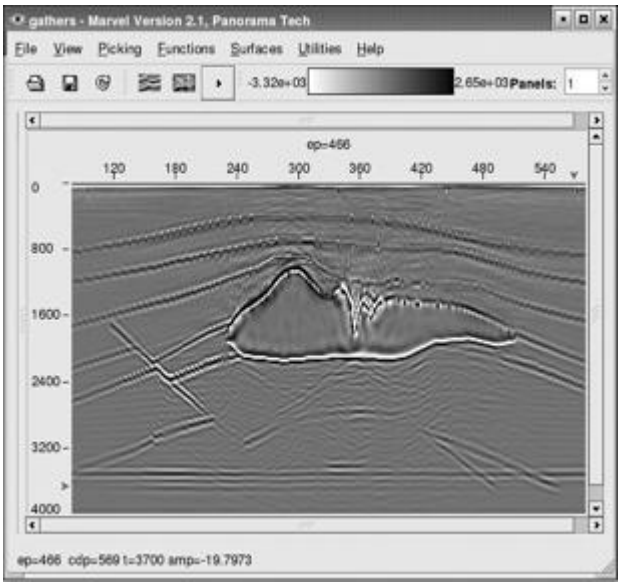

Anisotropic Earth Models

This section provides a simple example of how even simple anisotropic migrations can bring improved imaging to the migration arena. The Earth model in this section is based on an actual exploration problem that arose when drilling revealed a structure that was not apparent in the original imaging exercise. The vertical or well velocity of the highlighted turtle-like structure in the center of the model does not change. It is only the horizontal or NMO velocity that indicates its presence.

Figure 7-15 is an example of a simple 2D anisotropic Earth model. Shown are the vertical or well velocity (top left), the NMO velocity (top right), Thomsen's parameter δ (bottom left), and Thomsen's parameter η (bottom right).

Figure 7-15. An anisotropic Earth Model.

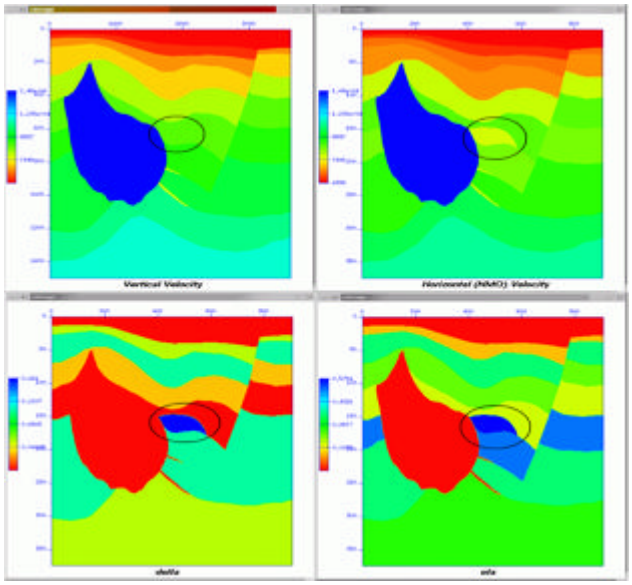

Although this figure contains four graphics, such models can be represented by only three parametric volumes. Given a vertical velocity, V_v, and Thomsen's parameters, δ and ε, we can express any of the others by suitable rearrangement of Equation 7-1 and Equation 7-2.

(7-1) $$V_{NMO} = V_v\sqrt{1+2\delta}$$

(7-2) $$\eta = \frac{\varepsilon - \delta}{\sqrt{1+2\delta}}$$

From a practical perspective, we usually estimate V_{NMO} using what has become traditional Kirchhoff based migration velocity analysis.

Since

(7-3) $$\delta = .5\frac{V_{NMO}}{V_v} - .5$$

it is clear that δ can be estimated through a simple combination of a well velocity and a velocity volume estimated through the usual migration velocity analysis process. Unfortunately, the same cannot be said for ε.

Figure 7-16 shows a set of images from several experiments to determine the extent to which anisotropic imaging might be of value.

Figure 7-16. Isotropic versus Anisotropic Imaging

(a). Isotropic with vertical velocity (left) and NMO (right)

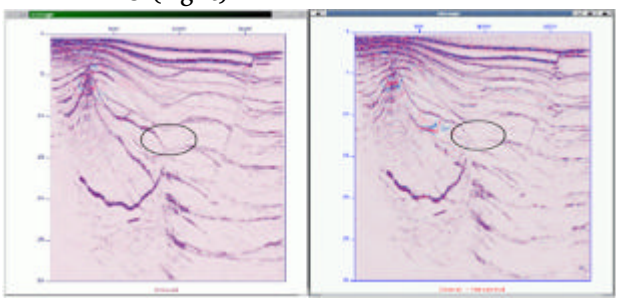

(b). Zoom of (a)

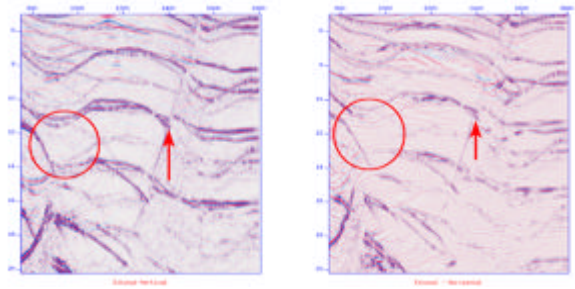

(c). Shot versus Eikonal

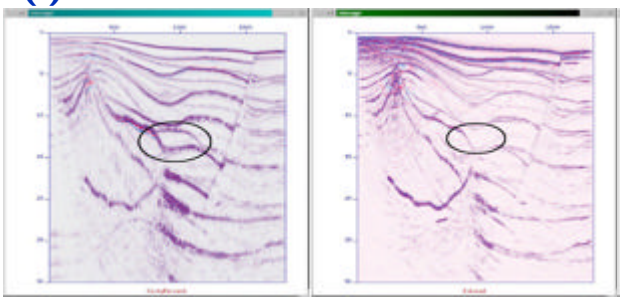

(d). Shot (left) versus Anisotropic Kirchhoff (right)

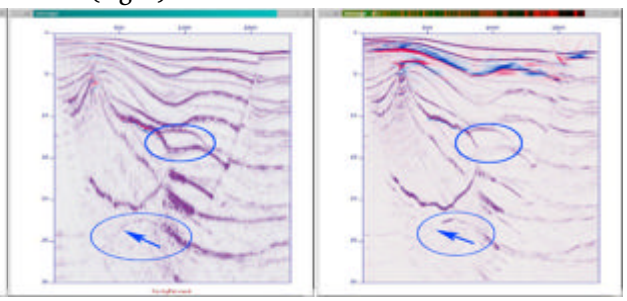

(e). Zoom of (d)

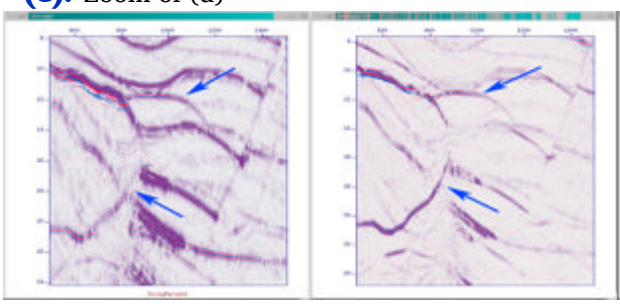

(f). Anisotropic (left) versus Isotropic (right) CDPs

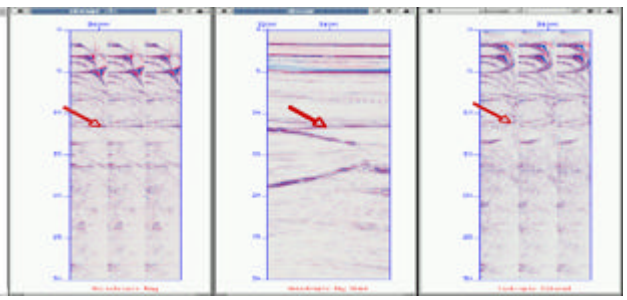

For this purpose, the model in Figure 7-15 was used to generate a series of shots. Figures 7-16(a) through (g) are various comparisons using different combinations of the underlying Earth model derived from that in Figure 7-15. Figure 7-16(a) and (b) show the results of using either the well velocity or the NMO velocity alone. The turtle back structure in these figures is essentially invisible so there is no reason to suspect its existence. While use of the vertical velocity does produce reasonable depth conversion when the reflecting horizon is relatively flat, steeply dipping events are either not imaged or are misplaced. Use of the NMO velocity tends to get steeply dipping events in their proper place, but does a poor job of depth conversion.

As shown in Figures 7-16(c) and (d), the issue changes quite quickly when an isotropic shot using the vertical velocity, or a full Kirchhoff anisotropic shot migration is applied. Now, the turtle back structure is clearly visible in both images, and depth conversion is quite good. However, while the shot migration is excellent, several of the steeply dipping events are still misplaced.

Figure 7-16(e) compares isotropic shot and Kirchhoff migrations using the vertical velocity. There is no question that the shot migration is worth the effort, but neither of these migrations accurately image steeply dipping events.

Figure 7-16(f) shows why anisotropic imaging is worth the effort. The left hand side of (f) shows anisotropically imaged CDP's, while the right hand side shows isotropically imaged CDP's. The middle image is just a representation of the location of the CDP's at the top of the turtle-like structure. The greater flatness, along with improved amplitude response of the anisotropic CDP's, is clear evidence of the need to utilize anisotropic methods when available.

Chapter 8

Data Acquisition

This chapter describes the principal ways in which data acquisition affects the seismic data processing effort. This includes information about array effects, aperture, aliasing, and the physical arrangement of the acquisition methods themselves.

The most frequently asked question about seismic data acquisition may be about the optimum approach to acquire the data. Fundamentally, this is a question about the geometry and sampling rate of the receiver array, but it easily expands to include what source we should use, what microphones we should employ, whether or not we should use geophone sub-arrays, how big our aperture should be, and, finally, what temporal and spatial sampling rates we should select. In the spatial sense, we have always acquired seismic data digitally. We never had continuous (analog) sampling in space; analog data was only acquired in time.

The answers to these questions are mathematically and physically clear. For each source, the receiver array should consist of point receivers (no arrays) densely sampled over a wide aperture array encompassing a large square area. The source, however it is formed, should be a point source (no arrays) generating energy uniformly in all directions. For maximum benefit, there should be full source-receiver reciprocity; that is, for each receiver position, there should be a source, and for each source there should be a receiver. Hopefully, this chapter will make the reason for these statements clear.

Unfortunately, there are many reasons why the mathematics and physics are almost always ignored—primarily, economics and practicality trump correctness. Furthermore, faced with budget limitations in an era when oil was relatively easy to find, little or no consideration was given to the underlying mathematical assumptions. Many geophysicists assumed that mathematics, including the wave equation, did not apply to the seismic acquisition process. Arrays were designed to control perceived noise, but frequently depressed the dip response. Fancy acquisition geometries were designed to reduce costs, but resulted in data sets that could not image geologic objectives. Illumination studies were conducted in an attempt to determine the impact of any given

acquisition style, but, because they were often based on one-way equations or rays, the studies had no real impact on the solution—such studies can be fairly meaningless since complicated waveforms exist in even relatively simple geologic environments.

In contrast, mathematics does not lie. Mathematics, physics and a tremendous amount of empirical evidence suggests that imaging is a complex process almost totally controlled by the degree to which mathematical assumptions are honored. While we will not go into the mathematics in detail, we hope to provide a reasonable clarification of why we should acquire data in a precise, mathematically-correct manner. We will show that acquisition schemes can and should be modified to meet implicit assumptions.

Array Effects

Instead of recording single, non-overlapping shots into straight-line arrays, acquisition became one in which each shot was recorded by a line of receivers laid out on either side of the central shot. When receivers are laid out on only one side of a source, the resulting acquisition is said to be single ended. Figure 8-1 shows a typical single-ended acquisition, where a modern land vibrator provides the energy source causing the subsurface wavefield and its reflection. Receiver arrays record the response.

Figure 8-1. Schematic of typical multi-fold, single-end seismic recording process

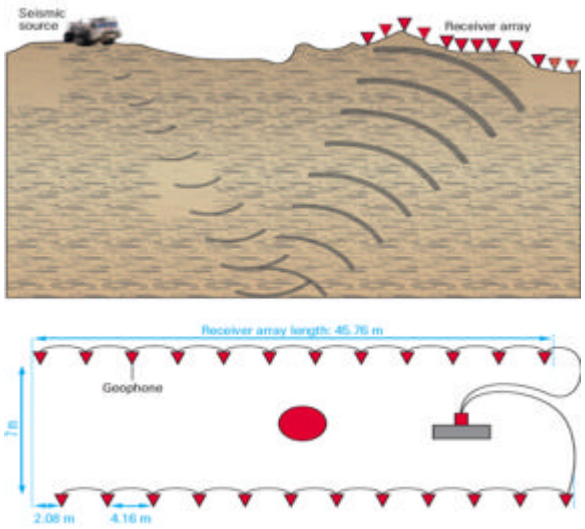

The bottom part of this figure shows how receiver arrays can be arranged and summed to produce a single trace. The output of this sub-array forces us to recognize that each trace can be affected by the array response. Although such arrays were supposed to reduce noise when it was not economically feasible to record the full output at each location, the mathematics says we should record and image using all receivers.

Array effects are rarely considered as part of the overall acquisition-data processing-imaging methodologies. In fact, the underlying mathematics is based on the assumption that each receiver is a so-called point receiver, but this assumption is wrong when an array is involved. Figure 8-2 demonstrates the smearing that arrays cause. The three images show the effect of recording every trace, a group of 8 traces, and a group of 16 traces. Note the considerable blurring caused by the mixing. While it appears to improve continuity and reduce noise, the net effect tends to be unwanted dip reduction.

Figure 8-2. The effect of seismic arrays.

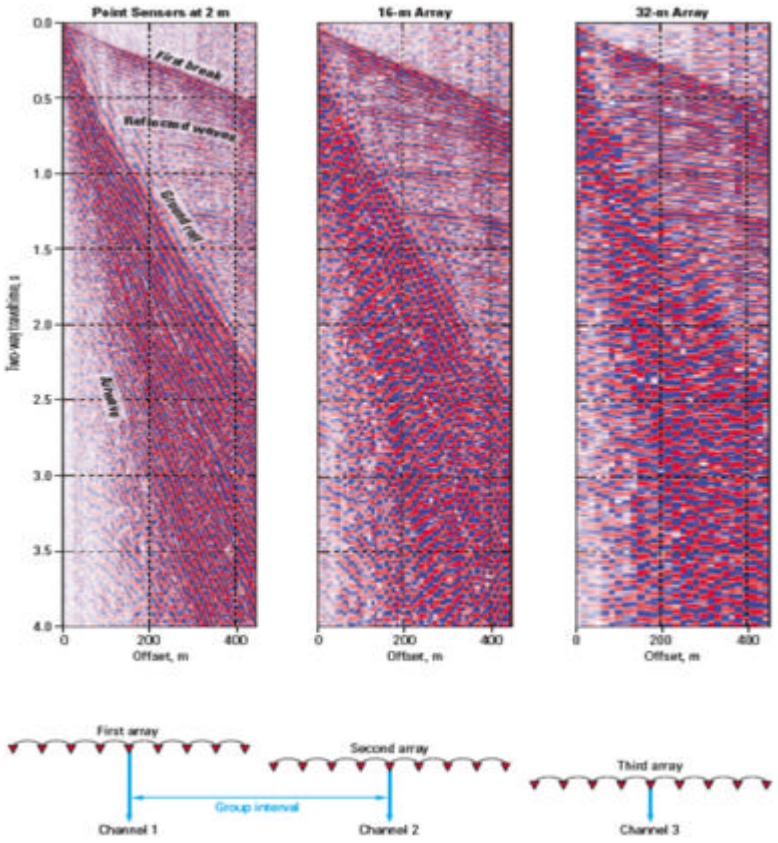

Among other things, smearing can reduce the dip response of the recording system and thereby seriously decrease the quality of the ultimate image. Although it seems like a good idea to use arrays, and, when steep dips are not an issue, it seems to make sense, that is never really the case. The use of arrays is a fundamental violation of the mathematical assumptions in all cases. Today, it is probably possible to record all the receivers. The affect of any given array can be emulated in the processing stage, so applying it in the field seems to be unnecessary and it is perhaps a big mistake.

Aperture

Figure 8-3 (courtesy of BP) provides an example of the kind of Earth model that you might see in the Gulf of Mexico. This model represents a typical salt imaging problem. Given that this model is a reasonably accurate representation of the subsurface, several facts are clear:

- every conceivable type of wave propagation will occur;
- since sea level represents a free-surface, every type of multiple will be evident;
- proper imaging will require that data acquisition be performed with a sufficiently wide aperture to capture a sufficient set of reflectors.

Figure 8-3. A complex model for data synthesis. Model courtesy BP, Modeling movie courtesy Panorama Technologies.

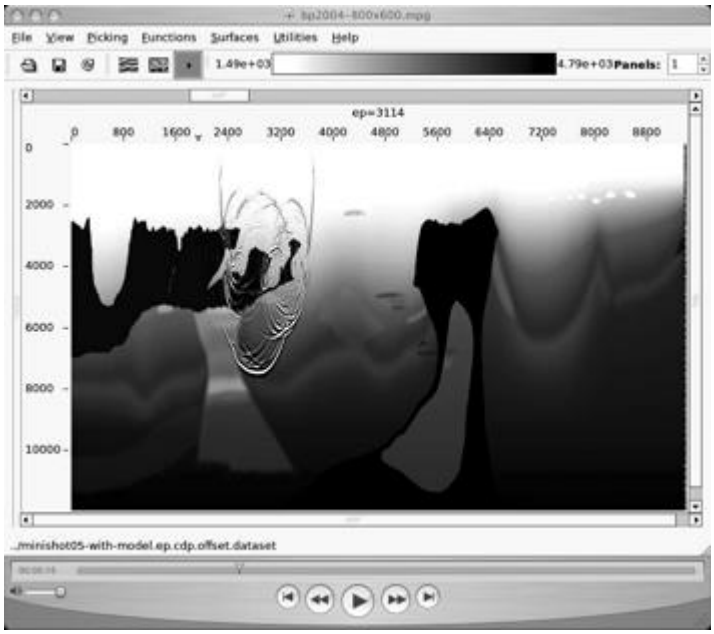

What modeling says is that producing an optimum image requires long offsets, long recording times, and small surface increments. What this means in three-dimensions is that we must use dense areal arrays as opposed to narrow-azimuth towed streamers. Another issue that is not fully appreciated is the importance of low frequencies. Full appreciation of this statement will become clear through the rest of the book.

Because it is from a Gulf of Mexico salt setting, many people conclude that the example represented by Figure 8-3 is of little value in a more worldly view of exploration. They say this kind of problem is simple to solve, and so should not be of much interest in the larger scheme of things. As we will see, this is far from the case. The salt-sediment contrast is on the order of 1.5 to 1, and a contrast this large is extremely difficult to handle for many of approximations used to produce imaging algorithms.

Figure 8-4 provides an example of the kind of complex geology we find on land. This perceived Oklahoma subsurface model from an over-thrust area in the southwestern part of the state faithfully represents a granitic overthrust in a very complex geologic setting. Once again, modeling tells us that to properly image subsurface structure, it is absolutely necessary to acquire long offsets and times. Thus, in both land and marine, satisfying mathematical assumptions means that acquisition arrays must be composed of point receivers, they must be areal in extent, and they must be densely sampled.

Figure 8-4. A complex model for data synthesis. Model courtesy Chesapeake Energy, Modeling movie courtesy Panorama Technologies.

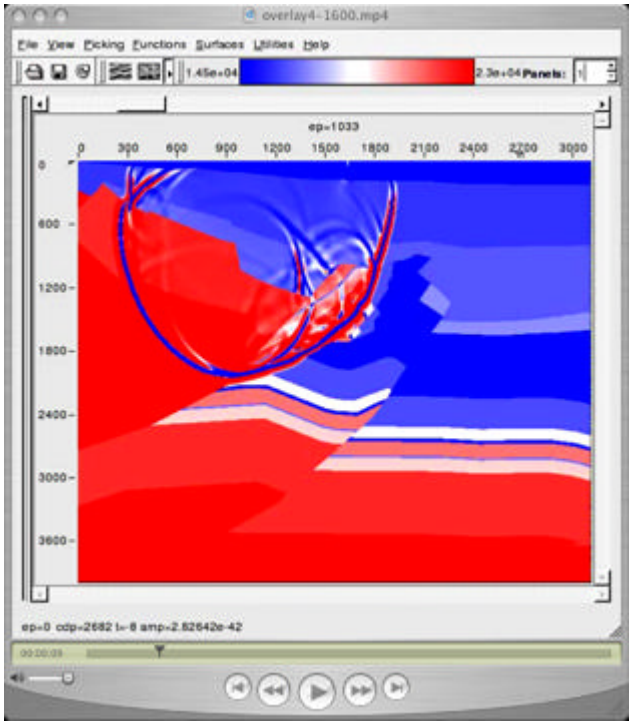

The rocks are hard, the near surface velocity is highly variable, and it is not unrealistic to assume that the true Earth model should really include anisotropy. Again, all waveforms are present in the simulation, and unraveling them requires that, to the extent possible, all waveforms be used in the imaging.

A big difference between imaging land and marine data is the lack of water cover for land data. When water is present, it is relatively easy to figure out what the near surface propagation parameters should be since it is not necessary to rely on the recorded data to determine the velocity of water. When water is not present, we must estimate the near surface velocity structure (compressional and shear) from the data itself, but this is very difficult to do because the number of traces that can be used to do this is highly restricted by the acquisition parameters. Sufficient offset is seldom available to do even simple semblance-based picking. What modern methods need is data that are fit for purpose; data must contain the information necessary to permit accurate estimation of the Earth model.

Aliasing

Aliasing happens when the frequency of repetition is too fast for the true nature of the repetition to be recognized. For example, everyone who has ever watched an old American Western movie has seen wagon wheels, maybe like those in Figure 8-5, spin diametrically opposed to the direction of travel (backwards). This occurs because the thirty-frame per second sampling rate of the movie camera is incapable of resolving the faster rate of the wheel spin. The net result is that the wheel appears to spin at a slower rate in the wrong (backwards) direction.

Figure 8-5. Wheels alias when in motion.

For our purposes, spatial aliasing in seismic exploration makes it impossible to correctly distinguish and image dipping events at their true position and angle. Many people argue that the mathematics of sampling is incorrect because they believe that if the human eye can recognize the correct pattern, the more mathematical migration algorithms should also be able to do so. But our brains make the event appear continuous, and handles it from there, while discrete mathematics cannot do this. The mathematics of discrete migration algorithms make strong demands on what kind of data they can handle because they cannot make the data continuous before they process it. Consequently, both acquisition design and the imaging algorithm must take aliasing into account. In some cases, the algorithm can be designed to handle any aliasing problem or issue automatically and directly. However, when this is not the case, aliasing must be avoided during the acquisition process itself. The elimination of aliasing ensures that dipping events are imaged as optimally as possible.

Data acquisition parameters play an important role in subsequent imaging exercises, while imaging algorithms vary considerably in their sensitivity to acquisition parameters. Understanding the impact of acquisition parameters on imaging techniques is the key to producing superior images.

Many geophysicists believe that there is some magic level of sampling, or that the sampling rules seemingly demanded by acquisition and processing are unnecessarily

strict. The basic idea that the human eye is better than the computer at being able to see through under-sampled data is probably true. However, ensuring that any given imaging application produces the most optimum results limits both the kind and style of the acquisition method. For the most part, data must be sampled sufficiently finely to ensure that the imaging algorithm can image target objects without loss of dip or image quality.

Figure 8-6 provides simple, conservative formulas relating the important parameters that affect the relationship of dipping reflectors at their true subsurface position to their apparent dip on a two-dimensional seismic recording when the source and receivers are coincident and the velocity is constant. The relationship between apparent dip, as specified by a change in time versus a change in space, coupled with Shannon's sampling theorem, tells us when to expect and how to handle potential aliasing caused by spatial sampling intervals.

Figure 8-6. Aliasing Formulas

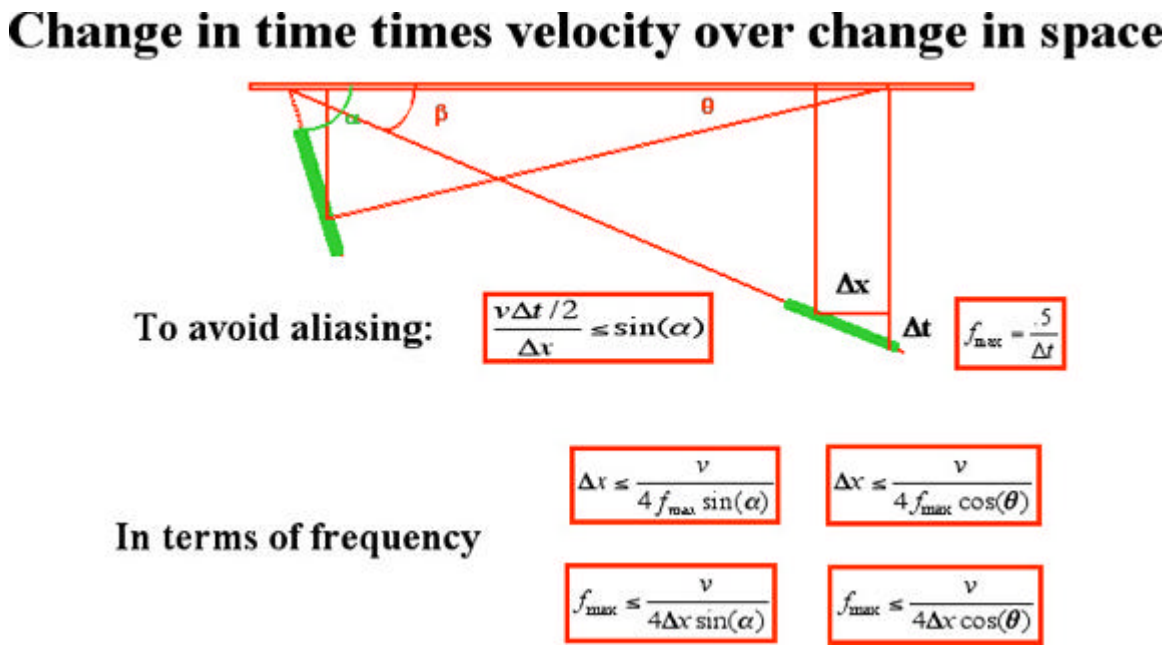

The trigonometric *sine* function of the true dip of the subsurface event turns out to be the ratio of half of the relative change in two-way time of the event at its apparent position, Δt, to the spatial range over which the time change takes place, Δx, multiplied by the assumed constant velocity of sound in the medium.

After this simple concept is understood, it is straightforward to use the Nyquist relationship between time sampling and frequency to rewrite the basic formula in terms of frequency. The Nyquist relationship states that a signal must be sampled at a rate greater than twice the highest frequency component of the signal to accurately reconstruct the waveform; otherwise, the high-frequency content will alias at a frequency inside the spectrum of interest.

Note that fixing any three parameters in the variety of formulas rewriting the basic formula produces provides a bound for the fourth. In 3D, it is important to do the calculations based on the largest spatial interval in the data set, Thus, if we want to make sure that we can image a given set of dips at a given frequency and velocity, we must make sure that the data has been recorded at the correct spatial spacing, or we must migrate it at the proper sampling interval.

You should understand that these are conservative formulas. The fact that velocities vary helps the imaging process because, in this kind of medium, ray bending improves the ability to image steeper dips. In precise mathematical terms, note that:

(8-1)
$$\frac{\partial t}{\partial x} = \frac{\Delta t}{\Delta x} = \frac{2 \sin \alpha}{v}$$

We all claim to understand the idea that when we sample a signal at a fixed even increment, the resulting set of samples can be used to reconstruct the original signal completely, but only up to a fixed frequency determined by the sampling rate (that is, the Nyquist frequency). Thus, if we sample at 250 samples per second (in other words, 4 milliseconds per sample), the highest possible frequency we can record correctly is 125 Hz, or exactly half the sampling rate. Note that in this case, the Nyquist frequency is determined equally from 250 or half of 1.0/.004. Thus, 125 = 1.0/.008. A similar equivalence is available for surface sampling parameters. If lines are spaced at 100 meters, the spatial Nyquist frequency in the line direction is 1.0/200. This Nyquist frequency specifies the maximum wavenumber or wavelength that can be safely recovered from the surface sampled data in the line direction.

Figure 8-7 shows a schematic of a single plane monochromatic wave front traveling at a slight angle relative to the vertical. The wave front on the right is recorded in time, while that on the left is recorded in depth. The wave front in this case is propagating in a constant velocity medium and is characterized by its vertical and horizontal wavenumbers, or their reciprocal wavelengths. The vertical wavenumber, k_0, is completely determined by the frequency, w, and the velocity, v. In contrast, the horizontal wavenumber, k_x, is impacted by the angle of propagation. Later, we will see that this dependence on angle can be used to specify a simple migration algorithm.

Figure 8-7. Wavenumbers

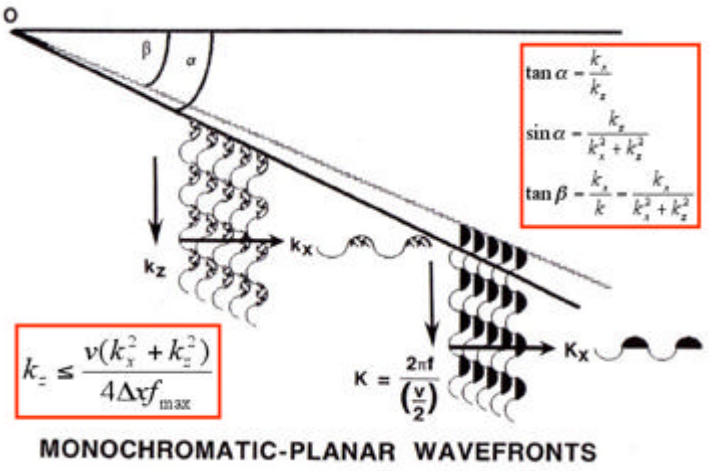

Figure 8-7 also shows the relationship between monochromatic wavefronts true dip. The figure shows how the trigonometric functions relating apparent dip to true dip are expressed in the frequency domain. The most important formulas say that the sine of the true dip angle, α, is equal to the tangent of the apparent dip angle, β.

It is important to note that in the real world, this means that we must consider measured seismic data to be digital in character, since the sources and receivers are at discrete locations. Since modern data is also digital in time, reflection seismic processing today is purely digital. Since wavenumbers of plane waves carry information about the angle of propagation, this suggests that there will be some issues with regard to the aliasing of dipping subsurface reflectors. The impact of aliasing on our ability to image subsurface events will be discussed in subsequent sections.

Aliasing appears in many ways. Figure 8-8 demonstrates the appearance of aliasing on zero offset sections. Here we see the difference between sampling at 27.5 feet and 110 feet. The figure on the left at 27.5 feet is clearly less aliased than the one on the right at 110 feet; that is, the section on the left has been sampled sufficiently finely to almost completely eliminate all aliasing for this level of dip. The section on the right was constructed by simply eliminating traces from the one on the left. Evidence of aliasing is represented by the grainy appearance and by the areas where events that follow some hyperbolic-like trajectory appear more like a single flat event.

Figure 8-8. Aliasing when the data are flat.

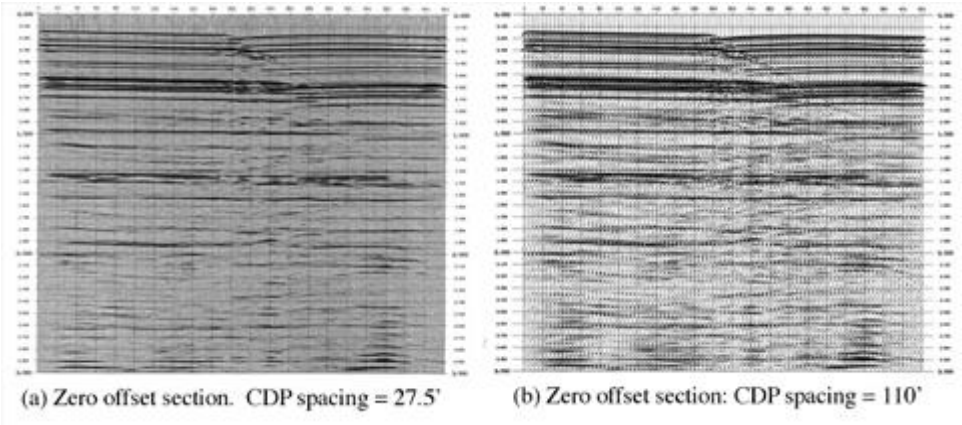

The synthetic CDP in Figure 8-9 is a normal moveout corrected CDP or midpoint gather with both flat and hyperbolic arrivals. It demonstrates a form of aliasing that occurs when the moveout of an event is so strong that the recorded spatial sampling cannot handle its rapidity adequately. This means that events can be aliased in offset even when all dips are perfectly sampled in space. This figure shows a synthetic (raytraced) CDP with multiples that are aliased in offset. While the human eye has no difficulty recognizing the pattern of these events, many noise suppression and migration algorithms will treat these events in a predictable, but incorrect manner. For example, a Radon transform is not be able to completely remove the event from the record.

Figure 8-9. Offset aliasing.

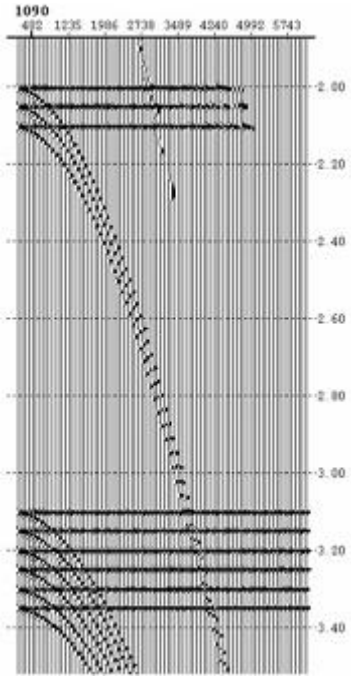

Modern Acquisition Geometries

This section describes the physical structure of the commonly used methods of acquiring seismic data over land and water environments.

Cross and Inline Spreads

Modern 3D land acquisition takes many forms. Figure 8-10(a) shows a typical cross-spread acquisition where shot lines are perpendicular to receiver lines. As the acquisition progresses, the entire pattern is rolled along to cover a large area. This represents true 3D acquisition with large azimuth variation.

Figure 8-10. Modern Land Acquisition

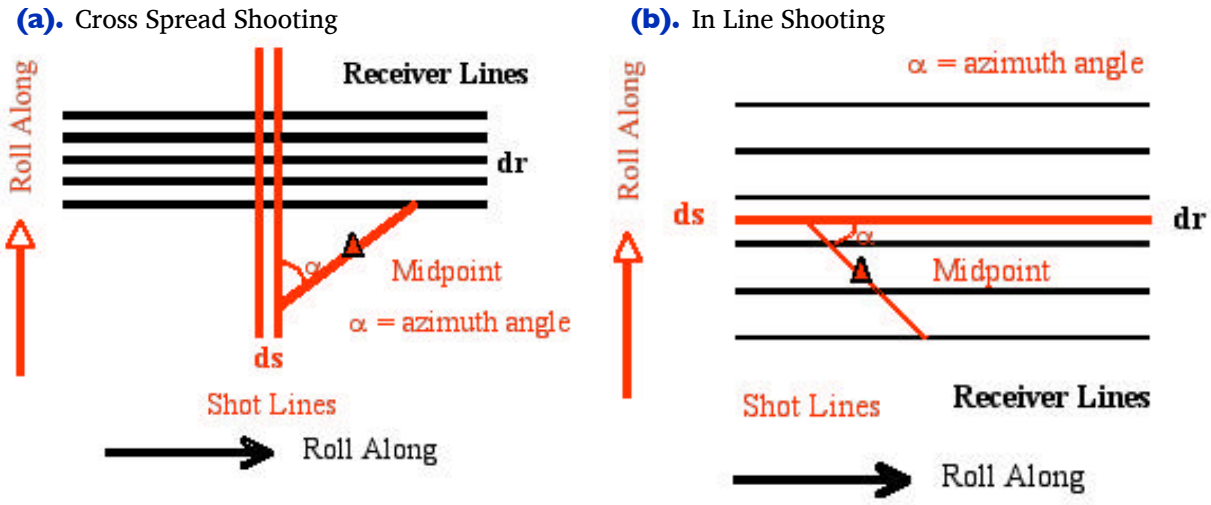

While the data from this kind of acquisition can still be sorted into the usual gathers, it can also be sorted into what are called common azimuth gathers. While this type of shooting produces uniform surface coverage, at least in terms of common midpoints, it usually does not fully satisfy underlying mathematical requirements.

Figure 8-10(a) shows the geometry of source lines relative to receiver lines for what is called cross-spread acquisition. Figure 8-10(b) shows acquisition for inline shooting. A grid of receiver lines records the output of sources aligned along source lines. The source lines are separated by *ds* and the receiver lines are sampled every *dr*. Both the source lines and receiver grids are rolled-along to achieve uniform surface redundancy. Part (b) shows a typical inline land acquisition geometry. This style is clearly reminiscent of typical 2D split-spread acquisition, and, in fact, the only real difference is that multiple parallel receiver lines recorded each shot response. Like its cross-spread cousin, inline

acquisition produces data sets with uniform surface coverage. Because the number of recording lines is small, it usually only produces narrow azimuth data.

As was the case for our split-spread acquisition, each gather from either of the recording geometries in Figure 8-10 can be migrated independently of any other similar gather. Thus, we can conceive of migrating common azimuth volumes for detailed illumination comparisons. Note that this kind of acquisition produces five dimensional data since there are two coordinates for the source, two coordinates for the receiver, and one coordinate for time. The most important point is that widely spaced lines are good for quick coverage but are bad for spatial sampling.

Sampling will become an issue later when we discuss its impact on high resolution migration algorithms. Although this style of sampling can generate many different azimuths, each azimuth is poorly sampled, meaning that, in some cases, azimuth migration cannot be performed.

CATS, NATS, and WATS

Marine data acquisition has evolved from single cable, single source acquisition to multi-cable multiple source, multiple boat and even ocean bottom (OBC) configurations that can record long offset data in record time. Again, redundant coverage can be sorted into any of the orders discussed in old-fashioned, split-spread shooting.

Figures 8-11(a) and 8-11(b) show current common azimuth towed streamer (CATS) and narrow azimuth towed streamer (NATS) geometries. There are typically 1 to 20 streamers spanning a cross-spread length from 0 to 2000 or 3000 meters. The geometry on the left has many receiver streamers, while the common azimuth geometry on the right has only one streamer. Although impossible in normal applications, the streamers in the single-ended marine experiment are never really straight. For migration purposes, the cross-spread width should be as large as possible.

Figure 8-11. Schematic of typical towed multi-streamer marine acquisition.

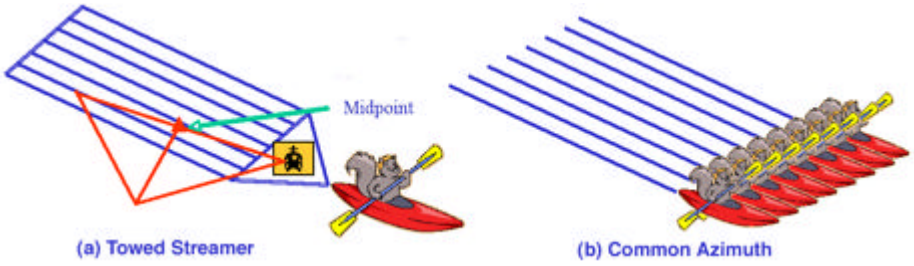

Towed streamers containing a few hundred receivers record data every time the sources, usually air guns just behind boats, like those shown in Figure 8-12, are fired. Because of boat movement, recording time is usually limited to at most 10 to 15 seconds. Receivers

in each streamer data are very finely sampled in each dimension. Cable spacing is rarely more than 100 meters with the number of cables ranging between 1 and 20. The number of traces per shot is large while the shot density per unit area can be relatively low. Although this kind of geometry has been used for many years and has proven to be reasonably good for advanced imaging techniques, it is still somewhat far from what the mathematics and physics demands. An important issue with this approach is cable feathering caused by water currents, which usually means that it is not possible to achieve the precise common azimuth form shown in the right half of Figure 8-11. Since most of the algorithms we consider must be run on a grid, traces may have to be regularized to that grid to ensure algorithm accuracy and final image quality.

Figure 8-12. Petroleum Geo-Services (PGS) boats in operation. Note the towed streamers and the triangular shape of the Ramform boats.

Figure 8-13(a) and (b) show a wide angle towed streamer (WATS) acquisition and composite shot. In WATS schemes, gunboats make multiple passes over the same shot line. One gunboat is placed at the head and to one side of the receiver array and the other is on the same side at the end of the array. The boat towing the receiver array parallels the gunboats, but traverses an every widening path in accordance with each pass of the source boats. Part (a) shows double gunboats recorded by a single eight streamer receiver boat to achieve shot centered receiver arrays. Four or more wider receiver swaths may have to be recorded to produce sufficient data to produce receiver arrays with areal coverage, as indicated by the surface coverage in the composite shot layout in Part (b). The WATS technology may be the first marine acquisition scheme that actually honors the mathematical assumptions underlying seismic imaging algorithms.

Figure 8-13. The geometry of wide azimuth towed streamer acquisition.

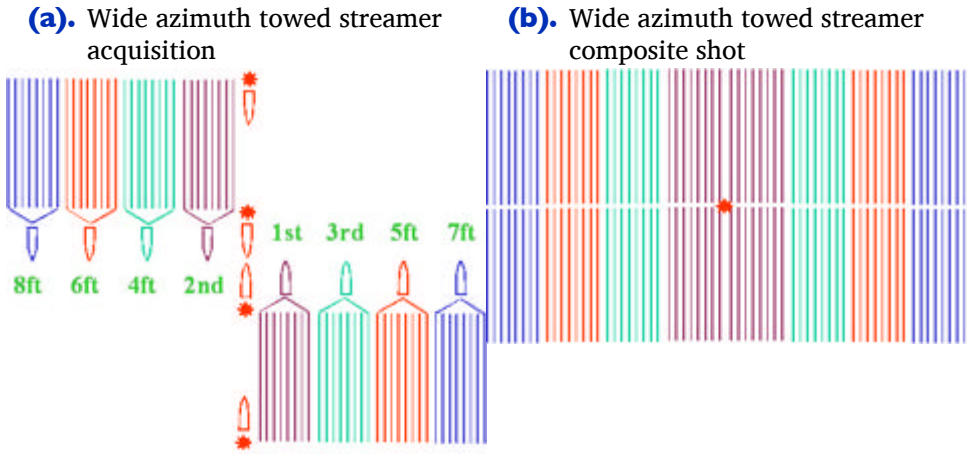

The composite shot in Figure 8-13(b) can contain a huge number of receivers. This figure was constructed based on the assumption that the receiver boat could effectively tow just eight streamers. Utilization of receiver boats towing 16 or more streamers would cut the work load significantly while still producing a composite shot that is much closer to the true mathematical ideal. When 8,000 meter streamers are separated by 100 meters, eight streamer WATS shots have an areal extent of approximately 6,000 meters by 16,000 meters but could certainly cover an area 16,000 meters on a side. As shown by BP, these types of acquisitions do, in fact, produce data sets fully capable of imaging complex subsurface geology.

Vertical Cables (VC)

Vertical cables, as shown in Figure 8-14, are just that. Receivers are actually placed along a vertical cable suspended at a fixed surface location either by sea anchors or by a tether attached to the ocean bottom. Usually source and receiver reciprocity is used to change the acquisition process into an equivalent one where the sources are

assumed to be along the cable and the receivers on the surface. While vertical cable acquisition is certainly capable of generating the equivalent of the composite shots of WATS, this particular approach has never achieved its promise, probably because of the inability to keep the cable in a fixed and completely vertical position. Furthermore, processing common receiver gathers as if they were common source gathers is much more computationally efficient than processing common-shot gathers.

Figure 8-14. Marine Vertical Cable Acquisition.

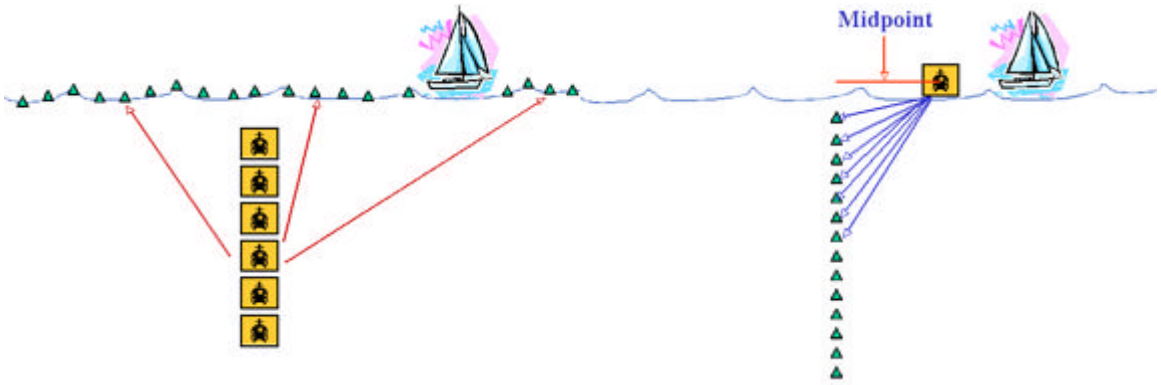

Ocean Bottom (OBC)

Since gunboats can shoot in a virtually unlimited set of locations, OBC acquisition can generate areal array shots quite easily. In Figure 8-15, receivers are laid on the ocean bottom and sources are located on the surface in gun boats like those shown in Figure 8-16. The receivers on the ocean bottom can be organized into a grid or as a small set of cables similar to those used on the surface. The grid can be positioned on the bottom by a remotely operated vehicle, by a manned submersible, or by simply allowing the cables or receiver unit to sink to the bottom. Wireless communication can be used to accurately locate the receivers when in position.

Figure 8-15. Schematic of a typical ocean bottom acquisition.

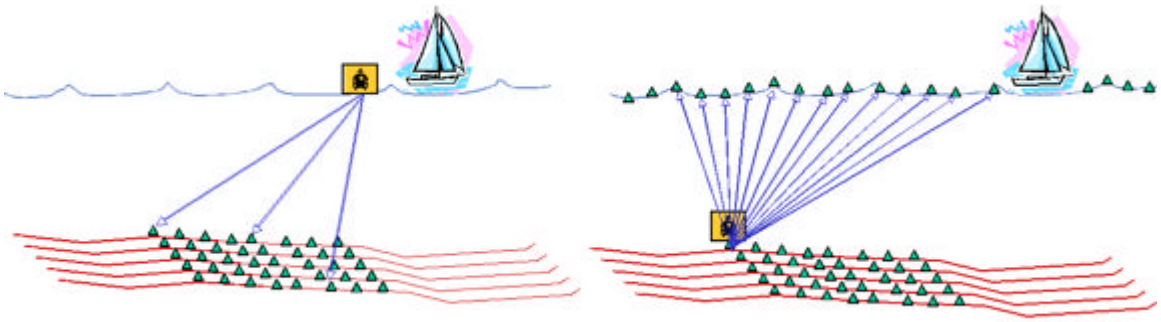

Figure 8-16. Fairfield gunboats near shore. OBC acquisition removes many restrictions on where source boats can sail.

Because the sources are at the surface, the gun boat can move in any direction desired. As a result, many azimuths can be recorded during the acquisition session. Data from the receivers can be recorded on the gun boat or on another boat especially designed for recording and processing. If sea-floor cables are used, this acquisition can be very similar to orthogonal shooting on land. The basic difference is that the source boat can move in any desired direction and consequently can generate full azimuth surveys. Usually source-receiver reciprocity is used to view a common-receiver gather as a single shot, making source spacing and density extremely important. Because receivers are actually on the ocean bottom, this data usually must be preprocessed almost as if it was land data. Certainly, receiver coupling or lack thereof, and the consequent amplitude differences must be addressed and eliminated or at least suppressed.

Regardless of how they are generated, seismic wavefields are the result of particle motion in the medium. Figure 8-17 shows two types of motion: compressional and shear. The red wavefront particles are vibrating tangentially to the wavefront as part of a shear wave. In a medium where velocity varies with angle (that is, an anisotropic medium), there are two orthogonal shear waves. Shear waves do not propagate in a fluid or gas. Particles on the blue wavefront vibrate perpendicular to the wavefront in the ray direction and consequently are part of a compressional wave. Perhaps the best example of a compressional wave is sound in air. Particles in air are compressed and rarified as the wave front progresses. Compressional waves travel in virtually all fluids and solids. Shear waves in solids generally travel at about 60% of the speed of compressional waves. Typical speeds of compressional waves are 330 m/s in air, 1450 m/s in water and about 5000 m/s in granite.

Figure 8-17. Shear versus Compressional waves

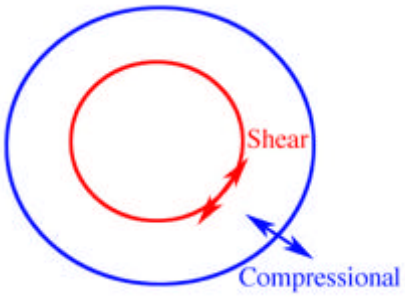

Shear waves are much more difficult to visualize than compressional waves. A good way to think of shear propagation is to consider a deck of cards. It is quite easy to slide the cards in the deck against each other and so generate a wave that propagates through the deck from one end to the other. While this is not necessarily how such waves propagate in the earth, the existence of shear propagation is not in question. Since shear waves cannot propagate in water, it is impossible to record shear waves in the water layer, but this does not mean that marine recordings do not contain shear wave information since all recordings, both land and marine, contain converted wave data. Seismic data from land and OBC data can both contain direct shear reflections, but data recorded in water contains only shear-related compressional waves that are direct conversions from shear to compressional at the water-ocean-bottom interface.

Practical acquisition of OBC data, as shown in Figures 8-18, 8-19, and 8-20 takes several forms. Whether the receivers are cables, as shown in Figure 8-18, or individual units like those shown in Figures 8-19 and 8-20, the primary objective is to place the receivers on the ocean bottom at precisely known locations, but this is not always easy to do. For example, cables are usually towed and then dropped, but even with radio sensors, it is not always possible to determine their exact ocean bottom position. The units in Figures 8-19 and the more modern version in Figure 8-20 contain computer systems that can accurately determine position and relay the information back to the recording instruments. In addition, they have sufficient local storage to record several shot responses before they must transmit the data to the primary storage system.

Figure 8-18. Ocean bottom layout and acquisition. This figure shows the cables and sensors used to acquire data from ocean bottom cables.

Figure 8-19. This figure shows boxlike ocean bottom receivers being deployed overboard (bottom left and top right) in both deep and shallow marine environments. The top left composite demonstrates that source boats can operate close to shore and platforms.

Figure 8-20. Fairfield Industries' latest ocean bottom recorder contains four phones and all the electronics necessary to record source-responses.

The secondary objective of OBC recording is to ensure that each component of the OBC receiver is correctly oriented. Each OBC phone contains a hydrophone, two shear phones, and one accelerometer. The two shear phones must be level and their orientation fixed relative to the rest of the receiver units. Consequently, they are gimbaled and adjustable based on each unit's digital compass. Clearly, OBC acquisition is difficult and potentially expensive.

Regardless of which acquisition method is employed, the net result are data volumes that are truly massive. Figure 8-21 shows a single time slice through 20,000 square miles of prestack, time-migrated Gulf of Mexico data with an average redundancy of about 90. Simple back of the envelope calculations suggest that the size of this data volume is several hundred terabytes or more. One can easily imagine ocean bottom acquisitions more than four times as large as this one.

Figure 8-21. This figure shows a time slice from a prestack time migration that essentially covers the Gulf of Mexico Continental shelf. (Image courtesy of Fairfield Industries.)

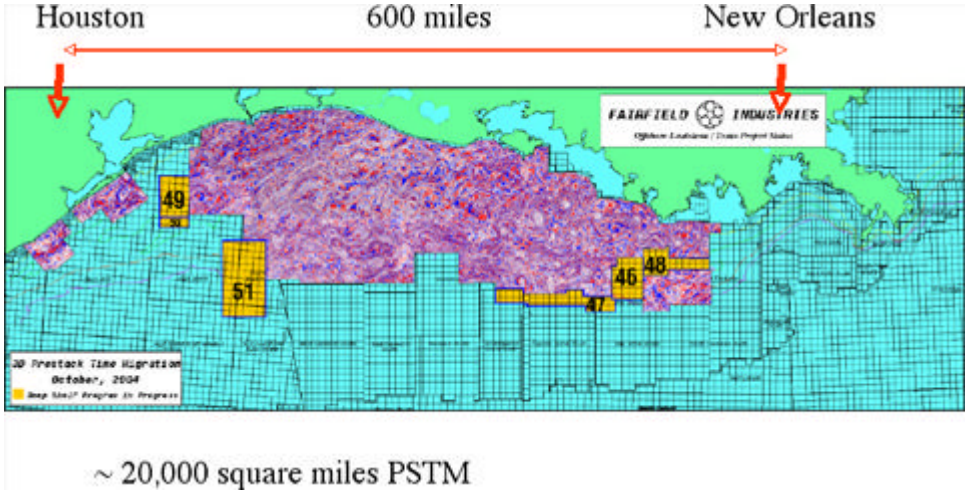

Data Acquisition Summary

The usual seismic sound fields we record are due to what we frequently consider to be point sources. As they propagate into the Earth, they radiate in all directions. The normal to the propagating wave front at any given subsurface location points in the direction of what you can think of as a ray. Since the propagation is normally not constrained with regard to direction, this normal can point in any direction consistent with the sound speed in the medium through which the field is propagating. If the normal points upward, it is an upward traveling wave; if the normal points downward, it is a downward traveling wave. Clearly such fields change directions at 45 degrees, and they become purely horizontal waves at 90 degrees.

If we arbitrarily assume that what was recorded only propagated upward, much of the true wavefield will not be properly imaged unless the assumption is true, but it should be clear that this kind of assumption cannot possibly be true. Nevertheless, the assumption that wavefields travel only in the upward direction is a major part of the migration/inversion/imaging algorithm set.

Note that while the Earth permits wave motion in all directions, migration algorithms may or may not be able to handle these motions. Table 8.1 summarizes the type of algorithms that are currently used in practice. We will consider each of these types of waves and how they impact the imaging process in the rest of the book.

Table 8.1. Wave Motion Hierarchy

Wave Motion	Wave Type
Waves move in all directions	Two-way wave motion
	Turning waves and rays
Waves move is almost all directions	Almost two-way wave motion
	Limited turning waves and rays
Waves move upward only	Propagation angles less than 90 degrees
	No turning waves or rays
Waves move downward only	Propagation angles less than 90 degrees
	No turning waves or rays

The measurement of seismic waves is accomplished using a variety of receivers or phones. These devices can measure the velocity of particle motion (accelerometers), pressure changes (marine geophones), and even the two shear waves. Modern OBC data is usually acquired using all four of these devices. Note that, although each class of phone records only data of that type, it also records all waves that converted from one form to another. Thus, unraveling, migrating, or imaging these data is only possible if they are all handled together. This is still a daunting task, even with today's massive computer power. The following list summarizes the type of microphones in use today.

- Accelerometers—Particle Velocity
- Geophone or hydrophone—Vertical Pressure change
- Shear Horizontal
- Shear Orthogonal

Chapter 9

Migration Summary

This chapter briefly summarizes the information about migration presented in previous chapters.

Computational Complexity

The hierarchy of algorithms in Figure 9-1 makes us wonder why this diagram has so many different one-way approaches. Why are there so many one-way methods and so few two-way or almost two-way technologies?

Figure 9-1. The migration algorithm hierarchy

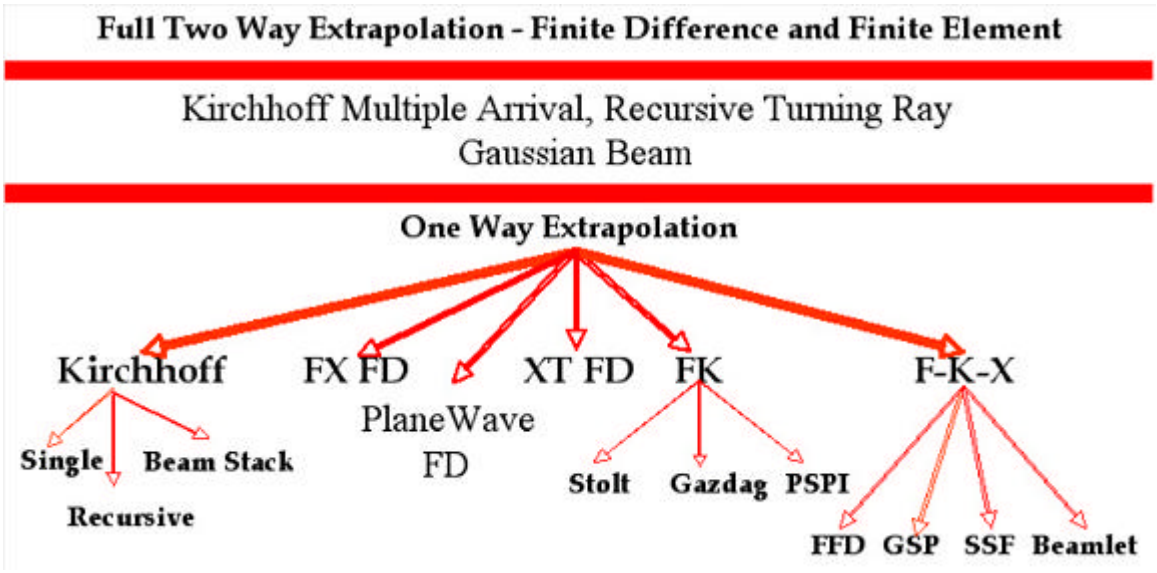

The simple answer is that the demarcation between one-way and two-way methods is one of computational efficiency. That is, one-way methods tend to be significantly more computationally efficient than two-way methods. This statement is certainly a function of algorithm implementation, but it is not a bad rule of thumb. Rumors have it that the Gaussian beam method can be made extremely efficient, and so the rule may be broken in that case. However, because all of the one-way methods function depth slice by depth slice or time slice by time slice, two-way approaches that must compute the entire wavefield at each propagation step usually lose the efficiency battle.

In spite of the apparent complexity of Figure 9-1, there are really only three basic algorithm styles. The first group might be best referred to as raytrace methods, and includes all of the Kirchhoff methods and the Gaussian beam. The second group generally includes methods that image depth slice by depth slice using either finite differences or some form of Fourier domain method. At the top of the hierarchy, the third group does imaging volume by volume. Thus, the computational complexity increases greatly as we move from the bottom to the top in Figure 9-1.

From a more practical viewpoint, raytrace-based methods are by far the most flexible. They can output data anywhere at any desired volumetric level. At some loss of overall accuracy, they can be made far more efficient than any other approach. In the slice-by-slice world, common azimuth methods rule the day. As we move up the accuracy chain, one-way shot profile methods are more efficient than two-way approaches. There is no question that as the computational complexity increases, efficiency decreases, but accuracy improves dramatically.

Velocity Sensitivity

Many geophysicists argue that high technology two-way methods are much more sensitive to errors in the velocity model than any of the one-way approaches. Both mathematical theory and experience contradict this assumption.

Any impulse analysis shows multi-arrival energy is very prevalent below complex geometries defined by anomalously high velocities. Such structures include salt domes and granitic overthrusts but can also be carbonate based.

Since rays, as computed by most raytraces, represent a high frequency approximation, virtually any ray-based migration may be excessively sensitive to sharp velocity discontinuities. This, together with the single arrival assumption, is certainly a major reason that single arrival Kirchhoff methods are extremely poor at imaging below salt.

Most one-way implementations do a much better job of handling multiple arrivals, and so it is not surprising that images produced with these methods are usually better than single arrival Kirchhoff applications. But, because one-way methods have a built-in angle limit, they also have a built in instability.

Two-way methods, or at least those that are above the one-way line in Figure 9-1, have almost no inherent restrictions on velocity variation, angle, or amplitude response. Depending on the implementation, they can produce significant amounts of grid dispersion resulting in something akin to a grid-based anisotropy, but, if that is handled properly, we can be assured that the two-way method will have the least sensitivity to velocity errors.

Amplitudes

The phrase *true amplitude imaging*, as used in this book, really means that, after migration, any amplitude within the imaged volume is directly proportional to reflectivity. There are, of course, so-called *true amplitude one-way methods*, but all of those methods are simply modifications of a one-way method of choice to include some aspect of two-way propagation. Jon Claerbout was the first to propose such a method in his 1986 book, so the idea of making a one-way migration into a two-way migration has been around for some time. However, as far as the author is concerned, the only methods that can be called true amplitude methods are the full two-way method and the Gaussian beam method.

Conclusions

Experience has shown that, given a good implementation, each of the one-way algorithms has a useful place in most, if not all, prestack migration projects. When implemented properly, almost any of the algorithms discussed here will produce a reasonable result. From a hierarchical perspective, the top of the pyramid is dominated by two-way methods. These full wavefield techniques always produce the best result when the velocity model is correct. Moreover, they almost always do a better job than their one-way counterparts when the velocity model is not correct. Moving down the hierarchy tends to reduce the computational complexity at the cost of image quality. Because they leave something out of the imaging process, one-way approaches are also much more sensitive to velocity errors.

Chapter 10

Isotropic Migration Velocity Analysis

Velocity analysis is one of the most important aspects of imaging seismic data. Regardless of whether the project is a prestack time or depth migration, finding an Earth model that produces the best possible image is seldom easy. What we know today is that finding the *optimum* isotropic velocity is directly related to the experience of the analyst, the quality of the migration tools at his or her disposal, and, of course, the quality of the seismic data itself.

Almost all velocity analysis done today is what is normally referred to as migration velocity analysis (MVA), and is usually based on some form of semblance calculation and picking. This works reasonably well so long as the Earth model is isotropic, but when the subsurface is anisotropic, it falls far short of producing reasonable estimates of the totality of parameters defining the anisotropic world. Moreover, as we saw the estimated velocity may produce a high quality image with excellent lateral positioning, but depth conversions will be inaccurate. In this case, the analyst must have proper tools for improving the number and accuracy of the parameters in the ultimate Earth model.

Almost nothing can be done about the seismic data from which the required Earth model parameters must be estimated. There are certain simple preprocessing steps that can at least reduce the possibility of limiting the quality of the final image. Some good and bad data preparation practices are summarized in the following list:

- Deconvolution is good, provided that it enhances low frequency content
- Removing low frequencies is bad
  - Velocity analysis requires many low but not so many high frequencies
  - Migration basically trades horizontal wavenumber for vertical wavenumbers
  - Migrate the data first to assess the need for low frequency removal

- Two dimensional linear noise reduction may reduce dips
  - FK or fan filters should be avoided unless absolutely necessary
  - Prestack migration usually images linear noise to a point or off the section

- Multiple suppression can be a necessary
  - SRME/Inverse Scattering is the optimum choice
  - Parabolic methods should be used with care

- Migration from topography should always be a priority
  - Sea floor topography is the same as topography
  - Refraction statics should really be refraction tomography

In the author's mind, there are four basic approaches to MVA.

- The first approach is what we will call *short-spread-semblance-based* velocity analysis. This velocity analysis is based on a short enough spread to avoid anisotropic effects and essentially provides what we have referred to as the NMO velocity. It is useful for both compressional and, when available, shear data. Typically, it does not consider issues related to any form of anisotropy. It can be completed with or without horizons. This approach has been the workhorse of MVA for many years.

- The second approach continues the use of the *short spread* approach, but adds residual tomography to the mix. When the short-spread analysis methodology is considered to have run its course, residual picks are used in a tomographic inversion to produce a refined update. Tomography sometimes suffers from a lack of redundancy that precludes its usefulness. It may also have problems due to short spread limitations. In the traditional formulation, it may not have sufficiently wide incidence angles to be effective. In some cases, the tomographic inversion can be used to estimate simple anisotropic parameters, but this does not appear to be routine.

- The third velocity analysis approach relaxes the short-spread assumptions, uses all the data, and incorporates well information directly into the mix. This combination of techniques requires the availability of additional data, usually in the form of shear measurements, but some form of subsurface information is a must. Subsurface knowledge can be empirical, rather then from a drill bit, but it is a must. This approach requires much more interpretive input than the other two. Perhaps its chief drawback is its continued dependence on semblance style picking.

- The fourth, and definitely least used and understood methodology, is what we will call *full-waveform inversion*. This is what we might refer to as a hands-off method. We formulate the problem in a purely mathematical sense and let a super computer do all the work. While this approach, for the most part, has failed miserably in the past, there are beginning to be indications that with the right data, full-waveform

inversion may eventually become a useful tool. What is becoming clear is that for full-waveform processing to become a useful technology, the industry must begin to acquire much lower frequency and more densely sampled data. In addition, computation power will have to increase several orders of magnitude, and the cost of compute cycles will also have to decrease significantly as well.

Migration Velocity Analysis Geometry

Figure 10-1 graphically represents the basic idea behind migration velocity analysis. Velocity analysis after migration estimates the velocity along the vertical from the surface to the migrated output point. Of course, because it assumes that the source and receiver are coincident, one cannot base a velocity analysis approach on this kind of concept alone.

Figure 10-1. Migration velocity analysis geometry

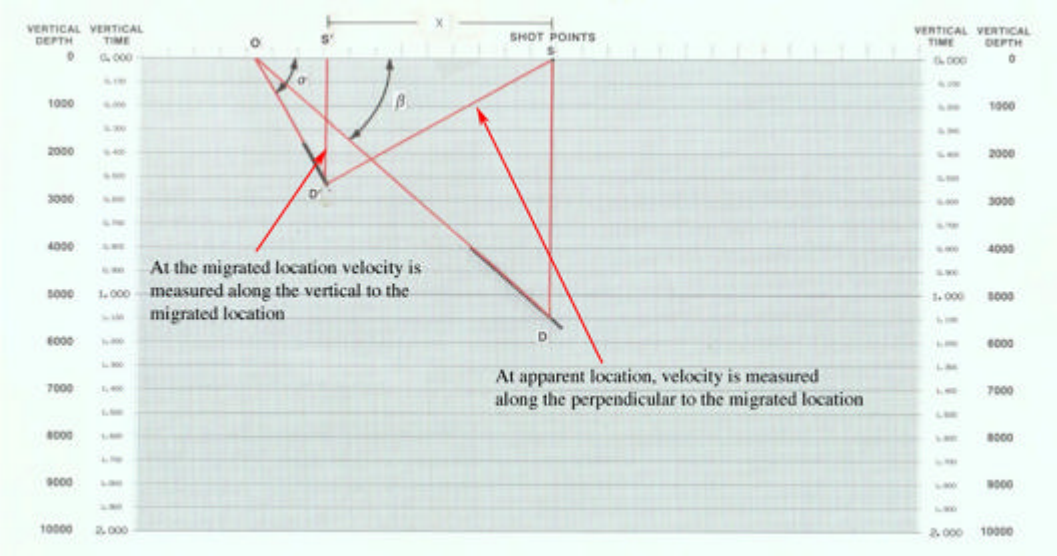

Developing a reasonable approach to velocity analysis requires that we have redundant data and that we exploit this redundancy in order to provide velocity estimates. Figure 10-2 illustrates the geometry in the case of non-zero offset from a ray-based modeling perspective. We see that the recorded data, in yellow, is placed below the surface midpoint. The red and green rays illustrate the paths taken by the illuminating energy. After migration, the yellow apparent event is now places at its true location below the vertical black image ray. Migration has moved the source and receiver locations directly above the correct location. Thus, after migration, source and receiver locations are lost. We can maintain redundancy by migrating common-offset sections and hopefully develop velocity analysis approaches that are applied after migration. Our goal is to provide velocity analysis methodologies that exploit residual redundancy to refine initial velocity estimates.

Figure 10-2. Migration velocity analysis geometry

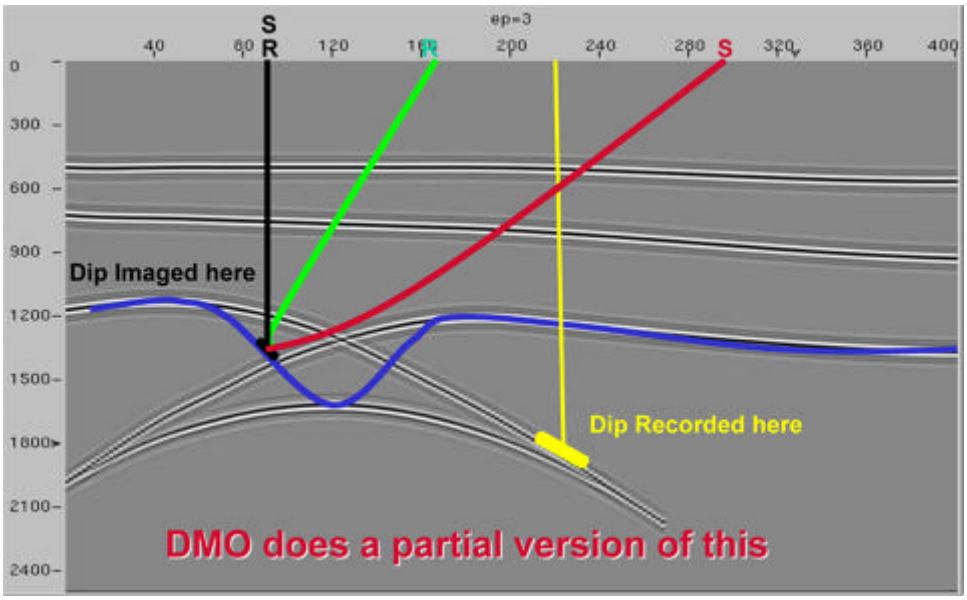

Constant Velocity Migration Velocity Analysis

An early approach to pre-stack-time migration velocity analysis is illustrated in Figure 10-3. The approach was popularized by Paul Fowler at the Stanford Exploration Project and later at Western Geophysical in Houston, Texas. In part (a) we see the general idea is to perform many constant velocity pre-stack time migrations and collect the resulting information into a cube with axis for time, CDP, and velocity. Each fixed CDP (y in this case) is then analyzed to select the optimum velocity at that location. Figure 10-3b compares more traditional stacking velocity and DMO based approaches to the one described by (a). The general conclusion is that the constant velocity approach is somewhat better than the other two.

Figure 10-3. Migration velocity analysis geometry

(a). Constant velocity PSTM gathers

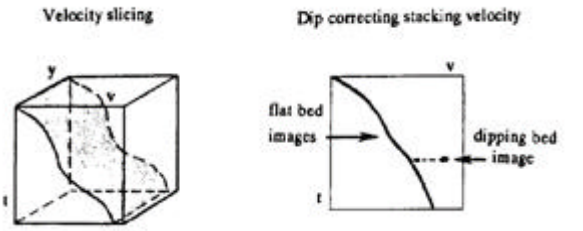

FIG. 1. (a) Extracting a stacked section corresponding to a specified velocity function by "slicing" through the three-dimensional velocity-midpoint-time data cube. (b) Correction of high stacking velocities due to dip, as seen in a (*v,t*) velocity panel.

(b). Constant velocity PSTM image comparisons

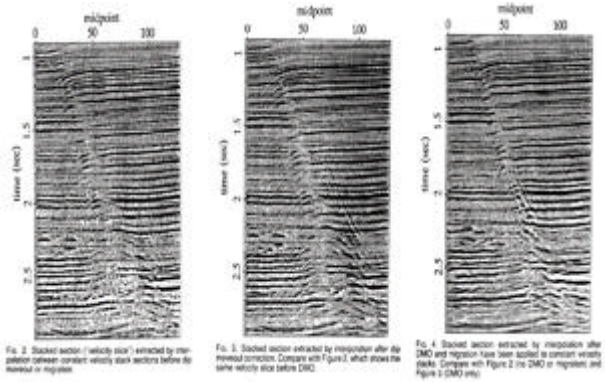

Velocity Independent Migration Velocity Analysis

Another early approach to PSTM velocity analysis is illustrated in Figure 10-4. The important issue with regard to Figure 10-4 is that we can apply this migration algorithm without knowledge of the velocity. Once applied, a detailed analysis can then be performed to determine the velocity that best flattens the gathers and produces the best image. It is very important to note that this approach produces velocities that are obtained at the migrated positions. Thus, the requirement of Figure 10-1 is met: The velocity is at the migrated or *vertical* position where it is actually needed.

Figure 10-4. Imaging without the velocity

(a). Midpoint and offset sorts of a point source

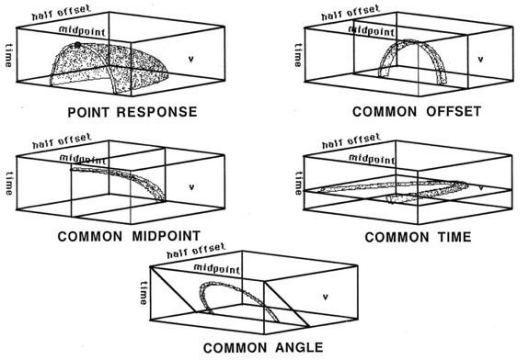

(b). Dip independent constant velocity imaging

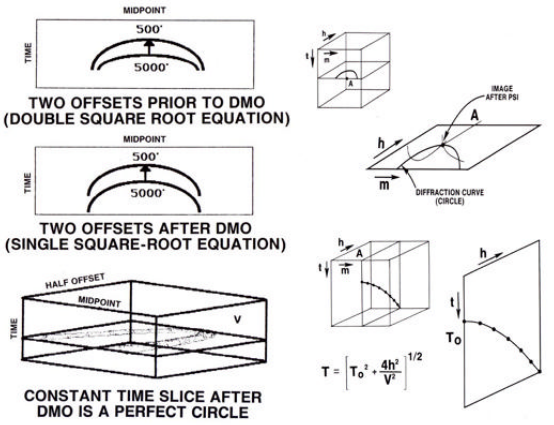

There are many variations of this approach. One, due to John C. Bancroft at the University of Calgary and his colleagues, is called Equivalent Offset Migration, but, except for the fact that it is not velocity independent, it is essentially equivalent to what is described here.

Because this so-called velocity-independent approach is predicated on a constant velocity assumption, it and the Fowler method are to a large extent identical in the kinds of velocity models they produce. They are easily extended to 3D and can form the basis for automatic estimation of initial velocity fields, but they are for the most part PSTM methodologies. As we will see, the semblance-based approach in item 2 on page 254 has a natural extension to depth migration based migration velocity analysis (MVA) methods.

Migrated Common Image Gathers

There are at least four types of common image gathers that are suited to velocity analysis after migration. You can probably find many more, but for our purposes, the four we explain in this section will suffice.

Common Offset Migrated Velocity Analysis

The best known of these methods is Kirchhoff-based and produces migrated trace ensembles based on migrating common input offset volumes. The advantage of the Kirchhoff method is that we need not output every CIG during the migration process. Indeed, we can focus on local areas, coarse grids, target lines, or just about any form of output to use in the velocity analysis stage. The assumptions of this method are best summarized in Figure 10-5. It is clear that offset information has been transfered to the output point by simply shifting the source and receiver locations so that the new mid-point is the current image or output location. Figure 10-6(a) provides the scheme by which such offset gathers are produced.

Figure 10-5. Migration velocity analysis geometry

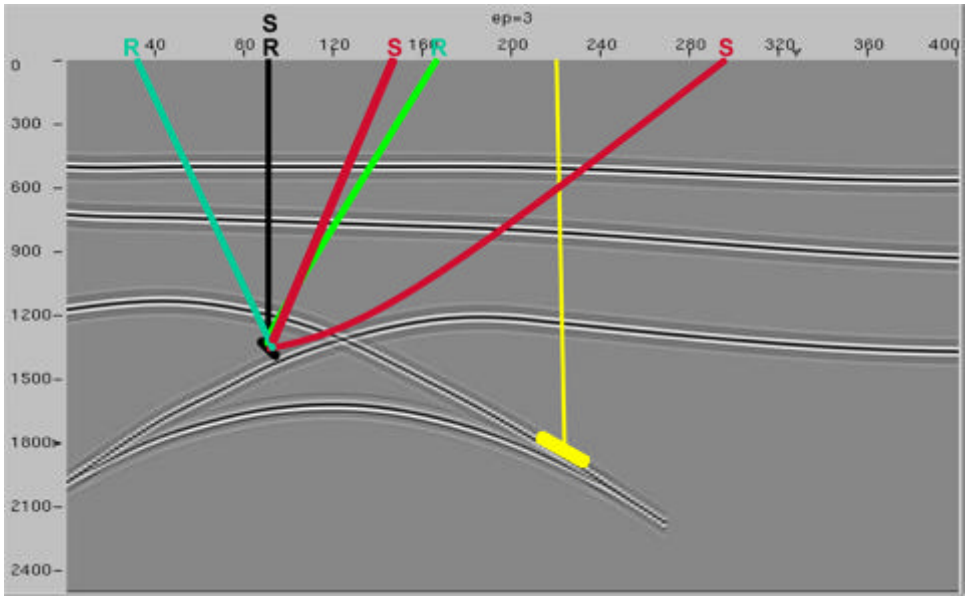

Figure 10-6(a) demonstrates the application of Kirchhoff migration on an offset-by-offset basis. Separating the output data by input offset means that we quite naturally produce input-offset gathers at each surface-defined image point. Such gathers are easily understood by processors used to thinking in stacking velocity analysis terms.

The Kirchhoff method is difficult but not impossible to extend to shot migration approaches. In the case of shot migrations, it is quite easy to produce three gather styles: Angle gathers, shot-profile migrated image gathers, and depth-focusing gathers. All three are based on time-shift, offset-shift, or vertical-shift gathers produced during the prestack migration stage. As we pointed out in the prestack algorithm chapter, these gathers carry information directly related to whether or not the velocity at any give point in the subsurface is accurate or not.

Common Angle Migration Velocity Analysis

Perhaps the best way to understand angle gathers is visualized in Figure 10-6(b). From a ray-theoretic point of view, we are holding the opening angle (or double the incidence angle) constant and producing output volumes parameterized by the opening angles. Relatively complex mathematics allows us to compute these gathers after the completion of the migration process but before removal of recording redundancy. An advantage of these gather styles is that they can convey considerable information about the kinds of analysis limits we might encounter prior to encountering them.

Figure 10-6. The three basic velocity analysis gathers

(a). Common-offset based Common Image Gathers (CIG)

(b). Common-angle gathers (CAG)

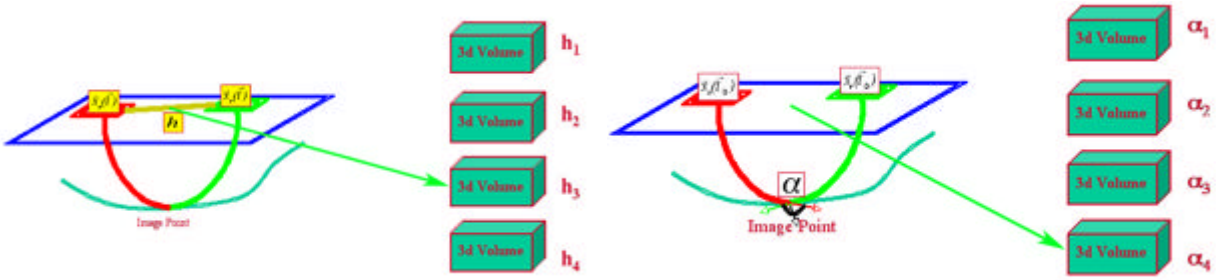

(c). Shot-profile migrated common image gathers (SMIGs)

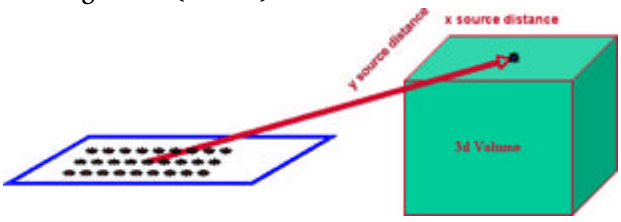

The production of common angle gathers as shown in Figure 10-6(b) is essentially the same as the process in (a). The difference is that, instead of holding the input offset constant, the process fixes the subsurface incidence angle to produce common angle gathers. Common angle gathers are certainly worth utilizing, but are somewhat difficult to use and are a bit costly to generate.

Shot Profile Migrated Image Gather Migration Velocity Analysis

Producing image gathers of any useful form from a set of shot-profile images hinges directly on the observation that after migration, the source and receiver are coincident. This fact is independent of migration algorithm—it does not matter whether the input data are migrated offset by offset, shot by shot, or common midpoint by common midpoint. When we migrate offset-by-offset and form common offset gathers based on the original input offset, we are assuming that the image point is directly below the midpoint of imaginary sources and receivers at half the offset distance on either side of the midpoint. Note that this also strongly implies that the migrated data have a fixed and common azimuth. We also expect this to produce precise velocity estimates.

Figure 10-6(c) represents what we call *shot-profile-common-image gathers*. A SMIG consists of all shots where the aperture contains a given fixed output image point. The migrated offset in this case is exactly half the distance from the image point to the source location for each trace in the gather. The reason for using half the distance will become clear in subsequent discussions. It is worth noting that SMIGs are not common receiver gathers. Since the fixed point is an output surface image location, they are true image gathers. They can also be three dimensional.

In the case of SMIGs, as depicted in Figure 10-7(a) and (b), we assume that, after the migration, the image point is directly below a source and receiver, and that it is again separated by a half offset, except that in this instance, the offset is the distance between the image point and the source. It is important to observe that these gathers are not common receiver gathers since surface receiver information is no longer available after migration.

Figure 10-7. Shot-profile-migrated common image gathers (SMIGs)

(a). Graphic explanation shot-profile-migrated common image gathers are formed

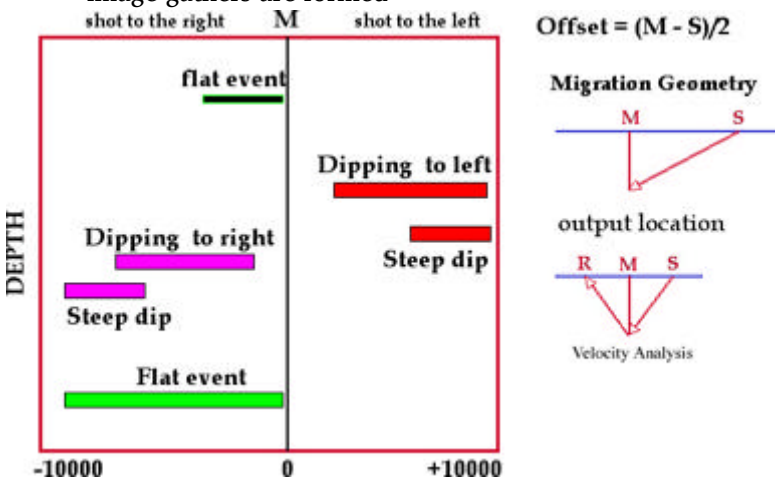

(b). Example shot-profile-migrated common image gather

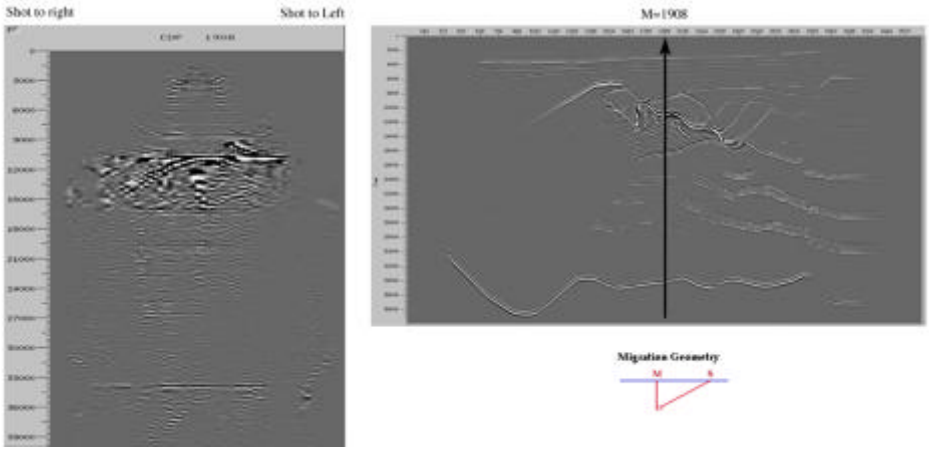

Depth Focusing Migration Velocity Analysis

Depth focusing analysis gathers are essentially the information used to produce angle gathers. They can be formed from either the time-shift or the offset-shift imaging conditions, or even vertical depth-shift imaging conditions described in the section on shot-profile migration.

Figure 10-8 illustrates the process. Part (a) is a cartoon of forward shot propagation, while (b) is a similar figure for the backward propagation of the receiver data. By shifting the arrivals vertically, laterally or temporally, we produce information that can be analyzed to find the maximum energy in the arrival.

Figure 10-8. Key Elements of depth focusing analysis.

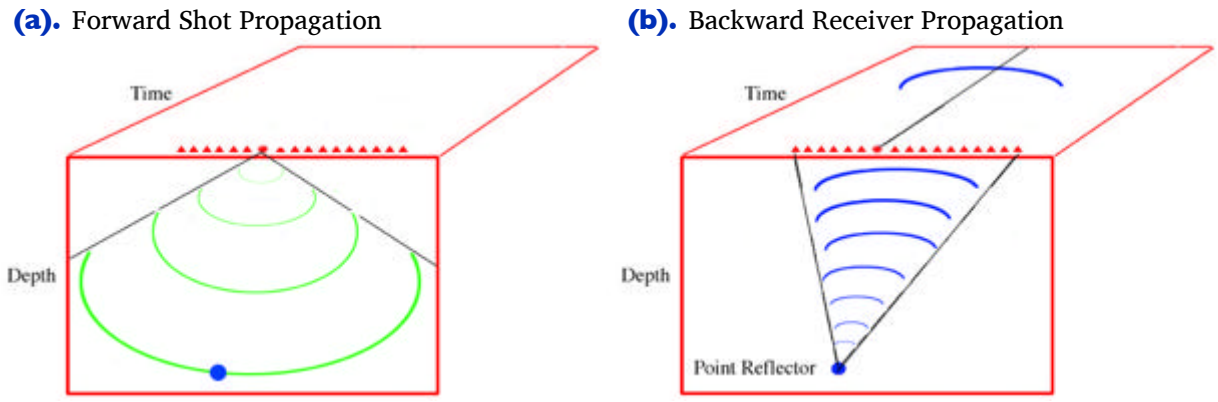

Figure 10-9(a) shows gathers produced by a time-shift imaging condition. The horizontal axis in this figure is depth and the vertical axis is time. Part (b) shows the relative depth shift from a fixed position. If the velocities at each depth are correct. the maximum energy arrivals will line up at zero time.

Figure 10-9. Depth Focusing Analysis. (After S. Mackay and R. Abma)

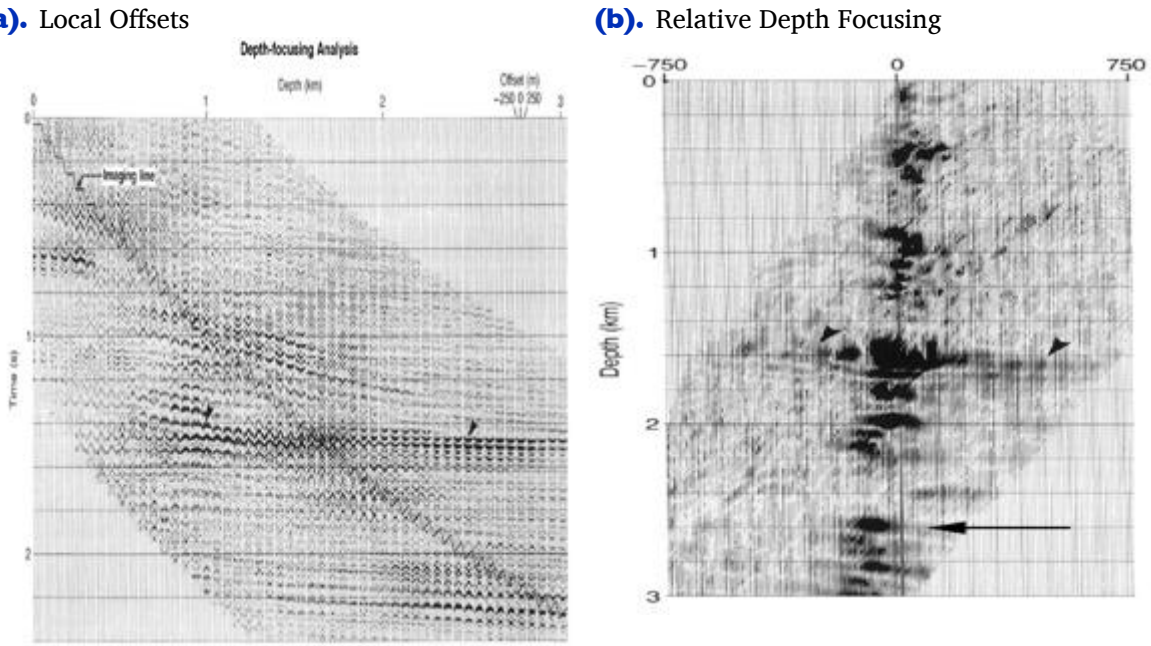

Semblance-Based Isotropic MVA on CIGs, CAGs, and SMIGs

Figure 10-10(a) shows common input offset image gathers generated by migrating each input sorted offset with a most energetic arrival Kirchhoff algorithm. Figure 10-10(b) shows common azimuth generated common angle gathers and associated common angle semblance panels. The angles range from 0 to 60 degrees in increments of 2 degrees.

Figure 10-10. Common input offset and common angle gathers.

(a). Input offset Kirchhoff common image gathers

(b). Input offset common azimuth common angle gathers

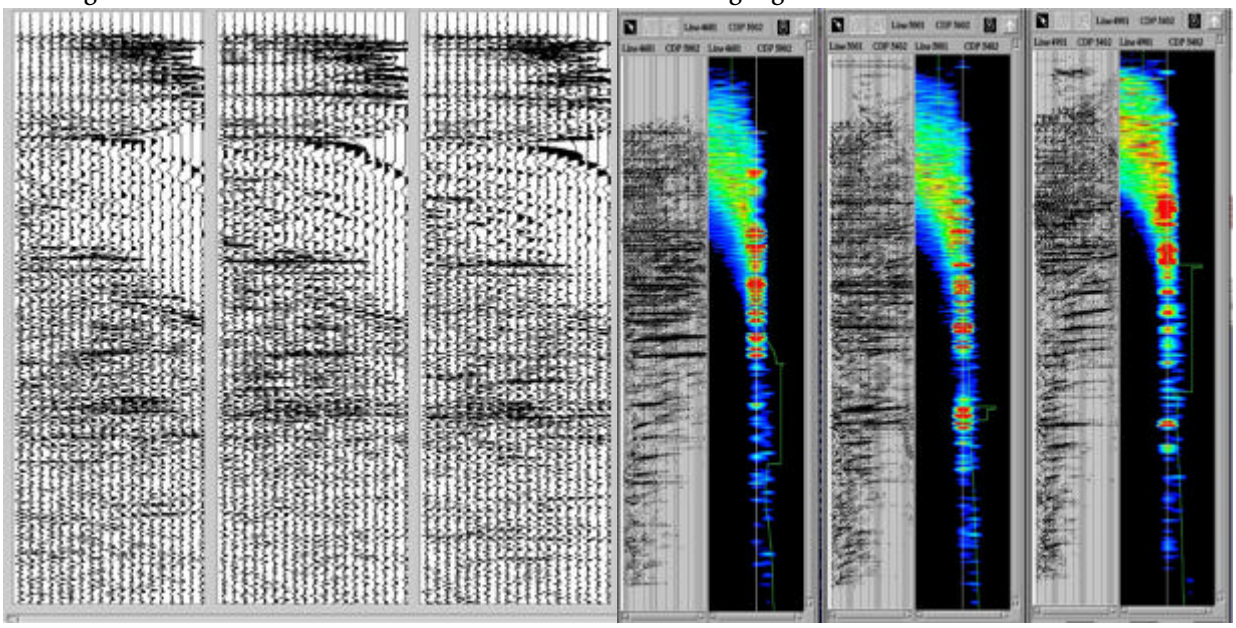

Figure 10-11(a) visualizes the kind of information angle gathers provide in sediments as compared to subsalt settings. In (a), the general loss of angle information is gradual as depth increases. In contrast, (b) shows that the loss of angle information below salt (or any high velocity anomaly) is quite dramatic. This is one reason angle gathers might be preferred over other forms of velocity analysis.

Figure 10-11. Common angle gathers. Sediments versus Salt

(a). Angle Gathers in Sediments **(b).** Angle Gathers below Salt

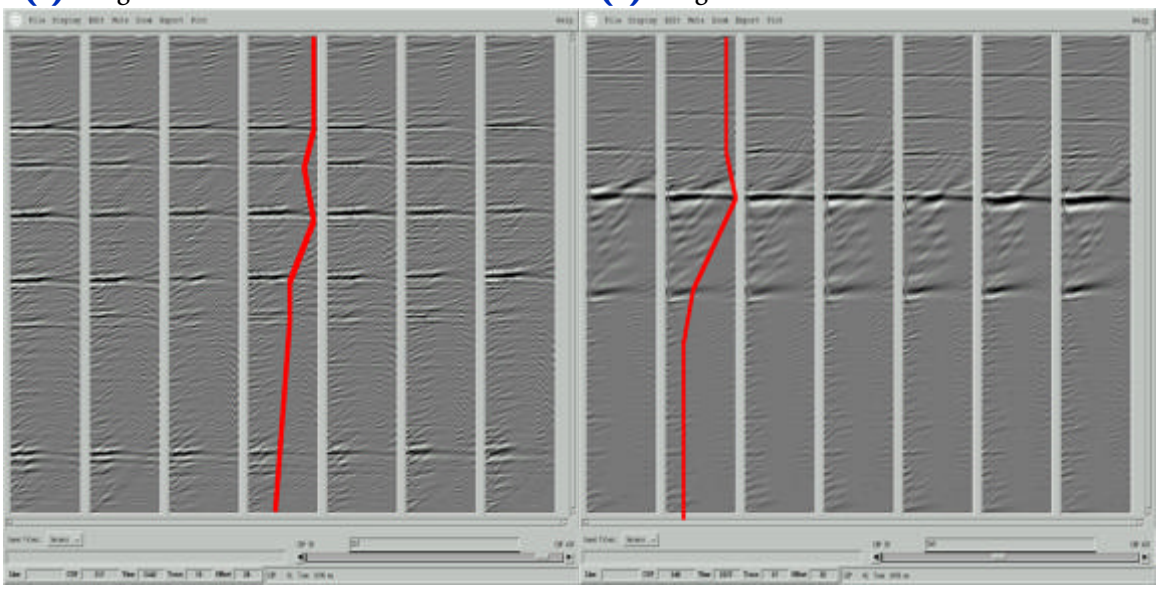

The velocity analysis/inversion formulas for estimating velocity models from either offset or angle gathers are shown in Figure 10-12. Note that the difference occurs because, in the old case, the method estimates velocity without any knowledge of the velocity used in the migration process, while in the new case, that information must be available. Regardless, both methods are based on producing a maximum energy or semblance display that can be directly picked to refine velocity estimates.

Figure 10-12. Angle Gather Velocity Analysis

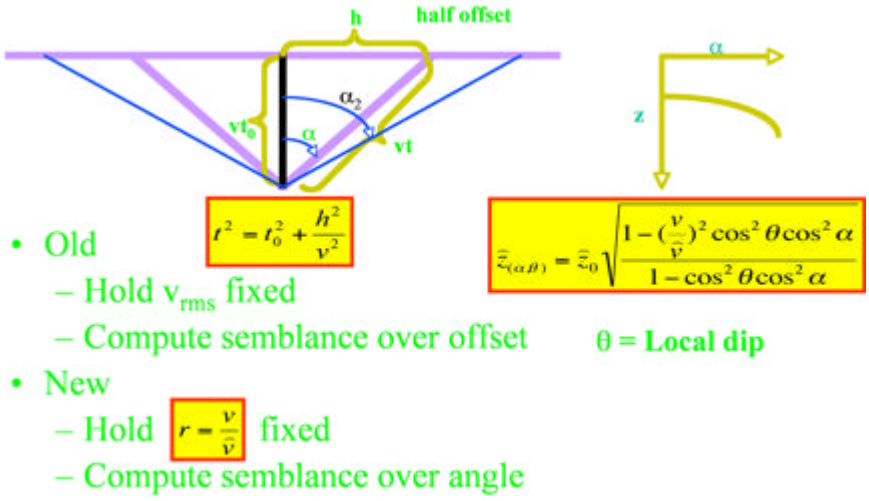

Whether we use $z(\alpha,\beta)$ or Equation 10-1, estimating v is usually based on semblance panels calculated from Equation 10-2 or Equation 10-3.

(10-1) $$t(v,h) = \sqrt{t_0^2 + \frac{h^2}{v^2}}$$

(10-2) $$s(t(v,h)) = \frac{\left(\sum_h d(x_s, x_r, t(v,h))\right)^2}{\sum_h d(x_s, x_r, t(v,h))^2}$$

(10-3) $$s(\alpha,\beta) = \frac{\left(\sum_h d(x_s, x_r, z(\alpha,\beta))\right)^2}{\sum_h d(x_s, x_r, t(\alpha,\beta))^2}$$

In this case, s is bounded between 0 and 1, but velocity at any given t or z is taken to be the value that maximize the semblance. In spite of the fact that theory underlying these equations assume flat lying reflectors, they have proven to very useful in development of seismic imaging velocity models for both time and depth imaging.

Figure 10-13(a) includes images of a depth-to-time converted SMIG, a semblance panel computed from the SMIG, the current section under analysis, and the velocity model under construction. The process of actually doing the velocity estimation is shown in Figure 10-13(b). From left to right, we see the raw depth-to-time converted SMIG and semblance panel, the picked SMIG with hyperbolic trajectories and semblance panel, and the moveout SMIG with semblance panel. This figure confirms that SMIGs can be used for migration velocity analysis and also demonstrates the current semblance based analysis process for developing short-spread velocity models.

Figure 10-13. Common image gather velocity analysis

(a). SMIG Gather, semblance panel, in progress work section, and estimated velocity model

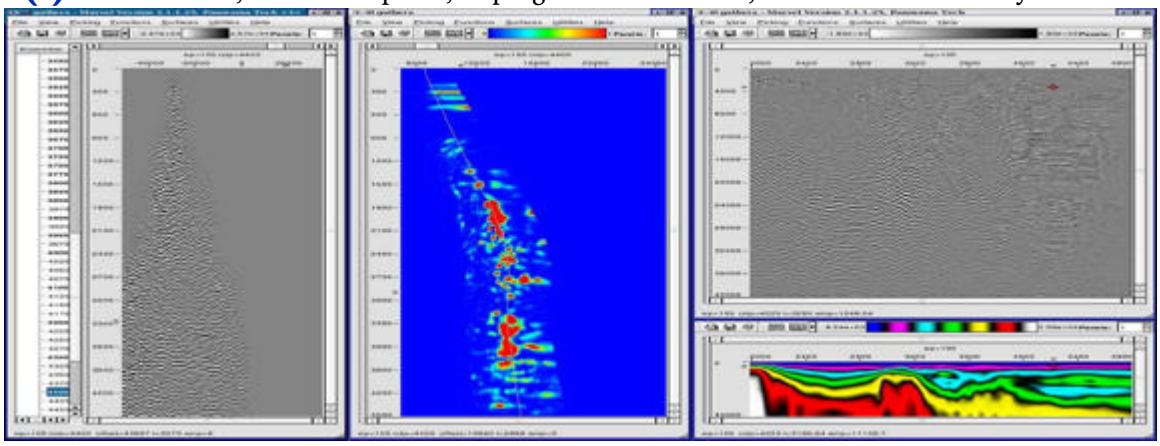

(b). Common image gather velocity analysis

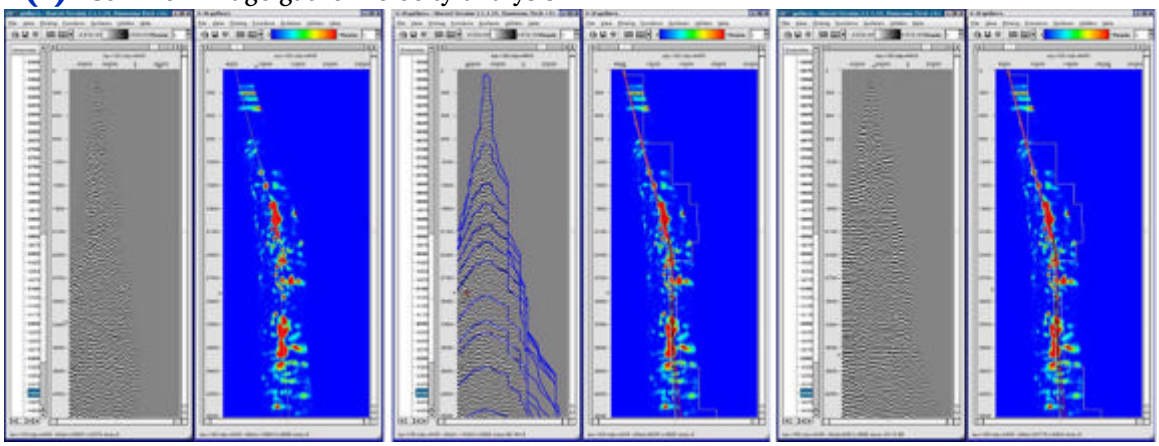

Figure 10-14 compares a common-midpoint gather, a common-midpoint gather with DMO, and a Kirchhoff depth migration common-image gather to assess the impact of partial and full migration, at least visually. The red line in the DMO stacks in (a) and (c) indicate a location where a CIG was selected for comparison. Part (a) is from an area where subsurface horizons do not dip severely, while Part (c) is from an area where subsurface horizons do dip severely. If our interpretation of the theory is correct, there should be little change in our velocity picks at (a), but considerable change for those at location (d). Changes from stacking velocity to DMO stacking velocity to migration velocity picks should be minimal in the former case and much more noticeable in the latter.

Figure 10-14. Barents Sea velocity analysis over flat and dipping horizons.

(a). Location of a CIG with relatively flat horizons

(b). Location of a CIG with steeply dipping horizons

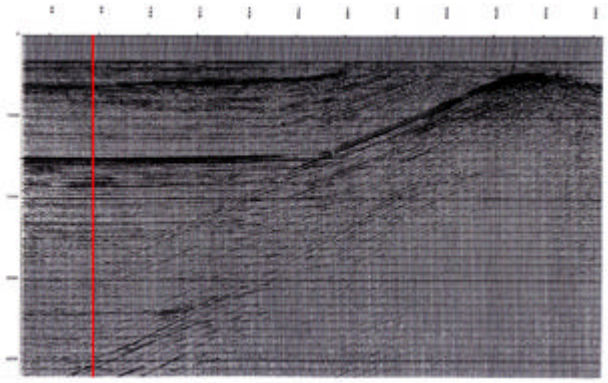

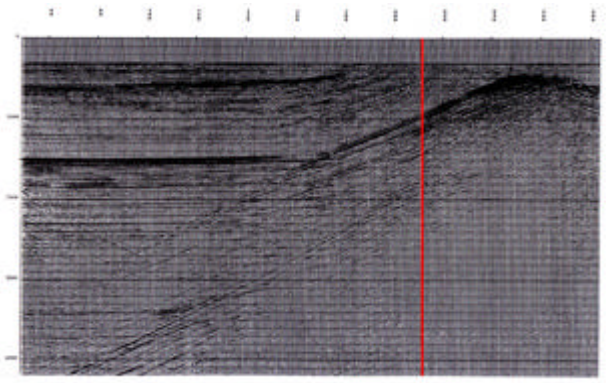

(c). Stacking, DMO, and Kirchhoff CIG semblance at (a)

(d). Stacking, DMO, and Kirchhoff CIG semblance at (b)

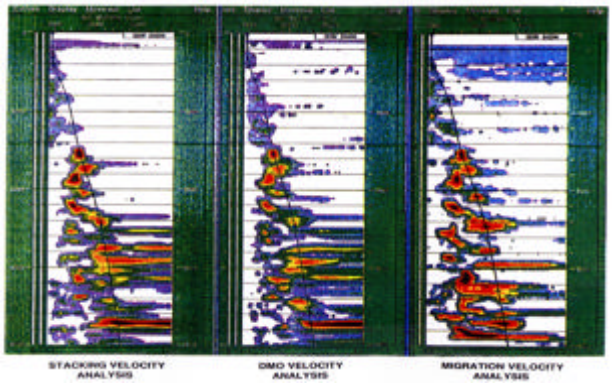

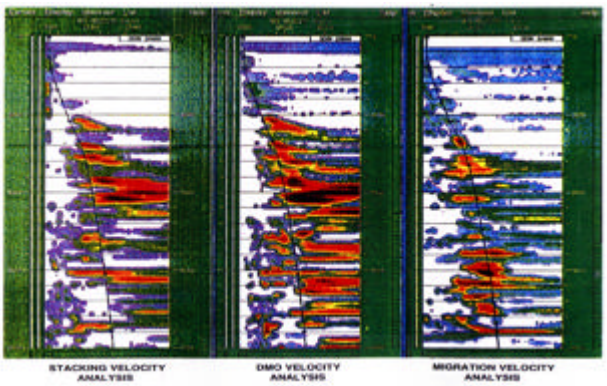

Figure 10-14(c) shows the picked curve from the migration analysis panel in (a) overlaid on the DMO panel and stacking velocity semblance panels. Note that while the panels differ in character, there is little reason to change the overall set of picks from one panel to the other. The theory seems to be reasonably solid when the horizons are flat.

In contrast to Figure 10-14(c), the picks in the panels in (d) are significantly different from each other. Even the DMO corrected panel in the middle, while better, is still

significantly different from the Kirchhoff migrated common-image gather. We would certainly be inclined to argue that stacking and DMO based velocity estimates are inferior to those obtained from this Kirchhoff based depth migration algorithm.

Figure 10-15 shows the result of three iterations of what we will ultimately call the *painless* approach to velocity model building. No horizons were used to estimate the migration velocity. While more modern migration algorithms may produce improved images, the common-image gathers are flat, and, in spite of the inability to image the base of salt, the process clearly works, even in areas where the geology is complex and the rocks are hard.

Figure 10-15. Full prestack depth migration of the Barents Sea data.

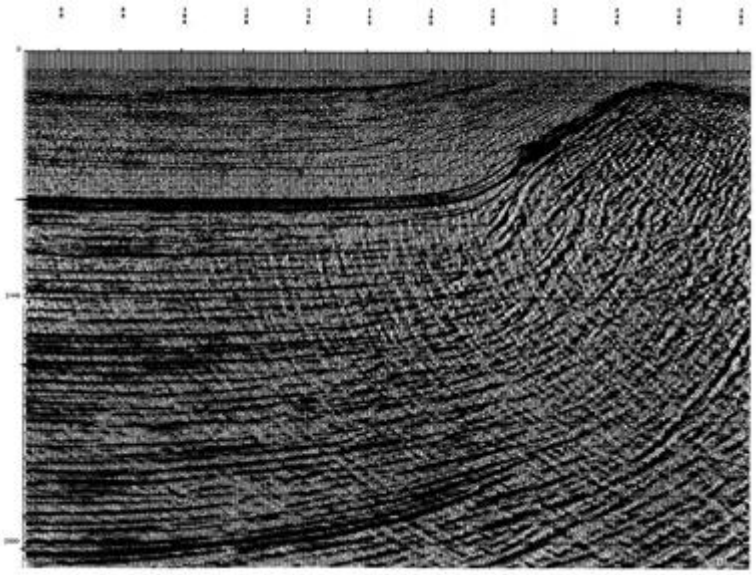

Painless (No Horizons) Velocity Model Construction

Figure 10-16 shows a typical velocity analysis-velocity model building workflow. This sequence of processes is typically used to convert data-driven-time dependent-stacking velocity estimates into depth-interval or time-RMS velocity volumes. In the painless approach, this process is carried out on flat-lying horizons, and is usually referred to as vertical updating or the Deregowski method. Since we are using a migration algorithm in an attempt to properly position events prior to velocity analysis, local dip information is usually an issue only when the lateral velocity variation is strong.

Figure 10-16. A no horizon based velocity analysis workflow

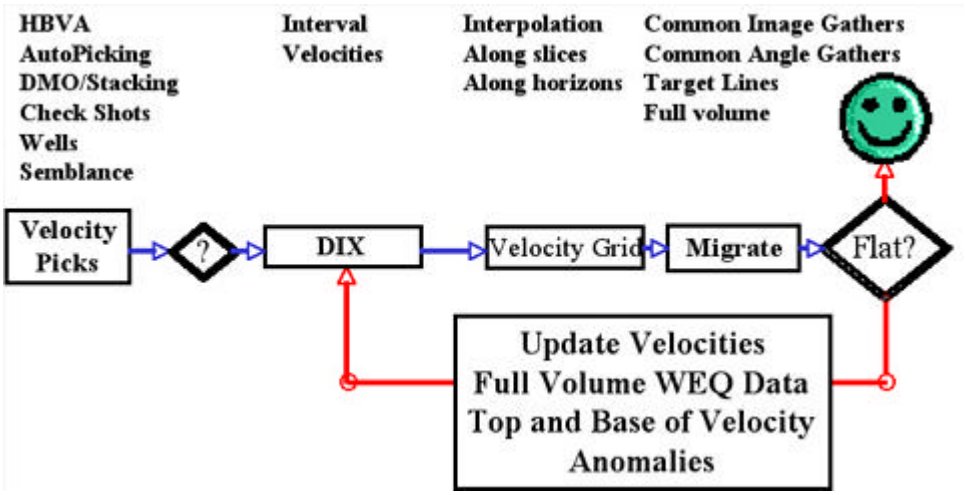

Figure 10-17 provides one approach to horizon-less velocity model construction. The idea is to directly map Dix intervals to an array of flat horizons at a user-selected fixed depth increment. Note that this Dix conversion is taking place on migrated gathers, and so should produce velocities at locations that are close to the true migrated positions. These intervals are then interpolated to a 3D model along these horizons, where a great variety of interpolation methods can be used. Such interpolation methods range from simple inverse-distance weighting to Gaussian direction oriented balls, or in some cases geostatistical prediction approaches.

Figure 10-17. Painless (no-horizon picking) approach to velocity model construction.

(a). Equally spaced flat horizons for painless picking

(b). Picked set of semblance panels

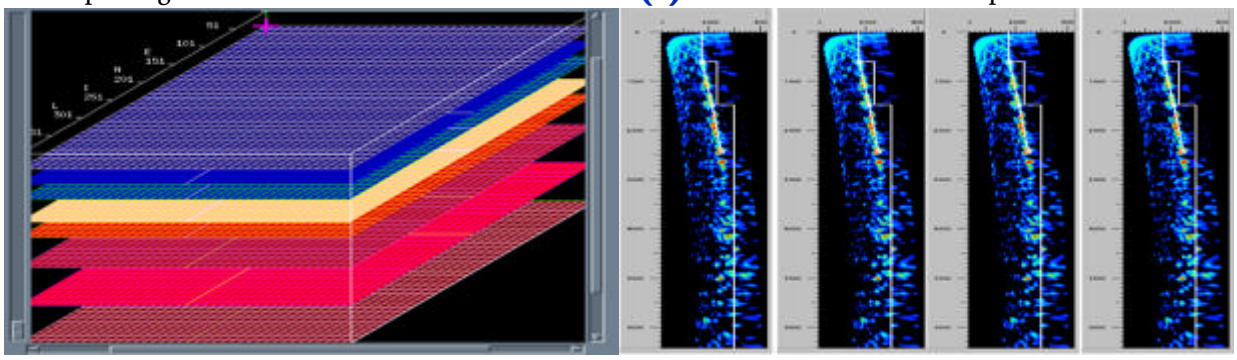

(c). Slice through the model from the initial velocity analysis

(d). Slice through the final velocity model

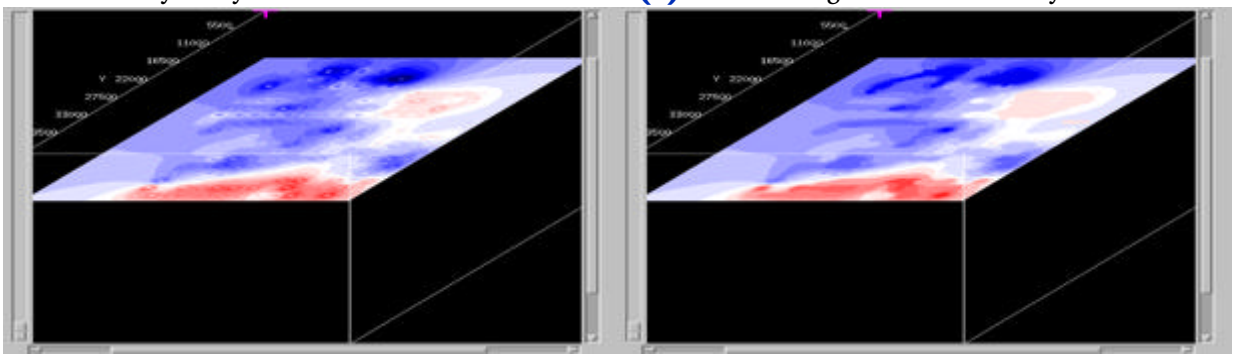

We can summarize the painless approach as follows: Begin with semblance panels like those in Figure 10-17(b). These can come from stacking velocities or velocity independent time migrations, or from depth migrations using any reasonable velocity field. When picking is complete, interpolation is used to *snap* Dix-interval velocities to each flat horizon. An example of the result of the interpolation is shown in Figure 10-17(c). The noticeable *bulls eyes* are intentional. The interpolation process was modified to ensure that these errors would produce an easy visualization of the location of the spatial velocity grid. In this case, the velocity gradient (blue to red) reflects a significant velocity change across a fault zone. No horizons were used in this process, but the velocity model still reflects local geology. Figure 10-17(d) shows a final velocity slice after three iterations. Again, the effect of geology is clearly evident in this graphic.

Figure 10-18(a) shows an initial velocity model generated using a single well hung from the water bottom. The water bottom horizon could come from a high-resolution analysis of the sea floor or from a shallow depth migration with water velocity. Typically, the well information comes from a well within the area extent of the seismic survey. In some cases, the resulting velocity field may be adjusted (sped up or slowed down) to account for depth discrepancies observed in other imaging projects.

As shown in Figure 10-18(b), MVA on CIGs can be used to painlessly update the initial well-derived velocity model. The model in (b) can then be used to perform a salt flood as shown in part (c). After the top and base of salt is determined, they can be directly inserted into the MVA updated model to obtain the final salt filled model in (d).

Figure 10-18. Well driven marine (Gulf of Mexico) velocity analysis

(a). A $v(z)$ hung off the water bottom

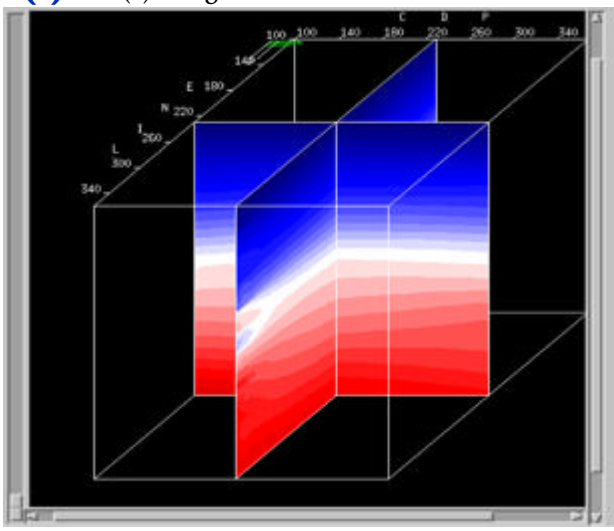

(b). Painless velocity update

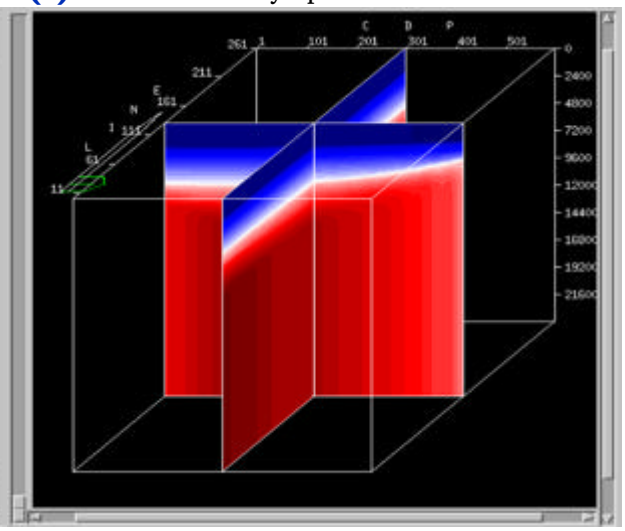

(c). A “salt flood” migration

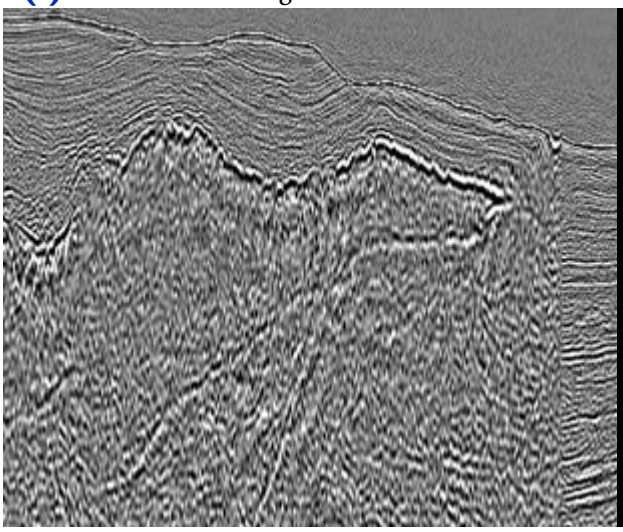

(d). Salt body insert

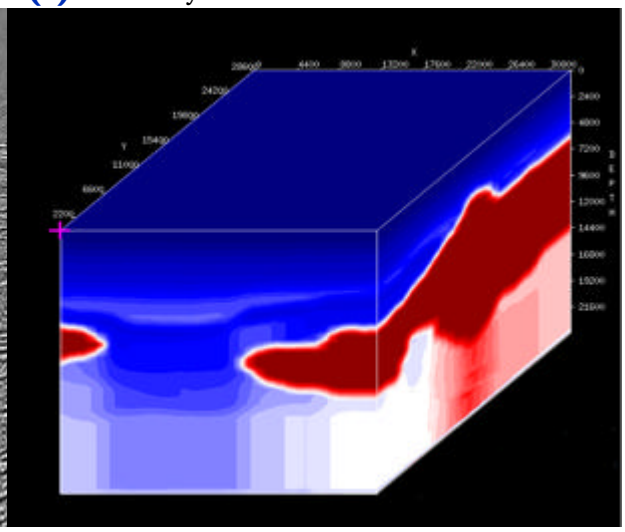

Figure 10-19(a) is a final image based on the process described in Figure 10-18. This volume was the result of a common azimuth migration. Note the excellent definition of the top, the base, and the subsalt reflectors. The associated flat image gathers in Figure 10-19(b) show that the painless approach to Earth model estimation can be quite successful.

Figure 10-19. Full volume common azimuth migration and associated image gathers.

(a). Full volume common azimuth migration

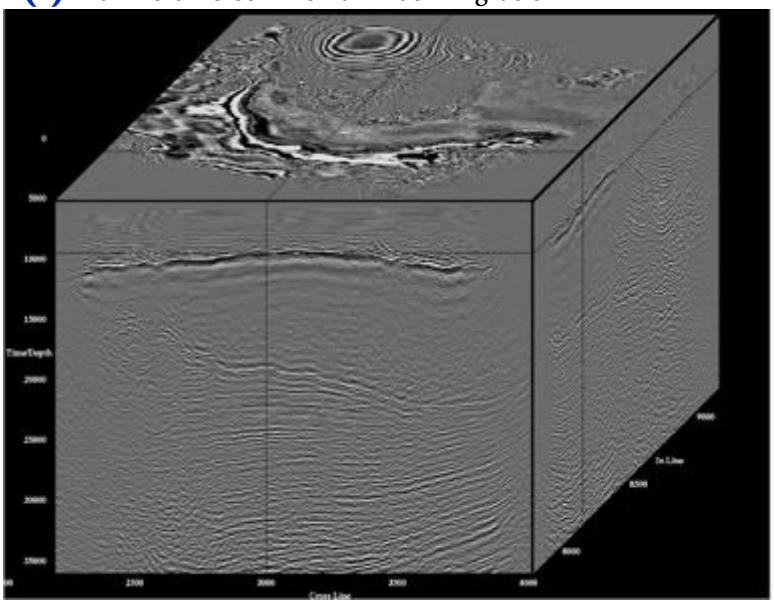

(b). Common image gathers from the migration in (a)

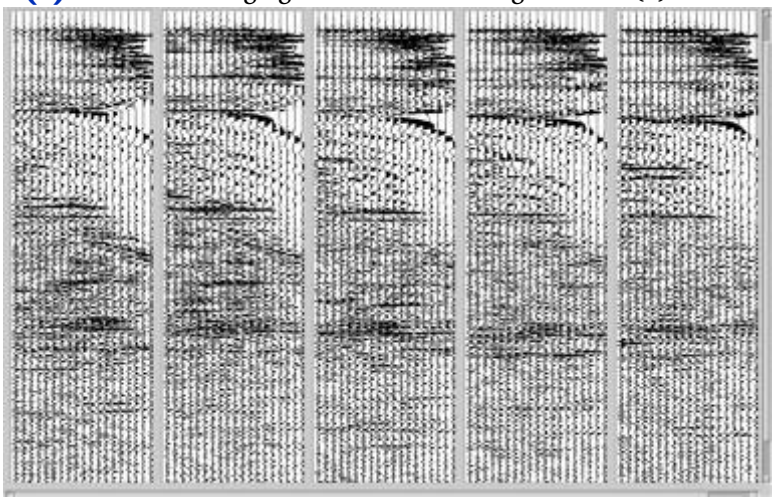

As detailed in Figure 10-20 (b), prestack time imaging can frequently be done using the painless approach with automatically picked CIGs. When the input data is of high quality, automatic picking can be a useful tool to both assess the need for preprocessing and to quickly provide a useable image.

Figure 10-20. Automatically picked prestack Kirchhoff time migration.

(a). Autopicked CIGs **(b).** Prestack time migration via autopicking

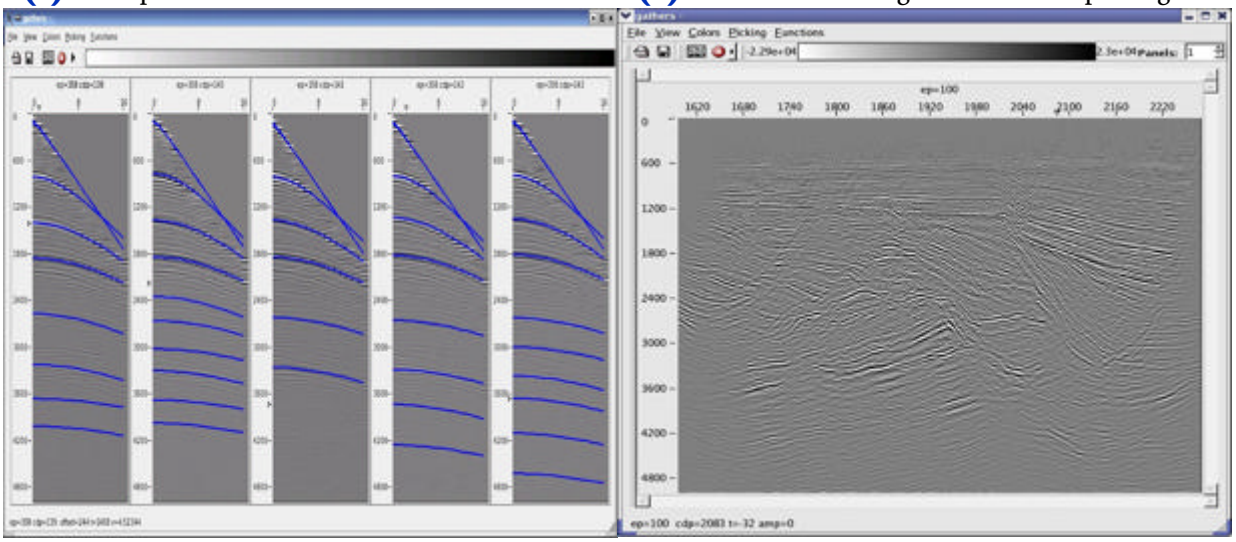

Horizon-Based Velocity Analysis

So the question is: *Do we ever need horizons?*

In some sense, the answer is driven by how well we can flatten the gathers we output from the Deregowski loop. It is great when the painless method does a good job of flattening the gathers because horizons certainly create a plethora of problems in an iterative scheme for velocity estimation. We would like to avoid these problems in all situations. Horizons change shape and position every time a new Earth model is part of a re-migration of the original input data. The processor is then either forced to reinterpret a new set of horizons or to edit the existing set prior to another iteration of velocity analysis. It would certainly be nice never to have to worry about horizons. There are also geologic environments where horizons are just as useless as the painless approach in those environments, but it is also probably true that in this kind of regime, nothing will produce acceptable results.

There are certainly many geologic settings where the use of horizons is absolutely necessary. Horizons are essential when strong, visible velocity anomalies, such as salt domes and sills, are present. The tops, sides, and bottoms of these visible bodies are

interpreted, defined as horizons and inserted into an existing Earth model. Figure 10-21 shows how the top of salt is interpreted in a salt flood exercise.

Figure 10-21. Horizon interpretation for a salt flood.

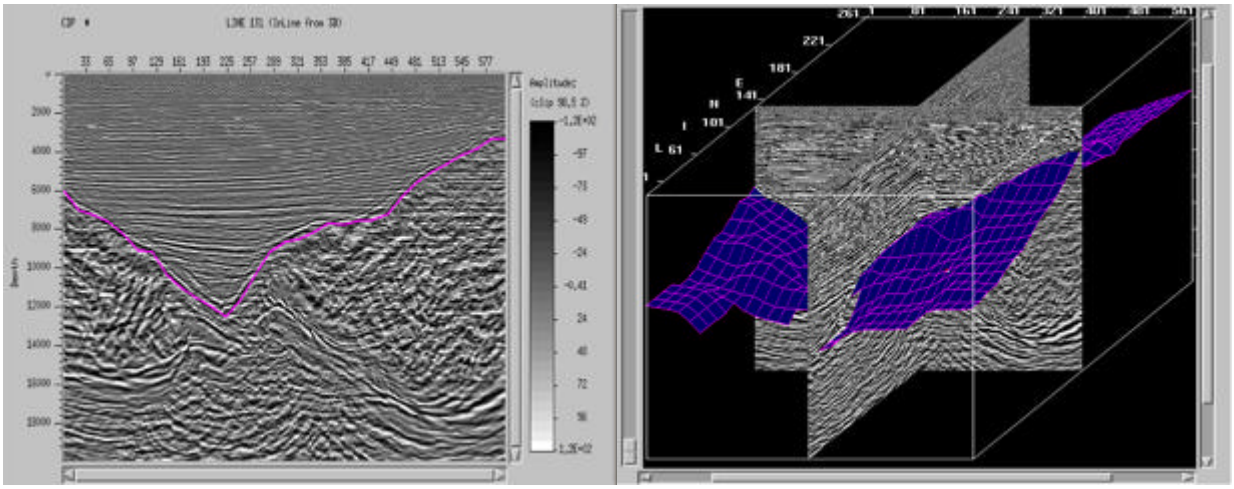

Horizons are probably also essential when velocity anomalies are invisible. In this case, we cannot interpret the tops, sides and bottoms, so horizons above and below the suspected area are the only option. In certain geologic settings, most notably in areas with strong carbonate bedding, fast velocities within relatively thin sections require utilization of interpreted horizons to produce adequate estimates of the velocity within the bedding planes. When data-based estimates are insufficient, horizons may also be useful as control surfaces allowing constant velocity insertion between specific layers to define a more accurate Earth model. Perhaps the most important setting where horizons are required is when it becomes clear that the painless approach has failed miserably. In this case, it is probable that an attempt to apply tomographic inversion will also be recommended. However, there are always exceptions to almost every rule. In geologic environments where subtle velocity variations are not easily seen, we may have to resort to more extreme approaches. This would definitely include very fine horizon based velocity model construction along with full utilization of tomography.

Figure 10-21 is an illustration of the interpretation of horizons on top of a base of salt. This kind of interpretation is also necessary for certain kinds of residual tomography. Typically, a reasonable set of horizons provides tomographic inversion with precisely the information necessary for success. It is not necessary to be as accurate as we might be for prospect generation, but it is necessary to define as many horizons as possible.

Once horizons have been defined, velocity picking can be done along the horizons themselves. While this should produce horizon consistent velocities, vertical updating through the Dix equation is still necessary to provide the required interval velocity estimates above the horizon under analysis.

Figure 10-22 shows the kind of model produced from a typical horizon based approach. It is difficult to believe that the blocky nature of this model is realistic. Because they use high frequency approximations, raytracers have considerable difficulty calculating accurate traveltimes unless the model is smoothed. The only real way to avoid the blocky nature evident in this image is to interpret a large number of densely spaced horizons or to insert a large number of invisible horizons between relatively sparse sets. Interpreting a large number of horizons requires a considerable amount of human time and cost. Interpolation of a fine set of horizons between sparse data seems to be moving back toward a more painless methodology. However, in situations where compaction plays an important role in vertical velocity variation, forcing the velocity structure to follow horizons when they are not the chief defining factor can be disastrous.

Figure 10-22. A horizon based velocity model

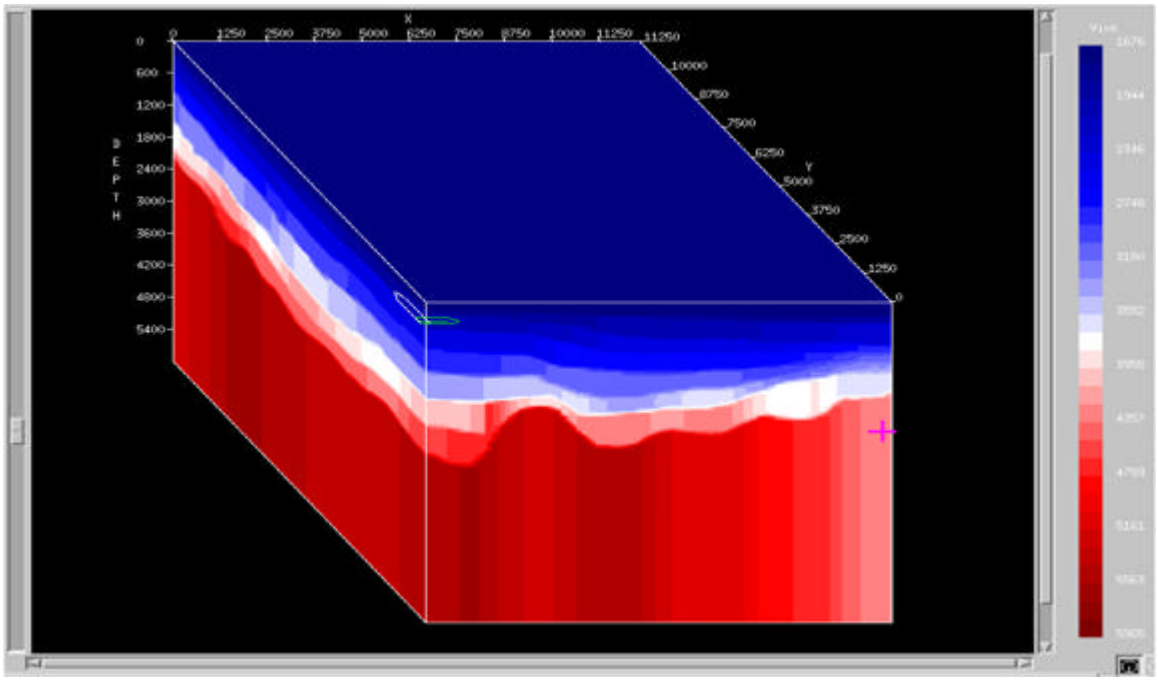

In Figure 10-23, we see a set of gathers that have been through several iterations of vertical or Dix updating. Note that the gathers on the right are reasonably flat while those on the left are not flat. Because these gathers produce poor images when stacked, this phenomenon cannot be improved by traditional horizon-based vertical methods. This three-dimensional effect was ultimately resolved only by careful application of tomography. While there are many approaches to tomography, recent experience has shown that residual methods work best. Residual approaches are usually applied only after an initial migration velocity volume is available. They also normally require reasonable information about local dip, which can be obtained from a horizon-based approach, or by direct estimation of the local dip from the current image, or from specific geologic knowledge. Since horizon-based methods tend to offer better accuracy than direct automatic estimation, we restrict our attention to that methodology. Note that this implicitly assumes some form of geologic interpretation of the study area.

Figure 10-23. Non flat gathers.

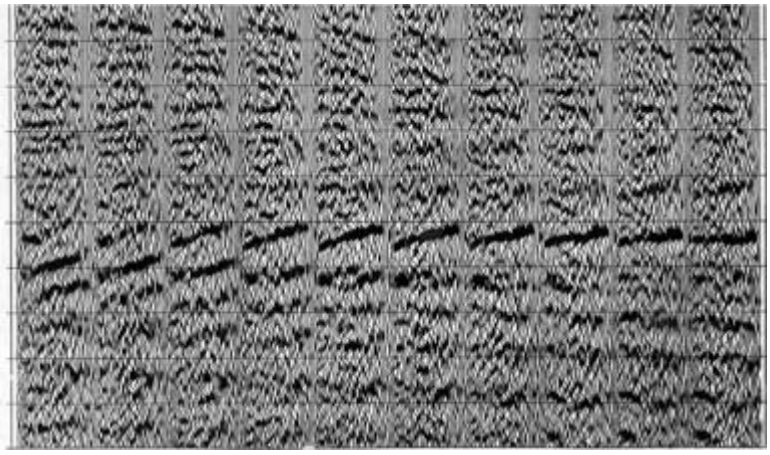

Figure 10-24 shows a typical horizon-based velocity analysis–velocity model building workflow. This sequence of processes is almost identical to that in Figure 10-16 on page 270, except that velocities are “snapped” to user-defined horizons rather than to an equally spaced set of flat horizons. Perhaps one benefit to this kind of analysis is that once the process has reached a stationary point, all the necessary information required to apply tomography is in place.

Figure 10-24. A horizon based velocity analysis workflow

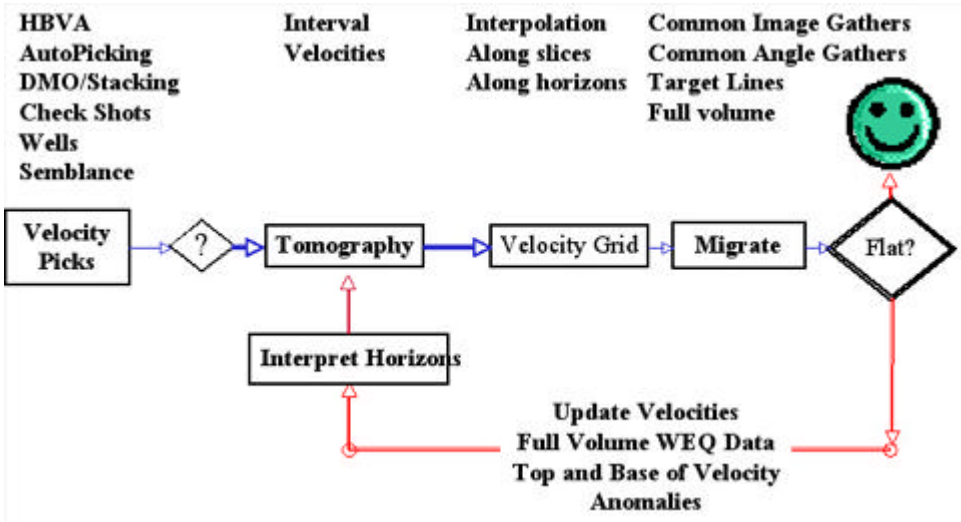

Residual Tomography

The basic geometry of residual-seismic tomography is explained by Figure 10-25. We see two source-image-point-receiver raypaths, one in red at a short offset and one in green at a longer offset,. These raypaths represent the migrated location of a reflector at each of these offsets. As each of these rays pass through the cells of the gridded model, it is possible to calculated the total distance traveled from source to receiver for the current migration velocity model.

Figure 10-25. Tomographic Geometry

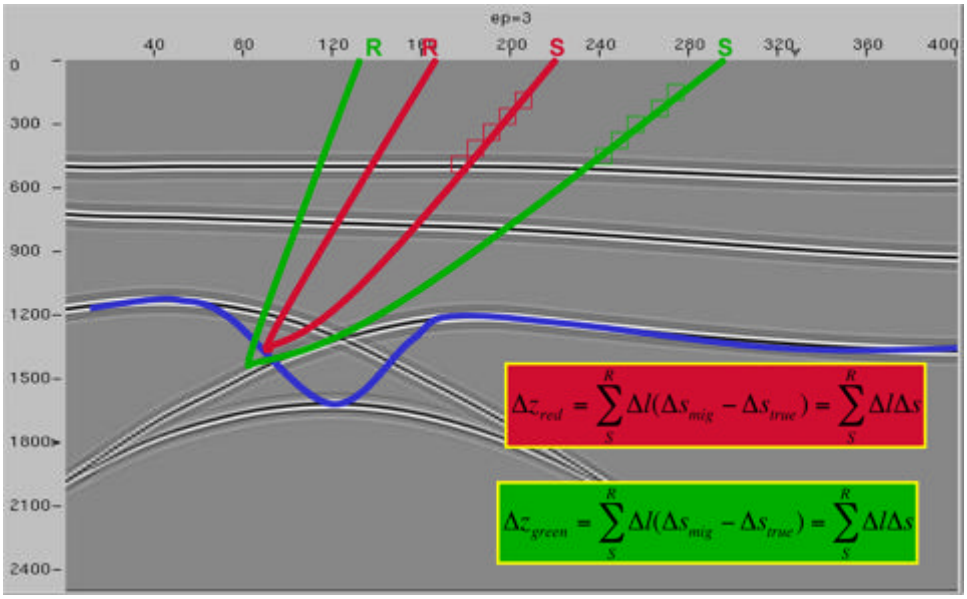

Whether calculated for the red or the green ray, that distance, d, is given by Equation 10-4, where Δl is the length of the ray in any given grid cell and Δs_{mig} is the actual migration velocity in that cell.

(10-4)
$$d = \sum_{S}^{R} \Delta l \Delta s_{mig}$$

What we are interested in finding is the true velocity, Δs_{true}. To do this, we calculate Δz for each ray path in the model using Equation 10-5.

(10-5)
$$\Delta z = \sum_{S}^{R} \Delta l(\Delta s_{mig} - \Delta s_{true})$$

Note that we can measure Δz for each horizon on a CIG, and so we assume we know this value for each and every possible ray. Algebraically, Equation 10-5 is a matrix equation

of the form shown in Equation 10-6, and it can be solved for Δs.

(10-6) $$\mathbf{A}\Delta\mathbf{s} = \mathbf{Z}$$

Once Δs is known, computation of s_{true} is straightforward.

In many respects, seismic tomography is very similar to common computer aided tomography (CAT) scans. The primary difference between the two is that CAT scans record purely transmitted energy, while seismic tomography is reflection based. Computer aided tomography reconstructs an image of human tissue by back projecting recorded transmission energy over a straight line. Seismic tomography back projects over a reflection cone. Seismic tomography is also a residual technique. It does not use directly recorded information to estimate the Earth model, and is always based on information extracted from an existing imaging exercise.

Figure 10-26(a) is an example of residual tomography as it would apply to residual offset dependent depth differences at two line and crossline locations. The figure shows back projected ray bundles indicating changes in velocity as a function of offset from the central line and crossline location.

Figure 10-26. Fundamentals of residual tomography

(a). Tomographic back projection

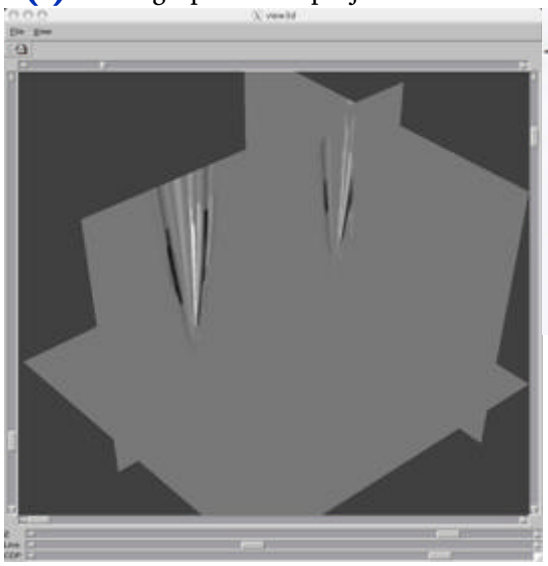

(b). Tomographic geometry

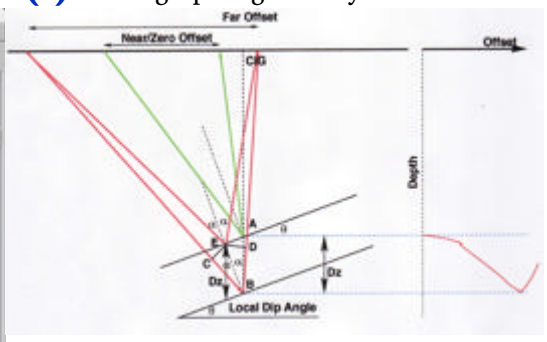

Residual tomography, as shown in Figure 10-26(b), is based on the assumption that after a prestack depth migration with velocities that are close to each other, lateral positioning of subsurface events will also be close to correct. This being the case, we can relate differences in depth differences as a function of offset to a residual velocity or slowness increment needed to make the arrival on the common image gather flat. To do so, we need to have reasonable estimates of the local dip everywhere in the volume

being analyzed. In this figure, the correct or reference dip is measured correctly at the offset determined by the near zero-offset trace (the green rays). What we measure is the residual depth difference at some other offset (the red rays). If we know the local dip, all this information can be related to a change in velocity that forces the next migration to produce much flatter common-image gathers.

Thus, the input required to perform a residual tomographic inversion is:

- a reasonable migration velocity field
- a picked set of residual depths
- a good set of horizons or some other method for estimating local dip. If horizons are used, there should be as many horizons as possible.

Figure 10-27 shows what we need to measure to have the proper information to use the method outlined in the previous figures. The right hand side of this figure is a common-image gather after a migration with an incorrect velocity. Note that the curved arrival is close to parabolic or even hyperbolic in shape, but is definitely not flat. The curved green line marks residual depth differences in reference to the shortest arrival. Because the arrival curves down, we know that a velocity above the horizon is too slow to properly correct the horizon at all offsets. Had it curved upward, the velocity in question would have been too fast. Knowing that the velocity is too slow is one thing, but knowing where it is too slow is another thing entirely. What residual tomography does is use redundancy of estimation to determine where to change the velocity to produce flat arrivals. This means that to be effective, tomographic inversion must have sufficient redundancy to do its job. This, in turn, means that we must solve a huge tomographic problem. It also means that a good tomographic solver will have been designed to work from automatically-picked residuals.

Figure 10-27. Residual depths as input to tomography.

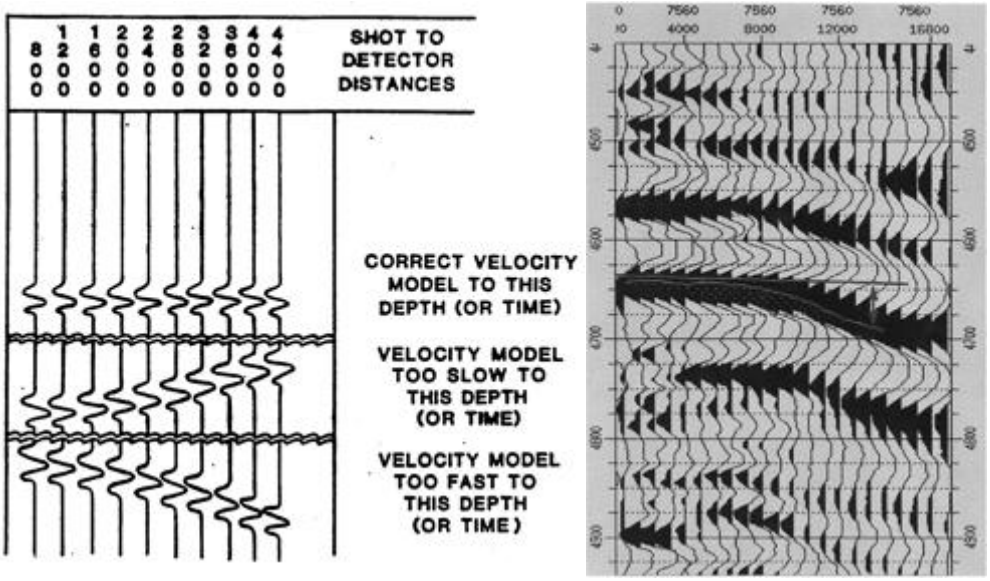

Figure 10-28 is an example of the use of automatic dip estimation and flattening on a set of CDPs from the SEG AA′ data set. Parts (a) and (b) of this figure are illustrative CDPs and their flattened counterparts. Figure 10-28(c) is the result of stacking the entire suite of CDPs in the line.

Figure 10-28. Automatic dip estimation, flattening and stacking.

(a). SEG AA′ Gathers before dip

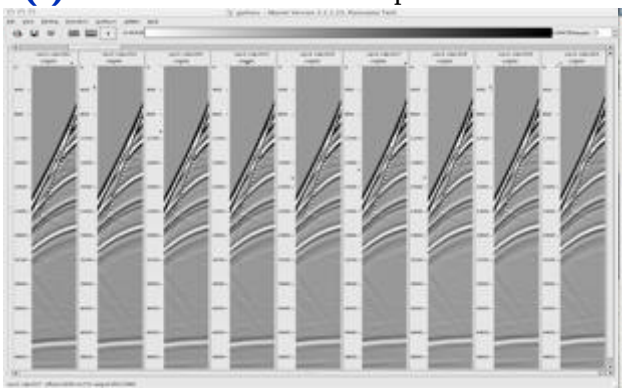

(b). SEG AA′ Gathers after dip

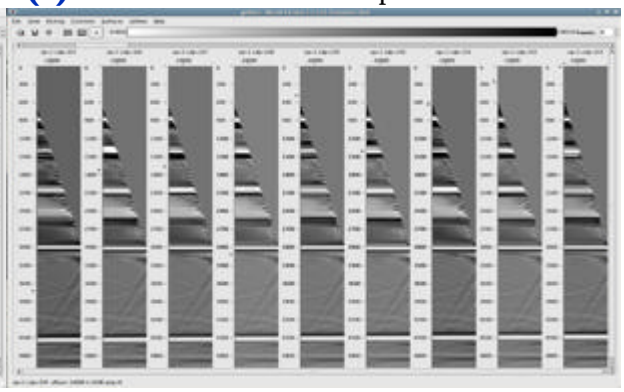

(c). SEG AA′ Auto Stack after dip

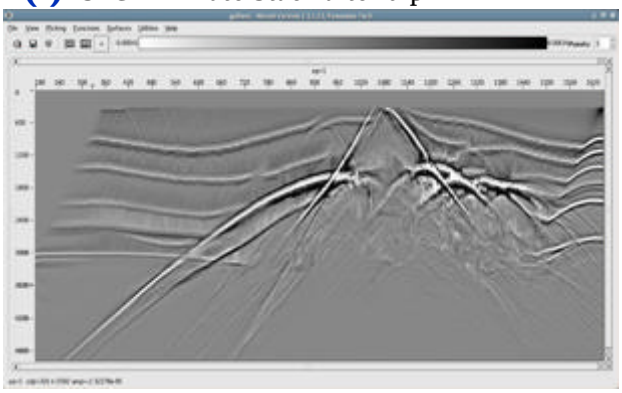

Figure 10-29 is for illustrative purposes only. Residual depths are estimated along horizons. Clearly there is no need for residual tomography at these locations. The colored lines just indicate the depths at which horizons intersect each offset plane.

Figure 10-29. Residual moveout along a horizon. This is Horizon Based Velocity Analysis or HBVA.

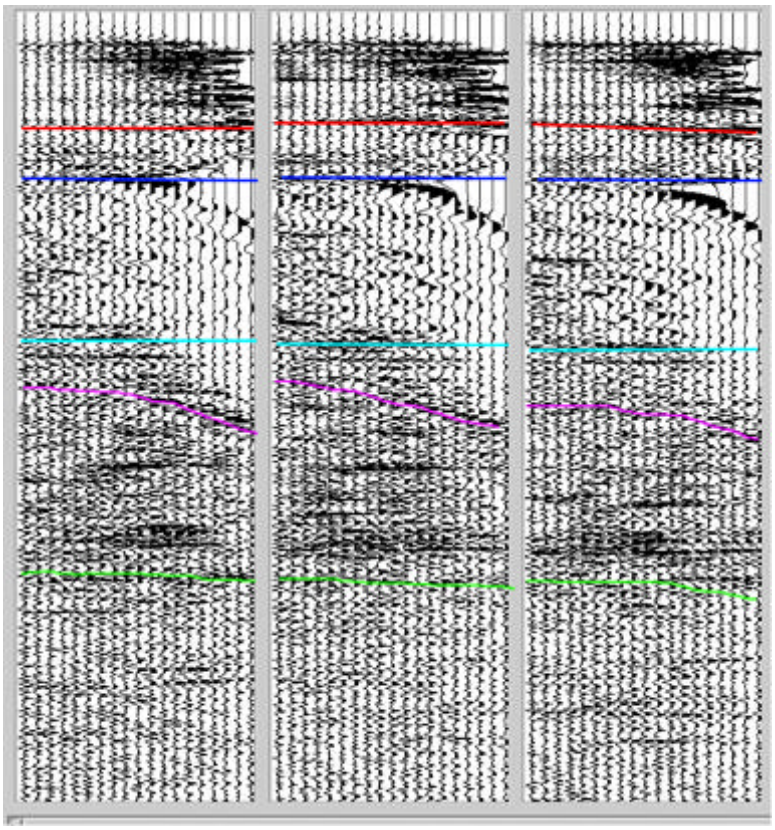

In certain cases, migrating along a predefined horizon (slab migration) reduces computation time and results in faster turnaround time. Figure 10-30 shows the stack of data migrated along a given 3D surface.

Figure 10-30. Imaging Along a Slab

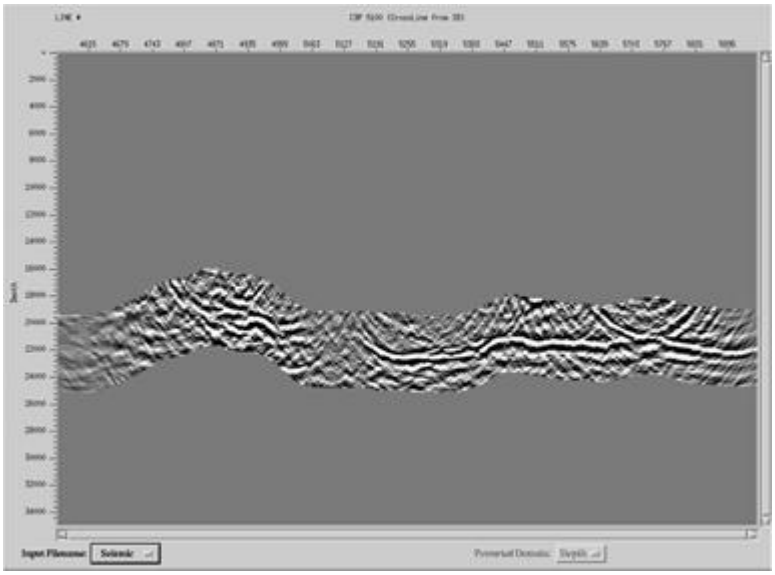

Performing percentage-based migration over a horizon can result in horizon-based analysis similar to that shown in Figure 10-31.

Figure 10-31. Residual Moveout Along Horizons

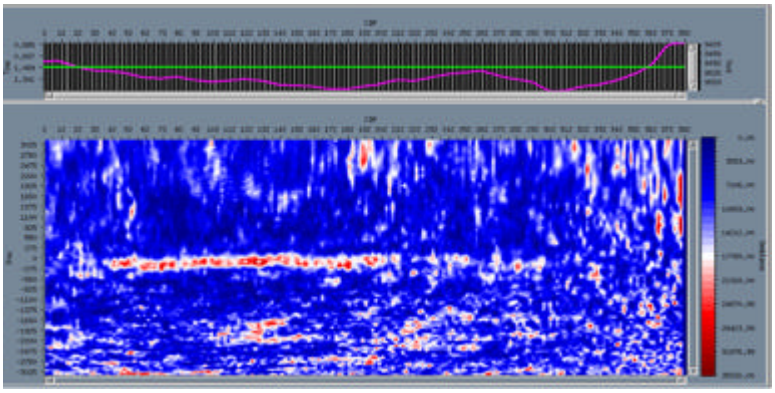

Tomographic updating should not be considered to be a technology that solves all velocity update problems. Like its semblance-based counterpart, tomographic accuracy is dependent on the angle range at any given point reflector. As depth increases, this angle range decreases in width until it is too narrow to be of value. Once the angle range reaches a width of less than 10 degrees, tomography is no more useful than traditional semblance-based analysis.

Tomography works best when at any given depth slice, its back projected cones, as displayed in Figure 10-26 on page 279, overlap. Again, as depth increases, the degree of overlap decrease and thereby reduces the effectiveness of the tomographic update. Some of these issues can be handled through interpolation or physical and geologic constraints of the type illustrated in Figure 10-32, but little can be done about the angle range.

Figure 10-32. Natural Tomographic Constraints

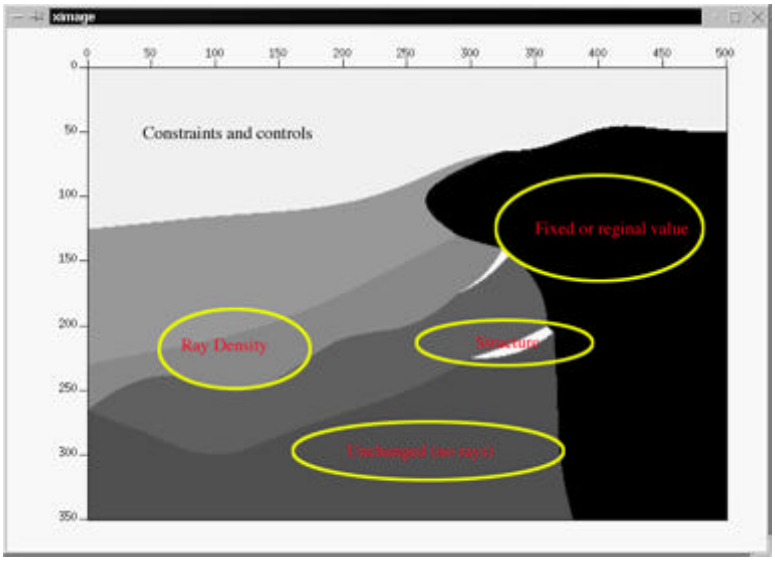

Figure 10-33 shows the tomographic exercise in graphical form. The left side of Figure 10-33 shows the horizons which were picked from the initial Dix-based velocity updating. The center graphic of this figure shows the residual depth differences from an automatic picker. The rightmost image in the figure] shows the updated velocity model after the completion of a residual tomographic update. Compare this to the original velocity field in a past slide.

Figure 10-33. Horizon Based Tomography

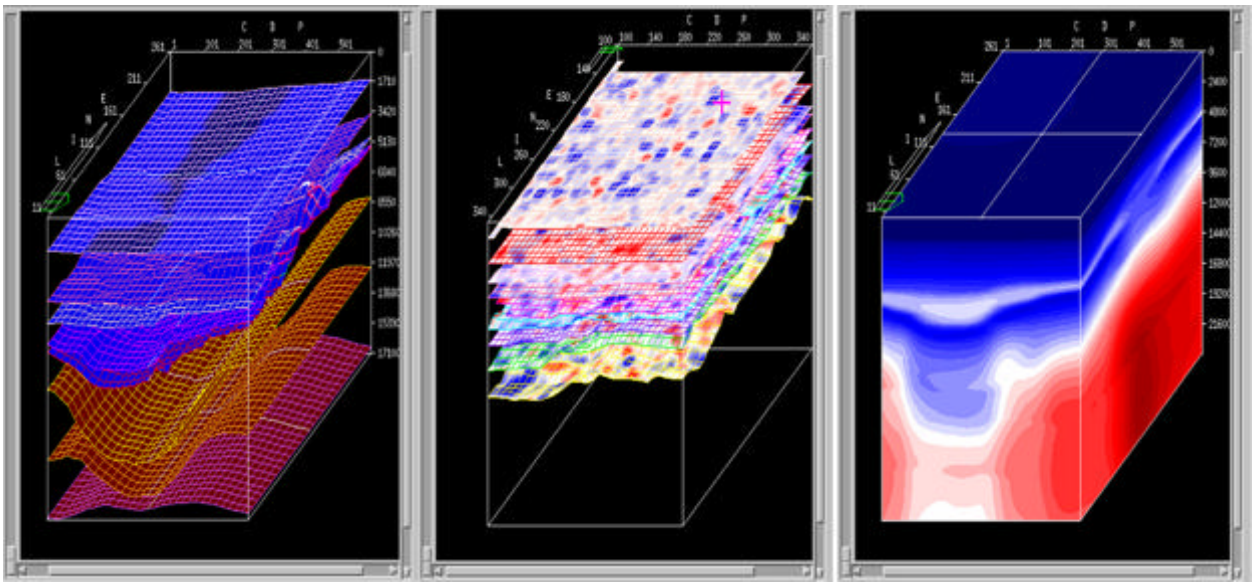

Figure 10-34 contains a side-by-side comparison between a vertical and a tomographic update. The vertical update is on the left and the tomographic update is on the right. Note the velocity inversion (the green on the right hand side of the right figure) and the increased dips roughly in the middle of the right-most figure. This data is over a granitic overthrust in the state of Wyoming in the USA.

Figure 10-34. Vertical versus Tomographic Velocity Update

(a). Vertical Update **(b).** Tomographic Update

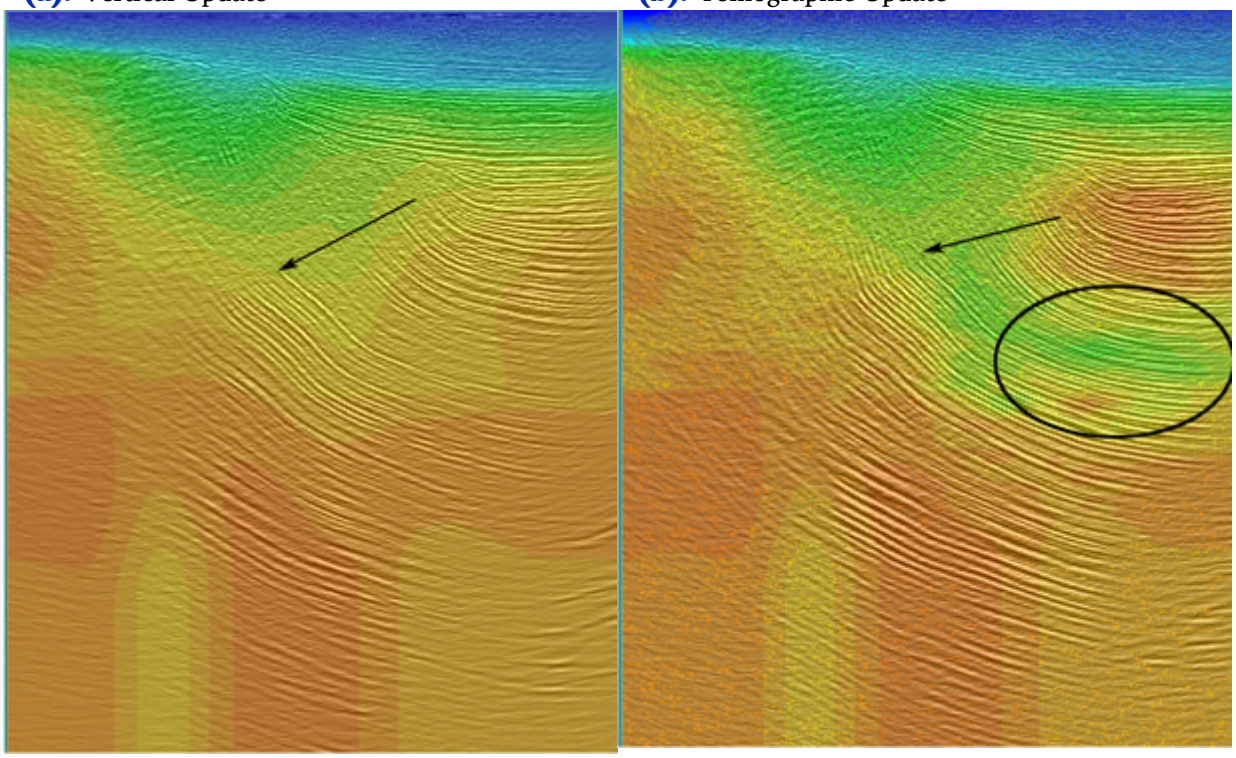

Figure 10-35 is an idealized flowchart summarizing the concepts and ideas discussed in this part of the course. The first part of this slide embodies what might be called vertical updating. It is only at the bottom the figure that we actually begin the option to use tomographic updating. Note that tomography is applied only when there is sufficient residual curvature in the output gathers to warrant it. Velocity defined structures, such as salt, are updated through velocity floods. After the top and base of the anomaly is well defined, residual tomography can be re-applied as needed.

Figure 10-35. Painless Model Estimation Finalized Workflow

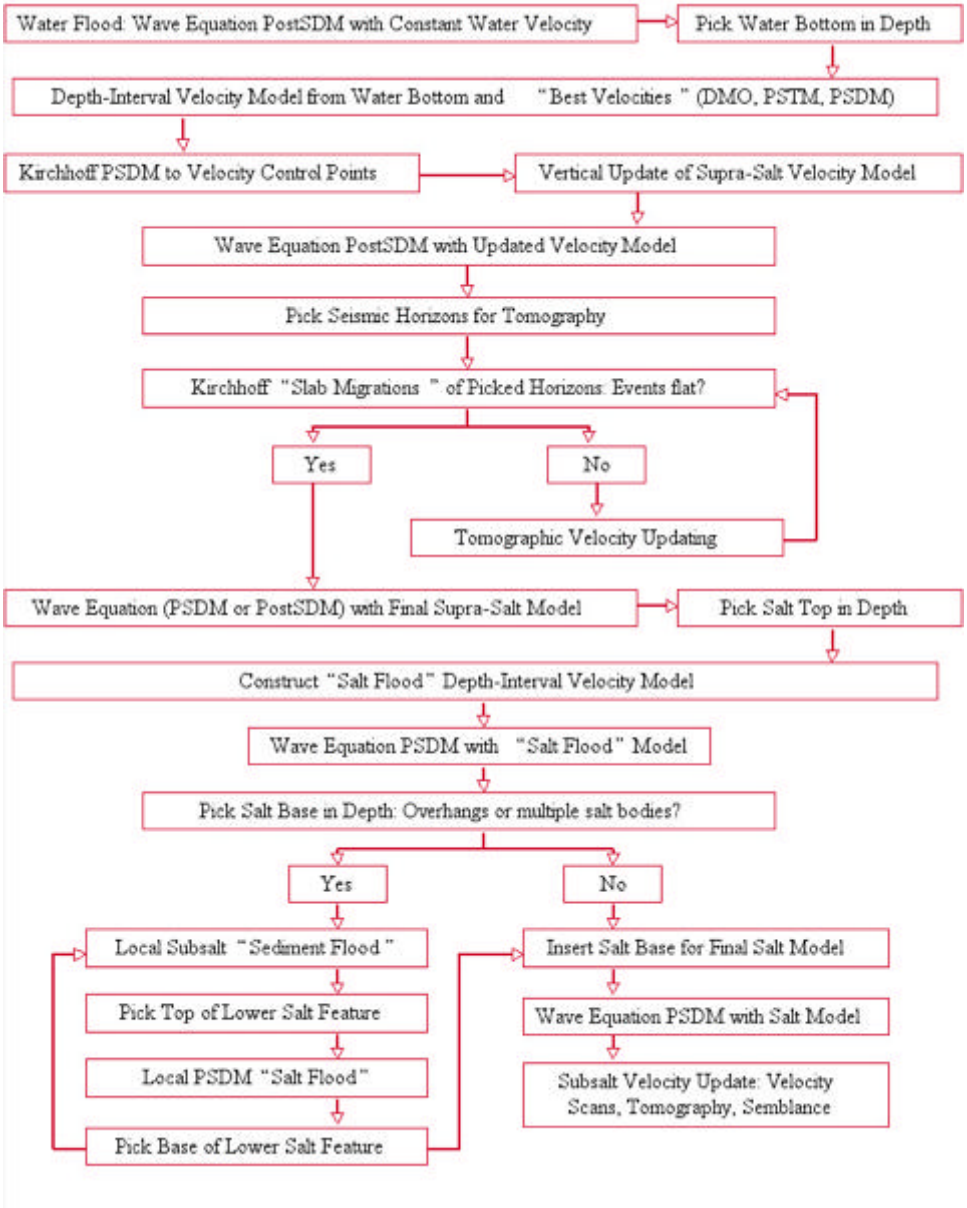

An essential feature of velocity model construction in hard rocks or on land is the increased utilization of wells when available. What is important for this book is the fact that depth migration continues to play its part in the ultimate velocity model definition. In some sense, Figure 10-36 is more or less identical to the previous soft-model slide. The only real difference is when wells are present is to convert the well information so that it matches seismic times. We can think of this process as check-shot correction, but it is just as easy to do when events at specific times can be matched to specific depths on borehole data. Frequently, velocity anomalies can be resolved in much the same manner as those caused by salt structures in the Gulf of Mexico.

Figure 10-36. Hard Rock Horizon Based Model Estimation Finalized Workflow

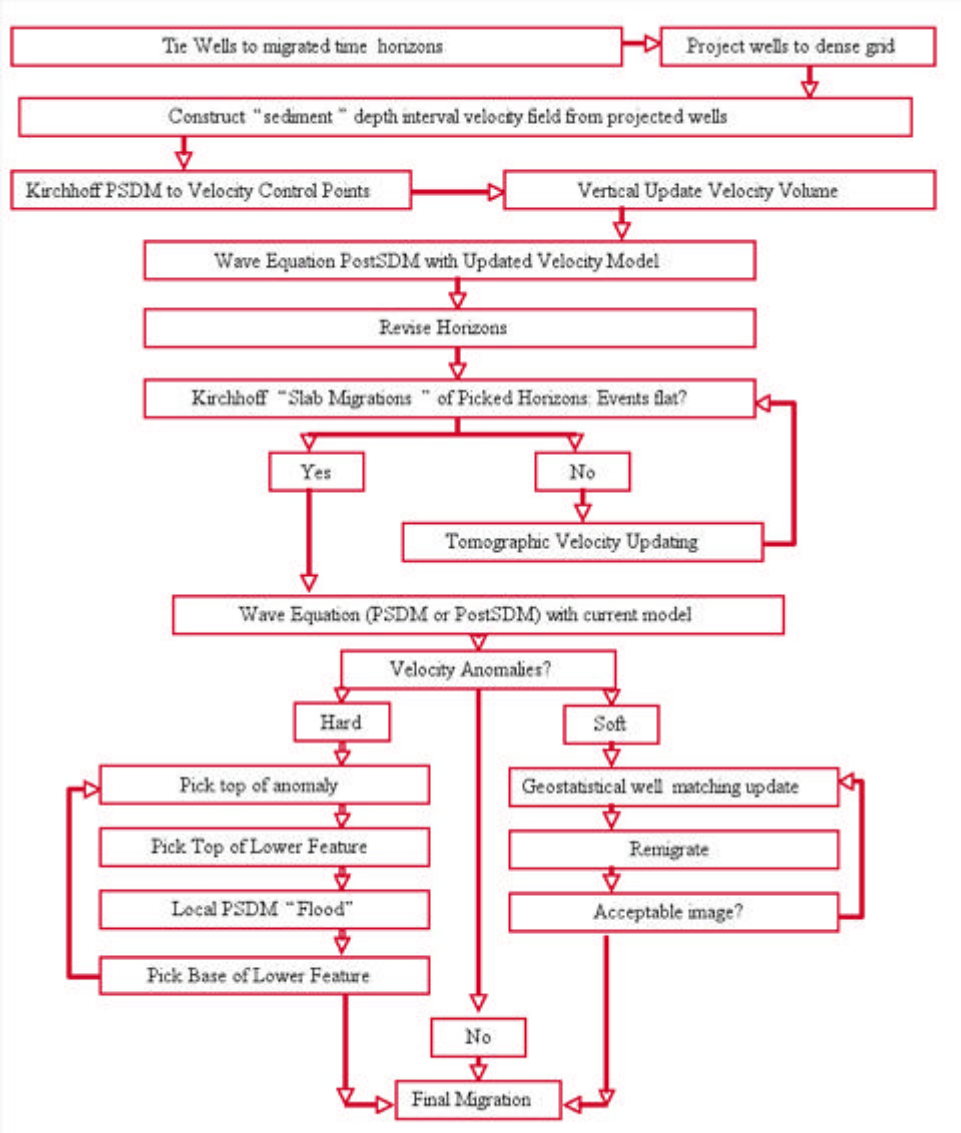

SEG AA′ Case Study

At this point, previous work flows and schemes for estimating depth migration velocity fields may seem a bit daunting. It is probably worth going through the process on a couple of selected synthetic examples where we know what the answer is. Our first example is based on the so-called SEG AA′ synthetic. It is really not proper to begin by showing the true velocity model at the start of this exercise, but the interested reader can find that image near the end of this section. An automatically stacked version of the input data is shown in Figure 10-28.

Figure 10-37. SEG AA′ coarsely picked background velocity (every 200).

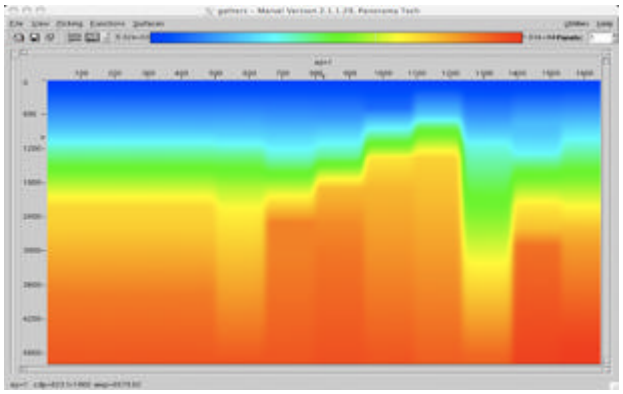

Figure 10-38. SEG AA′ First Iteration Auto Picking

(a). SEG AA′ Auto Picked CDP

(b). SEG AA′ Auto Picked Semblence

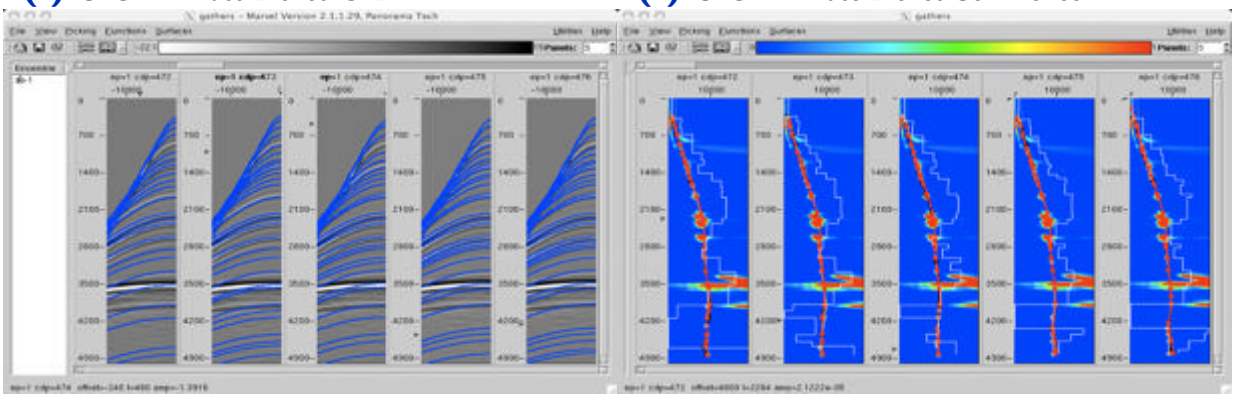

Figure 10-39. SEG AA′ First Iteration Auto Picked Models and Kirchhoff PSDM.

(a). SEG AA′ Auto Picked RMS **(b).** SEG AA′ Auto Picked Depth **(c).** SEG AA′ Migration using (b)

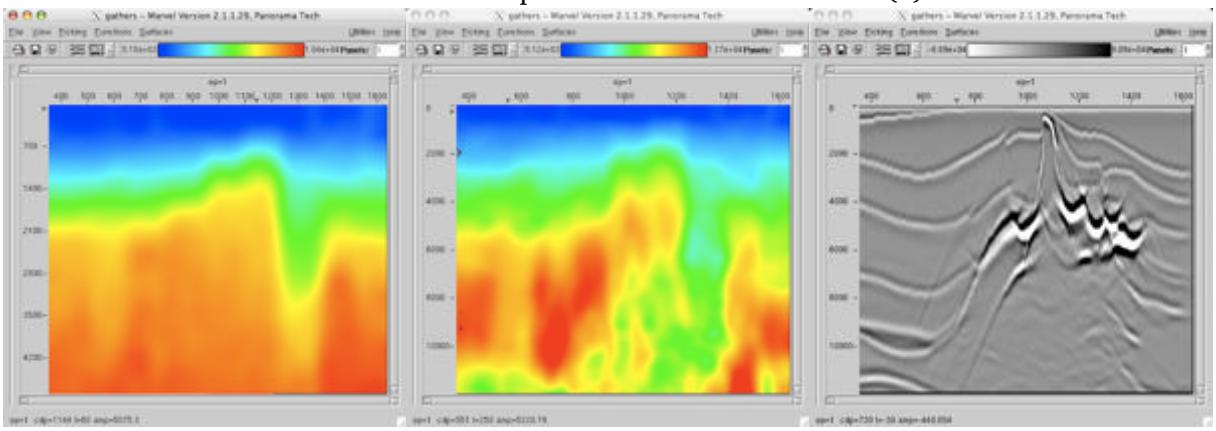

We start the process by first estimating a pre-stack time velocity profile, converting that to depth and then performing a migration of the recorded data. Figure 10-37 shows a stacking velocity model constructed by picking every 200th CDP from the input data. This is clearly a very coarse model, but its real purpose is to give us a background for automatic picking of the SEG AA′ input data. Figure 10-38(a) shows a selection of automatically picked gathers, while the graphic in (b) illustrates the corresponding semblance panels. The automatic picking used the model in Figure 10-37 to tightly constrain the picks. Thus, it is not surprising that the stacking velocity model in Figure 10-39(a) does not vary much from the coarse hand-picked model in Figure 10-37. The interval velocity model in Figure 10-39(b) was used to migrate and obtain the image in part (c).

It is clear that we need to repeat this picking process in hopes of improving our image substantially. To this end, we first use the model in Figure 10-39(b) to time-to-depth convert and apply inverse NMO. Figure 10-40 illustrates the process. The set of common image gathers (CIGs) in part (a) of this figure show that the initial stacking velocity analysis did not produce a very good model. The gathers are not flat and, in fact, appear to have little or no NMO correction. However, the fully inverse NMO corrected gathers in Figure 10-40(b) have considerably more moveout, so the migration did improve the flatness of the gathers to some extent. Parts (c) and (d) of Figure 10-40 are the automatically picked gathers and semblance functions from the inverse NMO corrected time-gathers.

Figure 10-40. SEG AA′ Autopicked First Iteration CIGs and Semblance

(a). 1st Auto Picked PSDM CIG

(b). 1st Auto Picked PSDM CIG after INMO

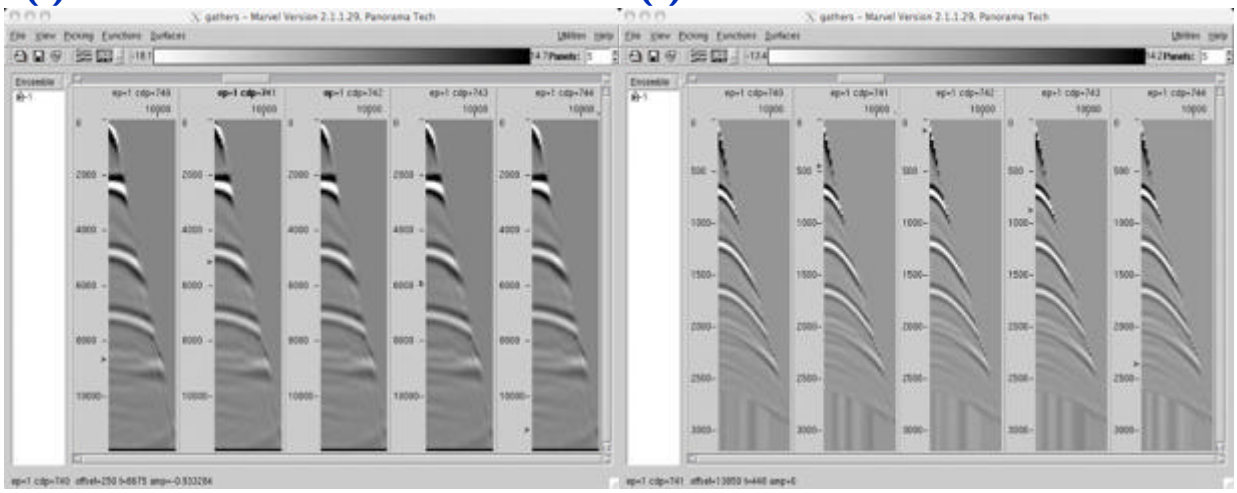

(c). 1st Auto Picked PSDM CIG

(d). 1st Auto Picked PSDM CIG Semblence

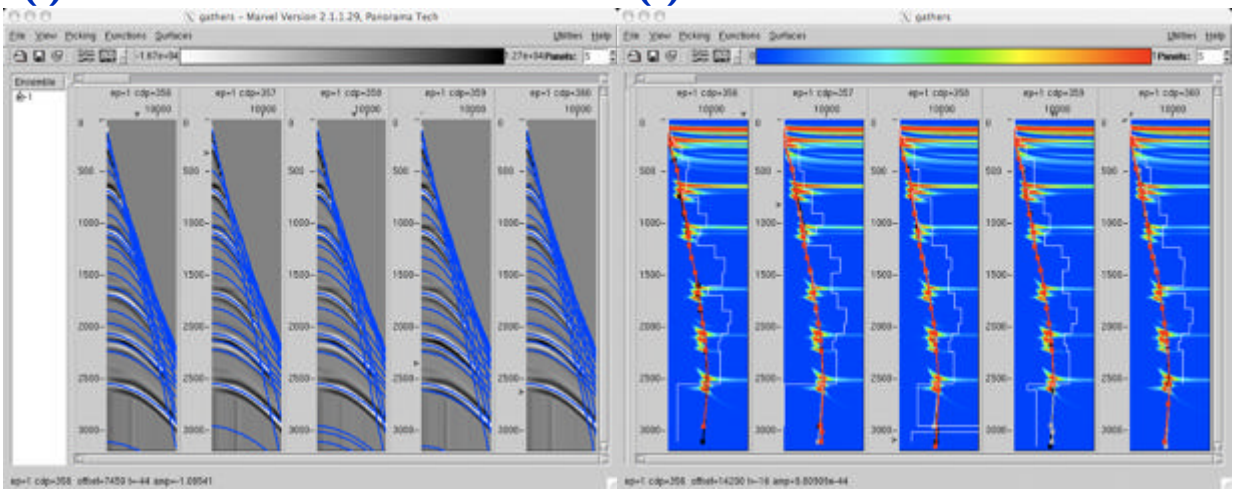

The newly computed velocity model from these picks is displayed in Figure 10-41(a) and the newly computed image based on this model is shown in part (b). A careful review of the CIGs from this second iteration suggested that it was time to estimate and insert the salt top and base. To this end, the top of salt was picked from the image in Figure 10-41(b). The salt flood based on the top of salt surface is displayed in Figure 10-41(c) and the resulting salt flood image is in part (c). The base of salt was defined from the image in Figure 10-41(c) and the resulting salt body inserted into the model in (a). The result is shown in Figure 10-41(d). Part (e) is the image based on the model in (d).

Figure 10-41. SEG AA′ Second Iteration Autopicked Models and Section

(a). 2nd Auto Picked Model

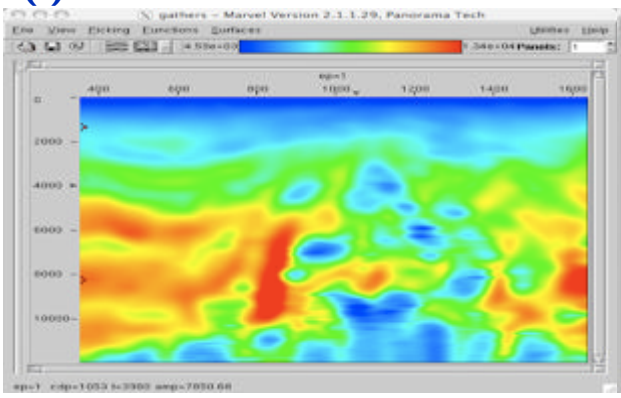

(b). 2nd Auto Picked Model Image

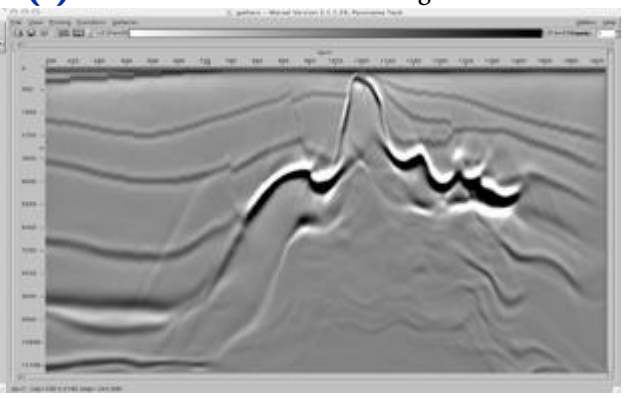

(c). 2nd Auto Picked Salt Flood Model

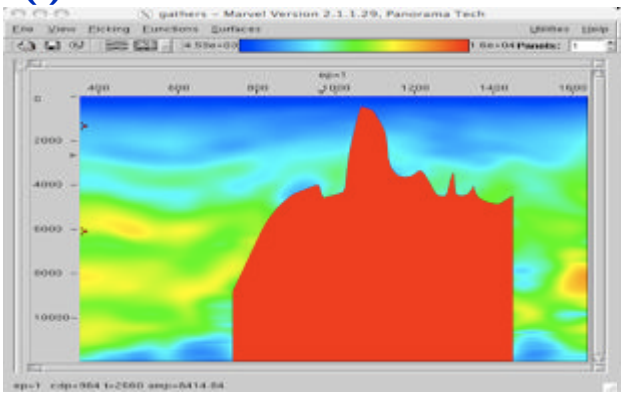

(d). 2nd Auto Picked Salt Flood Image

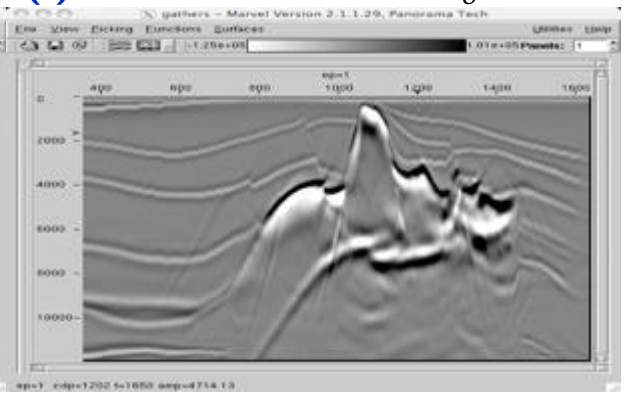

(e). 2nd Auto Picked Depth

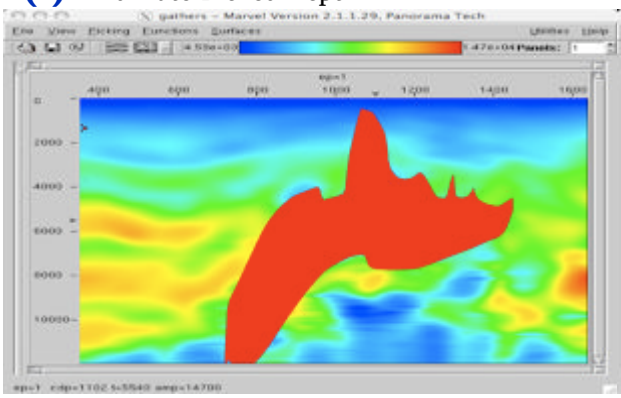

(f). 2nd Auto Picked Depth

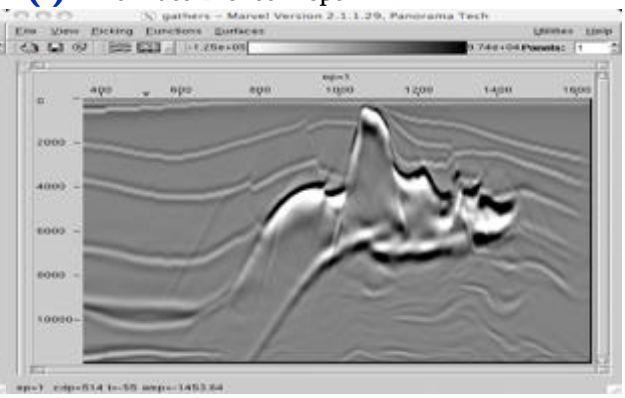

At this point, it is clear that the crude picking, Dix inversion-migration process has produced a reasonable image of what we might call sediments and the salt structure. It is also clear that the image below the salt is not fully sensible geologically. We would think that the way forward would be to keep the salt body in place and complete a very careful re-picking of the CIGs below salt. Unfortunately, the offset range was somewhat limited and almost any velocity below salt produces some kind of image.

Thus, it appears that our only option is to perform several additional migrations using models constructed with percentage differences or maybe even constant velocities below the salt. Figure 10-42 and Figure 10-43 illustrate this. Figure 10-42(a) through (k) graphically depict the utilization of what might be called estimated velocities in (a) and (b) through constant velocity increases from 5,000 ft/sec through 7,000 ft/sec in (c) through (l). Similarly Figure 10-43(a) through (l) depict the utilization of velocities ranging from 7,500 ft/sec through 10,000 ft/sec.

Figure 10-42. SEG AA′ Second Iteration Autopicked Models and Sections Using Increasing Velocities Below Salt

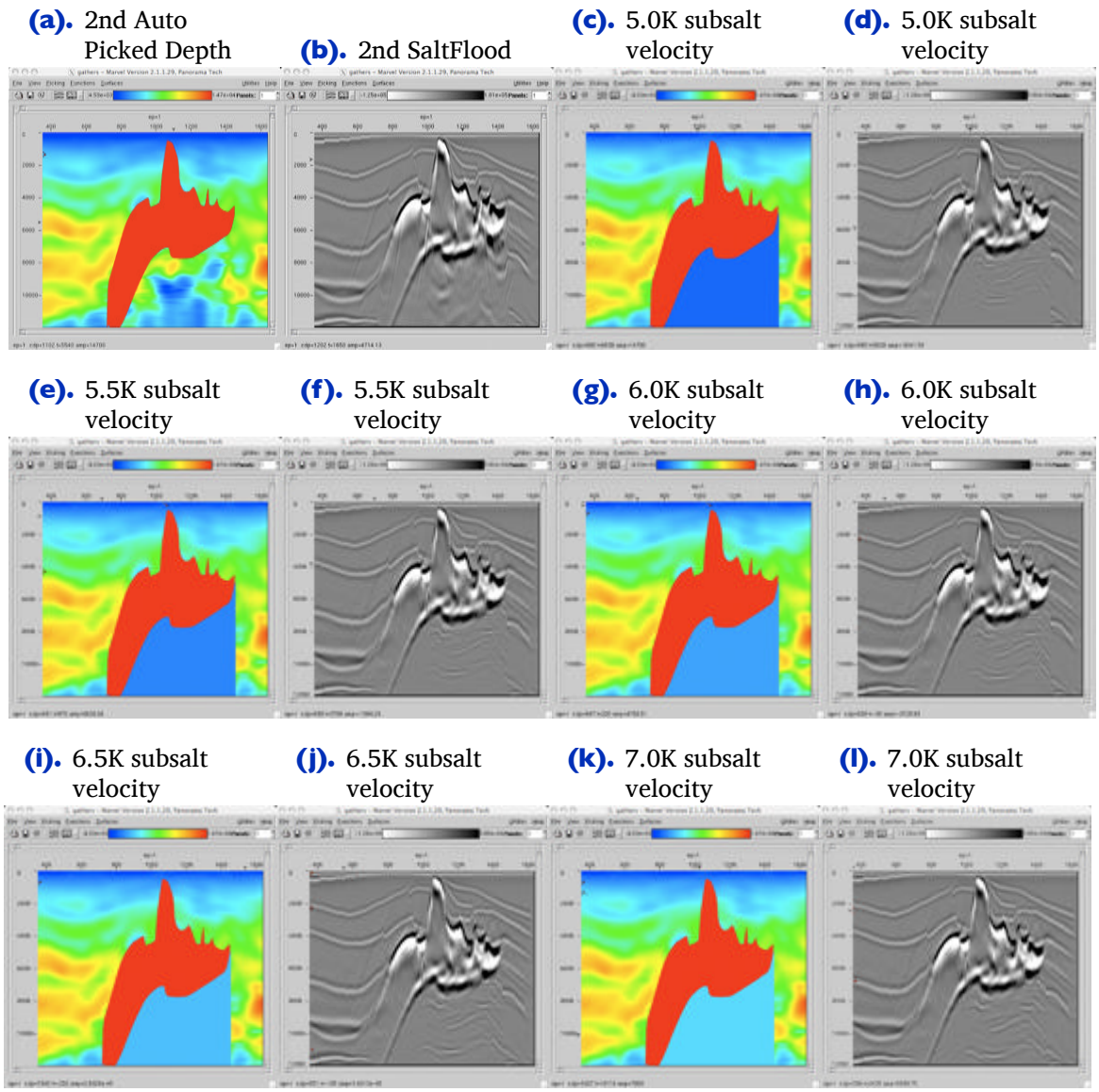

Figure 10-43. SEG AA′ Second Iteration Autopicked Models and Sections using increasing velocities below salt

(a). 7.5K subsalt velocityl **(b).** 7.5K subsalt velocity **(c).** 8.0K subsalt velocity **(d).** 8.0K subsalt velocity

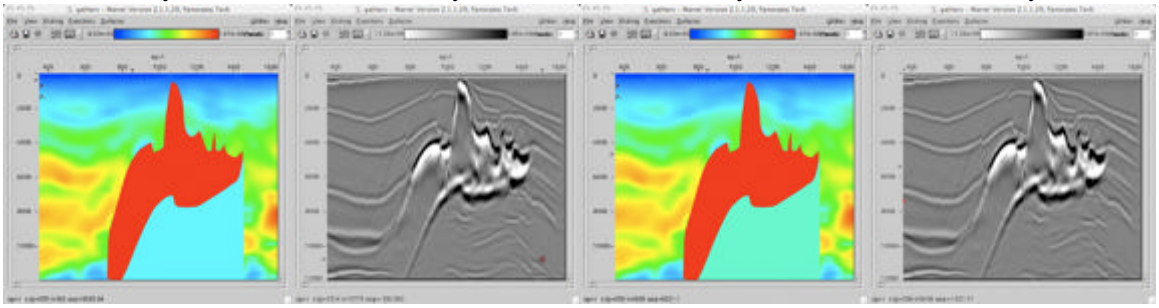

(e). 8.5K subsalt velocity **(f).** 8.5K subsalt velocity **(g).** 9.0K subsalt velocityl **(h).** 9.0K subsalt velocity

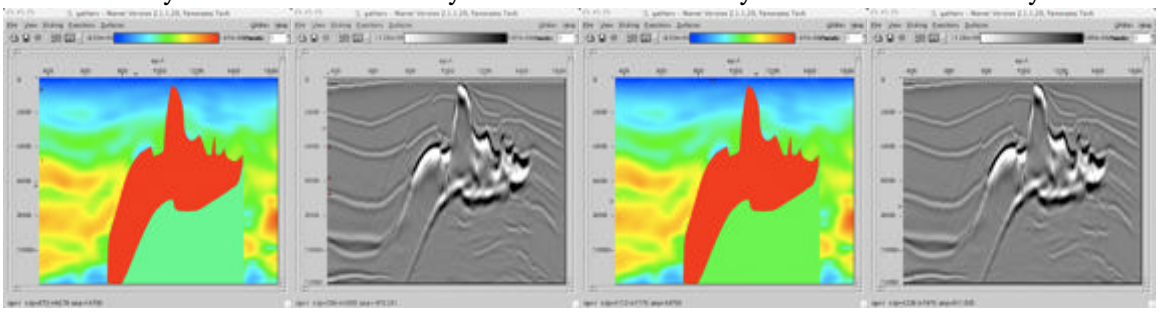

(i). 9.5K subsalt velocity **(j).** 9.5K subsalt velocity **(k).** 10K subsalt velocity **(l).** 10K subsalt velocityt

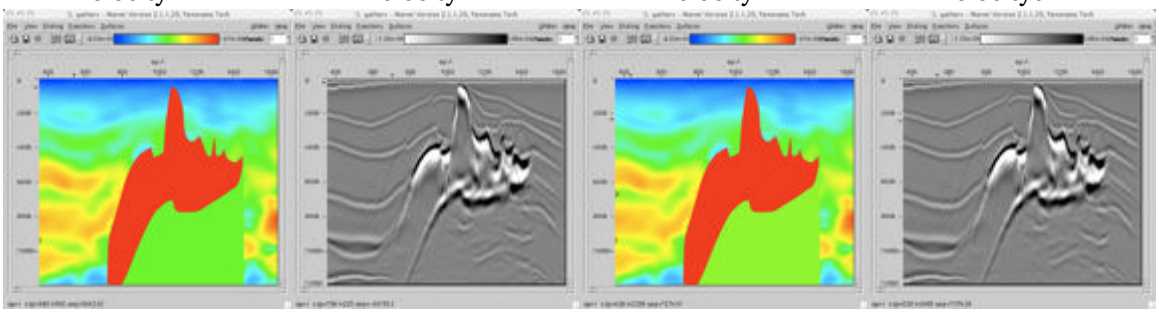

After Tomography

A careful analysis of the migration images in Figure 10-42 and Figure 10-43 suggests that the closest correct sub-salt velocity is about 9,000 ft/sec. Based on this assumption, the input data were re-migrated using 9,000 ft/sec below salt velocity and a dip-based-automatic-flattening analysis performed to generated the necessary input for residual tomography. Residual tomography was then applied to generate a new model and the data re-migrated. Figure 10-44(a) displays the tomographically-estimated velocity while (b) shows the true velocity model.

Figure 10-44. Estimated versus True Velocity model.

(a). Estimated Velocity Model **(b).** True Velocity Model

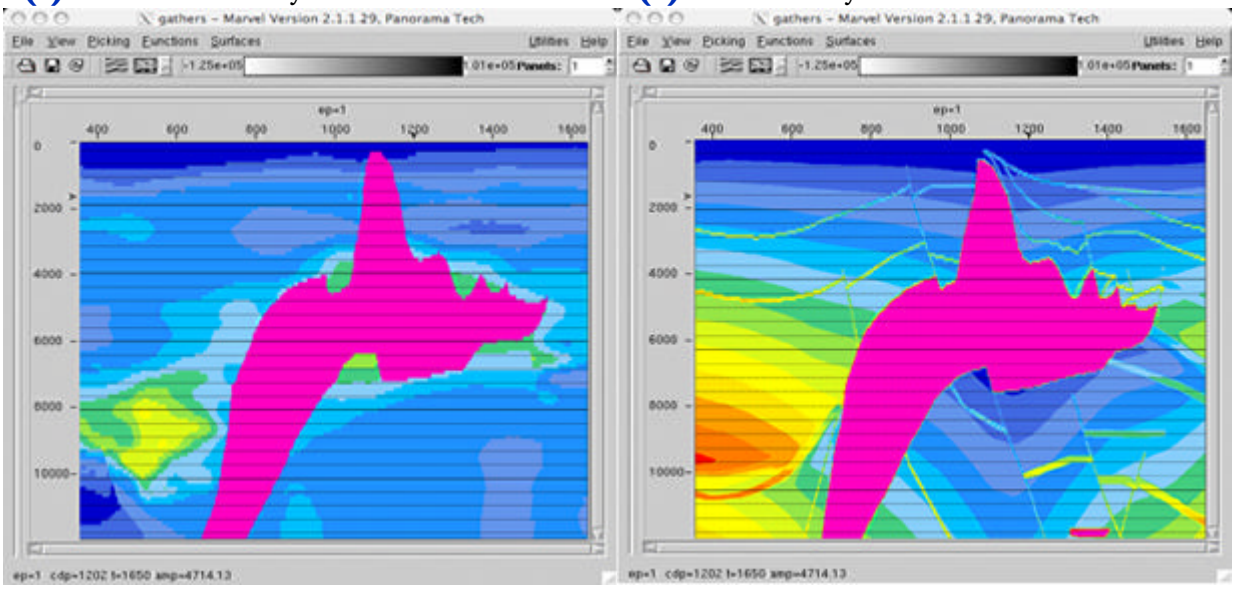

The flatness of the after-tomography gathers is illustrated in Figure 10-45(a) and (b). The gathers in Figure 10-45(a) figure are within what might be called sedimentary geology, while those in part (b) fall within the salt regime.

Figure 10-45. Gathers after Tomography

(a). After Tomography in Sediments **(b).** After Tomography in Salt

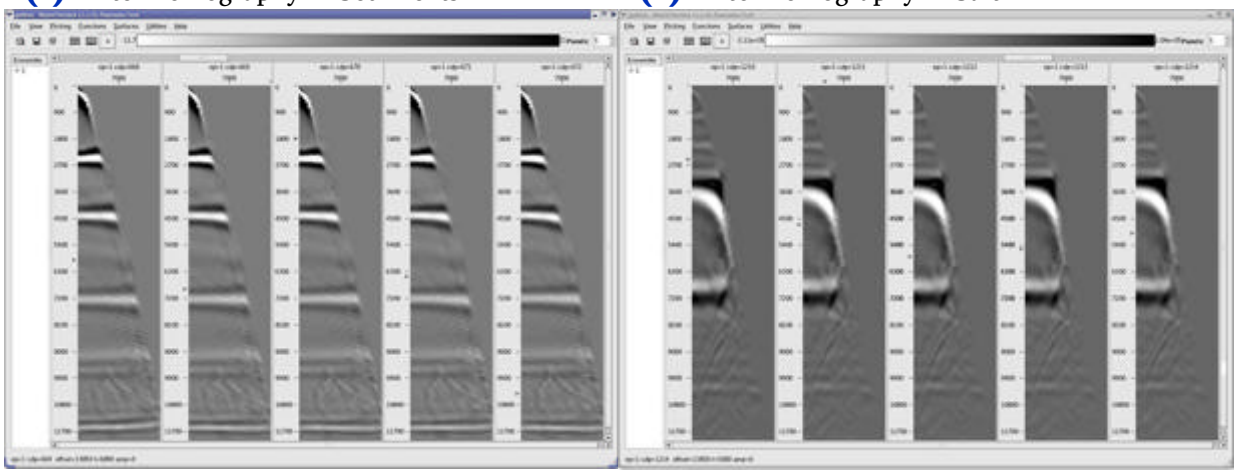

Figure 10-46 is a full comparison between utilization of the estimated velocity field in Figure 10-44(a) and the exact velocity field in (b). Note that in every case the one-way algorithm has produced an image that is significantly better than its Kirchhoff counterpart.

Figure 10-46. Estimated versus True Velocity Image Comparisons.

(a). Kirchhoff using Estimated Model

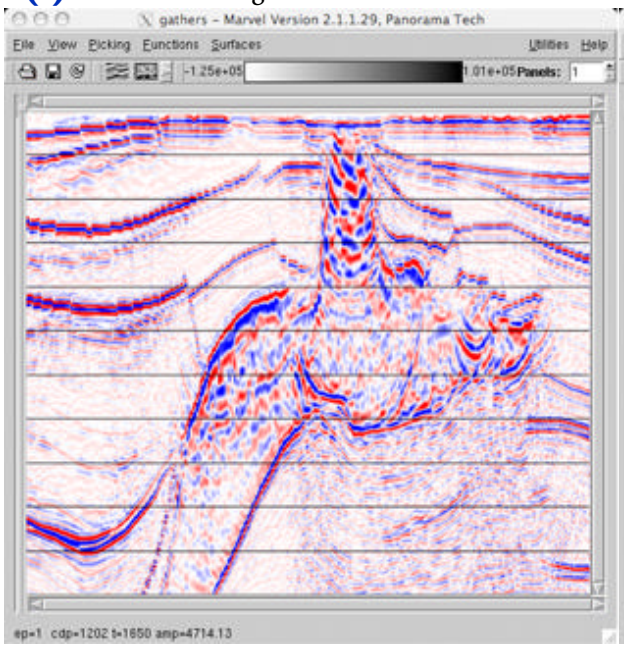

(b). Kirchhoff using Exact Model

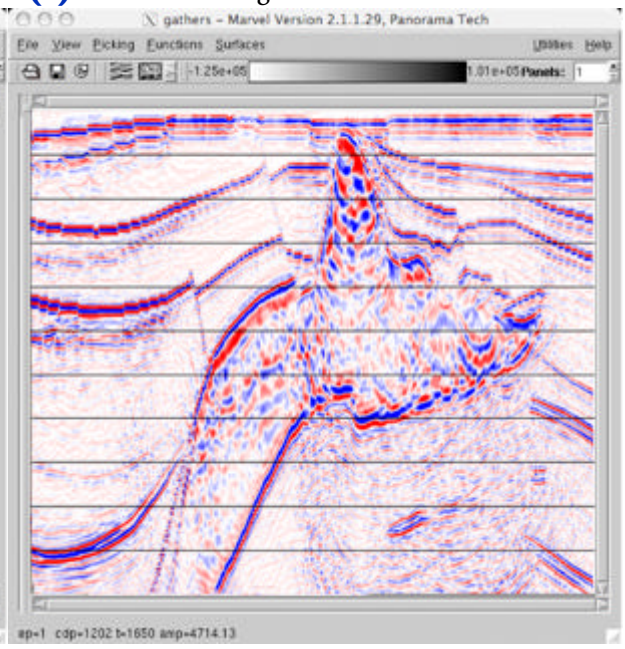

(c). One Way using Estimated Model

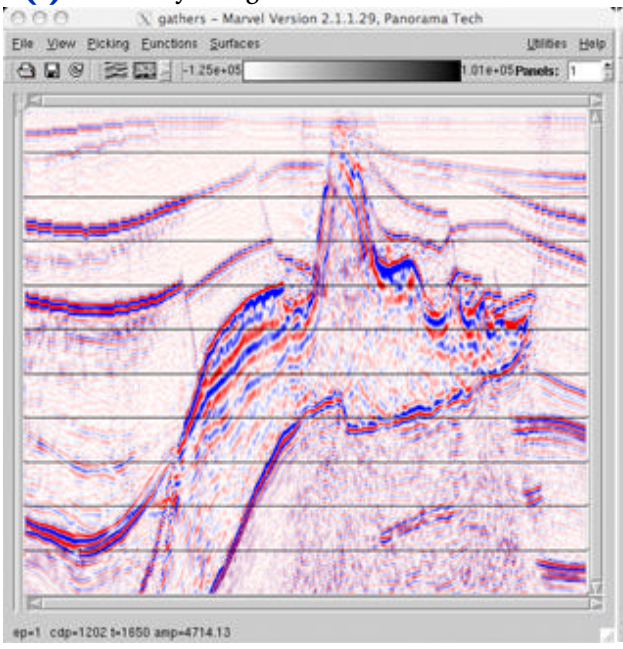

(d). One Way using Exact Model

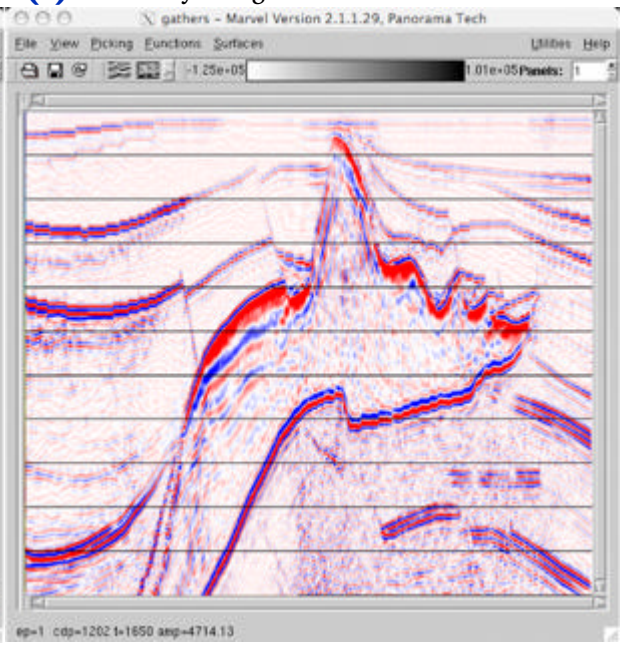

Marmousi Case Study

The original Marmousi data set is somewhat of an enigma. It was designed based on offshore Angola geology and represents a double anticline with the upper anticline sitting virtually directly on top of the lower. The lower structure was prospective but very difficult to image. Neither prestack time migrations or early depth migrations of the day could successfully image the reservoir. Because of this difficulty, Institute Francais de Petrol constructed a model closely resembling the interpreted structure, shot synthetic data over the model and then presented the data to the geophysical community of the day with a challenge to figure out the model from the data alone.

The synthetic data consisted of 240 96 channel shots spaced at 75 meters. The 96 receivers were separated by 25 meters at an offset 200 meters from the shot. Each receiver was the result of summing a more finely sampled array. The wavelet used in this case was neither minimum, maximum, nor zero delay, but produced an effective delay of about 60 ms in the synthesized data. The challenge thus included wavelet processing as well as velocity analysis or inversion and imaging. The goal was to find the velocity model as accurately as possible.

A paper in the 1990's by Sebastian Geoltrain and Roloff Versteeg suggested that Kirchhoff methods alone could never image this structure. While apparently true at the time, as we saw in the chapter on prestack algorithm examples, the real reason this hypothesis made sense was more closely related to the acquisition parameters than to the imaging algorithm.

Our goal here is to see just haw far we can go to produce something close to the actual true velocity. In this sense, we intend to use every available trick in order to achieve our goal

Figure 10-47 shows typical MVA panels based on the initial stacking velocity analysis shown in Figure 10-48. Of interest are that

- the stacking velocity model in (a) is extremely smooth
- the Dix depth-interval model in (b) is close to a $v(z)$
- the image in (c) is essentially what you get doing a PSTM

The smoothness in this case is directly related to the fact that picking was performed on every 100th CDP and that a rather long smoother was applied during the construction of the full model.

Figure 10-47. Marmousi velocity analysis and NMO CDP 1000.

(a). Marmousi CDP 1000l

(b). Marmousi CDP 1000 Semblance

(c). Marmousi CDP 1000 NMO

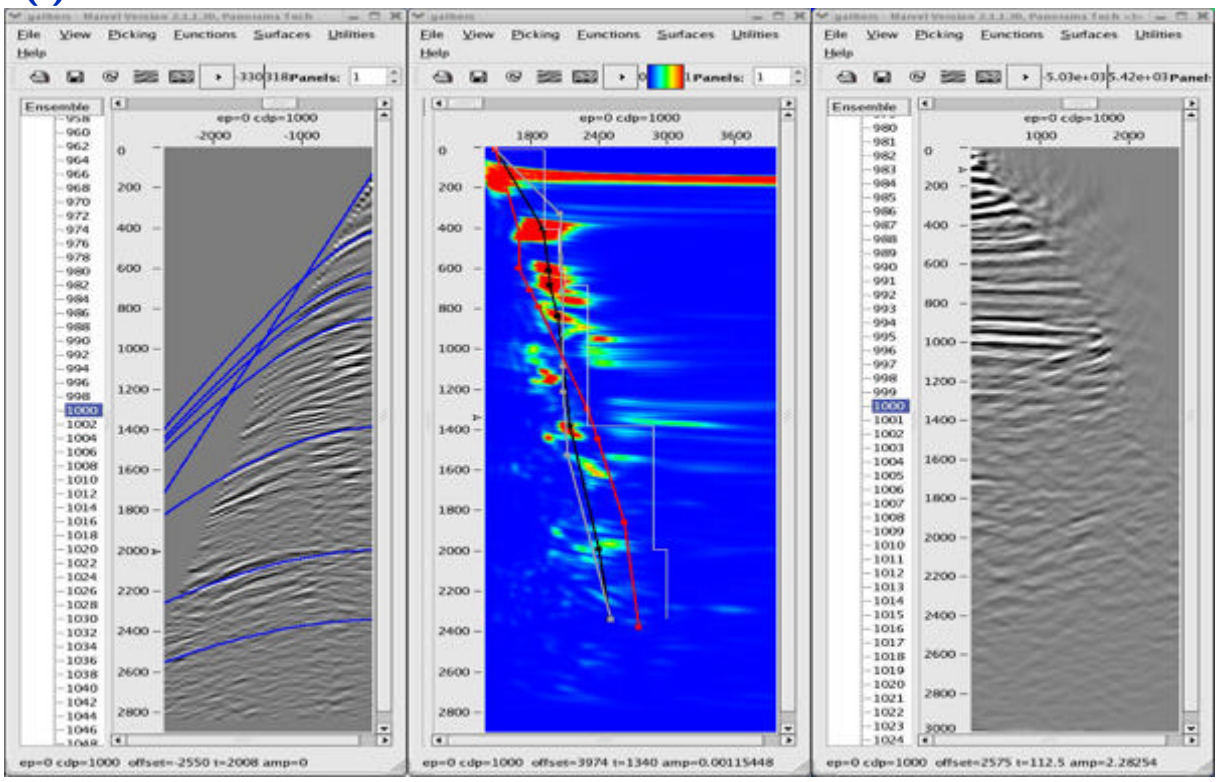

Figure 10-48. Initial Marmousi stacking velocity models and migration.

(a). Stacking Velocity Model

(b). Dix Depth-Interval Model

(c). Migration with (b)

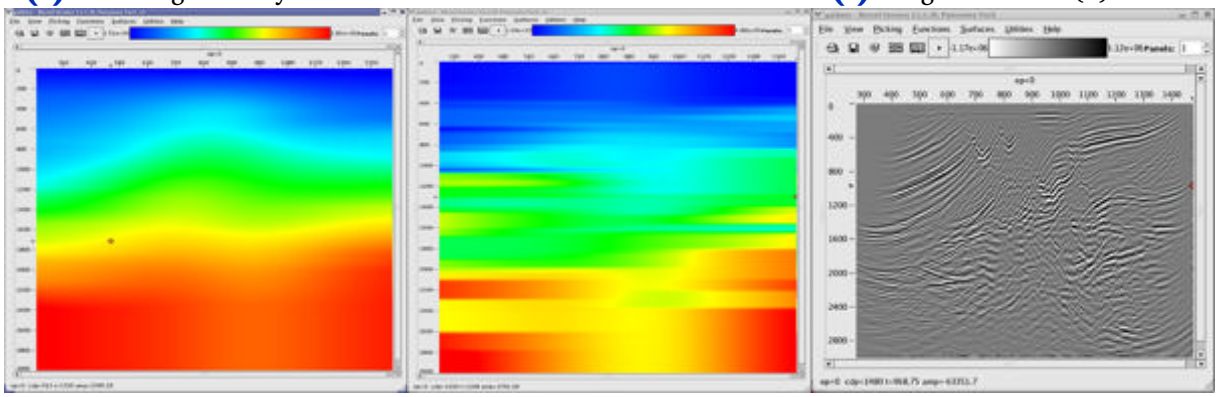

The panels in Figure 10-47 were used to construct the model in Figure 10-49. While the changes are not dramatic, it is clear from the depth-interval model in (b) that the geology does not really follow a $v(z)$ assumption. Note that the image in (c) is also much

more realistic. The only issue in the picking process relates to whether the clear speed up on the left hand side of the model is real or not.

Figure 10-49. Iteration 1 RMS and interval velocity models together with migration based on (b).

(a). Kirchhoff MVA RMS model

(b). Kirchhoff MVA interval velocity modell

(c). First iteration image with (b)

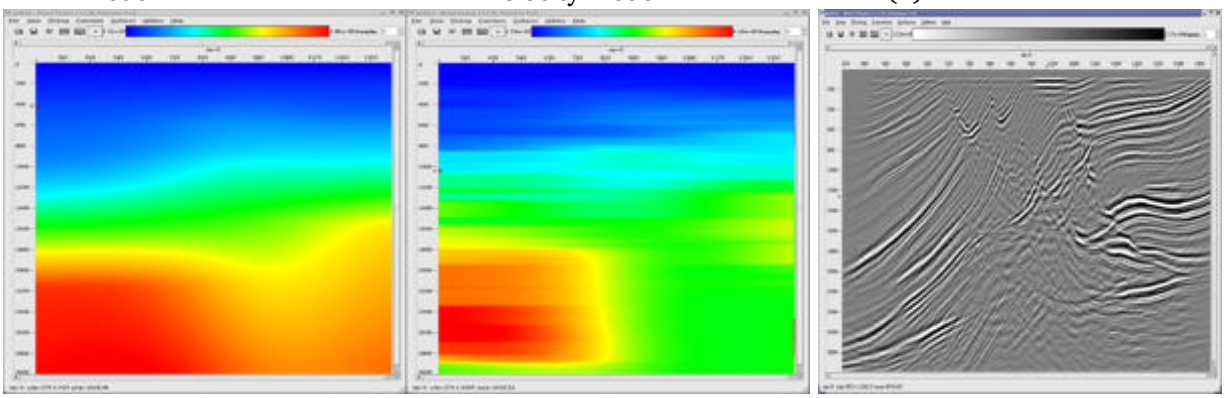

Using the model in Figure 10-49 as a guide, a new model was constructed from the current prestack data to effect a slow down of the left hand side high velocity zone. The result is shown in Figure 10-50(b). Note also that the image is now somewhat more realistic, but the gathers are still not completely flat.

Figure 10-50. First iteration velocity model slowdown together with migration based on (b).

(a). Kirchhoff MVA Interval velocity model

(b). Kirchhoff MVA Slowdown of (a)

(c). First iteration slowdown (b)

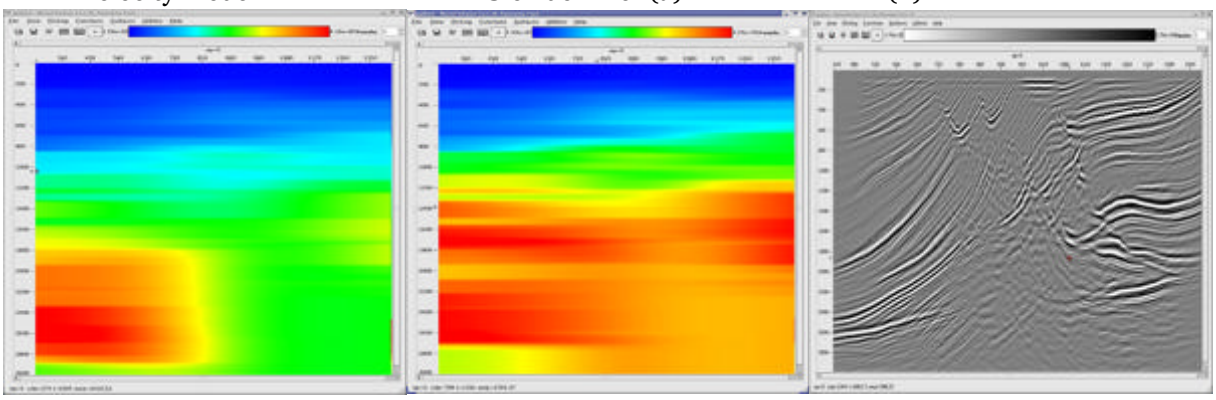

Using the data from the PSDM based on the model in Figure 10-50, panels like those in Figure 10-51 were picked and used to produce the model in Figure 10-52(a) and the migrated image in Figure 10-52(b). When compared to some of the best images produced in the original Marmousi velocity estimate exercise, this image is not too

bad. What is clear is that to improve the answer, several additional iterations will be necessary, but there is absolutely no guarantee that better results will be obtained. In fact, with a nominal maximum offset of just 2600 meters, it is unlikely that velocities below about 1,300 meters per second can be improved much at all.

Is it time to change gears?

Figure 10-51. Marmousi CDP 875 after inverse NMO using the model in Figure 10-50.

(a). Marmousi CDP 875 Semblance **(b).** Marmousi CDP 875

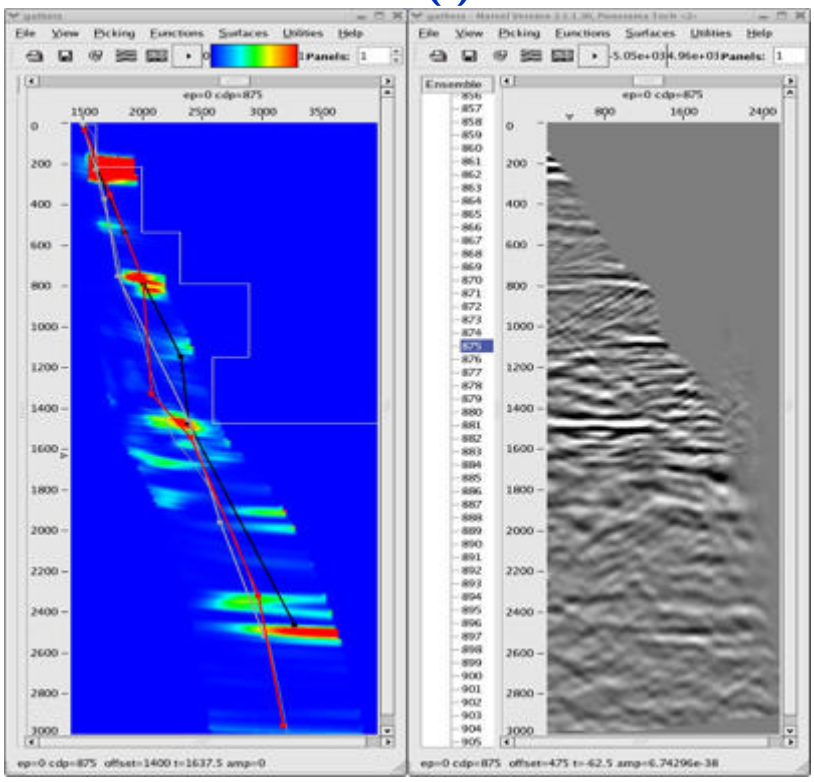

Figure 10-52. MVA Velocity model from migration based on Figure 10-50 model together with migration. In this case, picking was done every 25 CDPs between CDPs 700 and 1200.

(a). MVA Velocity Model **(b).** Migration with MVA model

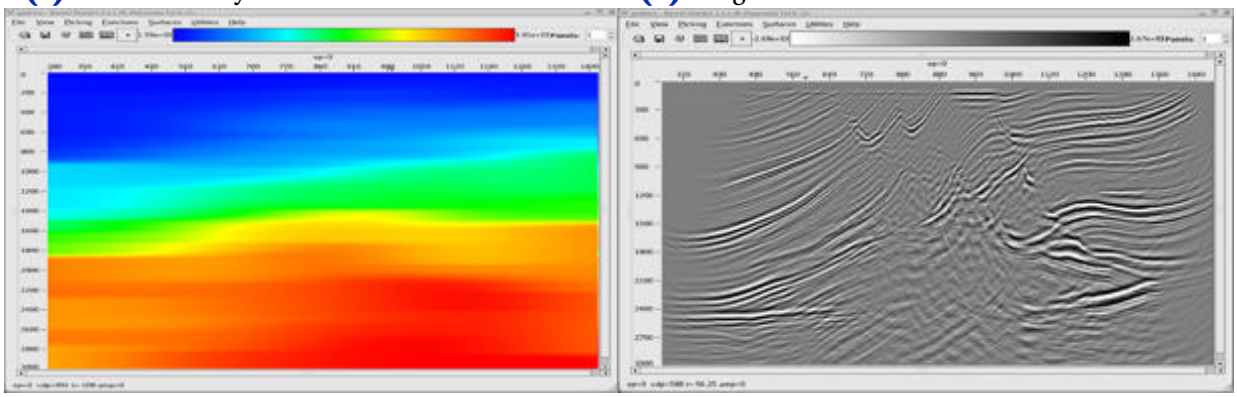

Inversion

At this point in any project, we have a velocity model and an image, but we have no idea how accurate the model is. Realistically, we have more velocity models than we know what to do with, and we don't have a clue as to which one is best.

We also have modeling algorithms, so if we believe our model is so good, why don't we test it by shooting data over the model and subtracting the synthetic from the observed data? That is, for each trace in the observed data, generate a synthetic trace, and then create a completely new data set using a trace-by-trace subtraction. If the model is perfect, we get nothing better than completely random noise and we simultaneously validate the model.

But what if we don't get random noise? Is there any way to use the information from the residual to estimate a new velocity model? The answer is yes, of course, and the mathematical recipe is relatively simple. All we have to do is prestack-reverse-time migrate the difference, normalize in the proper manner and add the result back to the current model. Given the new model, we repeat the process of synthetic generation and subtracting. If the new difference is still not zero, we repeat the exercise until the residual can no longer be reduced. This inversion approach was first presented in the geophysical literature by Lailly in 1983, and Tarantola in 1984. When they tested it, it failed rather miserably. We should not let that bother us. The idea looks sound. Maybe they did something wrong, or maybe they just did not have the computer power to test the theory in an optimum manner. Let us do our own test.

Figure 10-53 shows the result of testing the theory on synthetic data from the Marmousi model. Starting with the $v(z)$ model in (b) of this figure, we synthesized a survey with the same geometry as the data over the model in (a). We then ran the process described

above iteratively. The result after 100 iterations is shown in Figure 10-53(c), and after slightly more than 600 iterations, in (d). Note that the process has worked extremely well. The velocity error in Figure 10-53(e) is virtually zero, except for those areas outside a offset dependent cone. Note also that the RMS error in (f) has been reduced to a very low level. It is probable that we could have stopped after 300 iterations or so, but we cannot argue with the overall results.

Figure 10-53. Marmousi Full Waveform Inversion

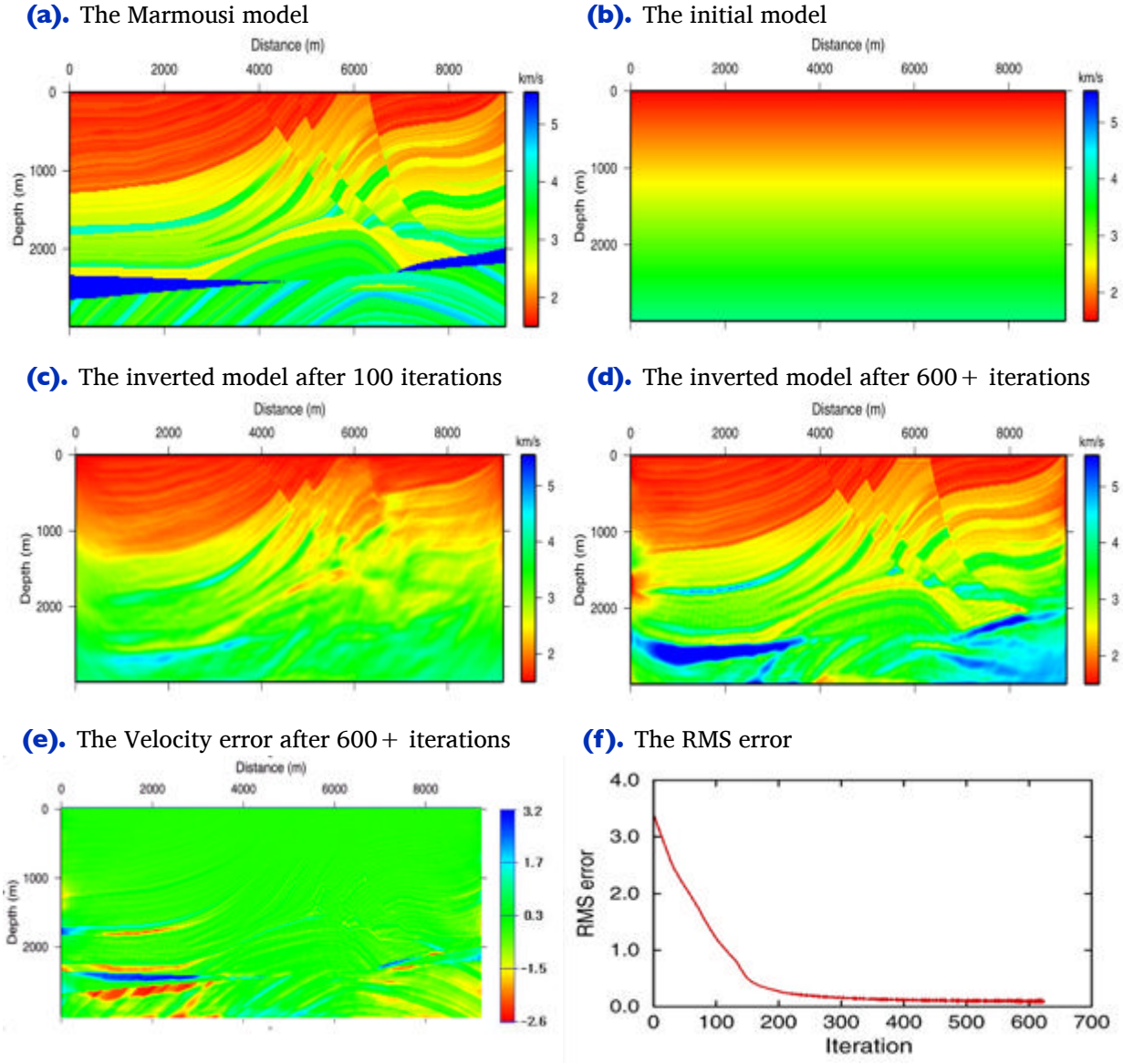

Figure 10-54 further confirms the high quality of the inversion process. This figure shows logs taken at distances of 3000 and 7000 meters from the left hand side of the model. The green line in this figure shows the initial $v(z)$ used to start the process, the red line is the true velocity while the blue line is the inverted velocity after 600+ iterations. Note that down to about 1500 meters, the results are truly outstanding.

Figure 10-54. Inverted Versus True Logs

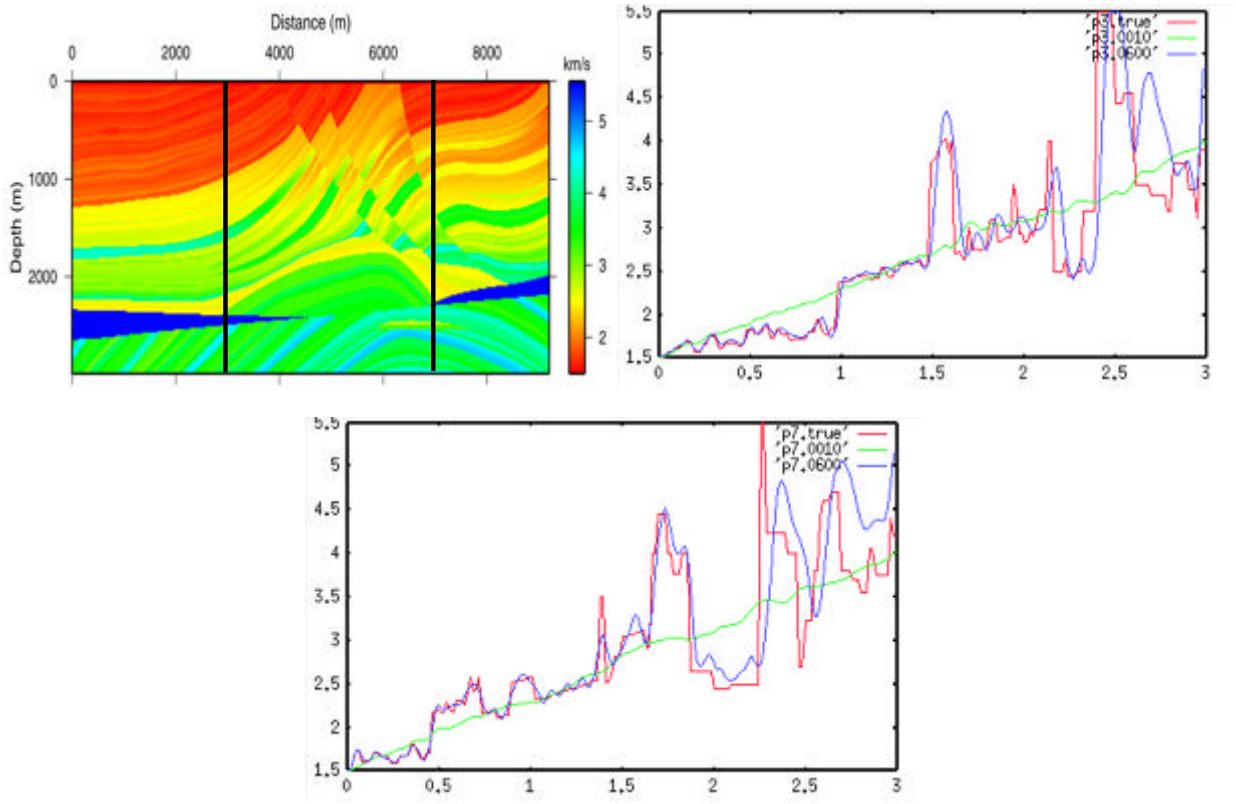

So why did this work now, when it failed so miserably before? Well, to tell the absolute truth, we actually ran the process on extremely low frequency data that we generated over the model in Figure 10-53(a). These data, shown in Figure 10-55, extended over the entire length of the model and had a bandwidth that extended from 0.3 Hz to 18.0 Hz. The model was sampled with a very fine grid to minimize dispersion and to ensure that each modeling exercise was as accurate as possible. However, there is no doubt that the real reason this process worked is directly related to the low frequency content of the data.

Figure 10-55. Marmousi Ultra Low Frequency Synthetic Data

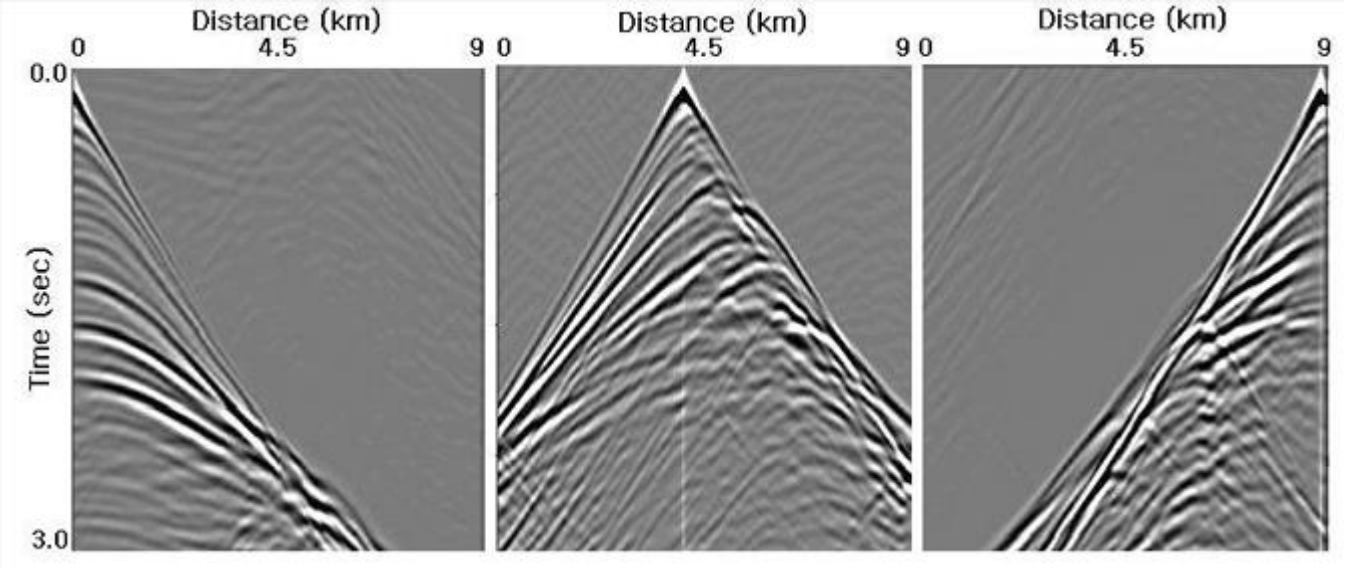

Chapter 11

Anisotropic Velocity Analysis

Tying well tops to seismic reflections requires detailed discussion of time-to-depth and depth-to-time conversion, as well as migration to true depth. Historically, tying wells to a seismic migration was called *depthing* and usually converted only a few horizons to depth. This depthing process was almost solely focused on ultimately providing an accurate conversion of an interpreted migrated time map to depth in such a manner that the horizon depth in all wells within the mapped area were matched as precisely as possible. This process was not concerned with producing depth volumes containing all horizons of interest; it was only concerned with matching well tops. Accomplishing this feat required that all well tops of interest be tied to the corresponding seismic time image with precise accuracy. When necessary, well velocities were modified to fit the observed discrepancies, and, after much trial and error, a suitable velocity $v_0(x,y)$ map for depth conversion of the given horizon was produced. The underlying assumption in all of this was that the time migrated volume was as accurate as necessary, and well discrepancies were just a function of measurement error. It is now known that the truth is not so simple. The reason we had to tie the seismic data to the well was that the migration was performed with no consideration for anisotropic wave propagation.

The single most important parameter associated with anisotropic migration is the 3D Earth model. Note that it is not just the simple velocity model normally used in prestack time (RMS) or prestack depth (INTERVAL) migrations. This model has at least three, and up to five, interrelated parameters.

The best known elements of this five-member set are the sound speed, determined through iterative migration velocity analysis, and the well-based or *true* depth velocity field. Frequently, these two fields are considered to be independent and totally unrelated, but the theoretical facts are completely out of phase with this concept. In fact, these two fields are the most important aspects of what is required to produce migrated images that exactly tie the wells.

While the two velocity fields are necessary, they are not sufficient to complete the process. In addition, we must also determine how these two fields are related to accurately image the recorded data at the precise subsurface location from which they were reflected. In the sections on velocity analysis and velocity model building, we develop and discuss the data, workflow, tools, and concepts necessary to construct the entire Earth model.

There is no doubt that there are still many geophysicists who believe that true depth imaging is not possible and will never be possible. What we argue is that all of these approaches have their place, but in the final analysis, the optimum approach must incorporate the full anisotropic model to achieve true depth conversion at all dips. Integration of all available data is key and must be performed accurately for this to produce high quality results.

Anisotropic Earth Models

Estimating an anisotropic Earth model is not easy. In the best case, the seismic data on which anisotropic parameters are based contain the necessary information to facilitate accurate velocity estimation. However, since this is not likely to be the case, we must make do with what we have.

Figure 11-1(a) is a graphic of why normal seismic velocity analysis does not generally provide an Earth model suitable for accurate depth imaging. The blue ray fronts indicate that the lateral velocity is faster than the vertical velocity shown in magenta. Semblance analysis tends to produce estimates of the lateral velocity variation and not the vertical variation. That is, in the specified Earth model used to compute the ray fronts, the magenta ray fronts are not present, so when velocities are estimated, the resulting interval velocity will be more proportional to the faster lateral sound speed. So long as we use a short spread analysis, as specified by Figure 11-1(b), our Earth model velocity field will be too fast. Nevertheless, it normally provides us with excellent images and a velocity field that can be used to estimate δ in conjunction with a suitable well field.

Figure 11-1. Anisotropic Ray Fronts and Short Spread Semblance Velocity Analysis

(a). Anisotropic ray fronts

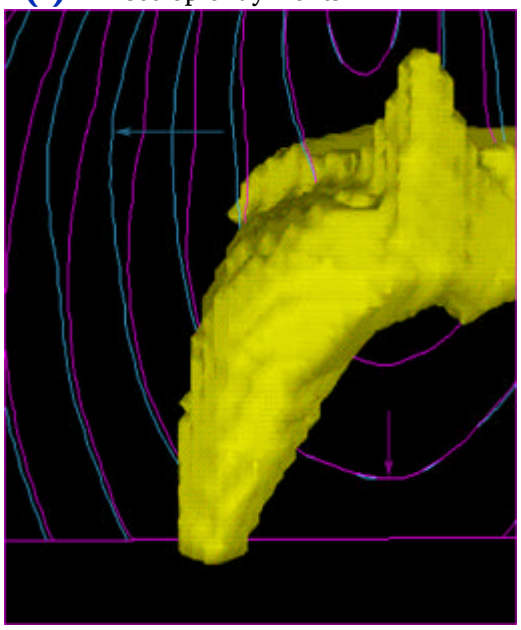

(b). Short spread semblance velocity analysis

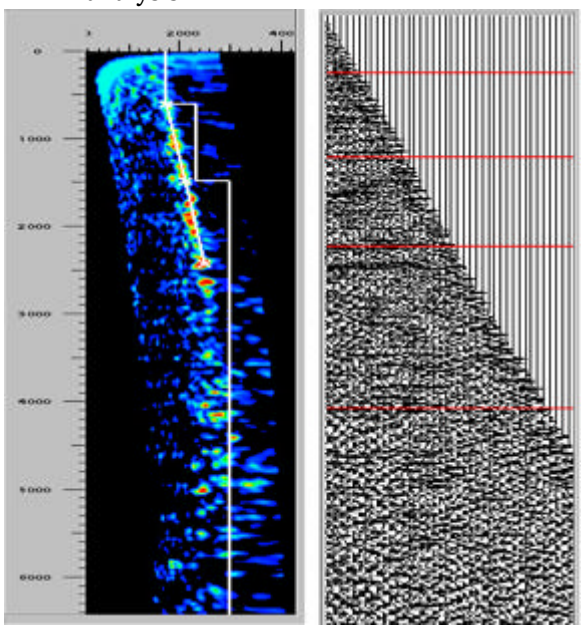

The Anisotropic Earth

Figure 11-2(a) shows conclusively that the Earth we know and love is definitely anisotropic. What we see in this figure is a comparison between an isotropic and an anisotropic migration of a small piece of a seismic section and well as a direct comparison to to data from a VSP-CDP transform section. The 3D vertical seismic profiles (VSPs), as shown in Figure 11-2(b), could provide virtually all of the additional anisotropic parameters in cone relative to the central well location. As shown in Figure 11-3, VSPs provide a superb approach for tying surface seismic data to reflecting horizons and are perhaps one of the best methods for both recognizing and proving the existence of anisotropy in real rocks. Unfortunately, VSPs provide information about anisotropy only at a relatively sparse set of well locations. To construct full wide area 3D anisotropic modes necessitates that we find methods for using recorded seismic data to extend the estimation area.

Figure 11-2. Vertical Seismic Profiles and Their Use in Depthing

(a). VSP-CDP transform, anisotropic versus isotropic migration

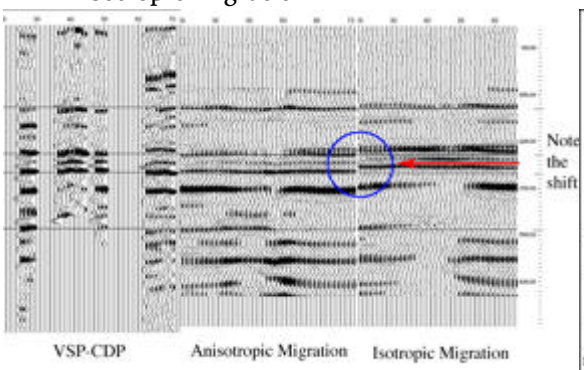

(b). 3D VSP after imaging

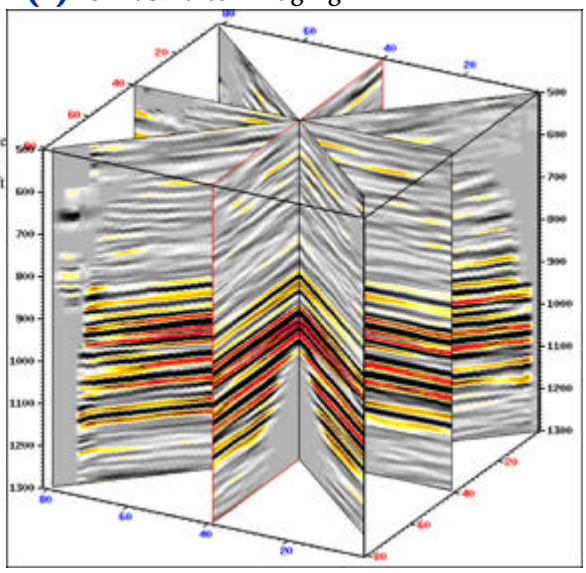

Figure 11-3. VSP tying surface data to reflecting horizons

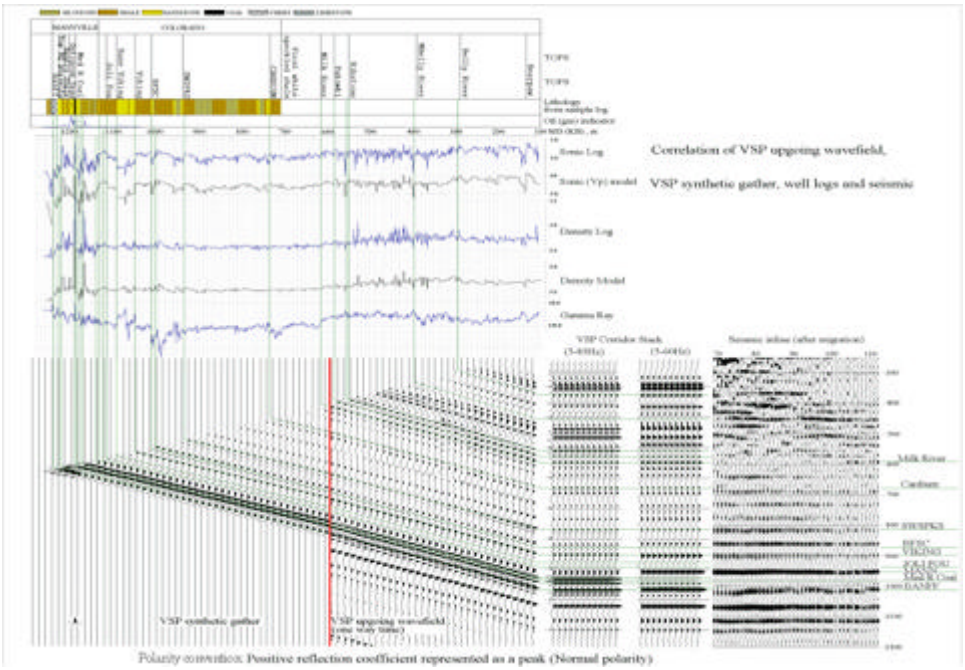

Anisotropic Normal Moveout

Today we know that the Earth is mostly anisotropic. When we estimate velocities in the isotropic case, we are trading offset information for what we think is vertical velocity. In an anisotropic world this necessarily implies that we are estimating angle dependent sound speeds and as a result we should not expect to produce images that match our wells in any form or fashion. We also should not expect our traditional isotropic velocity analysis to completely flatten common-midpoint gathers. Figure Figure 11-4 demonstrates what happens when we do. Here we see the so-called *hockey sticks* so prevalent in anisotropic media. In the past these patterns were usually muted off so as to improve overall image quality. What we really should have done was to try to figure out how to use this information to produce more accurate subsurface images.

Figure 11-4. After Leon Thomsen DSC 2002. Typical *hockey stick* character after application of *NMO* using the usual stacking velocity equation without the anisotripic term.

As we saw in the chapter on modeling, the moveout in a VTI medium is specified by the anisotropic normal moveout equation, Equation 2-26, which has been at least partially empirically corrected in Equation 11-1.

(11-1)
$$t^2(h) = t_0^2 + \frac{h^2}{v_{nmo}^2} - \frac{(v_{hor}^2 - v_{nmo}^2)h^4}{v_{nmo}^2(t_0^2 v_{nmo}^4 + 1.2 v_{hor}^2 h^2)}$$

Several important observations can be made concerning this equation. The first two terms are identical to the equation we currently use for both time and depth velocity estimation. Thus, we are already familiar with how they work and how we can use them to advantage. Because the difference between v_{nmo} and v_{hor} is usually small they are also the dominant terms when the half offset h is relative short.

At first glance this suggests that we can perform an anisotropic velocity analysis as a two step process. The first step ignores v_{hor} and just estimates v_{nmo}. Once v_{nmo} is available a second pass through the data provides estimates for v_{hor}. As we will see we can also perform a 3D velocity analysis at each vector midpoint for a simultaneous estimate of these important parameters.

Although known to be somewhat less statistically stable than Equation 11-1, Equation 11-2 relates the offset dependent traveltime $t^2(h)$ to v_{nmo} and the so-called η parameter defined by ε and δ as Equation 11-3.

(11-2) $$t^2(h) = t_0^2 + \frac{h^2}{v_{nmo}^2} - \frac{2\eta h^4}{v_{nmo}^2[t_0^2 v_{nmo}^2 + (1+2\eta)h^2]}$$

(11-3) $$\eta = \frac{\varepsilon - \delta}{\sqrt{1+2\delta}}$$

As was the case for Equation 11-1, once v_{nmo} has been determined, η can be estimated through a semblance-based process similar to the familiar stacking velocity analysis used to find v_{nmo}.

These two formulas can also be used in what you might call a simultaneous inversion for either v_{nmo} and v_{hor}, or for v_{nmo} and η. What is different is that the semblance panels are 3D volumes of two of the parameters and time.

Figure 11-5 is after Tsvankin (2001), where (a) shows an anisotropic arrival curve from a VTI media, and (b) shows the contours of a semblance analysis at 1.0 seconds; in this case, an estimate of $v_{hor} = 2.3$ and $v_{nmo} = 2.0$ is quite realistic. Part (c) shows that a value of $\eta \approx .16$ would not be completely inappropriate.

Figure 11-5. Estimating Vnmo and Vhor

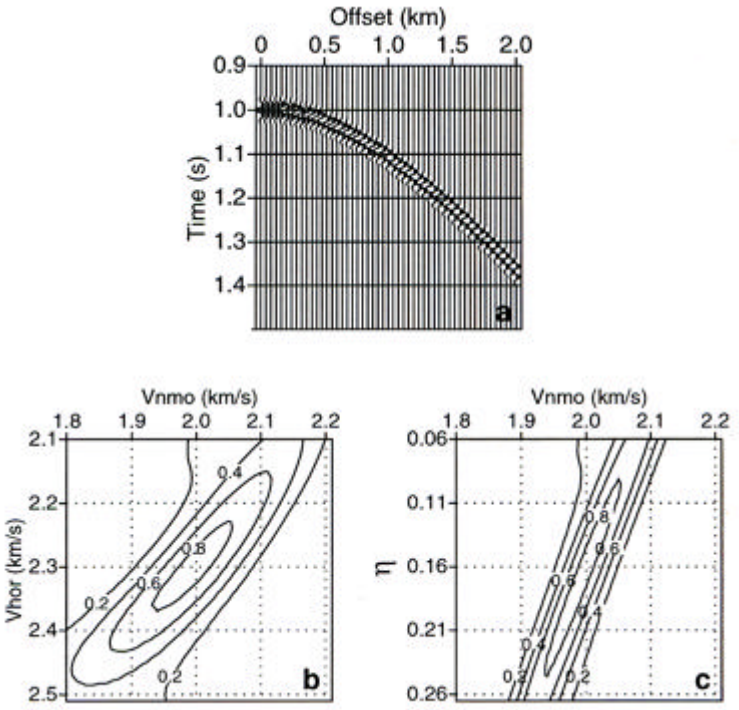

Figure Figure 11-5 provides a simple glimpse of the *NMO* based inversion process. Part (a) shows a single arrival from a reflector embedded in an anisotropic medium. The zero-offset time t_0 of this reflector is 1 second. In this case, the model *NMO* velocity is 2.0 meters/second, the model horizontal velocity, v_{hor}, is 2.3 kilometers/second and the η of the model is 0.16. Part (b) shows a slice at 1 second through a 3D $v_{nmo} - v_{hor}$ velocity analysis of the data in part (a). Clearly, values of $v_{nmo} = 2.0$ and $v_{hor} = 2.3$ kilometers per second are reasonable choices. Part (c) shows the similar panel for v_{nmo} and η. Since v_{nmo} is known from part (b) choosing $\eta = 0.16$ would not be out of line.

Following the process described above yields three parameters, v_{nmo}, v_{hor} and η. Because η is defined in terms of ε and δ, we must find some process which allows us to find either δ or ε. Once determined, we will have achieved the first step in developing a model that describes compressional wave propagation in an anisotropic medium. A quick review of the section on Thomsen parameters reveals that

(11-4)
$$\varepsilon \approx \frac{v_{hor}}{v_{P0}} - 1$$

Thus, we need a process to determine v_{P0} so we can estimate δ algebraically. To do so, we measure vertical velocities in a well. Although the measurements are at higher frequencies then seismic sound speeds, these can always be modified as the need arises. This means that we need a process for constructing a vertical well field. Once we have that, we can construct our VTI Earth model from our *NMO* based estimates, with the exception of γ.

Depthing

Geophysical approaches to finding vertical velocity fields abound. Some of the earliest were called *depthing*, or, perhaps more precisely, *depth conversion*. Depth conversion typically begins with a careful analysis of the wells of interest.

Figure 11-6(a) shows how the overburden above the potential reservoir is separated into different velocity units. Starting at the surface, we model the velocity behavior in layer 1 and create a depth map for horizon 1. We then model the velocity in layer 2 and hang the depth conversion from the depth horizon we already have for horizon 1. We repeat the process for each layer until we reach the maximum depth desired.

Figure 11-6. Analyzing wells for unitized velocities

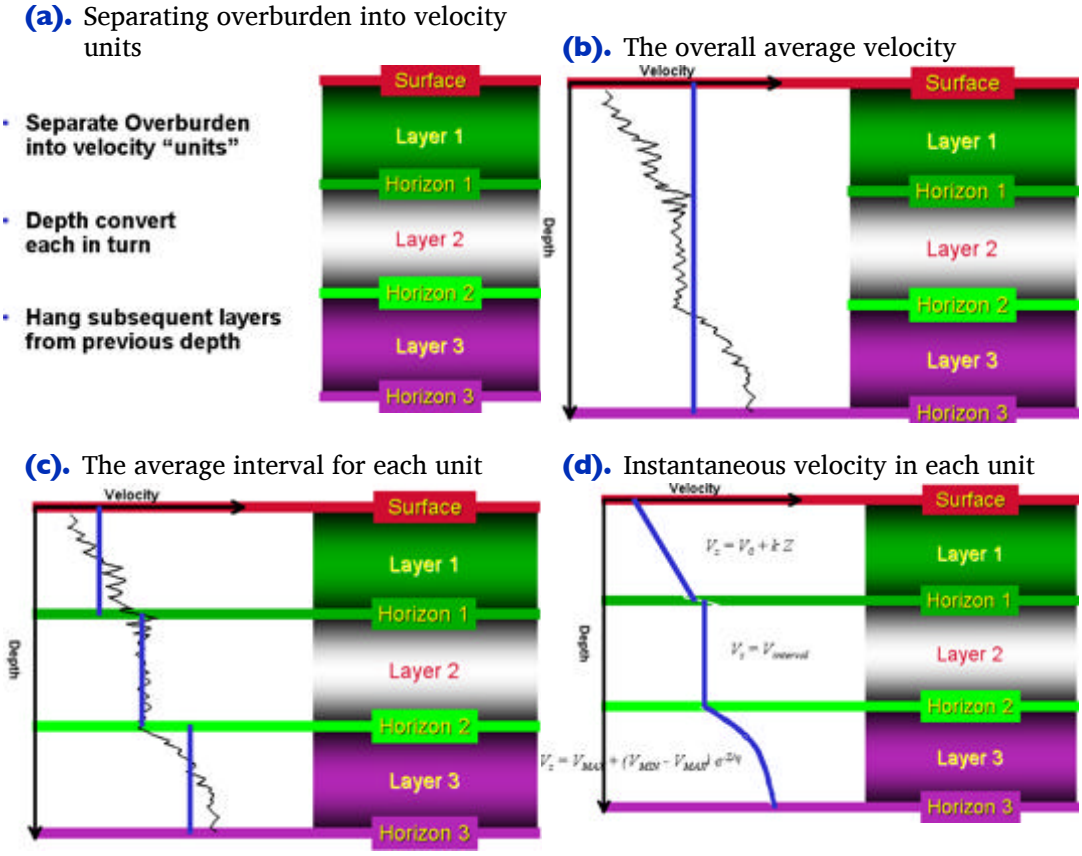

Figure 11-6 shows the typical approach to analyzing wells to determine a well or depthing velocity structure. The graphic in (a) of this figure presents the standard process. The well is separated into overburden units or well tops of horizons of interest. Each of these units can then be converted to depth. Analysis of each such unit can be simple, as indicated in Figure 11-6(b), or more complicated as indicated in (c) and (d). The more accurate approach is clearly represented by Figure 11-6(d).

Depending on the complexity and strength of the velocity variation within the well, we can minimize the number of depth units. Figure 11-6(b) shows the simplest technique using a single average velocity. We ignore the layering just described, and compute an average velocity from the surface to the target horizon. This has the advantage of being simple and quick to implement, but has the disadvantage that, since the behavior of the subsurface is not fully modeled, our confidence in the predictions may be reduced. This is a good domain for viewing stacking velocities, because they have seen all of the overburden anyway.

Moving to a more sophisticated approach in Figure 11-6(c), we look at interval velocity. Here, we assign a constant velocity to each layer. This velocity may vary spatially from well to well. We can model this by cross plotting interval velocity versus midpoint depth, for example, or we can contour the well interval velocities, perhaps geostatistically using our seismic processing velocities as a guide.

An even more sophisticated approach, as shown in Figure 11-6(d), is the use of instantaneous velocity functions. Here we are modeling the detailed velocity variation with depth on a layer-by-layer basis. The most commonly used relationship is the linear increase of velocity with depth (the V0Kz method), although modern software packages can handle any function, as shown in the third layer. Any of the parameters in these equations can be represented by grids, thus allowing full flexibility.

Constructing complex horizon-based models can be quite difficult. Figure 11-7 illustrates several requirements for different geological settings. What is important is to recognize that in a horizon-based model building exercise, we must interpret many more horizons than is usually necessary for exploration purposes. Moreover, many of the additional horizons have zero prospectivity and, consequently, are of little interest to interpreters, although these layers can be extremely important for depth imaging.

Figure 11-7. Complex model construction

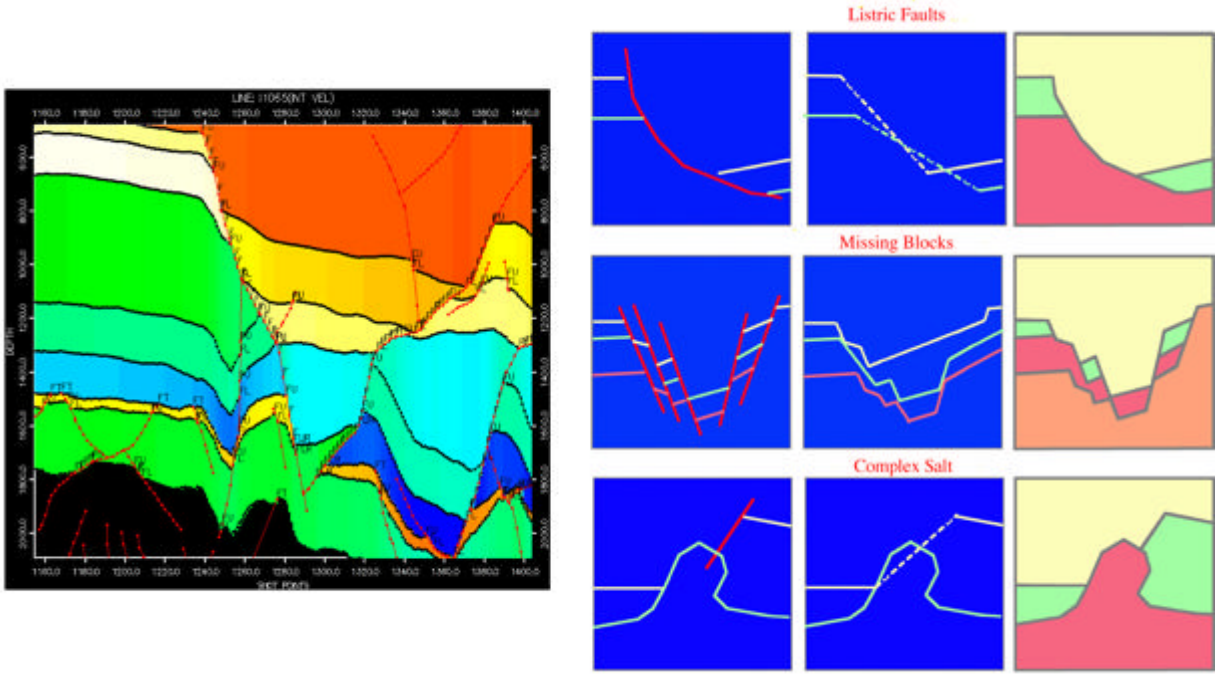

Horizontal velocity trends are thought to be linked with vertical velocity trends. Thus, using trends from the prestack depth migration velocity analysis can be used to statistically interpolate sparse well data sets. Figure 11-8 is an example velocity slice from a seismically derived Earth model. It could serve to define trends for extrapolating sparse wells to construct a detailed well field.

Figure 11-8. Seismic derived velocity slice.

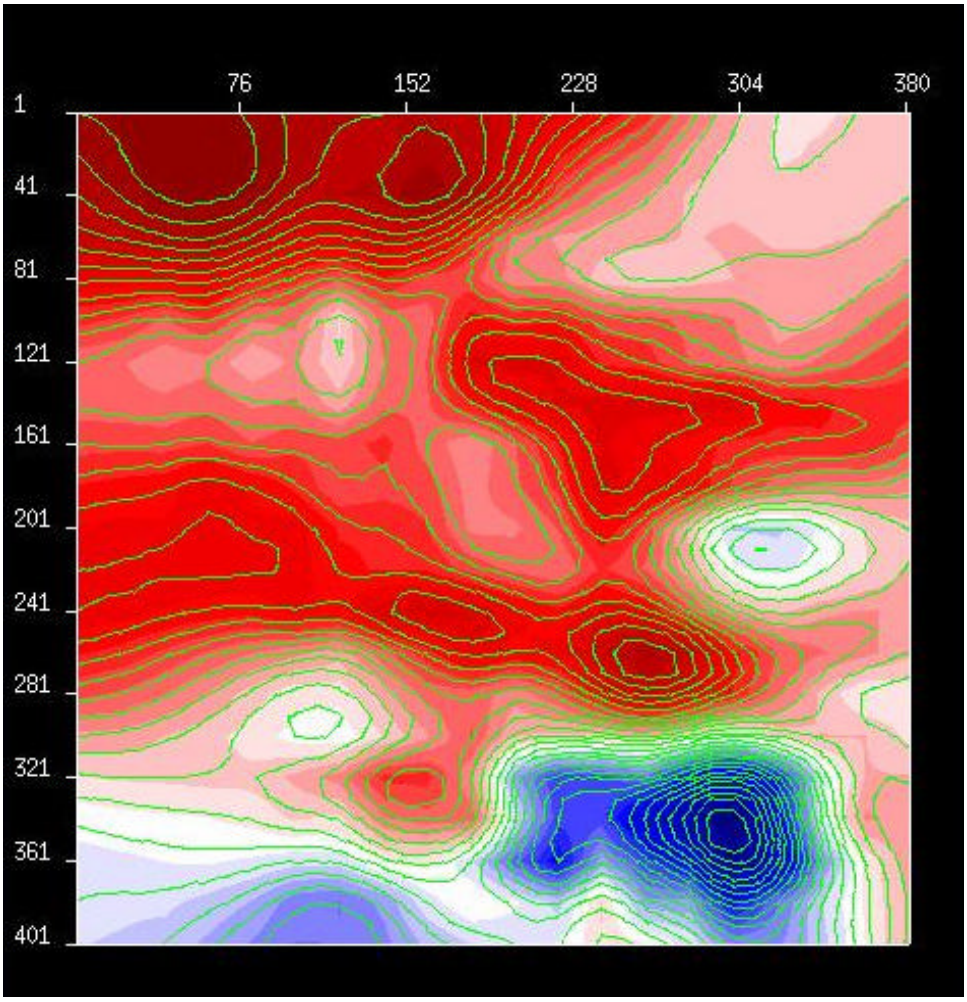

Horizons, like those in Figure 11-9(a), can be used to guide the interpolation process in a horizon consistent in a lap or off lap manner. If we decide that the subsurface geology follows the structure defined by the given horizons, a suitable projection of this estimated velocity functions on to a grid of locations defined by the user will produce a structure tracking velocity field.

Figure 11-9. Single Well Velocity Field

(a). A multiple horizon model

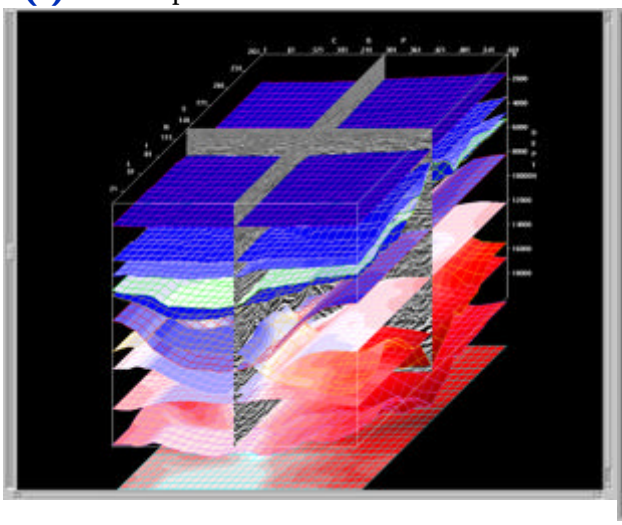

(b). A single well at the indicated location

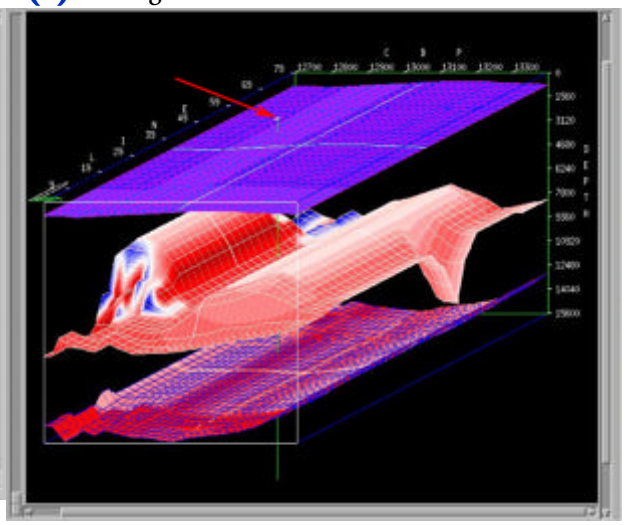

(c). Projected horizon tracking wells

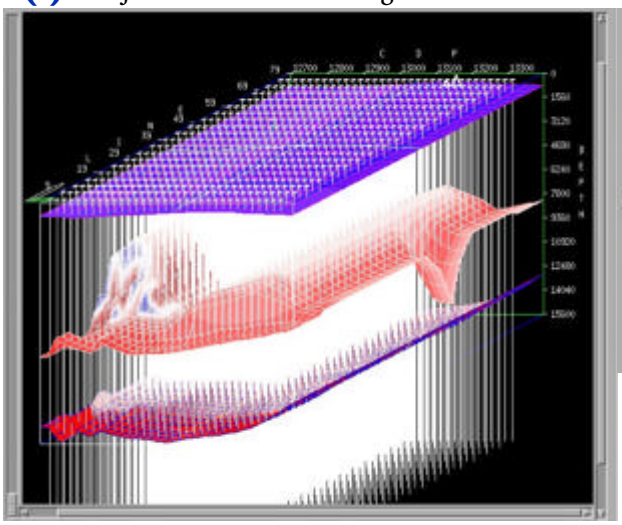

(d). A slice through the constructed model

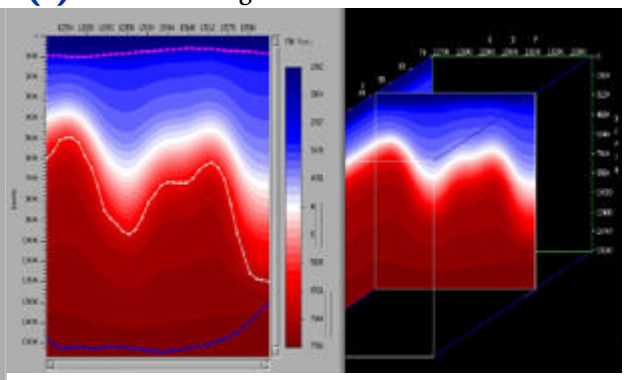

(e). Extracted RMS with interval velocity overlay

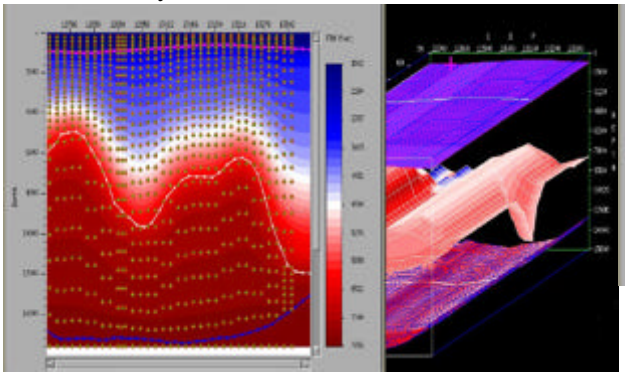

(f). Final Well field

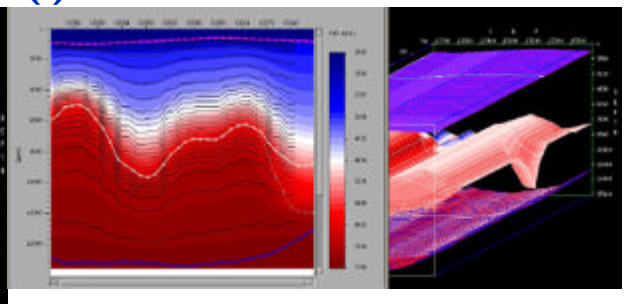

In Figure 11-9(b), a single well, at the location indicated by the arrow, is interactively projected into the three-dimensional grid. After projection, we have logs at an evenly sampled grid of surface locations, Figure 11-9(c). In this case, projection was based on shrinking and stretching the single input function to track the given horizons.

Figure 11-9(d) is a slice through the projected well field, while Figure (e) shows RMS velocities calculated from the well field. In a sense, this process reverses the usual process of estimating interval from RMS velocities. Figure (f) is a contoured version of (d) showing how the actual projection was performed.

A VTI example

Here we present an example of what one might expect from the analysis process discussed above. Figure 11-10 shows a vertical velocity (v_{P0}) field in (a) and a v_{nmo} field in (b). Because it is so similar to the vertical field the horizontal field v_{hor} is not shown. What we know from the previous analysis is that

(11-5) $$\varepsilon \approx \frac{v_{hor}}{v_{P0}} - 1$$

In this case, the ε volume is shown in Figure 11-12(b). Given Equation 11-6, we can easily solve for δ, thereby producing a complete three-dimensional volume. The result is shown in Figure 11-12(b).

(11-6) $$\eta = \frac{\varepsilon - \delta}{\sqrt{1 + 2\delta}}$$

Figure 11-10. Well and NMO Velocity Volume

(a). Estimated well velocity field

(b). Estimated short-spread MVA NMO velocity volume

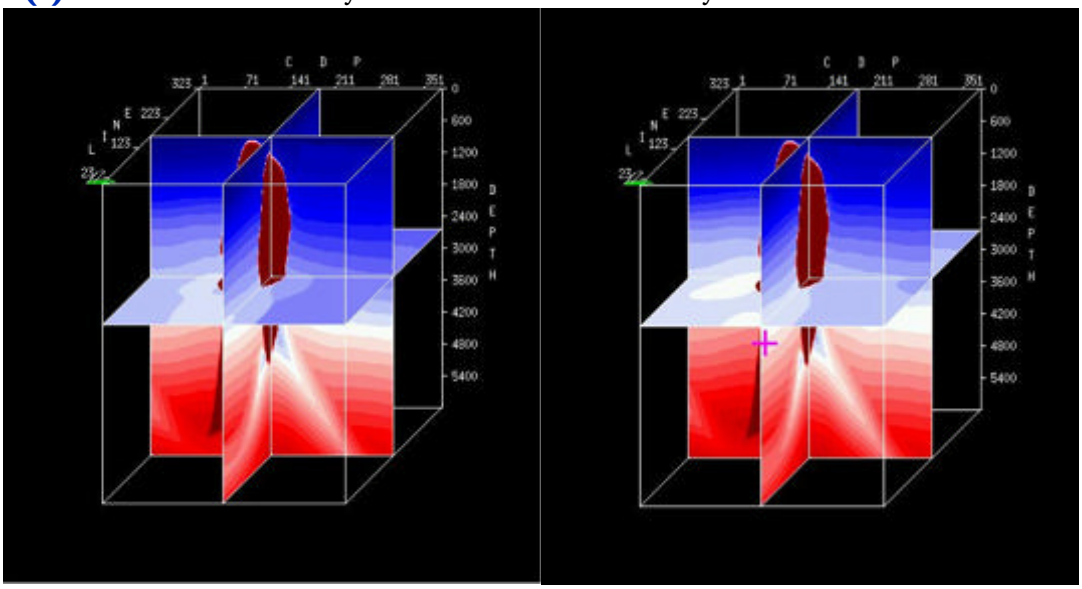

Figure 11-11. The η volume as estimated along with the v_{nmo} volume using Equation 11-2.

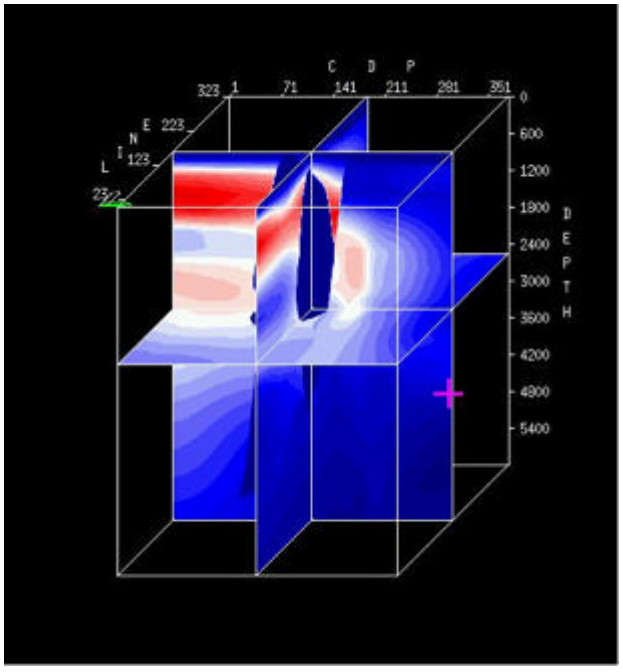

Figure 11-12. ε **and** η **volumes**

(a). The estimated ε volume.

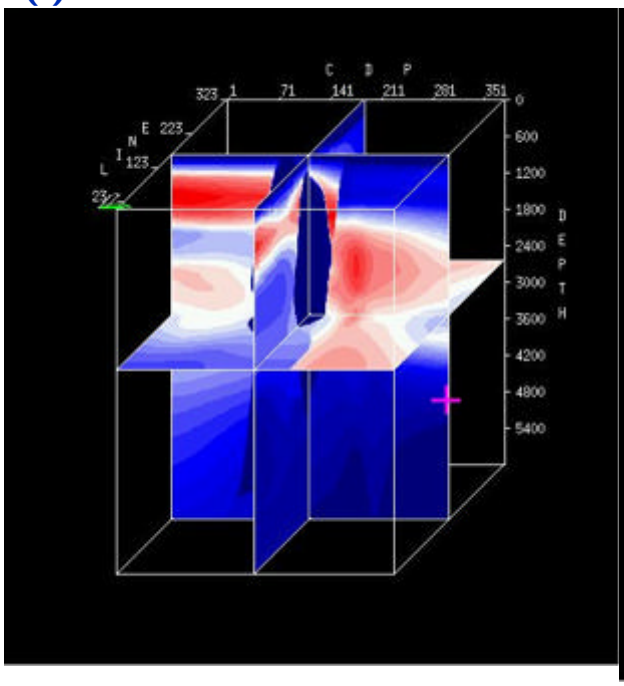

(b). The estimated δ volume.

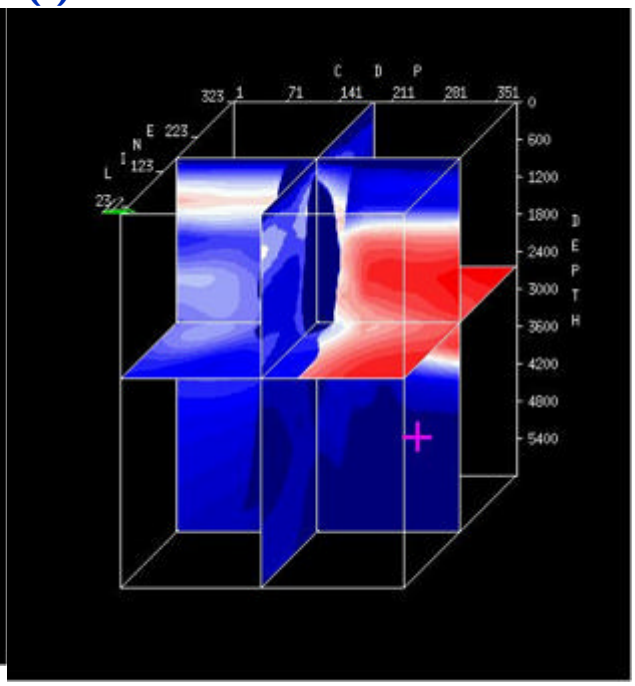

Chapter 12

Case Studies

This chapter presents several case studies showing the effects of various operational conditions.

Salt Flood and Body Insert

Figure 12-1 shows several examples of using short-offset salt floods to quickly determine the top and base of complex salt structures. In this case, the offset was limited to 1000 meters and a common azimuth algorithm was used to produce the image.

Figure 12-1. Short offset poststack salt Floods.

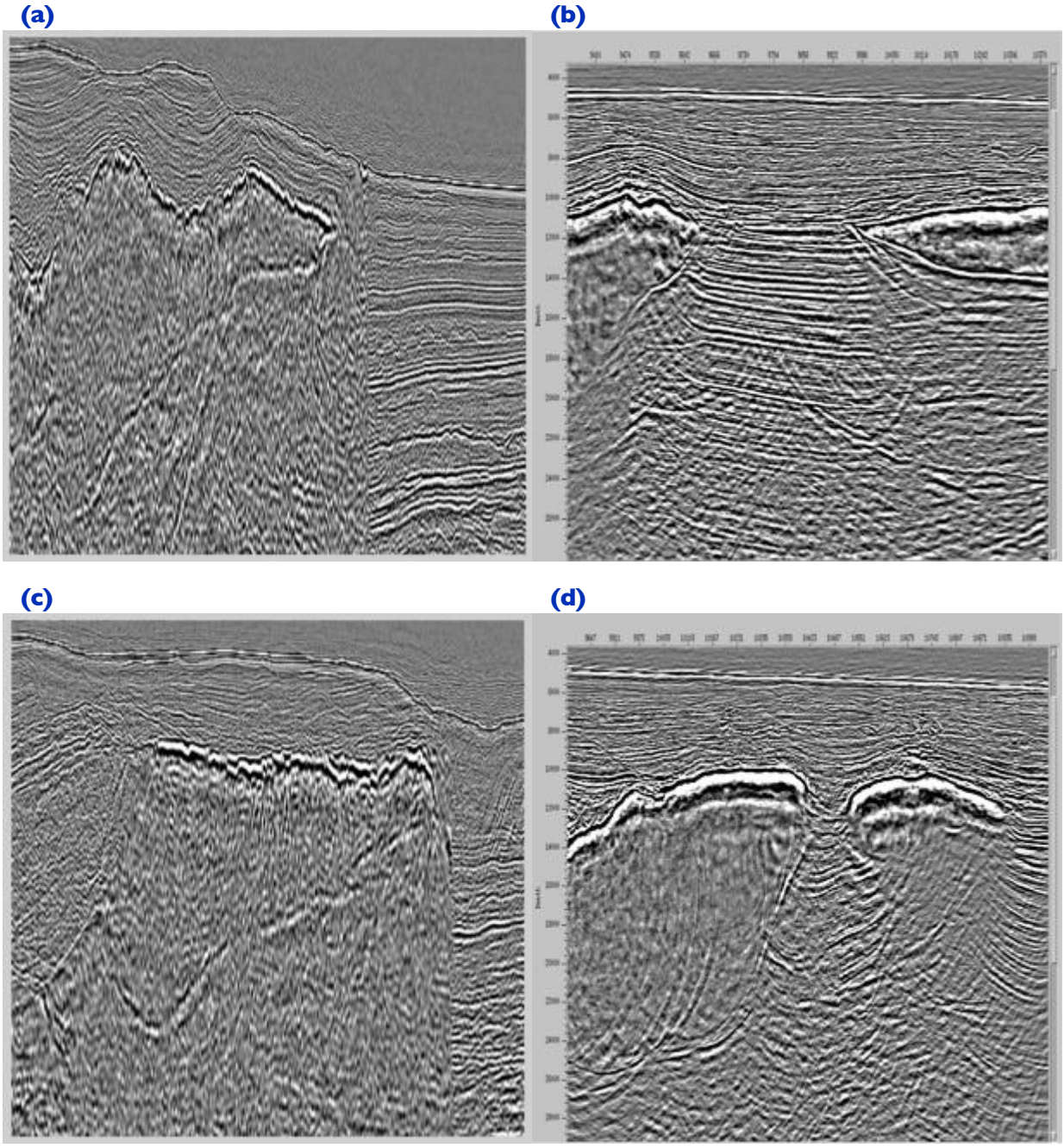

Each of these snapshots is from a Gulf of Mexico salt structure province and indicates the kinds of problems and issues that arise in this setting. Note that interpreting the top and base of salt is quite easy here, but that is not always the case. A major unsolved problem concerns why the salt base is not always visible.

Figure 12-2 shows a full volume image of a Gulf of Mexico salt structure after completion of detailed MVA and salt body insert. In this image, the salt base and sub-salt sediments are clearly imaged.

Figure 12-2. Full prestack Kirchhoff volume after salt body insert.

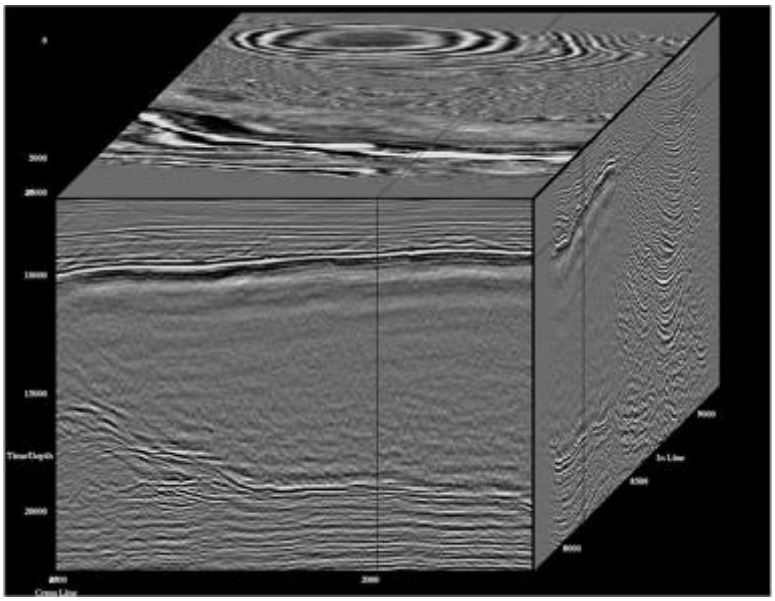

Comparing Figure 12-3(a) with (b), we observe excessive aliasing of the common azimuth section. This is very likely because the processor failed to properly assess and limit the input frequency content.

Figure 12-3. Wave Equation Aliasing

(a). Kirchhoff prestack xline image from the volume in Figure 12-2

(b). Common azimuth xline image from the volume in Figure 12-2

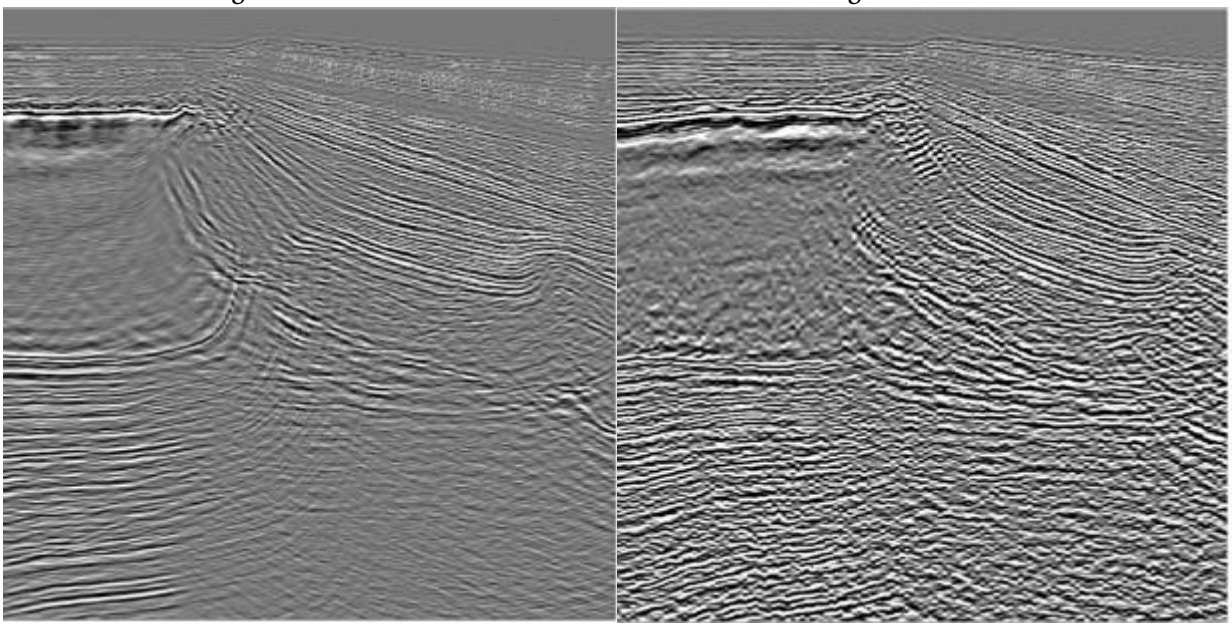

The two graphics in Figure 12-4 show that defining salt body shapes precisely when two salt structures almost overlap can be quite difficult.

Figure 12-4. Multi-level salt structures

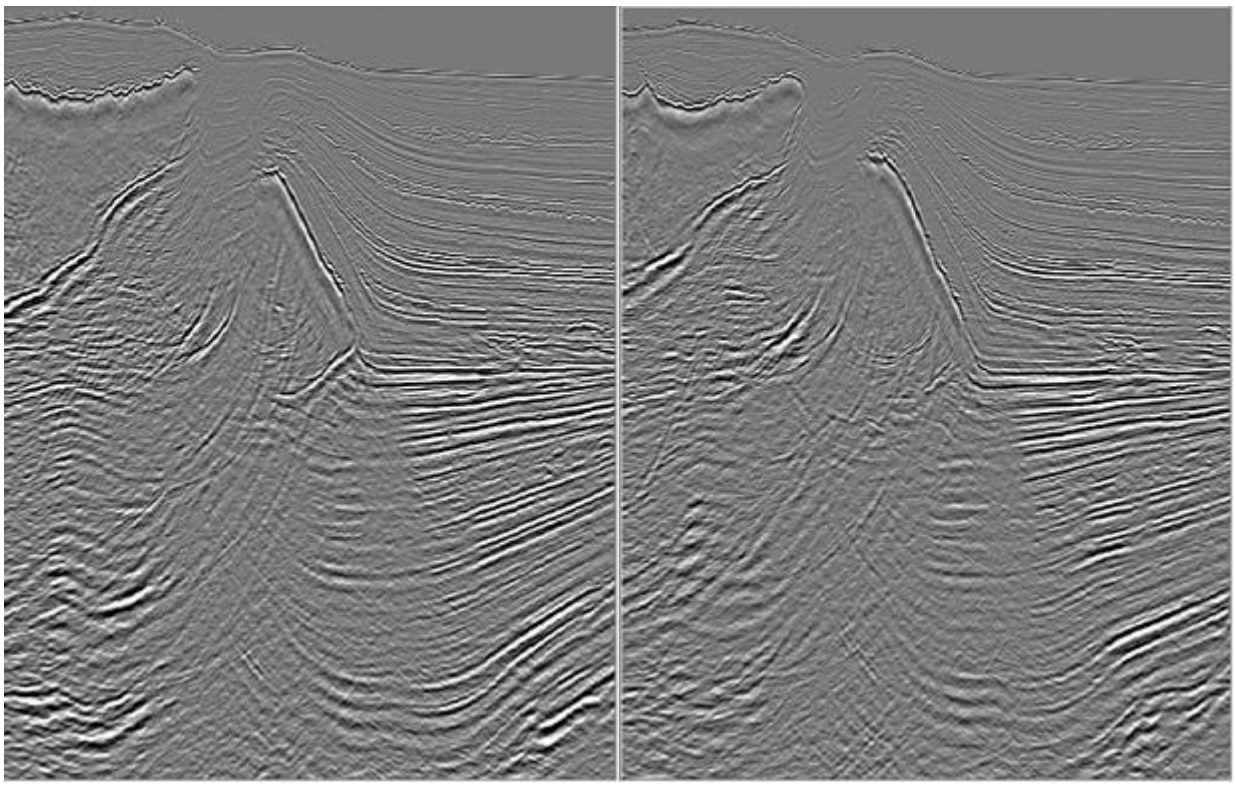

Salt structures, like the one in Figure 12-5, are relatively easy to image with single arrival Kirchhoff migrations. This is mostly due to the rugosity of the top of the salt.

Figure 12-5. Deep water laminate salt Kirchhoff imaging.

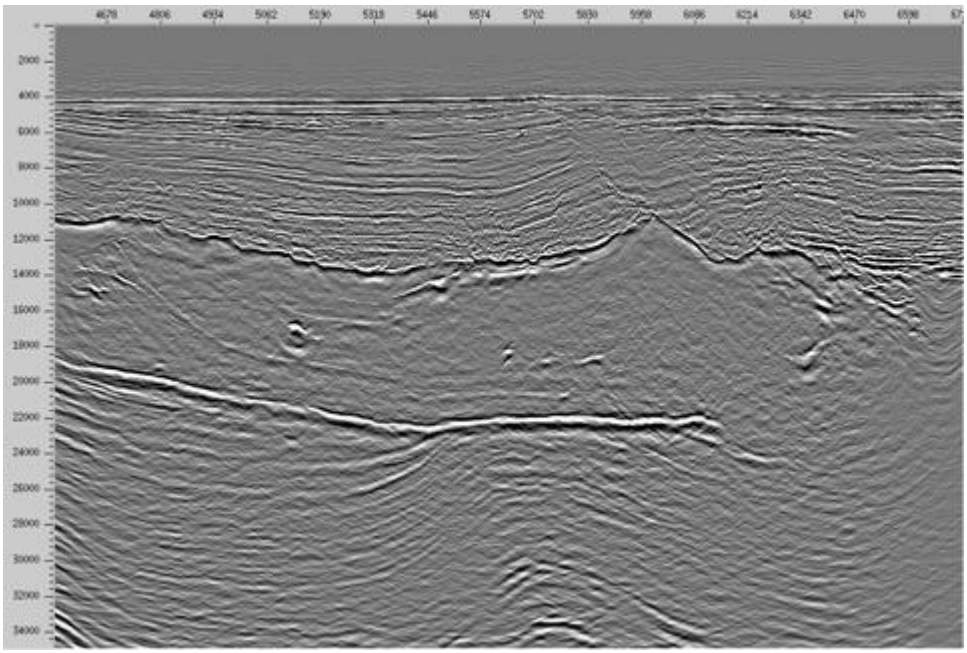

Amplitude Preservation

Figure 12-6 shows the relative amplitude differences between a full Kirchhoff migration (left) and a one-way phase-screen prestack depth migration (right).

Figure 12-6. Kirchhoff versus one-way shot profile offshore Florida

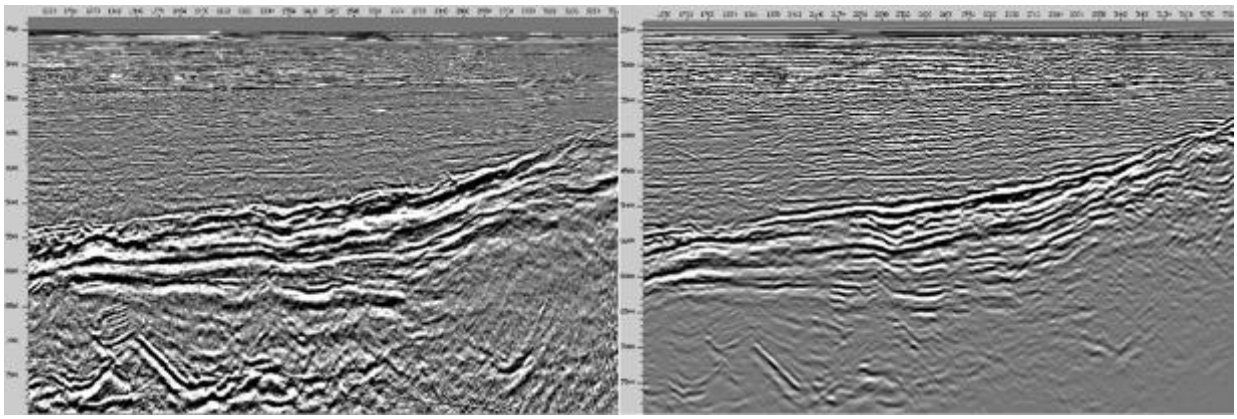

Which One Should I Use?

Figure 12-7. Inline slices through impulse responses

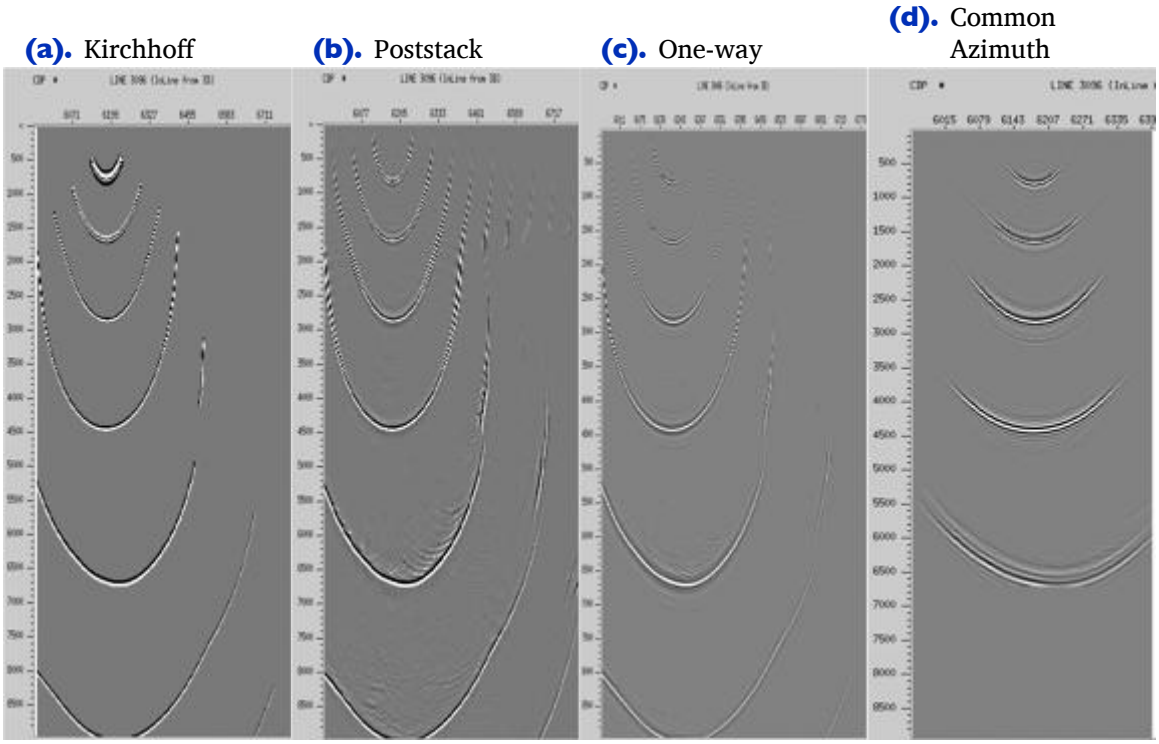

Figure 12-8. Crossline Slice Through Impulse Responses

(a). Kirchhoff **(b).** Poststack **(c).** One-way **(d).** Common Azimuth

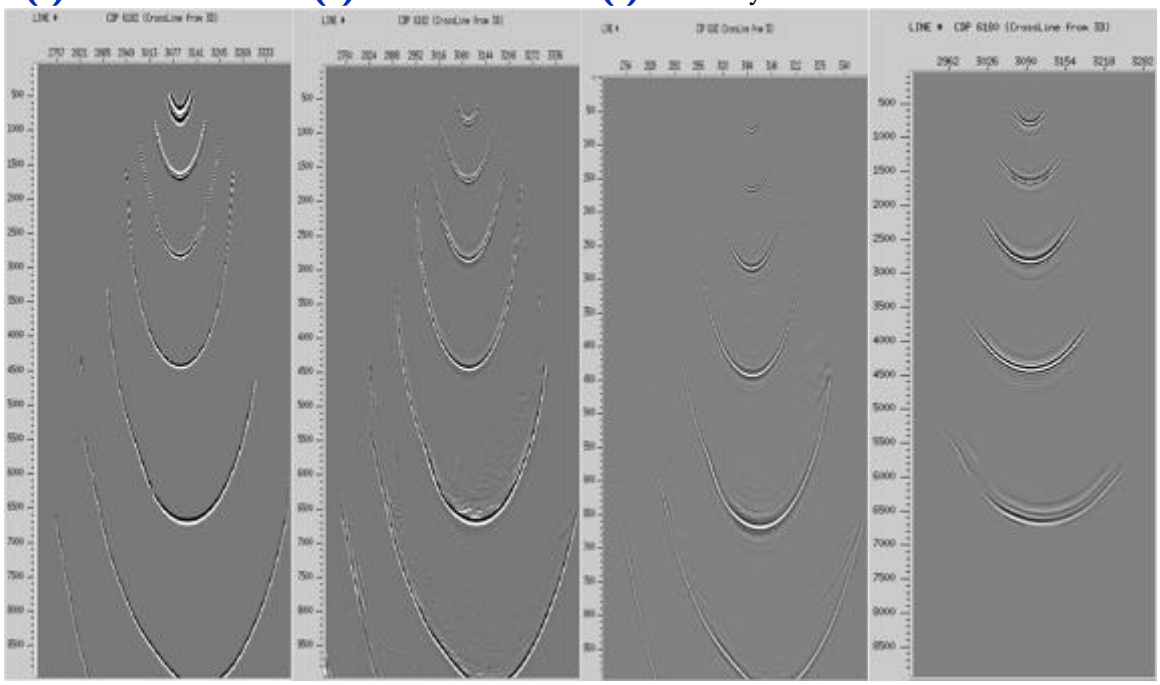

Figure 12-9. Depth slice through impulse responses

(a). Kirchhoff **(b).** Poststack **(c).** One-way **(d).** Common Azimuth

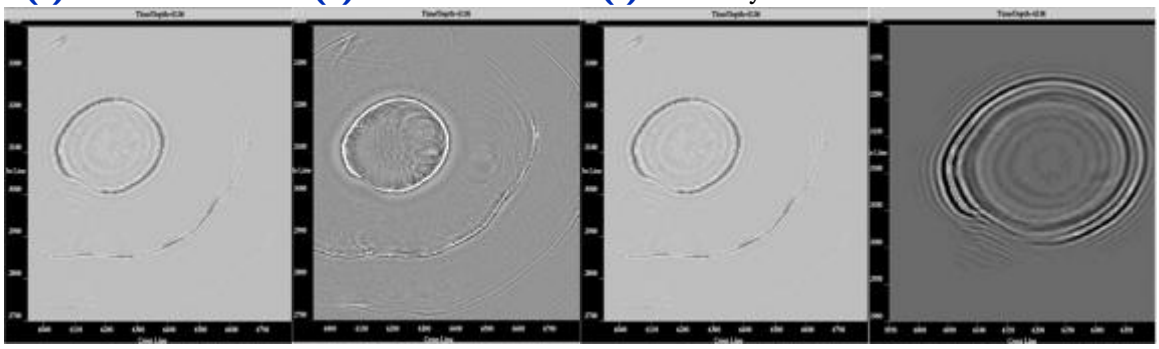

Land Data PSTM Versus PSDM Comparison

Figures 12-10, 12-11, 12-12, and 12-13, are examples from a 3D land survey near Daxing, China. What they all show is that wave equation migration is generally better at fault definition than single arrival based Kirchhoff methods. It is also much better at amplitude preservation, even when, as in the one way case, it is not perfect.

Figure 12-10. PSTM (top) versus PSDM (bottom) on land data near Daqing China

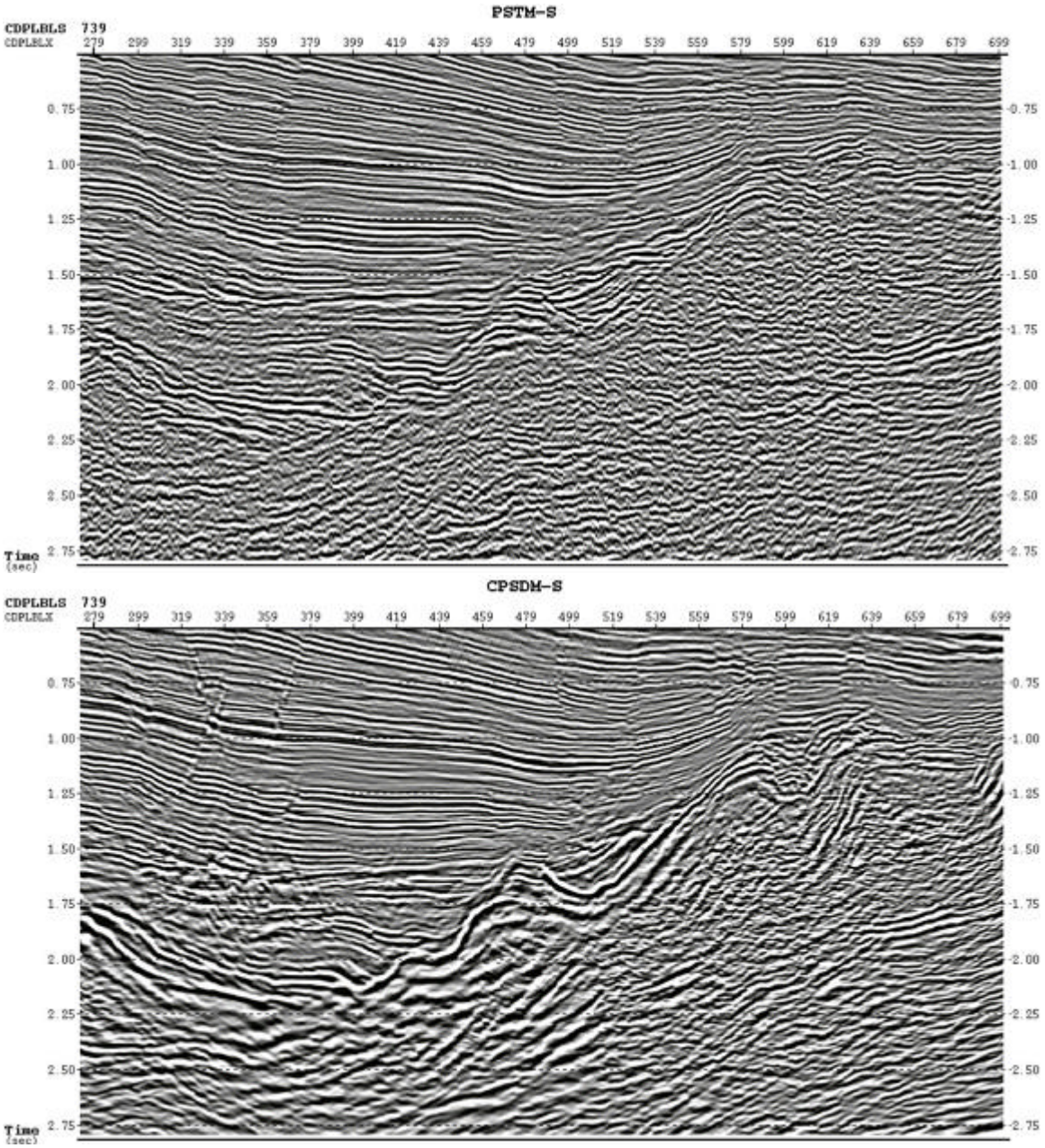

Figure 12-11. PSTM (top) versus PSDM (bottom) on land data near Daqing China

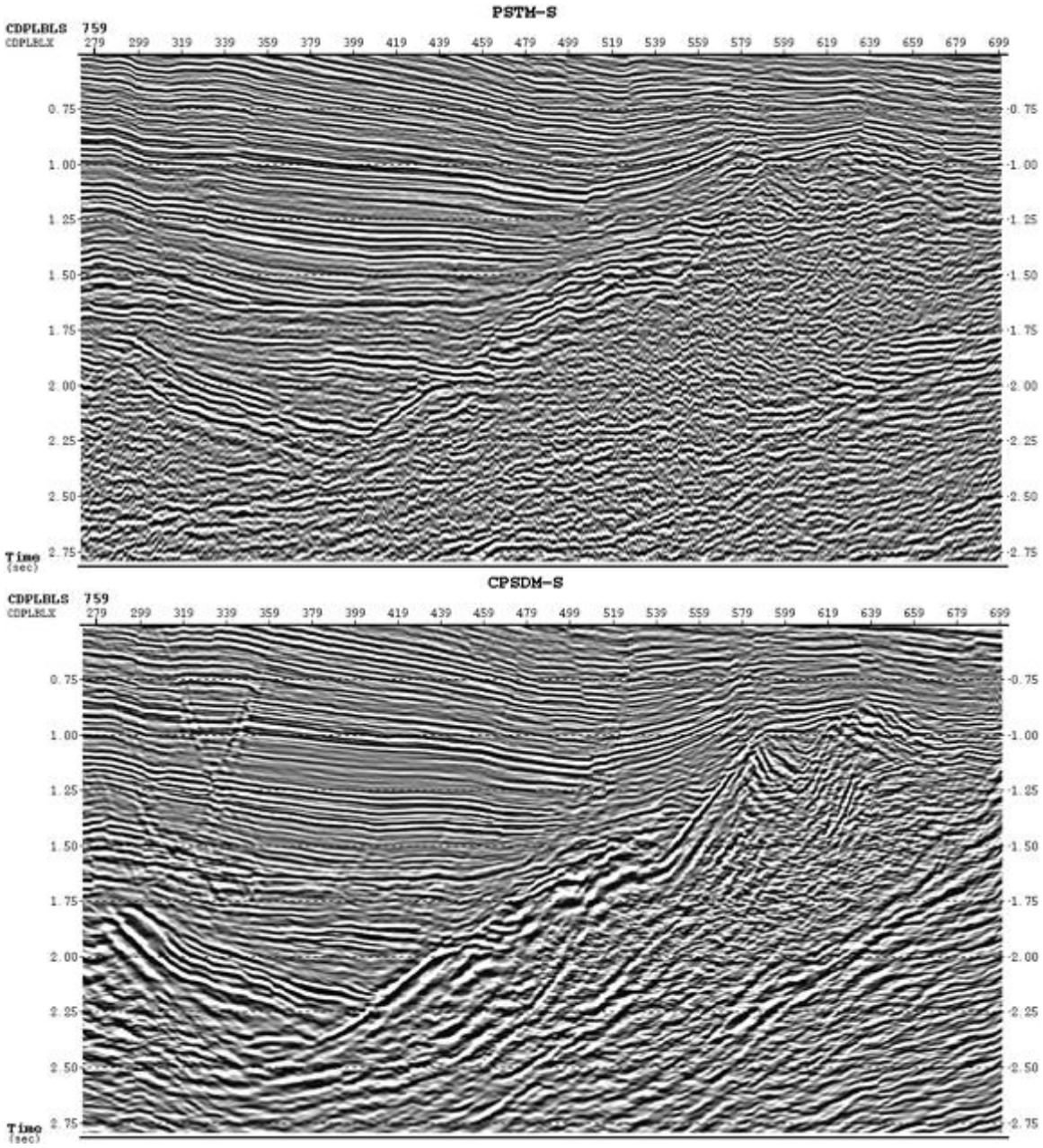

Figure 12-12. PSTM (top) versus PSDM (bottom) on land data near Daqing China

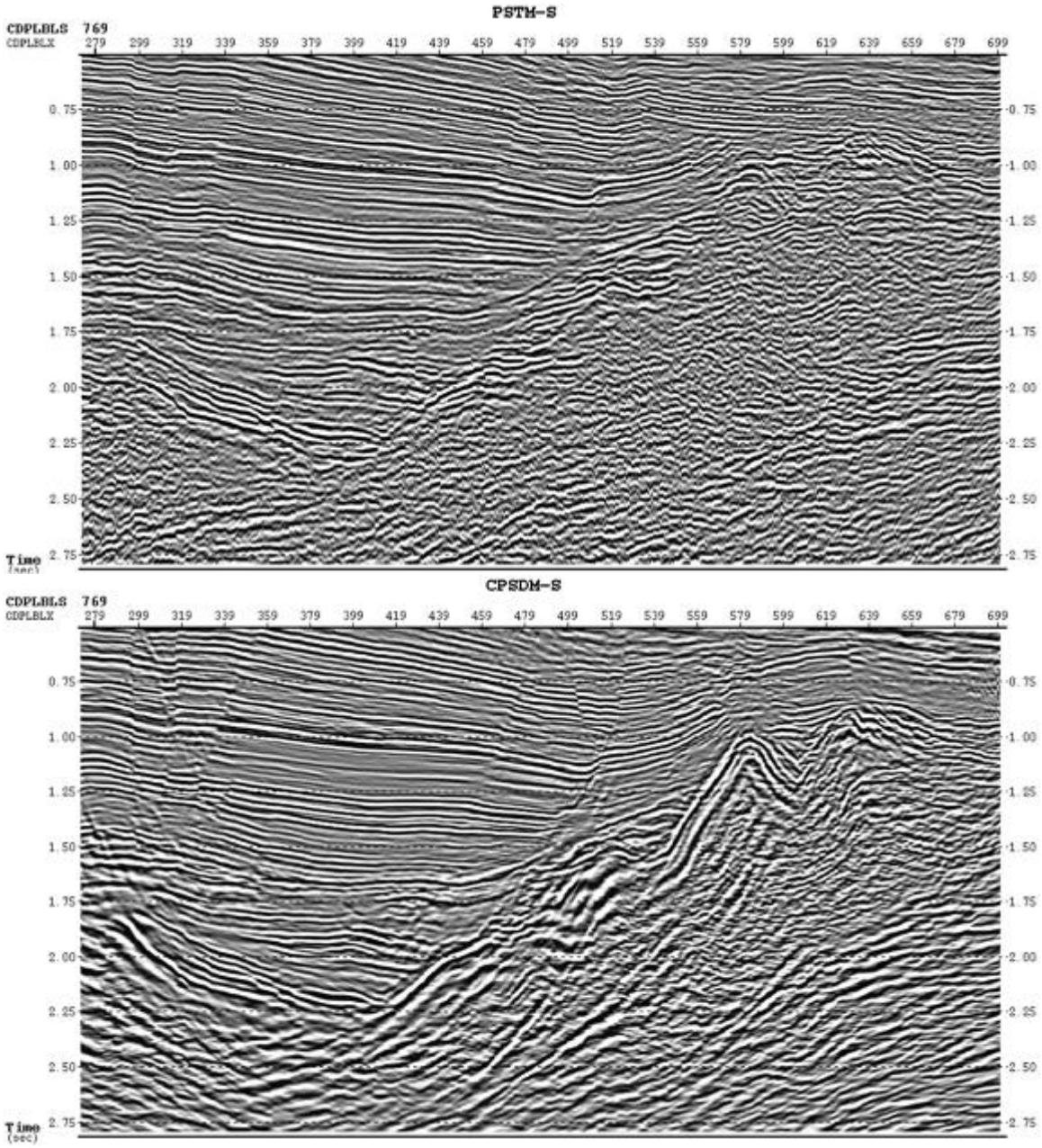

Figure 12-13 shows that when the data is over tertiary soft rock geology, the difference between various migration algorithms can be small. While certain parts of the top figure are better than the bottom figure, seeing the differences requires a sharp eye.

Figure 12-13. Curved ray PSTM versus Straight Ray on land data near Daqing China

(a). Curved Ray Kirchhoff PSTM

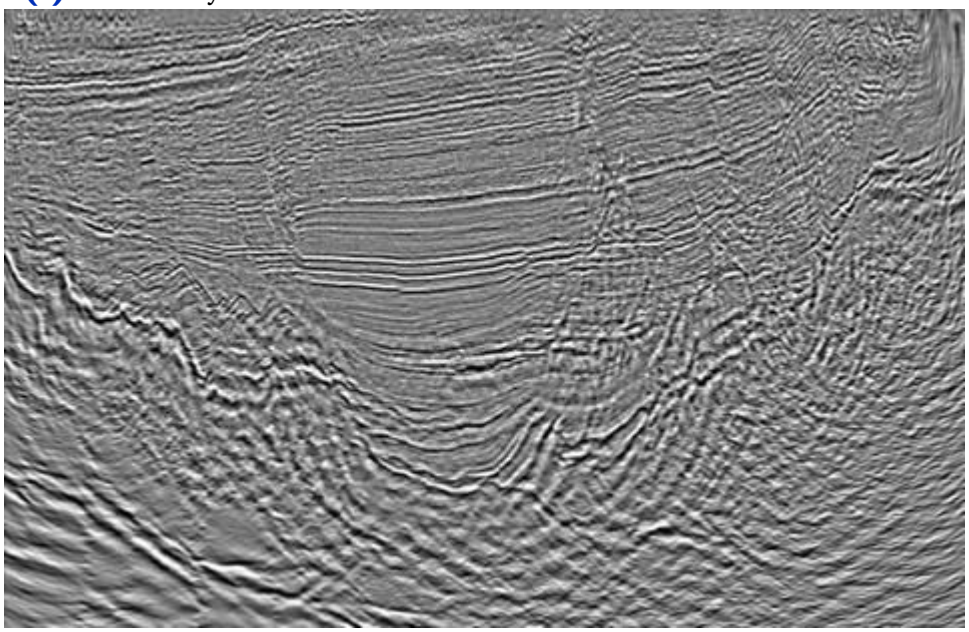

(b). Straight Ray Kirchhoff PSTM

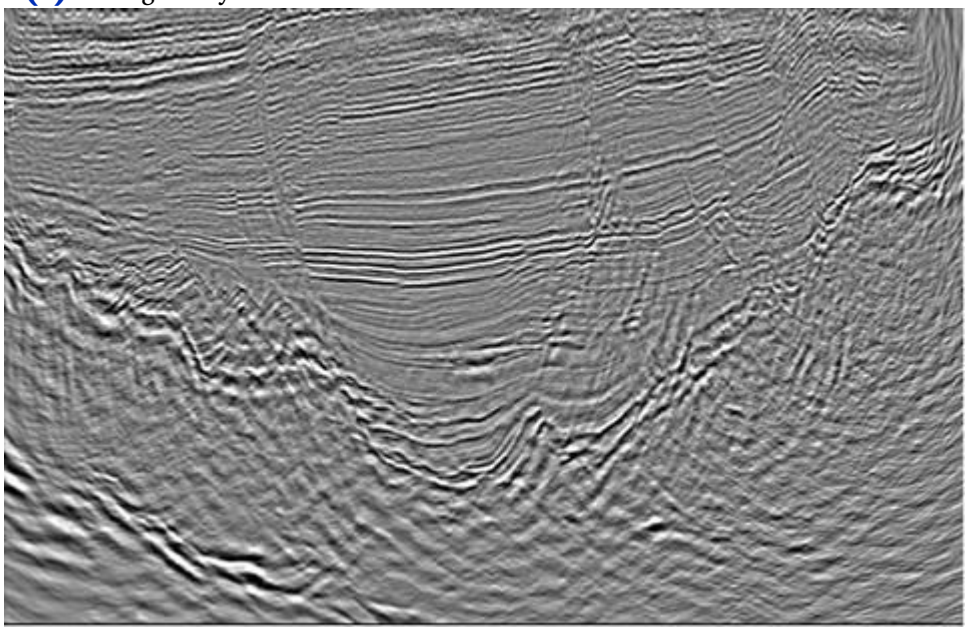

Autopicking PSTM

Figure 12-14 shows an image based on automatically picked velocities. In the image, the chase was the initial iteration of the imaging project.

Figure 12-14. Automatically picked and imaged PSTM

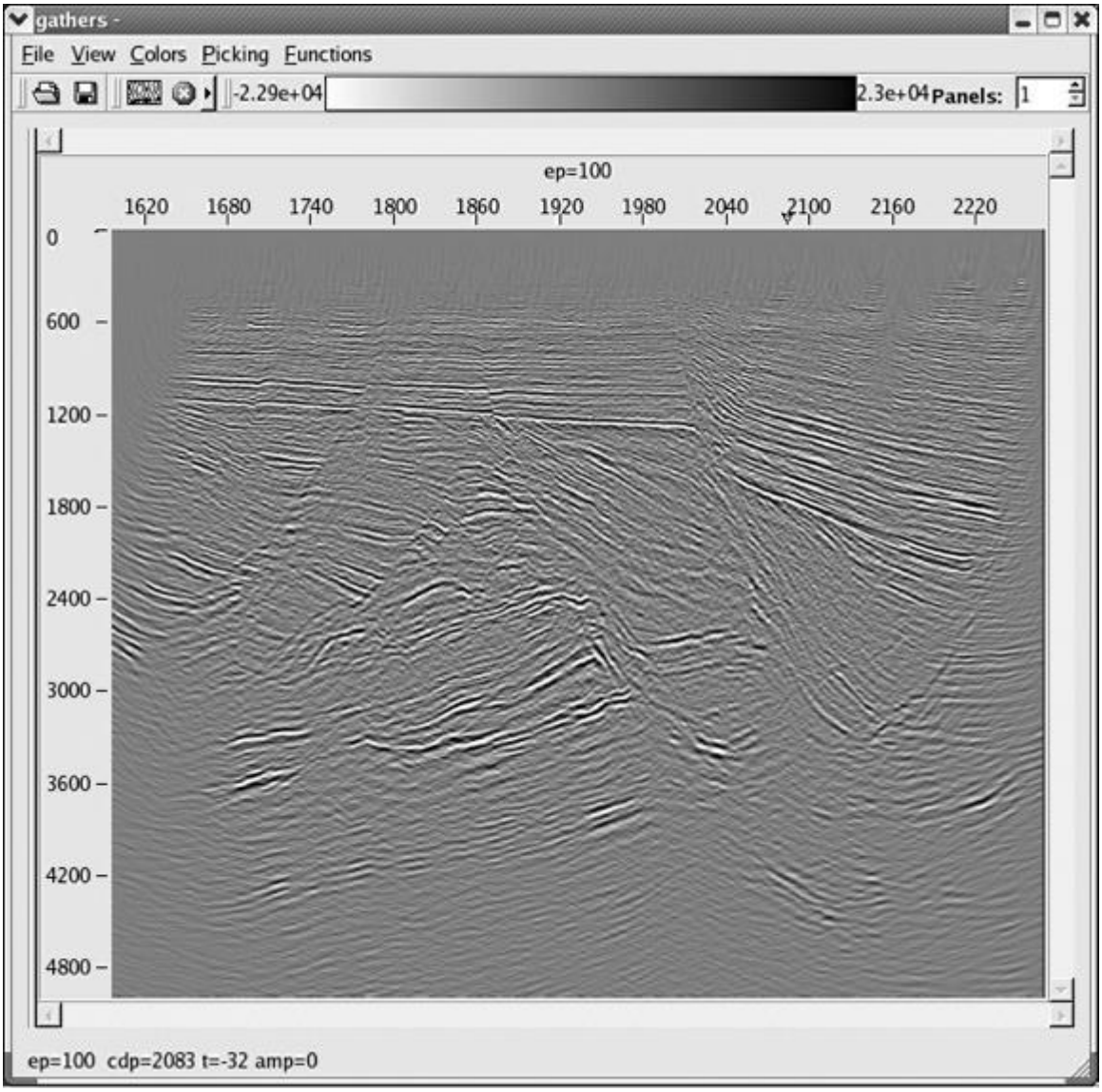

Tomography

Figure 12-15. A comparison of imaging with and without tomography

(a). Before tomography (left) and after tomography (right)

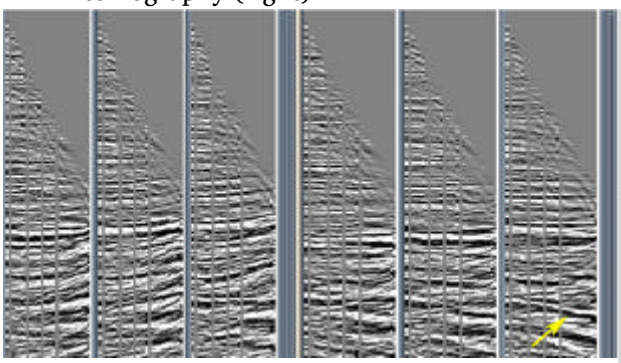

(b). Before tomography

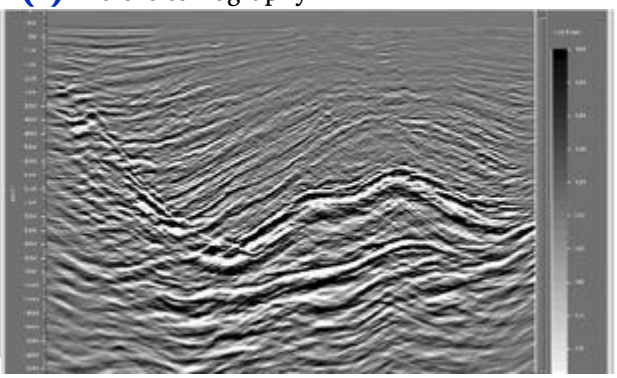

(c). After tomography

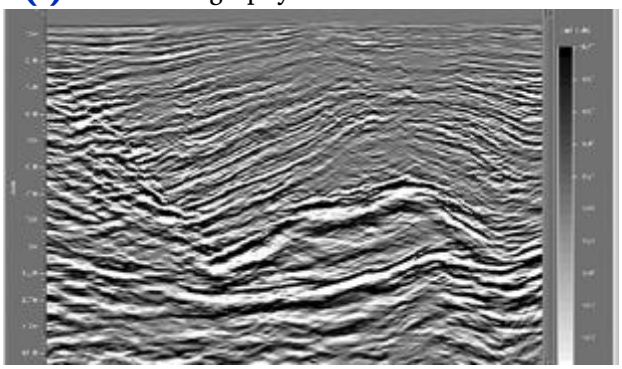

South Texas Fault Shadow

Figure 12-16(a) is a Kirchhoff PSTM that revealed a severe fault shadow imaging problem. Figure 12-16(b) shows that, while depth migration has generally improved the overall imaging quality, it has not completely solved the problem.

Figure 12-16. South Texas fault shadow

(a) South Texas fault shadow PSTM

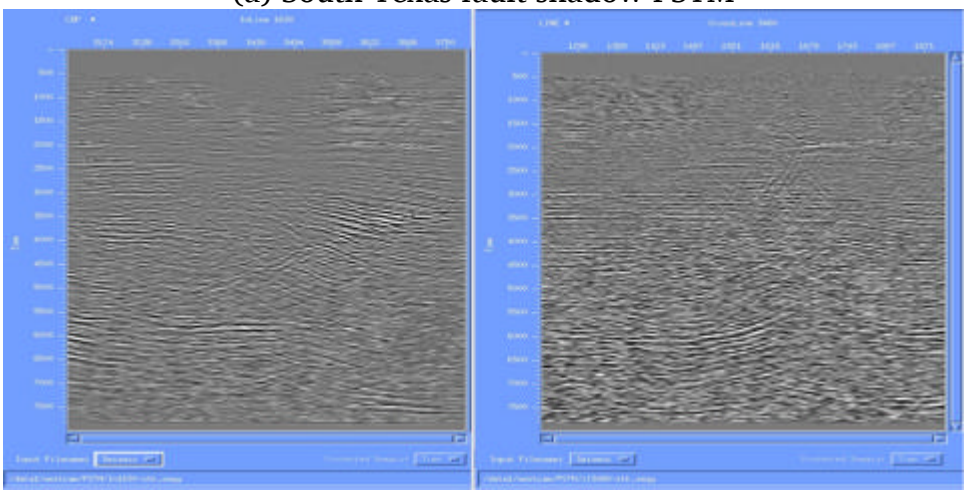

(b) South Texas fault shadow PSDM

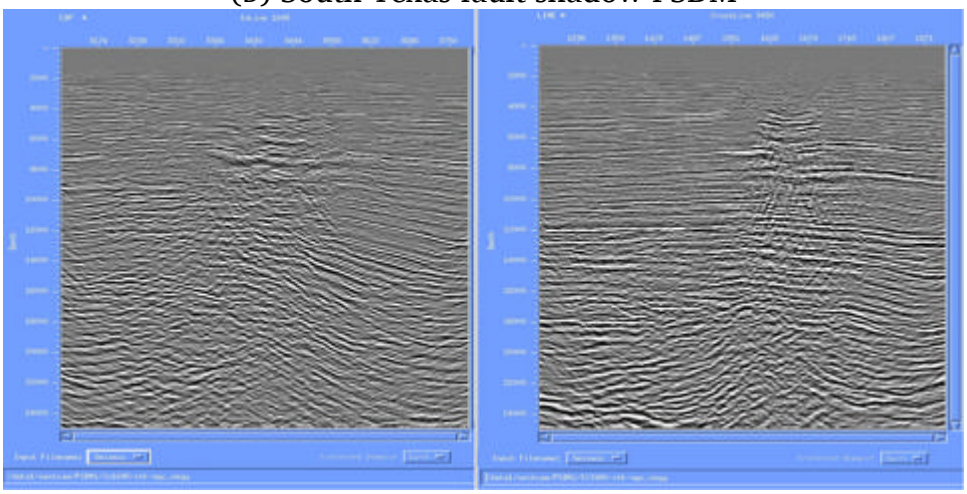

Blessing Texas Case Study

The availability of a small 3D Southeastern Texas Gulf of Mexico survey provided an excellent data set for directly comparing single arrival Kirchhoff migration with the much more computationally intensive full waveform reverse time migration. This study concluded that while there is an almost imperceptible difference between vertical time or depth sections, a high resolution fault analysis indicates that the more accurate method produces much higher resolution results. That this is the case, even when neither the geology nor the velocity model indicates any significant lateral gradients, is a bit surprising.

Figure 12-17 is a graphic montage depicting a 3D seismic survey acquired in the late 1980's or early 1990's near the town of Blessing in the state of Texas in the USA. The graphic in (a) shows the approximate location of the survey, (b) shows the CDP locations and fold, (c) shows the shot locations, and (d) shows an example shot where each shot was acquired by eight lines of receivers. There were approximately 1080 receivers per shot, and there were approximately 4265 shots. There are approximately 4,200,000 total traces in this survey.

Figure 12-17. Description of a 3D seismic survey Southwest of Houston near Blessing, Texas

(a). Blessing, Texas 3D survey location

(b). 3D CDP locations and Fold Map

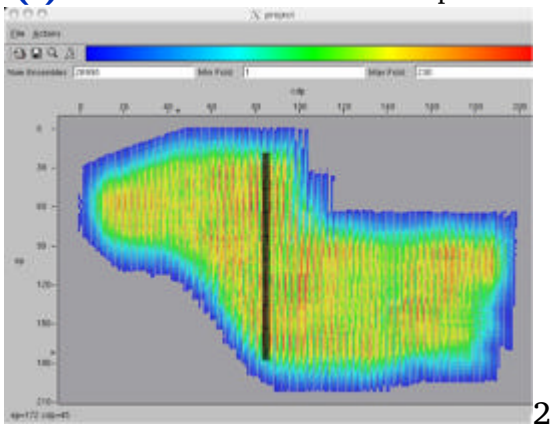

2

(c). Shot location map

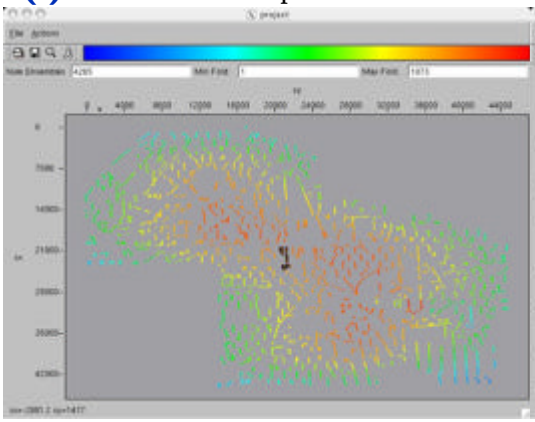

(d). Example shot record with 8 receiver spreads

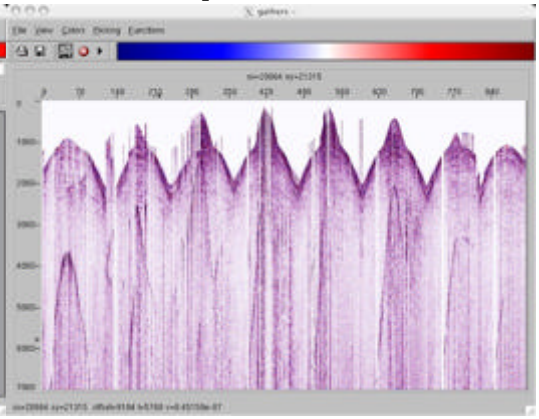

The migration in Figure 12-18 was one of the first done on the Blessing data. The target is indicated by the yellow square and the question was whether or not this clearly faulted zone contained one or two faults. A secondary question focused on whether the black square does or does not contain a continuation of the fault entering the square at the lower left corner.

Figure 12-18. A early Kirchhoff prestack depth migration of the Blessing data

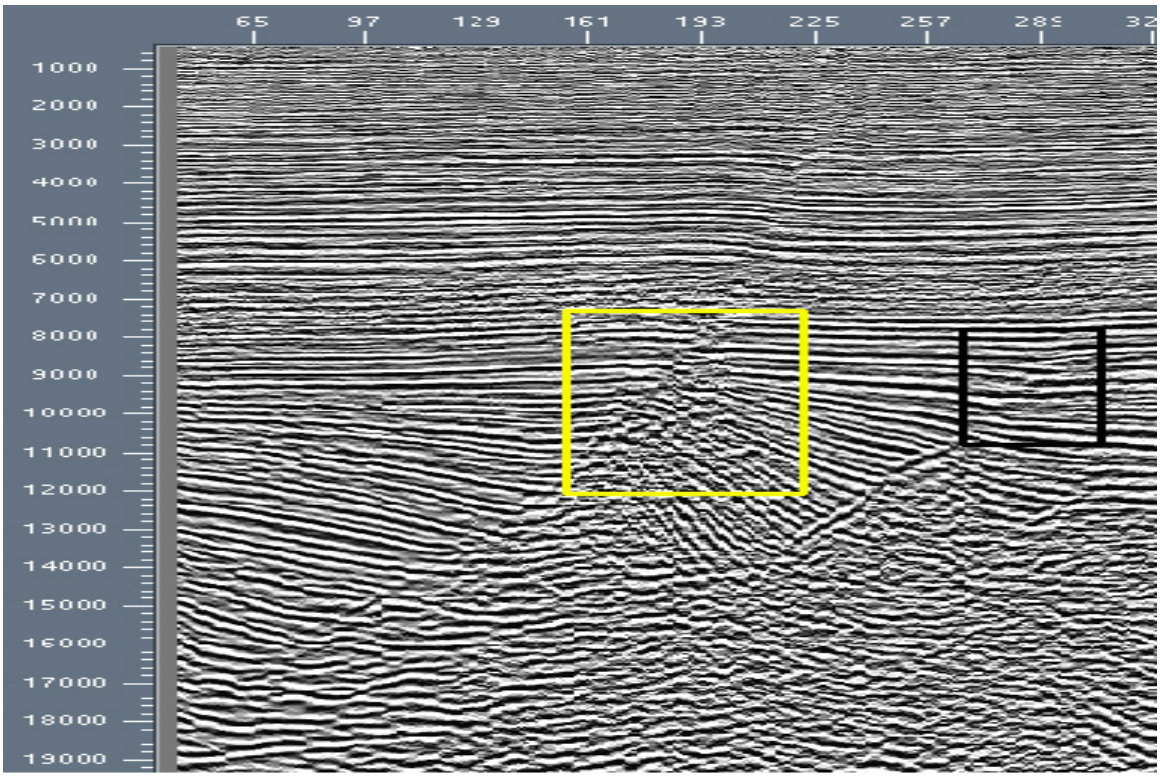

Figure 12-19(a) shows a straight ray time migration using the first iteration of velocity analysis, while (b) shows the second iteration result. Each of these initial iterations were performed using a semblance-based automatic picking routine. Figure 12-19(c) shows a curved ray PSTM with the final interval velocity volume. Part (d) is different because it used a migration algorithm that selected a velocity function at the source and another velocity function at the receiver to estimate the required traveltimes.

Figure 12-19. Four prestack time migrations of the 3D Blessing data

(a). Straight ray Kirchhoff with first velocity model

(b). Straight ray Kirchhoff with second velocity model

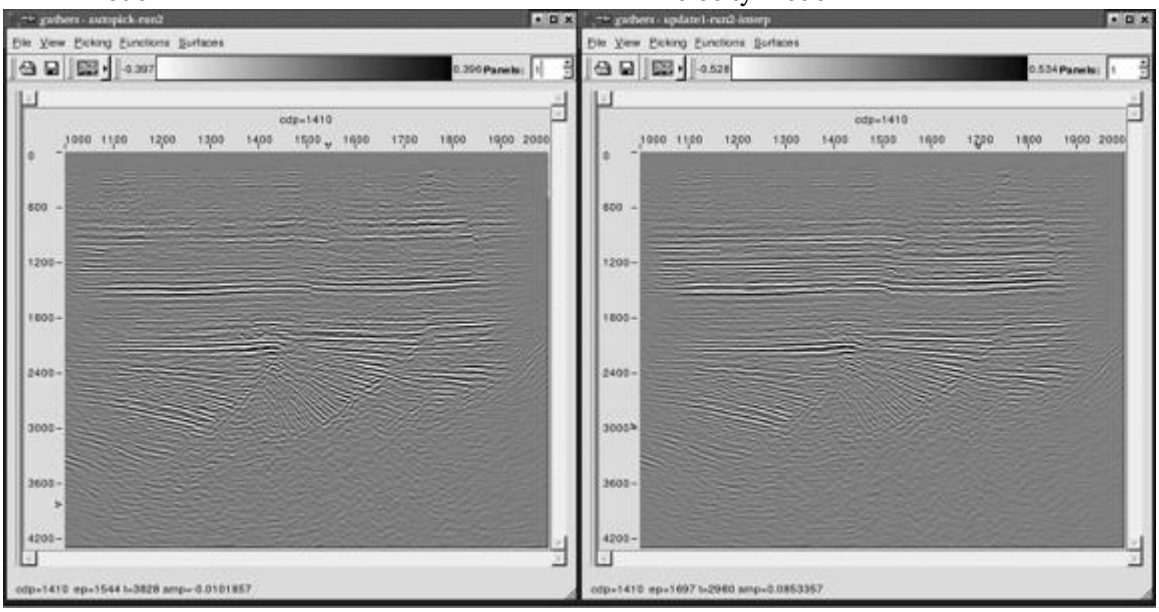

(c). Curved ray Kirchhoff with final velocity model

(d). Curved ray SR Kirchhoff with final velocity model

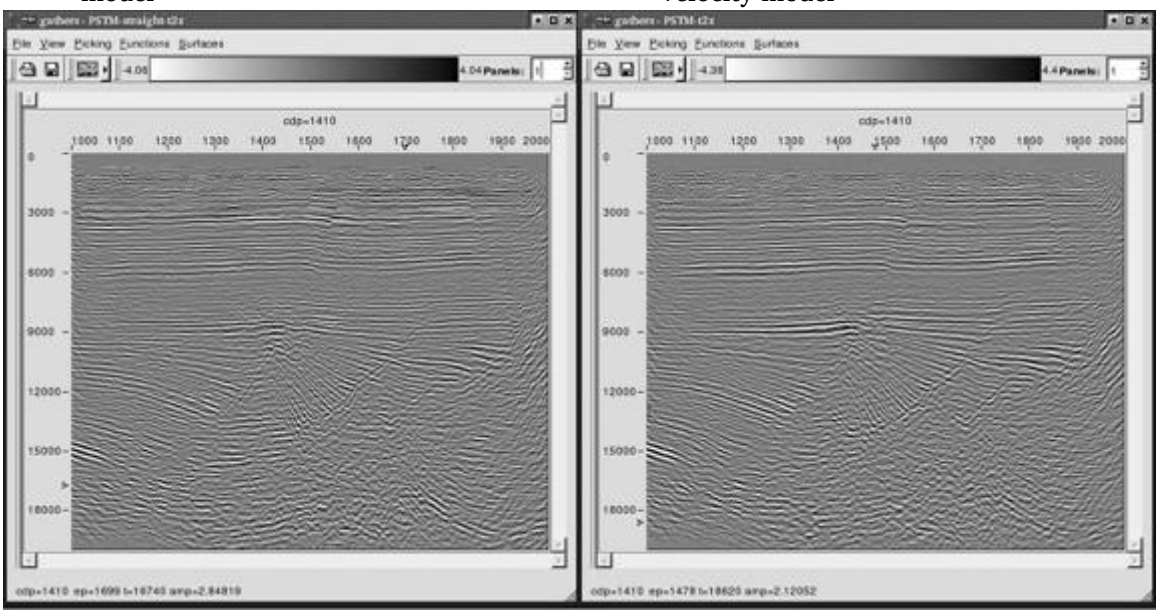

To ensure the highest possible velocity accuracy, tomography was applied to the Blessing data set. The before and after common image gather comparison in Figure 12-20 demonstrates that the painless velocity update method was sufficient to ensure high quality imaging.

Figure 12-20. A before and after comparison of tomography

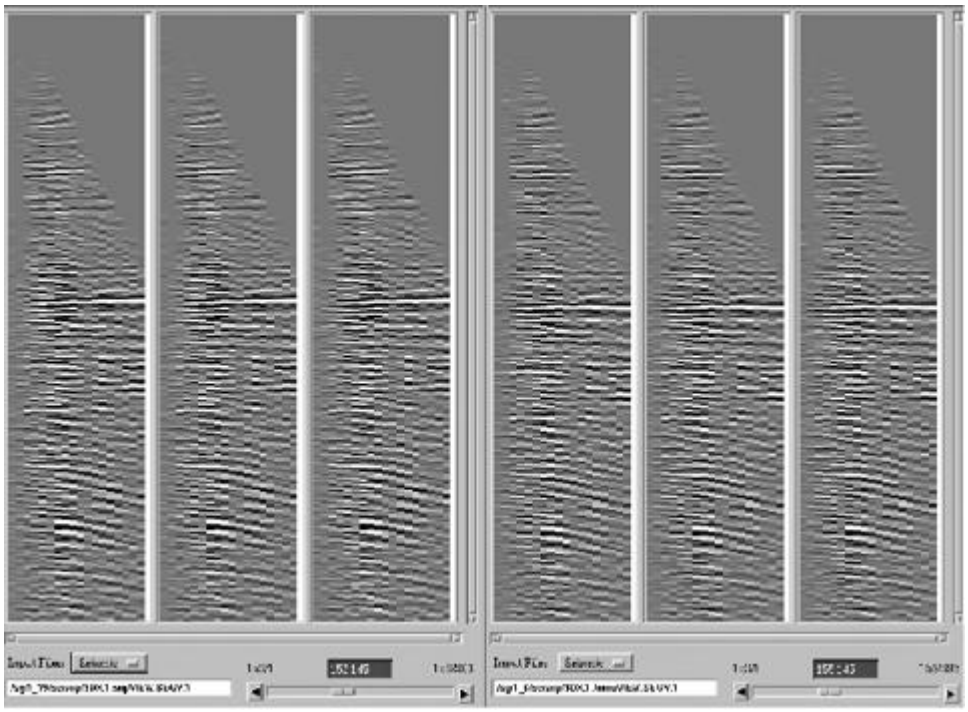

The images in Figure 12-21 represent the final depth-interval velocity volume and the final Kirchhoff maximum energy depth image at approximately line 1466.

Figure 12-21. Blessing Velocity Model and Kirchhoff PSDM

(a). Blessing interval velocity model

(b). Kirchhoff depth migration using the model in (a)

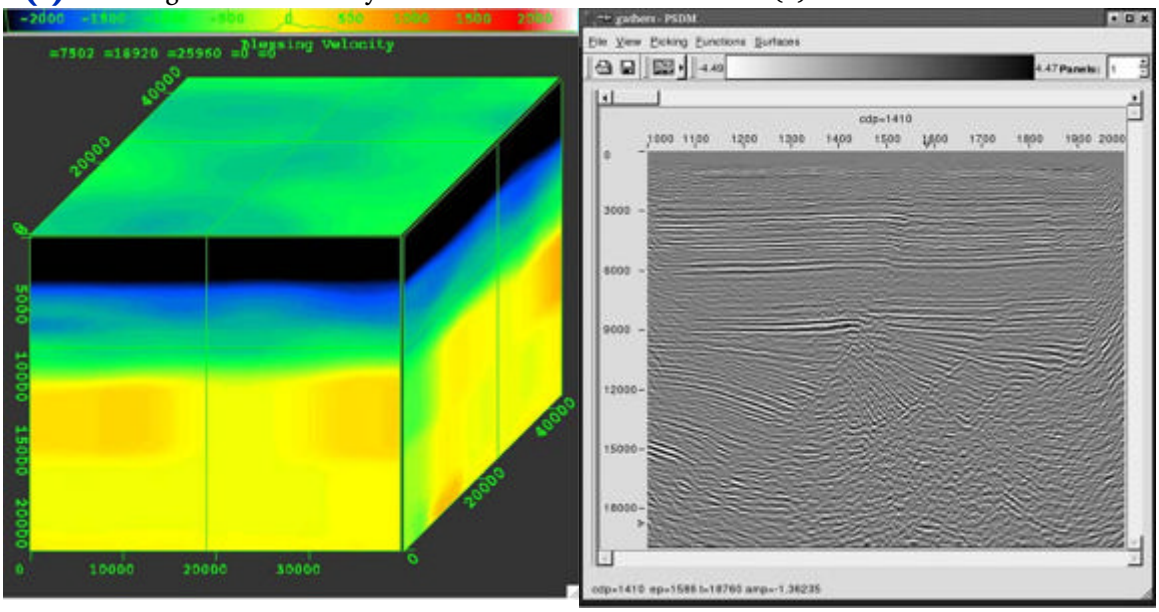

The key points of the images in Figure 12-22 are that, when viewed in sectional form, there appears to be little difference between the Kirchhoff single arrival in (a) and the much more computationally intensive reverse-time migration in (b). However, when viewed purely as depth slices, as in (c) and (d), the differences between the two methods are clear.

Figure 12-22. A Kirchhoff and Two-Way PSDM Comparison

(a). Kirchhoff PSDM and depth slice

(b). Two-way PSDM and depth slice

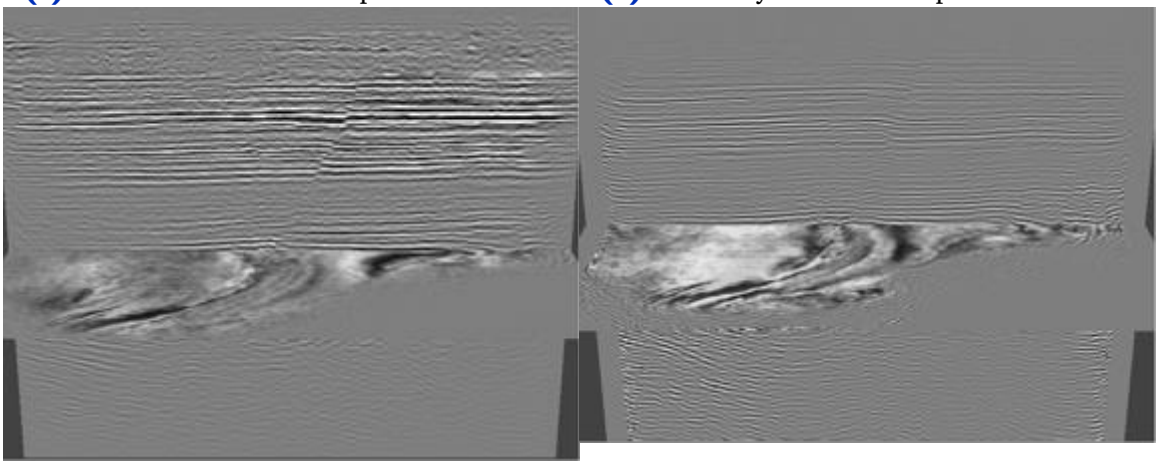

(c). Kirchhoff depth slice

(d). Two-way depth slice

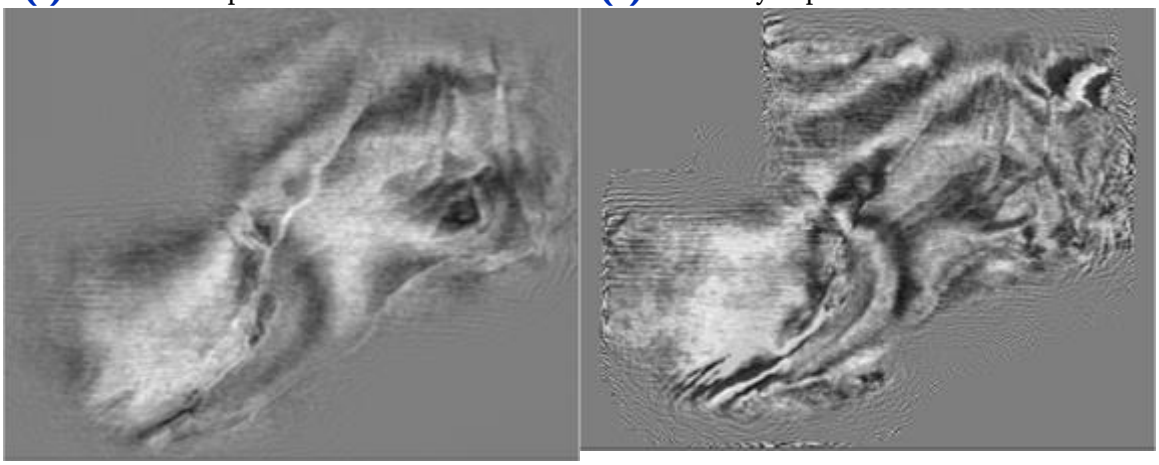

A high resolution fault analysis was run on both the Kirchhoff migration and the two-way volumes to verify the preliminary conclusion that the two-way method is of considerably higher resolution. A visual comparison of Figure 12-23(a) with Figure 12-23(b) confirms this basic hypothesis.

Figure 12-23. A high resolutions fault analysis of depth slices from a Kirchhoff migration and a full two-way 3D migration of the Blessing survey

(a). Fault analysis for Kirchhoff depth slice

(b). Fault analysis for two-way depth slice

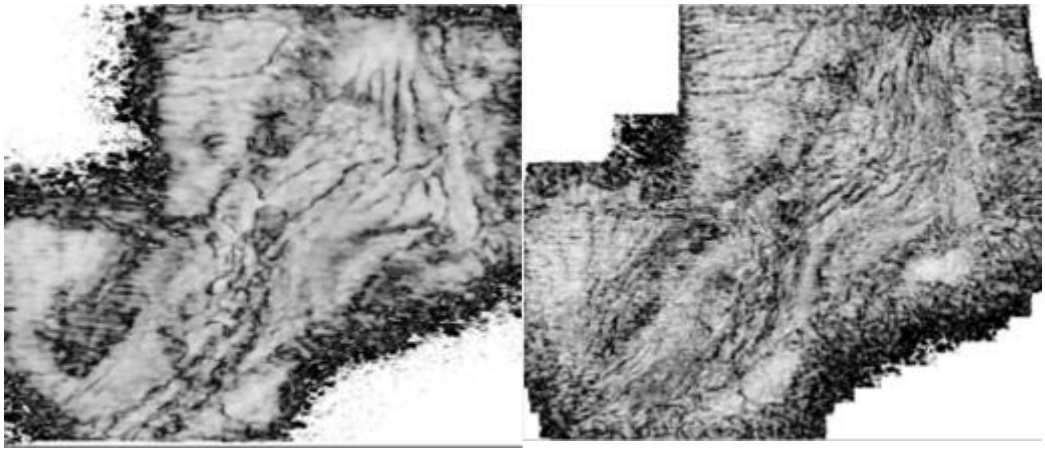

Figure 12-24 is another high-resolution fault analysis at a slightly different depth. The two-way still shows much higher resolution than the Kirchhoff.

Figure 12-24. A high resolution fault analysis of a second set of depth slice from the Blessing data volume.

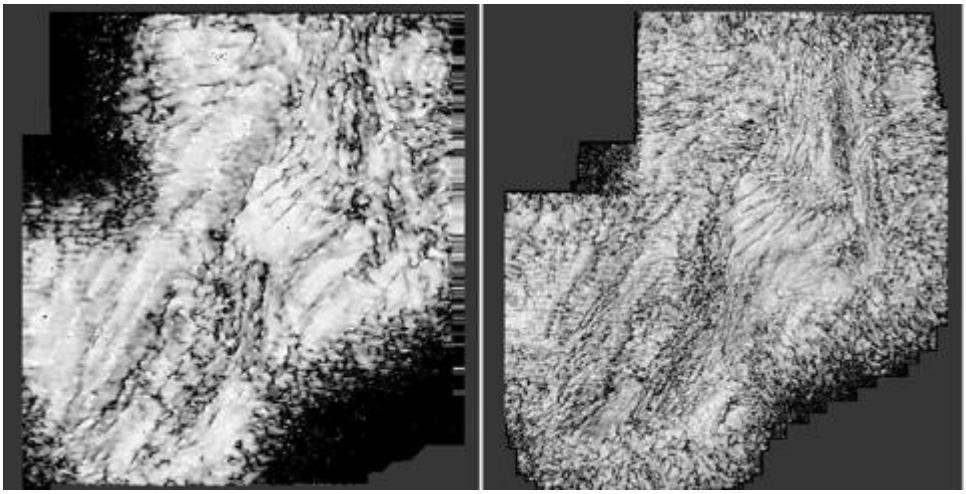

Data Mapping through AMO on the Blessing data

In this section, we consider the utilization of AMO as a data mapping technique. The idea is to construct large aperture rectangular densely sampled shots from either narrow azimuth or widely spaced receiver lines. Figure 12-25(a) shows an AMO based process for construction of large densely sampled areal array shots from otherwise narrow azimuth or widely spaced receiver arrays.

Figure 12-25. Regularization of land data to form a 3D wide azimuth shot.

(a). AMO as data mapping to regularize a 3D shot

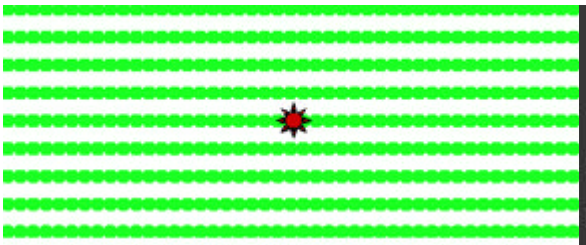

Method 1 - Regularize to output receiver grid
Fixed shot position
Offsets based on output receiver position
Method 2 - Regularize to output midpoint grid
Fixed shot position
Offsets based on output midpoints

(b). Objective fault image

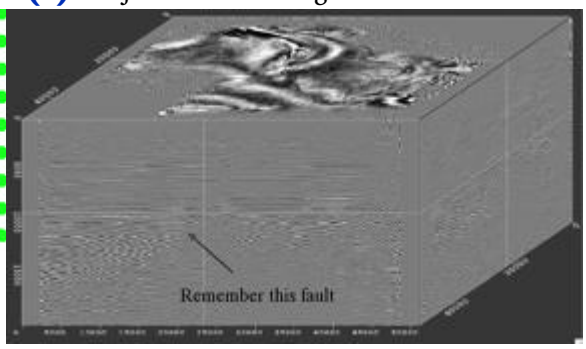

(c). AMO regularized 3D shot

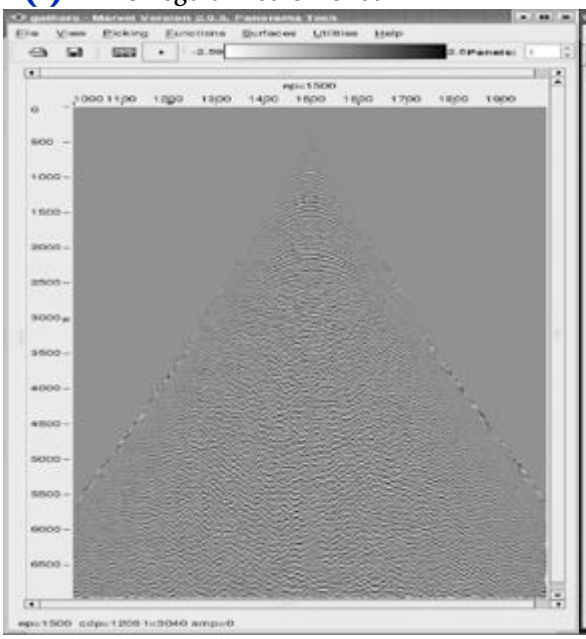

(d). Migrated regularized shot

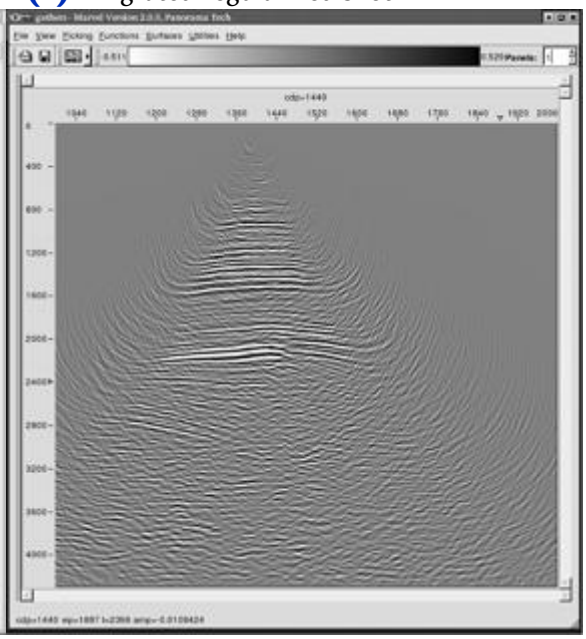

AMO in either FK, as described in previous sections, or in integral form as described by Biondi, *et al.*, can be used to directly construct output volumes of any offset and any azimuth. This can be done trace by trace or by computing all volumes at once. In any case, the data is sorted into common shot volumes and migrated shot by shot. Each migrated shot is a full 3D volume and, according to theory, should provide a superior image. Part (b) of this figure is a simple reminder of the fault that we wish to image. Part (c) shows a slice through a 3D rectangular and densely sampled shot generated to provide a reasonable image of the fault in (b). Part (d) shows that this process, at least for this land data set, is quite successful. There is no doubt that the fault is imaged quite well.

Chapter 13

Course Summary

The best one line summary I can give to modern seismic imaging is *to get the best image, use the most accurate technology you can afford*.

We can discuss the pros and cons of the various algorithms forever, but in my opinion, this comment is the only one that should be remembered.

On the other hand, attaining this goal usually requires starting at the lower end of the accuracy level and moving up the chain until the best possible image is obtained. Each step through this process increases the information content and also improves the quality of the estimated Earth model. Thus, the first step in any imaging project is a prestack time migration. This is generally followed by a Kirchhoff depth imaging exercise that leads quite naturally to a one-way wave equation method. Because of its inherent speed, common azimuth is usually the first one-way method to be applied. It is normally not until after the net improvements of the one-way techniques have been reached that expensive full waveform imaging is attempted.

However the process begins, depth imaging should be standard processing at the end of the process, and the final focus should be on estimating a full elastic Earth model. Hypothesis testing through modeling should be employed to answer questions that imaging alone cannot resolve. Modeling and migration are a necessary part of all exploration exercises.

Bibliography

[1] W. L. Abriel, N. R. Hill, G. S. Raskin, J. P. Sefani, and G. J. Surveyer, *Direct comparison of 3d prestack and poststack subsalt depth imaging on a physical model*, p. Session:A044.A044, Eur. Assn. Geosci. Eng., 1997.

[2] A. Adriansyah and G. A. McMechan, *Ava analysis and interpretation of a carbonate reservoir: northwest java basin, indonesia*, Geophysics **66** (2001), no. 3, 744–754.

[3] _____, *Analysis and interpretation of seismic data from thin reservoirs: Northwest java basin, indonesia*, Geophysics **67** (2002), no. 1, 14–26.

[4] T. Alkhalifah, *Kinematics of 3-d dmo operators in transversely isotropic media*, Geophysics **62** (1997), no. 04, 1214–1219.

[5] T. Alkhalifah and M. V. de Hoop, *Integral dmo in anisotropic media*, pp. 491–494, Soc. of Expl. Geophys., 1996.

[6] J. Anderson, T. Alkhalifah, and I. Tsvankin, *Fowler dmo and time migration for transversely isotropic media*, Geophysics **61** (1996), no. 03, 835–844.

[7] J. E. Anderson, T. A. Alkhalifah, and I. T. Tsvankin, *Fowler dmo and time migration in transversely isotropic media*, pp. 1217–1220, Soc. of Expl. Geophys., 1994.

[8] R. G. Anderson and G. A. McMechan, *Noise-adaptive filtering of seismic shot records*, p. Session:S4.3, Soc. of Expl. Geophys., 1987.

[9] _____, *Noise-adaptive filtering of seismic shot records*, Geophysics **53** (1988), no. 05, 638–649.

[10] _____, *Automatic editing of noisy seismic data*, Geophys. Prosp. **37** (1989), no. 08, 875–892.

[11] _____, *Weighted stacking of seismic data using amplitude-decay rates and noise amplitudes*, Geophys. Prosp. **38** (1990), no. 04, 365–380.

[12] P. Anno, J. K. Cohen, and N. Bleistein, *Waves and rays in acoustic variable density media*, pp. 1332–1336, Soc. of Expl. Geophys., 1992.

[13] K. Araya and N. Bleistein, *True amplitude ray tracing for seismic lines along the strike of cylindrical structures*, p. 1099, Soc. of Expl. Geophys., 1989.

[14] _____, *Prestack inversion of common-offset strike data*, pp. 1211–1214, Soc. of Expl. Geophys., 1990.

[15] E. Z. Ata, D. Corrigan, G. A. McMechan, and J. E. Gaiser, *Estimation of near-surface elastic parameters using multicomponent seismic data*, Geophysics **58** (1993), no. 07, 1017–1029.

[16] C. Bagaini, U. Spagnolini, and V. P. Pazienza, *Velocity analysis and missing offset restoration by prestack continuation operators*, pp. 1549–1552, Soc. of Expl. Geophys., 1994.

[17] R. Bale, R. Ferber, D. Nichols, C. Stolte, and S. Ronen, *Several field data examples of dealiasing dmo*, pp. 1168–1171, Soc. of Expl. Geophys., 1996.

[18] K. M. Barry and R. Drecun, *Some practical aspects of 3-d dmo*, p. 1148, Soc. of Expl. Geophys., 1989.

[19] C[] C[] Bates, T[] F[] Gaskell, and R[] B[] Rice, *Geophysics in the affairs of man*, Pergamon Press, 1982.

[20] E. Baysal, D. D. Kosloff, and J. W. C. Sherwood, *Reverse time migration*, Geophysics **48** (1983), no. 11, 1514–1524.

[21] C. Beasley, W. Lynn, K. Larner, and H. Nguyen, *Cascaded frequency-wavenumber migration - removing the restrictions on depth-varying velocity*, Geophysics **53** (1988), no. 07, 881–893.

[22] C. J. Beasley, *Quality assurance of spatial sampling for dmo*, pp. 544–547, Soc. of Expl. Geophys., 1993.

[23] C. J. Beasley and R. Klotz, *Equalization of dmo for irregular spatial sampling*, pp. 970–973, Soc. of Expl. Geophys., 1992.

[24] C. J. Beasley and E. Mobley, *Amplitude and antialiasing treatment in (x-t) domain dmo*, p. Session:S17.4, Soc. of Expl. Geophys., 1988.

[25] _____, *Spatial dealiasing of 3-d dmo*, The Leading Edge **17** (1998), no. 11, 1590–1594.

[26] J. Bednar and N. Bleistein, *Hybrid wave-equation-based beam-stack migration: Theory*, pp. 1024–1027, Soc. of Expl. Geophys., 2000.

[27] J. B. Bednar, *A theoretical comparison of equivalent-offset migration and dip moveout prestack imaging*, Geophysics **64** (1999), no. 1, 191–196.

[28] A. J. Berkhout, *Seismic migration, imaging of acoustic energy by wave field extrapolation*, Developments in solid earth Geophysics, vol. 12, Elsevier Scientific, New York, 1980.

[29] _____, *Wave-field extrapolation techniques in seismic migration - a tutorial*, Geophysics **46** (1981), no. 12, 1638–1656.

[30] _____, *Multidimensional linearized inversion and seismic migration*, Geophysics **49** (1984), no. 11, 1881–1895.

[31] _____, *Seismic migration, imaging of acoustic energy by wave field extrapolation a. theoretical aspects*, Developments in solid earth Geophysics, vol. 14A, Elsevier Scientific, New York, 1985.

[32] A. J. Berkhout and C. P. A. Wapenaar, *One-way versions of the kirchhoff integral*, Geophysics **54** (1989), no. 04, 460–467.

[33] J. R. Berryhill, *Wave equation datuming*, Geophysics **44** (1979), no. 08, 1329–1344.

[34] B. Biondi and N. Chemingui, *Transformation of 3-d prestack data by azimuth moveout (amo)*, pp. 1541–1544, Soc. of Expl. Geophys., 1994.

[35] B. Biondi and W. D. Moorhead, *A data parallel algorithm for kirchhoff 3-d dmo*, pp. 330–333, Soc. of Expl. Geophys., 1992.

[36] J. L. Black and M. S. Egan, *True-amplitude dmo in 3-d*, p. Session:S17.3, Soc. of Expl. Geophys., 1988.

[37] J. L. Black and K. Schleicher, *Effect of irregular sampling on prestack dmo*, p. 1144, Soc. of Expl. Geophys., 1989.

[38] N. Bleistein, *Wave equation migration deduced as an inversion method from the wave equation*, p. Session:S10.6, Soc. of Expl. Geophys., 1983.

[39] _____, *Asymptotic two-and-one-half-dimensional modeling from two-dimensional computations*, p. Session:S11.6, Soc. of Expl. Geophys., 1985.

[40] _____, *Inversion for sound-speed and density variations in complex background structure*, p. Session:S12.2, Soc. of Expl. Geophys., 1986.

[41] _____, *Two-and-one-half dimensional in-plane wave propagation*, Geophys. Prosp. **34** (1986), no. 05, 686–703.

[42] _____, *On the imaging of reflectors in the earth*, Geophysics **52** (1987), no. 07, 931–942.

[43] _____, *Born dmo revisited*, pp. 1366–1369, Soc. of Expl. Geophys., 1990.

[44] _____, *Memorial for jack k. cohen*, The Leading Edge **16** (1997), no. 07, 1049.

[45] _____, *2.5-d data mappings*, pp. 1353–1356, Soc. of Expl. Geophys., 1998.

[46] _____, *True amplitude 3-d constant background dmo - an implementation of data mapping*, pp. 1760–1763, Soc. of Expl. Geophys., 1998.

[47] _____, *Hagedoorn told us how to do kirchhoff migration and inversion*, The Leading Edge **18** (1999), no. 8, 918–927.

[48] N. Bleistein, Cohen, J. K., and J. W. Stockwell, *Mathematics of multidimensional seismic imaging migration, and inversion*, Interdisciplinary Applied Mathematics, vol. 13, Springer, New York, 2000.

[49] N. Bleistein, J. Cohen, and H. Jaramillo, *True-amplitude transformation to zero offset of data from curved reflectors*, Geophysics **64** (1999), no. 1, 112–129.

[50] N. Bleistein and J. K. Cohen, *Direct inversion procedure for claerbout's equations*, Geophysics **44** (1979), no. 06, 1034–1040.

[51] _____, *Velocity inversion - present status new directions*, Geophysics **47** (1982), no. 11, 1497–1511.

[52] _____, *An alternative approach to the cagniard de hoop method*, pp. 298–299, Eur. Assn. of Expl. Geophys., 1991.

[53] _____, *The cagniard methodin complex time revisited*, pp. 1584–1586, Soc. of Expl. Geophys., 1991.

[54] _____, *The cagniard method in complex time revisited*, Geophys. Prosp. **40** (1992), no. 06, 619–650.

[55] N. Bleistein, J. K. Cohen, and F. G. Hagin, *Computational and asymptotic aspects of velocity inversion*, p. Session:S19.8, Soc. of Expl. Geophys., 1984.

[56] _____, *Computational and asymptotic aspects of velocity inversion*, Geophysics **50** (1985), no. 08, 1253–1265.

[57] _____, *Two and one-half dimensional born inversion with an arbitrary reference*, Geophysics **52** (1987), no. 01, 26–36.

[58] N. Bleistein and S. H. Gray, *Inversion of cmp stacked data with a depth-dependent background velocity*, p. Session:S5.5, Soc. of Expl. Geophys., 1984.

[59] _____, *An extension of the born inversion method to a depth dependent reference profile*, Geophys. Prosp. **33** (1985), no. 07, 999–1022.

[60] _____, *An extension of the born inversion method to a depth dependent reference profile*, Inversion of geophysical data (L. R. Lines, ed.), Soc. of Expl. Geophys., 1988, pp. 111–134.

[61] _____, *From the hagedoorn imaging technique to kirchhoff migration and inversion*, Geophys. Prosp. **49** (2001), no. 06, 629–643.

[62] N. Bleistein and H. H. Jaramillo, *A platform for data mapping in scalar models of data acquisition*, pp. 1588–1591, Soc. of Expl. Geophys., 1998.

[63] _____, *A platform for kirchhoff data mapping in sealer models of data acquisition*, Geophys. Prosp. **48** (2000), no. 01, 135–162.

[64] N. Bleistein and T. Jorden, *Symmetric pre-stack inversion operator for multi-source, multi-geophone data*, Geophysical imaging, symposium of geophysical society of Tulsa (J. A. Scales, ed.), Soc. of Expl. Geophys., 1987, pp. 175–194.

[65] P. Blondel, *Amplitude preservation for kirchhoff dip moveout*, pp. 1529–1532, Soc. of Expl. Geophys., 1994.

[66] P. C. Blondel, *Recovering prestack kinematics with inverse dmo*, pp. 1987–1990, Soc. of Expl. Geophys., 1996.

[67] R. Bloor, S. Deregowski, and C. Beasley, *Dzo for irregular 3-d acquisition*, pp. 1475–1478, Soc. of Expl. Geophys., 1996.

[68] R. I. Bloor and S. M. Deregowski, *Demigration to zero offset*, pp. 1433–1436, Soc. of Expl. Geophys., 1995.

[69] J. H. Bradford, D. S. Sawyer, C. A. Zelt, and J. S. Oldow, *Imaging a shallow aquifer in temperate glacial sediments using seismic reflection profiling with dmo processing*, Geophysics **63** (1998), no. 04, 1248–1256.

[70] R. C. Bradley, *Personal communication*, October 2004.

[71] D. L. Brown, *Applications of operator separation in reflection seismology*, Geophysics **48** (1983), no. 03, 288–294.

[72] H. Brysk, *Numerical analysis of the forty-five-degree finite-difference equation for migration*, Geophysics **48** (1983), no. 05, 532–542.

[73] _____, *Slotnick revisited: Dmo with a linear velocity profile*, pp. 1350–1353, Soc. of Expl. Geophys., 1990.

[74] H. Brysk and T. Mojesky, *The 3-d isochron illuminates variable-velocity dmo*, pp. 1197–1200, Soc. of Expl. Geophys., 1991.

[75] M. A. Brzostowski and G. A. McMechan, *3-d tomographic imaging of near-surface seismic velocity and attenuation*, Geophysics **57** (1992), no. 03, 396–403.

[76] A. J. L. Budd, J. W. Ryan, K. Hawkins, and A. R. MacKewn, *Understanding the interaction between marine geometries and 3-d imaging methods*, pp. 945–948, Soc. of Expl. Geophys., 1995.

[77] J. Cabrera and S. Levy, *Shot dip moveout with logarithmic transformations (short note)*, Geophysics **54** (1989), no. 08, 1038–1041.

[78] J. Cai and G. A. McMechan, *Ray-based synthesis of bistatic ground-penetrating radar profiles*, Geophysics **60** (1995), no. 01, 87–96.

[79] _____, *2-d ray-based tomography for velocity, layer shape, and attenuation from gpr data*, Geophysics **64** (1999), no. 5, 1579–1593.

[80] A. Canning and G. H. F. Gardner, *Regularizing 3-d data sets with dmo*, Geophysics **61** (1996), no. 04, 1103–1114.

[81] _____, *Ava analysis after velocity-independent dmo and imaging*, Geophysics **63** (1998), no. 02s, 686–691.

[82] _____, *Reducing 3-d acquisition footprint for 3-d dmo and 3-d prestack migration*, Geophysics **63** (1998), no. 04, 1177–1183.

[83] J. A. Carter and L. N. Frazer, *Accommodating lateral velocity changes in kirchhoff migration by means of fermat's principle*, Geophysics **49** (1984), no. 01, 46–53.

[84] R. J. Castle, *Wave equation migration in the presence of lateral velocity variations*, Geophysics **47** (1982), no. 07, 1001–1011.

[85] _____, *A 2-d v(z) dmo algorithm*, pp. 1130–1133, Soc. of Expl. Geophys., 1993.

[86] W. F. Chang and G. A. McMechan, *Reverse-time migration of offset vertical seismic profiling data using the exitation-time imaging condition*, Geophysics **51** (1986), no. 01, 67–84.

[87] _____, *Elastic reverse-time migration*, Geophysics **52** (1987), no. 10, 1365–1375.

[88] W. F. Chang and G. A. McMechan, *3d acoustic reverse-time migration*, Geophys. Prosp. **37** (1989), no. 03, 243–256.

[89] _____, *3d acoustic prestack reverse-time migration*, Geophys. Prosp. **38** (1990), no. 07, 737–756.

[90] _____, *3-d elastic prestack, reverse-time depth migration*, Geophysics **59** (1994), no. 04, 597–610.

[91] N. Chemingui and B. L. Biondi, *Amplitude preserving azimuth moveout*, pp. 1453–1456, Soc. of Expl. Geophys., 1995.

[92] H. W. Chen and G. A. McMechan, *3-d physical modeling and pseudospectral simulation of seismic common-source data volumes*, Geophysics **58** (1993), no. 01, 121–133.

[93] G. Cheng and S. Coen, *The relationship between born inversion and migration for common-midpoint stacked data*, Geophysics **49** (1984), no. 12, 2117–2131.

[94] Y. T. Chon and A. Gonzalez, *Accuracy in rms-velocity determination using a kirchhoff dmo algorithm*, p. Session:S14.3, Soc. of Expl. Geophys., 1987.

[95] J. H. Chun and C. A. Jacewitz, *Fundamentals of frequency-domain migration*, Geophysics **46** (1981), no. 05, 717–733.

[96] J. F. Claerbout, *Coarse grid calculations of waves in inhomogeneous media with application to delineation of complicated seismic structure*, Geophysics **35** (1970), no. 03, 407–418.

[97] _____, *Toward a unified theory of reflector mapping*, Geophysics **36** (1971), no. 03, 467–481.

[98] _____, *Fundamentals of geophysical data processing*, International series in the earth and planetary sciences, McGraw-Hill, New York, 1976.

[99] _____, *Imaging the earth's interior*, Blackwell Scientific Publications, Oxford, 1985.

[100] _____, *Multidimensional recursive filters via a helix with application to velocity estimation and 3-d migration*, pp. 1995–1998, Soc. of Expl. Geophys., 1998.

[101] J. F. Claerbout and S. M. Doherty, *Downward continuation of moveout-corrected seismograms*, Geophysics **37** (1972), no. 05, 741–768.

[102] R. W. Clayton and B. Engquist, *Absorbing side boundary conditions for wave equation migration*, Geophysics **45** (1980), no. 05, 895–904.

[103] R. W. Clayton and G. A. McMechan, *Inversion of refraction data by wave-field continuation*, Geophysics **46** (1981), no. 06, 860–868.

[104] J. Cohen and N. Bleistein, *Velocity inversion procedure for acoustic waves*, Inversion of geophysical data (L. R. Lines, ed.), Soc. of Expl. Geophys., 1988, pp. 41–51.

[105] J. K. Cohen, *Analytic study of the effective parameters for determination of the nmo velocity function in transversely isotropic media*, pp. 1491–1494, Soc. of Expl. Geophys., 1996.

[106] J. K. Cohen and N. Bleistein, *Velocity inversion procedure for acoustic waves*, Geophysics **44** (1979), no. 06, 1077–1087.

[107] _____, *The influence of out-of-plane surface properties on unmigrated time sections*, Geophysics **48** (1983), no. 02, 125–132.

[108] J. K. Cohen, F. G. Hagin, and N. Bleistein, *Three-dimensional born inversion with an arbitrary reference*, Geophysics **51** (1986), no. 08, 1552–1558.

[109] _____, *Three-dimensional born inversion with an arbitrary reference*, pp. 179–184, Soc. of Expl. Geophys., 2001.

[110] C. L. Collins, *Imaging in 3-d dmo, part i: Geometrical optics models*, Geophysics **62** (1997), no. 01, 211–224.

[111] _____, *Imaging in 3-d dmo, part ii: Amplitude effects*, Geophysics **62** (1997), no. 01, 225–244.

[112] D. Connelly and M. Galbraith, *3-d design with dmo modeling*, pp. 933–934, Soc. of Expl. Geophys., 1995.

[113] N. J. Cooper, R. G. Williams, R. Wombell, and C. D. Notfors, *3-d dmo for cross-spread geometry: A practical approach and application to multi-fold field data*, pp. 1483–1486, Soc. of Expl. Geophys., 1996.

[114] R.M. Corbeanu, G. A. McMechan, R. B. Szerbiak, and K. Soegaard, *Prediction of 3-d fluid permeability and mudstone distributions from ground-penetrating radar (gpr) attributes: Example from the cretaceous ferron sandstone member, east-central utah*, Geophysics **67** (2002), no. 05, 1495–1504.

[115] E. J. Crouzy and J. Pion, *3d dmo simulation in land survey design using 2-d seismic data*, pp. 548–551, Soc. of Expl. Geophys., 1993.

[116] T. F. Dai and J. T. Kuo, *Real data results of kirchhoff elastic wave migration (short note)*, Geophysics **51** (1986), no. 04, 1006–1011.

[117] M. V. de Hoop and T. Alkhalifah, *Multi-parameter dmo/tzo in anisotropic media*, pp. 487–490, Soc. of Expl. Geophys., 1996.

[118] E. DeGoyler, *Notes on the early history of applied geophysics in the petroleum industry*, Early Geophysical Papers of the Society of Exploration Geophycisits, Society of Exploration Geophysicists, Tulsa, OK, 1947.

[119] S. M. Deregowski, *What is dmo*, First Break **04** (1986), no. 07, 7–24.

[120] J. A. Dickinson, *Evaluation of two-pass three-dimensional migration*, Geophysics **53** (1988), no. 01, 32–49.

[121] M. Dietrich and J. K. Cohen, *Migration to zero offset (dmo) for a constant velocity gradient: An analytical formulation*, Geophys. Prosp. **41** (1993), no. 05, 621–644.

[122] P. B. Dillon, *Vertical seismic profile migration using the kirchhoff integral*, Geophysics **53** (1988), no. 06, 786–799.

[123] C. H. Dix, *Seismic prospecting for oil*, Harper and Brothers, New York., 1952.

[124] M. B. Dobrin, *Introduction to geophysical prospecting*, McGraw-Hill, New York, 1976.

[125] P. Docherty and N. Bleistein, *A fast ray tracing routine for laterally inhomogeneous media*, p. Session:S24.6, Soc. of Expl. Geophys., 1984.

[126] G. P. Dohr and P. K. Stiller, *Migration velocity determination - part ii: Applications*, Geophysics **40** (1975), no. 01, 6–16.

[127] W. Dong and N. Bleistein, *Common-shot inversion in c(x,z) media*, p. 928, Soc. of Expl. Geophys., 1989.

[128] W. Dong, M. J. Emanuel, P. Bording, and N. Bleistein, *A computer implementation of 2.5-d common-shot inversion*, Geophysics **56** (1991), no. 09, 1384–1394.

[129] Z. Dong and G. A. McMechan, *3-d prestack migration in anisotropic media*, Geophysics **58** (1993), no. 01, 79–90.

[130] _____, *3-d viscoelastic anisotropic modeling of data from a multicomponent, multiazimuth seismic experiment in northeast texas*, Geophysics **60** (1995), no. 04, 1128–1138.

[131] A. A. Dubrulle, *Numerical methods for the migration of constant-offset sections in homogeneous and horizontally layered media*, Geophysics **48** (1983), no. 09, 1195–1203.

[132] A. A. Dubrulle and J. Gazdag, *Migration by phase shift - an algorithmic description for array processors*, Geophysics **44** (1979), no. 10, 1661–1666.

[133] D. Epili and G. A. McMechan, *Implementation of 3-d prestack kirchhoff migration, with application to data from the ouachita frontal thrust zone*, Geophysics **61** (1996), no. 05, 1400–1411.

[134] L. Y. Faust, *Application of geology and geophysics to war and post-war problems of the petroleum industry geophysics in the mid-continent*, Geophysics **07** (1942), no. 03, 272–273.

[135] _____, *Seismic velocity as a function of depth and geologic time*, Geophysics **16** (1951), no. 02, 192–206.

[136] _____, *Discussion of 'a velocity function including lithologic variation', by faust, l. y. (geo-18-02-0271-0288)*, Geophysics **18** (1953), no. 04, 970.

[137] _____, *A velocity function including lithologic variation*, Geophysics **18** (1953), no. 02, 271–288.

[138] _____, *Some values available to students*, Geophysics **19** (1954), no. 02, 337–338.

[139] _____, *The preparation of a paper*, Geophysics **23** (1958), no. 05, 944–952.

[140] _____, *Editorial - seg institutions - their continued improvement*, Geophysics **24** (1959), no. 04, 655–657.

[141] _____, *Reply to discussion of 'the preparation of a paper', by faust, l. y. (geo-23-05-0944-0952)*, Geophysics **24** (1959), no. 03, 637–638.

[142] _____, *Classics of geophysics*, Geophysics **25** (1960), no. 01, 2–18.

[143] _____, *Editorial - the silver anniversary of geophysics*, Geophysics **25** (1960), no. 01, 1.

[144] _____, *The fargo field - a case-history*, Geophysics **28** (1963), no. 06, 990–1000.

[145] _____, *Presidential address - some technological aspects of exploration effectiveness*, Geophysics **28** (1963), no. 01, 1–7.

[146] M. J. Faust, *Seismic stratigraphy of the mid-cretaceous unconformity (mcu) in the central gulf of mexico basin*, p. Session:S7.6, Soc. of Expl. Geophys., 1985.

[147] _____, *Seismic stratigraphy of the mid-cretaceous unconformity (mcu) in the central gulf of mexico basin*, Geophysics **55** (1990), no. 07, 868–884.

[148] R. Ferber, *What is dmo coverage?*, Geophys. Prosp. **48** (2000), no. 06, 995–1008.

[149] R. Ferber, B. Sanders, and O. Yilmaz, *Quick-look 3-d prestack time migration*, pp. 451–454, Soc. of Expl. Geophys., 1996.

[150] R. G. Ferber, *A filter, delay and spread technique for 3-d dmo*, Geophys. Prosp. **39** (1991), no. 06, 737–756.

[151] E. Fisher, G. A. McMechan, and A. P. Annan, *Acquisition and processing of wide-aperture ground-penetrating radar data*, Geophysics **57** (1992), no. 03, 495–504.

[152] E. Fisher, G. A. McMechan, A. P. Annan, and S. W. Cosway, *Examples of reverse-time migration of single-channel, ground-penetrating radar profiles*, Geophysics **57** (1992), no. 04, 577–586.

[153] S. Fomel, N. Bleistein, H. Jaramillo, and J. K. Cohen, *True amplitude dmo, offset continuation and ava/avo for curved reflectors*, pp. 1731–1734, Soc. of Expl. Geophys., 1996.

[154] S. B. Fomel and B. L. Biondi, *The time and space formulation of azimuth moveout*, pp. 1449–1452, Soc. of Expl. Geophys., 1995.

[155] D. Forel and G. H. F. Gardner, *A three-dimensional perspective on two-dimensional dip moveout*, Geophysics **53** (1988), no. 05, 604–610.

[156] W. S. French, *Two dimensional and three dimensional migration of model experiment reflection profiles*, Geophysics **39** (1974), no. 03, 265–277.

[157] _____, *Computer migration of oblique seismic reflection profiles*, Geophysics **40** (1975), no. 06, 961–980.

[158] _____, *Reply to discussion of 'computer migration of oblique seismic reflection profiles', by french, william s. (geo-40-06-0961-0980)*, Geophysics **41** (1976), no. 04, 776–777.

[159] J. R. Fricke, *Tutorial on reverse-time migration in parallel*, Geophysics **53** (1988), no. 09, 1143–1150.

[160] G. H. F. Gardner and D. Forel, *Amplitude preservation equations for dmo*, p. Session:S17.2, Soc. of Expl. Geophys., 1988.

[161] G. H. F. Gardner, W. S. French, and T. Matzuk, *Elements of migration and velocity analysis*, Geophysics **39** (1974), no. 06, 811–825.

[162] G. H. F. Gardner, S. Y. Wang, and S. Randazzo, *Examples of dmo for 3-d data over 3-d structures*, p. Session:POS2.7, Soc. of Expl. Geophys., 1987.

[163] J. P. Gates, *Descriptive geometry and the offset seismic profile*, Geophysics **22** (1957), no. 03, 589–609.

[164] J. Gazdag, *Wave equation migration with the phase-shift method*, Geophysics **43** (1978), no. 07, 1342–1351.

[165] J. Gazdag and P. Sguazzero, *Migration of seismic data by phase-shift plus interpolation*, Geophysics **49** (1984), no. 02, 124–131.

[166] S. Geoltrain and N. Bleistein, *Aspect of anisotropic wave propagation*, p. Session:S18.7, Soc. of Expl. Geophys., 1988.

[167] R. J. Godfrey, *Dmo and v(z)*, pp. 952–954, Soc. of Expl. Geophys., 1992.

[168] A. Gonzalez, F. K. Levin, R. Chambers, and E. Mobley, *A method of correcting 3-d dmo for the effects of wave propagation in an inhomogeneous earth*, pp. 966–969, Soc. of Expl. Geophys., 1992.

[169] H. Granser, *Shot gather dmo in the double log domain (short note)*, Geophysics **59** (1994), no. 08, 1305–1307.

[170] S. Gray, C. Notfors, and N. Bleistein, *Imaging using multi-arrivals: Gaussian beams or multi-arrival kirchhoff?*, pp. 1117–1120, Soc. of Expl. Geophys., 2002.

[171] S. H. Gray, *Efficient traveltime calculations for kirchhoff migration (short note)*, Geophysics **51** (1986), no. 08, 1685–1688.

[172] V. Y. Grechka and G. A. McMechan, *3-d two-point ray tracing for heterogeneous weakly transversely isotropic media*, Geophysics **61** (1996), no. 06, 1883–1894.

[173] _____, *Analysis of reflection traveltimes in 3-d transversely isotropic heterogeneous media*, Geophysics **62** (1997), no. 06, 1884–1895.

[174] V. Y. Grechka, G. A. McMechan, and V. A. Volovodenko, *Solving 1-d inverse problems by chebyshev polynomial expansion*, Geophysics **61** (1996), no. 06, 1758–1768.

[175] Z. Guan-Quan, Z. Shu-Lun, W. Ying-Xiang, and L. Chau-Ying, *A new algorithm for finite-difference migration of steep dips*, Geophysics **53** (1988), no. 02, 167–175.

[176] J. G. Hagedoorn, *A process of seismic reflection interpretation.*, Geophysical Prospecting **06** (1954), 449–453.

[177] D. Hale, N. R. Hill, and J. Stefani, *Imaging salt with turning seismic waves*, Geophysics **57** (1992), no. 11, 1453–1462.

[178] _____, *Imaging salt with turning seismic waves*, pp. 532–533, Eur. Assn. of Expl. Geophys., 1992.

[179] _____, *Imaging salt with turning seismic waves*, pp. 262–271, Soc. of Expl. Geophys., 2001.

[180] D. Hale, N. R. Hill, and J. P. Stefani, *Imaging salt with turning seismic waves*, pp. 1171–1174, Soc. of Expl. Geophys., 1991.

[181] III Hammon, W. S., X. Zeng, R.M. Corbeanu, and G. A. McMechan, *Estimation of the spatial distribution of fluid permeability from surface and tomographic gpr data and core, with a 2-d example from the ferron sandstone, utah*, Geophysics **67** (2002), no. 05, 1505–1515.

[182] C. E. Harris and G. A. McMechan, *Using downward continuation to reduce memory requirements in reverse-time migration (short note)*, Geophysics **57** (1992), no. 06, 848–853.

[183] L. Hatton, K. L. Larner, and B. S. Gibson, *Migration of seismic data from inhomogeneous media*, Geophysics **46** (1981), no. 05, 751–767.

[184] K. Hawkins, *The challenge presented by north sea central graben salt domes to all dmo algorithms*, First Break **12** (1994), no. 06, 327–343.

[185] K. Hawkins, C.-C. Cheng, S. A. Sadek, and M. A. Brzostowski, *A v(z) dmo developed with the north sea central graben in mind*, pp. 1429–1432, Soc. of Expl. Geophys., 1995.

[186] K. Helbig, *Personal communication*, October 2004.

[187] S. A. Henrys, A. R. Levander, N. R. Hill, and B. S. Gibson, *Seismic response of the surface layer at the ohaaki geothermal field, new zealand*, p. Session:ENG1.7, Soc. of Expl. Geophys., 1986.

[188] A. J. Herman, R. M. Anania, J. H. Chun, C. A. Jacewitz, and R. E. F. Pepper, *A fast three-dimensional modeling technique and fundamentals of three-dimensional frequency-domain migration*, Geophysics **47** (1982), no. 12, 1627–1644.

[189] P. Herrmann and J. Frelet, *Layer-oriented fk dmo*, pp. 1107–1110, Soc. of Expl. Geophys., 1996.

[190] J. H. Higginbotham, Y. Shin, and D. V. Sukup, *Directional depth migration (short note)*, Geophysics **50** (1985), no. 11, 1784–1796.

[191] S. T. Hildebrand, *Reverse-time depth migration - impedance imaging condition*, Geophysics **52** (1987), no. 08, 1060–1064.

[192] S. T. Hildebrand and G. A. McMechan, *1-d seismic inversion of dual wavefield data: Part i: Nonuniqueness and stability*, Geophysics **59** (1994), no. 05, 782–788.

[193] _____, *1-d seismic inversion of dual wavefield data: Part ii: A gulf of mexico example*, Geophysics **59** (1994), no. 05, 789–800.

[194] N. Hill, R. Langan, T. Nemeth, M. Zhao, and K. Bube, *Beam methods for predictive suppression of seismic multiples in deep water*, pp. 2118–2121, Soc. of Expl. Geophys., 2002.

[195] N. R. Hill, *Downward continuation of refracted arrivals to determine shallow complex structure*, p. Session:S1.2, Soc. of Expl. Geophys., 1985.

[196] _____, *Downward continuation of refracted arrivals to determine shallow structure*, Geophysics **52** (1987), no. 09, 1188–1198.

[197] _____, *Gaussian beam migration*, Geophysics **55** (1990), no. 11, 1416–1428.

[198] _____, *Prestack gaussian-beam depth migration*, Geophysics **66** (2001), no. 4, 1240–1250.

[199] N. R. Hill and I. Lerche, *Acoustic reflections from undulating surfaces (short note)*, Geophysics **51** (1986), no. 11, 2160–2161.

[200] N. R. Hill, T. H. Watson, M. H. Hassler, and K. L. Sisemore, *Salt-flank imaging using gaussian beam migration*, pp. 1178–1180, Soc. of Expl. Geophys., 1991.

[201] N. R. Hill and P. C. Wuenschel, *Numerical modeling of refraction arrivals in complex areas*, p. Session:S7.5, Soc. of Expl. Geophys., 1983.

[202] _____, *Numerical modeling of refraction arrivals in complex areas*, Geophysics **50** (1985), no. 01, 90–98.

[203] L. H. Howell and L. N. Trefethen, *Ill-posedness of absorbing boundary conditions for migration*, Geophysics **53** (1988), no. 05, 593–603.

[204] L. Z. Hu and G. A. McMechan, *Data processing system based on wave-field transformation sequences with application to vertical seismic profiles*, p. Session:S3.2, Soc. of Expl. Geophys., 1986.

[205] L. Z. Hu and G. A. McMechan, *Migration of vsp data by ray equation extrapolation in two-d variable velocity media*, Geophys. Prosp. **34** (1986), no. 05, 704–734.

[206] L. Z. Hu and G. A. McMechan, *Wave-field transformations of vertical seismic profiles*, Geophysics **52** (1987), no. 03, 307–321.

[207] L. Z. Hu, G. A. McMechan, and J. M. Harris, *Acoustic prestack migration of cross-hole data*, Geophysics **53** (1988), no. 08, 1015–1023.

[208] B. Hua and G. A. McMechan, *Parsimonious 2-d poststack kirchhoff depth migration*, Geophysics **66** (2001), no. 5, 1497–1503.

[209] _____, *Parsimonious 2d prestack kirchhoff dept migration*, Geophysics **68** (2003), no. 3, 1043–1051.

[210] P. Hubral, *Discussion of 'computer program - seismic raypath migration with the pocket calculator', by michaels, paul (geo-42-05-1056-1069)*, Geophysics **43** (1978), no. 05, 1023–1024.

[211] S. Jain and A. E. Wren, *Migration before stack - procedure and significance*, Geophysics **45** (1980), no. 02, 204–212.

[212] H. Jakubowicz, *A simple efficient method of dip-moveout correction*, Geophys. Prosp. **38** (1990), no. 03, 221–246.

[213] H. H. Jaramillo and N. Bleistein, *Demigration and migration in isotropic inhomogeneous media*, pp. 1673–1676, Soc. of Expl. Geophys., 1997.

[214] _____, *Seismic data mapping*, pp. 1991–1994, Soc. of Expl. Geophys., 1998.

[215] _____, *The link of kirchhoff migration and demigration to kirchhoff and born modeling*, Geophysics **64** (1999), no. 6, 1793–1805.

[216] T. E. Jorden, N. Bleistein, and J. K. Cohen, *A wave equation-based dip moveout*, p. Session:S14.2, Soc. of Expl. Geophys., 1987.

[217] D. R. Judson, J. Lin, P. S. Schultz, and J. W. C. Sherwood, *Depth migration after stack*, Geophysics **45** (1980), no. 03, 361–375.

[218] K. L. Kaila and V. G. Krishna, *A new computerized method for finding effective velocity from reversed reflection traveltime data*, Geophysics **44** (1979), no. 06, 1064–1076.

[219] I. B. Kang and G. A. McMechan, *Viscoelastic seismic responses of 2d reservoir models*, Geophys. Prosp. **41** (1993), no. 02, 149–164.

[220] C. L. Karcher, *The reflections seismograph, its invention and use in the discovery of oil and gas fields.*, American Institute of Physics, College Park, MD., 1973.

[221] T. H. Keho and W. B. Beydoun, *Paraxial ray kirchhoff migration*, Geophysics **53** (1988), no. 12, 1540–1546.

[222] G. A. Keller and G. A. McMechan, *Seismic studies of deep crustal structure in southwestern oklahoma*, p. Session:DC.6, Soc. of Expl. Geophys., 1985.

[223] S. Kelly, P. Baltensperger, and G. A. McMechan, *P-to-s conversion for a thin anisotropic zone produced by vertical fracturing*, Geophys. Prosp. **45** (1997), no. 04, 551–570.

[224] D. Kessler and W. K. Chan, *Dmo velocity analysis with jacubowicz's dip-decomposition method*, Geophysics **58** (1993), no. 10, 1517–1524.

[225] Y. C. Kim, R. Gonzalez, and J. R. Berryhill, *Recursive wavenumber-frequency migration*, Geophysics **54** (1989), no. 03, 319–329.

[226] A. P. Koesoemadinata and G. A. McMechan, *Empirical estimation of viscoelastic seismic parameters from petrophysical properties of sandstone*, Geophysics **66** (2001), no. 5, 1457–1470.

[227] _____, *Correlations between seismic parameters, em parameters, and petrophysical/petrological properties for sandstone and carbonate at low water saturations*, Geophysics **68** (2003), no. 3, 870–883.

[228] _____, *Petro-seismic inversion for sandstone properties*, Geophysics **68** (2003), no. 5, 1611–1625.

[229] D. Kosloff and D. Kessler, *Accurate depth migration by a generalized phase-shift method*, Geophysics **52** (1987), no. 08, 1074–1084.

[230] D. D. Kosloff and E. Baysal, *Migration with the full acoustic wave equation*, Geophysics **48** (1983), no. 06, 677–687.

[231] M. J. Kuhn and K. A. Alhilali, *Weighting factors in the construction and reconstruction of acoustical wave fields*, Geophysics **42** (1977), no. 06, 1183–1198.

[232] J. T. Kuo and T. F. Dai, *Kirchhoff elastic wave migration for the case of noncoincident source and receiver*, Geophysics **49** (1984), no. 08, 1223–1238.

[233] M. Lahlou, J. K. Cohen, and N. Bleistein, *Highly accurate inversion methods for three-dimensional stratified media*, p. Session:S7.1, Soc. of Expl. Geophys., 1983.

[234] W. J. Lamb, X. Zhu, G. A. McMechan, M. L. Greenberg, and J. P. Castagna, *Elastic wave propagation in composite media*, Geophysics **57** (1992), no. 09, 1155–1165.

[235] K. L. Larner, C. J. Beasley, and W. S. Lynn, *In quest of the flank*, Geophysics **54** (1989), no. 06, 701–717.

[236] K. L. Larner, L. Hatton, B. S. Gibson, and I. C. Hsu, *Depth migration of imaged time sections*, Geophysics **46** (1981), no. 05, 734–750.

[237] Y. A. Lau and K. Wilmott, *Common-offset processing with dmo-driven statics*, pp. 1391–1392, Soc. of Expl. Geophys., 1991.

[238] S. Lee, G. A. McMechan, and C. L. V. Aiken, *Phase field imaging of electromagnetic data*, p. Session:MIN1.1, Soc. of Expl. Geophys., 1985.

[239] _____, *Phase-field imaging - the electromagnetic equivalent of seismic migration*, Geophysics **52** (1987), no. 05, 678–693.

[240] _____, *Reply to discussion of 'phase-field imaging - the electromagnetic equivalent of seismic migration', by lee, s., et al (geo-52-05-0678-0693)*, Geophysics **53** (1988), no. 06, 863.

[241] E. L. Leiss and I. V. Kellimanis, *Implementation of two-dimensional dmo on the cray x-mp using multitasking and aq 10*, p. Session:S17.7, Soc. of Expl. Geophys., 1988.

[242] E. L. Leiss and R. Thapar, *3-d dmo on the sx-2 supercomputer: An xmu implementation*, p. 92, Soc. of Expl. Geophys., 1989.

[243] A. R. Levander and N. R. Hill, *Finite-difference simulations of noise problems caused by near-surface heterogeneity*, p. Session:S2.4, Soc. of Expl. Geophys., 1984.

[244] S. A. Levin, *Principle of reverse-time migration (short note)*, Geophysics **49** (1984), no. 05, 581–583.

[245] Z. Li, *Wave-field extrapolation by the linearly transformed wave equation*, Geophysics **51** (1986), no. 08, 1538–1551.

[246] Q. Liao and G. A. McMechan, *2.5d full-wavefield viscoacoustic inversion*, Geophys. Prosp. **43** (1995), no. 08, 1043–1059.

[247] _____, *Multifrequency viscoacoustic modeling and inversion*, Geophysics **61** (1996), no. 05, 1371–1378.

[248] _____, *Tomographic imaging of velocity and q, with application to crosswell seismic data from the gypsy pilot site, oklahoma*, Geophysics **62** (1997), no. 06, 1804–1811.

[249] C. Liner, *Dmo amplitude problem: Methods and goals*, p. 1152, Soc. of Expl. Geophys., 1989.

[250] C. L. Liner and N. Bleistein, *Comparative anatomy of common offset dip moveout*, p. Session:S17.1, Soc. of Expl. Geophys., 1988.

[251] C. L. Liner and J. K. Cohen, *An amplitude-preserving inverse of hale's dmo*, p. Session:S17.5, Soc. of Expl. Geophys., 1988.

[252] C. L. Liner, R. Gobeli, and W. D. Underwood, *Dmo amplitude*, pp. 1437–1440, Soc. of Expl. Geophys., 1995.

[253] L. R. Lines, *Personal communication*, October 2004.

[254] Z. Liu and N. Bleistein, *Velocity analysis by inversion*, pp. 1230–1233, Soc. of Expl. Geophys., 1991.

[255] _____, *Velocity analysis by residual moveout*, pp. 1034–1037, Soc. of Expl. Geophys., 1992.

[256] _____, *Velocity analysis by perturbation*, pp. 1191–1194, Soc. of Expl. Geophys., 1994.

[257] _____, *Mathematical analysis of residual moveout and velocity analysis*, pp. 1201–1203, Soc. of Expl. Geophys., 1995.

[258] _____, *Migration velocity analysis: Theory and an iterative algorithm*, Geophysics **60** (1995), no. 01, 142–153.

[259] D. Loewenthal and I. R. Mufti, *Reversed-time migration in spatial frequency-domain (short note)*, Geophysics **48** (1983), no. 05, 627–635.

[260] L. T. Long, J. J. Dwyer, R. M. White, and N. Faust, *Evaluation of causes of seismicity near charleston, south carolina: Development and analysis of multiple data sets*, p. 187, Soc. of Expl. Geophys., 1985.

[261] D. Lowenthal, L. Lu, R. Roberson, and J. W. C. Sherwood, *The wave equation applied to migration*, Migration of seismic data (G. H. F. Gardner, ed.), Soc. of Expl. Geophys., 1985, pp. 208–227.

[262] L. Lu, L. Bell, and K. Lim, *Parallel implementation of 3-d dmo on shared memory systems*, pp. 214–217, Soc. of Expl. Geophys., 1994.

[263] L. Lu, J. J. Chen, L. Bell, and R. Lara, *3-d flex binning and dmo*, pp. 43–46, Soc. of Expl. Geophys., 1996.

[264] S. Lu, S. Lu, and G. A. McMechan, *Estimation of gas hydrate and free gas saturation, concentration, and distribution from seismic data*, Geophysics **67** (2002), no. 2, 582–593.

[265] D. E. Lumley, J. E. Claerbout, and D. Bevc, *Anti-aliased kirchhoff migration*, p. Session:H027, Eur. Assn. of Expl. Geophys., 1994.

[266] D. E. Lumley, J. F. Claerbout, and D. Bevc, *Anti-aliased kirchhoff 3-d migration*, pp. 1282–1285, Soc. of Expl. Geophys., 1994.

[267] G. B. Madiba and G. A. McMechan, *Processing, inversion, and interpretation of a 2d seismic data set from the north viking graben, north sea*, Geophysics **68** (2003), no. 3, 837–848.

[268] _____, *Seismic impedance inversion and interpretation of a gas carbonate reservoir in the alverta foothills, western canada*, Geophysics **68** (2003), no. 5, 1460–1469.

[269] R. D. Martinez and G. A. McMechan, *Analysis of absorption and dispersion effects in tau-p synthetic seismograms*, p. Session:S24.2, Soc. of Expl. Geophys., 1984.

[270] _____, *Analysis of absorption and dispersion effects in synthetic tau-rho seismograms*, Geophysics **52** (1987), no. 08, 1033–1047.

[271] _____, *Multiparameter inversion for viscoelastic media*, p. Session:S7.8, Soc. of Expl. Geophys., 1988.

[272] _____, *Tau-p seismic data for viscoelastic media - part 1: Modelling*, Geophys. Prosp. **39** (1991), no. 02, 141–156.

[273] _____, *Tau-p seismic data for viscoelastic media - part 2: Linearized inversion*, Geophys. Prosp. **39** (1991), no. 02, 157–182.

[274] H. Mayne, *Common-reflection-point horizontal data stacking techniques*, Geophysics **50** (1985), no. 11, 1856–1867.

[275] W. H. Mayne, *Common reflection point horizontal data stacking techniques*, Geophysics **27** (1962), no. 06, 927–938.

[276] _____, *Practical considerations in the use of common reflection point techniques*, Geophysics **32** (1967), no. 02, 225–229.

[277] _____, *Seg presidential address - geopolitics and geophysics*, Geophysics **35** (1970), no. 02, 193–195.

[278] _____, *The evolution of geophysical technology*, The Leading Edge **01** (1982), no. 01, 75–76.

[279] _____, *Discussion of 'predictive deconvolution and the zero-phase source', by gibson, b., et al (geo-49-04-0379-0397)*, Geophysics **50** (1985), no. 01, 172.

[280] _____, *Discussion of 'high-resolution common-depth-point reflection profiling - field acquisition parameter design', by knapp, r. w., et al (geo-51-02-0283-0294)*, Geophysics **51** (1986), no. 10, 2011.

[281] _____, *50 years of geophysical ideas*, p. 96, Soc. of Expl. Geophys., 1989.

[282] W. H. Mayne and R. G. Quay, *Seismic signatures of large air-guns*, Geophysics **36** (1971), no. 06, 1162–1173.

[283] W. H. Mayne and Y. Russom, *Correlation side lobe amplitudes*, p. Session:S5.4, Soc. of Expl. Geophys., 1983.

[284] A. McMechan and G. A. McMechan, *Effects of attenuation and scattering on avo measurements*, Geophysics **63** (1998), no. 06, 2025–2034.

[285] G. McMechan and L. Z. Hu, *The effect of recording aperture in migration of vertical seismic profiling data (short note)*, Geophysics **51** (1986), no. 10, 2007–2010.

[286] G. A. McMechan, *Migration by extrapolation of time-dependent boundary values*, Geophys. Prosp. **31** (1983), no. 03, 413–420.

[287] _____, *Synthetic finite-offset vertical-seismic-profiles for laterally varying media*, Geophysics **50** (1985), no. 04, 627–636.

[288] G. A. McMechan, H. Chang, J. P. VanDyke, M. Solano, and D. Epili, *3-d prestack kirchhoff depth migration: From prototype to production in a massively parallel processor environment*, Geophysics **63** (1998), no. 02, 546–556.

[289] G. A. McMechan and H. W. Chen, *Implicit static corrections in prestack migration of common-source data*, Geophysics **55** (1990), no. 06, 757–760.

[290] G. A. McMechan, G. C. Gaynor, and R. B. Szerbiak, *Use of ground-penetrating radar for 3-d sedimentological characterization of clastic reservoir analogs*, Geophysics **62** (1997), no. 03, 786–796.

[291] G. A. McMechan, L. Z. Hu, and D. Stauber, *Determination of salt proximity by wave-field imaging of transmitted energy (short note)*, Geophysics **53** (1988), no. 08, 1109–1112.

[292] G. A. McMechan, R. G. Loucks, P. Mescher, and X. Zeng, *Characterization of a coalesced, collapsed paleocave reservoir analog using gpr and well-core data*, Geophysics **67** (2002), no. 04, 1148–1158.

[293] G. A. McMechan and R. Sun, *Depth filtering of first breaks and ground roll*, Geophysics **56** (1991), no. 03, 390–396.

[294] G. A. McMechan and T. Xu, *Efficient 3-d viscoelastic modeling with application to near-surface land seismic data*, Geophysics **63** (1998), no. 02, 601–612.

[295] G. A. McMechan and M. J. Yedlin, *Analysis of dispersive waves by wave-field transformation*, Geophysics **46** (1981), no. 06, 869–874.

[296] Z. Meng and N. Bleistein, *Wavefront construction (wf) ray tracing in tetrahedral models - application to 3-d traveltime and ray path computations*, pp. 1734–1737, Soc. of Expl. Geophys., 1997.

[297] _____, *On velocity/depth ambiguity in 3-d migration velocity analysis (short note)*, Geophysics **66** (2001), no. 1, 256–260.

[298] Z. Meng, N. Bleistein, and P. Valasek, *3-d analytical migration velocity analysis, part ii: Velocity gradient estimation*, pp. 1731–1734, Soc. of Expl. Geophys., 1999.

[299] Z. Meng, N. Bleistein, and K. Wyatt, *3-d analytical migration velocity analysis, part i: Two-step velocity estimation by reflector-normal update*, pp. 1727–1730, Soc. of Expl. Geophys., 1999.

[300] P. Michaels, *Computer program - seismic raypath migration with the pocket calculator*, Geophysics **42** (1977), no. 05, 1056–1069.

[301] _____, *Reply to discussion of 'computer program - seismic raypath migration with the pocket calculator', by michaels, paul (geo-42-05-1056-1069)*, Geophysics **43** (1978), no. 05, 1024–1025.

[302] D. Miller, M.L. Oristaglio, and G. Beylkin, *A new slant on seismic imaging - migration and integral geometry*, Geophysics **52** (1987), no. 07, 943–964.

[303] N. L. Mohan, *Discussion on 'regularizing 3-d data sets with dmo' by canning, a. and gardner, g. h. f. with reply from author (geo-61-4-1103-1114)*, Geophysics **62** (1997), no. 4, 1331–1333.

[304] G. Muller and P. Temme, *Fast frequency-wavenumber migration for depth-dependent velocity*, Geophysics **52** (1987), no. 11, 1483–1491.

[305] A. W. Musgrave, *Wavefront charts and construction of raypath plotter*, Ph.D. thesis, Colorado School of Mines, Golden, CO, February 1952.

[306] _____, *Wavefront charts and three-dimensional migration*, Geophysics **50** (1985), no. 11, 1810–1825.

[307] R. G. Nisle, *Considerations on the vertical migration of gases*, Geophysics **06** (1941), no. 04, 449–453.

[308] C. Notfors, S. H. Gray, and N. Bleistein, *Imaging using multi-arrivals gaussian beams or multi-arrival kirchhoff?*, p. E03, Eur. Assn. Geosci. Eng., 2003.

[309] V. Ohanian, *Dmo by huygens-fresnel diffraction integral*, pp. 1137–1140, Soc. of Expl. Geophys., 1993.

[310] V. Ohanian, T. M. Snyder, and A. Gunawardena, *Analytic properties of the f-k dmo operator*, pp. 1134–1136, Soc. of Expl. Geophys., 1993.

[311] V. Ohanian, T. M. Snyder, and D. P. Hampson, *Approximate regimes of the h-f dmo operator*, pp. 1533–1536, Soc. of Expl. Geophys., 1994.

[312] V. Ohanian, G. D. Young, C. R. Dick, D. F. Fouquet, and D. E. Larson, *Robust estimation of offset reflection-point coordinates without two-point ray-tracing*, pp. 54–56, Soc. of Expl. Geophys., 1996.

[313] A.A. Ortega and G. A. McMechan, *Synthesis ofmulticomponent quasi-p and converted quasi-p-s seismograms for intersecting fracture systems*, Geophysics **65** (2000), no. 4, 1261–1271.

[314] R. Ottolini and J. F. Claerbout, *The migration of common-midpoint slant stacks*, Geophysics **49** (1984), no. 03, 237–249.

[315] T. ozdenvar and G. A. McMechan, *Algorithms for staggered-grid computations for poroelastic, elastic, acoustic, and scalar wave equations*, Geophys. Prosp. **45** (1997), no. 02, 403–420.

[316] T. Ozdenvar, G. A. McMechan, and P. Chaney, *Simulation of complete seismic surveys for evaluation of experiment design and processing*, Geophysics **61** (1996), no. 02, 496–508.

[317] D. M. Pai, *Generalized f-k (frequency-wavenumber) migration in arbitrarily varying media*, Geophysics **53** (1988), no. 12, 1547–1555.

[318] N. Pan and W. S. French, *Generalized two-pass three-dimensional migration for imaging steep dips in vertically inhomogeneous media*, Geophysics **54** (1989), no. 05, 544–554.

[319] K. Pann, E. Eisner, and Y. Shin, *A collocation formulation of wave equation migration*, Geophysics **44** (1979), no. 04, 712–721.

[320] E. M. Parma, *Personal communication*, December 2004.

[321] Jr. Parr, J. O. and W. H. Mayne, *A new method of pattern shooting*, Geophysics **20** (1955), no. 03, 539–564.

[322] K. V. Paulson and S. C. Merdler, *Automatic seismic reflection picking*, Geophysics **33** (1968), no. 03, 431–440.

[323] H. Perroud, P. Hubral, G. Hocht, and E. de Bazelaire, *Common-reflection-point stacking in laterally inhomogeneous media*, pp. 495–498, Soc. of Expl. Geophys., 1996.

[324] R[] A[] Peterson and W[] C[] Waller, *Through the kaleidoscope: A doodlebugger in wonderland*, United Geophysical Corporation, 1974.

[325] R. A. Phinney and D. M. Jurdy, *Seismic imaging of deep crust*, Geophysics **44** (1979), no. 10, 1637–1660.

[326] A. W. Pieprzak and N. V. Bramblett, *Amplitude preserving dmo summation algorithm for 2-d and marine 3-d*, pp. 1358–1361, Soc. of Expl. Geophys., 1990.

[327] A. W. Pieprzak and P. A. Farmer, *Model studies of the effects of cable feathering and acquisition geometry on 3-d marine dmo*, p. Session:DA1.8, Soc. of Expl. Geophys., 1988.

[328] A. L. Pleshkevitch, B. D. Plyushchenkov, and V. I. Turchaninov, *3-d dmo of cross gather data*, pp. 1118–1121, Soc. of Expl. Geophys., 1996.

[329] A. M. Popovici, *From prestack migration to migration to zero-offset*, pp. 680–683, Soc. of Expl. Geophys., 1994.

[330] L[] A[] Rabinkin, I[] V[] Napalkov, V[] V[] Znamernskii, I[] N[] Voskresenskii, and M[] B[] Rapoport, *Theory and practice of the cdr seismic method (in russian)*, Transactions of the Gubkin institute of Petrochemical and Gas Productions (Moscow) **39** (1962).

[331] S. Rajasekaran and G. A. McMechan, *Prestack processing of land data with complex topography*, Geophysics **60** (1995), no. 06, 1875–1886.

[332] _____, *Tomographic estimation of the spatial distribution of statics*, Geophysics **61** (1996), no. 04, 1198–1208.

[333] M. Ramaswamy, M. Miley, and G. H. F. Gardner, *An example of full volume, 3-d, prestack depth migration*, pp. 990–992, Soc. of Expl. Geophys., 1996.

[334] J. Ramos-Martinez and G. A. McMechan, *Full wavefield inversion to estimate impact-source orientation from multicomponent land seismic data*, Geophysics **67** (2002), no. 2, 562–572.

[335] J. Ramos-Martinez, A. A. Ortega, and G. A. McMechan, *3-d seismic modeling for cracked media: Shear-wave splitting at zero-offset*, Geophysics **65** (2000), no. 01, 211–221.

[336] M. Reshef and D. Kessler, *Practical implementation of three-dimensional poststack depth migration*, Geophysics **54** (1989), no. 03, 309–318.

[337] M. Reshef and D. Kosloff, *Migration of common shot gathers*, Geophysics **51** (1986), no. 02, 324–331.

[338] J. Rickett, J. Claerbout, and S. B. Fomel, *Implicit 3-d depth migration by wavefield extrapolation with helical boundary conditions*, 68th Ann. Internat. Mtg, Soc. of Expl. Geophys., 1998, pp. 1124–1127.

[339] F. Rieber, *A new reflection system with controlled directional sensitivity*, Geophysics **01** (1936), no. 01, 97–106.

[340] _____, *Visual presentation of elastic wave patterns under various structural conditions*, Geophysics **01** (1936), no. 02, 196–218.

[341] _____, *Complex reflection patterns and their geologic sources*, Geophysics **02** (1937), no. 02, 132–160.

[342] _____, *Discussion of 'adverse effects associated with variably compounded seismograph records', by mott-smith, m. (geo-02-03-0265-0294)*, Geophysics **02** (1937), no. 03, 281–287.

[343] _____, *Complex reflection patterns and their geologic sources*, Migration of seismic data (G. H. F. Gardner, ed.), Soc. of Expl. Geophys., 1985, pp. 2–30.

[344] _____, *A new reflection system with controlled directional sensitivity*, Slant-stack processing (L. Lu, ed.), Soc. of Expl. Geophys., 1991, pp. 3–12.

[345] _____, *Visual presentation of elastic wave patterns under various structural conditions*, Slant-stack processing (L. Lu, ed.), Soc. of Expl. Geophys., 1991, pp. 13–35.

[346] _____, *Visualization of elastic wave patterns under various structural conditions*, Seismic physical modeling (J. A. McDonald, ed.), vol. 15, Soc. of Expl. Geophys., 1994, pp. 79–102.

[347] J. C. Robinson and T. R. Robbins, *Dip-domain migration of two-dimensional seismic profiles*, Geophysics **43** (1978), no. 01, 77–93.

[348] S. Rodriguez and C. Vuillermoz, *Solutions to near surface effects in mountainous thrust areas*, pp. 1644–1646, Soc. of Expl. Geophys., 1994.

[349] K. K. Roldan, A. Gonzalez, and D. A. Ebrom, *Effect of transverse isotropy on dip-moveout processing*, pp. 1221–1223, Soc. of Expl. Geophys., 1994.

[350] B. E. Rommel, *Kinematic tzo-response curves: An iterative approach for mode conversion and transverse isotropy*, pp. 1559–1562, Soc. of Expl. Geophys., 1996.

[351] S. Ronen, *Handling irregular geometry: Equalized dmo and beyond*, pp. 1545–1548, Soc. of Expl. Geophys., 1994.

[352] S. Ronen and C. L. Liner, *Least-squares dmo and migration*, Geophysics **65** (2000), no. 5, 1364–1371.

[353] S. Ronen, D. Nichols, R. A. Bale, and R. Ferber, *Dealiasing dmo: Good-pass, bad-pass, and unconstrained*, pp. 743–746, Soc. of Expl. Geophys., 1995.

[354] D. H. Rothman, S. A. Levin, and F. Rocca, *Residual migration - applications and limitations*, Geophysics **50** (1985), no. 01, 110–126.

[355] M. H. Safar, *On the lateral resolution achieved by kirchhoff migration*, Geophysics **50** (1985), no. 07, 1091–1099.

[356] J. W. Sattlegger, *Three-dimensional seismic depth computation using space-sampled velocity logs*, Geophysics **34** (1969), no. 01, 7–20.

[357] _____, *Migration velocity determination - part i: Philosophy*, Geophysics **40** (1975), no. 01, 1–5.

[358] J. Schleicher, M. Tygel, B. Ursin, and N. Bleistein, *The kirchhoff-helmholtz integral for anistropic elastic media*, p. Session:C0011, Eur. Assn. Geosci. Eng., 2000.

[359] W. A. Schneider, *Developments in seismic data-processing and analysis (1968-1970)*, Geophysics **36** (1971), no. 06, 1043–1073.

[360] _____, *Discussion of 'computer migration of oblique seismic reflection profiles', by french, william s. (geo-40-06-0961-0980)*, Geophysics **41** (1976), no. 04, 776.

[361] _____, *Integral formulation for migration in two-dimensions and three-dimensions*, Geophysics **43** (1978), no. 01, 49–76.

[362] P. S. Schultz and J. F. Claerbout, *Velocity estimation and downward-continuation by wavefront synthesis*, Geophysics **43** (1978), no. 04, 691–714.

[363] P. S. Schultz and J. W. C. Sherwood, *Depth migration before stack*, Geophysics **45** (1980), no. 03, 376–393.

[364] M. Schwab and G. H. F. Gardner, *2-d dmo for a medium with constant vertical velocity gradient*, pp. 1194–1196, Soc. of Expl. Geophys., 1991.

[365] Z. G. Sen, *Common reflection point travel time equation and dmo in vertically varying media*, pp. 1115–1117, Soc. of Expl. Geophys., 1996.

[366] Z. Shang and Jr. Starr, E. W., *A fast solution to the amplitude, phase and aliasing problems in integral dmo and migration*, pp. 1215–1217, Soc. of Expl. Geophys., 1991.

[367] _____, *Three-dimensional velocity-gradient dmo and overhang imaging*, pp. 1201–1203, Soc. of Expl. Geophys., 1991.

[368] S. D. Sheaffer and N. Bleistein, *2.5-d downward contiuation using data mapping theory*, pp. 1554–1557, Soc. of Expl. Geophys., 1998.

[369] J. W. C. Sherwood, *Personal communication*, October 2004.

[370] R. Silva and P. Kaskey, *Anti-aliasing and amplitude preserving 2-d and 3-d dmo - an integral implementation*, pp. 1211–1214, Soc. of Expl. Geophys., 1991.

[371] I. Sincer and T. Kayiran, *Relationship between deregowski-rocca and hale operators (short note)*, Geophysics **58** (1993), no. 09, 1373–1386.

[372] S. E. Slawson, D. J. Monk, and V. Sudhakar, *Dmo implications for 3-d survey design*, pp. 935–938, Soc. of Expl. Geophys., 1995.

[373] M. M. Slotnick, *Lessons in seismic computing*, Society of Exploration Geophysicists, Tulsa, OK., 1959.

[374] U. Spagnolini and S. Opreni, *3-d shot continuation operator*, pp. 439–442, Soc. of Expl. Geophys., 1996.

[375] P[] L[] Stoffa, J[] T[] Fokkema, R[] M[] de Luna Freire, and W[] P[] Kessinger, *Split-step Fourier migration*, Geophysics **55** (1990), no. 04, 410–421.

[376] R. H. Stolt, *Migration by fourier transform*, Geophysics **43** (1978), no. 01, 23–48.

[377] _____, *Migration by fourier transform*, Geophysics **50** (1985), no. 11, 2219–2244.

[378] R. H. Stolt and A. B. Weglein, *Migration and inversion of seismic data*, Geophysics **50** (1985), no. 12, 2458–2472.

[379] B. Sumner and N. Bleistein, *Prestack elastic kirchhoff migration and parameter estimation*, p. Session:S12.1, Soc. of Expl. Geophys., 1988.

[380] R. Sun and G. A. McMechan, *Nonlinear reverse-time inversion of elastic offset vertical seismic profile data*, Geophysics **53** (1988), no. 10, 1295–1302.

[381] _____, *Nonlinear reverse-time inversion of elastic offset vsp data*, p. Session:S6.2, Soc. of Expl. Geophys., 1988.

[382] _____, *Depth filtering for one-component seismic data (short note)*, Geophysics **56** (1991), no. 09, 1482–1485.

[383] C. Sword, *Tomographic determination of interval velocities from reflection seismic data: The method of controlled directional reception*, Ph.D. thesis, Stanford University, Stanford, CA., September 1987.

[384] R. B. Szerbiak, G. A. McMechan, R.M. Corbeanu, C. Forster, and S. H. Snelgrove, *3-d characterization of a clastic reservoir analog: From 3-d gpr data to a 3-d fluid permeability model*, Geophysics **66** (2001), no. 4, 1026–1037.

[385] A. Tarantola, *Inverse problem theory.*, Elsevier Science Publishing, Amsterdam, New York, 1987.

[386] W. M. Tedford, *Applied geophysics.*, Cambridge University Press, Cambridge, 1976.

[387] P. Temme, *A comparison of common-midpoint single-shot and plane-wave depth migration*, Geophysics **49** (1984), no. 11, 1896–1907.

[388] H. Trappe, G. Gierse, and J. Pruessmann, *Case studies show potential of common reflection surface stack - structural resolution in the time domain beyond the conventional nmo/dmo stack*, First Break **19** (2001), no. 11, 625–633.

[389] S. Treitel, *Personal communication*, October 2004.

[390] I. Tsvankin, *Analytic description of dip moveout in anisotropic media*, pp. 1209–1212, Soc. of Expl. Geophys., 1994.

[391] _____, *Moveout analysis for transversely isotropic media with a tilted symmetry axis*, pp. 731–734, Soc. of Expl. Geophys., 1995.

[392] M. Tygel and N. Bleistein, *An introduction to this special section*, The Leading Edge **19** (2000), no. 01, 37.

[393] M. Tygel, J. Schleicher, and P. Hubral, *2.5-d kirchhoff mzo in laterally inhomogeneous media*, pp. 483–486, Soc. of Expl. Geophys., 1996.

[394] A. van der Schoot, A. J. Duyndam, C. P. A. Wapenaar, and A. J. Berkhout, *Common-reflection-point stacking: A macro model-driven approach to dmo*, p. 1136, Soc. of Expl. Geophys., 1989.

[395] G. J. O. Vermeer, H. P. G. M Rooijen, and J. Douma, *Dmo in arbitrary 3-d acquisition geometries*, pp. 1445–1448, Soc. of Expl. Geophys., 1995.

[396] C. E. Wales, W. H. Mayne, and W. F. Massell, *Generation and utilization of nonlinear vibrator sweeps*, p. Session:S20.5, Soc. of Expl. Geophys., 1981.

[397] C.-S. Wang, *Dmo in radon domain*, pp. 1441–1444, Soc. of Expl. Geophys., 1995.

[398] _____, *Radon dmo amplitude and frequency preservation*, pp. 1479–1482, Soc. of Expl. Geophys., 1996.

[399] L. Wang and N. Bleistein, *Noise suppression in large wavenumber fourier imaging*, pp. 1312–1315, Soc. of Expl. Geophys., 1997.

[400] _____, *3-d multi-valued traveltime and amplitude maps*, pp. 1879–1882, Soc. of Expl. Geophys., 1998.

[401] C. P. A. Wapenaar, N. A. Kinneging, and A. J. Berkhout, *Principle of prestack migration based on the full elastic two-way wave equation*, Geophysics **52** (1987), no. 02, 151–173.

[402] B. B. Weatherby, *Early seismic discoveries in oklahoma*, Gephysics **10** (1945), no. 3.

[403] B. B. Weatherby and L. Y. Faust, *Influence of geological factors on longitudinal seismic velocities*, Early geophysical papers (SEG Staff, ed.), vol. 01, Soc. of Expl. Geophys., 1947, pp. 661–668.

[404] A[] B[] Weglein, F[] V[] Araujo, P[] M[] Carvalho, R[] H[] Stolt, K[] H[] Matson, R[] T[] Coates, D[] Corrigan, D[] J[] Foster, S[] A[] Shaw, and H[] Zhang, *Inverse scattering series and seismic exploration*, Inverse Problems **19** (2003), 27–83.

[405] J. Wen and G. A. McMechan, *Three-dimensional kinematic migration in variable velocity media*, Geophys. Prosp. **35** (1987), no. 03, 250–266.

[406] J. Wen, G. A. McMechan, and M. W. Booth, *Three-dimensional modeling and migration of seismic data using fourier transforms*, Geophysics **53** (1988), no. 09, 1194–1201.

[407] F. Wenzel and W. Soellner, *Multiple-velocity stack (mvs) - an alternative to dmo*, pp. 1297–1300, Soc. of Expl. Geophys., 1991.

[408] N. D. Whitmore and L. R. Lines, *Vertical seismic profiling depth migration of a salt dome flank*, Geophysics **51** (1986), no. 05, 1087–1109.

[409] J. W. Wiggins, *Kirchhoff integral extrapolation and migration of nonplanar data*, Geophysics **49** (1984), no. 08, 1239–1248.

[410] G. A. Winbow and E. C. Trantham, *Nonaliased amplitude-preserving avo*, pp. 719–722, Soc. of Expl. Geophys., 1994.

[411] R[] S[] Wu and L[] Y[] Huang, *Scattered field calculation in heterogeneous media using phase-screen propagation*, 62nd Ann. Internat. Mtg, Soc. of Expl. Geophys., 1992, pp. 1289–1292.

[412] R[]-S[] Wu and S[] Jin, *Windowed GSP (generalized screen propagators) migration applied to SEG-EAEG salt model data*, 67th Ann. Internat. Mtg, Soc. of Expl. Geophys., 1997, pp. 1746–1749.

[413] R[] S[] Wu and de Hoop M[] V, *Accuracy analysis of screen propagators for wave extrapolation using a thin-slab model*, 66th Ann. Internat. Mtg, Soc. of Expl. Geophys., 1996, pp. 419–422.

[414] Y. Wu and G. A. McMechan, *Estimation of fracture height using microseismicity associated with hydraulic fracturing*, Geophysics **63** (1998), no. 03, 908–917.

[415] _____, *Wave extrapolation in the spatial wavelet domain with application to poststack reverse-time migration*, Geophysics **63** (1998), no. 02, 589–600.

[416] T. Xu and G. A. McMechan, *Gpr attenuation and its numerical simulation in 2.5 dimensions*, Geophysics **62** (1997), no. 02, 403–414.

[417] T. Xu, G. A. McMechan, and R. Sun, *3-d prestack full-wavefield inversion*, Geophysics **60** (1995), no. 06, 1805–1818.

[418] X. Xu, C. L. V. Aiken, J. P. Bhattacharya, R. M. Corbeanu, K. C. Nielsen, G. A. McMechan, and M. G. Abdelsalam, *Creating virtual 3-d outcrop*, The Leading Edge **19** (2000), no. 02, 197–202.

[419] P. C. Yao, K. K. Sekharan, and D. Ebrom, *Data acquisition geometry and 3-d dmo*, pp. 552–554, Soc. of Expl. Geophys., 1993.

[420] O. Yilmaz, *Seismic data processing*, Society of Exploration Geophysicists, Tulsa, OK., 1987.

[421] O. Yilmaz and R. E. Chambers, *Migration velocity analysis by wave-field extrapolation*, Geophysics **49** (1984), no. 10, 1664–1674.

[422] O. Yilmaz and J. F. Claerbout, *Prestack partial migration*, Geophysics **45** (1980), no. 12, 1753–1779.

[423] _____, *Prestack partial migration*, DMO processing (D. Hale, ed.), Soc. of Expl. Geophys., 1995, pp. 7–33.

[424] K. H. Yoon and G. A. McMechan, *3-d finite-difference modeling of elastic waves in borehole environments*, Geophysics **57** (1992), no. 06, 793–804.

[425] L. Zanzi and C. Bagaini, *The design of prestack migration-demigration operators*, pp. 676–679, Soc. of Expl. Geophys., 1994.

[426] X. Zeng and G. A. McMechan, *Gpr characterization of buried tanks and pipes*, Geophysics **62** (1997), no. 03, 797–806.

[427] X. Zeng, G. A. McMechan, J. Cai, and H. W. Chen, *Comparison of ray and fourier methods for modeling monostatic ground-penetrating radar profiles*, Geophysics **60** (1995), no. 06, 1727–1734.

[428] X. Zeng, G. A. McMechan, and T. Xu, *Synthesis of amplitude-versus-offset variations in ground-penetrating radar data*, Geophysics **65** (2000), no. 01, 113–125.

[429] J. Zhang and G. A. McMechan, *3-d transmission tomography using wide aperture data for velocity estimation of irregular salt bodies*, Geophysics **59** (1994), no. 10, 1620–1630.

[430] _____, *Turning wave migration by horizontal extrapolation*, Geophysics **62** (1997), no. 01, 291–297.

[431] Y. Zhang and N. Bleistein, *Theory of true-amplitude one-way wave equations and true-amplitude common-shot migration*, pp. 925–928, Soc. of Expl. Geophys., 2003.

[432] Y. Zhang, J. Sun, S.H. Gray, C. Notfors, N. Bleistein, and G. Zhang, *True amplitude migration using common-shot one-way wavefield extrapolation*, p. E030, Eur. Assn. Geosci. Eng., 2002.

[433] L. Zhiming, R. Ottolini, and J. F. Claerbout, *Migrating reflections greater than 90 degrees via depth extrapolation*, 54th Ann. Internat. Mtg, Soc. of Expl. Geophys., 1984, p. Session:S19.3.

[434] H. Zhou and G. A. McMechan, *One-pass 3-d seismic extrapolation with the 45 degree wave equation*, Geophysics **62** (1997), no. 06, 1817–1824.

[435] _____, *Parallel butterworth and chebyshev dip filters with applications to 3-d seismic migration*, Geophysics **64** (1999), no. 5, 1573–1578.

[436] _____, *Analytic study of the geometrical spreading of p-waves in a layered transversely isotropic medium with a vertical symmetry axis*, Geophysics **65** (2000), no. 4, 1305–1315.

[437] _____, *Rigorous absorbing boundary conditions for 3-d one-way wave extrapolation*, Geophysics **65** (2000), no. 02, 638–645.

[438] T. Zhu, *Ray-kirchhoff migration in inhomogeneous media*, Geophysics **53** (1988), no. 06, 760–768.

[439] X. Zhu and G. A. McMechan, *Acoustic modeling and migration of stacked cross-hole data*, Geophysics **53** (1988), no. 04, 492–500.

[440] _____, *Estimation of near-surface velocities by tomography*, p. Session:S21.4, Soc. of Expl. Geophys., 1988.

[441] _____, *Numerical simulation of seismic responses of poroelastic reservoirs using biot theory*, Geophysics **56** (1991), no. 03, 328–339.

November 6, 2013